OPTICAL THERMOMETRY WITH ORGANOEUROPIUM(II) COMPLEXES

ROBERTO MANUEL DIAZ-RODRIGUEZ

Thesis submitted to the University of Ottawa
in partial Fulfillment of the requirements for the
degree of Doctorate in Philosophy Chemistry

Department of Chemistry and Biomolecular Sciences
Faculty of Science
University of Ottawa

© Roberto Manuel Diaz-Rodriguez, Ottawa, Canada, 2026

ABSTRACT

The measurement of temperature is of critical importance to a diverse array of fields and industries, such as heating, ventilation, and cooling, nutrition, molecular biology, medicine, engineering of all denominations, chemistry, climate science, and computing technologies, to name a few. As technologies in all these areas progress, measuring temperature more accurately and precisely under increasingly challenging conditions is an ever-evolving problem. One strategy to address these challenges is optical thermometry, which correlates changes in the optical characteristics (e.g. luminescence intensity, emission lifetime, colour, etc.) of a thermosensitive system to changes in temperature. In contrast to common thermometric methods employing thermistors, thermocouples, or even infrared thermography, optical thermometry is a remote-detection, minimally invasive technique with very high attainable spatial resolution, making it well-suited to probing temperature in difficult environments and sensitive systems. Due to their favourable (magneto-)optical properties, lanthanide-based materials are well-studied as optical thermometers. However, most of these materials operate *via* a ratiometric approach monitoring thermosensitive emission intensities on account of comprising trivalent lanthanides, which exhibit characteristic narrow, Laporte-forbidden 4*f*-4*f* absorbance and emission bands whose positions are almost invariant with temperature. This thesis explores a less-studied approach to lanthanide-based optical thermometry, exploring divalent europium and its Laporte-allowed, environment-sensitive, intense and broad 5*d*-4*f* transitions for thermal sensing, with a focus on emission band-shift. Moreover, organometallic complexes were targeted for these studies, as these are also not well-known for optical thermometry and the unique structure and bonding of such systems was envisioned to lead to unique properties.

Starting from the brightly emissive, synthetically convenient starting material $[Eu^{II}(BH_4)_2(THF)_2]$ (which was revealed to itself be a well-performing luminescence thermometer), the hemimetallocene dimer $[Cp^*Eu(\mu\text{-}BH_4)(THF)_2]_2$ (Cp^* = pentamethylcyclopentadienyl) was prepared and characterized. This complex exhibits strongly thermochromic luminescence, with the maximum of the 5*d*→4*f* emission band red-shifting by nearly 1900 cm^{-1} as the temperature is increased from 60-320 K. This defines a thermometric system that demonstrates the highest absolute sensitivity of any lanthanide-based band shift thermometer to date, reaching 8.2 cm^{-1} K^{-1} at 320 K. An opto-structural correlation study *via* variable-temperature single-crystal X-ray diffraction revealed that small changes in metrical parameters with temperature were correlated to these rather large changes in emission wavelength/energy, unveiling the potential of organoeuropium(II) systems as sensitive luminescence thermometers.

Building upon this discovery, a series of isostructural hemimetallocene dimers $[Cp^REu(\mu\text{-}BH_4)(solv)_n]_m$ (solv = tetrahydrofuran, 1,2-dimethoxyethane; n = 1 or 2; m = 2 or ∞) bearing systematically varying ligand sets was synthesized and examined for their thermometric performance, with an eye toward elucidating some of the factors governing the thermochromic luminescence that is clearly intrinsic to this type of system. Members of this series show widely varying emission properties despite their compositional similarities, demonstrating the tunability of the europium(II) hemimetallocene architecture. Opto-structural correlation studies *via* variable-temperature single-crystal X-ray diffraction revealed a convoluted dependence of the emission properties on various factors, which are difficult to disambiguate. However, a few factors of particular importance are identified, such as the distance between the europium(II) ion and the basal plane of the square-pyramidal coordination polyhedron, the presence of pendant electron density that might further interact with the excited-state 5*d* orbitals, and metal-ligand flexibility. These findings represent a step toward enabling the rational design of organoeuropium(II) luminescence thermometers for bespoke characteristics.

Finally, one of the substituted cyclopentadienides from the previous study, 1-(bis(dimethylamino)phosphino)-2,3,4,5-tetramethylcyclopentadienyl, was selected for further investigation due to the good thermometric performance exhibited by its hemieuropocene(II), and the possibility of further functionalizing the free phosphine moiety. Oxidizing this moiety with elemental sulfur, selenium, or tellurium yielded a corresponding series of novel phosphinochalcogenoyl-cyclopentadienides, which were coordinated to europium(II) to give a family of homoleptic europocenes(II) bound by both the cyclopentadienyl fragment and the pendant phosphinochalcogenoyl arms of the ligands. These complexes were characterized structurally and optically and, though they are not suited to band-shift luminescence thermometry, turn out to be extremely sensitive magneto-optical thermometers *via* magnetic circular dichroism, with relative sensitivity values reaching 170 % K^{-1} at ultralow temperatures inaccessible to conventional luminescence thermometry. This result corroborates our previous work introducing the concept of magnetic circular dichroism thermometry, and further strengthens the position of europium(II) as a valuable foundation for thermosensitive optical materials.

"I get by with a little help from my friends"
—Paul McCartney & John Lennon

Dedicated to Rosa Rodriguez and Manuel Diaz, who always encouraged me to follow my dreams, and to Alana Rangaswamy, who was always by my side while I did so

ACKNOWLEDGEMENTS

The time that I have spent at the University of Ottawa has been a crazy, whirlwind, rollercoaster of an experience that has truly left its mark upon my life. I look back on my undergraduate and M.Sc. degrees and notice that, just like my M.Sc. thesis represented the end of six years at Dalhousie University, my PhD thesis represents the end of six years at the University of Ottawa. I find it remarkable how, even after all this time, it is still possible to simultaneously feel like a grizzled veteran and a complete neophyte. Such, I suppose, is the journey of learning, scientific inquiry, and personal growth.

To begin, I must extend my sincerest thanks and appreciation to my supervisor, Dr. Muralee Murugesu. I ventured well outside my comfort zone when I decided to take on this PhD, not only for switching to a very different research discipline, but also because it was my first time living away from home. Dr. Murugesu saw me for who I was, saw my potential, and gave me the opportunity to develop that potential to the next level in huge, indelible ways; turns out that the shots for the moon really are worth taking. I thank him for his trust in me, his faith in my ideas and methods, and for giving me the space I needed to take my solid foundation and build it into an edifice. One of my favourite things about being in his group was that I learned something new every single day, and that is a treasure that cannot be replaced. Thanks also to my former supervisor, Dr. Alison Thompson (Dalhousie University), for keeping in touch and remaining my friend long after I graduated from her group, and for the continuing collaboration and warm encouragement. She gave me the foundation I needed to flourish as I move forward.

I would also like to thank my Thesis Advisory Committee, Drs. Jaclyn Brusso, Stephen Newman, and Darrin Richeson, for their welcoming attitudes, valuable support, and eagerness for engaging discussion at all stages of my degree, as well as Dr. Rebecca Abergel (University of California @ Berkeley) for kindly agreeing to serve as an external examiner for this thesis. I would like to acknowledge the Natural Sciences and Engineering Research Council of Canada for financial support by way of the Canada Graduate Scholarship – Doctoral, as well as the Province of Ontario for the Ontario Graduate Scholarship, and the University of Ottawa for financial support. These initiatives are critical to encouraging scientific excellence, and I am humbled to have been the recipient of such honours.

I have said it before, and I will say it again: good science comes from good collaborations. I sincerely thank all of the researchers and support staff that have contributed indispensably to my work here at uOttawa. Thank you to Dr. Jeffrey Ovens for teaching me to use the single-crystal diffractometers, enabling a pillar of my research and catalysing the advancement of a longtime obsession with crystallography. Thanks also to Sarah Osterholm for her support and continuing camaraderie; I don't think there is a better person to run a facility with. Thanks to Drs. Glenn Facey, Peter Pallister, and Patrick Szell for training and sharing their expertise on NMR spectroscopy; my collection of weird heteronuclei got quite a bit bigger while working here! Thanks to Ian Myers and Lukasz Andrzejewski at the Electronics Shop as well as Olivier Demers and Benoît Raymond at the Machine Shop for their camaraderie and unwavering support with all our laboratory technical queries. Thanks to each of the many staff at the Science Store, including but not limited to Alain, Kevin, Gabriel, Mike, Gregory, Nick, Max, André, Claude, and Josianne, for coordinating our procurement, chemicals, supplies, and sample submissions. Thanks to Dr. Sean Kirkwood, David Needham and Guillaume Blais for always being available to help us with our Facilities needs, and doing so with smiles and kind banter. Thanks to the team at the Office of the Chief Risk Officer, especially Dr. Alexander Daniels; we do a lot of dangerous work in the Murugesu Group, and they were critical to helping us maintain a high standard of safety and best laboratory practices. Special thanks go to Dr. Elizaveta Suturina (University of Bath) for her computational work on compound **2.1**, and to Drs. Thierry Maris and Daniel Chartrand (Université de Montréal) for variable-temperature single-crystal X-ray diffraction that

was crucial to the analyses in Chapters 2 and 3. I would also like to thank Dr. Sharon Barden of the John L. Holmes Mass Spectrometry Facility at uOttawa for the mass spectrometry of compounds **3.8**–**3.11** and Dr. Tom Woo for access to WebMO for the DFT calculations performed In Chapter 4. If you have helped me in any way during my degree and I have neglected to thank you by name, please know that you are appreciated.

Undertaking a PhD is a monumentally difficult endeavour, made no easier by the exceedingly difficult world in which we currently live. Through all of the highest highs and the lowest lows of this journey, my colleagues past and present, my esteemed friends, were the giants upon whose shoulders I stood, and whose steadfast positive presence gave me the drive I needed to keep going right to the very end.

Thanks to Armando Baca, Hussein Canoe, Sarah Castang, Bruno Chemel, Rayyan Ebrahim, Dr. Katie Harriman, Darren Herweyer, Elliot Jackson, Adriana Silvestre Llora, Dr. Sujithkumar Ganesh Moorthy, Merry Mulugeta, Aylin Nagel, Rémy Pierron, Vajeeha Urunikulavan, Laurence Yeh, and Clara Zwanziger; it was a pleasure getting to know and working alongside all of you, and I look fondly on the time we spent together.

Thanks to Maria Brzozowska for taking on several of my laboratory roles after I stopped my regular workflow, and for helping me finish off the refurbishing and setup of the argon glovebox. I hope it serves her and her successors well, and that a bounty of impactful and interesting results come her way.

Thanks to my "Spanish Gang", Carlos Díaz Fontenla and Josué Ortega Ramirez, for becoming my fast friends and never failing to share a coffee and a laugh. I know that you will both develop into successful scientists and I am excited to see the next steps on your paths forward.

Thanks to Antonia Pesch, a delightful character who never failed to brighten my day with her kindness and eccentric philosophy; to Essi Barkas, a passionate and curious scientist who I discovered was much like me in many ways; and to Dr. Airton Germano Bispo Jr., who dropped into our group for a brief stint and instantly fit in like he always belonged. I lament that our time together was so short, but I am certainly happy I got to experience it, and I hope we will see each other again.

Thank you to Dr. Chris Bamforth, my original glovebox roommate, who was somehow always in the lab whenever you were and never missed an opportunity to lend you a hand or share his deep knowledge of the literature and theory, beautiful diffraction frames, or bespoke memes. He also helped me a great deal as I was learning to perform my own crystallography, and would always be ready to dive into the strangest synthesis and esoteric fundamental research. Thanks also to Dylan Errulat, my second glovebox roommate, for trusting me to work alongside him in a highly rigorous environment, sharing his expertise with sensitive organometallic synthesis and magnetometric data interpretation, and always being open for problem-solving discussions and debates.

Thank you to Dr. Paul Richardson (and by extension his partner, Ellen) who, as for many before me, welcomed a complete stranger as though he were an old friend, and truly helped me begin to find my place and be comfortable in the group. His laboratory management skills were indispensable, and his willingness to fearlessly try chemistry from all corners of the field was inspiring. I had a great time discussing weird metal (of both the chemical and musical varieties) with him, and am glad that he is still nearby and makes the effort to come around for group milestones.

Thank you to Dr. Walace Doti do Pim, whose excellent sense of humour, effortlessly welcoming attitude, and unique perspective brought a whole group from all different corners of the Earth and walks of life together around him. His level-headed guidance formed a central pillar of one of the tightest group dynamics I have had the pleasure of working in. The lab is not quite the same without his little corner of MOFs, and I wish the best for him and his growing family.

Two huge, special thanks go to my third glovebox roommate Dr. Neha Bajaj, who I watched grow from an eager student starting a new chapter in Canada to a successful, confident, ambitious researcher and

impressive science communicator, and Claudia Manuela Santos Calado, a paragon of fierce independence, deep expertise, and making the most of life. Over the years we evolved from acquaintances to colleagues to good friends, and sharing a meal and a cathartic rant with these two exemplary women is always the highlight of my workday. I thank them for always thinking of me and including me in their shenanigans.

There are three people to whom I would like to extend my sincerest appreciation and most heartfelt thanks. Firstly, I am endlessly grateful for Dr. Niki Mavragani, an absolute powerhouse of a researcher and strong, inspiring leader. She was my go-to person for any questions about magnetochemistry, and she taught me so much about advanced air-free synthesis techniques, laboratory safety and organization, and new analytical techniques. Her laughter is contagious, and her quick wit, open heart and supportive nature made long days in the lab not just bearable, but downright enjoyable. I hope that all those she works alongside in the future can be uplifted by her the way I was.

Secondly, to Dr. Diogo Alves Gálico, a world-class scientist and bottomless encyclopedia of spectroscopy knowledge, with whom I worked closely on all the projects presented herein. I thank him for taking the time to teach me so much about lanthanides and lanthanide spectroscopy, for being patient with me when I made mistakes or worked slowly, for the countless enthusiastic discussions and exchanges of excellent ideas, and for always being available to kindly answer all my (sometimes stupid) questions. While I miss our dynamic-duo research approach, it brings me joy to see him thriving in his new faculty role.

Finally, to Dr. Alexandros Kitos, one of the most versatile and hardworking chemists I have ever known, with whom I probably spent the most time overall talking about all manner of topics, scientific or otherwise. I thank him in particular for being my "crystallography dad" (alongside my "crystallography mom" Dr. Katherine Robertson (St. Mary's University)); his eagerness to share his vast expertise, and assistance in honing my problem-solving skills, were instrumental (no pun intended) in turning me from a fledgling into something resembling a bona-fide crystallographer. I cherish our profound breaktime discussions and value him as a role model. Although it is strange to no longer have him as a coworker, I know he will accumulate great scientific outputs, mentees, colleagues, and friends wherever he goes.

In the preceding paragraphs, I have spoken mostly to the impact my colleagues have had on me from a professional perspective; but this is not the whole story, or even arguably the most important part. The most important part is the random weekday evenings we spent at La Maison; the beer, the shots, the pizza, the Indian Kebab and Curry House; the absurd night out with Juan from QD; the picnics in the park; the long, tough hours standing beside one another at the fumehood, the glovebox, the SQUID, the diffractometer; the hand on a fire extinguisher while someone performs a risky procedure; the potlucks, the birthdays, the Christmas parties, the defense celebrations, the conferences; the gossip sessions, the sharing and oversharing; the joy and the rage, the laughter, the blood, sweat, and tears; the names next to each other on the author line; the free therapy that comes from being surrounded by people you care about, that care about you. I believe that friendship is a form of love, and I was so fortunate to have existed in this group at the same time as all these wonderful people.

Above all, I would like to thank my family. To my parents, Rosa Rodriguez and Manuel Diaz Medina: thank you for enduring my leaving home to pursue this opportunity, and I hope that I have made you proud. To my "additional" parents, Donna Diaz, Diane McInnis, and Satish Rangaswamy: thank you for offering me a home away from home and welcoming me into your lives. Thanks to my favourite feline friend Jack, who was always waiting to welcome me home with a soft hug (and a banshee wail). And, last but not least, to my partner, Alana Rangaswamy: thank you for being the picture in my proverbial locket. The end of the tunnel is finally here.

TABLE OF CONTENTS

ABSTRACT ii
ACKNOWLEDGEMENTS v
TABLE OF CONTENTS viii
LIST OF FIGURES x
LIST OF TABLES xxiv
LIST OF ABBREVIATIONS AND SYMBOLS USED xxvi
CONTRIBUTIONS xxx
CHAPTER 1 Introduction to Lanthanide Luminescence, Luminescence Thermometry, and the Special Properties of Divalent Europium 1
1.1 Opening remarks 1
1.2 The electronic structure of lanthanide ions 1
1.3 Luminescence of trivalent lanthanide ions 3
1.4 The divalent lanthanides, and the special properties of Eu^{II} 6
1.5 Luminescence thermometry 9
1.6 Thesis scope and outlook 13
CHAPTER 2 Toward Opto-Structural Correlation to Investigate Luminescence Thermometry in an Organometallic Eu^{II} Complex 18
2.1 Preface 18
2.2 Abstract 18
2.3 Introduction 19
2.4 Synthesis and structural characterization 20
2.5 Magnetic properties 21
2.6 Photoluminescence 23
2.6 Variable-temperature structural analysis 27
2.7 Structural effects on optical properties 29
2.8 Conclusions 33
2.9 Experimental 34
CHAPTER 3 Ligand Effects on the Emission Characteristics of Molecular Eu^{II} Luminescence Thermometers 37
3.1 Preface 37
3.2 Abstract 37
3.3 Introduction 38
3.4 Synthesis and structural characterization of Eu complexes 39
3.5 Photoluminescence 41
3.6 Stereoelectronic effects 50
3.7 Variable-temperature structural analysis 52
3.8 Structural effects on the optical properties 70
3.9 Thermometric performance 73
3.10 Conclusion 74
3.11 Methods 75
3.13 Synthesis 77
CHAPTER 4 Exploring a New Family of (Phosphinochalcogenoyl)Europocenes for Magneto-Optical Thermometry 84

4.1 Preface 84
4.2 Abstract 84
4.3 Introduction 85
4.4 Synthesis and characterization of ligand precursors 86
4.5 Synthesis of europocenes 88
4.6 Structural analysis 90
4.7 Photoluminescence spectroscopy and luminescence thermometry 94
4.7 Magneto-optical properties and MCD thermometry 99
4.8 Conclusion 120
4.9 Methods 120
4.10 Synthesis 122
CHAPTER 5 Concluding Remarks and Future Directions 130
5.1 Organoeuropium(II) complexes as optical thermometers 130
5.2 Future directions 131
APPENDIX A Corresponding to Chapter 2 133
A.1 Nuclear magnetic resonance spectra 133
A.2 Electronic structure calculations 133
A.2 Photoluminescence 136
A.3 Crystallographic information 138
A.4 Absorption spectra calculations 141
APPENDIX B Corresponding to Chapter 3 152
B.1 Infrared spectra 152
B.2 Nuclear magnetic resonance spectra 158
B.3 Crystallographic information 164
B.4 Photoluminescence 178
B.5 Metrical analysis 180
APPENDIX C Corresponding to Chapter 4 183
C.1 Nuclear magnetic resonance spectra 183
C.2 Crystallographic information 191
C.3 Infrared spectra 196
C.5 Photoluminescence and luminescence thermometry 201
C.6 Magneto-optical properties and MCD thermometry 202
REFERENCES 209
LIST OF COPYRIGHT PERMISSIONS 235

LIST OF FIGURES

Figure 1.1. *Left*: Graphical representations of the general set of 4*f* orbitals. Reproduced with permission from [12]. *Right*: Radial distribution functions for the 4*f*, 5*s*, 5*p*, 5*d*, 6*s*, and 6*p* orbitals of Nd^0, illustrating the significantly low radial extension of the 4*f* orbitals relative to the others. Reproduced from [14] under the terms of the Creative Commons Attribution Non-Commercial No Derivatives License. 2

Figure 1.2. Schematic representation of the hierarchy of various factors affecting the electronic structure of lanthanide ions in coordination compounds. Reproduced with permission from [20]. 3

Figure 1.3. Diagram of energy levels for all trivalent lanthanide ions except Pm, obtained via optical absorption (blue boxes), photoluminescence excitation (grey boxes), and photoluminescence emission (red boxes) spectroscopy performed on the corresponding Ln^{III} aquo species as solutions in 100 mM $DClO_4$ in D_2O. Reproduced from [26] under the terms of the Creative Commons Attribution Non-Commercial No Derivatives License. 5

Figure 1.4. *Left:* Simplified schematic diagram of the "antenna effect" ("sensitized luminescence") showing the transfer of energy from an excited ligand chromophore to the bound metal center which eventually emits. The singlet and triplet excited states of the ligand are set at reasonable arbitrary positions[16] above Tb^{III} $^5D_4$, and the Tb manifold is based on the free-ion values from Carnall.[24] *Right:* Solid-state emission spectrum ($\lambda_{ex} = 323$ nm) of $Tb^{III}(acac)_3(PyAm)$ at 10 K, showing all seven $^5D_4 \rightarrow {}^7F_J$ transitions. 6

Figure 1.5. Photoluminescence spectra of Sm^{II} crown ether complexes in the solid state at 93 K, demonstrating emission from different types of transitions. $[Sm^{II}(15\text{-crown-}5)_2]I_2$ (red curve) exhibits emission only from intraconfigurational 4*f*-4*f* transitions; $[Sm^{II}(benzo\text{-}15\text{-crown-}5)_2]I_2$ (green curve) exhibits emission only from interconfigurational 4*f*-5*d* transitions; and $[Sm^{II}(15\text{-crown-}5)_2]I_2{\cdot}CH_3CN$ (blue curve) exhibits emission from a superimposed combination of both types of transition. Adapted with permission from [50]. 8

Figure 1.6. *Left:* Temperature-dependent upconversion emission spectra (λ_{ex} = 980 nm at 1.5 W cm^{-2}) of SrF_2:Yb/Er nanoparticles in the range 303-373 K, demonstrating the thermosensitive intensities of the $^4S_{3/2} \rightarrow {}^4I_{15/2}$ (I_1) and $^2H_{11/2} \rightarrow {}^4I_{15/2}$ (I_2) bands of Er^{III}. *Right*: Temperature dependence of the values $\Delta = \frac{I_1}{I_2}$ obtained from the temperature-dependent emission spectra, as a bare powder (black triangles) and as a suspension in water (red inverted triangles). The blue line represents the theoretical relationship between the observed intensity ratio and temperature. Adapted with permission from [96]. 11

Figure 1.7. *Left:* Temperature-dependent emission spectra (λ_{ex} = 370 nm) of $\{[Nd^{III}(acac)_3]_2(\mu\text{-bpm})\}$ in the range 11-310 K, demonstrating the thermosensitive intensities of the m_J sublevels in the $^4F_{3/2} \rightarrow {}^4I_{11/2}$ band of Nd^{III}. *Middle*: Temperature dependence of the values $\Delta = \frac{I_{1\prime,5\prime,6\prime}}{I_{1,4,5,6}}$ obtained from the temperature-dependent emission spectra. The red line represents the best fit to a Boltzmann-type equation. *Right*: Temperature dependence of the relative sensitivity S_r and temperature uncertainty δT based on the selected Δ. Adapted with permission from [98]. 12

Figure 1.8. *Left:* Temperature-dependent emission spectra (λ_{ex} = 330 nm) of $KSr(BH_4)_{2.8}Cl_{0.2}:Eu^{II}$ in the range 14-475 K, demonstrating the thermosensitive shifting of the $4f^6 5d^1 \rightarrow 4f^7$ band maximum of Eu^{II}. *Right*: Temperature dependence of the values $\Delta = \lambda_{em}$ obtained from the temperature-dependent emission spectra. Adapted with permission from [106]. 13

Figure 2.1. Molecular structure of **2.1**, shown as a ball-and-stick diagram (left) and as a thermal ellipsoid diagram (right). Labels are given only for the crystallographically unique atoms which coordinate the Eu^{II} centre; symmetry-related atoms are indicated elsewhere with a prime (e.g. B1′). Hydrogen atoms bonded to carbon are omitted for clarity. Selected bond lengths and angles are provided in Table A1. Packing diagrams are shown in Figure A7. 20

Figure 2.2. Infrared spectrum of complex **2.1** 21

Figure 2.3. Temperature dependence of the χT product at 1000 Oe (blue points) for complex **2.1**, with χ representing the molar magnetic susceptibility per molecule defined as M/H. The solid red line represents the fit; the calculated J value is +0.04 cm^{-1}. 22

Figure 2.4. Field dependence of the magnetization (left) and reduced magnetization (right) for **2.1** at the indicated temperatures 22

Figure 2.5. Excitation (gray) and emission (violet) spectra for **2.1** obtained at 10 K. 23

Figure 2.6. Temperature-dependent emission of **2.1**. (a) Temperature-dependent emission spectra (λ_{ex} = 330 nm) obtained in the solid state over the 60-320 K range with steps of 10 K. (b) Relevant section of the CIE diagram showing the luminescence colours at selected temperatures. (c) Temperature-dependence of the emission peak energy. The red line represents the Boltzmann function (Eqn. 2.1) used to fit the experimental data. Best-fitting parameters: $R^2 = 0.999$, $A_1 = 8583$, $A_2 = 145840$, and $x_0 = 2920$. (d) Absolute sensitivity obtained as the first derivative of the fitted function. 24

Figure 2.7. Temperature-dependent emission of $[Eu^{II}(BH_4)_2(THF)_2]$. (a) Temperature-dependent emission spectra (λ_{ex} = 330 nm) obtained in the solid state over the 30-320 K range with steps of 10 K. (b) Relevant section of the CIE diagram showing the luminescence colours at selected temperatures. (c) Temperature-dependence of the emission peak energy. The red line represents the Boltzmann function (Eqn. 2.1) used to fit the experimental data. Best-fitting parameters: $R^2 = 0.998$, $A_1 = 19336$, $A_2 = 21033$, and $x_0 = 219$. (d) Absolute sensitivity obtained as the first derivative of the fitted function. 25

Figure 2.8. (a) Wavelength dependence of the instrumental error $\boldsymbol{\sigma}$ for three different model spectroscopic systems (with wavelength resolution increasing from 0.5 nm in System 1 to 0.1 nm in System 2 to 0.025 nm in System 3). Temperature uncertainty ΔT values for (b) **2.1**, (c) **2.2**, and (d) $[Eu^{II}(BH_4)_2(THF)_2]$ (lower is better). 26

Figure 2.9. Plots of the emission peak energy of **2.1** as a function of the Eu-Cp*(cent) distance (a), the average Eu-O(THF) distance (b), the B1-B1′ distance (c), the intramolecular Eu-Eu′ distance (d), the average of all Eu-ligand distances (e), and the closest intermolecular Eu-Eu distance (f). The open green points represent data collected for a different crystal using the same diffractometer. The open orange points represent data collected on a different crystal using a different diffractometer. This demonstrates the consistency of the change in metrical parameters across the entire sample. Error bars are shown but overlap the points in some cases. The dashed blue lines are linear fits of the data to the equation $y = mx + b$. Best fitting parameters are as follows: (a) no correlation; (b) no correlation; (c) $m = 27.9$, $b = -94.5$, $R^2 = 0.5989$; (d) $m = 17.6$, $b = -59.0$, $R^2 = 0.7859$; (e) $m = 95.8$, $b = -240$, $R^2 = 0.8628$; (f) $m = 5.99$, $b = -40.7$, $R^2 = 0.9832$. 28

Figure 2.10. Variable-temperature structural analysis. (a) Temperature dependence of selected bond lengths from the crystal structure of **2.1**. The structure is truncated for clarity. Green = Eu, red = O, black = C, pink = B. Plots of emission peak energy as a function of the average Eu-B distance (b) and the relative

compression of the lattice (c). (d) Plot of emission peak energy as a function of the distortion of the coordination geometry around Eu. The distortion is represented by the continuous shape measure (CShM), which quantifies the deviation of the real coordination polyhedron from an idealized square pyramid. A value of zero represents exact agreement with the idealized geometry. (e) Plot of emission peak energy as a function of the distance between the Eu ion and the basal plane of the coordination pyramid, defined by the atoms B1, B1′, O1 and O2 (see Figure 2.1). The solid black points represent data collected from the same crystal at varying temperatures. The open green points represent data collected for a different crystal using the same diffractometer. The open orange points represent data collected on a different crystal using a different diffractometer. This demonstrates the consistency of the change in metrical parameters across the entire sample. Error bars are shown but overlap the points in some cases. The dashed blue lines are linear fits of the data to the equation $y = mx + b$. Best fitting parameters are as follows: (b) $m = 35.7, b = -87.8$, $R^2 = 0.9108$; (c) $m = 29.3, b = -12.9, R^2 = 0.9975$; (d) $m = 7.6, b = 6.6, R^2 = 0.9875$; (e) $m = 45.4$, $b = -33.4, R^2 = 0.8810$. 29

Figure 2.11. Schematic diagram of the general effect of Eu-ligand distance on ligand field splitting and emission peak energy in a Eu^{II} complex. The energy levels represent generalized "low-" and "high-" energy ligand-field states. 30

Figure 2.12. Temperature-dependent emission of **2.2**. (a) Temperature-dependent emission spectra (λ_{ex} = 330 nm) for **2.2** obtained in the solid state over the 30-320 K range with steps of 10 K. (b) Temperature-dependence of the emission peak energy. The red line represents the Boltzmann function (eq. 2.1) used to fit the experimental data. Best-fitting parameters: $R^2 = 0.999, A_1 = 13362, A_2 = 19214$, and $x_0 = 261$. (c) Absolute sensitivity obtained as the first derivative of the fitted function. 31

Figure 2.13. *Left:* Infrared spectrum of complex **2.2**. *Right:* Infrared spectra of **2.1** and **2.2** overlaid for comparison. The centre frequency of the BX_4 vibration band shifts by 630 cm^{-1} upon substitution of D for H, from approx. 2260 cm^{-1} to approx. 1630 cm^{-1}. A very weak absorbance is observed at 2337 cm^{-1} in the spectrum of **2.2**, which is most likely due to a small amount of ^1H incorporation from the 98%-D $NaBD_4$ used in the synthesis. 32

Figure 2.14. Comparison of the emission peak energy (top) and absolute sensitivity (bottom) of $[Eu(BH_4)_2(THF)_2]$, **2.1**, and **2.2** as a function of temperature. 33

Figure 3.1. Synthesis of organometallic Eu^{II} complexes **3.1–3.7** for optostructural correlation investigation. 39

Figure 3.2. Solid-state structures of complexes **3.1–3.4**, **3.6** and **3.7** at 200-213 K. Ellipsoid diagrams and packing diagrams for all complexes are given in Appendix B. Labels are given only to selected crystallographically unique atoms. Hydrogen atoms bonded to carbon have been omitted for clarity. 40

Figure 3.3. *Left:* Solid-state structure of **3.5**. Two units of the infinite one-dimensional coordination polymer are depicted. Labels are only given to selected, crystallographically unique atoms. Hydrogen atoms bonded to carbon have been omitted for clarity. For clarity, only one component of the disordered Cp^{iPr4} ring is shown. *Right:* Thermal ellipsoid diagram (30% probability for clarity) of **3.5**. Large thermal ellipsoids are a consequence of the significant disorder present in this structure. Only one repeating unit of the polymeric structure and one component of the disorder is shown for clarity. Hydrogen atoms bonded to carbon are omitted for clarity. Labels are given only to the crystallographically unique atoms which coordinate the Eu^{II} centre. Packing diagrams are shown in Figure B9. 41

Figure 3.4. Solid-state excitation (grey) and emission (red) spectra for **3.1** obtained at 10 K. 42

Figure 3.5. Temperature-dependent emission spectra (λ_{ex} = 357 nm) for **3.1** obtained in the solid state over the 100−320 K range with steps of 10 K. 42

Figure 3.6. Solid-state excitation (grey) and emission (blue) spectra for **3.2** obtained at 10 K. 43

Figure 3.7. Temperature-dependent emission spectra (λ_{ex} = 352 nm) for **3.2** obtained in the solid state over the 30−300 K range with steps of 10 K. 43

Figure 3.8. Solid-state excitation (grey) and emission (purple) spectra for **3.3** obtained at 10 K. 44

Figure 3.9. Temperature-dependent emission spectra (λ_{ex} = 356 nm) for **3.3** obtained in the solid state over the 40−310 K range with steps of 10 K. 44

Figure 3.10. Solid-state excitation (grey) and emission (green) spectra for **3.4** obtained at 10 K. 45

Figure 3.11. Temperature-dependent emission spectra (λ_{ex} = 356 nm) for **3.4** obtained in the solid state over the 30−320 K range with steps of 10 K. 45

Figure 3.12. Solid-state excitation (grey) and emission (orange) spectra for **3.5** obtained at 10 K. 46

Figure 3.13. Temperature-dependent emission spectra (λ_{ex} = 350 nm) for **3.5** obtained in the solid state over the 110−290 K range with steps of 10 K. 46

Figure 3.14. Solid-state excitation (grey) and emission (yellow) spectra for **3.6** obtained at 10 K. 47

Figure 3.15. Temperature-dependent emission spectra (λ_{ex} = 345 nm) for **3.6** obtained in the solid state over the 80−320 K range with steps of 10 K. 47

Figure 3.16. Solid-state excitation (grey) and emission (light blue) spectra for **3.7** obtained at 10 K. 48

Figure 3.17. Temperature-dependent emission spectra (λ_{ex} = 355 nm) for **3.7** obtained in the solid state over the 120−260 K range with steps of 10 K. 48

Figure 3.18. Thermometric performance of complexes **3.1**–**3.7** in comparison to the original complex **2.1**. (a) Temperature dependence of the energy at the emission band maximum, extracted from the temperature-dependent emission spectra. The solid lines represent the Boltzmann function used to fit the experimental data. Best-fitting parameters for each dataset are given in Table B1. (b) Absolute sensitivities obtained as the first derivative of the fitted functions shown in panel (a). 49

Figure 3.19. Temperature-dependence of various metrical parameters of **3.1**. (a) The Eu-Cp^{xph}(cent) distance; (b) the average Eu-O(THF) distance; (c) the average Eu-B distance; (d) the B1-B1′ distance; (e) the B1-Eu-B1′ angle; (f) the intramolecular Eu-Eu′ distance; (g) the average of all Eu-ligand distances; (h) the volume of the crystallographic unit cell; (i) the crystallographic density; (j) the closest intermolecular Eu-Eu distance; (k) the relative compression of the lattice; (l) the distance between the Eu ion and the basal plane of the coordination pyramid, defined by the atoms B1, B1′, O1, and O2; (m) distortion of the coordination geometry around Eu as represented by the continuous shape measure (CShM), which quantifies the deviation of the real coordination polyhedron from an idealized square pyramid (a value of zero represents exact agreement with the idealized geometry). Error bars (as ±3x esu of the measurement) are shown but overlap the points in some cases. The dashed lines are linear fits of the equation $y = mx + b$ to the data. Best fitting parameters are given in Table 3.4. 54

Figure 3.20. Plots of the energy at the emission band maximum for **3.1** as a function of (a) The Eu-Cp^{xph}(cent) distance; (b) the average Eu-O(THF) distance; (c) the average Eu-B distance; (d) the B1-B1′ distance; (e) the B1-Eu-B1′ angle; (f) the intramolecular Eu-Eu′ distance; (g) the average of all Eu-ligand distances; (h) the volume of the crystallographic unit cell; (i) the crystallographic density; (j) the closest intermolecular Eu-Eu distance; (k) the relative compression of the lattice; (l) the distance between the Eu ion and the basal plane of the coordination pyramid, defined by the atoms B1, B1′, O1, and O2; (m) distortion of the coordination geometry around Eu as represented by the continuous shape measure (CShM), which quantifies the deviation of the real coordination polyhedron from an idealized square pyramid (a value of zero represents exact agreement with the idealized geometry). Error bars (as ±3x esu of the measurement) are shown but overlap the points in some cases. The dashed lines are linear fits of the equation $y = mx + b$ to the data. Best fitting parameters are given in Table 3.5. 55

Figure 3.21. Temperature-dependence of various metrical parameters of **3.2**. (a) The Eu-$^{TMS}Cp^{\#}$(cent) distance; (b) the average Eu-O(THF) distance; (c) the average Eu-B distance; (d) the B1-B1′ distance; (e) the B1-Eu-B1′ angle; (f) the intramolecular Eu-Eu′ distance; (g) the average of all Eu-ligand distances; (h) the volume of the crystallographic unit cell; (i) the crystallographic density; (j) the closest intermolecular Eu-Eu distance; (k) the relative compression of the lattice; (l) the distance between the Eu ion and the basal plane of the coordination pyramid, defined by the atoms B1, B1′, O1, and O2; (m) distortion of the coordination geometry around Eu as represented by the continuous shape measure (CShM), which quantifies the deviation of the real coordination polyhedron from an idealized square pyramid (a value of zero represents exact agreement with the idealized geometry). Error bars (as ±3x esu of the measurement) are shown but overlap the points in some cases. The dashed lines are linear fits of the equation $y = mx + b$ to the data. Best fitting parameters are given in Table 3.7. 57

Figure 3.22. Plots of the energy at the emission band maximum for **3.2** as a function of (a) The Eu-$^{TMS}Cp^{\#}$(cent) distance; (b) the average Eu-O(THF) distance; (c) the average Eu-B distance; (d) the B1-B1′ distance; (e) the B1-Eu-B1′ angle; (f) the intramolecular Eu-Eu′ distance; (g) the average of all Eu-ligand distances; (h) the volume of the crystallographic unit cell; (i) the crystallographic density; (j) the closest intermolecular Eu-Eu distance; (k) the relative compression of the lattice; (l) the distance between the Eu ion and the basal plane of the coordination pyramid, defined by the atoms B1, B1′, O1, and O2; (m) distortion of the coordination geometry around Eu as represented by the continuous shape measure (CShM), which quantifies the deviation of the real coordination polyhedron from an idealized square pyramid (a value of zero represents exact agreement with the idealized geometry). Error bars (as ±3x esu of the measurement) are shown but overlap the points in some cases. The dashed lines are linear fits of the equation $y = mx + b$ to the data. Best fitting parameters are given in Table 3.8. 58

Figure 3.23. Temperature-dependence of various metrical parameters of **3.3**. (a) The Eu-$^{TMG}Cp^{\#}$(cent) distance; (b) the average Eu-O(THF) distance; (c) the average Eu-B distance; (d) the B1-B1′ distance; (e) the B1-Eu-B1′ angle; (f) the intramolecular Eu-Eu′ distance; (g) the average of all Eu-ligand distances; (h) the volume of the crystallographic unit cell; (i) the crystallographic density; (j) the closest intermolecular Eu-Eu distance; (k) the relative compression of the lattice; (l) the distance between the Eu ion and the basal plane of the coordination pyramid, defined by the atoms B1, B1′, O1, and O2; (m) distortion of the coordination geometry around Eu as represented by the continuous shape measure (CShM), which quantifies the deviation of the real coordination polyhedron from an idealized square pyramid (a value of zero represents exact agreement with the idealized geometry). Error bars (as ±3x esu of the measurement) are shown but overlap the points in some cases. The dashed lines are linear fits of the equation $y = mx + b$ to the data. Best fitting parameters are given in Table 3.10. 60

Figure 3.24. Plots of the energy at the emission band maximum for **3.3** as a function of (a) The Eu-^{TMG}Cp$^{\#}$(cent) distance; (b) the average Eu-O(THF) distance; (c) the average Eu-B distance; (d) the B1-B1′ distance; (e) the B1-Eu-B1′ angle; (f) the intramolecular Eu-Eu′ distance; (g) the average of all Eu-ligand distances; (h) the volume of the crystallographic unit cell; (i) the crystallographic density; (j) the closest intermolecular Eu-Eu distance; (k) the relative compression of the lattice; (l) the distance between the Eu ion and the basal plane of the coordination pyramid, defined by the atoms B1, B1′, O1, and O2; (m) distortion of the coordination geometry around Eu as represented by the continuous shape measure (CShM), which quantifies the deviation of the real coordination polyhedron from an idealized square pyramid (a value of zero represents exact agreement with the idealized geometry). Error bars (as ±3x esu of the measurement) are shown but overlap the points in some cases. The dashed lines are linear fits of the equation $y = mx + b$ to the data. Best fitting parameters are given in Table 3.11. 61

Figure 3.25. Temperature-dependence of various metrical parameters of **3.4**. (a) The Eu-^{bdp}Cp$^{\#}$(cent) distance; (b) the average Eu-O(THF) distance; (c) the average Eu-B distance; (d) the B1-B1′ distance; (e) the B1-Eu-B1′ angle; (f) the intramolecular Eu-Eu′ distance; (g) the average of all Eu-ligand distances; (h) the volume of the crystallographic unit cell; (i) the crystallographic density; (j) the closest intermolecular Eu-Eu distance; (k) the relative compression of the lattice; (l) the distance between the Eu ion and the basal plane of the coordination pyramid, defined by the atoms B1, B1′, O1, and O2; (m) distortion of the coordination geometry around Eu as represented by the continuous shape measure (CShM), which quantifies the deviation of the real coordination polyhedron from an idealized square pyramid (a value of zero represents exact agreement with the idealized geometry). Error bars (as ±3x esu of the measurement) are shown but overlap the points in some cases. The dashed lines are linear fits of the equation $y = mx + b$ to the data. Best fitting parameters are given in Table 3.13. 63

Figure 3.26. Plots of the energy at the emission band maximum for **3.4** as a function of (a) The Eu-^{bdp}Cp$^{\#}$(cent) distance; (b) the average Eu-O(THF) distance; (c) the average Eu-B distance; (d) the B1-B1′ distance; (e) the B1-Eu-B1′ angle; (f) the intramolecular Eu-Eu′ distance; (g) the average of all Eu-ligand distances; (h) the volume of the crystallographic unit cell; (i) the crystallographic density; (j) the closest intermolecular Eu-Eu distance; (k) the relative compression of the lattice; (l) the distance between the Eu ion and the basal plane of the coordination pyramid, defined by the atoms B1, B1′, O1, and O2; (m) distortion of the coordination geometry around Eu as represented by the continuous shape measure (CShM), which quantifies the deviation of the real coordination polyhedron from an idealized square pyramid (a value of zero represents exact agreement with the idealized geometry). Error bars (as ±3x esu of the measurement) are shown but overlap the points in some cases. The dashed lines are linear fits of the equation $y = mx + b$ to the data. Best fitting parameters are given in Table 3.14. 64

Figure 3.27. Temperature-dependence of various metrical parameters of **3.6**. (a) The Eu-Cp*(cent) distance; (b) the average Eu-O(DME) distance; (c) the average Eu-B distance; (d) the B1-B1′ distance; (e) the B1-Eu-B1′ angle; (f) the intramolecular Eu-Eu′ distance; (g) the average of all Eu-ligand distances; (h) the volume of the crystallographic unit cell; (i) the crystallographic density; (j) the closest intermolecular Eu-Eu distance; (k) the relative compression of the lattice; (l) the distance between the Eu ion and the basal plane of the coordination pyramid, defined by the atoms B1, B1′, O1, and O2; (m) distortion of the coordination geometry around Eu as represented by the continuous shape measure (CShM), which quantifies the deviation of the real coordination polyhedron from an idealized square pyramid (a value of zero represents exact agreement with the idealized geometry). Error bars (as ±3x esu of the measurement) are shown but overlap the points in some cases. The dashed lines are linear fits of the equation $y = mx + b$ to the data. Best fitting parameters are given in Table 3.16. 66

Figure 3.28. Plots of the energy at the emission band maximum for **3.6** as a function of (a) The Eu-Cp*(cent) distance; (b) the average Eu-O(DME) distance; (c) the average Eu-B distance; (d) the B1-B1′ distance; (e) the B1-Eu-B1′ angle; (f) the intramolecular Eu-Eu′ distance; (g) the average of all Eu-ligand distances; (h) the volume of the crystallographic unit cell; (i) the crystallographic density; (j) the closest intermolecular Eu-Eu distance; (k) the relative compression of the lattice; (l) the distance between the Eu ion and the basal plane of the coordination pyramid, defined by the atoms B1, B1′, O1, and O2; (m) distortion of the coordination geometry around Eu as represented by the continuous shape measure (CShM), which quantifies the deviation of the real coordination polyhedron from an idealized square pyramid (a value of zero represents exact agreement with the idealized geometry). Error bars (as ±3x esu of the measurement) are shown but overlap the points in some cases. The dashed lines are linear fits of the equation $y = mx + b$ to the data. Best fitting parameters are given in Table 3.17. 67

Figure 3.29. Plots of the energy at the emission band maximum for all complexes at 90 K as a function of (a) The Eu-Cp(cent) distance at 90 K; (b) the average Eu-O(solv) distance at 90 K; (c) the average Eu-B distance at 90 K; (d) the B1-B1′ distance at 90 K; (e) the B1-Eu-B1′ angle at 90 K; (f) the intramolecular Eu-Eu′ distance at 90 K; (g) the average of all Eu-ligand distances at 90 K; (h) the volume of the crystallographic unit cell at 90 K; (i) the crystallographic density at 90 K; (j) the closest intermolecular Eu-Eu distance at 90 K; (k) the distortion of the coordination geometry around Eu at 90 K as represented by the continuous shape measure (CShM), which quantifies the deviation of the real coordination polyhedron from an idealized square pyramid (a value of zero represents exact agreement with the idealized geometry). Error bars (as ±3x esu of the measurement) are shown but overlap the points in some cases. 68

Figure 3.30. Plots of the energy at the emission band maximum for all complexes at 270 K as a function of (a) The Eu-Cp(cent) distance at 270 K; (b) the average Eu-O(solv) distance at 270 K; (c) the average Eu-B distance at 270 K; (d) the B1-B1′ distance at 270 K; (e) the B1-Eu-B1′ angle at 270 K; (f) the intramolecular Eu-Eu′ distance at 270 K; (g) the average of all Eu-ligand distances at 270 K; (h) the volume of the crystallographic unit cell at 270 K; (i) the crystallographic density at 270 K; (j) the closest intermolecular Eu-Eu distance at 270 K; (k) the distance between the Eu ion and the basal plane of the coordination pyramid, defined by the atoms B1, B1′, O1, and O2; (l) the distortion of the coordination geometry around Eu at 270 K as represented by the continuous shape measure (CShM), which quantifies the deviation of the real coordination polyhedron from an idealized square pyramid (a value of zero represents exact agreement with the idealized geometry). Error bars (as ±3x esu of the measurement) are shown but overlap the points in some cases. The dashed blue lines are linear fits of the equation $y = mx + b$ to the data. Best fitting parameters are (a) $m = 40.2, b = -84.9, R^2 = 0.9612$ (the point for **3.6** is excluded from the fit); (d) $m = -13.2, b = 68.8, R^2 = 0.8435$. 69

Figure 3.31. Energy at the emission band maximum for complexes **2.1**, **3.1**–**3.4** and **3.6** as a function of their Eu-basal plane distance at 90 K. Error bars are shown as 3x esu of the measurement but overlap the points. The dashed blue line is a linear fit of the equation $y = mx + b$ to the data; the points for **3.1** and **3.4** are excluded from the fit. Best fitting parameters are $m = 27.9, b = -14.7, R^2 = 0.9844$. 71

Figure 3.32. Schematic diagram showing how the Eu-basal plane distance in complexes with square-pyramidal coordination spheres might affect the interactions between the ligands defining the basal plane and the electron density in the $5d_{xz}$ and $5d_{yz}$ orbitals of Eu^{II}. 72

Figure 3.33. Electron localizability indicator (ELI-D) maps for **3.4** (left) and **3.1** (right). For **3.4**, the selected plane is defined by Eu1, C1 (1-position of $^{bdp}Cp^{\#}$), and P1. For **3.1**, the selected plane is defined by Eu1, C5 (1-position of Cp^{xph}), C10 (*ipso*-Ph), and C13 (*para*-Ph). Each plot is overlaid with a portion of the

theoretical, normalized radial distribution function for a Eu^{II} 5*d* orbital[212,247] from (left) 0 to 4 Å (0 to 7.56 bohr) or (right) 0 to 7 Å (0 to 13.2 bohr)..... 73

Figure 4.1. Synthesis of (phosphinochalcogenoyl)cyclopentadienides **KCp$^{\#}$PCh** and their corresponding Eu^{II} complexes **4.1Ch**. 87

Figure 4.2. Variable-temperature $^{31}P\{^{1}H\}$ NMR spectra of **KCp$^{\#}$PTe** within 6 hr of sample preparation (left) and after one week of stabilization time (right). Spectra are normalized to the room-temperature spectrum in both cases. 88

Figure 4.3. Solid-state structure of **4.1S·THF**. Thermal ellipsoids are shown at 50% probability. For clarity, only one component of the disorder is shown; hydrogen atoms and THF of solvation are omitted. Selected metrical parameters are also given in the appended table (right). Distances are given in Å and angles are given in degrees. Twist angle τ is the torsion angle C-Cp(cent)-Cp(cent)-C between the cyclopentadienyl carbon atoms directly bound to the P atoms of the phosphinothioyl moiety and the corresponding cyclopentadienyl centroids.[294] The value obtained for this complex corresponds to an antiperiplanar staggered geometry. N planarity is defined as the distance between the nitrogen atom and the plane defined by the phosphorus atom and the two methyl carbon atoms on N.[298] This complex contains one planarized and three pyramidal dimethylamino substituents. 89

Figure 4.4. Crystallographic packing diagrams of **4.1S·THF**, shown along the a) *a*-axis, b) *b*-axis, and c) *c*-axis of the unit cell. For clarity, only one component of the disorder is shown, and hydrogen atoms are omitted. 89

Figure 4.5. Solid-state structures of Eu^{II} complexes **4.1Ch**. Labels are given only to crystallographically unique atoms. Thermal ellipsoids are shown at 50% probability; hydrogen atoms are omitted for clarity. Packing diagrams are given in Figures C2-4. 90

Figure 4.6. Experimental infrared spectrum of **KCp$^{\#}$PS** (yellow curve) compared to the corresponding simulated spectrum (obtained from vibrational frequencies calculated via DFT at the CAM-B3LYP/def2-TZVPD level) (blue curve). The raw (grey ticks) and scaled (blue ticks) vibrational frequencies are also shown. The simulated spectrum was obtained by applying a 4 cm^{-1} Gaussian broadening to the calculated vibrational frequencies. *Left:* full spectra. *Right:* closeup of the fingerprint region (525–1750 cm^{-1}). 92

Figure 4.7. Experimental infrared spectrum of **KCp$^{\#}$PSe** (brown curve) compared to the corresponding simulated spectrum (obtained from vibrational frequencies calculated via DFT at the CAM-B3LYP/def2-TZVPD level) (blue curve). The raw (grey ticks) and scaled (blue ticks) vibrational frequencies are also shown. The simulated spectrum was obtained by applying a 4 cm^{-1} Gaussian broadening to the calculated vibrational frequencies. *Left:* full spectra. *Right:* closeup of the fingerprint region (525–1750 cm^{-1}). 92

Figure 4.8. Experimental infrared spectrum of **KCp$^{\#}$PTe** (green curve) compared to the corresponding simulated spectrum (obtained from vibrational frequencies calculated via DFT at the CAM-B3LYP/def2-TZVPD level) (blue curve). The raw (grey ticks) and scaled (blue ticks) vibrational frequencies are also shown. The simulated spectrum was obtained by applying a 4 cm^{-1} Gaussian broadening to the calculated vibrational frequencies. *Left:* full spectra. *Right:* closeup of the fingerprint region (525–1750 cm^{-1}). 93

Figure 4.9. Top-down view of truncated structures of **4.1S** (left), **4.1Se** (middle) and **4.1Te** (right) highlighting the torsional angle τ that defines the metallocene conformation. Hydrogen and chalcogen atoms as well as dimethylamino substituents have been omitted. Black = C, orange = P, green = Eu. 93

Figure 4.10. Solid-state excitation (grey) and emission (yellow) spectra for **4.1S** obtained at 10 K..... 95

Figure 4.11. Temperature-dependent emission spectra (λ_{ex} = 395 nm) for **4.1S** obtained in the solid state over the 70−330 K range with steps of 10 K. 95

Figure 4.12. Temperature dependence of the energy at the emission band maximum of **4.1S**, extracted from the emission spectra shown in Figure 4.11 (left axis). The blue line represents the Boltzmann function fitted to the experimental data. Best fitting parameters: $A_1 = 14838$, $A_2 = 33468$, $x_0 = 2308$, $R^2 = 0.9954$. Absolute sensitivity obtained as the first derivative of the fitted function (right axis)..... 96

Figure 4.13. Solid-state excitation (grey) and emission (brown) spectra for **4.1Se** obtained at 10 K..... 96

Figure 4.14. Temperature-dependent emission spectra (λ_{ex} = 395 nm) for **4.1Se** obtained in the solid state over the 10−120 K range with steps of 10 K. 97

Figure 4.15. Solid-state diffuse reflectance spectra for **4.1Ch** transformed via the Kubelka-Munk function (a) and as raw reflectance (b). Comparison of the Kubelka-Munk-transformed diffuse reflectance spectra for **4.1S** (c) and **4.1Se** (d) (yellow and brown lines, respectively) with their solid-state photoluminescence excitation spectra at 10 K (blue curve) and room temperature, where applicable (red curve). 98

Figure 4.16. Mott-Seitz plots for the relative photoluminescence intensity of **4.1S** (yellow points) and **4.1Se** (brown points). A double-crossover model was employed, and the best-fitting parameters are as follows: for **4.1S**, $A_1 = 1.79$ x10^6, $A_2 = 1.29$, $\Delta E_1 = 2479$, $\Delta E_2 = 202$, $R^2 = 0.9993$; for **4.1Se**, $A_1 = 4.13$, $A_2 = 1090$, $\Delta E_1 = 50$, $\Delta E_2 = 223$, $R^2 = 0.9989$. 99

Figure 4.17. Temperature dependence of the χT product at 1000 Oe for complexes **4.1Ch**, with χ representing the molar magnetic susceptibility per molecule defined as *M/H*. 100

Figure 4.18. Isothermal field-dependence of the magnetization for **4.1S** (a), **4.1Se** (b), and **4.1Te** (c), and reduced magnetization for **4.1S** (d), **4.1Se** (e), and **4.1Te** (f) at the indicated temperatures. 101

Figure 4.19. Variable-field magnetic circular dichroism (VH-MCD) spectra of **4.1S** at 1.9 K (top) and 7.0 K (bottom) under applied magnetic fields of 0.1 – 7 T. Spectra were collected with the magnetic field oriented parallel to the direction of light propagation ("positive field", solid lines) and a spectrum was also collected with a 1 T magnetic field oriented antiparallel to the direction of light propagation ("negative" 1 T), indicated by the dashed line. 102

Figure 4.20. Variable-field magnetic circular dichroism (VH-MCD) spectra of **4.1Se** at 1.9 K (top) and 7.0 K (bottom) under applied magnetic fields of 0.1 – 7 T. Spectra were collected with the magnetic field oriented parallel to the direction of light propagation ("positive field", solid lines) and a spectrum was also collected with a 1 T magnetic field oriented antiparallel to the direction of light propagation ("negative" 1 T), indicated by the dashed line. 103

Figure 4.21. Variable-field magnetic circular dichroism (VH-MCD) spectra of **4.1Te** at 1.9 K (top) and 7.0 K (bottom) under applied magnetic fields of 0.1 – 7 T. Spectra were collected with the magnetic field oriented parallel to the direction of light propagation ("positive field", solid lines) and a spectrum was also collected with a 1 T magnetic field oriented antiparallel to the direction of light propagation ("negative" 1 T), indicated by the dashed line. 104

Figure 4.22. Comparison of VH-MCD spectra at selected fields with solid-state diffuse reflectance (coloured lines in lower portion) and photoluminescence excitation spectra (where applicable, filled grey curves in

lower portion) for **4.1S** (top), **4.1Se** (middle), and **4.1Te** (bottom). Dotted blue lines indicate the distinguishable components observed in the MCD spectra, as described in the text. 105

Figure 4.23. Variable-temperature magnetic circular dichroism (VT-MCD) spectra of **1-S** under applied magnetic fields of (a) 0.1, (b) 0.25, (c) 0.5, and (d) 1.0 T. Regions I_n of the spectra from which MCD thermometric parameters Δ are derived are indicated by yellow boxes. 107

Figure 4.24. Variable-temperature magnetic circular dichroism (VT-MCD) spectra of **4.1S**e under applied magnetic fields of 0.25 (top), 0.5 (middle), and 1.0 T (bottom). Regions I_n of the spectra from which MCD thermometric parameters Δ are derived are indicated by brown boxes. 108

Figure 4.25. Variable-temperature magnetic circular dichroism (VT-MCD) spectra of **4.1Te** under applied magnetic fields of 0.25 (top), 0.5 (middle), and 1.0 T (bottom). Regions I_n of the spectra from which MCD thermometric parameters Δ are derived are indicated by green boxes. 109

Figure 4.26. Temperature-dependence of the Δ parameters of **4.1S** under applied magnetic fields of (a) 0.1, (b) 0.25, (c) 0.5, and (d) 1.0 T. The solid lines represent the sigmoidal logistic function fitted to the experimental data; best fitting parameters are given in Table C6. 110

Figure 4.27. Temperature-dependence of the Δ parameters of **4.1Se** under applied magnetic fields of 0.25 (top), 0.5 (middle), and 1.0 T (bottom). The solid lines represent the sigmoidal logistic function fitted to the experimental data; best fitting parameters are given in Table C6. 111

Figure 4.28. Temperature-dependence of the Δ parameters of **4.1Te** under applied magnetic fields of 0.25 (top), 0.5 (middle), and 1.0 T (bottom). The solid lines represent the sigmoidal logistic function fitted to the experimental data; best fitting parameters are given in Table C6. 112

Figure 4.29. Relative sensitivities calculated for each Δ parameter of **4.1S** under applied magnetic fields of (a) 0.1, (b) 0.25, (c) 0.5, and (d) 1.0 T. The blue line labelled "MP" indicates the sensitivity derived from a multiparametric thermal readout method that combines the temperature-dependence of all Δ for a given set of conditions into one parameter. 113

Figure 4.30. Relative sensitivities calculated for each Δ parameter of **4.1Se** under applied magnetic fields of 0.25 (top), 0.5 (middle) and 1.0 T (bottom). The blue line labelled "MP" indicates the sensitivity derived from a multiparametric thermal readout method that combines the temperature-dependence of all Δ for a given set of conditions into one parameter. 114

Figure 4.31. Relative sensitivities calculated for each Δ parameter of **4.1Te** under applied magnetic fields of 0.25 (top), 0.5 (middle) and 1.0 T (bottom). The blue line labelled "MP" indicates the sensitivity derived from a multiparametric thermal readout method that combines the temperature-dependence of all Δ for a given set of conditions into one parameter. 115

Figure 4.32. Temperature uncertainty δT obtained for **4.1S** under applied magnetic fields of (a) 0.1, (b) 0.25, (c) 0.5, and (d) 1.0 T, based on the temperature-dependent signal fluctuations shown in Figure C13. The dashed grey line indicates the "useful threshold" of δT = 1.0 K. 116

Figure 4.33. Temperature uncertainty δT obtained for **4.1Se** under applied magnetic fields of 0.25 (top), 0.5 (middle), and 1.0 T (bottom), based on the temperature-dependent signal fluctuations shown in Figure C14. The dashed grey line indicates the "useful threshold" of δT = 1.0 K. 117

Figure 4.34. Temperature uncertainty δT obtained for **4.1Te** under applied magnetic fields of 0.25 (top), 0.5 (middle), and 1.0 T (bottom), based on the temperature-dependent signal fluctuations shown in Figure C15. The dashed grey line indicates the "useful threshold" of δT = 1.0 K. 118

Figure 4.35. Reaction scheme for the synthesis of $H^{bdp}Cp^{\#}$. 125

Figure 5.1. Chemical structure of the "mausolate" dianion.[360] 132

Figure A1. ^{1}H NMR spectrum of complex **2.1** in THF-d_8. Note the extremely downfield-shifted resonance ascribable to the Cp* methyl substituents, in addition to the resonances at 3.66 and 1.79 ppm that are attributable to THF. Residual THF and coordinated THF are indistinguishable due to the broadness of the resonances. 133

Figure A2. Spin density plot (iso-value 0.001) of the broken-symmetry solution for **2.1**. 134

Figure A3. Computed energies of the excited states arising from *f-f* transitions in **2.1**. 135

Figure A4. Comparison of the 90 K and 270 K crystal structures of a mononuclear fragment of **2.1**. 135

Figure A5. Solid-state emission spectra of crystalline **2.1** (λ_{ex} = 330 nm) obtained in the 10-60 K range. Note that the emission peak energy remains constant over this temperature range. 136

Figure A6. Relative sensitivities for **2.1**, **2.2**, and $[Eu^{II}(BH_4)_2(THF)_2]$. Relative sensitivities were calculated with the equation: S_r (%) = [(*∂Peak position / ∂T) / Peak position*] x 100. 137

Figure A7. Crystallographic packing diagrams of **2.1**, shown along the (a) *a*-axis, (b) *b*-axis, and (c) *c*-axis of the unit cell. Hydrogen atoms bonded to carbon are omitted for clarity. 140

Figure A8. *Left:* comparison of the idealized square pyramidal geometry (green polyhedron) to the actual coordination sphere of **2.1**. *Right:* comparison of the next-best-fitting idealized geometry (vacant octahedron, red polyhedron), demonstrating the poor agreement of this model with the real structure. 140

Figure A9. Computed TD-DFT absorption spectra of **2.1** calculated based on the crystal structures at 90 K (black) and 270 K (red). The bars represent vertical electronic transitions, and the envelope is obtained with 1000 cm^{-1} Gaussian broadening. 141

Figure A10. Visualization of the intermolecular interactions in **2.1** at various temperatures. Left to right: Hirshfeld fingerprint plot; sum of intermolecular contacts derived from the Hirshfeld surface analysis; and specific intermolecular contacts in the crystal structure, at each indicated temperature. Only the asymmetric unit is shown, and components of the molecule that do not participate in any intermolecular contacts are omitted for clarity. X-axis labels were added manually for clarity. 151

Figure B1. Thermal ellipsoid diagram (50% probability) of **3.1**. Hydrogen atoms bonded to carbon are omitted for clarity. Labels are given only to the crystallographically unique atoms which coordinate the Eu^{II} centre. 171

Figure B2. Crystallographic packing diagrams of **3.1**, shown along the (a) *a*-axis, (b) *b*-axis, and (c) *c*-axis of the unit cell. Hydrogen atoms bonded to carbon are omitted for clarity. 171

Figure B3. Thermal ellipsoid diagram (50% probability) of **3.2**. Hydrogen atoms bonded to carbon are omitted and only one component of the disorder [of O1-THF] is shown for clarity. Labels are given only to the crystallographically unique atoms which coordinate the Eu^{II} centre. 172

Figure B4. Crystallographic packing diagrams of **3.2**, shown along the (a) *a*-axis, (b) *b*-axis, and (c) *c*-axis of the unit cell. Hydrogen atoms bonded to carbon are omitted for clarity. 172

Figure B5. Thermal ellipsoid diagram (50% probability) of **3.3**. Hydrogen atoms bonded to carbon are omitted and only one component of the disorder [of O2-THF] is shown for clarity. Labels are given only to the crystallographically unique atoms which coordinate the Eu^{II} centre. 173

Figure B6. Crystallographic packing diagrams of **3.3**, shown along the (a) *a*-axis, (b) *b*-axis, and (c) *c*-axis of the unit cell. Hydrogen atoms bonded to carbon are omitted for clarity. 173

Figure B7. Thermal ellipsoid diagram (50% probability) of **3.4**. Hydrogen atoms bonded to carbon are omitted for clarity. Labels are given only to the crystallographically unique atoms which coordinate the Eu^{II} centre. 174

Figure B8. Crystallographic packing diagrams of **3.4**, shown along the (a) *a*-axis, (b) *b*-axis, and (c) *c*-axis of the unit cell. Hydrogen atoms bonded to carbon are omitted for clarity. 174

Figure B9. Crystallographic packing diagrams of **3.5**, shown along the (a) *a*-axis, (b) *b*-axis, and (c) *c*-axis of the unit cell. Only one component of the disorder is shown for clarity. Hydrogen atoms bonded to carbon are omitted for clarity. 175

Figure B10. Thermal ellipsoid diagram (50% probability) of **3.6**. Hydrogen atoms bonded to carbon are omitted for clarity. Labels are given only to the crystallographically unique atoms which coordinate the Eu^{II} centre. 176

Figure B11. Crystallographic packing diagrams of **3.6**, shown along the (a) *a*-axis, (b) *b*-axis, and (c) *c*-axis of the unit cell. Hydrogen atoms bonded to carbon are omitted for clarity. 176

Figure B12. Thermal ellipsoid diagram (50% probability) of **3.7**. Only one component of the disorder is shown for clarity. Hydrogen atoms bonded to carbon are omitted for clarity. Labels are given only to the crystallographically unique atoms which coordinate the Eu^{II} centre. 177

Figure B13. Crystallographic packing diagrams of **3.7**, shown along the (a) *a*-axis, (b) *b*-axis, and (c) *c*-axis of the unit cell. Only one component of the disorder is shown for clarity. Hydrogen atoms bonded to carbon are omitted for clarity. 177

Figure B14. Temperature uncertainty of complexes **3.1–3.4**, **3.6** and **3.7** in comparison to the original complex **2.1**, assuming a wavelength resolution of 0.1 nm (lower is better).[224] 178

Figure B15. Thermometric performance of complex **3.5**. *Top:* Temperature dependence of the energy at the emission band maximum, extracted from the temperature-dependent emission spectra shown in Figure 3.13. The solid line represents the Boltzmann function fitted to the experimental data. Best fitting parameters: $A_1 = 17050$, $A_2 = 24466$, $x_0 = 1236$, $R^2 = 0.9950$. *Bottom:* Absolute sensitivity obtained as the first derivative of the fitted function (left axis), and the temperature uncertainty assuming a wavelength resolution of 0.1 nm (right axis).[224] 179

Figure B16. Distance between the cyclopentadienyl centroid and the Eu ion for complexes **2.1**, **3.1–3.4** as a function of the donor strength of the cyclopentadienyl ligand C_5Me_4R, as estimated via the Hammett σ_P parameter (a), the modified Swain-Lupton *F* parameter (b), and the Hammett σ_M parameter (c) of the substituent R, as well as the A_1 carbonyl stretching frequency (d) and the ^{13}C δ_{CO} of the corresponding

complex $(C_5Me_4R)Mn^I(CO)_3$, demonstrating the lack of meaningful correlation between these parameters. Error bars are shown as ±3x esu of the measurement. 180

Figure B17. Steric maps of the ligands used in complexes **2.1**, **3.1–3.7**. 181

Figure B18. Energy at the emission band maximum for complexes **2.1**, **3.1–3.4** as a function of steric bulk (measured as $\%V_{bur}$), demonstrating the lack of meaningful correlation between these parameters. The 10 and 90 K points for **3.1** overlap..... 181

Figure B19. Total change in emission energy ΔE of each complex **2.1**, **3.1–3.4**, and **3.6** over the temperature range 90-270 K (left) and the maximum values of the absolute sensitivity of **2.1**, **3.1–3.4**, and **3.6** (right) plotted against the slopes of the linear fits calculated for plots of energy vs. relative compression of the lattice (i.e., the rate of change of emission energy as a function of lattice compression, see Tables 3.[5, 8, 11, 14, 17]) of each complex. This demonstrates that in general, complexes with a more compressible lattice are expected to show better thermometric performance. Best fitting parameters are (left) $m = 40.3$, $b = 2.38$, $R^2 = 0.8963$; (right) $m = 0.23$, $b = 1.09$, $R^2 = 0.7671$. 182

Figure C1. Variable-temperature ^{1}H NMR spectra of **KCp$^{\#}$PTe** within 6 hr of sample preparation (left) and after one week of stabilization time (right). Spectra are normalized to the room-temperature spectrum in both cases. 190

Figure C2. Crystallographic packing diagrams of **4.1S**, shown along the (a) *a*-axis, (b) *b*-axis, and (c) *c*-axis of the unit cell. Hydrogen atoms are omitted for clarity. 192

Figure C3. Crystallographic packing diagrams of **4.1Se**, shown along the (a) *a*-axis, (b) *b*-axis, and (c) *c*-axis of the unit cell. Hydrogen atoms are omitted for clarity. 192

Figure C4. Crystallographic packing diagrams of **4.1Te**, shown along the (a) *a*-axis, (b) *b*-axis, and (c) *c*-axis of the unit cell. Hydrogen atoms are omitted for clarity. 192

Figure C5. Solid-state structures of both unique molecules in the unit cell of **4.1Se** (two half molecules are uniquely defined). These are similar but differ slightly in their metrical parameters; the differences are listed in Table C1. Thermal ellipsoids are shown at 50% probability, and hydrogen atoms have been omitted for clarity. 193

Figure C6. Infrared spectra of ligand precursors **KCp$^{\#}$PCh**. *Left:* full spectra. *Right:* closeup of the fingerprint region (525–1750 cm^{-1})..... 196

Figure C7. Infrared spectra of complexes **4.1Ch**. 196

Figure C8. Infrared spectrum of **KCp$^{\#}$PS** (black curve) compared to the corresponding Eu complex 4.1S (yellow curve). *Left:* full spectra. *Right:* closeup of the fingerprint region (525–1750 cm^{-1}). 197

Figure C9. Infrared spectrum of **KCp$^{\#}$PSe** (black curve) compared to the corresponding Eu complex 4.1Se (brown curve). *Left:* full spectra. *Right:* closeup of the fingerprint region (525–1750 cm^{-1}). 197

Figure C10. Infrared spectrum of **KCp$^{\#}$PTe** (black curve) compared to the corresponding Eu complex 4.1Te (green curve). *Left:* full spectra. *Right:* closeup of the fingerprint region (525–1750 cm^{-1})..... 198

Figure C11. CAM-B3LYP/def2-TZVPD optimized geometries of **KCp$^{\#}$PCh**. White = H, black = C, blue = N, orange = P, yellow = S, purple = K, brown = Se, light green = Te. 198

Figure C12. Comparison of experimental and calculated vibrational frequencies for **KCp$^{\#}$PS** (left), **KCp$^{\#}$PSe** (middle), and **KCp$^{\#}$PTe** (right) The solid blue lines are linear fits of the equation $y = mx + b$ to the data. Best-fitting parameters are given in Table C2..... 198

Figure C13. Temperature-dependent signal fluctuation $\delta I/I$ in the range 675-775 nm (outside the Eu^{II} components) for **4.1S** under applied magnetic fields of (a) 0.1, (b) 0.25, (c) 0.5, and (d) 1.0 T. The solid blue lines are linear fits of the equation $y = mx + b$ to the data. Best-fitting parameters are given in Table C7. 204

Figure C14. Temperature-dependent signal fluctuation $\delta I/I$ in the range 675-775 nm (outside the Eu^{II} components) for **4.1Se** under applied magnetic fields of 0.25 (top), 0.5 (middle), and 1.0 T (bottom). The solid blue lines are linear fits of the equation $y = mx + b$ to the data. Best-fitting parameters are given in Table C7. 205

Figure C15. Temperature-dependent signal fluctuation $\delta I/I$ in the range 675-775 nm (outside the Eu^{II} components) for **4.1Te** under applied magnetic fields of 0.25 (top), 0.5 (middle), and 1.0 T (bottom). The solid blue lines are linear fits of the equation $y = mx + b$ to the data. Best-fitting parameters are given in Table C7. 206

LIST OF TABLES

Table 1.1. Comparison of the characteristics of 4*f*-4*f* and 4*f*-5*d* transitions in lanthanide spectroscopy. 8

Table 1.2. Survey of Eu^{II}-based luminescence thermometers until 2022. 15

Table 2.1. Comparison of the highest-performing band-shift luminescence thermometers reported to date. Adapted from [99]. 24

Table 2.2. Selected metrical parameters from crystal structures of **2.1** at various temperatures, in comparison to the emission peak energy. 28

Table 2.3. Comparison of metrical parameters between **2.1** and **2.2** at 203 K. 32

Table 3.1. Luminescence properties and thermometric performance of complexes **2.1**, **2.2**, **3.1–3.7**. 49

Table 3.2. Comparison of various methods of estimating the donor strength of cyclopentadienyl ligands L = η^5-C_5Me_4R, and evaluation of how accurately each predicts the experimentally-determined emission energies of complexes $[LEu(\mu\text{-}BH_4)(THF)_2]_2$ (**2.1**, **3.1–3.4**). 52

Table 3.3. Selected metrical parameters from crystal structures of **3.1** at various temperatures, in comparison to the energy at the emission band maxima. A statistically significant difference between two values is indicated via coloured dividing lines (*vide supra*). 53

Table 3.4. Best-fitting parameters for the linear fits given in Figure 3.19. 53

Table 3.5. Best-fitting parameters for the linear fits given in Figure 3.20. 53

Table 3.6. Selected metrical parameters from crystal structures of **3.2** at various temperatures, in comparison to the energy at the emission band maxima. A statistically significant difference between two values is indicated via coloured dividing lines (*vide supra*). 56

Table 3.7. Best-fitting parameters for the linear fits given in Figure 3.21. 56

Table 3.8. Best-fitting parameters for the linear fits given in Figure 3.22. 56

Table 3.9. Selected metrical parameters from crystal structures of **3.3** at various temperatures, in comparison to the energy at the emission band maxima. A statistically significant difference between two values is indicated via coloured dividing lines (*vide supra*). 59

Table 3.10. Best-fitting parameters for the linear fits given in Figure 3.23. 59

Table 3.11. Best-fitting parameters for the linear fits given in Figure 3.24. 59

Table 3.12. Selected metrical parameters from crystal structures of **3.4** at various temperatures, in comparison to the energy at the emission band maxima. A statistically significant difference between two values is indicated via coloured dividing lines (*vide supra*). 62

Table 3.13. Best-fitting parameters for the linear fits given in Figure 3.25. 62

Table 3.14. Best-fitting parameters for the linear fits given in Figure 3.26. 62

Table 3.15. Selected metrical parameters from crystal structures of **3.6** at various temperatures, in comparison to the energy at the emission band maxima. A statistically significant difference between two values is indicated via coloured dividing lines (*vide supra*). 65

Table 3.16. Best-fitting parameters for the linear fits given in Figure 3.27. 65

Table 3.17. Best-fitting parameters for the linear fits given in Figure 3.28. 65

Table 3.18. Temperature-dependence of the Eu-basal plane distance (in Å) of complexes **2.1**, **3.1–3.4** and **3.6**, which are visualized in Figures 3.[20, 21, 22, 23, 24, 25, 26, 27, 28]l, 3.30k, 3.31 and 3.33. 71

Table 4.1. Selected metrical parameters of **4.1Ch**. Distances are given in Å and angles are given in degrees. 91

Table 4.2. Summary of thermometric figures of merit obtained for **4.1Ch** applied as probes for MCD-based thermometry. 119

Table A1. Selected bond lengths/interatomic distances and angles around europium of **2.1** 140

Table A2. Shape analysis of **2.1**, from the 203 K crystal structure, using SHAPE 2.1. Values in table are the continuous shape measures (dimensionless) for each idealized geometry. 140

Table A3. TD-DFT (B3LYP) calculated vertical excitations for the first 50 electronic transitions, with the corresponding oscillator strength and difference densities of **2.1** (truncated structure) measured at 90 K (isovalue 0.003). Transitions are sorted by their oscillator strength. 142

Table A4. TD-DFT (B3LYP) calculated vertical excitations for the first 50 electronic transitions with the corresponding oscillator strength and difference densities of **2.1** (truncated structure) measured at 270 K (isovalue 0.003). Transitions are sorted by their oscillator strength. 145

Table B1. Best-fitting parameters for the Boltzmann-type function $y = A_2 + \frac{(A_1 - A_2)}{1 + e^{[x - x_0/dx]}}$ fitted to the energies at the emission band maxima for complexes **3.1–3.4**, **3.6** and **3.7** (Figure 3.18a). Best-fitting parameters for **2.1** are given in Figure 2.6. 178

Table B2. Thermal expansion coefficients[56,176] for complexes studied via variable-temperature SCXRD. 182

Table C1. Comparison of metrical parameters between the two uniquely-defined half-molecules in the asymmetric unit of the crystal structure of **4.1Se**. "Fragment 1" contains Eu1 and associated atoms, and "Fragment 2" contains Eu2 and associated atoms. All distances are given in angstroms, and all angles are given in degrees. 193

Table C2. Best-fitting parameters for the linear fits given in Figure C12. 199

Table C3. Selected vibrational modes used to scale the frequencies of **KCp$^{\#}$PCh**, and their assignments. Raw calculated frequencies were scaled according to the parameters in Table C2. 199

Table C5. Performance comparison of selected band-shift luminescence thermometers. 201

Table C6. Best-fitting parameters for the sigmoidal logistic function $\Delta = \frac{A_1 - A_2}{1 + (x/x_0)^p} - A_2$ fitted to the thermometric parameters Δ shown in Figures 4.26-4.28. 202

Table C7. Best-fitting parameters for the linear fits given in Figures C13-15. 207

Table C8. Performance comparison of magnetic circular dichroism thermometers reported to date. 208

LIST OF ABBREVIATIONS AND SYMBOLS USED

Å	Angstrom (10^{-10} meters)
ΔA	differential absorption
α_V	isotropic thermal expansion coefficient
AC	alternating current
acac	acetylacetone, acetylacetonate, 2,4-pentanedion(ate) [ligand]
Ad	adamantane, or 1-adamantyl [group, substituent]
amu	atomic mass unit
Ar*	2,6-bis(2,4,6-triisopropylphenyl)phenyl [group, substituent]
ATR	attenuated total reflectance
Avg.	average
bdp	bis(dimethylamino)phosphino [group, substituent]
bpm	2,2′-bipyrimidine [ligand]
CASSCF	complete active-space self-consistent field
CCD	charge-coupled device
CCDC	Cambridge Crystallographic Data Centre
cent	centroid
CGC	constrained-geometry complex
Ch	chalcogen [group 16 element]
CIE	Commission Internationale de L'Éclairage
cm^{-1}	wavenumber
CMOS	complementary metal oxide semiconductor
COT	cyclooctatetraendiyl
Cp	cyclopentadienyl
Cp#	1,2,3,4-, *OR* a 1-substituted 2,3,4,5-, tetramethylcyclopentadienyl
Cp*	pentamethylcyclopentadienyl
CSD	Cambridge Structural Database
CShM	continuous shape measure
χ	magnetic susceptibility
χT	magnetic susceptibility-temperature product
d	doublet [e.g., as an NMR resonance descriptor]
D	axial zero-field splitting parameter
DC	direct current
DEPT	distortionless enhancement by polarization transfer [NMR technique]
DFT	density functional theory
DME	1,2-dimethoxyethane [solvent]
δ	chemical shift [NMR spectroscopy] [when used alone]
Δ	thermometric parameter [when used alone]
ΔE	change in energy
E	energy
E	rhombic zero-field splitting parameter
E^0	standard electrode potential vs. the standard hydrogen electrode
EI	electron impact [mass spectrometry]
ELI	electron localizability indicator

eq.	molar equivalents
eqn.	equation
esu	estimated standard uncertainty
Et	ethyl [group, substituent]
FTIR	Fourier transform infrared [spectroscopy]
g_J	Landé [total angular momentum] *g*-factor
GB	gigabytes [computing]
GHz	gigahertz
GP	general procedure
H	auxiliary magnetic field [also called "applied" or "external" field]
HAR	Hirshfeld atom refinement
HMBC	heteronuclear multiple bond correlation [NMR technique]
hr	hour
HRMS	high-resolution mass spectrum/spectrometry
HSQC	heteronuclear single quantum coherence [NMR technique]
Hz	hertz
I_n	integrated intensity of a selected spectral region *n*
*i*Pr	isopropyl [group, substituent]
J	total angular momentum quantum number *OR* magnetic coupling constant *OR* NMR coupling constant
KHMDS	potassium hexamethyldisilazide
L	total orbital angular momentum quantum number
λ	wavelength
λ_{em}	wavelength at the emission maximum
λ_{ex}	excitation wavelength
lcp	left circularly polarized [light]
LIR	luminescence intensity ratio
Ln	lanthanide(s)
m	medium [IR spectral feature descriptor] OR multiplet [e.g. as an NMR resonance descriptor]
M	magnetization
M	molarity [moles/liter]
MCD	magnetic circular dichroism
mdeg	millidegree
Me	methyl [group, substituent]
MHz	megahertz
m_ℓ	magnetic quantum number
MLCT	metal-to-ligand charge transfer
mmu	milli(mass unit) [x10^{-3} mass units]
MOF	metal-organic framework
mmol	millimole
MPMS	Magnetic Property Measurement System
m/z	mass-to-charge ratio
μ_B	Bohr magneton (also written β)
μs	microsecond

n	"normal" [i.e., straight-chain]
N	Avogadro's number
n.c.	no correlation
n.d.	not determined
NIR	near-infrared [spectral region]
NMR	nuclear magnetic resonance [spectroscopy]
ns	nanosecond
$\tilde{\nu}$	spatial frequency
Oe	Oersted [unit of auxiliary magnetic field $H \approx 0.0001$ T]
Ph	phenyl [group, substituent]
phen	phenanthroline [ligand]
PL	photoluminescence
PmAm	2-amidinopyrimidine [ligand]
PMT	photomultiplier tube
ppm	parts per million
PTFE	poly(tetrafluoroethylene) [Teflon]
py	pyridine [ligand]
PyAm	2-amidinopyridine [ligand]]
quant.	quantitative [≥95%] yield
RAM	random-access memory [computing]
RASSI	restricted active-space self-consistent field
rcp	right circularly polarized [light]
R_f	chromatographic retention factor
r.t.	room temperature
s	singlet [e.g. as an NMR resonance descriptor] *OR* strong [IR spectral feature descriptor]
S	total spin quantum number *OR* sensitivity
S_a	absolute sensitivity
S_r	relative sensitivity
S_1	first singlet excited state
SCF	self-consistent field
SCXRD	single-crystal X-ray diffraction
SHE	standard hydrogen electrode
SOC	spin-orbit coupling
solv	solvent ligand
SQUID	superconducting quantum interference device
SVP	double-zeta valence + polarization [of a basis set]
σ	uncertainty of a measurement
T	Tesla [unit of magnetic flux density $B \approx 10\,000$ Oe]
T_1	first triplet excited state
TD-DFT	time-dependent density functional theory
THF	tetrahydrofuran
THT	tetrahydrothiophene
TMEDA	*N,N,N′,N′*-tetramethylethylenediamine
TMG	trimethylgermanyl [group, substituent]
TMS	trimethylsilyl [group, substituent]

TPPO	triphenylphosphine oxide
TZVP	triple-zeta valence + polarization [of a basis set]
TZVPD	diffuse triple-zeta valence + polarization [of a basis set]
TZVPP	triple-zeta valence + double polarization [of a basis set]
ΔT	temperature uncertainty (also written δT)
τ	excited-state lifetime *OR* torsional twist angle
UDEFT	uniform driven equilibrium Fourier transform [NMR technique]
UV	ultraviolet [spectral region]
UVA	ultraviolet-A [spectral region], taken as 315-400 nm (31 746–25 000 cm^{-1})
V	volt
V	volume [of a unit cell]
V_{bur}	buried volume
V_0	volume [of a unit cell] at the highest measured temperature
Vis	visible [spectral region]
vs	very strong [IR spectral feature descriptor]
VTVH	variable-temperature and variable-field
vw	very weak [IR spectral feature descriptor]
w	weak [IR spectral feature descriptor]
W	watt
wt%	percent by weight
Z	number of formula units (i.e., molecules) in the unit cell of the crystal structure
ZFS	zero-field splitting

CONTRIBUTIONS

Peer-reviewed contributions

A list of works contributed during this degree is given below. The symbol † denotes an equal contribution to the indicated work.

1. **Diaz-Rodriguez, R. M.**;† Gálico, D. A.;† Chartrand, D.; Suturina, E. A.; Murugesu, M. Toward Opto-Structural Correlation to Investigate Luminescence Thermometry in an Organometallic Eu(II) Complex. *J. Am. Chem. Soc.* **2022**, *144* (2), 912–921. DOI: 10.1021/jacs.1c11076
2. **Diaz-Rodriguez, R. M.**; Kitos, A. A.; Murugesu, M. Expanding the Series of Alkali Metal Plumbolyl Complexes to Na and K. *Dalton Trans.* **2022**, *51* (38), 14420–14428. DOI: 10.1039/D2DT02615E *[Not included in this thesis]*
3. Bispo-Jr, A. G.; Gálico, D. A.; **Diaz-Rodriguez, R. M.**; Ovens, J. S.; Sigoli, F. A.; Murugesu, M. The Role of Terminal Ligands in the Slow Relaxation of Magnetisation and Luminescence Thermometry of Dinuclear Nd^{III} Complexes. *Inorg. Chem. Front.* **2023**, *10* (13), 3929–3939. DOI: 10.1039/D3QI00969F *[Not included in this thesis]*
4. **Diaz-Rodriguez, R. M.**; Gálico, D. A.; Chartrand, D.; Murugesu, M. Ligand Effects on the Emission Characteristics of Molecular Eu(II) Luminescence Thermometers. *J. Am. Chem. Soc.* **2024**. DOI: 10.1021/jacs.4c13805
5. **Diaz-Rodriguez, R. M.**; Gálico, D. A.; Murugesu, M. Exploring a New Family of (Phosphino-chalcogenoyl)Europocenes for Magneto-Optical Thermometry. *Angew. Chem. Int. Ed.* **2025**, *64* (50), e202517812. DOI: 10.1002/anie.202517812

CHAPTER 1
Introduction to Lanthanide Luminescence, Luminescence Thermometry, and the Special Properties of Divalent Europium

1.1 Opening remarks

The *f*-block elements, occupying their distinctive position at the foot of the periodic table, are often regarded as mere curiosities by many, including many chemists. However, it might be surprising to discover that these elements are responsible for numerous phenomena that define our daily lives. High-strength permanent magnets used in data storage devices, electric motors, generators, and audio devices such as loudspeakers, are made possible by neodymium and samarium. The red, green, and blue pixels in LED displays primarily come courtesy of europium and terbium.[1] Gadolinium has attracted fame and notoriety for its well-known use as a contrast agent for magnetic resonance imaging.[2,3] Holmium[4,5] and thulium[6] are used broadly in medical and industrial radiography and lasing technologies. Even radioactive elements have their place in society; for example, americium is a common component of smoke detectors.[7] Perhaps the best-known among these elements are uranium[8] and thorium,[9] whose radioactive decay can be harnessed to provide abundant, low-emission energy to power entire cities or even countries. Indeed the internet, one of the most transformative technologies ever developed, depends on the specific properties of erbium and praseodymium; their role in long-distance fiber-optic telecommunications is crucial to connecting the world at great speed.[1,10]

Although the heavy *actinides* that populate the 5*f* series do see practical applications in nuclear medicine and atomic energy, their oftentimes intense radioactivity and general lack of natural abundance limit their utility. The elements of the 4*f* series on the other hand, given the moniker *lanthanides* after their prototype lanthanum (element 57), are broadly employed in a plethora of critical applications, and are among the most important classes of natural resources in the world. As can be inferred from the examples given above, the applications of lanthanides arise largely from two factors: their powerful magnetic properties, and their unique and interesting luminescence.

1.2 The electronic structure of lanthanide ions

The defining feature of the lanthanides (hereinafter abbreviated Ln where appropriate) is the participation of 4*f* orbitals in the valence electron configurations of these elements. Each elemental lanthanide has an electronic configuration of [Xe]$4f^n6s^2$ (Pr, Nd, Pm, Sm, Eu, Tb, Dy, Ho, Er, Tm, Yb) or [Xe]$4f^n5d^16s^2$ (La, Ce, Gd, Lu).[11] As a result, the most stable oxidation state for all the lanthanides is +3, and the majority of lanthanide compounds are those of the trivalent ions. With a few exceptions (including La^{III} itself!), lanthanide ions have a valence consisting only of 4*f* electrons, and this electronic configuration gives rise to several factors that form the origin of their sought-after characteristics.

Firstly, there are seven n*f* orbitals, corresponding to magnetic quantum numbers $m_\ell = 0, \pm1, \pm2, \pm3$; this means that an *f*-block element can carry up to seven unpaired electrons, the most possible for a single ion based on our current understanding of the periodic table. Compounds of lanthanides therefore often bear large total spin *S*, which is one component of their favourable magnetic properties. Secondly, the three nodes present in 4*f* orbitals and hence the many (4, 6 or 8) small lobes impart a strong directionality (Figure 1.1, left), which ultimately results in the electron density of free lanthanide ions having a substantial intrinsic anisotropy.[12] This characteristic has been thoroughly explored and exploited in the field of single-molecule magnetism, where tailored ligand fields designed to maximize the

intrinsic anisotropy of a given ion are used to enhance the ability of bespoke lanthanide complexes to emulate the behaviour of bulk permanent magnets.[13] Thirdly, and perhaps most importantly, the 4*f* valence orbitals have the unusual property of being extremely spatially contracted, held tightly to the lanthanide nucleus and buried by a shield of filled 5*s* and 5*p* orbitals with greater radial extension (Figure 1.1, right).[14–16] This has two implications. The first is that the chemical properties of the lanthanide elements are broadly very similar, which is both an advantage (isostructural materials across the series are often attainable, therefore periodic trends can be easily studied) and a challenge (separation of *f*-block elements from one another tends to be very difficult).[16–19] The major distinction between the lanthanides is that the 4*f* valence electrons themselves provide ineffective shielding of the nuclear charge, resulting in the well-known "lanthanide contraction": a much larger-than-expected decrease in atomic/ionic radius across the period.[19] The second implication is that the limited radial extension prevents efficient overlap of the 4*f* valence electron density with the electron density of ligands, thus resisting the influence of the coordination sphere on the electronic structure of the ion. Consequently, lanthanide ions retain a large total orbital angular momentum L, as the small ligand-field splitting is insufficient to cause appreciable disruption. Lanthanide ions therefore exhibit a significant spin-orbit coupling (from 600 to nearly 3000 cm^{-1}),[15,16] such that a Russel-Saunders (LS) "intermediate" coupling scheme and the use of the total angular momentum quantum number $J = L + S$ becomes most appropriate to describe their electronic structure.[11]

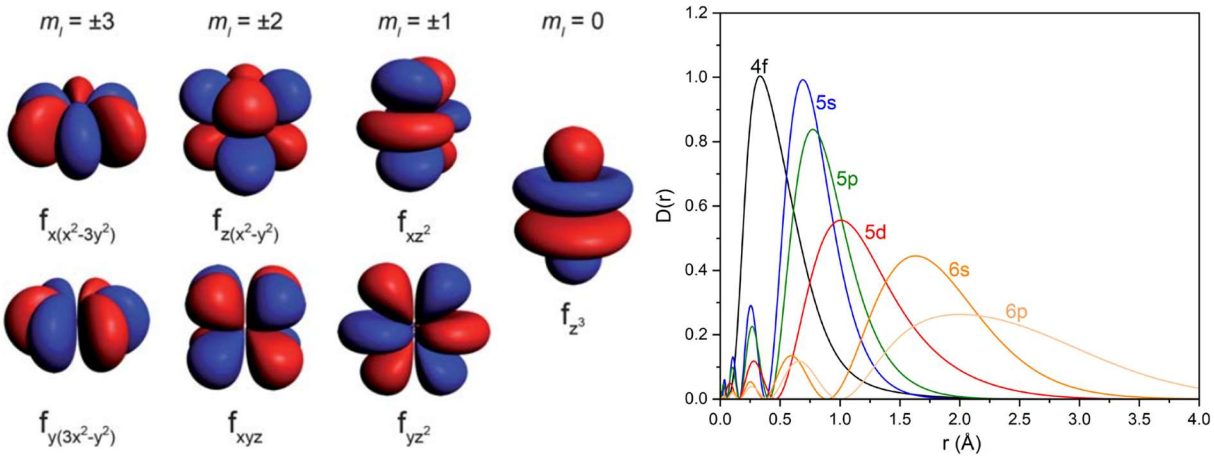


Figure 1.1. *Left*: Graphical representations of the general set of 4*f* orbitals. Reproduced with permission from [12]. *Right*: Radial distribution functions for the 4*f*, 5*s*, 5*p*, 5*d*, 6*s*, and 6*p* orbitals of Nd^0, illustrating the significantly low radial extension of the 4*f* orbitals relative to the others. Reproduced from [14] under the terms of the Creative Commons Attribution Non-Commercial No Derivatives License.

Taken together, the above factors give rise to a characteristic energy landscape for the lanthanide ions, which can be imagined as a hierarchical perturbation on a "central field",[16,20] illustrated in Figure 1.2.[20] In the case of a Ln^{III} compound, the $4f^n$ electronic configuration is split into several ^{2S+1}L terms by interelectronic repulsion of the 4*f* electrons, which is the most significant effect in the manifold (on the order of 10^4 cm^{-1}). Each of the ^{2S+1}L terms are further split by the spin-orbit coupling into various $^{2S+1}L_J$ levels according to the total angular momentum of the system in question, with a magnitude on the order of 1000 cm^{-1}. Finally, the ligand field is applied to split each $^{2S+1}L_J$ level into a number of m_J states separated by some 100s of cm^{-1}. In the presence of an applied magnetic field H, the Zeeman effect can cause the m_J states to be even further split, by a few wavenumbers, into $\pm m_J$ sublevels.[20] The result of all of this is that

the trivalent lanthanide ions exhibit a complex, "ladder-like" pattern of 4*f* energy levels (see Figure 1.3) which, due to the typically minor effect of the ligand field on the highly-shielded 4*f* valence orbitals, are almost invariant with coordination environment for ions of a given element.[15]

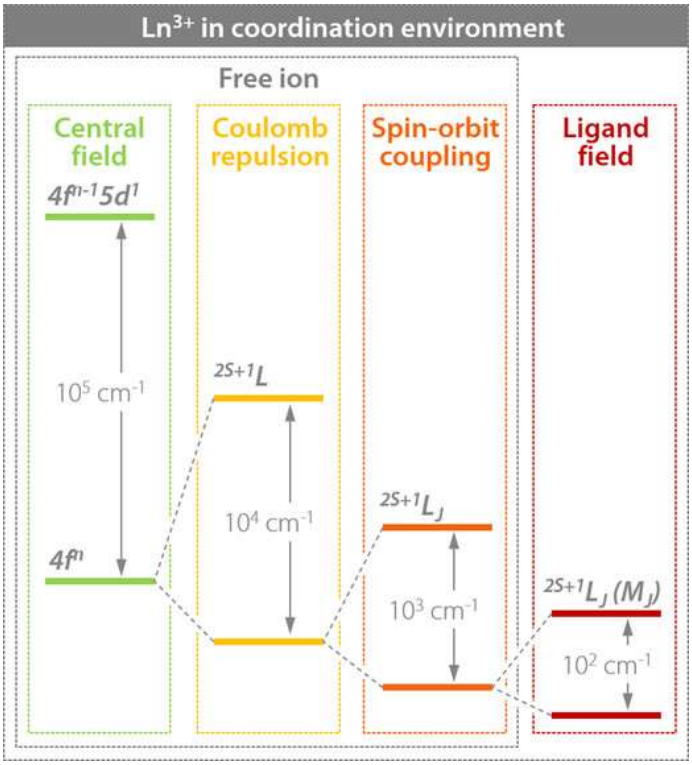


Figure 1.2. Schematic representation of the hierarchy of various factors affecting the electronic structure of lanthanide ions in coordination compounds. Reproduced with permission from [20].

1.3 Luminescence of trivalent lanthanide ions

The unique pattern of 4*f* energy levels in trivalent lanthanide ions is responsible for a correspondingly unique set of optical properties in Ln^{III} compounds, which in general are extremely well-studied for their luminescence. Given the characteristics of 4*f* orbitals, the particular arrangement of energy levels in the $4f^n$ manifold for these ions, and the fact that any alternative electronic configurations tend to be quite energetically high-lying, electronic absorption and emission occur primarily via intraconfigurational 4*f*-4*f* transitions.[21] These transitions manifest as distinctive, very narrow bands, many of which fall in the ultraviolet (UV) to near-infrared (NIR) spectral regions. Since the positions of the associated levels are usually affected very little by changes in the coordination environment, the positions of the absorption and emission bands are also little affected; hence, the optical spectra of Ln^{III} compounds are highly diagnostic "fingerprints" of the ion(s) involved.[20,22]

The optical properties of lanthanide ions can be exploited and studied in the solid state or in solution *via* several matrices, including by doping into various inorganic host lattices, as simple Ln salts, or in organic-ligand-bound Ln coordination complexes. A comprehensive picture of the energy landscapes of all Ln^{III} were developed using spectroscopic methods, and the landmark studies by Dieke[23] and Carnall[24] tabulating values for and assignments of the identities of the energy levels in each Ln^{III} are of particular importance. Obtaining information on the energy levels of the true free ions can be achieved by analyzing

ionized gases of the elements.[25] Doing so would allow full disambiguation of all environmental effects, since any coordinating species will have some effect, even if small, on the energy levels. Doping of the ions into a fluoride host lattice (e.g. LaF_3) is a much more practical alternative, and provides a useful approximation to the free-ion behaviour. This is because of the weak ligand field generated by fluoride alongside the assumption that the Ln-F interactions are essentially completely ionic with a negligible covalent component. Studying the corresponding homoleptic aquo complexes serves a similar purpose. Due to the ongoing technological importance of lanthanide luminescence, the values and the associated assignments of the energy levels have been continually refined; the most current version to date, prepared by Nielsen and Sørensen for Ln^{III} aquo species in 2025, is shown in Figure 1.3.[26]

Studies of simple lanthanide salts are useful from a fundamental perspective, and Ln-doped inorganic solids are important for a number of applications (phosphors, scintillators, and lasers, for example).[1] However, in this thesis, we will focus instead on the molecular materials; that is, discrete lanthanide coordination complexes with organic ligands. Molecular materials have a distinct advantage over other types of systems, in that the coordination environment of a given molecular compound can be finely and rationally tuned, and therefore its characteristics can be finely and rationally controlled. Furthermore, molecular materials with defined and reproducible structures allow for very detailed structural characterization, which can then be correlated to their optical and magnetic (and other) properties. These factors form the basis of a "*structure-property relationship"* approach to investigation.

Another reason metal-organic complexes are valuable when it comes to the luminescence of trivalent lanthanides in particular is related to a fundamental property of the 4*f*-4*f* transitions that characterize that luminescence. The oscillator strength of a transition (i.e., the probability that a given transition will occur) is governed by a set of quantum mechanical principles called *selection rules*, and transitions are either *allowed* or *forbidden* according to those rules.[16] Crucially, the characteristic 4*f*-4*f* intraconfigurational transitions of the Ln^{III} are formally forbidden by the Laporte rule and "should" have no oscillator strength at all.[27] It is important to note that Laporte's rule is valid specifically for electric dipole-type transitions in centrosymmetric systems.[21,28] Most real transitions do not occur at absolute zero in free ions between perfectly pure electronic states, nor in complexes with perfect centrosymmetry, so we can rationalize how the 4*f*-4*f* transitions can gain a bit of oscillator strength and become observable. Nevertheless, these transitions are in most cases very weak, translating to low absorbance and weak emission and hampering potential applications. On the other hand, the forbidden nature of these transitions lends them long lifetimes relative to e.g. organic chromo/fluorophores, on the order of microseconds up to some milliseconds.[16]

The limitation of low oscillator strength can be circumvented by choosing ligands for the Ln^{III} ion that contain, or are themselves, strong chromophores. The ligand, rather than the metal, can then be excited to a singlet excited state with suitable light, then, typically *via* the first triplet excited state after intersystem crossing, transfer the absorbed energy to the appropriate excited states of the coordinated Ln^{III} ion. The population of the excited states then relaxes by emission of photons in a manner consistent with the aforementioned energetic structure of the 4*f* levels, leading to a large enhancement in luminescence intensity and effectively combining the high oscillator strength of ligand-based transitions with the unique nature of lanthanide-centered emission. This arrangement is termed *sensitized luminescence*, often called the "*antenna effect*" in this context (Figure 1.4, left),[20–22] and offers the further benefit of very large pseudo-Stokes shifts.[16] A common ligand set for luminescent Ln^{III} complexes consists of a combination of β-diketonate (e.g., acetylacetonate, "acac") and neutral N^N-donor ligands (e.g. phenanthroline, "phen").[16]

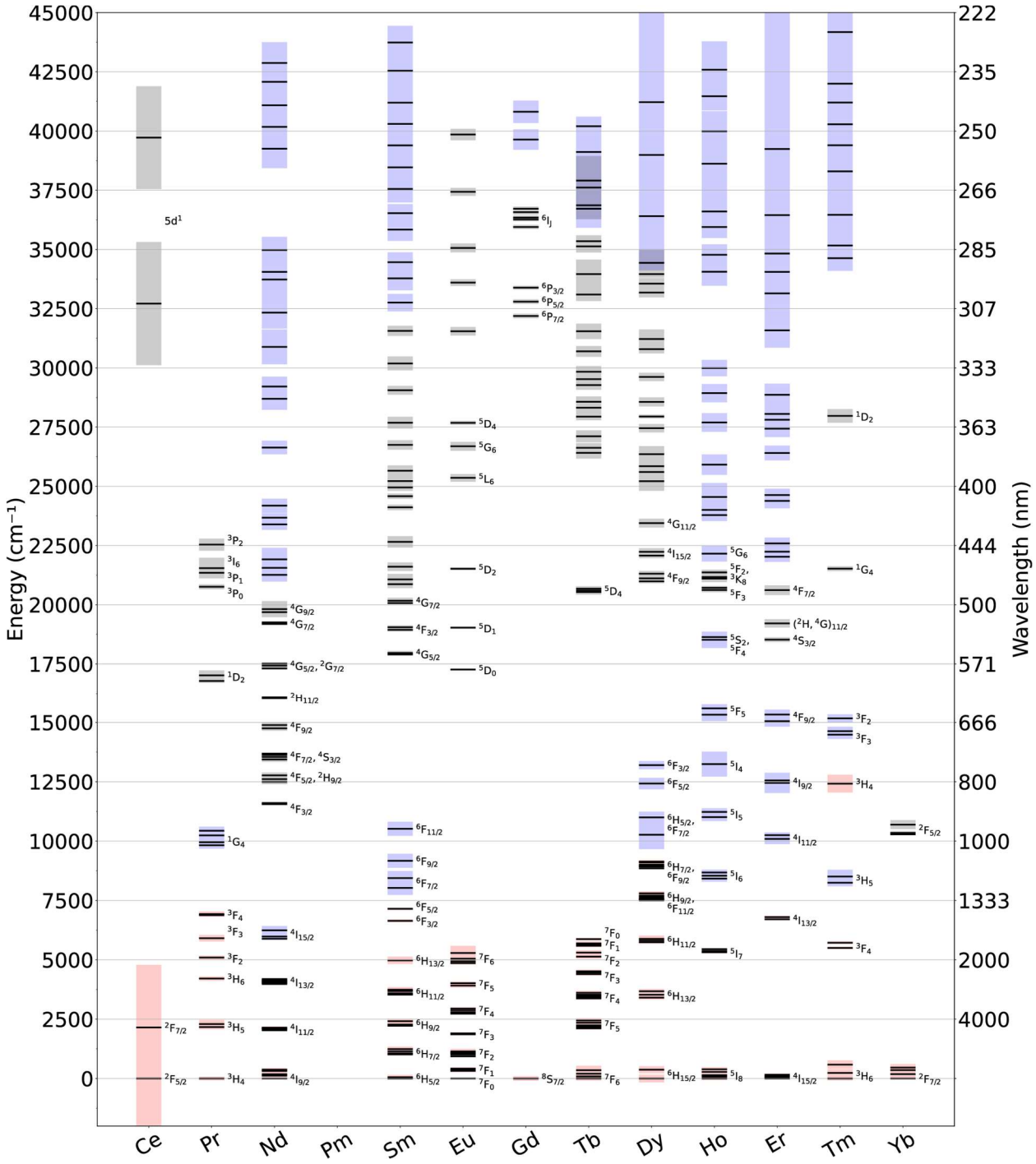


Figure 1.3. Diagram of energy levels for all trivalent lanthanide ions except Pm, obtained via optical absorption (blue boxes), photoluminescence excitation (grey boxes), and photoluminescence emission (red boxes) spectroscopy performed on the corresponding Ln^{III} aquo species as solutions in 100 mM $DClO_4$ in D_2O. Reproduced from [26] under the terms of the Creative Commons Attribution Non-Commercial No Derivatives License.

As a brief example, the emission spectrum of the trivalent terbium complex [$Tb^{III}(acac)_3(PyAm)$] (PyAm = 2-amidinopyridine)[29] is shown in Figure 1.4 (right), which demonstrates all the phenomena described in this section. The visible emissions of Tb^{III} originate from the $^5D_4$ emitter level and terminate in the ^7F manifold, which are separated due to the interelectronic repulsion splitting. The ^7F term is further split by the spin-orbit coupling into seven ^7F_J levels with $J = 0$–6, and the $^5D_4 \rightarrow {}^7F_J$ transitions produce several narrow (a few tens of nanometers wide) bands in the spectrum. The $^5D_4 \rightarrow {}^7F_5$ transition, whose barycenter occurs in the green region of the spectrum (~545 nm), is always the most intense, therefore Tb^{III} exhibits a characteristic bright green emission.[16]

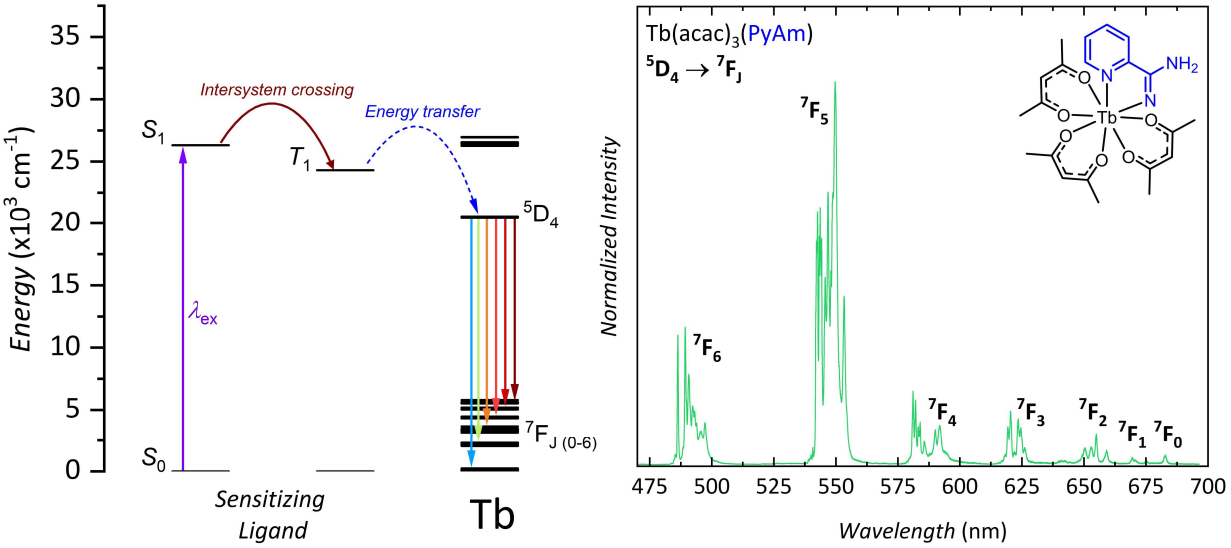


Figure 1.4. *Left:* Simplified schematic diagram of the "antenna effect" ("sensitized luminescence") showing the transfer of energy from an excited ligand chromophore to the bound metal center which eventually emits. The singlet and triplet excited states of the ligand are set at reasonable arbitrary positions[16] above Tb^{III} $^5D_4$, and the Tb manifold is based on the free-ion values from Carnall.[24] *Right:* Solid-state emission spectrum ($\lambda_{ex} = 323$ nm) of $Tb^{III}(acac)_3(PyAm)$ at 10 K, showing all seven $^5D_4 \rightarrow {}^7F_J$ transitions.

Moreover, it is evident that the predominant effect of the ligand field splitting in Ln^{III} complexes is to impart a fine structure to each of the transition bands (the m_J states). The number, intensity, and position of these peaks can vary drastically depending on the particular coordination environment of the ion, but do not much alter the observed colour of the emission. Nevertheless, these small perturbations applied by the ligand field are a rich field of opportunity when it comes to the design, study, and application of lanthanide luminophores.

1.4 The divalent lanthanides, and the special properties of Eu^{II}

Although the +3 oxidation state is the most stable for all the lanthanides, it is not the only one that is attainable or interesting. All the lanthanides can be obtained in their divalent forms with varying degrees of effort,[30,31] and some (Ce, Pr, Tb) have an accessible tetravalent state.[16,21] The divalent lanthanides are strongly reducing species and are generally unstable to oxygen and especially unstable to water, meaning that they are typically synthesized and studied in the solid state and/or under inert, non-aqueous conditions.[16] They find applications in chemical synthesis; e.g., the well-known blue solution of $SmI_2(THF)_n$ (THF = tetrahydrofuran) in THF is a flexible and selective reductant for a variety of organic functional groups,[32]

and complexes of various Ln^{II} are well-studied in photoredox, cross-coupling, and (de-)polymerization catalysis.[33–41]

Among the Ln^{II}, Eu^{II}, Yb^{II}, and Sm^{II} stand out from the others. These are frequently referred to as the "classical" divalent lanthanides and are the most thoroughly studied, because they are, in the given order, the most stable of the series. The relative stability of these ions can be explained by their electronic configurations, and is reflected in their reduction potentials. The reduction of Eu^{III} to Eu^{II} is rendered quite facile by the generation of a highly stabilized half-filled 4*f* valence shell, hence the reduction potential of the Eu^{II}-Eu^{III} redox couple is the smallest of all the Ln at only -0.35 V vs. the standard hydrogen electrode (SHE). Similarly, the reduction of Yb^{III} to Yb^{II} is facilitated by the generation of a full 4*f* shell, and the the Yb^{II}-Yb^{III} redox couple has the second-lowest reduction potential of -1.15 V vs. SHE. Samarium is somewhat of a unique case; the reduction of Sm^{III} to Sm^{II} generates an "almost half-full" $4f^6$ configuration that also bears zero total angular momentum *J* (*vide infra*), yielding the third-most stable Ln^{II} with a Sm^{II}-Sm^{III} redox potential of -1.55 V vs. SHE.[30]

The divalent ions also have useful optical and magnetic properties that are distinct from those of the trivalent ions. Although the Ln^{II} also exhibit similarly arranged intraconfigurational 4*f*-4*f* transitions in their optical spectra, those transitions are lower in energy and experience less splitting than the isoelectronic Ln^{III} congeners. This is a consequence of a lower effective nuclear charge in the more reduced species, which decreases the magnitude of both the interelectronic repulsion and the spin-orbit splitting.[30] However, perhaps the most important difference between the Ln^{II} and Ln^{III} is the presence of absorption and emission from *inter*configurational 4*f*-5*d* transitions in the former. The 5*d* excited states are well outside the UV-Vis-NIR region of the electromagnetic spectrum for most Ln^{III}, but are accessible to Ln^{II}, and are a defining property of many Ln^{II} systems. (Ce^{III} is the chief exception; compounds of this ion are also known for characteristic 4*f*-5*d* optical features.[42–46]) Unlike the 4*f*-4*f* transitions, 4*f*-5*d* transitions are allowed by the Laporte selection rule and therefore have much higher oscillator strengths, sometimes dominating the observed spectral features of the associated material. They also display shorter lifetimes, up to hundreds of nanoseconds in typical cases.[46] The 5*d* excited-state orbitals do not share the stereoelectronic characteristics that distinguish the 4*f* orbitals, being much more diffuse and radially expanded with a greater capacity for overlap with other orbitals, and exhibiting greater electron-phonon coupling than the 4*f* levels.[47] The 5*d* orbitals and therefore the energy of the excited states are accordingly strongly affected by the ligand field, and vary broadly with coordination environment[30,48] as a confluence of several factors. These include but are not limited to donor atom identity, metal-donor distance, distortion of the coordination polyhedron, metal-ligand covalency, and ligand polarizability.[46,49] In stark contrast to the sharp, highly-structured, diagnostic emission bands observed for Ln^{III} luminophores, 4*f*-5*d* emissions tend to be broad (up to hundreds of nm) and featureless (or grossly structured), and vary according to the particularities of each unique coordination environment in different compounds of the same ion. To illustrate, Figure 1.5 shows photoluminescence spectra for a series of Sm^{II} 15-crown-5 iodide complexes[50] that, depending on the coordination environment, exhibit emission arising from only 4*f*-4*f*, only 4*f*-5*d*, or both types of transitions simultaneously. The environmental sensitivity of 4*f*-5*d* transitions allows for tuning of the luminescence characteristics of 4*f*-5*d* emissive lanthanide materials over a broad range. A comparison of the properties of 4*f*-4*f* and 4*f*-5*d* transitions is summarized in Table 1.1.

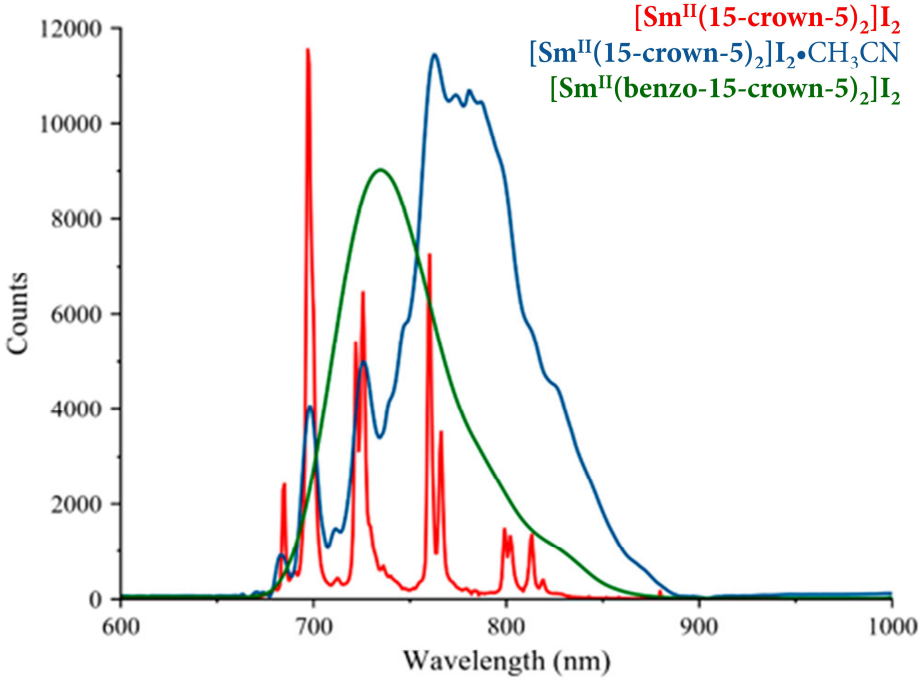


Figure 1.5. Photoluminescence spectra of Sm^{II} crown ether complexes in the solid state at 93 K, demonstrating emission from different types of transitions. $[Sm^{II}(15\text{-crown-}5)_2]I_2$ (red curve) exhibits emission only from intraconfigurational 4*f*-4*f* transitions; $[Sm^{II}(benzo\text{-}15\text{-crown-}5)_2]I_2$ (green curve) exhibits emission only from interconfigurational 4*f*-5*d* transitions; and $[Sm^{II}(15\text{-crown-}5)_2]I_2{\cdot}CH_3CN$ (blue curve) exhibits emission from a superimposed combination of both types of transition. Adapted with permission from [50].

Table 1.1. Comparison of the characteristics of 4*f*-4*f* and 4*f*-5*d* transitions in lanthanide spectroscopy.

Property	4*f*-4*f*	4*f*-5*d*
Bandwidth	Narrow (10^1 nm)	Often quite broad (10^2 nm)
Laporte selection	forbidden	allowed
Intrinsic intensity	Very weak	Strong to very strong
Environment sensitivity	Low; element-dependent	High; coordination-dependent
Lifetime	Long (up to some ms)	Moderate (up to ~10^2 ns)

With regard to the work presented in this thesis, we are most interested in the particular combination of properties exhibited by Eu^{II}, which make it an excellent candidate for application-focused functional luminescent materials. Eu^{III} already has a suite of unique properties, even among the lanthanides, that makes it valuable as a luminophore. For example, it has a $4f^6$ electron configuration with six unpaired electrons, but Hund's rules dictate that the ground state must have minimum J since the shell is less than half-full, resulting in a $^7F_0$ ground state for this particular combination of L and S.[16] (This also occurs for Sm^{II}, which is a reason for its relative stability, *vide supra*.) The lack of total angular momentum means that the ion should be diamagnetic,[11] making Eu^{III}-based materials generally uninteresting for applications focusing on magnetic properties, at least on paper. However, the first-excited $^7F_1$ level is very close to ground, being separated by only ~300-400 cm^{-1} from $^7F_0$;[24] it is only the thermal population of this state that imparts a small magnetic susceptibility to Eu^{III} compounds.[11] This enables some applications of the

magnetic properties of Eu^{III}, such as its complexes often being used as "shift reagents" for nuclear magnetic resonance (NMR) spectroscopy.[51–53] The visible emissions of Eu^{III} originate from the $^5D_0$ emitter level, and the most intense transition in Eu^{III} compounds tends to be the $^5D_0 \rightarrow {}^7F_2$ centered at ~615 nm, producing a distinctive red luminescence.

In dramatic contrast, the $4f^7$ configuration of Eu^{II} is strongly paramagnetic, having zero L due to the half-full shell but making full use of its seven unpaired electrons for a ground state described as $^8S_{7/2}$, isoelectronic with its heavier neighbour, Gd^{III}. As for Gd^{III}, the lowest excited $4f$ level ($^6P_{7/2}$) is well into the near-UV, so the low-lying $4f^65d^1$ excited state dominates the properties of this ion with a high-intensity, often visible, $5d \rightarrow 4f$ emission.[30,46,54] Crucially, the energy of this emission is extremely variable with coordination environment, and Eu^{II}-containing compounds taking various forms have been reported with emission maxima that span the near-UV all the way to the near-IR. [48,55–61] On the high end, for example, $BaAl_3BO_7:Eu^{II}$ has a $4f^6[\,^7F_0]5d^1 \rightarrow 4f^7[\,^8S_{7/2}]$ emission in the UVA, at 360 nm (27 727 cm^{-1}).[48,62] $Eu^{II}I_2$, a common Eu^{II} starting material, exhibits blue $5d \rightarrow 4f$ luminescence at 432 nm (~23 148 cm^{-1}).[63] Similarly on the low end, $Ba_4Li(BN_2)_3:Eu^{II}$ shows a broad emission in the near-IR, reaching a maximum at 880 nm (11 364 cm^{-1}).[64] Further, as described above, the high relative stability of Eu^{II} means that its compounds are the most synthetically accessible of all Ln^{II}, despite ambient stability still being a concern in many cases. This expands the chemical space that can be investigated for novel architectures with favourable properties. Indeed, molecular complexes of Eu^{II}, in particular crown ether/cryptand complexes,[55,59,65–81] pyrazolylborates,[57,82–85] and substituted metallocenes,[58,60,61,86–89] are also well-studied luminescent materials, and demonstrate a similar exquisite tunability of emission properties to the well-understood doped inorganic matrices. The fact that Eu^{II} has luminescence characteristics that are extremely susceptible to modification, in addition to strong paramagnetism, suggests that powerful multifunctional systems might be attainable with Eu^{II}. That versatility, in our view, makes it an attractive target for new (magneto-)optical materials towards applications including theranostics, advanced lighting, spintronics, sensors, and, most interestingly to us, luminescence thermometry.

1.5 Luminescence thermometry

Control over temperature is of paramount importance to many technological applications, and temperature sensors claim, by a significant margin, the largest market share of sensors overall.[90] For example, the generation and dissipation of heat is a significant (and sometimes the most important) factor limiting the performance of high-power computing systems. The importance is further magnified with the progression of miniaturization and advent of quantum computing, where increasingly dense packing of nanosized (or smaller) electronic or spintronic elements may challenge the ability of a device to dissipate generated heat. Thermal stress is also poorly tolerated in biological systems; advanced theranostic techniques that examine and treat diseases at or below the cellular level may require temperature control to curtail damage or to effect therapeutic outcomes. Generally speaking, the measurement of temperature in moving objects is also difficult. In such applications, there is a requirement to measure temperature in locations that are difficult to access with conventional thermometric devices, which usually require colocation and good contact between the system and the measurement probe. Where this is not possible, an alternative measurement method is required. One such method is called *luminescence thermometry*,[91–93] a term which describes several related approaches whereby temperature is quantified *via* corresponding changes in the electronic emission of a luminescent chemical probe. Luminescence thermometry is a so-called "remote detection" method, meaning that the probe and the detector do not have to be physically coupled, which greatly increases the flexibility of measurement systems and prevents the thermometer itself

from disturbing the system under test. Given that the thermometric probe can theoretically consist of any emissive species, down to a single molecule,[94] luminescence thermometry can achieve ultrahigh spatial resolution, making it well-suited to nanoscale applications. As the probe is a chemical entity, myriad possible options exist for selecting a probe with the exact physicochemical characteristics necessary for an arbitrary application, and burgeoning research continues to expand these options.

There are several different luminescence characteristics that can be used, alone or in combination, for temperature readout.[91] When used in this way, these characteristics are termed *thermometric parameters* (Δ). Thermometry can, in principle, be achieved by monitoring the intensity of a single transition, although this is seldom practiced. Emission intensities are strongly dependent on the specific conditions of each experimental setup and not intuitively proportional to the nature of the emitting species, so it cannot be expected that a predictable intensity will be obtained at a given temperature on different batches, different instruments, or even at different times. This limitation is handily circumvented by instead using the ratio between the intensities of two (or more) different emission bands, a self-calibrating approach termed *luminescence intensity ratio* (LIR) or *ratiometric thermometry*. As the emission bands in many materials are broadened as a direct result of phonon coupling, thermometry is possible *via* quantitative tracking of changes in emission bandwidth with an appropriate system. Some materials exhibit temperature-dependent optical polarization, which can similarly be leveraged for temperature quantitation. In *band-shift thermometry*, temperature can be measured based on a correlated change in the position of the barycenter or maximum of an emission band. One advantage of this approach is that the emission wavelength is an intrinsic property of the emitting species and is thus invariant with experimental conditions, making for a robust methodology with high repeatability. Finally, changes in emission lifetime with temperature comprise a sensitive thermal probe, despite requiring more complex instrumentation to quantify.

When evaluating the performance of a given luminescence thermometer, various figures of merit are used to enable comparison. Some of the most important ones are described as follows. The *sensitivity,* S, of a thermometer reflects its ability to respond to changes in temperature (higher is better), and usually takes a maximum value at some temperature. Two kinds of sensitivities are defined: the absolute sensitivity S_a (Eqn. 1.1), expressed in units of the monitored parameter per increment temperature,

$$S_a = \frac{\partial \Delta}{\partial T} \tag{1.1}$$

and the relative sensitivity S_r (Eqn. 1.2), often expressed as percent per increment temperature,

$$S_r(\%) = \left[\frac{\left(\frac{\partial \Delta}{\partial T}\right)}{\Delta}\right] \cdot 100 \tag{1.2}$$

A value of 1 % K^{-1} is usually taken as a threshold of practicality.[91,95] The *temperature uncertainty* ΔT (Eqn. 1.3) is a measure of the smallest increment of temperature that can be resolved by the thermometer (lower is better),

$$\Delta T = \frac{1}{S} * \sigma \tag{1.3}$$

where $\sigma = \frac{\delta \Delta}{\Delta}$ is the uncertainty in the instrumental determination of Δ. Each thermometer will have a *sensing range* representing the limits of temperature that can be measured with it. A larger range is usually better, but there exist very sensitive thermometers with very small sensing ranges and relatively insensitive thermometers with very broad sensing ranges, which are both still useful depending on the desired application. Additional figures of merit are considered depending on the systems at hand and their target applications.[90]

Due to their special optical properties, lanthanide-based luminescent materials are a popular choice for luminescence thermometry applications across all approaches. Those materials based on Ln^{III} are very commonly employed as ratiometric thermometers. Thermometric parameters are traditionally constructed as a combination of different emission bands.[92] For example, Balabhadra et al. reported a thermometer based on the ratio between the thermally-coupled $^4S_{3/2} \rightarrow {}^4I_{15/2}$ and $^2H_{11/2} \rightarrow {}^4I_{15/2}$ bands of Er^{III} in SrF_2:Yb/Er upconverting nanoparticles (Figure 1.6), giving S_r up to ~1.2 % K^{-1} and ΔT as low as 0.265 K over a sensing range of 298-383 K.[96]

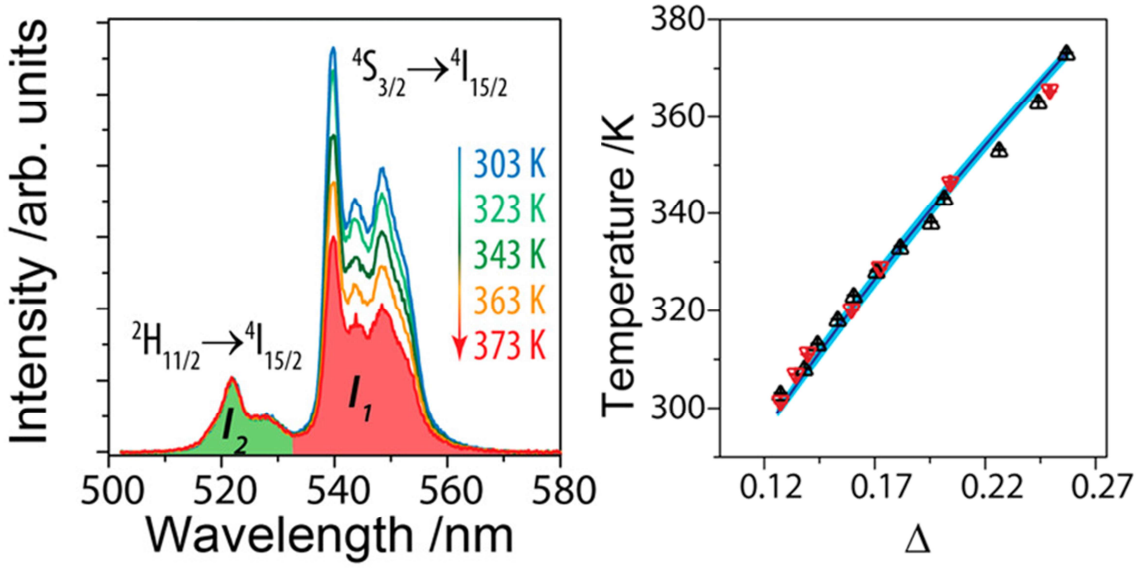


Figure 1.6. *Left:* Temperature-dependent upconversion emission spectra (λ_{ex} = 980 nm at 1.5 W cm^{-2}) of SrF_2:Yb/Er nanoparticles in the range 303-373 K, demonstrating the thermosensitive intensities of the $^4S_{3/2} \rightarrow {}^4I_{15/2}$ (I_1) and $^2H_{11/2} \rightarrow {}^4I_{15/2}$ (I_2) bands of Er^{III}. *Right*: Temperature dependence of the values $\Delta = \frac{I_1}{I_2}$ obtained from the temperature-dependent emission spectra, as a bare powder (black triangles) and as a suspension in water (red inverted triangles). The blue line represents the theoretical relationship between the observed intensity ratio and temperature. Adapted with permission from [96].

Energy transfer between entirely different emitting centers can be another source of thermosensitive LIRs, such as the ratio between Eu^{III} $^5D_0 \rightarrow {}^7F_4$ and Tb^{III} $^5D_4 \rightarrow {}^7F_5$ in a Eu-Tb discrete molecular dyad reported by Bao et al.,[97] which gives an S_r of 1.86 % K^{-1} from 10-298 K and ΔT less than 1 K above 200 K. The intensities of the m_J sublevels within a single band can also be used,[29] as their relative intensities are quite responsive to temperature. This approach is demonstrated e.g. by Gil et al., with the dimeric molecular complex {[Nd^{III}(acac)$_3$]$_2$(μ-bpm)} (bpm = 2,2′-bipyrimidine).[98] There, a thermometric parameter comprising different components of the $^4F_{3/2} \rightarrow {}^4I_{11/2}$ band of Nd^{III} yields a maximum S_r of 2.1 % K^{-1} with a ΔT of 0.5 K at 85 K, and a sensing range of 85-285 K, when excited via the ligands (Figure 1.7). Since the ligand field is the origin of the m_J splitting in Ln^{III}, some tuning of the thermometric performance of m_J-based thermometers is attainable by modulating the coordination environment. Indeed, our group previously demonstrated that the complexes [Dy(acac)$_3$(PyAm)] (S_r = 2.03 % K^{-1} at 18.25 K) and [Dy(acac)$_3$(PmAm)] (PmAm = 2-amidinopyrimidine) (S_r = 0.76 % K^{-1} at 82 K) have dramatically different thermometric performances based on the $^4F_{9/2} \rightarrow {}^6H_{13/2}$ band, despite having ligand sets differing by a

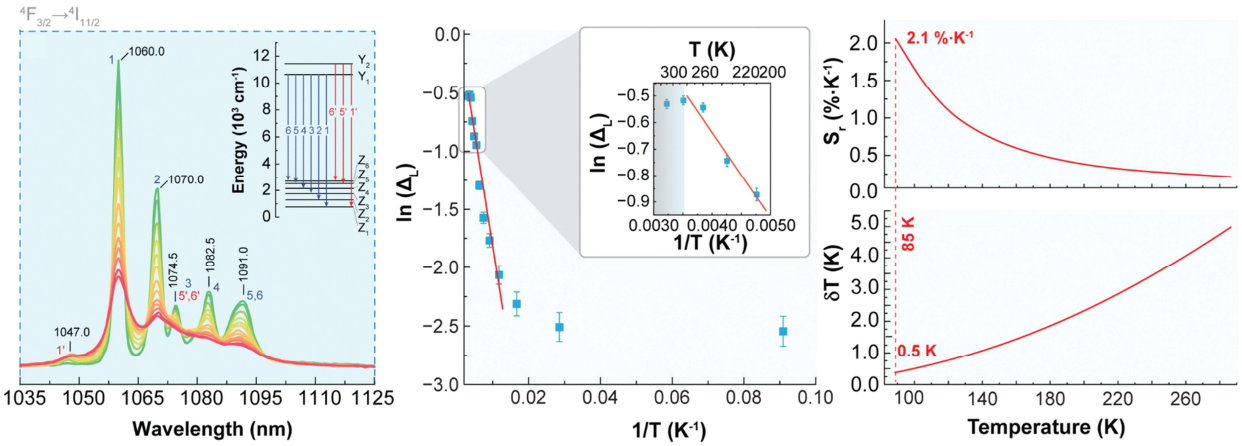


Figure 1.7. *Left:* Temperature-dependent emission spectra (λ_{ex} = 370 nm) of {[$Nd^{III}(acac)_3$]$_2$(μ-bpm)} in the range 11-310 K, demonstrating the thermosensitive intensities of the m_J sublevels in the $^4F_{3/2} \rightarrow {}^4I_{11/2}$ band of Nd^{III}. *Middle*: Temperature dependence of the values $\Delta = \frac{I_{1',5',6'}}{I_{1,4,5,6}}$ obtained from the temperature-dependent emission spectra. The red line represents the best fit to a Boltzmann-type equation. *Right*: Temperature dependence of the relative sensitivity S_r and temperature uncertainty δT based on the selected Δ. Adapted with permission from [98].

mere single atom in the secondary coordination sphere. Alternatively, the ratio between the interconfigurational $5d \rightarrow 4f$ and intraconfigurational $4f \rightarrow 4f$ transition bands of a system that exhibits both types of transitions simultaneously can be used to define a ratiometric Δ. Via this method, Ćirić et al. obtained a very high S_r = 4.8 % K^{-1} at 298 K with a ΔT of 0.04 K and a sensing range 298-648 K in a coating of γ-Al_2O_3:Sm^{II} by using the ratio between the $4f^5 5d^1 \rightarrow 4f^6$ and $^5D_0 \rightarrow {}^7F_J$ emission bands of Sm^{II} in that matrix.[99] While this type of Δ is often achieved with a Ln^{II} luminescent center like Sm^{II} or Eu^{II}, the energy-transfer approach described above can also be leveraged for this sort of mixed-mode LIR. This is exemplified by Yue et al. in a mixed Ce^{III}-Tb^{III} metal-organic framework (MOF) system, where the ratio between Ce^{III} $4f^0 5d^1 \rightarrow 4f^1$ and Tb^{III} $^5D_4 \rightarrow {}^7F_5$ gave a thermometer with maximum S_r = 1.37 % K^{-1} at 473 K over a sensing range of 313-473 K, with ΔT as low as 0.36 K.[100]

Despite their general success in optical thermometry, Ln-based materials are, on the whole, historically understudied as band-shift thermometers. This represents an interesting gap, which exists because most studies of Ln-based band-shift thermometry have been conducted with Ln^{III}. The band positions (i.e., the emission energies) in most Ln^{III} luminophores are simply not very environment sensitive for reasons detailed earlier in this chapter, and therefore fall short of the conditions necessary for good thermometric performance.[90,92,93,101] The electron-beam excited $^5D_0 \rightarrow {}^7F_0$ transition of Y_2O_2S:Eu^{III} was an early example, exhibiting S_a = 0.04 cm^{-1} K^{-1} in the range 257-345 K (i.e., a total ΔE of only ~5 cm^{-1}) with ΔT of ~1 K, and was leveraged to measure the temperature of colour television cathode ray tubes *in situ*.[99,102] Rocha et al. investigated the thermosensitive shift of the NIR $^4F_{3/2} \rightarrow {}^4I_{9/2}$ transition of LaF_3:Nd^{III} nanoparticles for thermal sensing in simulated human skin, attaining an S_a of 0.14 cm^{-1} K^{-1} between 283-333 K with a ΔT of ~2 K.[103] The YVO_4:Ln^{III} (for Eu, Dy, Nd) are also well known in this space;[104,105] the $^5D_0 \rightarrow {}^7F_1$ band-shift of the Eu analogue has maximum S_a = 0.20 cm^{-1} K^{-1} at 733 K in the range 295-733 K, the $^4F_{9/2} \rightarrow {}^6H_{15/2}$ band-shift of the Dy analogue has maximum S_a = 0.13 cm^{-1} K^{-1} at 295 K in the range 295-653 K, and the $^4F_{3/2} \rightarrow {}^4I_{11/2}$ band-shift of the Nd analogue has maximum S_a = 0.03 cm^{-1} K^{-1} at

873 K in the range 123-873 K.[i] All of these examples have rather poor performance when considering the magnitude of the band-shift, with very small values <1 cm^{-1} K^{-1}.

Unsurprisingly, the $5d \rightarrow 4f$ emissions of Ln^{II} are much better suited for band-shift thermometry, on account of the higher sensitivity of the $5d$ excited-state orbitals to the surroundings. In this regard, it is interesting to note that the γ-Al_2O_3:Sm^{II} coating reported by Ćirić et al. is also a standout band-shift thermometer, having maximum S_a of 8 cm^{-1} K^{-1} at 298 K in the range 298-648 K when tracking the barycenter of the whole Sm^{II} emission band (i.e., considering both the $4f^5 5d^1 \rightarrow 4f^6$ and $^5D_0 \rightarrow {}^7F_J$ emission bands of Sm^{II} simultaneously). Indeed, prior to the work described in this thesis, this was the best-performing Ln-based band-shift thermometer reported to date.

1.6 Thesis scope and outlook

Given the dominance of the highly environment-sensitive $4f^6 5d^1 \rightarrow 4f^7$ transition in the emission of Eu^{II}, constructs using this ion are of course other potential candidates for high-performance luminescence thermometry. Several examples of Eu^{II}-based luminescence thermometers exist, which are summarized in Table 1.2. It is notable that despite the favourable properties, there was effectively only one reported example of a system demonstrating band-shift thermometry with Eu^{II} (the $MSr(BH_4)_xCl_{1-x}$:Eu^{II}, M = K, Rb, Cs, Figure 1.8)[106] until January 2022 (the date of the first publication included in this thesis).

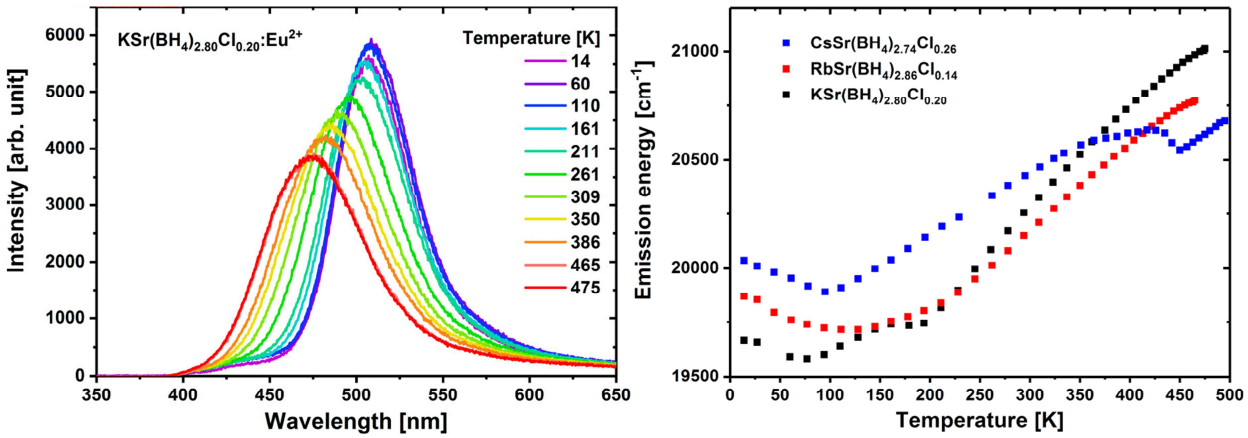


Figure 1.8. *Left:* Temperature-dependent emission spectra (λ_{ex} = 330 nm) of $KSr(BH_4)_{2.8}Cl_{0.2}$:Eu^{II} in the range 14-475 K, demonstrating the thermosensitive shifting of the $4f^6 5d^1 \rightarrow 4f^7$ band maximum of Eu^{II}. *Right*: Temperature dependence of the values $\Delta = \lambda_{em}$ obtained from the temperature-dependent emission spectra. Adapted with permission from [106].

Further, there is a glaring lack of Eu^{II}-based band shift thermometers built on discrete molecular platforms, and therefore a concomitant lack of knowledge on the structure-property relationships that govern the thermometric performance of these systems. With this in mind, the overarching goal of our research was to explore exactly this: the potential for discrete molecular, Eu^{II}-based optical thermometers, with a focus on luminescence thermometry *via* band-shift. Moreover, we chose to focus on organometallic systems given that Eu^{II} metallocenes are already established as luminescent materials, and we were inspired by the additional layer of unique properties that might be imparted by carbon-donor ligands. We were further encouraged by the exciting properties of the simple coordination polymer $[Eu^{II}(BH_4)_2(THF)_2]$ originally reported by Marks et al.,[56] which demonstrates extremely bright cyan emission at room temperature. The lanthanide tetrahydroborate THF solvates are well-appreciated as excellent starting materials for the

synthesis of tailored molecular architectures due to their stability, solubility, ease of synthesis, and favourable reactivity,[107] so we surmised that this material would be an excellent platform from which to begin our studies.

Three projects representing the indicated theme are detailed in this thesis, all of which have generated peer-reviewed publications that form the content herein. In Chapter 2, we describe the synthesis and opto-structural characterization of the hemimetallocene dimer $[Cp^*Eu(\mu\text{-}BH_4)(THF)_2]_2$ (Cp^* = pentamethylcyclopentadienyl), the first example of an organometallic, discrete molecular, Eu^{II}-based band-shift thermometer, which also exhibits the highest S_a (8.2 $cm^{-1}\,K^{-1}$) reported to date for a lanthanide-based band-shift thermometer. We also study the temperature-dependent luminescence of $[Eu^{II}(BH_4)_2(THF)_2]$ and find that it is a competent band-shift thermometer in its own right. Observing the exceptional performance of $[Cp^*Eu(\mu\text{-}BH_4)(THF)_2]_2$, we then sought to elucidate the design principles that would allow for tuning (and perhaps improvement) of its properties. Hence, Chapter 3 describes a systematic study where the dimeric Eu^{II}-BH_4 hemimetallocene architecture was decorated with a range of different ligands, and the optical properties were studied and correlated to their thermometric performance. Following that study, we became interested in a particular family of substituted cyclopentadienides, namely the 1-(bis(dimethylamino)phosphinochalcogenoyl)-2,3,4,5-tetramethylcyclopentadienides, and their complexes with Eu^{II}. While we intended firstly to obtain Eu^{II}-BH_4 hemimetallocenes with these ligands, and secondly to investigate their performance as band-shift thermometers, we discovered instead a family of homoleptic europocenes(II) with excellent performance as magneto-optical thermometers *via* their strongly temperature-dependent magnetic circular dichroism. The synthesis and magneto-optical characterization of these complexes is detailed in Chapter 4. Finally, Chapter 5 concludes the thesis with a summary of the obtained results and perspectives for the future development of molecular Eu^{II}-based systems for optical thermometry. Overall, we demonstrate that molecular Eu^{II}-based systems are a severely understudied but very promising family of materials for remote-detection temperature sensing.

Table 1.2. Survey of Eu^{II}-based luminescence thermometers until 2022.

System	Approach	Δ	S_a (K^{-1})	S_r (% K^{-1})	Sensing Range (K)	ΔT (K)	Ref.
$Li_4SrCa(SiO_4)_2:Eu^{II}$ [a]			n.d.	2.87 @ 440 K	370-470	n.d.	[108]
$Li_4SrCa(SiO_4)_2:Eu^{II}$ [c]	LIR	$I(Eu^{II}_{Ca})$: $I(Eu^{II}_{Sr})$[b]	n.d.	1.51 @ 460 K	370-470	n.d.	
$Li_4SrCa(SiO_4)_2:Eu^{II}$			0.051 @ 473 K	3.18 @ 423 K	303-473	0.35	[109]
	Lifetime	Eu^{II} τ_{433}	1.47 @ 363 K	15 @ 573 K	363-573	n.d.	
$Ca_9Mg_{1.5}(PO_4)_7:(Eu^{II},Eu^{III})$[d]	LIR	$I(Eu^{II}\ 4f^6 5d^1 \rightarrow 4f^7)$: $I(Eu^{III}\ {}^5D_0 \rightarrow {}^7F_2)$	8.4 x10^{-5}	n.d.	293-473	n.d.	[110]
$Ca_9Mg_{1.5}(PO_4)_7:(Eu^{II},Eu^{III})$[e]	LIR	Eu^{II} I_{600}: I_{415} bands	0.064 @383 K	1.19 @ 383 K	293-473	n.d.	[110]
$Ca_2Mg_{0.5}AlSi_{1.5}O_7:Eu^{II}$	LIR	Eu^{II} I_{425}: I_{525} bands	n.d.	1.62 @ 350 K	200-425	~0.05	[111]
$BaMgAl_{10}O_{17}:Eu^{II}$	"Lifetime"[f]	Eu^{II} I_{445} phase shift	[g]	[g]	600-841	8.6	[112,113]
Eu^{II}/Cr^{III} activated oxyfluoride glass ceramic	LIR	$I(Eu^{II}\ 4f^6 5d^1 \rightarrow 4f^7)$: $I(Cr^{III}\ {}^2E \rightarrow {}^4A_2)$	n.d.	0.8	313-563	n.d.	[114]
$Ca_6BaP_4O_{17}:Eu^{II}$	LIR	$I(Eu^{II}_{Ca})$: $I(Eu^{II}_{Ba})$[b]	0.011 @ 430 K	1.53 @ 500 K	250-500	n.d.	[115]
$SrAl_2O_4:(Eu^{II},Dy^{III},Tb^{III})$	LPL[h] LIR	Eu^{II} I_{446}: I_{524} bands	8 @ ~145 K	10 @ 240 K	60-240	n.d.	[116]
$Ca_2Na_2La_6(SiO_4)_4(PO_4)_2O:(Eu^{II},Eu^{III})$	LIR	$I(Eu^{II}\ 4f^6 5d^1 \rightarrow 4f^7)$: $I(Eu^{III}\ {}^5D_0 \rightarrow {}^7F_2)$	n.d.	2.82 @ 473 K	298-473	n.d.	[117]
$Sr(HCO_2)_2:(Eu^{II},Eu^{III})$	LIR	$I(Eu^{II}\ 4f^6 5d^1 \rightarrow 4f^7)$: $I(Eu^{III}\ {}^5D_0 \rightarrow {}^7F_2)$	0.004	0.38	9-293	n.d.	[118]
$KSr(BH_4)_{2.80}Cl_{0.20}:Eu^{II}$				0.029 @ 245 K	14-475	n.d.	[106]
$RbSr(BH_4)_{2.86}Cl_{0.14}:Eu^{II}$	Band-shift	$\lambda_{em}(Eu^{II}\ 4f^6 5d^1 \rightarrow 4f^7)$	n.d.	0.021 @ 324 K	14-463	n.d.	
$CsSr(BH_4)_{2.74}Cl_{0.26}:Eu^{II}$				0.015 @ 178 K	14-495	n.d.	
$Mg_2Al_4Si_5O_{18}:Eu^{II}$	LIR	Eu^{II} I_{445}: I_{615} bands	n.d.	0.45 @ 673 K	373-673	n.d.	[119]
$Ca_8Mg_3Al_2Si_7O_{28}:(Eu^{II},Ce^{III})$	LIR	$I(Eu^{II}\ 4f^6 5d^1 \rightarrow 4f^7)$: $I(Ce^{III}\ 4f^0 5d^1 \rightarrow 4f^1)$	0.019 @250 K	1.35 @ 500 K	200-250	n.d.	[120]
$Sr_4La(PO_4)_3O:(Eu^{II},Sm^{III})$	LIR	$I(Eu^{II}\ 4f^6 5d^1 \rightarrow 4f^7)$: $I(Sm^{III}\ {}^4G_{5/2} \rightarrow {}^6H_J)$	7.9 x10^{-4} @ 573 K	0.48 @ 573 K	293-573	n.d.	[121]
$Na_3Sc_2P_3O_{12}:(Eu^{II},Mn^{II})$	LIR	$I(Eu^{II}\ 4f^6 5d^1 \rightarrow 4f^7)$: $I(Mn^{II}\ {}^4G \rightarrow {}^6S)$	n.d.	1.56 @ 473 K	293-473	n.d.	[122]
$NaZr_2(PO_4)_3:(K,Eu^{II},Eu^{III})$	LIR	$I(Eu^{II}\ 4f^6 5d^1 \rightarrow 4f^7)$: $I(Eu^{III}\ {}^5D_0 \rightarrow {}^7F_1)$	0.026 @ 413 K	3.84 @ 293 K	293-413	0.075	[123]
$LaGdAlO_3:(Eu^{II},Eu^{III})$	LIR	$I(Eu^{II}\ 4f^6 5d^1 \rightarrow 4f^7)$: $I(Eu^{III}\ {}^5D_0 \rightarrow {}^7F_2)$	0.084 @ 473 K	3.23 @ 303 K	303-473	n.d.	[124]
$MgAl_2O_4:(Eu^{II},Eu^{III})$	LIR	$I(Eu^{II}\ 4f^6 5d^1 \rightarrow 4f^7)$:	0.084 @ 523 K	0.83 @ 473 K	298-523	0.6	[125]

		$I(Eu^{III}\ ^5D_0 \rightarrow\ ^7F_4)$					
$Sr_4Al_{14}O_{25}$:Eu^{II}	LIR	Eu^{II} I_{400}: I_{490} bands	0.004 @ 373 K	0.62 @ 373 K	293-423	n.d.	[126]
$Ca_9NaZn(PO_4)_7$:Eu^{II}	LIR	$I(Eu^{II}_{Ca})$: $I(Eu^{II}_{Na})$[b]	0.023 @ 498 K	0.81 @ 398 K	298-498	n.d.	[127]
$Ca_9Zn_{1.5}(PO_4)_7$:(Eu^{II},Eu^{III})	LIR	$I(Eu^{II}\ 4f^6 5d^1 \rightarrow 4f^7)$: $I(Eu^{III}\ ^5D_0 \rightarrow\ ^7F_2)$	0.0034 @ 453 K	1.4 @ 453 K	293-473	n.d.	[128]
$SrAl_2Si_2O_8$:(Eu^{II},Eu^{III})	LIR	$I(Eu^{II}\ 4f^6 5d^1 \rightarrow 4f^7)$: $I(Eu^{III}\ ^5D_0 \rightarrow\ ^7F_4)$	0.056 @ 583 K	0.30 @ 583 K	303-583	n.d.	[129]
$Ca_2Al_2SiO_7$:(Eu^{II},Eu^{III})	LIR	$I(Eu^{II}\ 4f^6 5d^1 \rightarrow 4f^7)$: $I(Eu^{III}\ ^5D_0 \rightarrow\ ^7F_4)$	0.024 @ 303 K	2.46 @ 443 K	303-443	n.d.	[130]
Eu^{II}/Eu^{III} activated oxyfluoride glass ceramic	LIR	$I(Eu^{II}\ 4f^6 5d^1 \rightarrow 4f^7)$: $I(Eu^{III}\ ^5D_0 \rightarrow\ ^7F_2)$	n.d.	4.28	300-563	n.d.	[131]
$LaAlO_3$:(Eu^{II},Eu^{III})	LIR	$I(Eu^{II}\ 4f^6 5d^1 \rightarrow 4f^7)$: $I(Eu^{III}\ ^5D_0 \rightarrow\ ^7F_2)$	0.014 @ 473 K	1.19 @ 403 K	293-473	n.d.	[132]
$Sr_3P_4O_{13}$:(Eu^{II},Eu^{III})	LIR	$I(Eu^{II}\ 4f^6 5d^1 \rightarrow 4f^7)$: $I(Eu^{III}\ ^5D_0 \rightarrow\ ^7F_1)$	0.008 @ 573 K	1.06 @ 353 K	293-573	n.d.	[133]
$Ca_3Mg_3(PO_4)_4$:(Eu^{II},Eu^{III})	LIR	$I(Eu^{II}\ 4f^6 5d^1 \rightarrow 4f^7)$: $I(Eu^{III}\ ^5D_0 \rightarrow\ ^7F_2)$	0.049 @ 523 K	0.024 @ 303 K	303-523	n.d.	[134]
$K_5Y(P_2O_7)_2$:Eu^{II}	LIR	$I(Eu^{II}_{K})$: $I(Eu^{II}_{Y})$[b]	~0.03 @ 100 K	1.2 @ 125 K	100-350	0.1	[135]
$BaY_2Si_3O_{10}$:Eu^{II}	LIR	Eu^{II} I_{420}: I_{520} bands	0.0087	0.58 @ 293 K	293-533	n.d.	[136]
Ca(Eu^{II},Eu^{III})Al_3O_7	LIR	$I(Eu^{II}\ 4f^6 5d^1 \rightarrow 4f^7)$: $I(Eu^{III}\ ^5D_0 \rightarrow\ ^7F_4)$	0.069 @ 313 K	n.d.	313-573	n.d.	[137]
$Ba_5SiO_4Cl_6$:Eu^{II}	LIR	Eu^{II} I_{441}: I_{506} bands	0.031 @ 498 K	0.87 @ 498 K	303-498	n.d.	[138]
Li_2CaSiO_4:(Eu^{II},Eu^{III})	LIR	$I(Eu^{II}\ 4f^6 5d^1 \rightarrow 4f^7)$: $I(Eu^{III}\ ^5D_0 \rightarrow\ ^7F_J)$	0.003 @ 303 K[i]	0.29 @ ~550 K[i]	300-583	0.25	[139]
$Ca_8ZrMg(PO_4)_6(SiO_4)$:(Eu^{II},Eu^{III})	LIR	$I(Eu^{II}\ 4f^6 5d^1 \rightarrow 4f^7)$: $I(Eu^{III}\ ^5D_0 \rightarrow\ ^7F_1)$	n.d.	5.94	293-473	n.d.	[140]
Sc_2O_3:(Eu^{II},Eu^{III})	LIR	$I(Eu^{II}\ 4f^6 5d^1 \rightarrow 4f^7)$: $I(Eu^{III}\ ^5D_0 \rightarrow\ ^7F_2)$	n.d.	3.06 @ 267 K	77-267	n.d.	[141]
Sc_2O_3:(Tb^{III},Eu^{II},Eu^{III})		$I(Eu^{II}\ 4f^6 5d^1 \rightarrow 4f^7)$: $I(Tb^{III}\ ^5D_4 \rightarrow\ ^7F_5)$	n.d.	2.65 @ 267 K	137-267	n.d.	
$Sr_3La(PO_4)_3$:Eu^{II}	LIR	Eu^{II} I_{420}: I_{550} bands	n.d.	1.32 @ 423 K	303-530	n.d.	[142]
$Li_4(SrCa)(SiO_4)_2$:Eu^{II}	LIR	$I(Eu^{II}_{Ca})$: $I(Eu^{II}_{Sr})$[b]	n.d.	1.71 @ 463 K[i]	303-583	n.d.	[143]
$LiSr_4(BO_3)_3$:(Ce^{III},Eu^{II})	LIR	$I(Eu^{II}\ 4f^6 5d^1 \rightarrow 4f^7)$: $I(Ce^{III}\ 4f^0 5d^1 \rightarrow 4f^1)$	0.057 @ 293 K	4.02 @ 293 K	293-473	0.09	[144]

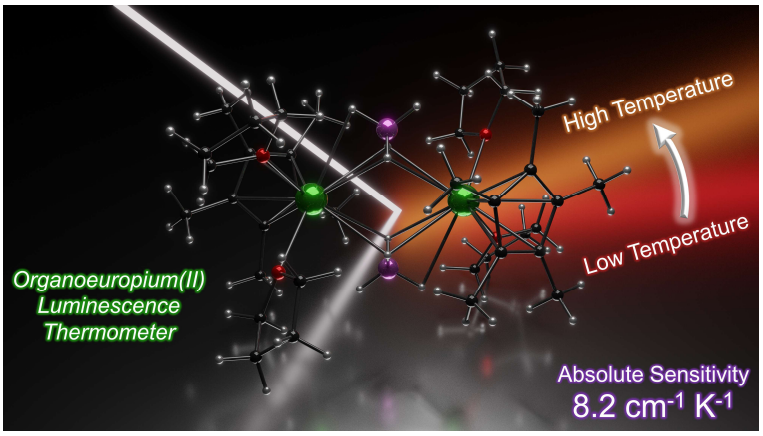
Eu^{II}/Eu^{III} activated (Si,Zn,K,Al) oxide glass	LIR	$I(Eu^{II}\ 4f^6 5d^1 \rightarrow 4f^7)$: $I(Eu^{III}\ {}^5D_0 \rightarrow {}^7F_2)$	0.043	n.d.	298-573	n.d.	[145]
$CaSrMgSi_2O_7$:(Ce^{III},Eu^{II})	LIR	$I(Eu^{II}\ 4f^6 5d^1 \rightarrow 4f^7)$: $I(Ce^{III}\ 4f^0 5d^1 \rightarrow 4f^1)$	n.d.	2.43 @ 293 K	293-473	n.d.	[146]
$SrMg_2(PO_4)_2$:(Ce^{III},Eu^{II})	LIR	$I(Eu^{II}\ 4f^6 5d^1 \rightarrow 4f^7)$: $I(Ce^{III}\ 4f^0 5d^1 \rightarrow 4f^1)$	0.017 @ 568 K	1.57 @ 568 K	298-568	n.d.	[147]
$CaMgSi_2O_6$:(Ce^{III},Eu^{II})	LIR	$I(Eu^{II}\ 4f^6 5d^1 \rightarrow 4f^7)$: $I(Ce^{III}\ 4f^0 5d^1 \rightarrow 4f^1)$	0.049 @ 505 K	2.12 @ 480 K	80-505	n.d.	[148]
$CaSrMgSi_2O_6$:(Eu^{II},Tb^{III})	LIR	$I(Eu^{II}\ 4f^6 5d^1 \rightarrow 4f^7)$: $I(Tb^{III}\ {}^5D_4 \rightarrow {}^7F_5)$	0.047 @ 280 K	0.6 @ 280 K	77-280	n.d.	[149]

[a] "As-prepared" (never measured). [b] Eu^{II}_E denotes Eu^{II} occupying an E lattice site of the host. [c] Following UV + thermal treatment. [d] Excited at 254 nm. [e] Excited at 350 nm. [f] Not a conventional lifetime thermometry application, but rather an emission phase shift measurement used for thermographic velocimetry in hot gas streams. This application is somewhat adjacent to the work discussed herein but is included for comparison purposes. [g] the sensitivity in conventional terms of luminescence thermometry was not specified. [h] "Long persistent luminescence"; intensity of the afterglow was used. [i] strongly dependent on dopant concentration; maximum values among all systems studied is given. n.d. = not determined.

CHAPTER 2

Toward Opto-Structural Correlation to Investigate Luminescence Thermometry in an Organometallic Eu^{II} Complex

2.1 Preface



The work detailed in this chapter was published as an Article in *Journal of the American Chemical Society* and is reprinted with permission from Diaz-Rodriguez, R. M., Gálico, D. A., Chartrand, D., Suturina, E. A., Murugesu, M., *J. Am. Chem. Soc.* **2022**, *144*, 912–921. Copyright 2022 American Chemical Society.

R. M. Diaz-Rodriguez performed all chemical synthesis; characterized the synthesized complexes by IR and NMR spectroscopy; collected and interpreted DC magnetometry data on **2.1**; collected, solved and refined SCXRD data for basic characterization of **2.1** and **2.2**; interpreted all structural data; contributed equally with D. A. Gálico to design photoluminescence experimental protocols and to collect and interpret photoluminescence spectra for all complexes; and wrote the original manuscript. D. A. Gálico contributed writing and editing of parts of the manuscript in addition to the above. D. Chartrand collected, solved and refined variable-temperature SCXRD data for **2.1**. E. A. Suturina performed and interpreted DFT and *ab initio* calculations. M. Murugesu oversaw all aspects of the project.

Additional data and discussion pertaining to this chapter are given in Appendix A.

2.2 Abstract

Lanthanide-based luminescent materials have unique properties and are well-studied for many potential applications. In particular, the characteristic $5d \rightarrow 4f$ emission of divalent lanthanide ions such as Eu^{II} allows for tunability of the emissive properties via modulation of the coordination environment. We report the synthesis and photoluminescence investigation of pentamethylcyclopentadienyl-europium(II) tetrahydroborate bis(tetrahydrofuran) dimer (**2.1**), the first example of an organometallic, discrete molecular Eu^{II} band-shift luminescence thermometer. Complex **2.1** exhibits an absolute sensitivity of 8.2 cm^{-1} K^{-1} at 320 K, the highest thus far observed for a lanthanide-based band-shift thermometer. Opto-structural correlation via variable-temperature single-crystal X-ray diffraction and fluorescence spectroscopy allows rationalization of the remarkable thermometric luminescence of complex **2.1** and reveals the significant potential of molecular Eu^{II} compounds in luminescence thermometry.

2.3 Introduction

In recent years, materials based on molecular systems have shown remarkable optical/luminescent properties.[29,56,150–154] If such properties can be used to monitor changes in structure and/or temperature of the material, then applications employing these materials become viable. To that end, control over the interaction between light and matter is key to leading technological advancement in a wide range of fields. Molecular systems offer a remarkable advantage over traditional bulk materials when it comes to probing structural changes at the molecular level, and enable unparalleled flexibility to fine-tune the coordination environment around an emissive metal center. Structural parameters can be probed *via* single-crystal X-ray diffraction, while thermosensitive optical properties can provide subtle spectral changes with varying temperature. By careful association between the molecular structure and optical features, opto-structural correlation can be performed. Such analysis provides a unique insight into the connection between a material's structure and its optical properties. By taking advantage of such opto-structural correlation, an understanding of the factors that govern the change in physical properties is achievable, thus subsequent fine-tuneability of the optical properties becomes a reality.

When it comes to luminescent properties, trivalent lanthanide ions reign supreme, as they exhibit long-lived narrow emission lines which enable optical probing.[21] That being said, as the most stable divalent lanthanide ion, Eu^{II} is by far the most studied with respect to luminescence.[30] In contrast to most trivalent lanthanide ions, the presence of a low-lying 5*d* state gives rise to a strong $d \rightarrow f$ emission, allowed *via* selection rules. Luminescent molecular Eu^{II} compounds have been known for a long time, however studies involving them mostly focus on basic spectroscopic characterization.[55,57,65,80,85,155–158] Hence, applications of luminescent molecular Eu^{II} compounds[60,84,85,159] remain an underexplored area of study with tremendous potential. One such application is luminescence thermometry, wherein changes in the luminescence behaviour of a chemical probe as a function of temperature are used as a contactless temperature measurement technique.[20,29,91,97,150,154,160–164] Luminescence parameters of a probe that may vary with temperature include: emission peak energy; fluorescence lifetime and/or intensity; or the ratio of intensity between multiple emission bands, among others.[91–93,165]

In the family of divalent lanthanides, Sm^{II} and Eu^{II} are especially well-suited to this application, as their associated emissive *5d* state is very sensitive to the coordination environment.[48,166] Although luminescence thermometry has previously been achieved in Eu^{II}-containing inorganic materials,[106,108,110–118] it is surprising to note that no examples of discrete molecular Eu^{II} luminescence thermometers have been reported to date. This may be due to the highly air- and moisture-sensitive nature of most molecular divalent lanthanide compounds, making the synthesis, isolation and characterization of systems exhibiting the desired properties quite challenging. This is especially true of organometallic divalent lanthanide compounds, which are nevertheless highly desirable thanks to the unique stereoelectronic characteristics accessible using carbon-donor ligands. We therefore sought to explore avenues toward such compounds.

The small negative reduction potential of the Eu^{II}-Eu^{III} redox couple ($E°$ = -0.35 V)[167] allows the facile synthesis of $[Eu^{II}(BH_4)_2(THF)_2]$ from the reaction of $EuCl_3$ with $NaBH_4$, wherein Eu^{III} is reduced in situ.[56] This complex is unique among the simple lanthanide tetrahydroborates in that it displays intense blue luminescence in the solid state,[56,168] and yellow-green luminescence in THF solution. This observation implies that tetrahydroborate ligands are effective at promoting luminescence in Eu^{II}, making this compound a good starting point for the application-focused design of luminescent Eu^{II} compounds. Tetrahydroborate ligands are coordinatively flexible and labile, often acting as pseudohalides in salt metathesis reactions, and are consequently well suited to the construction of more sophisticated complexes, including organometallic complexes.[107] Furthermore, Eu^{II} is isoelectronic to Gd^{III} ($4f^7$, with an $^8S_{7/2}$ ground

state) and is accordingly highly paramagnetic. However, it is important to note that Gd^{III} is "optically silent", exhibiting no emissive transitions within the visible spectrum.[21] One can, therefore, envision applications employing Eu^{II} as a highly tunable luminescent analogue to its isoelectronic trivalent congener, the Gd^{III} ion. All considered, we surmised that $[Eu^{II}(BH_4)_2(THF)_2]$ could be a useful precursor for the preparation of exciting luminescent and optomagnetic molecular compounds.

In this chapter, we report the synthesis, characterization, and photoluminescence of the divalent europium complex $[Cp^*Eu(\mu\text{-}BH_4)(THF)_2]_2$ (**2.1**). In the solid state, complex **2.1** acts as a highly sensitive band-shift luminescence thermometer operating over a broad temperature range (60-320 K), properties which are extremely sought-after for viability in such applications.[99] An opto-structural correlation study on this unique Eu^{II} luminescence thermometer highlights the versatility of molecular organometallic systems over traditional inorganic materials. The synthetic flexibility and stereoelectronic tunability afforded by organometallic constructs, combined with the remarkable luminescence properties of **2.1**, demonstrate the great potential of molecular Eu^{II} systems as luminescence thermometers, with incipient applications in the control of sensitive spintronic devices or organic electronics.

2.4 Synthesis and structural characterization

The equimolar reaction of $[Eu^{II}(BH_4)_2(THF)_2]$ with potassium pentamethylcyclopentadienide (KCp^*) in THF led to the formation of complex **2.1** as a microcrystalline yellow solid. Upon recrystallization from THF at -20 °C, transparent yellow, blocklike crystals suitable for analysis by X-ray diffraction were isolated. Complex **2.1** crystallizes in the monoclinic space group $P2_1/n$; the structure is shown in Figure 2.1.

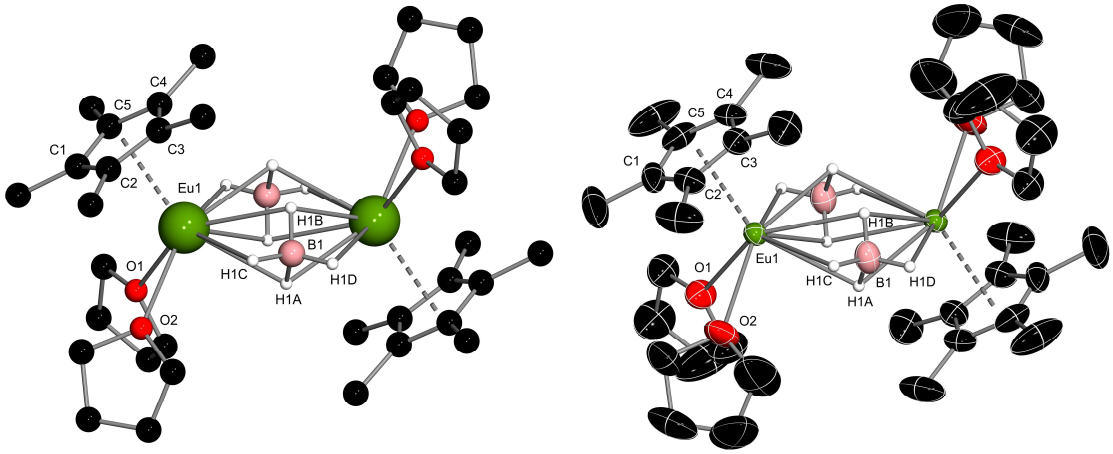


Figure 2.1. Molecular structure of **2.1**, shown as a ball-and-stick diagram (left) and as a thermal ellipsoid diagram (right). Labels are given only for the crystallographically unique atoms which coordinate the Eu^{II} centre; symmetry-related atoms are indicated elsewhere with a prime (e.g. B1′). Hydrogen atoms bonded to carbon are omitted for clarity. Selected bond lengths and angles are provided in Table A1. Packing diagrams are shown in Figure A7.

The solid-state structure of **2.1** consists of a dimer where the Eu^{II} centers are bridged by two $(\mu_3\text{-}H)_2B(\mu_2\text{-}H)_2$ units,[169] with a monoanionic Cp* ligand and two molecules of THF completing the coordination environment of each Eu^{II} ion. It is noteworthy that **2.1** is only the second example of a bis(tetrahydroborate)-bridged homobimetallic Ln^{II} hemimetallocene, the first being the isostructural Sm^{II} complex $[Cp^*Sm(\mu\text{-}BH_4)(THF)_2]_2$ reported by Jaroschik *et al.*, obtained *via* a similar synthetic route.[170] In

the IR spectrum of **2.1** (Figure 2.2), a group of absorption peaks centered around 2260 cm^{-1} is observed. This spectral feature is reminiscent of that which was previously observed for $[(COT)Nd^{III}(BH_4)(THF)]_2$, which exhibits the same tetrahydroborate coordination mode as **2.1**.[171] Additionally, a pair of absorption peaks at 2243 and 2191 cm^{-1} are present, which comprise a doublet (splitting of 52 cm^{-1}) that is highly diagnostic of the B-$H_{bridging}$ stretch of a κ^3-tetrahydroborate.[172] Coordinated THF is also evidenced by the very strong absorption peaks at 881 and 1034 cm^{-1}.

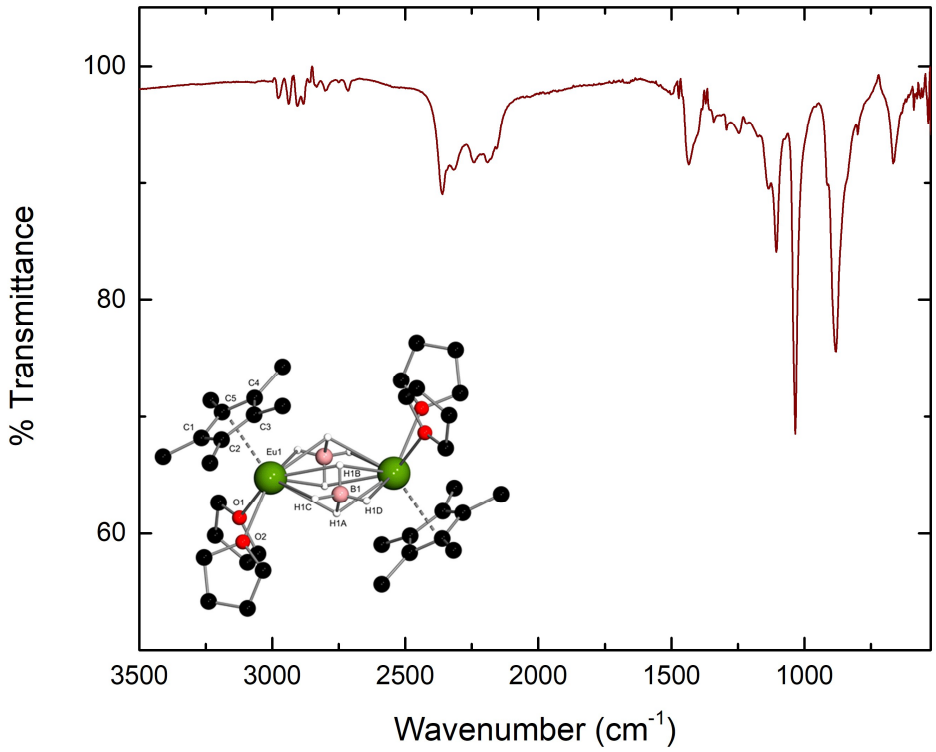


Figure 2.2. Infrared spectrum of complex **2.1**.

Attempts to observe **2.1** by ^1H NMR spectroscopy (Figure A1) revealed a resonance at +235 ppm attributable to the Cp* methyl substituents. The tetrahydroborate ligands could not be observed by ^1H or ^{11}B NMR spectroscopy, even when decoupled. This is unsurprising given the significant paramagnetic broadening from the two Eu^{II} centers, in conjunction with the quadrupolar broadening intrinsic to boron.

No decomposition was observed when crystalline **2.1** was stored for several months at -20 °C under inert atmosphere. A borodeuteride analogue (**2.2**) was also prepared, which is discussed in detail below (see Section 2.7).

2.5 Magnetic properties

The magnetic properties of **2.1** were measured via SQUID magnetometry. From DC measurements, a χT product of 15.68 cm^3 K mol^{-1} is observed at 300 K and 1000 Oe (Figure 2.3), which is in good agreement with the expected value of 15.76 cm^3 K mol^{-1} for two non-interacting $4f^7$, $^8S_{7/2}$ ions with $L = 0$ and $g = 2$. The χT value remains essentially constant until approximately 20 K, where it increases slowly to 16.93 cm^3 K mol^{-1} at 6 K before increasing sharply to a maximum of 20.32 cm^3 K mol^{-1} at 1.8 K. This increase in χT below 20 K can be attributed to weak ferromagnetic interactions between spin carriers occurring at

low temperatures. This data can be fitted using the Hamiltonian $\mathcal{H} = -2JS_1S_2$, which yields a small positive Eu-Eu coupling constant of J = +0.04 cm^{-1}. At 1.9 K, the field-dependent magnetization reaches a value of 13.91 μ_B at a field of 7 T (Figure 2.4), which is in good agreement with the theoretical value of 14 μ_B for a system with ground state S_T = 7. As expected for an isotropic system, complex **2.1** is devoid of any slow magnetic relaxation dynamics (i.e., no AC signal at zero field or under an applied DC field of 1000 Oe).

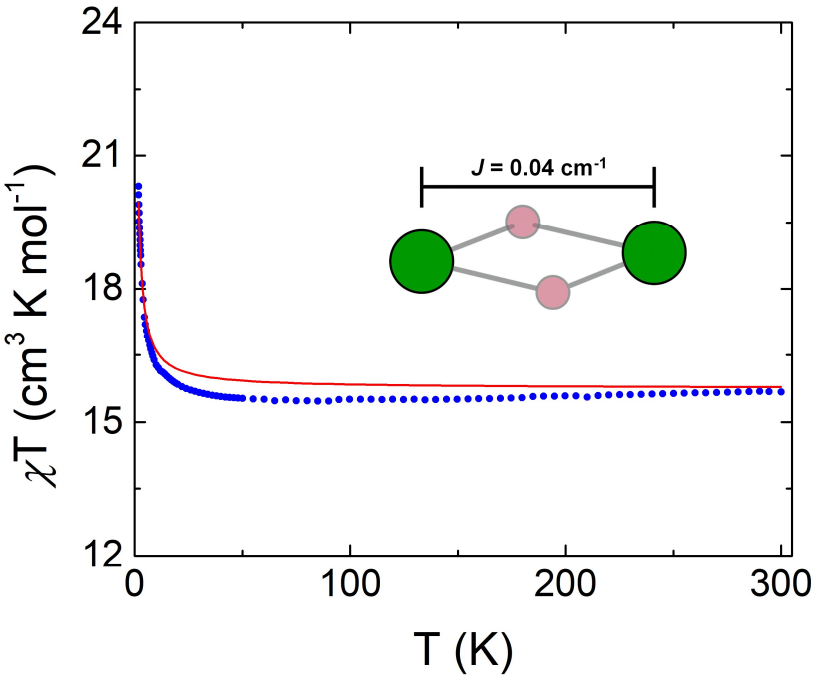


Figure 2.3. Temperature dependence of the χT product at 1000 Oe (blue points) for complex **2.1**, with χ representing the molar magnetic susceptibility per molecule defined as M/H. The solid red line represents the fit; the calculated J value is +0.04 cm^{-1}.

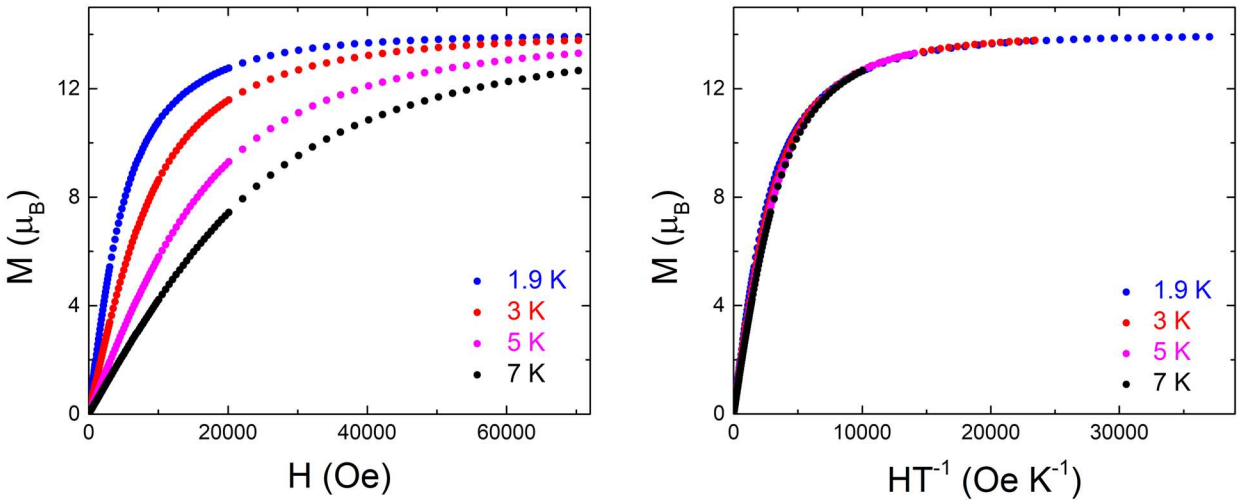


Figure 2.4. Field dependence of the magnetization (left) and reduced magnetization (right) for **2.1** at the indicated temperatures.

2.6 Photoluminescence

With the goal of understanding the spectroscopic features of **2.1** and rationalizing the potential of molecular organometallic Eu^{II} compounds as luminescence thermometers, the solid-state luminescence properties of single crystals of **2.1** were studied at varying temperatures. Excitation and emission spectra obtained at 10 K are shown in Figure 2.5.

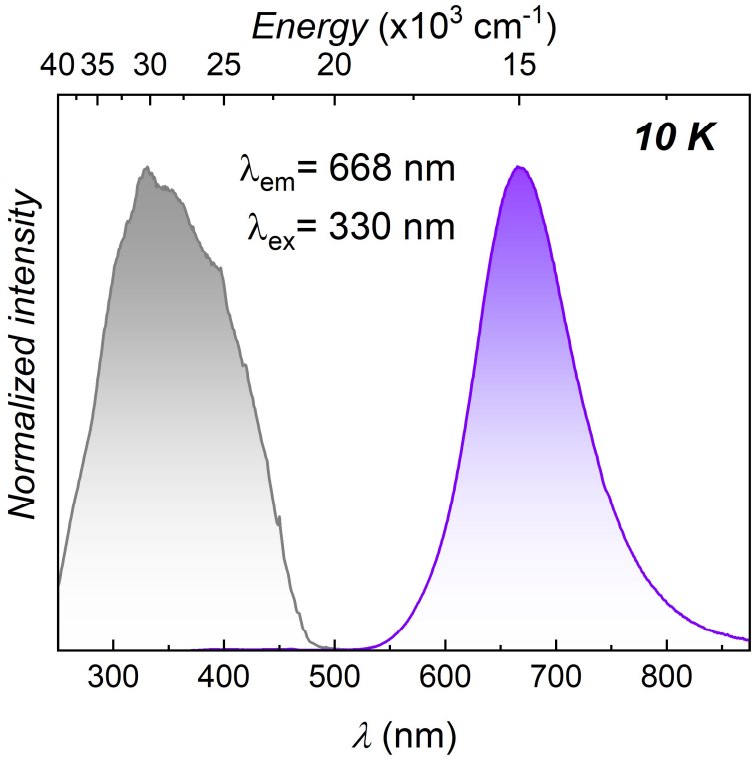


Figure 2.5. Excitation (gray) and emission (violet) spectra for **2.1** obtained at 10 K.

The excitation spectrum reveals bands from the Eu^{II} 5*d* state as well as ligand-based states over the UV and blue spectral region. Excitation at 330 nm results in a strong and broad *d*→*f* transition, as expected for divalent europium, centered at 669 nm (≈14 959 cm^{-1}). Increasing the temperature does not result in any spectral change until 60 K (Figure A5). However, above 60 K, a blue-shift of the band is observed, i.e., the band peak shifts to higher energies (Figures 2.6a and c). From 60 to 320 K, the emission maximum is shifted from 14 959 to 16 858 cm^{-1} (ΔE = 1899 cm^{-1}). Correspondingly, the output color of the emission is shifted from deep red to orange, as demonstrated on the *Commission Internationale de l'éclairage* (CIE) chromaticity diagram (Figure 2.6b). The observed shift of the band peak can be explored for band-shift based luminescence thermometry, as previously demonstrated for Sm^{II}, Eu^{III}, and Dy^{III} inorganic solids.[99] The energy shift can be fitted by a Boltzmann function (Eqn. 2.1) as implemented in OriginPro 2018 (see Figure 2.6c):

$$y = A_2 + \frac{(A_1 - A_2)}{1 + e^{[(x - x_0)/dx]}} \tag{2.1}$$

Absolute sensitivity S_a (Figure 2.6d) was calculated by taking the first derivative of the fitted function, and the maximum absolute sensitivity obtained was 8.2 cm^{-1} K^{-1} at 320 K. This is the highest absolute sensitivity thus far observed for a lanthanide-based band-shift thermometer.

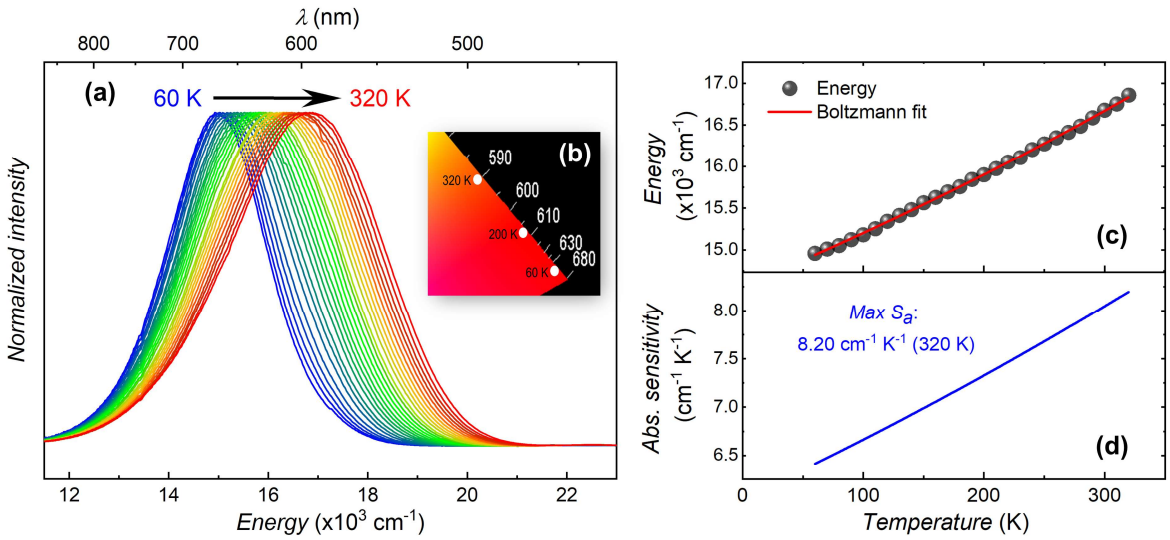


Figure 2.6. Temperature-dependent emission of **2.1**. (a) Temperature-dependent emission spectra ($\boldsymbol{\lambda_{ex}}$ = 330 nm) obtained in the solid state over the 60-320 K range with steps of 10 K. (b) Relevant section of the CIE diagram showing the luminescence colours at selected temperatures. (c) Temperature-dependence of the emission peak energy. The red line represents the Boltzmann function (Eqn. 2.1) used to fit the experimental data. Best-fitting parameters: $R^2 = 0.999$, $A_1 = 8583$, $A_2 = 145840$, and $x_0 = 2920$. (d) Absolute sensitivity obtained as the first derivative of the fitted function.

For intensity-based luminescence thermometry methods, the intensity of a given luminescent probe varies with different equipment and experimental conditions. Contrarily, the position of the emission peak is an intrinsic property of a compound at a given temperature, independent of other factors. Therefore, absolute sensitivity is a reliable metric for comparing the performance of different band-shift thermometers. For completeness, we also report the relative sensitivity S_r (Figure A6) that shows lower performance compared to other Ln-based thermometric systems (see Section 1.5).

The precursor compound $[Eu^{II}(BH_4)_2(THF)_2]$ itself demonstrates thermochromic luminescence (Figure 2.7), displaying a shift in the $d \rightarrow f$ emission band over the range 30 to 320 K from 19 501 to 20 679 cm^{-1} (ΔE = 1178 cm^{-1}); this represents a change in output colour from cyan to green. The maximum absolute sensitivity calculated for $[Eu^{II}(BH_4)_2(THF)_2]$ is 5.37 cm^{-1} K^{-1} at 220 K. Table 2.1 compares the thermometric performance of our complex to other high-performing band-shift thermometers in the literature.

Table 2.1. Comparison of the highest-performing band-shift luminescence thermometers reported to date. Adapted from [99].

Thermometer	S_a (cm^{-1} K^{-1})	Sensing Range (K)
Ag_2S quantum dots[173]	11	295-317
$[Cp^*Eu(\mu\text{-}BH_4)(THF)_2]_2$ [a]	8.2 @ 320 K	60-320
$\gamma\text{-}Al_2O_3:Sm^{II}$ [99]	8.0 @ 298 K[b]	298-648
$[Cp^*Eu(\mu\text{-}BD_4)(THF)_2]_2$ [a]	7.07 @260 K	30-320
$[Eu(BH_4)_2(THF)_2]$[56,a]	5.37 @ 220 K	30-320
CdTe quantum dots[174]	5	300-353

[a] This work. [b] using the barycentre of the entire Sm^{II} emission band as the sensor.

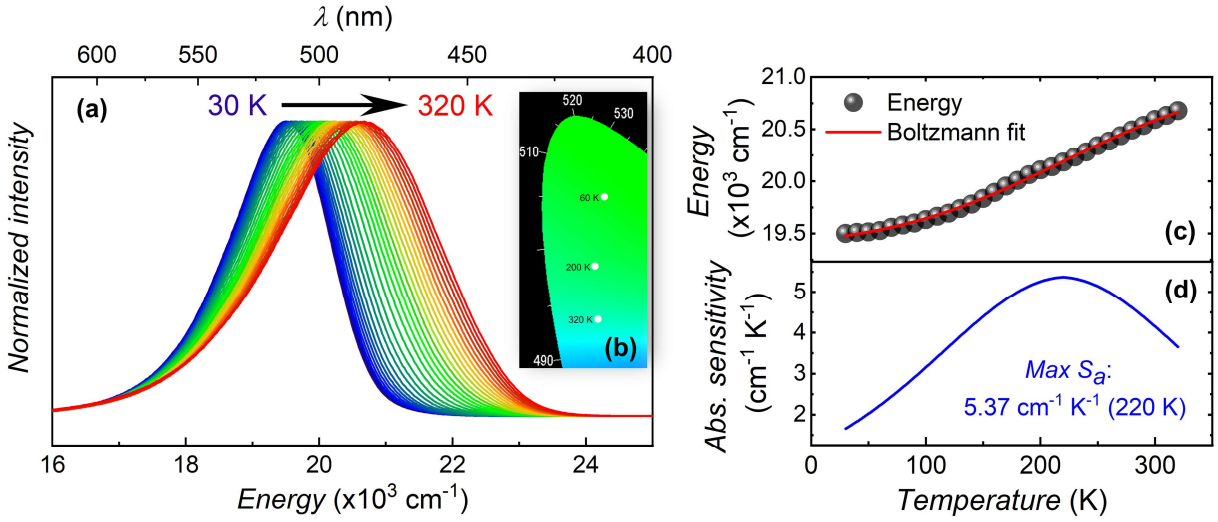


Figure 2.7. Temperature-dependent emission of $[Eu^{II}(BH_4)_2(THF)_2]$. (a) Temperature-dependent emission spectra (λ_{ex} = 330 nm) obtained in the solid state over the 30-320 K range with steps of 10 K. (b) Relevant section of the CIE diagram showing the luminescence colours at selected temperatures. (c) Temperature-dependence of the emission peak energy. The red line represents the Boltzmann function (Eqn. 2.1) used to fit the experimental data. Best-fitting parameters: $R^2 = 0.998$, $A_1 = 19336$, $A_2 = 21033$, and $x_0 = 219$. (d) Absolute sensitivity obtained as the first derivative of the fitted function.

To further evaluate the thermometric performance, the temperature uncertainty ΔT, also known as the temperature resolution, was estimated. The ΔT parameter is extremely dependent on the instrumental setup, and correlates the instrumental error with the thermometer's sensitivities *via* Eqn. 1.3:

$$\Delta T = \frac{1}{S} * \sigma \tag{1.3}$$

where the sensitivity S may be either absolute (S_a) or relative (S_r), and σ is the absolute or relative instrumental error, depending on the chosen sensitivity. Most of the methodologies presented in the literature for calculating ΔT do so for intensity-based thermometric methods. For intensity-based methods, σ is related to the detector's signal-to-noise ratio and is wavelength independent (except at the limits of the detector's wavelength range). Conversely, σ for band-shift thermometry is extremely dependent on the wavelength range. Thus, σ is associated with the wavelength accuracy and wavelength repeatability of the whole spectrofluorometer system (i.e., the monochromator/spectrograph size, gratings, and detector). Herein, we propose an estimation of ΔT for a band-shift thermometric setup, considering the wavelength dependence of different spectroscopic systems. For this, we select 3 hypothetical but typical instrumental peak resolution values:

System 1: 0.5 nm (commonly observed for portable optical detectors).
System 2: 0.1 nm (commonly observed for typical laboratory spectrometers).
System 3: 0.025 nm (commonly observed for high-resolution spectrometers).

As the energy values are inversely proportional to the wavelength (Energy = $10^7/\lambda$), σ possesses different values over different spectral regions (Figure 2.8). Consequently, σ values are higher in the blue region and smaller in the red region. For example, given a wavelength resolution of 0.025 nm (as for a high-resolution

spectrometer), the value of σ is 0.61 cm^{-1} at 650 nm (red region) and 1.24 cm^{-1} at 450 nm (blue region). Therefore, for different band-shift thermometers possessing the same temperature sensitivity, the one with the emission occurring at longer wavelengths/lower energies will result in smaller ΔT (i.e., higher temperature resolution). Figures 2.8b-d show the temperature uncertainty for the three complexes studied in this work. Values as low as 0.09 K are obtained for **2.1**, further confirming it as a highly competent band-shift luminescence thermometer.

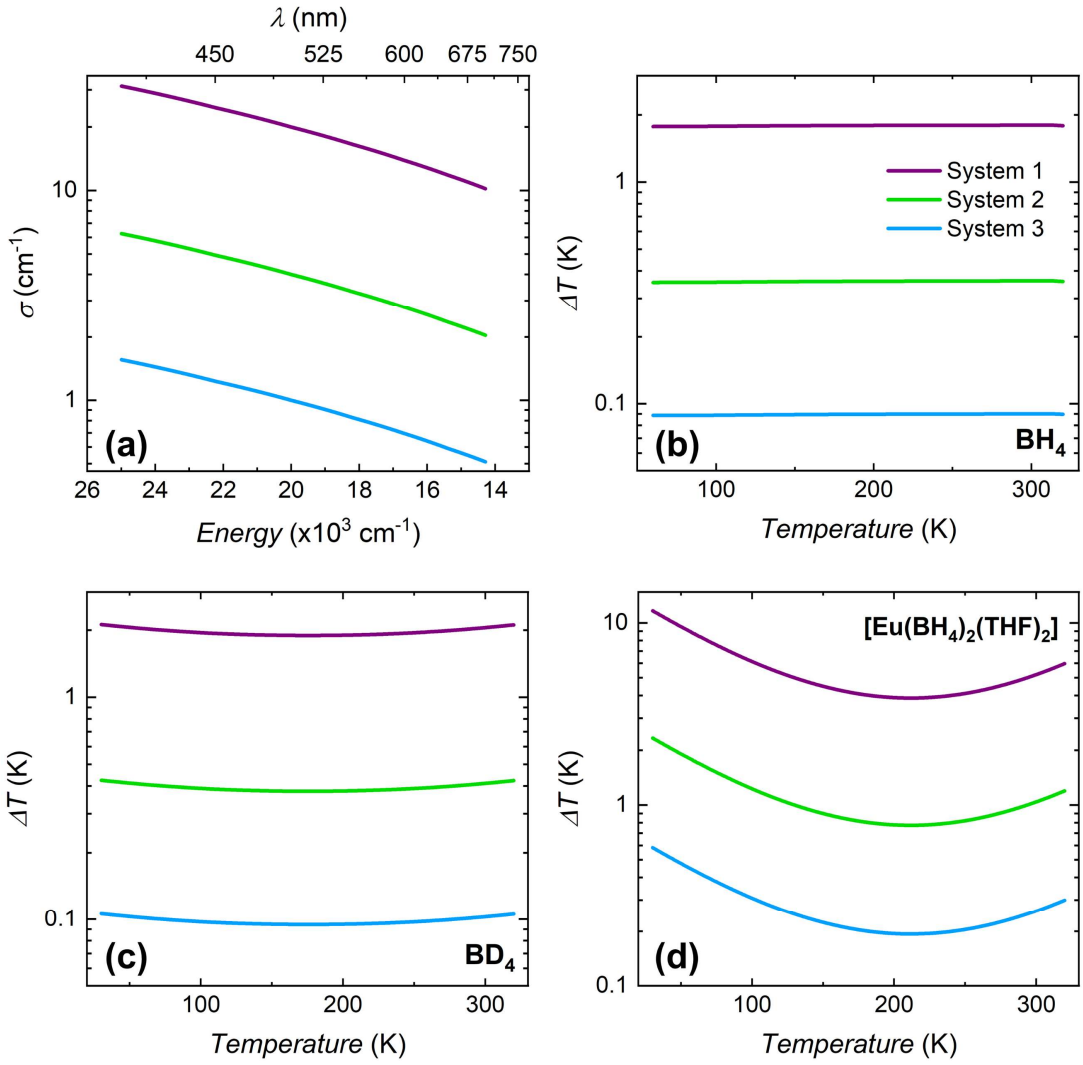


Figure 2.8. (a) Wavelength dependence of the instrumental error σ for three different model spectroscopic systems (with wavelength resolution increasing from 0.5 nm in System 1 to 0.1 nm in System 2 to 0.025 nm in System 3). Temperature uncertainty ΔT values for (b) **2.1**, (c) **2.2**, and (d) $[Eu^{II}(BH_4)_2(THF)_2]$ (lower is better).

While the thermometric performance of the precursor $[Eu^{II}(BH_4)_2(THF)_2]$ already matches that of some high-performing quantum-dot based sensors, complex **2.1** undergoes a 67% larger energy shift over its sensing range and exhibits a 53% improvement in sensitivity in comparison. Crucially, **2.1** emits in the red spectral range, thus has inherently higher temperature resolution than a blue-green emitter such as $[Eu^{II}(BH_4)_2(THF)_2]$; this is because the wavelength resolution of optical detectors is higher at longer

wavelengths, as described above. As anticipated, **2.1** represents a unique example of an organometallic, discrete molecular Eu^{II} luminescence thermometer. The present result showcases the value of carbon-donor ligands in promoting high thermometric performance and suggests that molecular organometallic Eu^{II} compounds have tremendous potential as luminescence thermometers.

2.6 Variable-temperature structural analysis

To understand such luminescence thermometric behaviour and performance, it is critical to closely examine the molecular level. Especially, contrary to trivalent lanthanides, the *5d* orbitals involved in the $4f^6 5d^1$ excited-state configuration of Eu^{II} interact strongly with ligands, and thus the energy of the excited state and properties of the metal-centered luminescence are highly sensitive to ligand field effects.[30] Therefore, to elucidate the remarkable temperature-dependent emission of **2.1**, we carried out luminescence-structural correlation studies through variable-temperature single crystal X-ray diffraction within the range where thermometric behaviour was observed. The metrical parameters obtained from several crystal structures of **2.1** measured at 90, 175, 200, 203 and 270 K were carefully compared (Table 2.2, Figures 2.9 and 2.10) and correlated to the corresponding energy of the emission band maximum at each temperature. We expected that variations in the Eu-ligand distances with temperature would be major contributors to the observed changes in luminescence with temperature, as is frequently the case for Ln^{II}-doped inorganic solids.[30,99,106,175] Surprisingly, however, the Eu-Cp*(cent) and Eu-O(THF) distances remain almost constant across the measured temperature range (within 0.004 and 0.006 Å, respectively). Meanwhile, the Eu-B distances increase by 0.03 Å with increasing temperature, concurrent with an equal increase in the B-B′ distances and an increase in the intramolecular Eu-Eu′ distance of 0.06 Å. The coordination geometry of a mononuclear fragment of **2.1** was analyzed using SHAPE 2.1 (Table A2 and Figure A8) and is best described as a distorted square pyramid around each Eu^{II} ion, with the ion above the basal plane of the pyramid. Notably, the complex increasingly distorts from the idealized square pyramidal geometry with increasing temperature, and furthermore, the Eu^{II} ions(s) migrate further from the basal plane (by 0.025 Å) with increasing temperature. As might be expected, the unit cell volume increases by 93.1 $Å^3$ (with a concomitant decrease in the crystal density of -0.06 g/cm^3), as does the closest intermolecular Eu-Eu distance (by 0.21 Å) with increasing temperature. From these data, a thermal expansion coefficient $\alpha_V = 2.54 \times 10^{-4}\ K^{-1}$ can be calculated for crystals of **2.1**,[106] consistent with the expectation for organic crystals.[176] Over the selected temperature range (90-270 K), the emission peak energy increases by 1288 cm^{-1} (i.e., the emission peak is blue-shifted by 52 nm).

Table 2.2. Selected metrical parameters from crystal structures of **2.1** at various temperatures, in comparison to the emission peak energy.

Temperature (K)	Eu-Cp*(cent) distance (Å)	Avg. Eu-O(THF) distance (Å)	Avg. Eu-B distance (Å)	B1-B1′ distance (Å)	B1-Eu-B1′ angle (°)	Intramolecular Eu-Eu′ distance (Å)	Avg. of all Eu-ligand bonds (Å)	Unit cell volume (Å^3)	Crystal density (g/cm^3)	Closest intermolecular Eu-Eu distance (Å)	Emission peak energy (cm^{-1})
90	2.5259(5)	2.5917(60)	2.8885(132)	3.9258(158)	85.608(351)	4.2387(7)	2.6687(66)	2015.6(2)	1.470	9.3132(8)	15124
175	2.5224(3)	2.6071(23)	2.9019(41)	3.9547(51)	85.899(108)	4.2483(4)	2.6771(22)	2058.2(1)	1.440	9.4142(4)	15721[b]
200	2.5226(4)	2.6011(53)	2.9015(105)	3.9399(142)	85.521(278)	4.2606(7)	2.6750(54)	2068.3(2)	1.433	9.4553(6)	15900
203	2.5185(3)	2.6081(18)	2.9068(31)	3.9547(41)	85.720(81)	4.2616(5)	2.6778(17)	2071.6(2)	1.431	9.4600(5)	15925[b]
270	2.5222(4)	2.5976(61)	2.9233(134)	3.9594(154)	85.248(283)	4.3022(7)	2.6810(66)	2108.7(2)	1.406	9.5211(6)	16412
Δ(parameter)[a]	-	-	**+0.0349**	**+0.0336**	**-0.360**	**+0.0635**	**+0.0124**	**+93.1**	**-0.064**	**+0.2079**	**+1288**

[a] Change in the corresponding parameter over the selected temperature range, expressed in the indicated units. [b] Interpolated using the Boltzmann-type equation described in the main text.

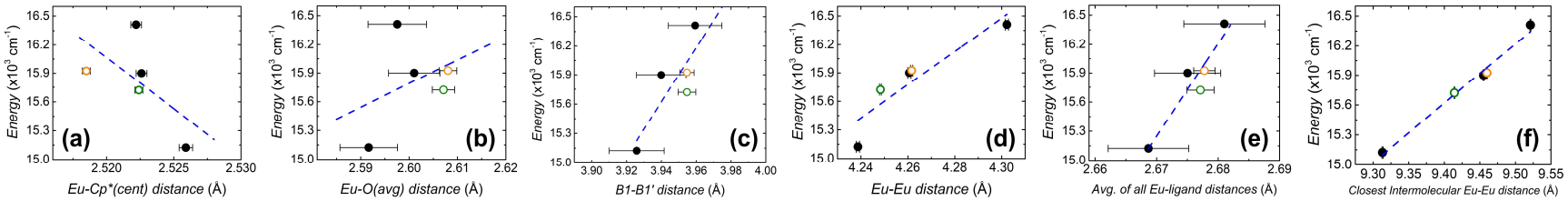


Figure 2.9. Plots of the emission peak energy of **2.1** as a function of the Eu-Cp*(cent) distance (a), the average Eu-O(THF) distance (b), the B1-B1′ distance (c), the intramolecular Eu-Eu′ distance (d), the average of all Eu-ligand distances (e), and the closest intermolecular Eu-Eu distance (f). The open green points represent data collected for a different crystal using the same diffractometer. The open orange points represent data collected on a different crystal using a different diffractometer. This demonstrates the consistency of the change in metrical parameters across the entire sample. Error bars are shown but overlap the points in some cases. The dashed blue lines are linear fits of the data to the equation $y = mx + b$. Best fitting parameters are as follows: (a) no correlation; (b) no correlation; (c) $m = 27.9$, $b = -94.5$, $R^2 = 0.5989$; (d) $m = 17.6$, $b = -59.0$, $R^2 = 0.7859$; (e) $m = 95.8$, $b = -240$, $R^2 = 0.8628$; (f) $m = 5.99$, $b = -40.7$, $R^2 = 0.9832$.

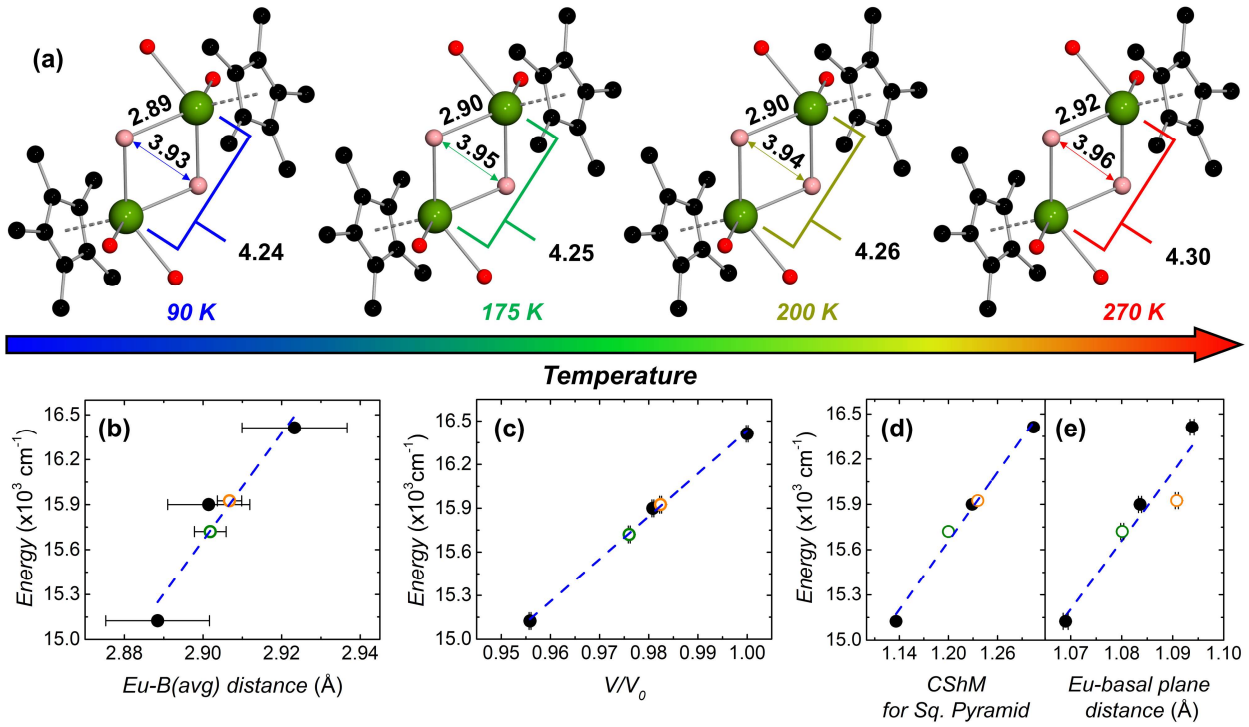


Figure 2.10. Variable-temperature structural analysis. (a) Temperature dependence of selected bond lengths from the crystal structure of **2.1**. The structure is truncated for clarity. Green = Eu, red = O, black = C, pink = B. Plots of emission peak energy as a function of the average Eu-B distance (b) and the relative compression of the lattice (c). (d) Plot of emission peak energy as a function of the distortion of the coordination geometry around Eu. The distortion is represented by the continuous shape measure (CShM), which quantifies the deviation of the real coordination polyhedron from an idealized square pyramid. A value of zero represents exact agreement with the idealized geometry. (e) Plot of emission peak energy as a function of the distance between the Eu ion and the basal plane of the coordination pyramid, defined by the atoms B1, B1′, O1 and O2 (see Figure 2.1). The solid black points represent data collected from the same crystal at varying temperatures. The open green points represent data collected for a different crystal using the same diffractometer. The open orange points represent data collected on a different crystal using a different diffractometer. This demonstrates the consistency of the change in metrical parameters across the entire sample. Error bars are shown but overlap the points in some cases. The dashed blue lines are linear fits of the data to the equation $y = mx + b$. Best fitting parameters are as follows: (b) $m = 35.7, b = -87.8, R^2 = 0.9108$; (c) $m = 29.3, b = -12.9, R^2 = 0.9975$; (d) $m = 7.6, b = 6.6, R^2 = 0.9875$; (e) $m = 45.4, b = -33.4, R^2 = 0.8810$.

2.7 Structural effects on optical properties

The thermochromism of **2.1** can be considered as a dynamic extension of the well-documented principles governing the emission peak energy in Eu^{II}-containing inorganic compounds, namely the geometry, ligand field splitting, metal-ligand covalency, and ligand polarizability of the coordination environment,[42,48,175,177–180] all of which are interrelated. The excited state configuration is strongly affected by the ligand field, as the overlap of the *5d* orbitals and the ligand orbitals is considerable.[30,42,49] These relatively strong interactions lead to significant variability of the *5d* manifold energy with the ligand field.[166,178] Metal-ligand covalency

also increases as the polarizability of the ligand increases, leading to increasing red-shifts of the emitting state energy.[42,48] The deep red (i.e., low energy) emission of **2.1** at low temperatures is thus a result of the large ligand-field splitting imparted by the strongly donating Cp* ligand, in concert with the high polarizability of the tetrahydroborate ligands,[181] which favour lower-energy emitting states.[166] The pliability of borohydride lattices has been demonstrated to yield materials that are highly sensitive to pressure[180] and temperature,[106] consistent with the properties of our complex **2.1**. The structural changes observed in **2.1** point to an overall distancing of the ligands from the Eu^{II} ion with increasing temperature, e.g., the increasing volume of the crystalline lattice and lengthening of Eu-[BH_4] distances. It is well known that the lengthening of metal-ligand bonds decreases the strength of the ligand field exerted by the ligand(s), thereby decreasing the magnitude of the ligand field splitting (in this case, of the Eu^{II} $4f^{n-1}5d^1$ state).[30] This then drives the emitting level (lowest $f^{n-1}d^1$)[21] to higher energies and thus shorter emission wavelengths, as observed for **2.1** with increasing temperature (Figures 2.10b and 2.11, also see Figure 2.9e).

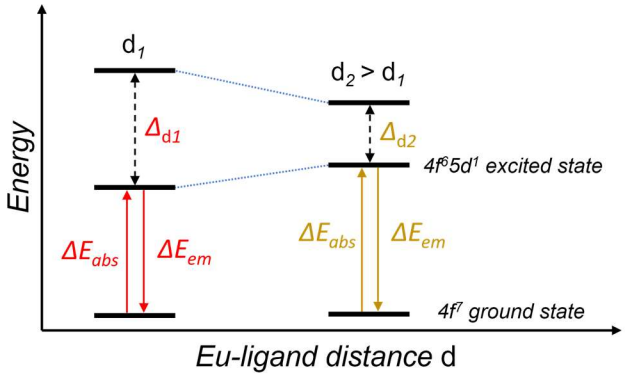


Figure 2.11. Schematic diagram of the general effect of Eu-ligand distance on ligand field splitting and emission peak energy in a Eu^{II} complex. The energy levels represent generalized "low-" and "high-" energy ligand-field states.

The magnitude of the change in transition energy as a function of Eu-[BH_4] bond length in **2.1** (*ca.* 37 000 cm^{-1}/Å) is comparable to the analogous change as a function of Ce-Cl distance computed for Cs_2NaYCl_6:Ce^{III} (*ca.* 30 000 cm^{-1} $Å^{-1}$), an archetypal lanthanide-doped inorganic solid with *5d*→*4f* emission.[177] The effects of the distortion of the square-pyramidal Eu^{II} coordination geometry (*vide supra*) must also be considered, as the change in position of the ion relative to the basal plane of the pyramid will influence the ligand-field splitting in the *5d* excited state.[182] Indeed, the emission peak energy of **2.1** correlates strongly to the magnitude of these distortions (Figure 2.10d and e). It has been demonstrated for octahedrally-coordinated *f*-element ions that the metal-ligand bond lengths shorten upon $f^{n-1}d(t_{2g})^1 \leftarrow f^n$ excitation, regardless of the environment.[177,183–185] This contraction arises from a combination of the *5d* and ligand orbital interactions previously described and a stabilization of the *4f* hole generated in the excitation process *via* charge-transfer interactions with the ligands.[30,186] It is possible that the maximal excited-state bond contraction for **2.1** occurs at 60 K, below which no closer approach of the ligands to the central ion is possible, leading to the observed invariability of emission peak energy with temperature in the range 10-60 K.

To further investigate ligand effects on the thermochromic luminescence of **2.1**, an analogue bearing bridging tetradeuteroborate moieties (**2.2**) was prepared, and its solid-state luminescence properties analyzed.

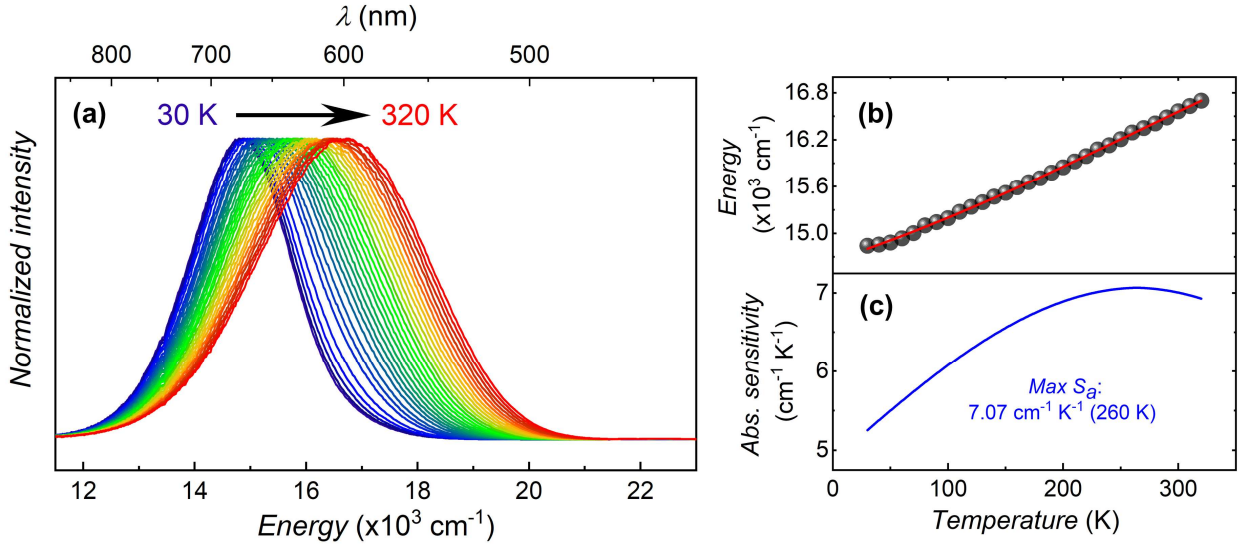


Figure 2.12. Temperature-dependent emission of **2.2**. (a) Temperature-dependent emission spectra ($\boldsymbol{\lambda_{ex}}$ = 330 nm) for **2.2** obtained in the solid state over the 30-320 K range with steps of 10 K. (b) Temperature-dependence of the emission peak energy. The red line represents the Boltzmann function (eq. 2.1) used to fit the experimental data. Best-fitting parameters: $R^2 = 0.999$, $A_1 = 13362$, $A_2 = 19214$, and $x_0 = 261$. (c) Absolute sensitivity obtained as the first derivative of the fitted function.

Complex **2.2** exhibits slightly red-shifted luminescence at 10 K (674 nm ≅ 14 839 cm^{-1}) *cf.* **2.1**, and a very similar blue-shift of the emission band peak with increasing temperature (Figure 2.12a, ΔE = 1858 cm^{-1}). However, the band shift of **2.2** begins at 30 K, rather than 60 K as observed for 2.**1**. While the emission peak energies of **2.1** and **2.2** follow virtually the same trend with increasing temperature (Figure 2.12b), the peak energies of **2.2** become increasingly lower *cf.* **2.1** at 150 K and above, though the largest difference in energy is only 158 cm^{-1} at 320 K. These slight differences cause the maximum absolute sensitivity of **2.2** to be somewhat lower (7.07 cm^{-1} K^{-1}) than that of **2.1** and reach this maximum at a lower temperature (260 K) (Figure 2.12c). Due to the significantly higher mass of deuterium relative to protium, the vibrational energies of a B-D bond will be lower than an otherwise identical B-H bond. Indeed, these differences can be readily observed when comparing the IR spectra of **2.1** and **2.2** (Figure 2.13), wherein the BX_4 vibrational band is shifted to lower energy by 630 cm^{-1}. The differences in emission peak energy between these complexes can thus be attributed primarily to the significantly different vibrational energies of the bridging BX_4 ligands, which manifests most obviously at higher temperatures. Table 2.3 compares the metrical parameters of **2.1** and **2.2** from crystal structures of each obtained at the same temperature (203 K). The average Eu-O(THF) distance and average of all Eu-ligand distances are longer in **2.2** than **2.1**, but the average Eu-B distance is identical, and the intramolecular Eu-Eu distance is distinctly shorter. Most notably, **2.2** has a larger unit cell volume (by 15 $Å^3$) than **2.1**, suggesting that the compressibility of crystals of **2.2** may be higher than those of **2.1**. This, combined with the observation that the emission peak of **2.2** begins shifting at lower temperature *cf.* **2.1**, supports the premise that the lower limit of the temperature sensing range is correlated with the compressibility of the lattice. This comparison further demonstrates the

importance of the tetra(hydro/deutero)borate ligand(s) toward the thermochromic luminescence properties of these complexes. A comparison of the emission peak energies and sensitivities for each of $[Eu(BH_4)_2(THF)_2]$, **2.1**, and **2.2** are presented in Figure 2.14.

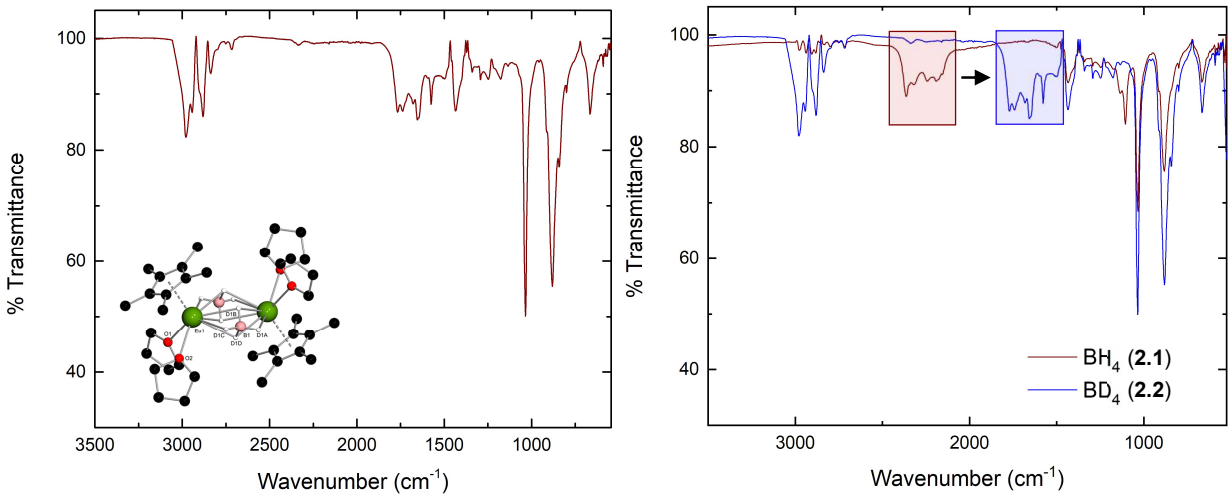


Figure 2.13. *Left:* Infrared spectrum of complex **2.2**. *Right:* Infrared spectra of **2.1** and **2.2** overlaid for comparison. The centre frequency of the BX_4 vibration band shifts by 630 cm^{-1} upon substitution of D for H, from approx. 2260 cm^{-1} to approx. 1630 cm^{-1}. A very weak absorbance is observed at 2337 cm^{-1} in the spectrum of **2.2**, which is most likely due to a small amount of ^1H incorporation from the 98%-D $NaBD_4$ used in the synthesis.

Table 2.3. Comparison of metrical parameters between **2.1** and **2.2** at 203 K.

Parameter	**2.1**	**2.2**
Eu-Cp*(cent) distance (Å)	2.5185(3)	2.5208(6)
Eu-O(avg) distance (Å)	2.6081(18)	2.6207(30)
Eu-B(avg) distance (Å)	2.9068(31)	2.9060(58)
B1-B1' distance (Å)	3.9547(41)	3.9638(76)
Eu-Eu distance (Å)	4.2616(5)	4.2508(12)
Avg of Eu-L distances (Å)	2.6778(17)	2.6825(31)
Unit Cell Volume ($Å^3$)	2071.6(2)	2086.9(1)
Crystal Density (g/cm^3)	1.431	1.433

Time-dependent DFT calculations (Figure A9 and Tables A3 and A4) predict intense *5d←4f* absorption in the range 24-29 000 cm^{-1}, consistent with the experimentally determined excitation profile (*vide supra*). However, these calculations also show a lower-energy charge transfer band involving the THF ligands, which is not visible in the excitation profile. The energy of this predicted absorption band also changes substantially with increasing temperature (by ~1500 cm^{-1}). The *5d←4f* absorption bands calculated for the 90 and 270 K crystal structures of **2.1** have only a small energy shift, suggesting that the origin of the thermochromic luminescence might be more complex than a simple change in vertical transition energy; charge-transfer states intermediate to the *4f-5d* transition may play a role in the observed photoluminescence of complex **2.1**. The Hirshfeld surfaces of **2.1** at each temperature were analyzed, and only weak H-H and H-C intermolecular crystal packing interactions were observed (Figure A10), the

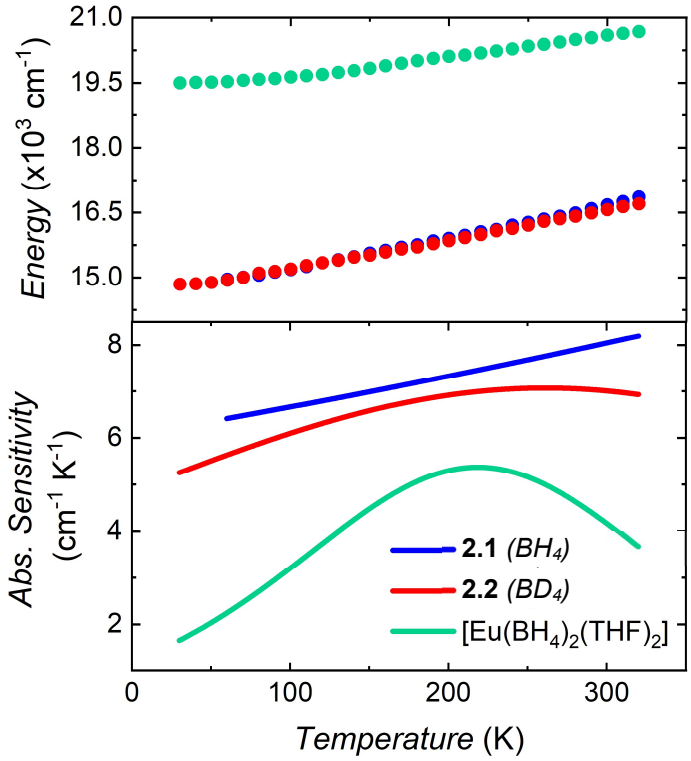


Figure 2.14. Comparison of the emission peak energy (top) and absolute sensitivity (bottom) of $[Eu(BH_4)_2(THF)_2]$, **2.1**, and **2.2** as a function of temperature.

strength and nature of which did not appear to correlate meaningfully with temperature. No intermolecular interactions whatsoever involving Eu, O or B were observed. It is thus unlikely that the thermochromic luminescence of **2.1** is due to intermolecular interactions. This opto-structural analysis suggests the thermochromism of **2.1** is dictated by the overall distortion of the Eu^{II} coordination environment with temperature, i.e., a simultaneous combination of all effects described above.

2.8 Conclusions

In summary, we report a notable example of an organometallic Eu^{II} molecular complex that acts as an efficient luminescence thermometer over a broad temperature range (60-320 K). The opto-structural correlation presented here represents a starting point for understanding how to modulate the thermometric performance of molecular Eu^{II} compounds. The high absolute sensitivity of 8.2 cm^{-1} K^{-1} obtained for complex **2.1**, the highest reported to date, reveals the potential of Eu^{II} compounds as viable molecular thermometers. The emission occurring in the red spectral region guarantees high temperature resolution. The emission peak energy of **2.1** is correlated with a change in Eu-ligand bond lengths, particularly of Eu-$[BH_4]$ bonds, and other geometric distortions of the Eu^{II} coordination environment as a function of temperature, though charge-transfer interactions may also play a role in the observed emission. Further studies with different Eu^{II} complexes are anticipated to elucidate the exact origin of the temperature-sensitive luminescence and unlock the applicability of these compounds as luminescence thermometers through a deep and systematic study of how the structural features affect the band-shift behaviour.

2.9 Experimental

General. All manipulations were conducted under stringently oxygen- and moisture-free conditions under argon or nitrogen atmospheres using Schlenk line and glovebox techniques. All solvents were dried on columns of activated alumina using a J.C. Meyer Phoenix solvent system and degassed via repeated freeze-pump-thaw cycles, then stored over activated 4 Å molecular sieves. All reagents were purchased from STREM Chemicals, Sigma-Aldrich, or Fisher Scientific and used as received. Potassium pentamethylcyclopentadienide (KCp^*)[187] and $[Eu(BH_4)_2(THF)_2]$[56] were prepared by reported procedures. $[Eu(BD_4)_2(THF)_2]$ was prepared according to the literature,[56] using protiated tetrahydrofuran rather than deuterated tetrahydrofuran. The $NaBD_4$ used was 98 atom % deuterium (Sigma).

Elemental analysis. Elemental analysis was performed by Midwest Microlab (Indianapolis, USA). Organolanthanide complexes, especially those of divalent ions, are well-known to suffer incomplete combustion and formation of carbides during microanalysis, yielding consistently and artificially low values.[60] Complexes bearing solvent ligands are further plagued by artificially low values due to loss of coordinated solvent during sample loading and/or combustion, thus microanalysis values should be considered within a wider tolerance than usually expected. Here, elemental analysis has been treated in a manner consistent with the literature regarding divalent organolanthanide compounds.

Infrared spectroscopy. Fourier transform infrared (FTIR) spectra were recorded in the $\tilde{\nu}$ = 4000-525 cm^{-1} range on a Nicolet 6700 FTIR spectrometer equipped with an attenuated total reflectance (ATR) attachment. Samples comprised suspensions of crushed polycrystalline solid in a thin layer of Parabar 10312 oil; background spectra were corrected for the presence of the oil.

NMR spectroscopy. All NMR spectra were recorded using a Bruker AVANCE II 300 MHz spectrometer. Samples were prepared inside the glove box and sealed with a septum, Teflon tape and a layer of Parafilm to minimize incursion of air and moisture. ^1H chemical shifts are reported in ppm relative to tetramethylsilane using the THF-d_8 residual solvent signal at δ = 1.72 as an internal standard.

X-ray crystallography. X-ray crystallography of **2.1** and **2.2** were performed using a Bruker AXS KAPPA single-crystal diffractometer equipped with an APEX II CCD detector, using graphite-monochromated Mo Kα radiation (λ = 0.71073 Å) from a sealed tube source. The crystals chosen were mounted on the tip of a 200 μm MicroLoop using Parabar 10312 oil and cooled to 203.15 K. Raw data collection and processing were performed with the Bruker APEX II software package.[188,189] A multi-scan absorption correction was applied (SADABS).[190] The crystal structures were solved via direct methods and refined using a full-matrix least-squares method on F^2 using the SHELXTL program suite[191–193] and the Olex2 user interface.[194] Non-hydrogen atoms were refined anisotropically. The positions of all hydrogen atoms except for those bonded to boron were calculated based on the geometry of their respective atoms and are included at geometrically idealized positions [riding model]. Hydrogen atoms bonded to boron were located in the Fourier difference map and allowed to refine freely.

Variable-temperature X-ray structural analysis. Additional crystallographic analysis of **2.1** at varying temperatures (90, 175, 200, and 270 K) was performed using a Bruker D8 VENTURE METALJET single-crystal diffractometer equipped with a Photon III CMOS detector, using Ga Kα radiation (λ = 1.34139 Å) from a liquid Ga source (Bruker METALJET D2 PLUS with HELIOS MX optics). The crystals chosen were

mounted on a loop fiber using Parabar 10312 oil and cooled to the indicated temperatures. Raw data collection and processing were performed as above, using the Bruker APEX 3 software package.[195–197] The H atoms of the BH_4 moieties were refined with an isotropic displacement parameter with a SADI restraint applied on all B-H distances. All other H atoms were generated geometrically and were included in the refinement in the riding model approximation; their temperature factors were set to a multiple of the equivalent isotropic temperature factors of the parent site (aromatic 1.2 times; methyl 1.5 times the factor). There was positional disorder of the Cp* moiety; the occupancy ratio was left to refine freely.

All diagrams were prepared using Diamond 4[198,199] or Mercury 2020.1[200] and POV-Ray.[201] The data has been deposited with the Cambridge Crystallographic Data Centre under deposition numbers 2107457-61 and 2126609. Analysis of the coordination geometry was performed using SHAPE 2.1,[202,203] using the THF oxygen atoms, centroid of the Cp* ligand, and the central boron atoms of the tetrahydroborate ligands as vertices. Hirshfeld surface analysis was performed using CrystalExplorer21.[204]

Photoluminescence spectroscopy. Photoluminescence data was obtained using a Horiba QuantaMaster 8075-21 spectrofluorometer. An ozone-free PowerArc 75 W xenon lamp was used as the radiation source. The excitation spectra were corrected in real time according to the lamp intensity and the optical system of the excitation monochromator using a silicon diode as a reference. The emission spectra were corrected according to the optical system of the emission monochromator and the photomultiplier response (Hamamatsu R13456 red-extended PMT). Samples were prepared inside the glove box and comprised a small amount of crystalline solid placed inside a screw-top quartz cuvette, which was then sealed with an additional layer of Teflon tape. Low-temperature measurements were performed with the samples mounted inside a CS202*E-DMX-1AL closed-cycle helium cryostat system (Advanced Research Systems), controlled via a LakeShore 335 temperature controller.

Magnetometry. Magnetic susceptibility measurements were performed using a Quantum Design MPMS-XL7 SQUID magnetometer operating in the temperature range 1.8-300 K. DC measurements were performed on crushed polycrystalline samples of **2.1** restrained in a matrix of vacuum grease (Corning) and wrapped in a polyethylene membrane. The magnetization data were collected at 100 K to check for ferromagnetic impurities, which were absent. Diamagnetic corrections were applied for the sample holder, and the inherent diamagnetism of the prepared sample was estimated with the use of Pascal's constants. $\chi_M T$ data was fitted using PHI 3.1.5.[205]

Synthesis of $[Cp^*Eu(BH_4)(THF)_2]_2$ (2.1). In a glove box under a positive pressure of nitrogen gas, $[Eu(BH_4)_2(THF)_2]$ (100 mg, 0.31 mmol) and KCp* (54 mg, 0.31 mmol) were dissolved in dry tetrahydrofuran (5 mL) with stirring. The solution immediately attained a yellow-orange colour, and orange luminescence was observed when the solution was excited with a 405 nm laser pointer. The mixture was stirred for 24 hr. at room temperature, during which a substantial quantity of precipitate formed. The mixture was filtered over a pad of Celite, and the pad rinsed with several 0.5 mL portions of tetrahydrofuran until the washings ran colourless. The filtrate was concentrated *in vacuo* until incipient crystallization, then tetrahydrofuran was added dropwise until all the solid just dissolved. The so-formed saturated solution was stored at -20 °C, resulting in the formation of yellow blocklike crystals. These were isolated by decantation of the supernatant and dried briefly under vacuum. This process was repeated with the supernatant to give **2.1** (71 mg, 51% yield over three crops). ^{1}H NMR (300 MHz, THF-d_8) δ: 235 ppm (s, Cp* methyl); $B(H)_4$ was not observed and coordinated THF could not be distinguished from residual THF. IR: $\tilde{\nu}$ = 2976 (w),

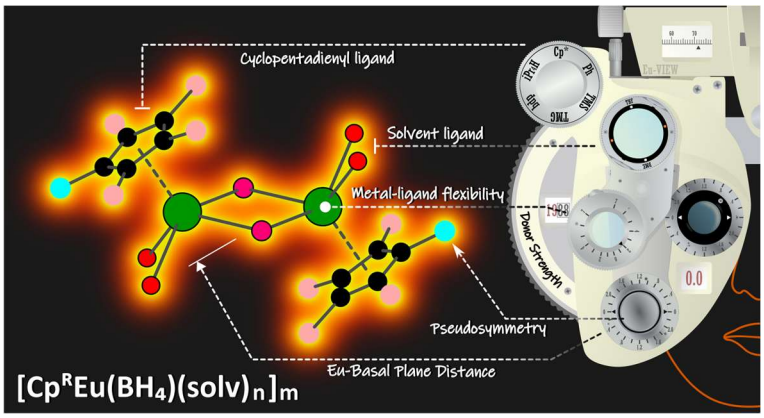
2939 (w), 2904 (w), 2883 (w), 2832 (vw), 2800 (w), 2715 (w), 2360 (m), 2318 (m), 2243 (m), 2191 (m), 1435 (br, m), 1340 (w), 1292 (w), 1246 (w), 1136 (m), 1105 (s), 1034 (vs), 881 (br, vs), 667 (br, m) cm^{-1}. Elemental analysis was consistent with the fully desolvated complex: Anal. calc'd. (%) for $C_{20}H_{38}B_2Eu_2$ (604.07) (**2.1** with loss of 4x coordinated THF): C, 39.77; H, 6.34. Found: C, 39.74; H, 6.63.

Synthesis of [Cp*Eu(BD$_4$)(THF)$_2$]$_2$ (2.2). Prepared following the same procedure as for **2.1** with $[Eu(BD_4)_2(THF)_2]$ (77 mg, 0.23 mmol) and KCp* (40 mg, 0.23 mmol) to give **2.2** (50 mg, 48% yield over two crops). IR: $\tilde{\nu}$ = 2980 (s), 2943 (s), 2881 (s), 2839 (w), 2717 (w), 1768 (s), 1740 (s), 1680 (s), 1655 (s), 1576 (s), 1498 (w), 1435 (br, s), 1340 (w), 1294 (w), 1248 (w), 1176 (w), 1036 (vs), 881 (br, vs), 843 (s, sh), 800 (m, sh), 665 (br, s) cm^{-1}.

These compounds are highly air- and moisture-sensitive. Samples coated in Parabar oil appear to have increased stability and can be stored under ambient conditions for several days with only very slow decomposition. Decomposed samples present as off-white or pinkish powders rather than yellow crystalline solid.

CHAPTER 3
Ligand Effects on the Emission Characteristics of Molecular Eu^{II} Luminescence Thermometers

3.1 Preface



The work detailed in this chapter was published as an Article in *Journal of the American Chemical Society* and is reprinted with permission from Diaz-Rodriguez, R. M., Gálico, D. A., Chartrand, D., Murugesu, M., *J. Am. Chem. Soc.* **2024**, *146*, 34118–34129. Copyright 2024 American Chemical Society.

R. M. Diaz-Rodriguez performed all chemical synthesis; characterized the synthesized compounds by IR and NMR spectroscopy; collected, solved and refined SCXRD data for basic characterization of all Eu^{II} complexes and performed NoSpherA2 refinements; interpreted structural data; collected and interpreted photoluminescence spectra for all complexes; and wrote the original manuscript. D. A. Gálico interpreted photoluminescence and structural data and contributed to writing and editing of parts of the manuscript. D. Chartrand collected, solved and refined variable-temperature SCXRD data for complexes **3.1**, **3.2**, **3.3** and **3.4**. M. Murugesu oversaw all aspects of the project.

Additional data and discussion pertaining to this chapter are given in Appendix B.

3.2 Abstract

Discrete molecular organometallic europium(II) complexes are promising functional materials due to their ability to behave as highly sensitive band-shift luminescence thermometers. Furthering our understanding of the design principles salient to the emission behaviour of such systems is important for developing them in this emerging application. To this end, a series of pseudo-C_{4v}-symmetric organometallic europium(II) complexes bearing systematically varying ligand sets was synthesized and characterized to probe the influence of subtle structural modification on their optical properties. Opto-structural correlation analyses via variable-temperature single-crystal X-ray diffraction and photoluminescence spectroscopy reveal a remarkable variability in properties among structurally similar complexes, and a convoluted dependence of the emission characteristics on the stereoelectronic properties of the ligands. A few factors of particular influence are nevertheless identified, including the distance between the europium(II) ion and the basal plane of the square-pyramidal coordination polyhedron, the presence of pendant electron density that might further interact with the excited-state 5*d* orbitals, and, qualitatively, the metal-ligand flexibility of the construct. These results help to elucidate principles that govern the luminescence properties of

organometallic europium(II) complexes, with an eye to enabling the rational design of high-performance luminescence thermometers of this genre.

3.3 Introduction

Luminescence thermometry is a remote-detection temperature measurement technique that relies upon a change in the emission properties of a luminescent probe, such as a doped solid, nanoparticle, or molecule, as a function of temperature.[93] This technique has many potential applications in advanced devices, as the spatial resolution of a nanosized thermometric probe is unparalleled by any existing thermometric technology.[92] Luminescent materials based on trivalent lanthanide ions have been extensively studied for luminescence thermometry applications[91] due to the narrow emission band structure and thermosensitive emission intensity of these ions, which allow for a "ratiometric" temperature measurement strategy based on emission intensity.[29,160,163,206] Additionally, the Laporte-forbidden $f \rightarrow f$ transitions that characterize the luminescence of the trivalent lanthanides are very long-lived, allowing for changes in excited-state lifetimes with temperature to be employed as an alternative thermometric parameter ("lifetime thermometry").[207–209] More recently, materials based on divalent lanthanide ions, especially Eu^{II} and Sm^{II}, have been increasingly investigated in this regard, as the luminescence of these ions is dominated by Laporte-allowed $d \rightarrow f$ emission which are broad and intense.[30,43,46,66,210] The shift in energy of these emission bands with changing temperature can then be taken as a thermometric parameter for "band-shift" luminescence thermometry.[99,106,211]

The distinctive luminescence properties of divalent europium have been the subject of a wealth of studies. The relationship between structure and emission of Eu^{II} doped into myriad inorganic matrices[46,48,106,108,110–115,117,118,143,166,175,179,180,185,212,213] and in a variety of Werner-type coordination complexes,[157,211,214–218] e.g., those featuring (pyrazolyl)borate[57,82–85,158,219,220] and crown ether/cryptand ligands,[55,59,65–79,81,221–223] is now well understood. Luminescence studies of organometallic Eu^{II} complexes, on the other hand, are dominated by metallocenes.[58,60,61,86,88,89] However, our group recently reported on the organoeuropium(II) complex $[Cp^*Eu(\mu\text{-}BH_4)(THF)_2]_2$ (**2.1**), which is distinguished from other luminescent organoeuropium(II) systems by its marked thermochromism. It was the first (and, to the best of our knowledge, remains the only) example of an organometallic, discrete molecular band-shift luminescence thermometer, which also exhibited the highest absolute sensitivity of any lanthanide-based band-shift thermometer to date (8.2 $cm^{-1}\ K^{-1}$).[224] The thermochromism in the luminescence of this complex was found to correlate with a combination of structural distortions with varying temperature, and small structural changes had an unexpectedly large effect on the emission band energies. This study revealed the great potential that molecular Eu^{II} compounds have as luminescence thermometers.

The singular existing member of this promising category of molecular materials is insufficient to gain profound insight into the structural properties that influence its luminescence. Rather, comparing a variety of analogues would enable a systematic investigation of that relationship, advancing our currently limited understanding of the entire category. Therein lies a significant advantage presented by discrete molecular systems: the potential for precise structural control, which can allow targeted investigations of structure-property relationships and, eventually, application-focused design of tailored systems. The dimeric hemimetallocene architecture exemplified by **2.1** represents an ideal starting point from which to forge better optostructural correlations, as it is well-positioned to accommodate a broad variety of substituted cyclopentadienyl moieties and supporting solvent ligands. Considering also the high thermometric performance demonstrated by **2.1**, we envisioned that analysis of analogues of this system bearing different ligands could shed light on how the emission characteristics of molecular Eu^{II} luminescence thermometers could be controlled through engineering of the coordination sphere. To this

end, herein we report the synthesis, structural and photoluminescence characterization of several divalent europium complexes of the form $[Cp^{R}Eu(\mu\text{-}BH_4)(solv)_n]_m$ (solv = THF, 1,2-dimethoxyethane (DME); n = 1 or 2; m = 2 or ∞) with varying ligand sets. All these complexes share a similar square-pyramidal coordination geometry, with two solvento oxygen atoms and two tetrahydroborate boron atoms defining the basal plane, and the cyclopentadienyl centroid in the axial position. Despite this similarity, the emission characteristics and thermometric performance differ greatly across the series; we are therefore able to perform the first systematic comparison of the luminescence properties of thermochromic organoeuropium(II) complexes as a function of their varying coordination environments. Variable-temperature single-crystal X-ray diffraction analysis highlights the subtle structural factors that affect the emission band energies in these compounds and emphasizes the complex and highly convoluted relationship between these parameters.

3.4 Synthesis and structural characterization of Eu complexes

The synthetic pathways to the complexes described herein are presented in Figure 3.1.

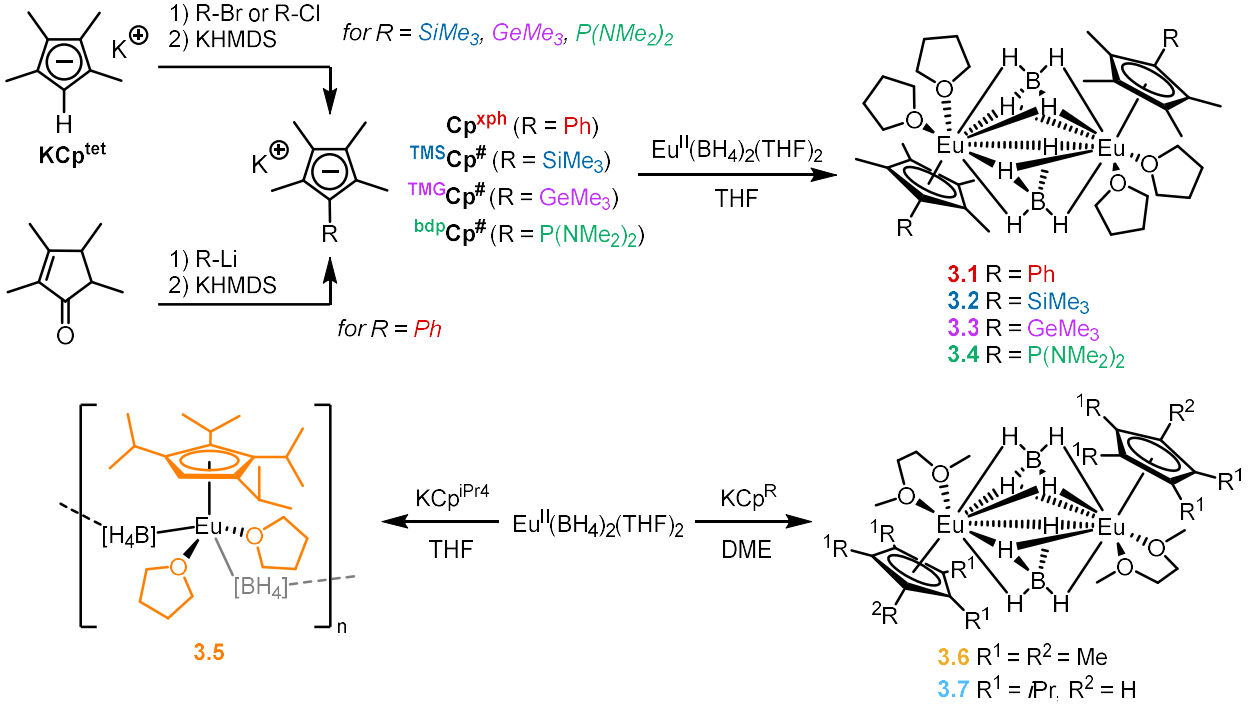


Figure 3.1. Synthesis of organometallic Eu^{II} complexes **3.1**–**3.7** for optostructural correlation investigation.

To investigate the electronic effect of the organometallic fragment of the complexes on their structural features and luminescence, a series of complexes $[(\eta^5\text{-}C_5Me_4R)Eu(\mu\text{-}BH_4)(THF)_2]_2$ was prepared with R = Ph (**3.1**), $SiMe_3$ (**3.2**), $GeMe_3$ (**3.3**), and $P(NMe_2)_2$ (**3.4**). These ligands were selected for their synthetic accessibility and to span a range of electronic profiles based on the chosen substituent. The ligand precursors $K(C_5Me_4R)$ were synthesized via either electrophilic addition of R-X (X = Cl or Br) to KCp^{tet} (for R = $SiMe_3$, $GeMe_3$, and $P(NMe_2)_2$; Cp^{tet} = $[C_5Me_4H]^-$)[225–227] followed by deprotonation with potassium hexamethyldisilazide (KHMDS), or nucleophilic addition of R-Li to 2,3,4,5-tetramethylcyclopenten-2-one (for R = Ph)[60,187] followed by deprotonation with KHMDS. The equimolar reaction of these $K(C_5Me_4R)$ with $[Eu^{II}(BH_4)_2(THF)_2]$ in THF followed by crystallization gave the desired complexes **3.1**–**3.4** in moderate to

good yields. Crystals suitable for X-ray diffraction analysis were obtained for all compounds, and each of them crystallized in the triclinic space group $P\bar{1}$. Complexes **3.1**–**3.4** are isostructural dimers where the square-pyramidal Eu^{II} centers are bridged by two $(\mu_3\text{-H})_2B(\mu_2\text{-H})_2$ units,[169] with a monoanionic cyclopentadienyl ligand and two molecules of THF completing the coordination environment of each Eu^{II} ion (Figures B1-8), as previously observed for 2.**1**.[224] Additionally, to better understand the steric effects of the organometallic ligand, we chose $[C_5iPr_4H]^-$ ("Cp^{iPr4}")[228–230] as a sterically encumbering ligand with which to compare to the above series [**2.1, 3.1**–**3.4**]. We prepared the corresponding ligand precursor by hydrolysis of previously prepared $NaCp^{iPr4}$ with stoichiometric water to give the parent cyclopentadiene,[231,232] followed by deprotonation with KHMDS. Unexpectedly, the equimolar reaction of KCp^{iPr4} with $[Eu^{II}(BH_4)_2(THF)_2]$ in THF followed by crystallization from THF/alkanes reproducibly gave the one-dimensional coordination polymer $[Cp^{iPr4}Eu(\mu\text{-}BH_4)(THF)_2]_\infty$ (**3.5**), which crystallized in the orthorhombic space group Pbcn (Figure 3.3). An analogous reaction using DME as the reaction and crystallization solvent instead gave the desired dimer $[Cp^{iPr4}Eu(\mu\text{-}BH_4)(DME)]_2$ (**3.7**), which crystallized in the triclinic space group $P\bar{1}$ (Figures B12-13). The equimolar reaction of less bulky cyclopentadienides, e.g. KCp or KCp′ (Cp′ = $[C_5H_4(SiMe_3)]^-$), with $[Eu^{II}(BH_4)_2(THF)_2]$ in THF failed to completely consume either of the starting materials and otherwise gave only intractable, insoluble, and/or non-emissive residues. Finally, to examine the effects of the solvent ligand on the luminescence properties of these complexes, we prepared the DME-solvated dimer $[Cp^*Eu(\mu\text{-}BH_4)(DME)]_2$ (**3.6**) in an analogous manner to **2.1** and **3.7**. This complex crystallized in the orthorhombic space group Pbca and is isostructural to the other dimeric complexes **2.1, 3.1**–**3.4** and **3.7** (Figures B10-11). The solid-state structures of the complexes **3.1**–**3.4** and **3.6**–**3.7** are shown in Figure 3.2.

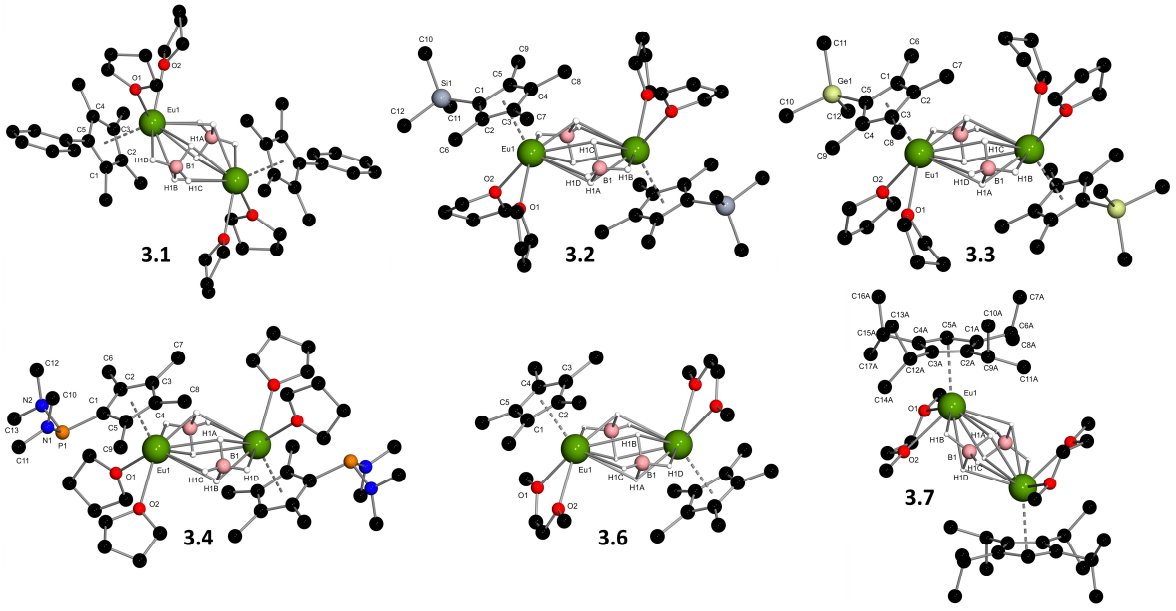


Figure 3.2. Solid-state structures of complexes **3.1**–**3.4**, **3.6** and **3.7** at 200-213 K. Ellipsoid diagrams and packing diagrams for all complexes are given in Appendix B. Labels are given only to selected crystallographically unique atoms. Hydrogen atoms bonded to carbon have been omitted for clarity.

Several other solvents were investigated as supporting ligands for these complexes, with little success. Reactions of equimolar KCp* and $[Eu^{II}(BH_4)_2(THF)_2]$ conducted in tetrahydrothiophene (THT), N-methylpyrrolidine, tetramethylethylenediamine (TMEDA), or tetrahydropyran were confounded by the

poor- or insolubility of $[Eu^{II}(BH_4)_2(THF)_2]$ and/or any potential products in those solvents, and no tractable or crystalline product was recovered in any case.

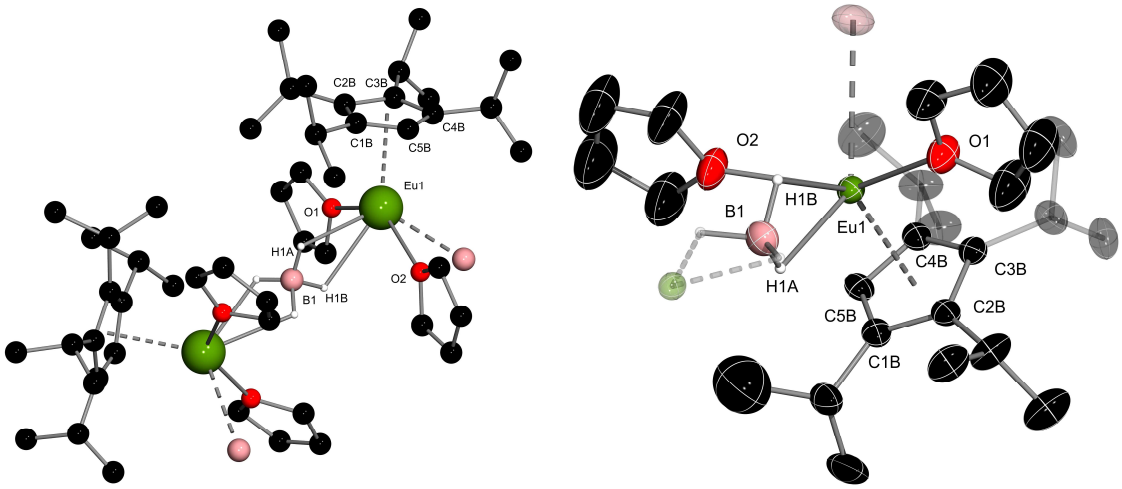


Figure 3.3. *Left:* Solid-state structure of **3.5**. Two units of the infinite one-dimensional coordination polymer are depicted. Labels are only given to selected, crystallographically unique atoms. Hydrogen atoms bonded to carbon have been omitted for clarity. For clarity, only one component of the disordered Cp^{iPr4} ring is shown. *Right:* Thermal ellipsoid diagram (30% probability for clarity) of **3.5**. Large thermal ellipsoids are a consequence of the significant disorder present in this structure. Only one repeating unit of the polymeric structure and one component of the disorder is shown for clarity. Hydrogen atoms bonded to carbon are omitted for clarity. Labels are given only to the crystallographically unique atoms which coordinate the Eu^{II} centre. Packing diagrams are shown in Figure B9.

The same reaction was attempted using pyridine as a solvent, which on one occasion gave non-emissive red-violet blocklike crystals that decomposed upon attempted isolation, after which the investigation was discontinued. Furthermore, the synthesis of $[Eu^{II}(BH_4)_2(THT)_2]$ from $EuCl_3$ and $NaBH_4$ in THT was attempted, but the reaction did not proceed. We also attempted to exclude the solvent ligand entirely by introducing triphenylphosphine oxide (TPPO) as a supporting ligand, given the known strong affinity of lanthanide ions for phosphine oxide ligands.[233,234] Treatment of **2.1** with 1 eq. TPPO in THF caused an instantaneous darkening of the yellow solution and quenching of the visible luminescence thereof. Unfortunately, attempts to crystallize the mixture from a variety of solvents and solvent mixtures returned only orange-coloured, non-emissive, oily residue that could not be characterized.

3.5 Photoluminescence

To determine the emission properties and thermometric performance of the complexes **3.1**–**3.7**, solid-state photoluminescence spectra of crystalline samples of each complex were obtained at varying temperatures. Excitation and emission spectra of each compound obtained at 10 K are shown in Figures 3.[4, 6, 8, 10, 12, 14, and 16]. As expected, the emission spectra of all complexes are dominated by a strong, broad $d \rightarrow f$ emission, varying in colour from yellow-green to red depending on the ligand set. As reported for **2.1**, excitation to the Eu^{II} 5*d* band is observed alongside ligand-based states in the UV and blue region from the excitation spectra of all complexes. As the temperature is increased, each of the complexes demonstrates a blue-shift in the energy at the emission band maximum; the temperature-dependent emission spectra of each compound are shown in Figures 3.[5, 7, 9, 11, 13, 15, and 17].

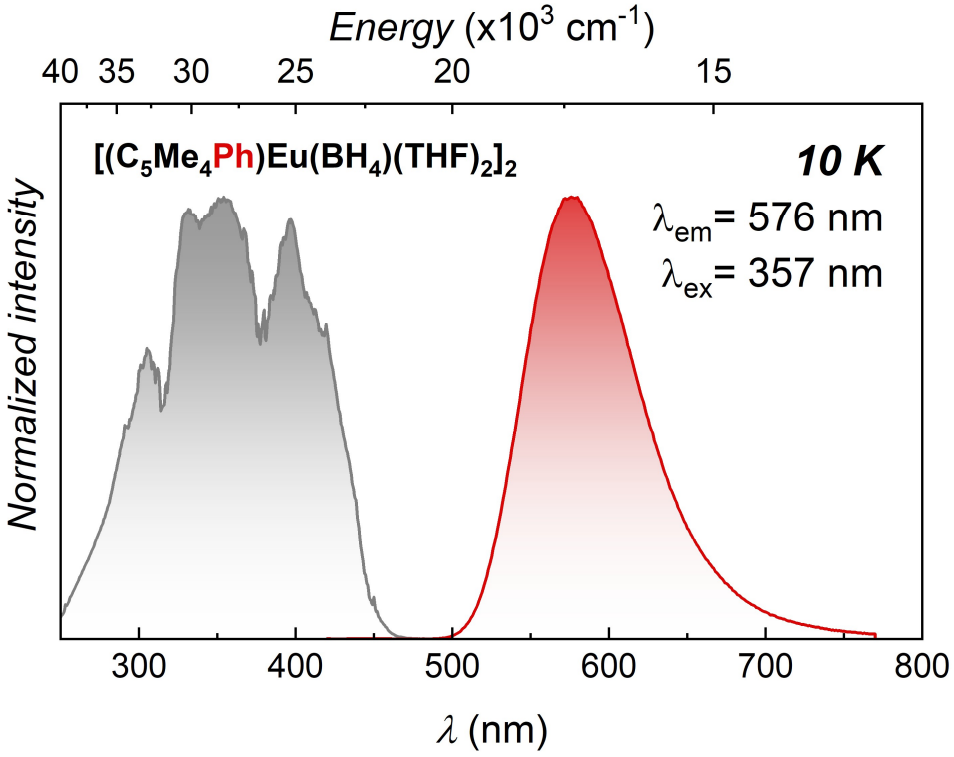


Figure 3.4. Solid-state excitation (grey) and emission (red) spectra for **3.1** obtained at 10 K.

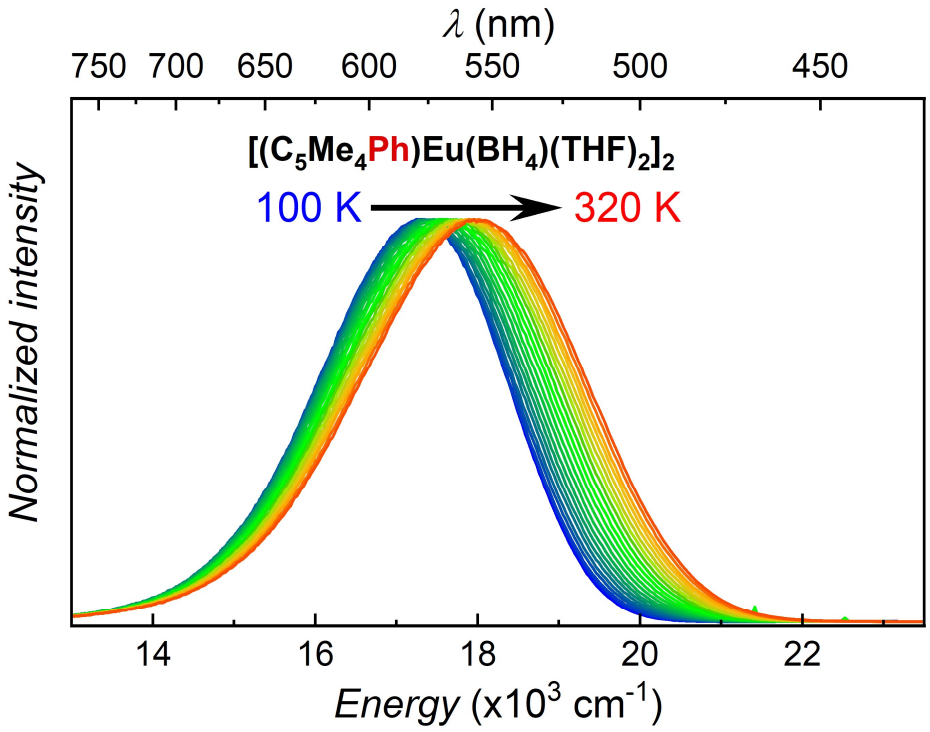


Figure 3.5. Temperature-dependent emission spectra (λ_{ex} = 357 nm) for **3.1** obtained in the solid state over the 100–320 K range with steps of 10 K.

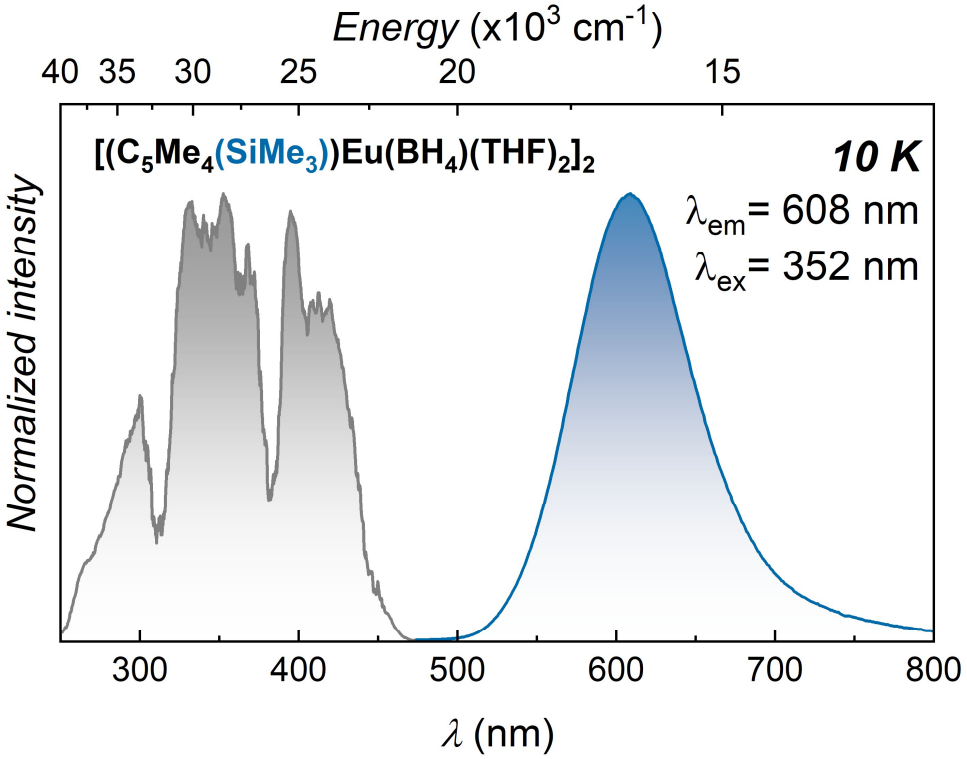


Figure 3.6. Solid-state excitation (grey) and emission (blue) spectra for **3.2** obtained at 10 K.

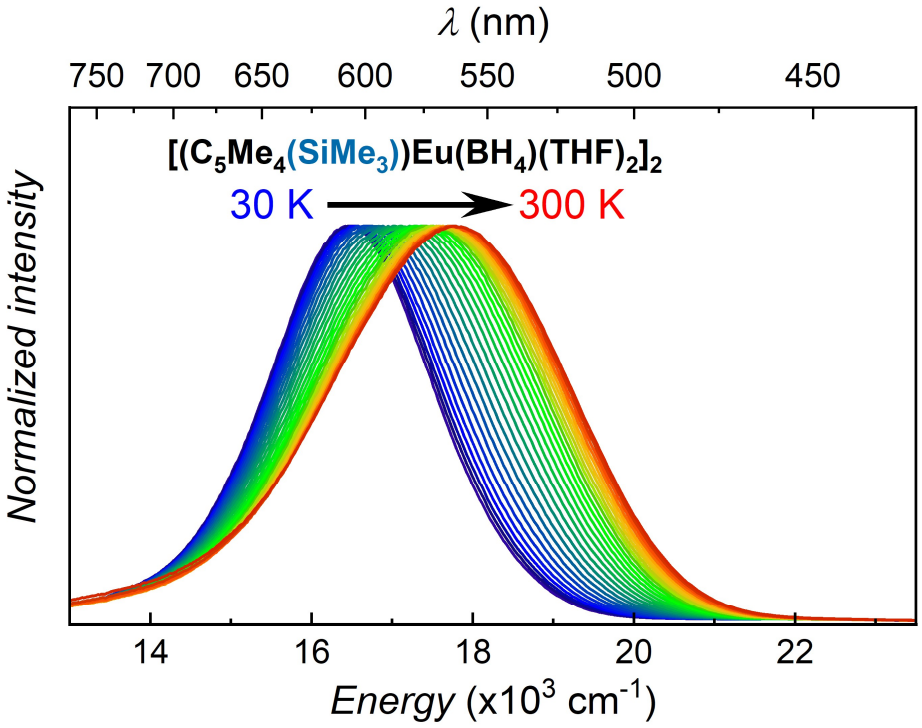


Figure 3.7. Temperature-dependent emission spectra (λ_{ex} = 352 nm) for **3.2** obtained in the solid state over the 30–300 K range with steps of 10 K.

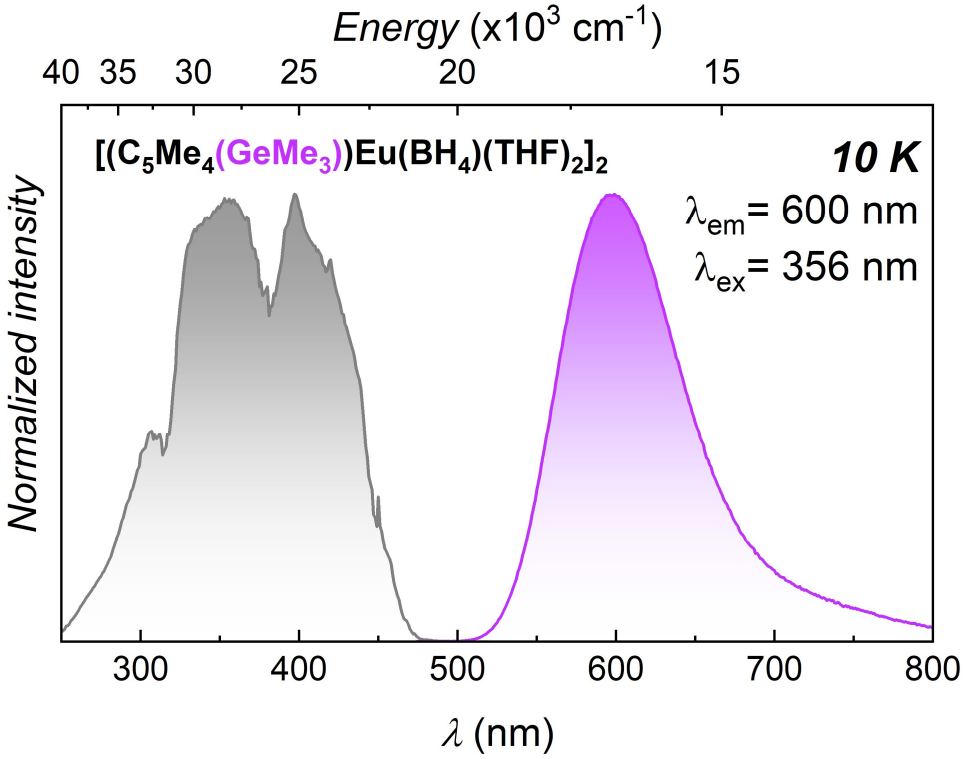


Figure 3.8. Solid-state excitation (grey) and emission (purple) spectra for **3.3** obtained at 10 K.

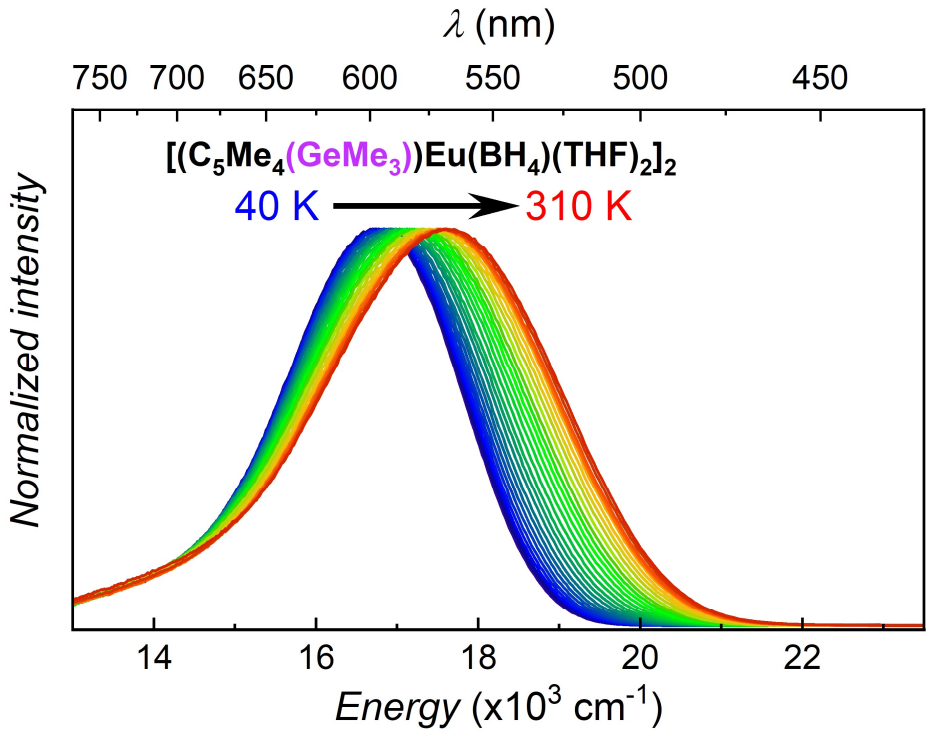


Figure 3.9. Temperature-dependent emission spectra (λ_{ex} = 356 nm) for **3.3** obtained in the solid state over the 40–310 K range with steps of 10 K.

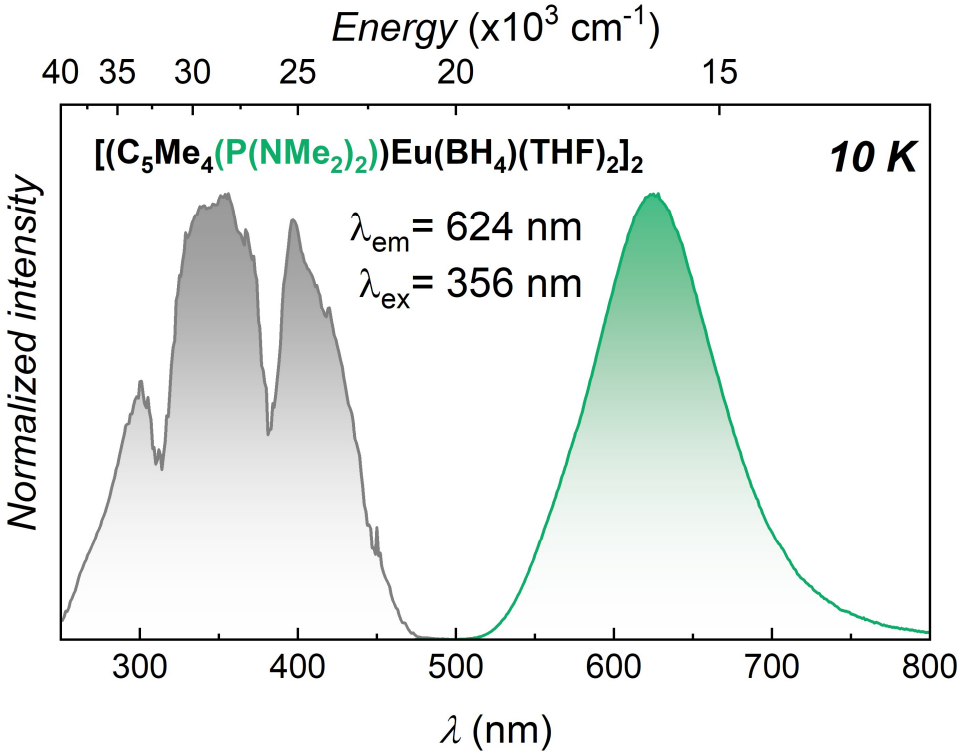


Figure 3.10. Solid-state excitation (grey) and emission (green) spectra for **3.4** obtained at 10 K.

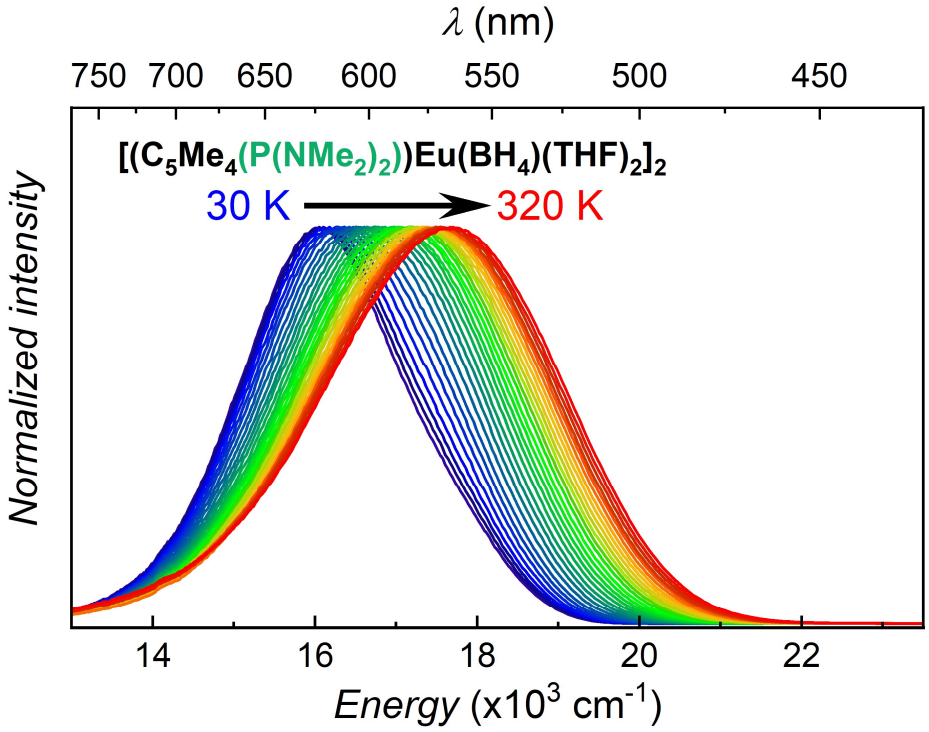


Figure 3.11. Temperature-dependent emission spectra (λ_{ex} = 356 nm) for **3.4** obtained in the solid state over the 30−320 K range with steps of 10 K.

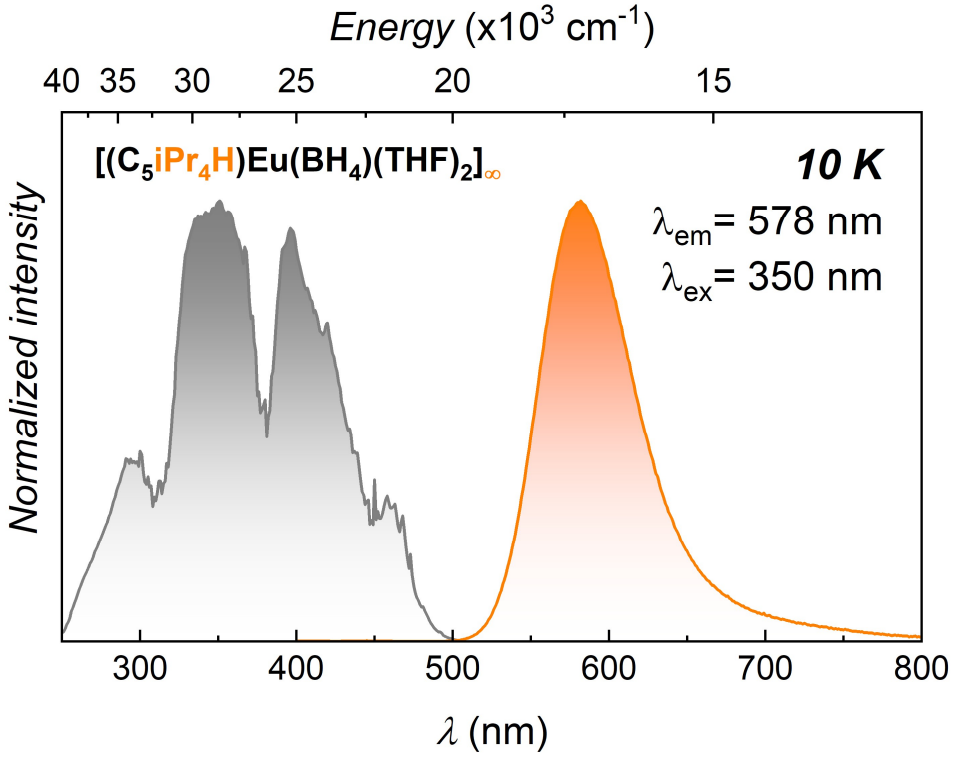


Figure 3.12. Solid-state excitation (grey) and emission (orange) spectra for **3.5** obtained at 10 K.

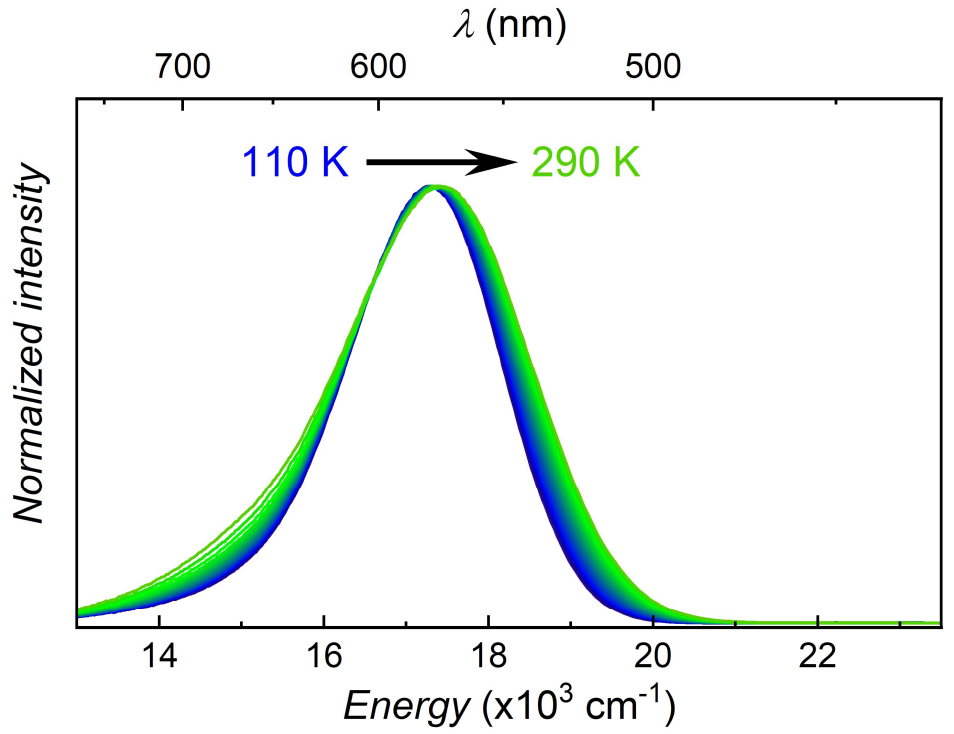


Figure 3.13. Temperature-dependent emission spectra (λ_{ex} = 350 nm) for **3.5** obtained in the solid state over the 110–290 K range with steps of 10 K.

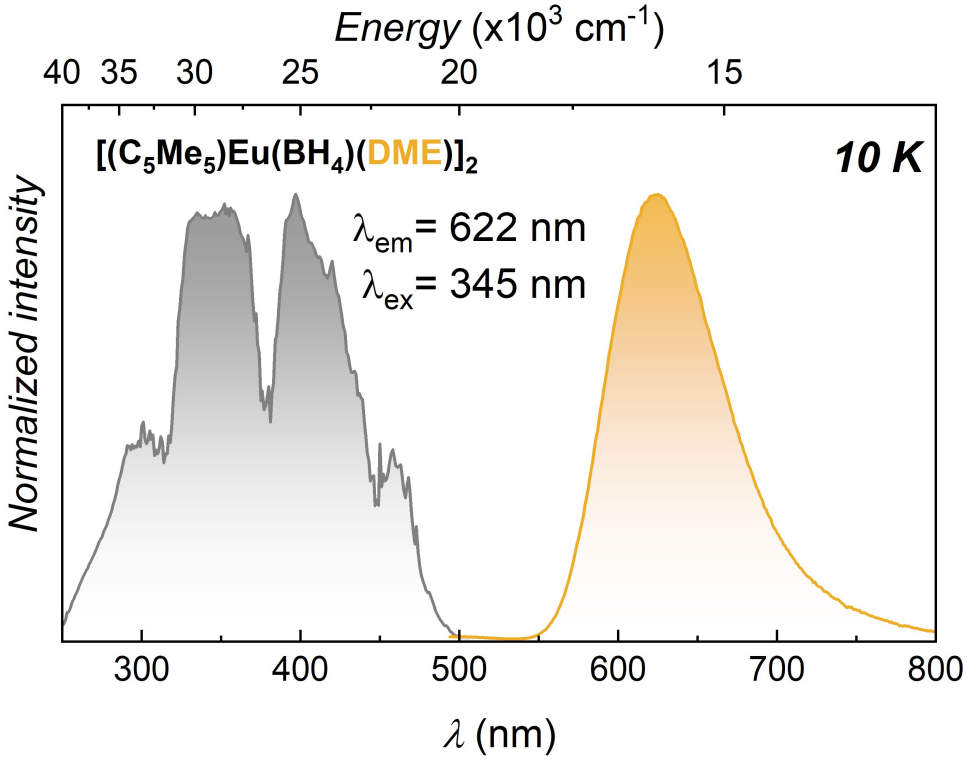


Figure 3.14. Solid-state excitation (grey) and emission (yellow) spectra for **3.6** obtained at 10 K.

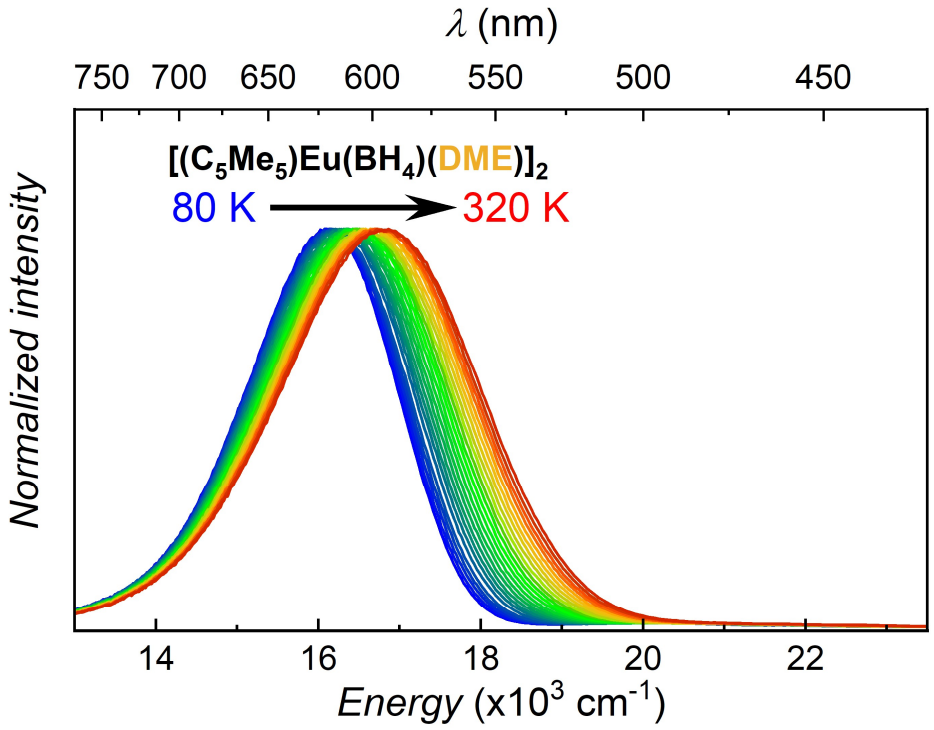


Figure 3.15. Temperature-dependent emission spectra (λ_{ex} = 345 nm) for **3.6** obtained in the solid state over the 80−320 K range with steps of 10 K.

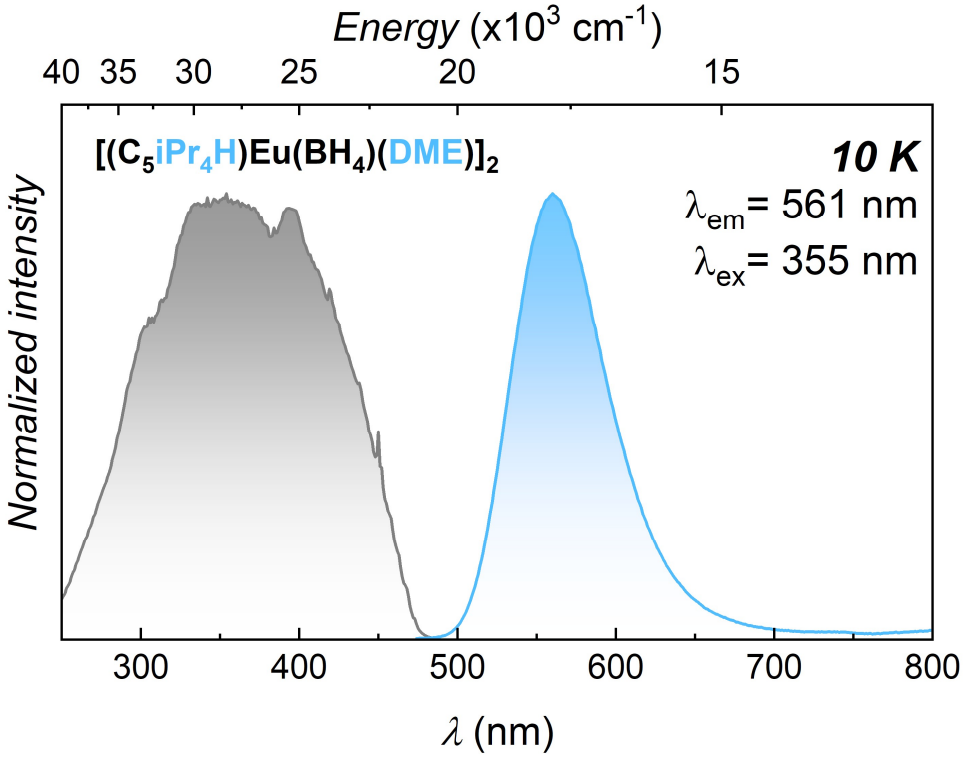


Figure 3.16. Solid-state excitation (grey) and emission (light blue) spectra for **3.7** obtained at 10 K.

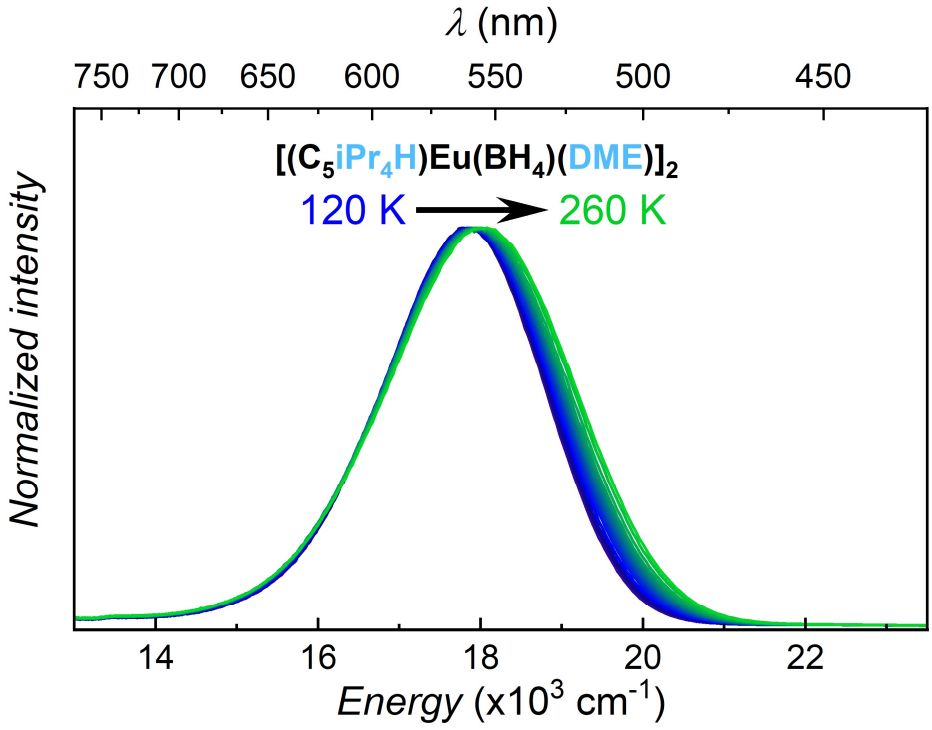


Figure 3.17. Temperature-dependent emission spectra (λ_{ex} = 355 nm) for **3.7** obtained in the solid state over the 120–260 K range with steps of 10 K.

Thus, as we previously demonstrated for **2.1**, complexes **3.1–3.4**, **3.6** and **3.7** act as luminescence thermometers, with the temperature-induced band shift acting as the thermometric parameter. On the other hand, complex **3.5** exhibits only a minimal band shift over the temperature range probed (≅2 nm ≡ 60 cm^{-1}), which is insufficient to be considered a luminescence thermometer (*vide infra*). Figure 3.18 and Table 3.1 summarize the relevant luminescence properties of all complexes discussed herein.

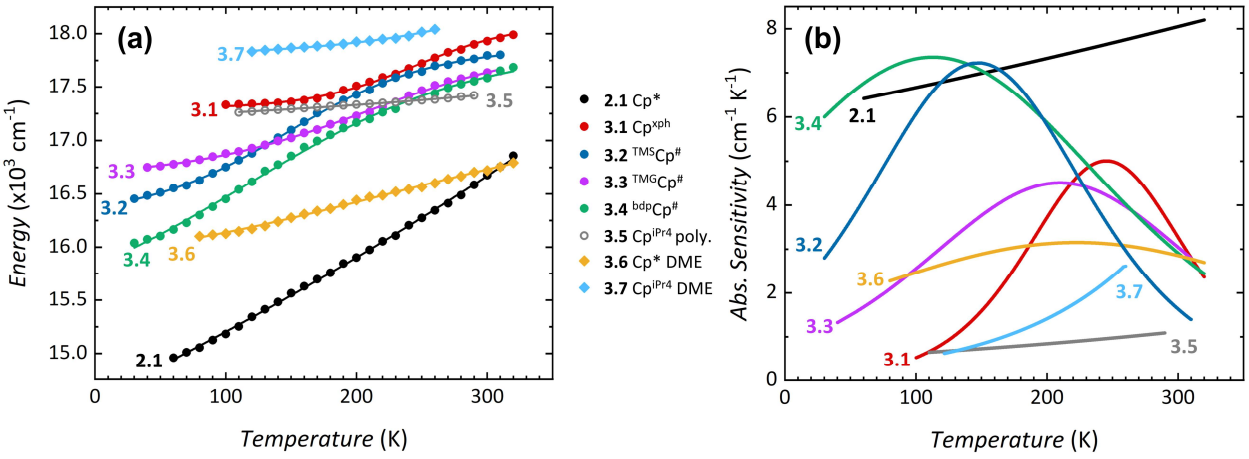


Figure 3.18. Thermometric performance of complexes **3.1–3.7** in comparison to the original complex **2.1**. (a) Temperature dependence of the energy at the emission band maximum, extracted from the temperature-dependent emission spectra. The solid lines represent the Boltzmann function used to fit the experimental data. Best-fitting parameters for each dataset are given in Table B1. (b) Absolute sensitivities obtained as the first derivative of the fitted functions shown in panel (a).

Table 3.1. Luminescence properties and thermometric performance of complexes **2.1**, **2.2**, **3.1–3.7**.

Compound	**2.1**[224]	**2.2**[224]	**3.1**[a]	**3.2**[a]	**3.3**[a]	**3.4**[a]	**3.5**[a]	**3.6**[a]	**3.7**[a]
Organometallic ligand	Cp*	Cp*	Cp^{xph}	$^{TMS}Cp^{\#}$	$^{TMG}Cp^{\#}$	$^{bdp}Cp^{\#}$	Cp^{iPr4}	Cp*	Cp^{iPr4}
Solvent ligand	THF	THF	THF	THF	THF	THF	THF	DME	DME
Bridging group	BH_4	BD_4	BH_4	BH_4	BH_4	BH_4	BH_4	BH_4	BH_4
Nuclearity *n*	2	2	2	2	2	2	∞	2	2
Sensing Range (K)	60-320	30-320	100-320	30-300	40-310	30-320	110-290	80-320	120-260
Energy at Band Maximum (cm^{-1})[b]	14 959	14 839	17 331	16 453	16 667	16 039	17 301	16 077	17 833
	16 858	16 697	17 953	17 803	17 606	17 686	17 361	16 863	18 040
ΔE (cm^{-1})[c]	1899	1858	622	1350	939	1647	60	786	207
S_a (cm^{-1} K^{-1})[d]	8.20	7.07	5.00	7.22	4.51	7.36	1.08	3.15	2.61
Temp. of max. S_a (K)	320	260	243	150	210	113	290	220	260
ΔT (K)[e]	0.35	0.39	0.63	0.40	0.66	0.37	2.79	0.86	1.24

[a] This work. [b] The first value is the energy at the low-temperature limit of the sensing range, and the second value is the energy at the high-temperature limit of the sensing range. [c] Change in the energy at the emission band maximum over the indicated sensing range. [d] Maximum value of the absolute sensitivity. [e] Temperature uncertainty at the temperature of maximum sensitivity, calculated as described in [224] assuming a wavelength resolution of 0.1 nm.

The temperature dependence of the maximum band energies for each complex can be fitted using a Boltzmann function (Figure 3.18a), and the absolute sensitivities S_a (Table 3.1, Figure 3.18b) are calculated from the first derivative of the fitted function, as previously described.[224] Despite the complexes **2.1, 3.1–3.4**, **3.6** and **3.7** being isostructural with respect to the atoms bound to Eu, we observe remarkable variability in their luminescence characteristics. Thus, we carefully examined each complex in terms of their stereoelectronic properties and metrical parameters, seeking correlations that would help us elucidate the factors affecting their emission behaviour.

3.6 Stereoelectronic effects

The π-coordinated Cp* ligand is employed broadly in applications that take advantage of its electron-richness and steric encumbrance, especially compared to the parent Cp. The former effect is due to the inductive donation of electron density into the ring that results from the five additional methyl groups that are appended. This increased electron density also leads Cp* to have strong donicity, and therefore cause a substantial ligand field splitting of n*d* states in its complexes. We previously proposed that the significantly red-shifted emission of complex **2.1** was in part a result of such large splitting of the 5*d* excited state leading to accordingly low-energy emissive levels.[224] The series of complexes **3.1–3.4** each bear a cyclopentadienyl ligand $[C_5Me_4R]^-$ that exchanges one methyl group of Cp* (*cf.* **2.1**) for a different substituent (*vide supra*). Using these, we can probe whether modulating the donor strength of the cyclopentadienyl ligand leads to a correlated modulation of the emission energy. The comparative donor strength of each of these ligands might be estimated by examining the electronics of the substituent R.[235] Analysis of the Hammett σ_P values of each substituent predicts that donor strength will increase as $P(NMe_2)_2 << GeMe_3 \approx Ph < SiMe_3 < Me$, according to electron-donating potential via both induction and resonance. A similar trend is predicted from the modified Swain-Lupton *F* parameter: $P(NMe_2)_2 < Ph < GeMe_3 < SiMe_3 \approx Me$. A concurring trend is again predicted by considering instead the Hammett σ_M values, which exclude contributions from resonance: $P(NMe_2)_2 < Ph < GeMe_3 < SiMe_3 < Me$. The energies at the emission band maxima of complexes **2.1, 3.1–3.4** at 10 K decrease as $Ph > GeMe_3 > SiMe_3 > P(NMe_2)_2 >> Me$. These trends agree except for the position of $P(NMe_2)_2$, suggesting that the donor strength of the ligand is inversely proportional to the emission energy of the complex, as expected. However, the position of the $P(NMe_2)_2$ substituent in the experimental series is curious, as the emission energy of the corresponding complex **3.4** is expected to be higher than that of the phenyl-substituted complex **3.1** based on substituent electronics alone. Instead, we find that **3.4** has the second-lowest energy (after the original complex **2.1**) at all temperatures, despite the ligand being ostensibly the weakest donor. Indeed, the electron-withdrawing power of the substituent itself is surprising, given that the two dimethylamino moieties provide considerable electron density to the phosphorous atom, and $[^{bdp}Cp^{\#}]^-$ is considered exceptionally electron-rich among known cyclopentadienylphosphanes.[227] The high emission energy of **3.1** can be partially rationalized by analysis of its crystal structure (Figure B1), which demonstrates that in the solid state, the phenyl substituent is locked in a conformation that is not coplanar with the cyclopentadienyl ring (the two rings are canted by ~50°). This maximizes its electron-withdrawing power by cancelling the mesomeric contribution. The trends derived from the electronic parameters of the substituents R correctly predict that the most strongly-donating ligand Cp* produces the complex with the lowest emission energy (i.e., **2.1**). It is, however, surprising that the trimethylsilyl-substituted complex **3.2** has emission energies dramatically (>1000 cm^{-1}) higher than **2.1** at all temperatures, despite the corresponding substituents being electronically very similar; they have identical *F* parameters (0.01) and differ in σ_M by only 0.03 units.[235] This may be explained by considering that R = Me is a much better resonance donor (σ_P = -0.17) than R = $SiMe_3$ (σ_P = -0.07). Finally,

it might be expected that an increase in the donicity of the organometallic fragment should lead to a shorter Eu-Cp(cent) distance. However, we observe no meaningful correlation between these metrics (Figure B16).

To further investigate the suitability of extrapolating the ligand donor strength based on substituent electronics, we attempted to directly measure the relative donor strength of each of the ligands. To do so, we prepared a series of cymantrenes $(C_5Me_4R)Mn^I(CO)_3$ bearing each of the ligands of interest, and measured the frequency of their A_1 carbonyl stretching mode via infrared spectroscopy in the solid state. In principle, this value is proportional to the donor strength of the ligand; the measurement is analogous to the classical Tolman parameter,[236,237] but adapted to a monoanionic, π-coordinated ligand framework. This analysis suggests an order of donor strength among these ligands of Ph < $P(NMe_2)_2$ < $SiMe_3$ ≈ Me < $GeMe_3$. The result that **3.1** has the highest emission energies among the series is correctly predicted by this method. Meanwhile, complex **3.4** still has lower-than-expected emission energies given its position in the donicity series. The most surprising result obtained from this probe is the implication that $^{TMG}Cp^{\#}$ is more donating than Cp*. This result is perhaps rationalizable given that the large size and polarizability of the $GeMe_3$ fragment may lead to increased electron density at the cyclopentadienyl centroid to which it is proximal (Ge-Cp(cent) distance 3.1474(3) Å). It might therefore be expected that the ensuing Eu complex **3.3** should have lower emission energy than **2.1**, but this is not the case. Additionally, the donor strength of the ligands $^{TMS}Cp^{\#}$ and Cp* are predicted to be virtually identical by this method, concurring with the trend predicted from the Swain-Lupton *F* parameter. One might therefore expect that the trimethylsilyl-substituted complex **3.2** would have largely similar emission energies to **2.1**. However, as discussed above, **3.2** has considerably higher emission energies than **2.1** at all temperatures.

The use of ν(CO) as a donicity probe in this manner is limited by an additional factor, which is that the total shift in frequency between all complexes measured is only 6 cm^{-1}, rendering it neither as sensitive nor as accurate as the Tolman parameter. Thus, we examined an alternative method that leverages the same $(C_5Me_4R)Mn^I(CO)_3$ complexes, this time comparing the chemical shifts of the carbonyl carbon resonances as measured by ^{13}C NMR spectroscopy. We surmised that ligands with higher donicity should result in a downfield shift of this resonance, in a manner analogous to the now well-established Huynh electronic parameter.[238] Here, we observe a Δδ of 0.1-0.2 ppm between complexes, and this analysis suggests an order of donor strength among these ligands of $P(NMe_2)_2$ < Ph ≈ $SiMe_3$ < $GeMe_3$ < Me. This method agrees with the Hammett and Swain-Lupton parameters regarding the most- and least-donating substituents, but otherwise does not accurately reproduce either the experimental energy series or the trends predicted from σ_P, σ_M, or *F*. A comparison of these different methods is given in Table 3.2. The Hammett σ_M parameter most accurately reproduces the measured emission energies of **2.1, 3.1–3.4**, suggesting that substituent electronics can provide a reasonable estimation of the effect that a given substituted cyclopentadienyl ligand will have on the emission energies of Eu^{II} hemimetallocenes.

Alongside the electronic differences among the cyclopentadienyl ligands of complexes **2.1, 3.1–3.4**, the accompanying steric differences should also be considered for a more thorough optostructural analysis. Figure B17 shows steric maps of each corresponding ligand, generated using SambVca 2.1.[239,240] Despite the different substituents, the steric profiles of each ligand are relatively similar, with $\%V_{bur}$ in the range 33-35. The steric maps demonstrate that the Cp* and $^{TMS}Cp^{\#}$ ligands are sterically similar in addition to being electronically similar, with buried volumes differing by only 0.1%. $^{TMG}Cp^{\#}$ is the bulkiest ligand in this series and Cp* is the least bulky, although there appears to be no meaningful overall correlation between bulkiness and emission energy (Figure B18).

Table 3.2. Comparison of various methods of estimating the donor strength of cyclopentadienyl ligands L = η^5-C_5Me_4R, and evaluation of how accurately each predicts the experimentally-determined emission energies of complexes $[LEu(\mu\text{-}BH_4)(THF)_2]_2$ (**2.1**, **3.1–3.4**).

R =	**Me**	**Ph**	**$SiMe_3$**	**$GeMe_3$**	**$P(NMe_2)_2$**	**(Predicted) emission energy trend**
Emission energy @ 10 K (cm^{-1})[a]	14 959[224]	17 331	16 453	16 667	16 039	Ph > $GeMe_3$ > $SiMe_3$ > $P(NMe_2)_2$ >> Me
σ_P[235]	-0.17	-0.01	-0.07	0	+0.25	$P(NMe_2)_2$ >> $GeMe_3$ ≈ Ph > $SiMe_3$ > Me
$\boldsymbol{\sigma_M}$[235]	**-0.07**	**+0.06**	**-0.04**	**0**	**+0.18**	**$P(NMe_2)_2$ > Ph > $GeMe_3$ > $SiMe_3$ > Me**
F[235]	+0.01	+0.12	+0.01	+0.03	+0.17	$P(NMe_2)_2$ > Ph > $GeMe_3$ > $SiMe_3$ ≈ Me
A_1 ν(CO) of $LMn(CO)_3$ (cm^{-1})	1988	1992	1988	1986	1990	Ph > $P(NMe_2)_2$ > $SiMe_3$ ≈ Me > $GeMe_3$
^{13}C δ(CO) of $LMn(CO)_3$ (ppm)	226.95	226.52	226.60	226.76	226.42	$P(NMe_2)_2$ > Ph ≈ $SiMe_3$ > $GeMe_3$ > Me

[a] of complexes **2.1, 3.1–3.4**, experimentally determined, as in Table 3.1 and Figures 3.[4, 6, 8, 10].

The preferential formation of the polymeric complex **3.5** from the equimolar reaction of KCp^{iPr4} and $[Eu^{II}(BH_4)_2(THF)_2]$ in THF confounds further analysis of steric effects on the emission properties, as a complex isostructural to **2.1** cannot be obtained with the bulky cyclopentadienide $[Cp^{iPr4}]^-$. It seems that the large steric profile of Cp^{iPr4} promotes the BH_4 ligand to coordinate in a κ^2-mode rather than a κ^3-mode,[170,172] leading to the formation of a polymer in THF. To accommodate the polymeric structure, the two THF ligands in **3.5** adopt a "trans-disposed" geometry in the Eu^{II} coordination sphere. In contrast, the THF ligands in the other complexes reported herein are "cis" to each other because of the BH_4-bridged dimeric structure. Complex **3.7** is forced to adopt a dimeric structure resembling **2.1** and **3.1–3.4** only due to chelation by DME. This suggests that there is an upper limit to the bulkiness of a bound cyclopentadienide that can be expected to form μ-BH_4 dimeric, THF-solvated complexes, ostensibly with good thermometric performance. Taken together, these results suggest that the stereoelectronic characteristics of the cyclopentadienyl ligand alone cannot account for the differences in luminescence properties among these complexes, though analysis of substituent electronics does have useful predictive power.

3.7 Variable-temperature structural analysis

In our previous work with **2.1**, variable-temperature single-crystal X-ray diffraction proved to be a valuable analytical tool; it demonstrated the significant effect that small geometric changes had on the emission energy of the complex and allowed us to determine which geometric distortions were most impactful.[224] Hence, we chose to employ a similar study in this work. Several crystal structures of each complex **3.1–3.4** and **3.6** were collected at 90, 150, 175, ~210, and 270 K, and metrical parameters were carefully compared. A summary of the temperature-dependent structural changes for each complex can be found Tables 3.3-3.17 and Figures 3.19-3.30. In addition to error bars, we have implemented a code of coloured lines between values in Tables 3.[3, 6, 9, 12, and 15] to help visualize statistical significance between measured values. In the case that two adjacent values have $|\Delta| \geq 3^*\sqrt{esu_1^2+esu_2^2}$, a blue line is drawn between them to indicate that the difference is significant. If this criterion is not met, a red line is drawn between them instead. The bottom row of each table ("Δ(parameter)") is populated with a value only if the difference between the value at 90 K and the value at 270 K meets the above criterion; this is independent of the presence of a correlation among these values (which is communicated via Tables 3.[4, 5, 7, 8, 10, 11, 13, 14, 16, 17] and visualized in Figures 3.19-3.30).

Table 3.3. Selected metrical parameters from crystal structures of **3.1** at various temperatures, in comparison to the energy at the emission band maxima. A statistically significant difference between two values is indicated via coloured dividing lines (*vide supra*).

Temperature (K)	Eu-Cp^{xph}(cent) distance (Å)	Avg. Eu-O(THF) distance (Å)	Avg. Eu-B distance (Å)	B1-B1′ distance (Å)	B1-Eu-B1′ angle (°)	Intramolecular Eu-Eu′ distance (Å)	Avg. of all Eu-ligand bonds (Å)	Unit cell volume (Å^3)	Crystal density (g/cm^3)	Closest intermolecular Eu-Eu distance (Å)	Emission band max. (cm^{-1})
90	2.5515(2)	2.5777(20)	2.8880(27)	3.8711(43)	84.161(76)	4.2871(3)	2.6724(16)	1143.46(7)	1.476	9.3300(4)	17 329
150	2.5421(4)	2.5740(64)	2.8888(97)	3.8435(157)	83.403(282)	4.3136(5)	2.6683(55)	1154.93(16)	1.462	9.3609(9)	17 358
175	2.5454(3)	2.5888(50)	2.9043(76)	3.8855(124)	83.969(217)	4.3176(6)	2.6795(43)	1158.73(9)	1.457	9.3721(6)	17 418[b]
208	2.5488(2)	2.5980(33)	2.9035(38)	3.8488(62)	83.024(109)	4.3484(3)	2.6834(24)	1171.35(11)	1.441	9.4186(6)	17 527[b]
270	2.5557(2)	2.6041(44)	2.9285(67)	3.8791(107)	82.950(195)	4.3884(4)	2.6961(38)	1188.23(9)	1.421	9.4713(5)	17 824
Δ(parameter)[a]	**+0.0042**	**+0.0264**	**+0.0405**	-	-	**+0.1013**	**+0.0237**	**+44.8**	**-0.055**	**+0.1413**	**+495**

[a] Change in the corresponding parameter over the selected temperature range, expressed in the indicated units. A value is given in each cell of this row only if the absolute difference between the parameter at 90 K and the parameter at 270 K is equal or greater than $3^{*}\sqrt{esu_{90}{}^2+esu_{270}{}^2}$. [b] Interpolated using the Boltzmann-type equation described above.

Table 3.4. Best-fitting parameters for the linear fits given in Figure 3.19.

	(a)	(b)	(c)	(d)	(e)	(f)	(g)	(h)	(i)	(j)	(k)	(l)	(m)
m		1.54 x10^{-4}	1.78 x10^{-4}			5.53 x10^{-4}	1.13 x10^{-4}	0.246	-3.12 x10^{-4}	7.80 x10^{-4}	2.13 x10^{-4}	9.10 x10^{-5}	-4.76 x10^{-4}
b	n.c.	2.56	2.87	n.c.	n.c.	4.23	2.66	1120	1.51	9.25	0.941	1.02	0.975
R^2		0.8828	0.8442			0.9770	0.8358	0.9742	0.9722	0.9630	0.9716	0.9050	0.8411

Table 3.5. Best-fitting parameters for the linear fits given in Figure 3.20.

	(a)	(b)	(c)	(d)	(e)	(f)	(g)	(h)	(i)	(j)	(k)	(l)	(m)
m		13.9	11.8			5.02	17.8	0.0113	-9.15	3.53	13.5	28.2	
b	n.c.	-18.6	-16.8	n.c.	n.c.	-4.24	-30.3	4.32	30.8	-15.6	4.32	-11.7	n.c.
R^2		0.7253	0.9087			0.9160	0.8910	0.9054	0.8988	0.9190	0.9054	0.8972	

n.c. = no correlation.

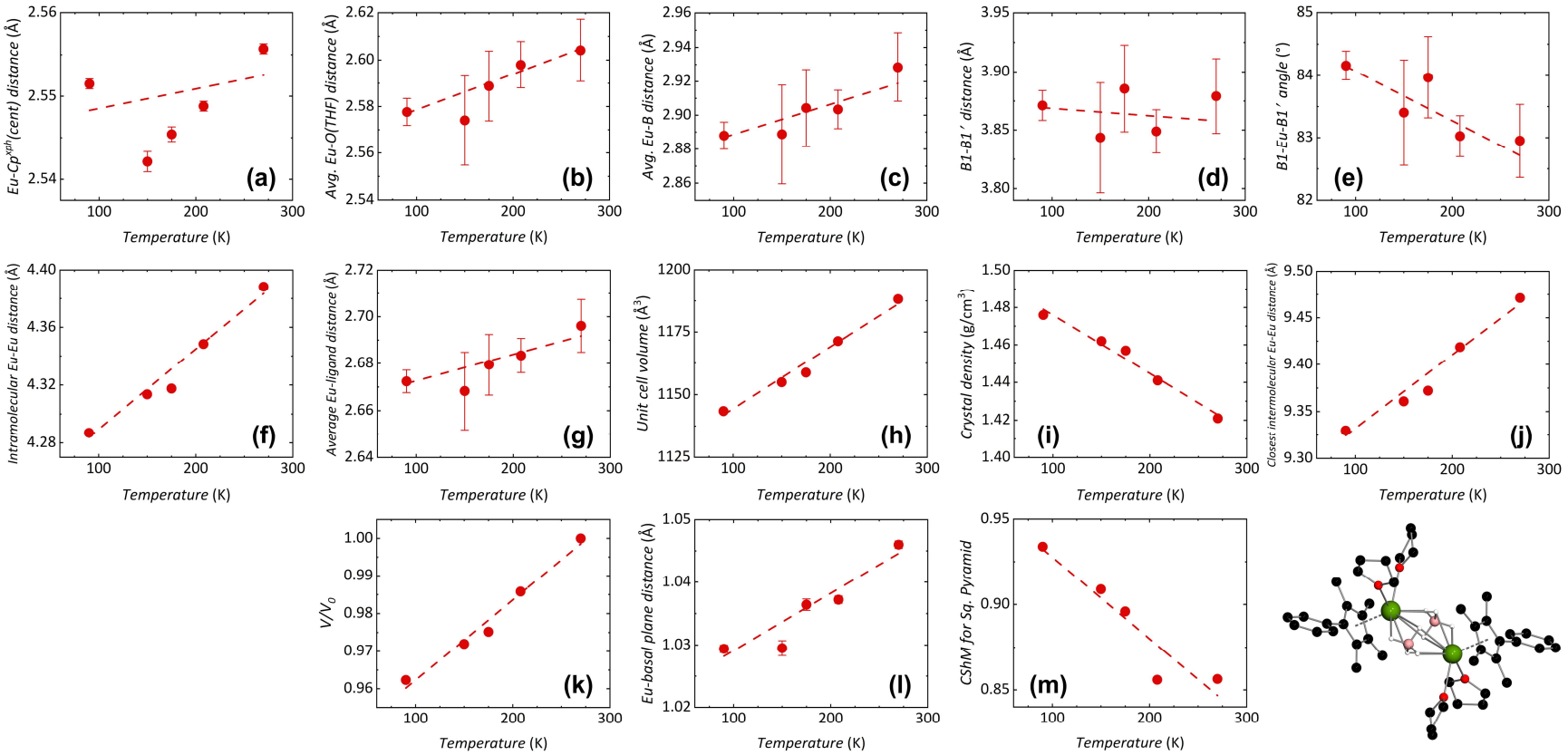


Figure 3.19. Temperature-dependence of various metrical parameters of **3.1**. (a) The Eu-Cp^{xph}(cent) distance; (b) the average Eu-O(THF) distance; (c) the average Eu-B distance; (d) the B1-B1′ distance; (e) the B1-Eu-B1′ angle; (f) the intramolecular Eu-Eu′ distance; (g) the average of all Eu-ligand distances; (h) the volume of the crystallographic unit cell; (i) the crystallographic density; (j) the closest intermolecular Eu-Eu distance; (k) the relative compression of the lattice; (l) the distance between the Eu ion and the basal plane of the coordination pyramid, defined by the atoms B1, B1′, O1, and O2; (m) distortion of the coordination geometry around Eu as represented by the continuous shape measure (CShM), which quantifies the deviation of the real coordination polyhedron from an idealized square pyramid (a value of zero represents exact agreement with the idealized geometry). Error bars (as ±3x esu of the measurement) are shown but overlap the points in some cases. The dashed lines are linear fits of the equation $y = mx + b$ to the data. Best fitting parameters are given in Table 3.4.

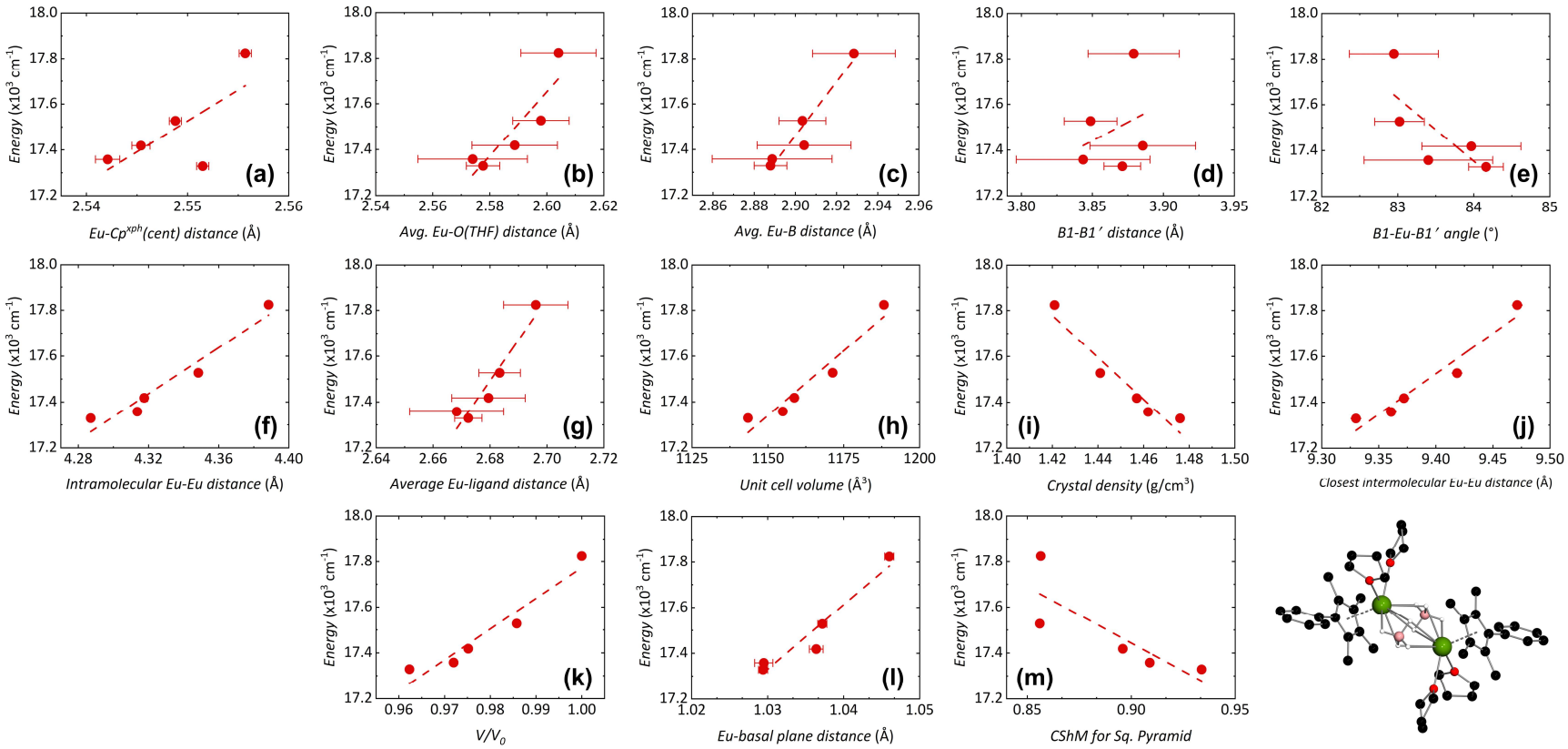


Figure 3.20. Plots of the energy at the emission band maximum for **3.1** as a function of (a) The Eu-Cp^{xph}(cent) distance; (b) the average Eu-O(THF) distance; (c) the average Eu-B distance; (d) the B1-B1′ distance; (e) the B1-Eu-B1′ angle; (f) the intramolecular Eu-Eu′ distance; (g) the average of all Eu-ligand distances; (h) the volume of the crystallographic unit cell; (i) the crystallographic density; (j) the closest intermolecular Eu-Eu distance; (k) the relative compression of the lattice; (l) the distance between the Eu ion and the basal plane of the coordination pyramid, defined by the atoms B1, B1′, O1, and O2; (m) distortion of the coordination geometry around Eu as represented by the continuous shape measure (CShM), which quantifies the deviation of the real coordination polyhedron from an idealized square pyramid (a value of zero represents exact agreement with the idealized geometry). Error bars (as ±3x esu of the measurement) are shown but overlap the points in some cases. The dashed lines are linear fits of the equation $y = mx + b$ to the data. Best fitting parameters are given in Table 3.5.

Table 3.6. Selected metrical parameters from crystal structures of **3.2** at various temperatures, in comparison to the energy at the emission band maxima. A statistically significant difference between two values is indicated via coloured dividing lines (*vide supra*).

Temperature (K)	Eu-^{TMS}Cp$^{\#}$(cent) distance (Å)	Avg. Eu-O(THF) distance (Å)	Avg. Eu-B distance (Å)	B1-B1′ distance (Å)	B1-Eu-B1′ angle (°)	Intramolecular Eu-Eu′ distance (Å)	Avg. of all Eu-ligand bonds (Å)	Unit cell volume (Å^3)	Crystal density (g/cm^3)	Closest intermolecular Eu-Eu distance (Å)	Emission band max. (cm^{-1})
90	2.5607(2)	2.5885(20)	2.8874(41)	3.9210(54)	85.514(115)	4.2405(4)	2.6789(21)	1172.67(7)	1.428	9.4323(4)	16 695
150	2.5552(2)	2.5961(29)	2.9008(46)	3.9284(68)	85.223(125)	4.2702(4)	2.6840(26)	1186.03(9)	1.412	9.4696(5)	17 096
175	2.5582(2)	2.5968(29)	2.9036(46)	3.9226(68)	84.972(125)	4.2828(4)	2.6862(26)	1195.19(7)	1.402	9.4805(4)	17 273[b]
213	2.5603(3)	2.6055(20)	2.9123(34)	3.9182(55)	84.536(88)	4.3107(5)	2.6927(19)	1211.70(14)	1.382	9.5365(7)	17 503[b]
270	2.5566(3)	2.6043(37)	2.9084(59)	3.8930(95)	84.007(170)	4.3229(5)	2.6898(33)	1225.46(12)	1.367	9.5688(6)	17 711
Δ(parameter)[a]	**-0.0041**	**+0.0159**	-	-	**-1.507**	**+0.0824**	-	**+52.8**	**-0.061**	**+0.1365**	**+1016**

[a] Change in the corresponding parameter over the selected temperature range, expressed in the indicated units. A value is given in each cell of this row only if the absolute difference between the parameter at 90 K and the parameter at 270 K is equal or greater than $3^{*}\sqrt{esu_{90}^2+esu_{270}^2}$. [b] Interpolated using the Boltzmann-type equation described above.

Table 3.7. Best-fitting parameters for the linear fits given in Figure 3.21.

	(a)	(b)	(c)	(d)	(e)	(f)	(g)	(h)	(i)	(j)	(k)	(l)	(m)
m		1.13 x10^{-4}			-0.00846	4.83 x10^{-4}	8.46 x10^{-5}	0.29	-3.55 x10^{-4}	7.60 x10^{-4}	2.50 x10^{-4}	1.16 x10^{-4}	-5.33 x10^{-4}
b	n.c.	2.58	n.c.	n.c.	86.4	4.20	2.67	1145	1.46	9.36	0.933	1.11	1.43
R^2		0.8660			0.9599	0.9685	0.7600	0.9800	0.9776	0.9512	0.9795	0.8968	0.9110

Table 3.8. Best-fitting parameters for the linear fits given in Figure 3.22.

	(a)	(b)	(c)	(d)	(e)	(f)	(g)	(h)	(i)	(j)	(k)	(l)	(m)
m		54.1			-0.635	11.8	67.8	0.0184	-15.9	6.94	22.6	44.3	-9.70
b	n.c.	-123	n.c.	n.c.	71.1	-33.4	-165	-4.81	39.5	-48.7	-4.81	-32.8	30.2
R^2		0.8936			0.9059	0.9859	0.8090	0.9566	0.9586	0.9272	0.9566	0.7994	0.8092

n.c. = no correlation.

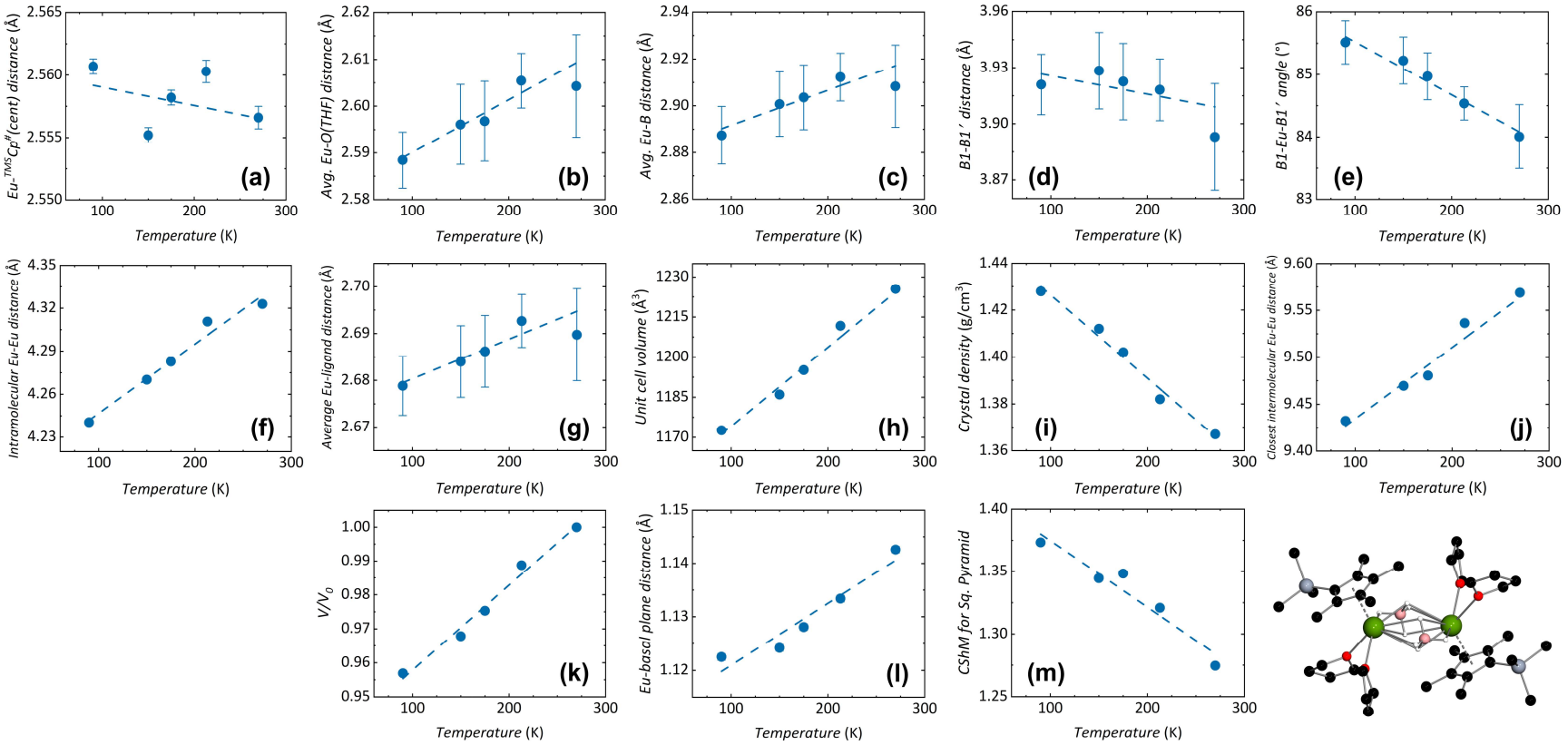


Figure 3.21. Temperature-dependence of various metrical parameters of **3.2**. (a) The Eu-^{TMS}Cp$^{\#}$(cent) distance; (b) the average Eu-O(THF) distance; (c) the average Eu-B distance; (d) the B1-B1′ distance; (e) the B1-Eu-B1′ angle; (f) the intramolecular Eu-Eu′ distance; (g) the average of all Eu-ligand distances; (h) the volume of the crystallographic unit cell; (i) the crystallographic density; (j) the closest intermolecular Eu-Eu distance; (k) the relative compression of the lattice; (l) the distance between the Eu ion and the basal plane of the coordination pyramid, defined by the atoms B1, B1′, O1, and O2; (m) distortion of the coordination geometry around Eu as represented by the continuous shape measure (CShM), which quantifies the deviation of the real coordination polyhedron from an idealized square pyramid (a value of zero represents exact agreement with the idealized geometry). Error bars (as ±3x esu of the measurement) are shown but overlap the points in some cases. The dashed lines are linear fits of the equation $y = mx + b$ to the data. Best fitting parameters are given in Table 3.7.

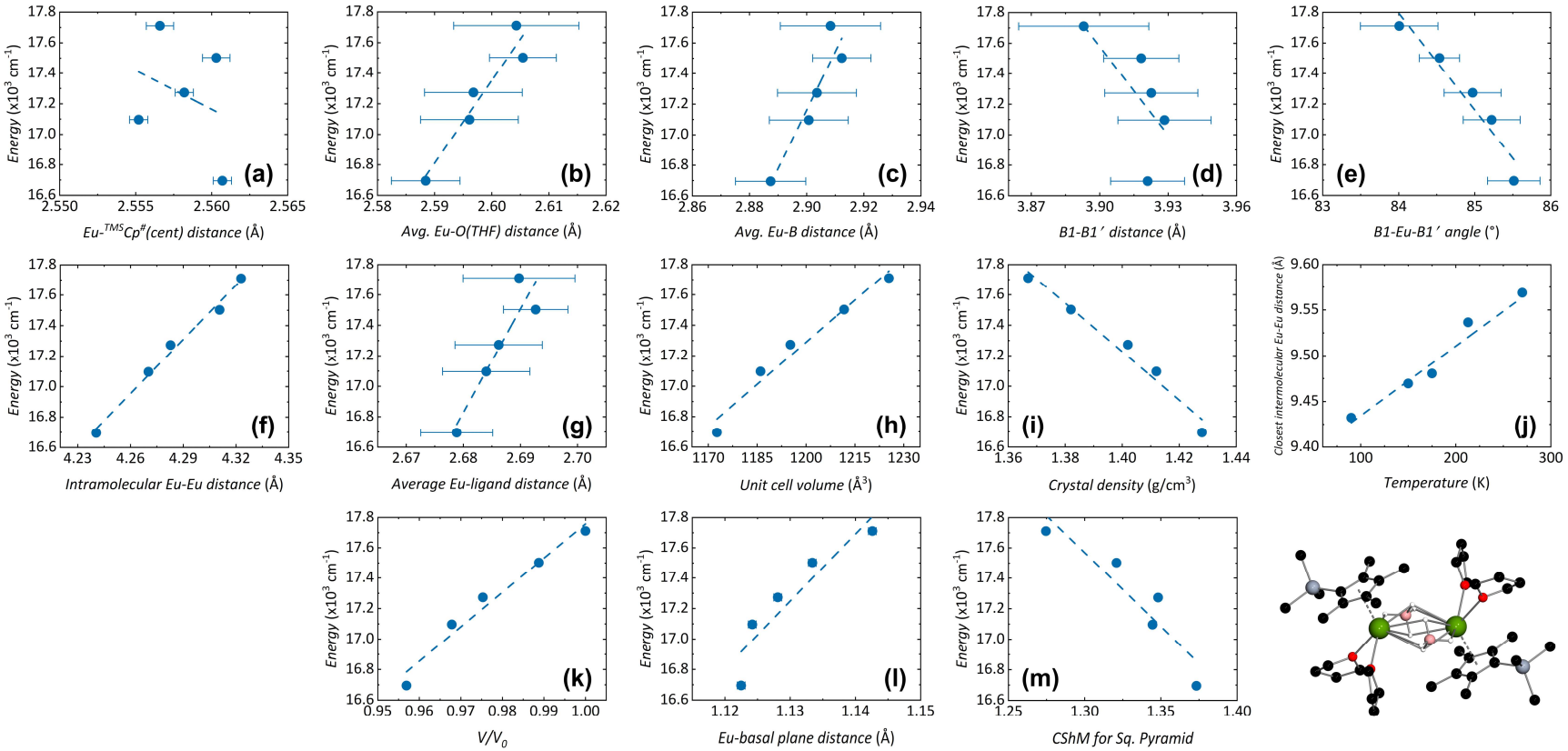


Figure 3.22. Plots of the energy at the emission band maximum for **3.2** as a function of (a) The Eu-^{TMS}Cp$^{\#}$(cent) distance; (b) the average Eu-O(THF) distance; (c) the average Eu-B distance; (d) the B1-B1′ distance; (e) the B1-Eu-B1′ angle; (f) the intramolecular Eu-Eu′ distance; (g) the average of all Eu-ligand distances; (h) the volume of the crystallographic unit cell; (i) the crystallographic density; (j) the closest intermolecular Eu-Eu distance; (k) the relative compression of the lattice; (l) the distance between the Eu ion and the basal plane of the coordination pyramid, defined by the atoms B1, B1′, O1, and O2; (m) distortion of the coordination geometry around Eu as represented by the continuous shape measure (CShM), which quantifies the deviation of the real coordination polyhedron from an idealized square pyramid (a value of zero represents exact agreement with the idealized geometry). Error bars (as ±3x esu of the measurement) are shown but overlap the points in some cases. The dashed lines are linear fits of the equation $y = mx + b$ to the data. Best fitting parameters are given in Table 3.8.

Table 3.9. Selected metrical parameters from crystal structures of **3.3** at various temperatures, in comparison to the energy at the emission band maxima. A statistically significant difference between two values is indicated via coloured dividing lines (*vide supra*).

Temperature (K)	Eu-$^{TMG}Cp^{\#}$(cent) distance (Å)	Avg. Eu-O(THF) distance (Å)	Avg. Eu-B distance (Å)	B1-B1′ distance (Å)	B1-Eu-B1′ angle (°)	Intramolecular Eu-Eu′ distance (Å)	Avg. of all Eu-ligand bonds (Å)	Unit cell volume (Å^3)	Crystal density (g/cm^3)	Closest intermolecular Eu-Eu distance (Å)	Emission band max. (cm^{-1})
90	2.5348(2)	2.5864(25)	2.8891(45)	3.9002(67)	84.893(122)	4.2642(4)	2.6701(24)	1161.68(9)	1.569	8.8089(5)	16 850
150	2.5377(5)	2.5915(38)	2.8992(63)	3.9090(95)	84.762(165)	4.2835(7)	2.6761(35)	1176.50(30)	1.549	8.8240(10)	17 023
175	2.5404(2)	2.5956(29)	2.8992(47)	3.8996(70)	84.508(123)	4.2923(4)	2.6784(26)	1179.32(7)	1.546	8.8175(4)	17 126[b]
213	2.5414(3)	2.6053(17)	2.9107(28)	3.9053(42)	84.254(74)	4.3178(6)	2.6858(16)	1193.10(20)	1.528	8.8262(9)	17 294[b]
270	2.5469(5)	2.6106(63)	2.9217(110)	3.9023(166)	83.784(286)	4.3502(8)	2.6930(59)	1206.20(30)	1.511	8.8260(10)	17 551
Δ(parameter)[a]	**+0.0121**	**+0.0242**	-	-	**-1.109**	**+0.0860**	**+0.0230**	**+44.5**	**-0.058**	**+0.0171**	**+701**

[a] Change in the corresponding parameter over the selected temperature range, expressed in the indicated units. A value is given in each cell of this row only if the absolute difference between the parameter at 90 K and the parameter at 270 K is equal or greater than $3*\sqrt{esu_{90}^2+esu_{270}^2}$. [b] Interpolated using the Boltzmann-type equation described above.

Table 3.10. Best-fitting parameters for the linear fits given in Figure 3.23.

	(a)	(b)	(c)	(d)	(e)	(f)	(g)	(h)	(i)	(j)	(k)	(l)	(m)
m	6.18 x10^{-5}	1.53 x10^{-4}	1.78 x10^{-4}		-0.00565	4.44 x10^{-4}	1.29 x10^{-4}	0.23	-3.25 x10^{-4}		2.07 x10^{-4}	2.16 x10^{-4}	
b	2.53	2.57	2.87	n.c.	85.5	4.22	2.66	1140	1.60	n.c.	0.94	1.11	n.c.
R^2	0.9661	0.9379	0.9439		0.9361	0.9445	0.9691	0.9726	0.9860		0.9871	0.9588	

Table 3.11. Best-fitting parameters for the linear fits given in Figure 3.24.

	(a)	(b)	(c)	(d)	(e)	(f)	(g)	(h)	(i)	(j)	(k)	(l)	(m)
m	58.6	26.6	21.2		-0.602	8.01	30.0	0.0157	-12.1		18.9	18.0	
b	-132	-51.9	-44.4	n.c.	68.0	-17.3	-63.2	-1.39	35.7	n.c.	-1.39	-3.53	n.c.
R^2	0.9717	0.9621	0.9733		0.9778	0.9933	0.9923	0.9830	0.9796		0.9830	0.9716	

n.c. = no correlation.

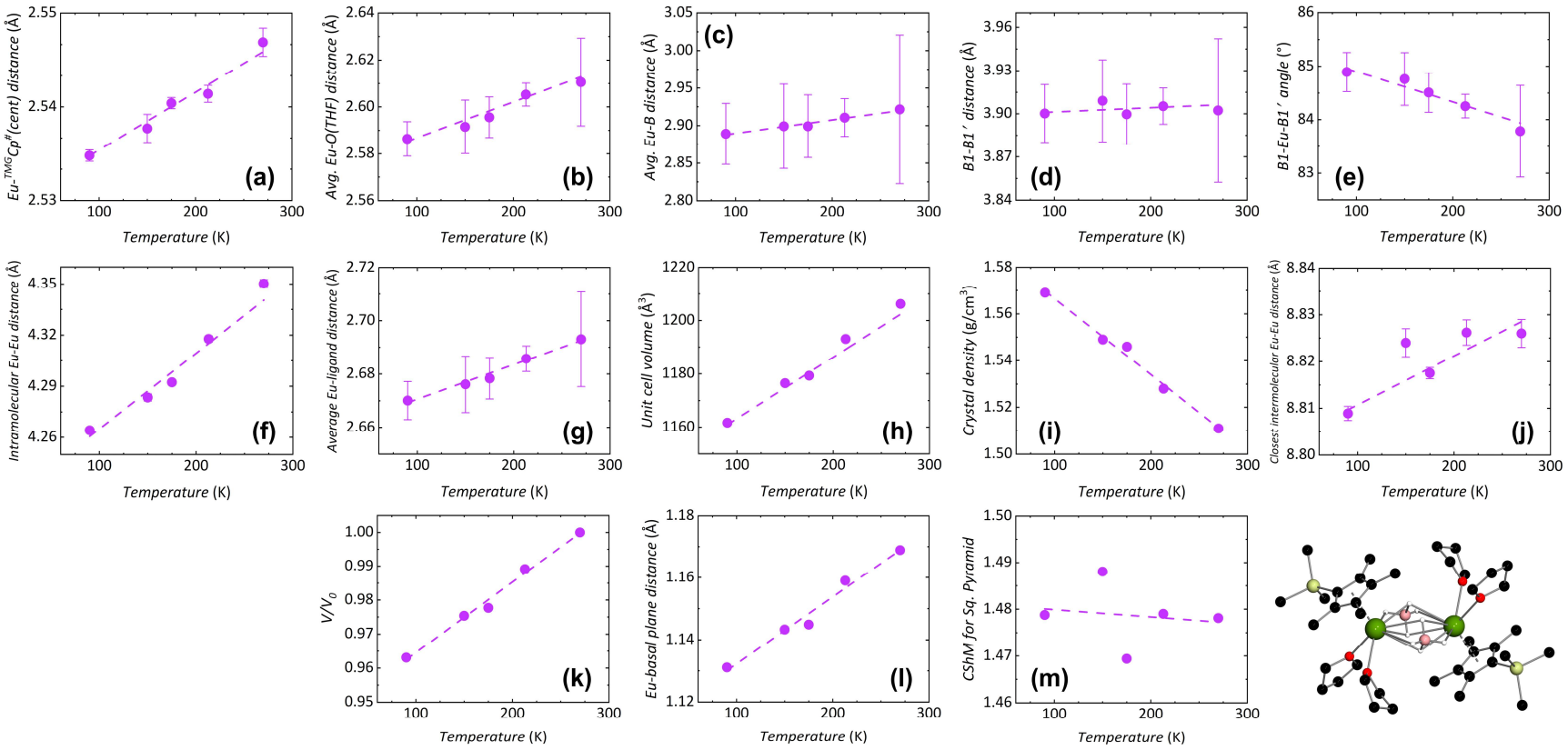


Figure 3.23. Temperature-dependence of various metrical parameters of **3.3**. (a) The Eu-^{TMG}Cp$^{\#}$(cent) distance; (b) the average Eu-O(THF) distance; (c) the average Eu-B distance; (d) the B1-B1′ distance; (e) the B1-Eu-B1′ angle; (f) the intramolecular Eu-Eu′ distance; (g) the average of all Eu-ligand distances; (h) the volume of the crystallographic unit cell; (i) the crystallographic density; (j) the closest intermolecular Eu-Eu distance; (k) the relative compression of the lattice; (l) the distance between the Eu ion and the basal plane of the coordination pyramid, defined by the atoms B1, B1′, O1, and O2; (m) distortion of the coordination geometry around Eu as represented by the continuous shape measure (CShM), which quantifies the deviation of the real coordination polyhedron from an idealized square pyramid (a value of zero represents exact agreement with the idealized geometry). Error bars (as ±3x esu of the measurement) are shown but overlap the points in some cases. The dashed lines are linear fits of the equation $y = mx + b$ to the data. Best fitting parameters are given in Table 3.10.

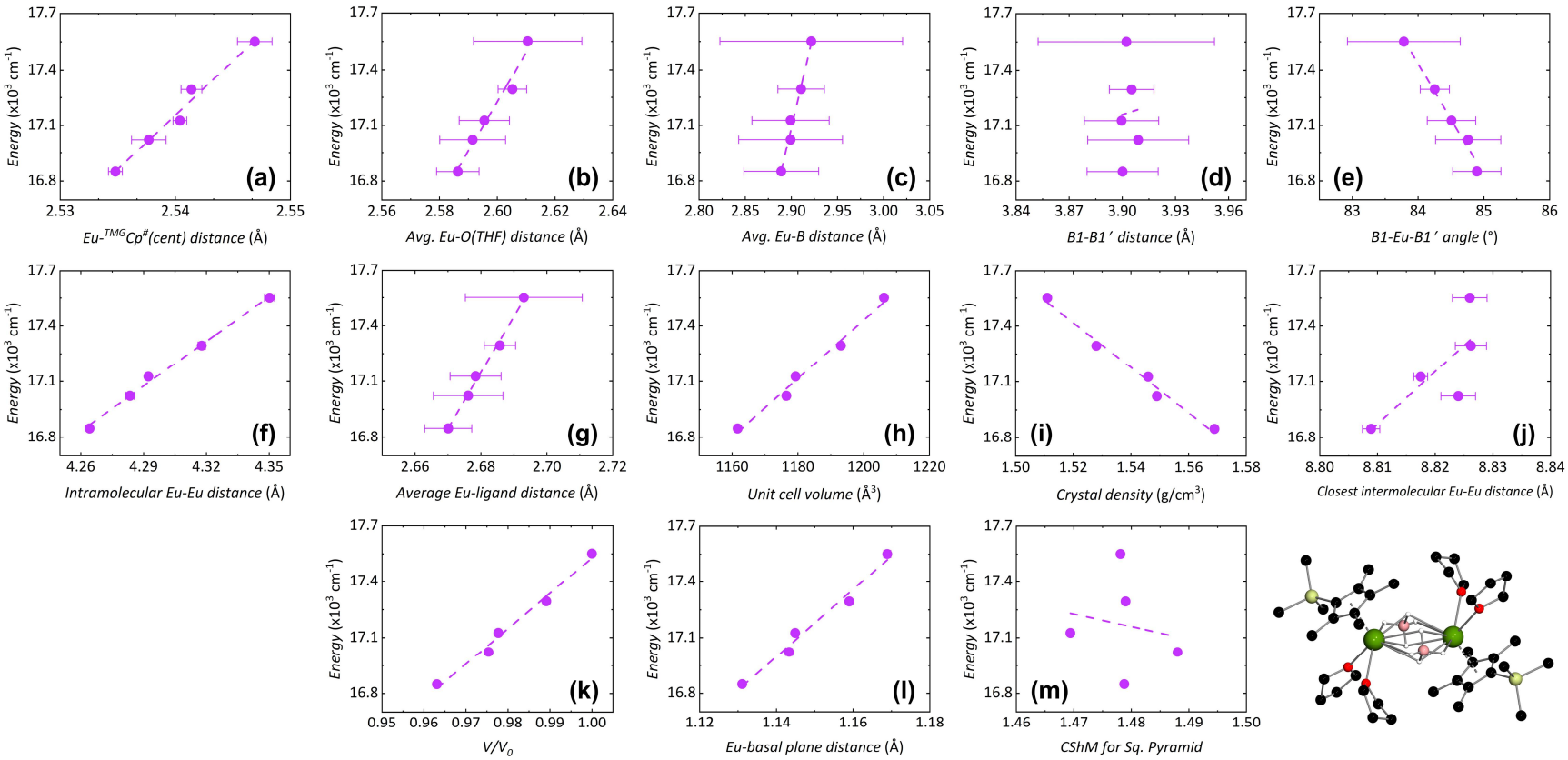


Figure 3.24. Plots of the energy at the emission band maximum for **3.3** as a function of (a) The Eu-^{TMG}Cp$^{\#}$(cent) distance; (b) the average Eu-O(THF) distance; (c) the average Eu-B distance; (d) the B1-B1′ distance; (e) the B1-Eu-B1′ angle; (f) the intramolecular Eu-Eu′ distance; (g) the average of all Eu-ligand distances; (h) the volume of the crystallographic unit cell; (i) the crystallographic density; (j) the closest intermolecular Eu-Eu distance; (k) the relative compression of the lattice; (l) the distance between the Eu ion and the basal plane of the coordination pyramid, defined by the atoms B1, B1′, O1, and O2; (m) distortion of the coordination geometry around Eu as represented by the continuous shape measure (CShM), which quantifies the deviation of the real coordination polyhedron from an idealized square pyramid (a value of zero represents exact agreement with the idealized geometry). Error bars (as ±3x esu of the measurement) are shown but overlap the points in some cases. The dashed lines are linear fits of the equation $y = mx + b$ to the data. Best fitting parameters are given in Table 3.11.

Table 3.12. Selected metrical parameters from crystal structures of **3.4** at various temperatures, in comparison to the energy at the emission band maxima. A statistically significant difference between two values is indicated via coloured dividing lines (*vide supra*).

Temperature (K)	Eu-^{bdp}Cp*(cent) distance (Å)	Avg. Eu-O(THF) distance (Å)	Avg. Eu-B distance (Å)	B1-B1′ distance (Å)	B1-Eu-B1′ angle (°)	Intramolecular Eu-Eu′ distance (Å)	Avg. of all Eu-ligand bonds (Å)	Unit cell volume (Å^3)	Crystal density (g/cm^3)	Closest intermolecular Eu-Eu distance (Å)	Emission band max. (cm^{-1})
90	2.5443(2)	2.5771(24)	2.8859(42)	3.8979(64)	84.946(117)	4.2577(4)	2.6691(23)	1275.81(14)	1.433	8.7649(6)	16 379
150	2.5485(2)	2.5790(41)	2.8986(65)	3.9095(103)	84.797(174)	4.2815(5)	2.6754(36)	1290.06(9)	1.417	8.7807(5)	16 855
175	2.5484(3)	2.5866(52)	2.8972(78)	3.8973(123)	84.520(211)	4.2889(5)	2.6774(44)	1300.17(18)	1.406	8.7971(8)	17 004[b]
213	2.5473(2)	2.5920(18)	2.9161(29)	3.9180(45)	84.402(77)	4.3206(4)	2.6851(16)	1309.99(11)	1.395	8.7998(5)	17 233[b]
270	2.5456(3)	2.5987(55)	2.9108(77)	3.8766(122)	83.495(209)	4.3436(6)	2.6850(45)	1322.40(20)	1.382	8.8084(8)	17 490
Δ(parameter)[a]	**+0.0013**	**+0.0217**	-	-	**-1.451**	**+0.0859**	**+0.0159**	**+46.6**	**-0.051**	**+0.0435**	**+1111**

[a] Change in the corresponding parameter over the selected temperature range, expressed in the indicated units. A value is given in each cell of this row only if the absolute difference between the parameter at 90 K and the parameter at 270 K is equal or greater than $3*\sqrt{esu_{90}^2+esu_{270}^2}$. [b] Interpolated using the Boltzmann-type equation described above.

Table 3.13. Best-fitting parameters for the linear fits given in Figure 3.25**.**

	(a)	(b)	(c)	(d)	(e)	(f)	(g)	(h)	(i)	(j)	(k)	(l)	(m)
m		1.25 x10^{-4}	2.09 x10^{-4}		-0.00590	4.93 x10^{-4}	1.17 x10^{-4}	0.274	-2.90 x10^{-4}	2.60 x10^{-4}	2.00 x10^{-4}	1.86 x10^{-4}	
b	n.c.	2.57	2.87	n.c.	85.6	4.21	2.66	1250	1.46	8.74	0.947	1.05	n.c.
R^2		0.9388	0.8022		0.7566	0.9675	0.9103	0.9863	0.98836	0.9242	0.9899	0.9433	

Table 3.14. Best-fitting parameters for the linear fits given in Figure 3.26.

	(a)	(b)	(c)	(d)	(e)	(f)	(g)	(h)	(i)	(j)	(k)	(l)	(m)
m		43.8	31.7		-0.652	12.0	59.3	0.0232	-21.1	23.5	30.6	32.1	
b	n.c.	-96.4	-75.0	n.c.	72.1	-34.8	-142	-13.1	46.7	-190	-13.1	-17.9	n.c.
R^2		0.8524	0.7547		0.7067	0.9270	0.9114	0.9775	0.9802	0.9325	0.9775	0.9716	

n.c. = no correlation.

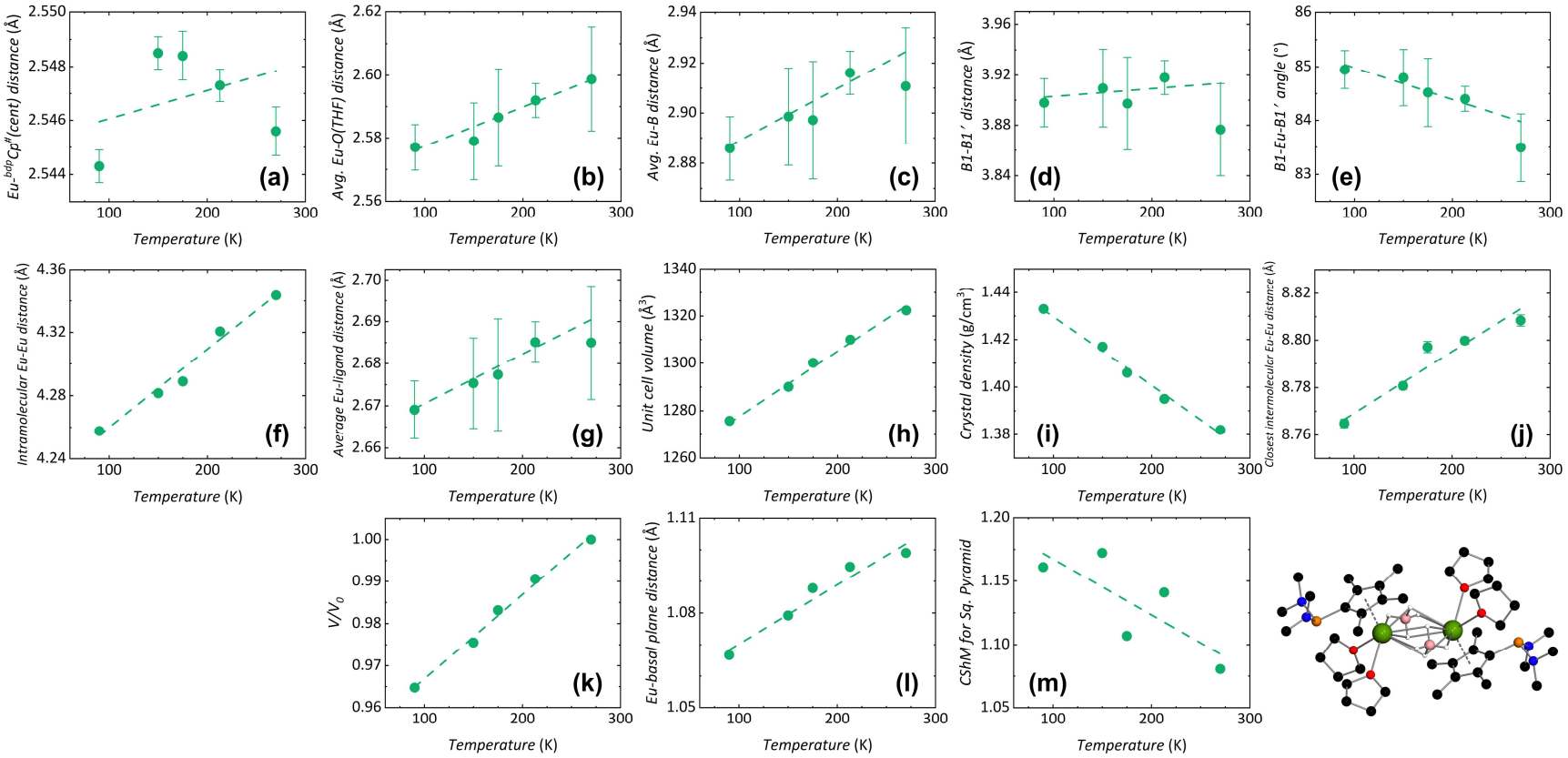


Figure 3.25. Temperature-dependence of various metrical parameters of **3.4**. (a) The Eu-^{bdp}Cp$^{\#}$(cent) distance; (b) the average Eu-O(THF) distance; (c) the average Eu-B distance; (d) the B1-B1′ distance; (e) the B1-Eu-B1′ angle; (f) the intramolecular Eu-Eu′ distance; (g) the average of all Eu-ligand distances; (h) the volume of the crystallographic unit cell; (i) the crystallographic density; (j) the closest intermolecular Eu-Eu distance; (k) the relative compression of the lattice; (l) the distance between the Eu ion and the basal plane of the coordination pyramid, defined by the atoms B1, B1′, O1, and O2; (m) distortion of the coordination geometry around Eu as represented by the continuous shape measure (CShM), which quantifies the deviation of the real coordination polyhedron from an idealized square pyramid (a value of zero represents exact agreement with the idealized geometry). Error bars (as ±3x esu of the measurement) are shown but overlap the points in some cases. The dashed lines are linear fits of the equation $y = mx + b$ to the data. Best fitting parameters are given in Table 3.13.

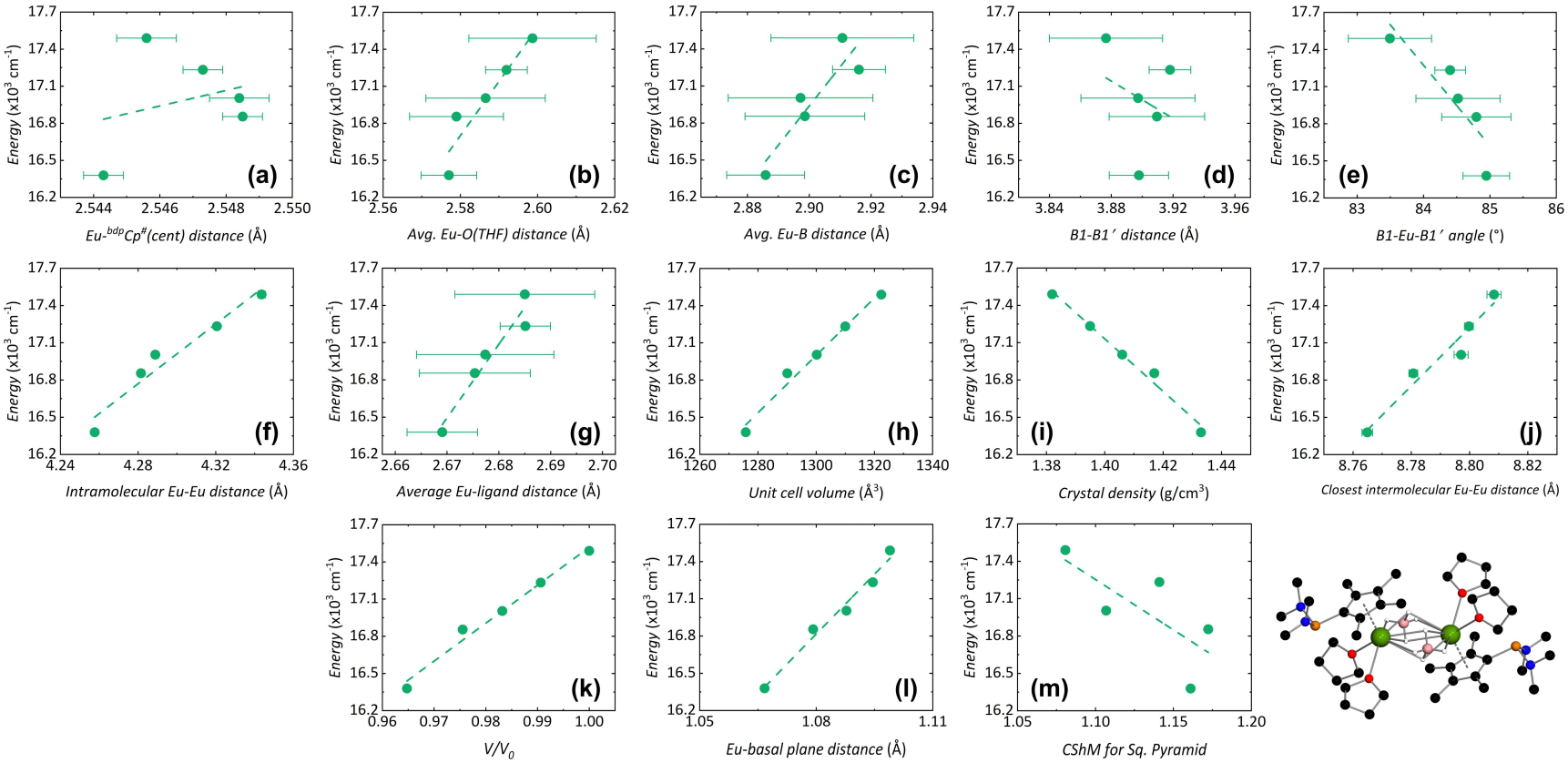


Figure 3.26. Plots of the energy at the emission band maximum for **3.4** as a function of (a) The Eu-^{bdp}Cp$^{\#}$(cent) distance; (b) the average Eu-O(THF) distance; (c) the average Eu-B distance; (d) the B1-B1′ distance; (e) the B1-Eu-B1′ angle; (f) the intramolecular Eu-Eu′ distance; (g) the average of all Eu-ligand distances; (h) the volume of the crystallographic unit cell; (i) the crystallographic density; (j) the closest intermolecular Eu-Eu distance; (k) the relative compression of the lattice; (l) the distance between the Eu ion and the basal plane of the coordination pyramid, defined by the atoms B1, B1′, O1, and O2; (m) distortion of the coordination geometry around Eu as represented by the continuous shape measure (CShM), which quantifies the deviation of the real coordination polyhedron from an idealized square pyramid (a value of zero represents exact agreement with the idealized geometry). Error bars (as ±3x esu of the measurement) are shown but overlap the points in some cases. The dashed lines are linear fits of the equation $y = mx + b$ to the data. Best fitting parameters are given in Table 3.14.

Table 3.15. Selected metrical parameters from crystal structures of 3.6 at various temperatures, in comparison to the energy at the emission band maxima. A statistically significant difference between two values is indicated via coloured dividing lines (*vide supra*).

Temperature (K)	Eu-Cp*(cent) distance (Å)	Avg. Eu-O(DME) distance (Å)	Avg. Eu-B distance (Å)	B1-B1′ distance (Å)	B1-Eu-B1′ angle (°)	Intramolecular Eu-Eu′ distance (Å)	Avg. of all Eu-ligand bonds (Å)	Unit cell volume (Å^3)	Crystal density (g/cm^3)	Closest intermolecular Eu-Eu distance (Å)	Emission band max. (cm^{-1})
90	2.5077(4)	2.6005(35)	2.8760(49)	4.0044(84)	88.243(166)	4.1291(5)	2.6614(29)	3481.35(40)	1.496	8.5911(6)	16 116
150	2.5105(3)	2.5981(28)	2.8754(45)	3.9921(63)	87.924(125)	4.1394(4)	2.6613(25)	3512.81(30)	1.483	8.6336(5)	16 276
175	2.5075(3)	2.5969(35)	2.8758(52)	3.9813(72)	87.610(146)	4.1509(4)	2.6601(30)	3542.76(17)	1.470	8.6795(4)	16 347[b]
208	2.5124(4)	2.5944(51)	2.8851(81)	3.9764(114)	87.122(227)	4.1813(6)	2.6640(45)	3581.36(78)	1.455	8.7081(9)	16 449[b]
270	2.4966(3)	2.5955(41)	2.8908(68)	3.9743(93)	86.849(188)	4.1991(4)	2.6609(37)	3630.88(15)	1.435	8.7890(4)	16 639
Δ(parameter)[a]	**-0.0111**	-	-	-	**-1.394**	**+0.07**	-	**+149.53**	**-0.061**	**+0.1979**	**+523**

[a] Change in the corresponding parameter over the selected temperature range, expressed in the indicated units. A value is given in each cell of this row only if the absolute difference between the parameter at 90 K and the parameter at 270 K is equal or greater than $3^*\sqrt{esu_{90}^2+esu_{270}^2}$. [b] Interpolated using the Boltzmann-type equation described above.

Table 3.16. Best-fitting parameters for the linear fits given in Figure 3.27.

	(a)	(b)	(c)	(d)	(e)	(f)	(g)	(h)	(i)	(j)	(k)	(l)	(m)
m				-1.78 x10^{-4}	-0.00831	4.29 x10^{-4}		0.902	-3.53 x10^{-4}	0.00115	2.38 x10^{-4}	1.63 x10^{-4}	3.45 x10^{-5}
b	n.c.	n.c.	n.c.	4.02	89.1	4.08	n.c.	3386	1.53	8.48	0.935	1.08	1.92
R^2				0.8300	0.9408	0.9165		0.9889	0.9750	0.9818	0.9733	0.9656	0.9138

Table 3.17. Best-fitting parameters for the linear fits given in Figure 3.28.

	(a)	(b)	(c)	(d)	(e)	(f)	(g)	(h)	(i)	(j)	(k)	(l)	(m)
m				-14.5	-0.34	6.44		0.00332	-8.14	2.57	12.0	17.5	7.83
b	n.c.	n.c.	n.c.	74.0	45.7	-10.4	n.c.	4.60	28.3	-5.98	4.60	-3.08	0.843
R^2				0.8110	0.9417	0.9180		0.9816	0.9822	0.9843	0.9816	0.9622	0.8872

n.c. = no correlation.

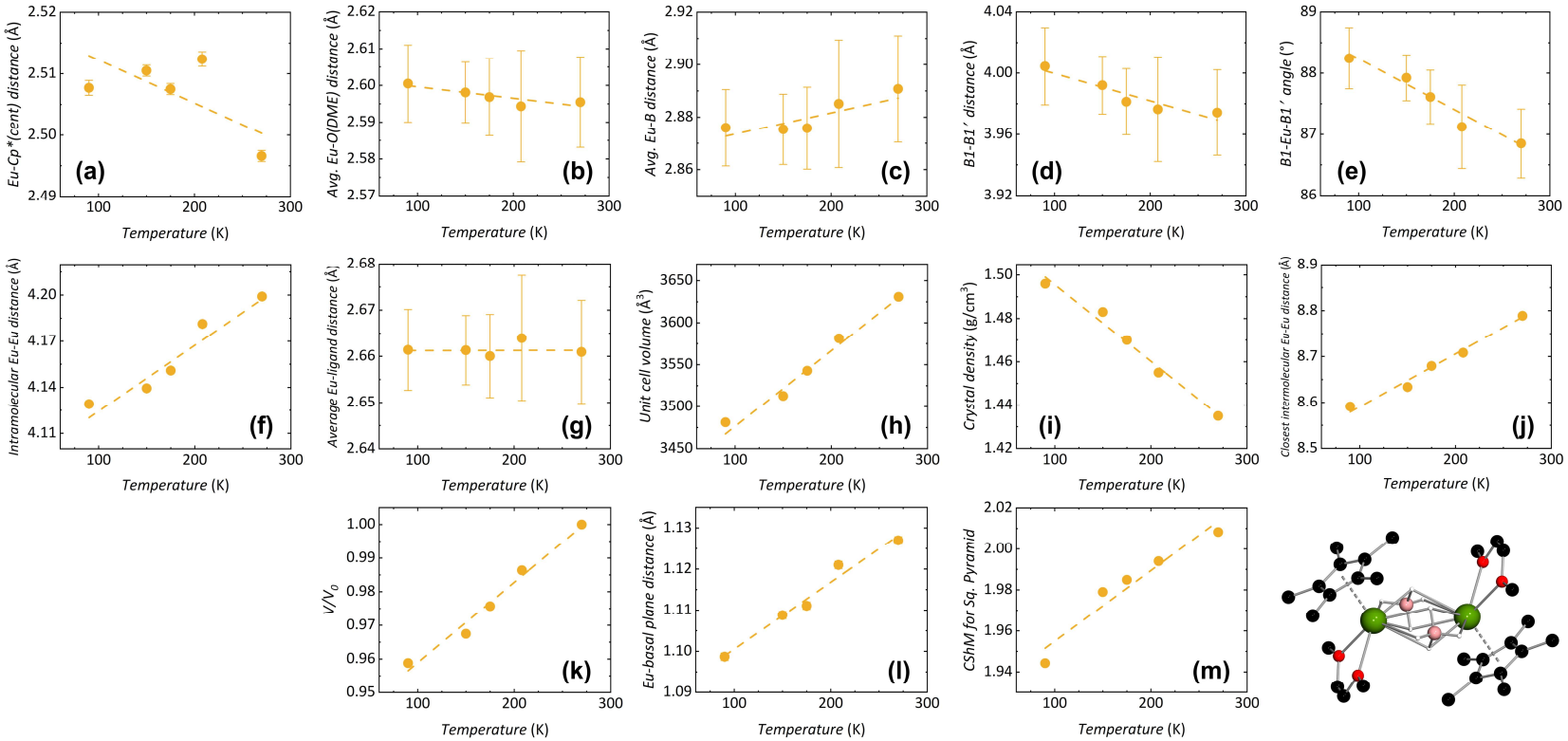


Figure 3.27. Temperature-dependence of various metrical parameters of **3.6**. (a) The Eu-Cp*(cent) distance; (b) the average Eu-O(DME) distance; (c) the average Eu-B distance; (d) the B1-B1′ distance; (e) the B1-Eu-B1′ angle; (f) the intramolecular Eu-Eu′ distance; (g) the average of all Eu-ligand distances; (h) the volume of the crystallographic unit cell; (i) the crystallographic density; (j) the closest intermolecular Eu-Eu distance; (k) the relative compression of the lattice; (l) the distance between the Eu ion and the basal plane of the coordination pyramid, defined by the atoms B1, B1′, O1, and O2; (m) distortion of the coordination geometry around Eu as represented by the continuous shape measure (CShM), which quantifies the deviation of the real coordination polyhedron from an idealized square pyramid (a value of zero represents exact agreement with the idealized geometry). Error bars (as ±3x esu of the measurement) are shown but overlap the points in some cases. The dashed lines are linear fits of the equation $y = mx + b$ to the data. Best fitting parameters are given in Table 3.16.

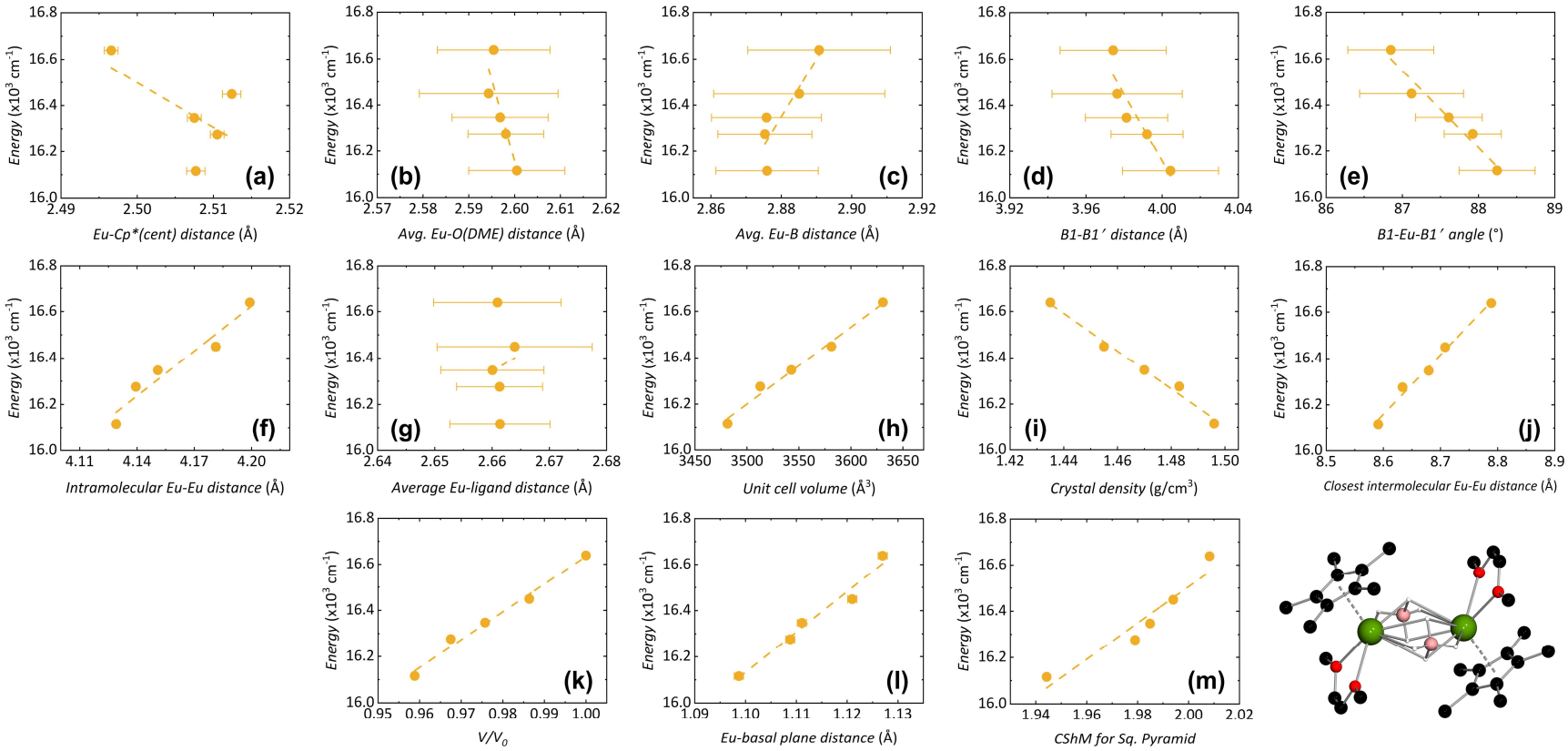


Figure 3.28. Plots of the energy at the emission band maximum for **3.6** as a function of (a) The Eu-Cp*(cent) distance; (b) the average Eu-O(DME) distance; (c) the average Eu-B distance; (d) the B1-B1′ distance; (e) the B1-Eu-B1′ angle; (f) the intramolecular Eu-Eu′ distance; (g) the average of all Eu-ligand distances; (h) the volume of the crystallographic unit cell; (i) the crystallographic density; (j) the closest intermolecular Eu-Eu distance; (k) the relative compression of the lattice; (l) the distance between the Eu ion and the basal plane of the coordination pyramid, defined by the atoms B1, B1′, O1, and O2; (m) distortion of the coordination geometry around Eu as represented by the continuous shape measure (CShM), which quantifies the deviation of the real coordination polyhedron from an idealized square pyramid (a value of zero represents exact agreement with the idealized geometry). Error bars (as ±3x esu of the measurement) are shown but overlap the points in some cases. The dashed lines are linear fits of the equation $y = mx + b$ to the data. Best fitting parameters are given in Table 3.17.

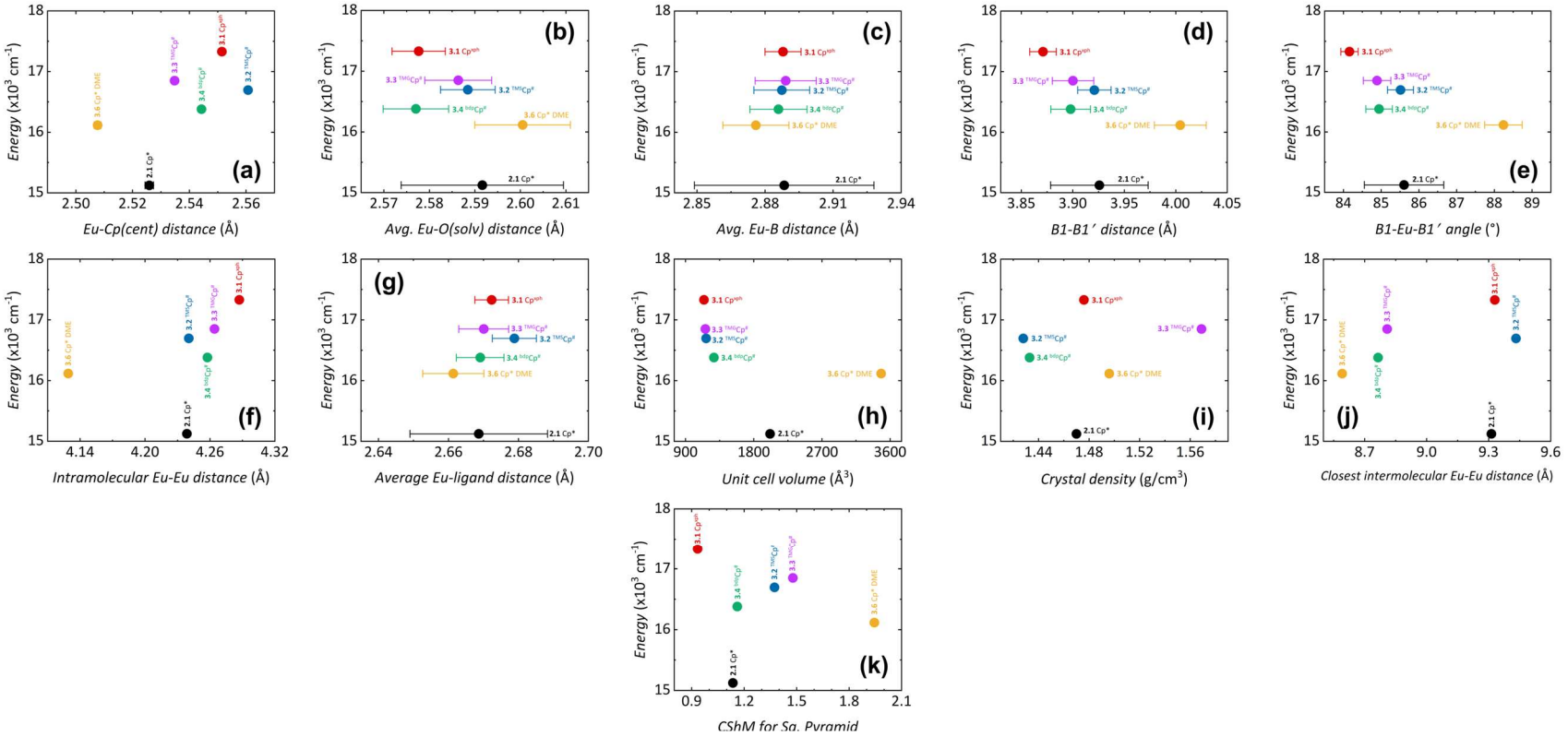


Figure 3.29. Plots of the energy at the emission band maximum for all complexes at 90 K as a function of (a) The Eu-Cp(cent) distance at 90 K; (b) the average Eu-O(solv) distance at 90 K; (c) the average Eu-B distance at 90 K; (d) the B1-B1′ distance at 90 K; (e) the B1-Eu-B1′ angle at 90 K; (f) the intramolecular Eu-Eu′ distance at 90 K; (g) the average of all Eu-ligand distances at 90 K; (h) the volume of the crystallographic unit cell at 90 K; (i) the crystallographic density at 90 K; (j) the closest intermolecular Eu-Eu distance at 90 K; (k) the distortion of the coordination geometry around Eu at 90 K as represented by the continuous shape measure (CShM), which quantifies the deviation of the real coordination polyhedron from an idealized square pyramid (a value of zero represents exact agreement with the idealized geometry). Error bars (as ±3x esu of the measurement) are shown but overlap the points in some cases.

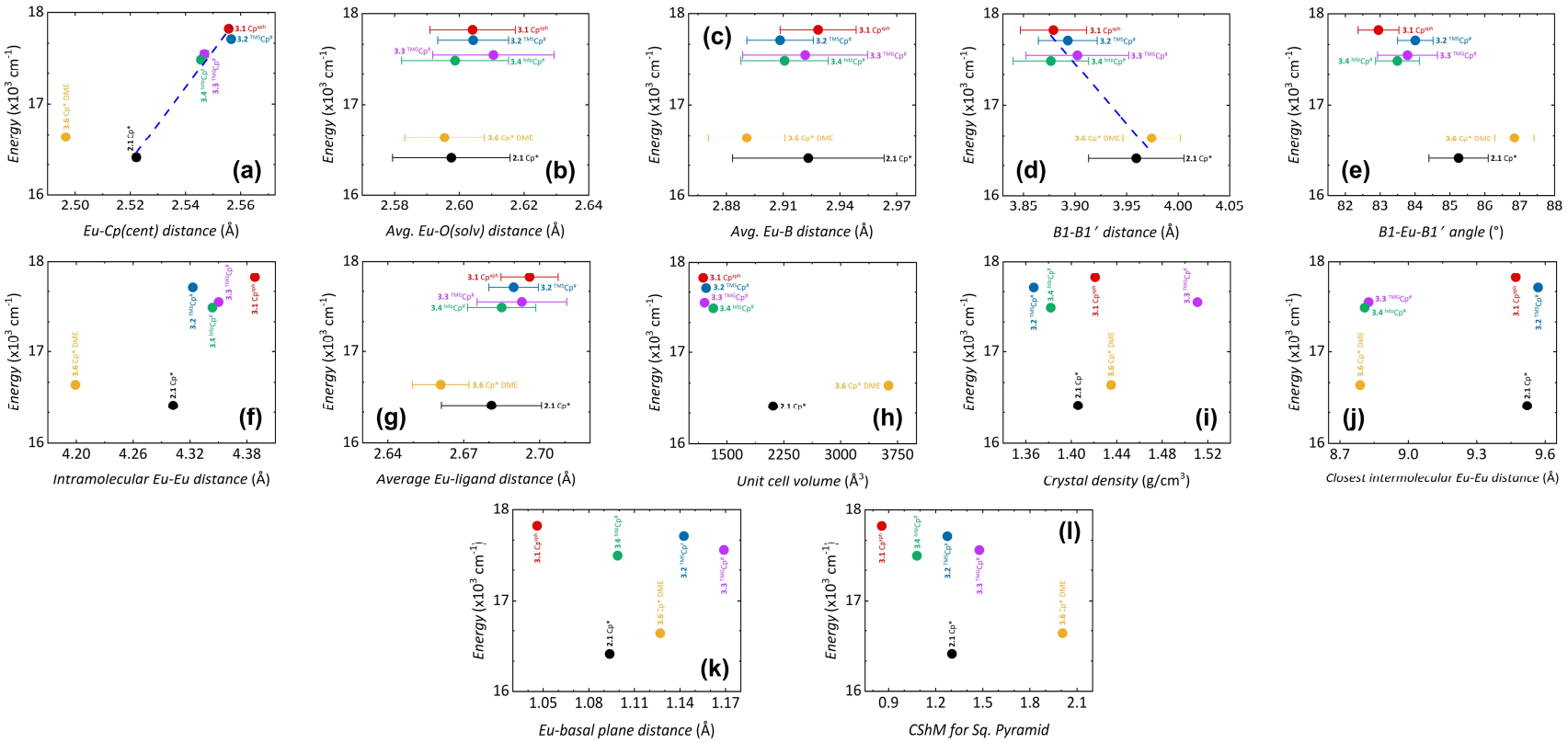


Figure 3.30. Plots of the energy at the emission band maximum for all complexes at 270 K as a function of (a) The Eu-Cp(cent) distance at 270 K; (b) the average Eu-O(solv) distance at 270 K; (c) the average Eu-B distance at 270 K; (d) the B1-B1′ distance at 270 K; (e) the B1-Eu-B1′ angle at 270 K; (f) the intramolecular Eu-Eu′ distance at 270 K; (g) the average of all Eu-ligand distances at 270 K; (h) the volume of the crystallographic unit cell at 270 K; (i) the crystallographic density at 270 K; (j) the closest intermolecular Eu-Eu distance at 270 K; (k) the distance between the Eu ion and the basal plane of the coordination pyramid, defined by the atoms B1, B1′, O1, and O2; (l) the distortion of the coordination geometry around Eu at 270 K as represented by the continuous shape measure (CShM), which quantifies the deviation of the real coordination polyhedron from an idealized square pyramid (a value of zero represents exact agreement with the idealized geometry). Error bars (as ±3x esu of the measurement) are shown but overlap the points in some cases. The dashed blue lines are linear fits of the equation $y = mx + b$ to the data. Best fitting parameters are (a) $m = 40.2$, $b = -84.9$, $R^2 = 0.9612$ (the point for **3.6** is excluded from the fit); (d) $m = -13.2$, $b = 68.8$, $R^2 = 0.8435$.

The temperature-dependence of certain geometric changes are common to all the complexes (including **2.1**). For example, all these complexes exhibit an increase in the intramolecular Eu-Eu distance (ranging from 0.06-0.1 Å, Figures 3.[19, 21, 23, 25, 27]f) and an increase in unit cell volume (ranging from 40-150 $Å^3$, Figures 3.[19, 21, 23, 25, 27]h) and concomitant decrease in crystal density (*ca.* -0.06 g/cm^3 in all cases, Figures 3.[19, 21, 23, 25, 27]i) with increasing temperature. All the complexes show strongly correlated decreases in emission energy with increasing lattice compression (Figures 3.[22, 24, 26, 28, 30]k), in an analogous fashion to that observed previously for **2.1**. Beyond this, there are significantly different trends in the temperature-dependent geometric distortions between the complexes over the measured temperature range. Whereas the Eu-Cp(cent) distances of **2.1**,[224] **3.1**, **3.2**, **3.4** and **3.6** are not correlated to the change in temperature (Figures 3.[19, 21, 25, 27]a), the Eu-Cp(cent) distance of complex **3.3** increases linearly (by 0.012 Å) with increasing temperature (Figure 3.23a). The average Eu-O(solv) distances for complexes **3.3** and **3.4** (and not the others) show correlated increases of 0.024 and 0.022 Å, respectively, with increasing temperature (Figures 3.23b, 3.25b), although the uncertainties on these distances are somewhat large. The average Eu-B distance of **3.1** shows a uniquely significant correlated increase of 0.041 Å with increasing temperature (Figure 3.19c). Most of the complexes show a substantial (0.1-0.2 Å) increase in the closest intermolecular Eu-Eu distance with increasing temperature (Figures 3.19j, 3.21j, 3.27j), whereas this distance remains comparatively nearly constant for **3.3** (less than 0.02 Å, Figure 3.23j) and changes by only a relatively small amount (~0.04 Å, Figure 3.25j) for **3.4**.[i]

The most interesting results are obtained when considering the geometry of the coordination polyhedra. Each complex exhibits a square-pyramidal coordination geometry with pseudo-C_{4v} symmetry and the Eu^{II} ion above the basal plane of the pyramid. A mononuclear fragment of each complex was compared to an idealized square pyramid using SHAPE 2.1,[203,241] taking the cyclopentadienyl centroid as the axial position and using the oxygen and boron atoms of the remaining ligands to define the basal plane. For complexes **2.1**[224] and **3.6** (Figure 3.27m), the true geometry becomes increasingly distorted from the idealized geometry with increasing temperature. However, surprisingly, the polyhedral distortion *decreases* (i.e., the true geometry becomes more idealized) with increasing temperature for **3.1** and **3.2** (Figures 3.19m and 3.21m), and no correlation is observed between the polyhedral distortion and temperature for **3.3** or **3.4** (Figures 3.23m and 3.25m). However, the Eu^{II} ion is increasingly distanced from the basal plane in all cases, though the magnitude of the displacement is somewhat less for **3.1** (less than 0.02 Å, Figure 3.19l) than the others (0.03-0.04 Å, Figures 3.[21, 23, 25, 27]l). This is accompanied by correlated increases in emission energy with increasing Eu-basal plane distance for all complexes (Figure 3.3).

3.8 Structural effects on the optical properties

The results obtained thus far clearly demonstrate that there is no single factor that governs the emission energies of these complexes. At 90 K, there is no meaningful correlation across complexes between most of the isolated metrical parameters and the corresponding emission energy. It is notable, however, that there is a trend towards increasing emission energy with increasing intramolecular Eu-Eu distance (Figure 3.29f); complex **3.6** is an outlier due to its substantially shorter (4.1291(5) Å) intramolecular Eu-Eu distance compared to the others (4.23 – 4.29 Å). Furthermore, we observe that an increased Eu-basal plane distance is strongly linearly correlated with increasing energy at the emission band maximum for complexes **2.1**, **3.2**, **3.3** and **3.6**, with complexes **3.1** and **3.4** being outliers (Figure 3.31). This is particularly interesting because the trend is defined by complexes with distinct characteristics. For example, complexes **2.1** and **3.6** have unit cells distinct from the others in the series (**3.1–3.4** are triclinic systems with $Z=1$, whereas **2.1** is a

monoclinic system with $Z = 2$ and *ca.* double the cell volume of the triclinic examples, and **3.6** is an orthorhombic system with $Z = 4$ and a unit cell about triple the volume of the triclinic examples). Complex **3.6** also naturally has higher polyhedral distortion than the others, due to the geometric constraints imposed by the chelating DME ligand.

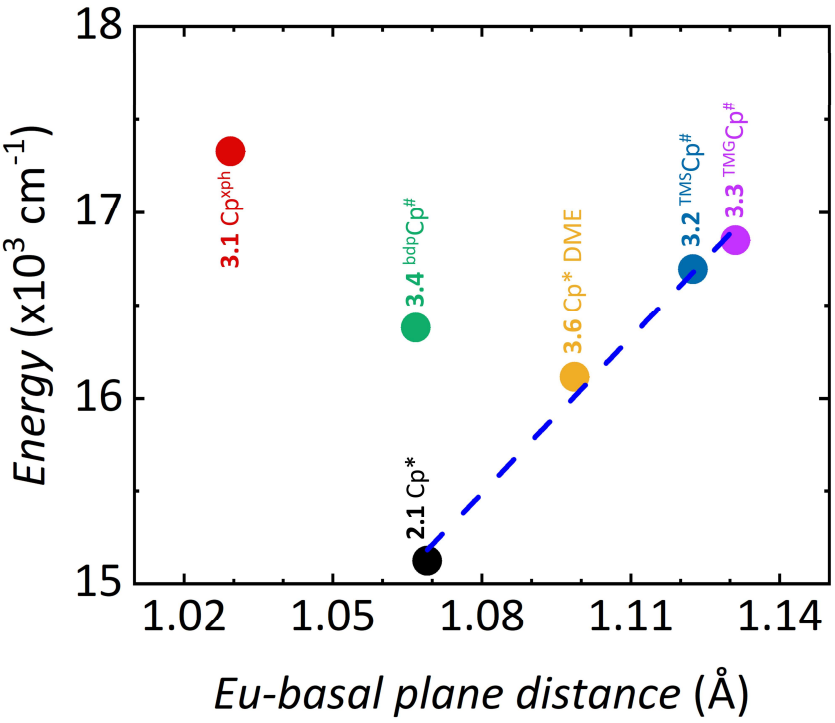


Figure 3.31. Energy at the emission band maximum for complexes **2.1**, **3.1–3.4** and **3.6** as a function of their Eu-basal plane distance at 90 K. Error bars are shown as 3x esu of the measurement but overlap the points. The dashed blue line is a linear fit of the equation $y = mx + b$ to the data; the points for **3.1** and **3.4** are excluded from the fit. Best fitting parameters are $m = 27.9$, $b = -14.7$, $R^2 = 0.9844$.

Table 3.18. Temperature-dependence of the Eu-basal plane distance (in Å) of complexes **2.1**, **3.1–3.4** and **3.6**, which are visualized in Figures 3.[20, 21, 22, 23, 24, 25, 26, 27, 28]l, 3.30k, 3.31 and 3.33.

Temperature (K)	**1**[36]	**2**	**3**	**4**	**5**	**7**
90	1.0690(5)	1.0294(2)	1.1225(2)	1.1311(2)	1.0667(2)	1.0987(3)
150	1.0801(3)	1.0295(4)	1.1242(2)	1.1433(3)	1.0792(2)	1.1088(3)
175	1.0836(3)	1.0364(3)	1.1281(2)	1.1449(2)	1.0878(3)	1.1111(3)
~200	1.0908(3)	1.0372(2)[b]	1.1334(2)[c]	1.1590(2)[c]	1.0946(2)[c]	1.1210(3)[b]
270	1.0938(4)	1.0460(2)	1.1426(2)	1.1689(3)	1.0990(2)	1.1270(3)
Δ(parameter)[a]	**+0.0248**	**+0.0166**	**+0.0201**	**+0.0378**	**+0.0323**	**+0.0283**

[a] Change in the corresponding parameter over the selected temperature range, expressed in the indicated units. A value is given in each cell of this row only if the absolute difference between the parameter at 90 K and the parameter at 270 K is equal or greater than $3*\sqrt{esu_{90}{}^2+esu_{270}{}^2}$. [b] at 208 K. [c] at 213 K.

Given that we also observe correlated increases in emission energy with increasing Eu-basal plane distance among all complexes (Figures 3.[20, 22, 24, 26, 28]l), we infer that the spatial arrangement of donor atoms about the basal plane of the coordination polyhedron has the greatest relative influence on the emission energies of these complexes, particularly at low temperature. This behaviour also suggests that the emission in this class of complex may originate from a 5*d* excited state that involves the d_{xz} and d_{yz} orbitals. This is because distortion of the Eu ion out of the basal plane of the coordination pyramid would bring the ligand electron density closer to the lobes of these *d*-orbitals, increasing interelectronic repulsion and therefore driving them to higher energy (Figure 3.32).

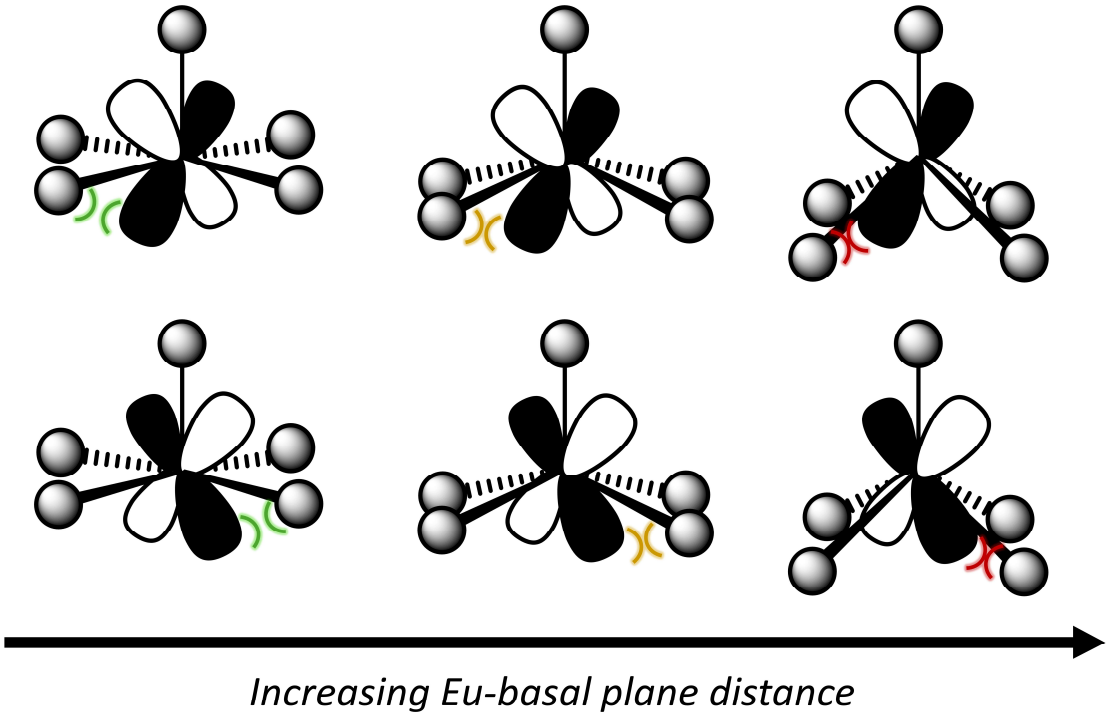


Figure 3.32. Schematic diagram showing how the Eu-basal plane distance in complexes with square-pyramidal coordination spheres might affect the interactions between the ligands defining the basal plane and the electron density in the $5d_{xz}$ and $5d_{yz}$ orbitals of Eu^{II}.

As predicted for **2.1**, there may be some charge-transfer character to the electronic transitions that lead to the observable emissions, which are otherwise predominantly 5*d*→4*f* in nature. Thus, the different ligand sets examined in this study may also modulate the charge-transfer character of the transitions. This may be another reason for some of the anomalous behaviour we observe, although the exact nature and magnitude of this effect is unclear.

As a possible rationale for the anomalous behaviour of **3.1** and **3.4** in this correlation, we consider that the $^{bdp}Cp^{\#}$ and Cp^{xph} ligands are unique among the series because they have substituents featuring significant π-type electron density, i.e., the formally sp^3-hybridized lone pair on the phosphorus atom of the $P(NMe_2)_2$ substituent, or the delocalized π-system of the phenyl substituent, respectively. To visualize, the 90 K crystal structures of **3.1** and **3.4** were refined using NoSpherA2[242] and electron localizability indicator (ELI-D)[243] maps were generated using the computed wavefunction (PBE0/x2c-TZVPP)[244–246] (Figure 3.33). Electron density from the phosphorus lone pair in **3.4** and the delocalized π-system in **3.1** is clearly visible

in the maps, and furthermore, are spatially located in regions that coincide with the second and/or third maximum of the expected radial distribution of a Eu^{II} 5*d* orbital.[212,247] This suggests that the electron density is accumulated close enough to the Eu ion that it could promote appreciable secondary interactions with the excited-state 5*d* orbitals, driving these to higher energy due to increased interelectronic repulsion. Under these circumstances, the secondary interactions arising from the pendant electron density can break the pseudosymmetry, which may help to explain the unexpectedly high emission energies of **3.1** and **3.4** relative to their Eu-basal plane distance.

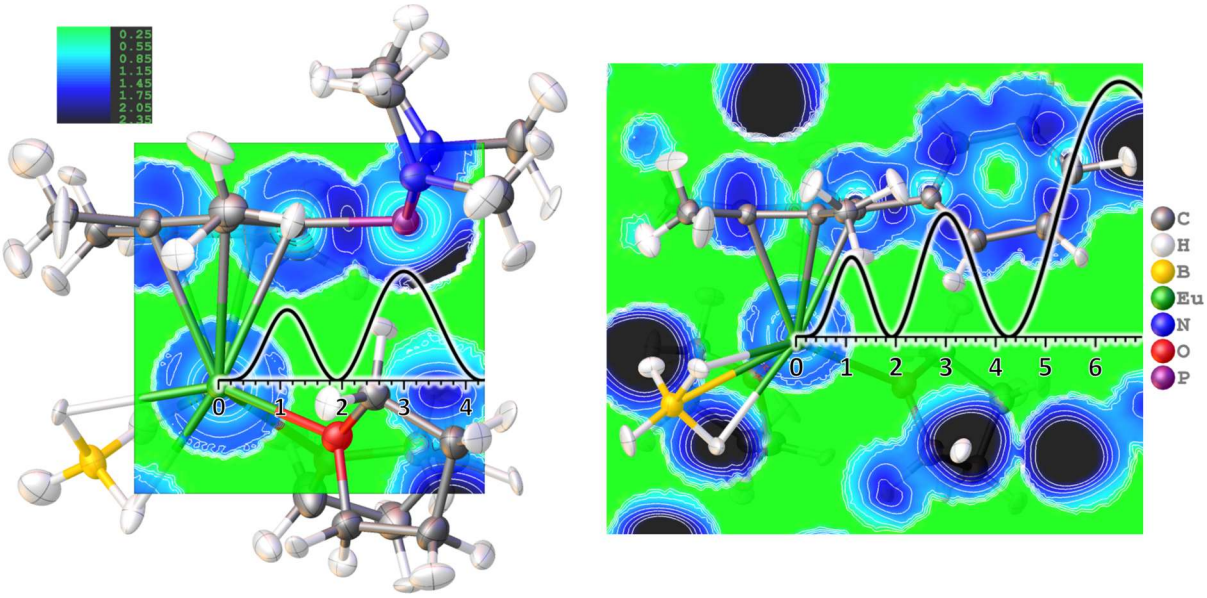


Figure 3.33. Electron localizability indicator (ELI-D) maps for **3.4** (left) and **3.1** (right). For **3.4**, the selected plane is defined by Eu1, C1 (1-position of $^{bdp}Cp^{\#}$), and P1. For **3.1**, the selected plane is defined by Eu1, C5 (1-position of Cp^{xph}), C10 (*ipso*-Ph), and C13 (*para*-Ph). Each plot is overlaid with a portion of the theoretical, normalized radial distribution function for a Eu^{II} 5*d* orbital[212,247] from (left) 0 to 4 Å (0 to 7.56 bohr) or (right) 0 to 7 Å (0 to 13.2 bohr).

At 270 K, vibronic effects play a much larger role in describing the emission properties of these complexes, and even the correlations described above are weakened. However, at this temperature, it is notable that the Eu-Cp(cent) distance becomes much more predictive, with **3.6** having a much shorter distance (2.4966(3) Å) than the others (2.52 – 2.54 Å) and thus being the only significant outlier to an otherwise linear increase in energy at the emission band maximum with increasing distance (Figure 3.30a). Aside from a moderately correlated decrease in emission energy with increasing B1-B1′ distance (Figure 3.30d) that also arises at this temperature, the relative influence of each individual metrical parameter is obfuscated, and no further interpretation is possible.

3.9 Thermometric performance

Gratifyingly, all the complexes $[Cp^{R}Eu(\mu\text{-}BH_4)(solv)_n]_2$ exhibit thermochromic luminescence, further fortifying the suitability of this architecture for luminescence thermometry applications. Among all examples, the original complex **2.1** remains the highest-sensitivity thermometer, and the one with the greatest ΔE (the borodeuteride-bridged analogue **2.2** is included for comparison). Exchanging the two THF

solvent ligands of **2.1** for DME, as in **3.6**, engenders a dramatic reduction in ΔE and sensitivity. Complexes **3.2** and **3.4** approach the sensitivity of **2.1**, with values of 7.22 and 7.36 cm^{-1} K^{-1} respectively, while the other complexes exhibit much lower values from ~3-5 cm^{-1} K^{-1}. The temperatures at which each complex attains its maximum value of sensitivity also vary widely; for example, complex **3.4** has by far the lowest temperature of maximum sensitivity (113 K) while also having the second highest S_a in the series. This phenomenon is also hypersensitive to the coordination environment, as even the slightest possible modification to the ligand field (substitution of BH_4 for BD_4) leads to a change in the temperature of maximum sensitivity of 60 K. It is also noteworthy that complexes **3.2** and **3.3** have very different thermometric performance despite being direct congeners. Complex **3.5** exhibits negligible band shift and correspondingly low sensitivity.

Our results indicate that, for this class of complex, there is no single structural parameter that can dictate or predict the luminescence thermometric performance. The synergy between temperature-dependent structural modulations, electronic structure, and vibrational effects can lead to the distinct performances observed here. However, in a qualitative sense, it appears that the metal-ligand flexibility of the coordination sphere plays an important role in modulating the emission characteristics in these complexes. It is notable in this regard that ΔE and S_a appear to decrease with increasing rigidity of the coordination sphere. Complex **2.1** has arguably the most flexible coordination sphere, as it bears monodentate solvent ligands and Cp^* is the least sterically encumbering of all the cyclopentadienyl ligands investigated herein. Thus, it follows that it displays the largest ΔE and S_a among the series. The performance is diminished upon rigidification of the coordination sphere by introducing a chelating solvent ligand, as in **3.6**. Conversely, complex **3.7** has the bulkiest cyclopentadienyl fragment and bears chelating solvent ligands, and therefore can be considered to have the most rigid coordination sphere among the dimers; accordingly, it has the lowest ΔE and S_a by considerable margin. A similar argument can help explain the differences between **3.2** and **3.3**: the bulkier trimethylgermanyl substituent of **3.3** rigidifies the coordination sphere, diminishing the ΔE and S_a relative to the smaller trimethylsilyl substituent of **3.2** while all else remains equal. Complexes **3.1** and **3.4** emerge again as outliers in this examination, emphasizing that the relative importance of the various effects governing the thermometric performance are altered when the pseudosymmetry of the coordination sphere is lowered or broken. The $^{bdp}Cp^{\#}$ ligand is slightly bulkier than the $^{TMS}Cp^{\#}$ ligand, and due to the unique electronic properties of the -$P(NMe_2)_2$ fragment, is probably more rigid, yet **3.4** has higher ΔE and S_a than **3.2**. Similarly, Cp^{xph} is not bulkier than $^{TMG}Cp^{\#}$, yet **3.1** has a lower ΔE but a curiously higher S_a than **3.3**. These differences may be related to specific ligand-field perturbations or excited-state dynamics engendered by the extra pendant π-type electron density of these two ligands, as described above. Furthermore, an examination of the relationship between thermometric figures of merit and the rate of change of emission energy as a function of lattice compression (Figure B19) shows a general trend of increasing sensitivity and increasing ΔE as the compressibility of the crystal lattice increases. This correlation is preserved across different crystal morphologies, and corroborates our previous observations on **2.1**.[224]

3.10 Conclusion

In summary, we have expanded the family of organometallic Eu^{II}-based luminescence thermometers by six additional members, spanning a range of stereoelectronic profiles in an isostructural framework. Investigating the factors that govern the optical properties of systems of this nature is key to understanding, modulating, and eventually improving them. We have shed some light towards this goal by identifying several factors of particular importance within this family of complexes, namely the Eu-basal plane distance,

presence of pendant π-type electron density, and metal-ligand flexibility. This study demonstrates that thermochromic emission is an intrinsic property of Eu^{II} hemimetallocenes and highlights the complex interactions that give rise to this property and the challenges in elucidating and disambiguating their influence. We expect that the insights gained herein will aid in driving and directing the development of increasingly advanced molecular optical materials based on Eu^{II}, with finely tunable photophysical characteristics.

3.11 Methods

General Remarks. All manipulations were conducted under stringently oxygen- and moisture-free conditions under argon or nitrogen atmospheres using Schlenk line and glovebox techniques. Tetrahydrofuran (THF), hexanes, pentane, 1,2-dimethoxyethane (DME), diethyl ether, and toluene were dried on columns of activated alumina using a J.C. Meyer Phoenix solvent system and degassed via repeated freeze-pump-thaw cycles, then stored over activated 4 Å molecular sieves. All chemicals were purchased from STREM Chemicals, Oakwood Scientific, Sigma-Aldrich, or Fisher Scientific and used as received unless otherwise noted. Potassium pentamethylcyclopentadienide (KCp*),[187] $[Eu(BH_4)_2(THF)_2]$,[56] potassium tetramethylcyclopentadienide (KCp^{tet}),[225] potassium 1-(trimethylsilyl)-2,3,4,5-tetramethylcyclopentadienide ($K^{TMS}Cp^{\#}$),[226] $MnBr(CO)_3(py)_2$,[248] and pentamethylcymantrene $[Cp^*Mn(CO)_3]$[249] were prepared according to reported procedures.

Elemental analysis. Elemental analysis was performed by Midwest Microlab (Indianapolis, IN, USA). Organolanthanide complexes, especially those of divalent ions, are well known to suffer incomplete combustion and formation of carbides during microanalysis, yielding consistently and artificially low values. Complexes bearing solvent ligands are further plagued by artificially low values due to loss of coordinated solvent during sample loading and/or combustion; thus, microanalysis values should be considered within a wider tolerance than usually expected.[60,250–256] Here, elemental analysis has been treated in a manner consistent with the literature regarding divalent organolanthanide compounds.

Mass spectrometry. Mass spectrometry was performed from solid samples using a Kratos Concept 2S magnetic sector electron impact high-resolution mass spectrometer.

NMR spectroscopy. All NMR spectra were recorded using either a Bruker AVANCE II 300 MHz spectrometer or a Bruker AVANCE III HD 600 MHz spectrometer equipped with a triple resonance inverse 5 mm H-C/N-D cryoprobe. ^1H chemical shifts are reported in ppm relative to tetramethylsilane using the $CDCl_3$ residual solvent signal at $\delta = 7.26$ as an internal standard. ^{13}C NMR spectra recorded on the 300 MHz spectrometer were collected using the proton-decoupled UDEFT pulse sequence,[257] and chemical shifts are reported in ppm relative to tetramethylsilane referenced to the $CDCl_3$ resonance at $\delta = 77.16$. ^{29}Si NMR spectra were recorded using the DEPT35 pulse sequence, and chemical shifts are reported in ppm, externally referenced to tetramethylsilane ($\delta = 0.00$). ^{31}P chemical shifts are reported in ppm, externally referenced to 85% aqueous H_3PO_4 ($\delta = 0.00$).

Infrared spectroscopy. Fourier transform infrared (FTIR) spectra were recorded in the $\tilde{\nu}$ = 4000-525 cm^{-1} range on a Nicolet 6700 FTIR spectrometer equipped with an attenuated total reflectance (ATR) attachment. Samples of air-sensitive materials comprised suspensions of crushed polycrystalline solid in a thin layer of Parabar 10312 oil; background spectra were corrected for the presence of the oil. Air-stable materials were measured as is.

X-ray crystallography. X-ray crystallography was performed using Bruker AXS KAPPA or SMART single-crystal diffractometers equipped with APEX II CCD detectors, using graphite-monochromated Mo Kα radiation (λ = 0.710173 Å) from sealed tube sources. The crystals chosen were mounted on the tips of 100 or 200 μm MicroLoops (depending on the crystal size) using Parabar 10312 oil and cooled to the indicated temperatures. Raw data collection and processing were performed with the Bruker APEX II software package.[188,189] A multiscan absorption correction was applied (SADABS).[190] The crystal structures were solved via direct methods and refined using a full-matrix least-squares method on F^2 using the SHELXTL program suite[191–193] and the Olex2 user interface.[194] Non-hydrogen atoms were refined anisotropically. The position of all hydrogen atoms except for those bonded to boron were calculated based on the geometry of their respective atoms and are included at geometrically idealized positions [riding model]. Hydrogen atoms bonded to boron were located in the Fourier difference map and allowed to refine freely.

Variable-temperature X-ray structural analysis. Additional crystallographic analysis at varying temperatures (90, 150, 175, and 270 K) was performed using a Bruker D8 VENTURE METALJET single-crystal diffractometer equipped with a PHOTON III CMOS detector, using Ga Kα radiation (λ = 1.341 39 Å) from a liquid Ga source (Bruker METALJET D2 PLUS with HELIOS MX optics). The crystals chosen were mounted on a loop fiber using Parabar 10312 oil and cooled to the indicated temperatures. Raw data collection and processing were performed as above, using the Bruker APEX 3 software package.[195–197]

NoSpherA2. The 90 K crystal structures of **3.1** and **3.4** were refined using the non-spherical atom refinement protocol NoSpherA2[242] as implemented in Olex2. The calculations were performed on a laptop computer bearing a 6-core 2.60/4.50 GHz Intel Core i7-9750H with hyperthreading, 16 GB RAM and solid-state drives. The *.tsc* wavefunction was calculated using ORCA 5.0[258–260] and the following settings: basis set x2c-TZVPP;[246] method PBE0;[244,245] 6 threads and 10 GB memory allocation; "Max" integration accuracy; "Relativistics", "H Aniso", "No Afix", and "DISP" activated; automatic HAR; SCF threshold "Strong"; SCF strategy "Normal"; updated SHELXTL-type weighting scheme activated. EXTI was activated for **3.1** as dictated by the original refinement, but not for **3.4**. The entire [dimeric] molecule was taken as input for the wavefunction calculation, yielding a charge of 0 and a multiplicity of $2 * \left(\frac{7}{2} + \frac{7}{2}\right) + 1 = 15$, which was specified in the calculation settings.
All diagrams were prepared using Olex2, Diamond 4,[198,199] or Mercury 2020.1[200] and POV-Ray.[201] The data have been deposited with the Cambridge Crystallographic Data Centre under the deposition numbers 2387284 – 2387312. Analysis of coordination geometry was performed using SHAPE 2.1,[203,241] using the solvent oxygen atoms, centroid of the cyclopentadienyl ligand, and the central boron atoms of the tetrahydroborate ligands as vertices.

Photoluminescence spectroscopy. Photoluminescence data was obtained using a Horiba QuantaMaster 8075-21 spectrofluorometer. An ozone-free PowerArc 75 W xenon lamp was used as the radiation source. The excitation spectra were corrected in real time according to the lamp intensity and the optical system of the excitation monochromator using a silicon diode as a reference. The emission spectra were corrected according to the optical system of the emission monochromator and the photomultiplier response (Hamamatsu R13456 red-extended PMT). Samples were prepared inside the glovebox and comprised a small amount of crystalline solid placed inside a screw-top quartz cuvette, which was then sealed with additional layers of Teflon tape and electrical tape. Low-temperature measurements were performed with

the samples mounted inside a CS202*E-DMX-1AL closed-cycle helium cryostat system (Advanced Research Systems), controlled via a LakeShore 335 temperature controller.

3.13 Synthesis

(1 or 2 or 5)-phenyltetramethylcyclopentadiene (HCp^{xph}). This compound was prepared via a modified literature procedure,[261] as follows: an oven-dried Schlenk flask was purged with dry argon and charged with a stir bar and a 1.9 M solution of phenyllithium in di-*n*-butyl ether (Aldrich) (4.6 mL, 8.68 mmol, 1.2 eq.), then cooled to 0 °C using an ice bath. 2,3,4,5-tetramethyl-2-cyclopentenone (1.0 g, 7.24 mmol, 1 eq.) was added dropwise via syringe at 0 °C. The solution changed from a deep orange to a pale yellow-orange colour as the addition proceeded. The reaction mixture was allowed to warm to room temperature while stirring overnight, giving a cloudy, straw-coloured suspension. The mixture was poured over ice, then acidified to pH 1 via dropwise addition of concentrated HCl (2 mL) with shaking. The solution was extracted with diethyl ether and the organic phase dried over anhydrous sodium carbonate. The solvent was evaporated to give a yellow oil, which was vacuum-distilled using a short-path apparatus. Residual dibutyl ether was collected as a brief colourless forerun and discarded, then the title compound was obtained as a yellow oil (1.3 g, 90% yield). The NMR spectrum of this material was consistent with the literature, and comparison with the reported resonances indicates our sample contained 80% 2-phenyl-, 18% 1-phenyl-, and ~2% 5-phenyl cyclopentadiene. The obtained oil was degassed via repeated freeze-pump-thaw cycles and transferred into a nitrogen-filled glove box for further manipulation and used in the next step without further purification.

Potassium 1-phenyl-2,3,4,5-tetramethylcyclopentadienide (KCp^{xph}). This compound was prepared via a modified literature procedure,[187,261] as follows: in a glovebox under a positive pressure of nitrogen gas, HCp^{xph} (1.3 g, 6.56 mmol, 1 eq.) was dissolved in dry diethyl ether (3.5 mL) and chilled to -20 °C. Potassium hexamethyldisilazide (KHMDS) (1.7 g, 8.52 mmol, 1.3 eq.) was separately dissolved in dry diethyl ether (3.5 mL), and this solution was added dropwise to the stirring, chilled solution of HCp^{xph}. The mixture was allowed to warm to room temperature with stirring overnight to give an opaque, pale yellow suspension. The solid was collected on a fine-porosity fritted glass filter, washed with hexanes (4x 5 mL), and dried *in vacuo* to give the title compound as a light beige powder (1.43 g, 92% yield) which was used without further purification.

Potassium 1-(trimethylgermanyl)-2,3,4,5-tetramethylcyclopentadienide ($K^{TMG}Cp^{\#}$). This compound was prepared via a modified literature procedure,[226] as follows: in a glovebox under a positive pressure of nitrogen gas, KCp^{tet} (250 mg, 1.56 mmol, 1 eq.) was dissolved in dry toluene (2.5 mL) with stirring. A solution of trimethylgermanium bromide (309 mg, 1.56 mmol, 1 eq.) in dry toluene (2.5 mL) was added dropwise at room temperature, and the mixture stirred for 48 hr at room temperature to give an opaque, pale yellow suspension. Hexanes (5 mL) was added, and the mixture was filtered over a pad of Celite to give a clear solution, which was subsequently chilled to -20 °C. A solution of KHMDS (312 mg, 1.56 mmol, 1 eq.) in dry toluene was added dropwise to the chilled, stirring filtrate, and the mixture was allowed to warm to room temperature with stirring overnight. The resulting heavy precipitate was collected on a fine-porosity fritted glass filter, washed with hexanes (4x 5 mL), and dried *in vacuo* to give the title compound as a white solid (333 mg, 77% yield) which was used without further purification.

Potassium 1-(bis(dimethylamino)phosphino)-2,3,4,5-tetramethylcyclopentadienide ($K^{bdp}Cp^{\#}$). This compound was prepared via a modified literature procedure,[227] as follows: in a glovebox under a positive pressure of nitrogen gas, a Schlenk flask was charged with KCp^{tet} (996 mg, 6.21 mmol, 1 eq.), dry diethyl ether (30 mL), dry hexanes (30 mL), and a stir bar. The flask was sealed with a rubber septum and transferred to a Schlenk line under a flow of argon, then cooled to 0 °C using an ice bath. Bis(dimethylamino)chlorophosphine (1.0 g, 6.21 mmol, 1 eq.) was added via syringe to the stirring suspension of KCp^{tet} at 0 °C. The mixture was allowed to warm to room temperature with stirring overnight, giving a cloudy, pale yellow suspension. The diethyl ether was removed *in vacuo*, and the remaining mixture was transferred back into the glovebox for further processing. The mixture was filtered over a pad of Celite and the pad rinsed with many small volumes of hexanes to ensure maximal product recovery. The colourless filtrate was concentrated to *ca.* 10 mL and chilled to -20 °C (some colourless crystalline 1-(bis(dimethylamino)phosphino)-2,3,4,5-tetramethylcyclopentadiene formed upon cooling). A solution of KHMDS (1.36 g, 6.83 mmol, 1.1 eq.) in 5 mL dry toluene was added dropwise to the stirring, chilled filtrate. The filtrate immediately attained a yellow colour and became significantly cloudy at the end of the KHMDS addition. The mixture was allowed to warm to room temperature with stirring over 48 hr, giving an opaque, yellowish suspension. The solid was collected on a fine-porosity fritted glass filter, washed with pentane (4x 5 mL), and dried *in vacuo* to give the title compound as an off-white powder (1.45 g, 84% yield) which was used without further purification.

Potassium 1,2,3,4-tetraisopropylcyclopentadienide (KCp^{iPr4}). In a glovebox under a positive pressure of nitrogen gas, a Schlenk flask was charged with $NaCp^{iPr4}$ (1 g, 3.9 mmol), dry THF (10 mL) and a stir bar. The flask was sealed with a rubber septum and transferred to a Schlenk line under a flow of argon. Distilled water (71 µL, 3.9 mmol, 1 eq) was added with a pipettor, causing the solution to turn cloudy immediately. The mixture was stirred under argon for 30 min, then filtered through a column comprising a plug of cotton wool, 1 cm of Celite, and 1 cm of Na_2SO_4 packed in a Pasteur pipette to give a cloudy, pale yellow solution. The solution was blown dry under a stream of air to give a white solid, which was redissolved in minimal pentane and blown dry again to give a yellowish crystalline solid. Analysis via ^{1}H NMR spectroscopy confirmed the identity of this material as HCp^{iPr4} alongside minor impurities.[231] The solid was dissolved in minimal pentane once more and the solution filtered through a 0.45 µM PTFE syringe filter to give a clear yellow solution, from which the solvent was removed and the residue dried *in vacuo* overnight before being transferred into a nitrogen-filled glove box.

The crude HCp^{iPr4} was dissolved in dry hexanes (5 mL) with stirring, and a solution of KHMDS (856 mg, 4.3 mmol, 1.1 eq. assuming quantitative yield of HCp^{iPr4}) in toluene (3 mL) was added dropwise. The mixture rapidly turned yellow and cloudy and was stirred overnight at room temperature to give an opaque, yellowish suspension. The solid was collected on a fine-porosity fritted glass filter, washed with pentane (4x 5 mL), and dried *in vacuo* to give the title compound as an off-white powder (827 mg, 78% yield) which was used without further purification.

$[Cp^{xph}Eu(BH_4)(THF)_2]_2$ (3.1). In a glovebox under a positive pressure of nitrogen gas, $[Eu(BH_4)_2(THF)_2]$ (40 mg, 0.123 mmol, 1 eq.) and KCp^{xph} (29 mg, 0.123 mmol, 1 eq.) were dissolved in dry THF (3 mL) with stirring. The solution immediately attained a yellow-orange colour, and orange luminescence was observed when the solution was excited with a 405 nm laser pointer. The mixture was stirred for 48 hr at room temperature, during which a substantial quantity of precipitate formed. The mixture was filtered over a pad of Celite, and the pad rinsed with several 0.5 mL portions of THF until the washings ran colorless. The filtrate was concentrated *in vacuo* until incipient crystallization; then THF was added dropwise until all the

solid just dissolved. The so-formed saturated solution was stored at −20 °C, resulting in the formation of yellow-green blocklike crystals. These were isolated by decantation of the supernatant and dried briefly *in vacuo*. This process was repeated with the supernatant to give **3.1** (32 mg, 52% yield over two crops). IR: $\tilde{\nu}$ = 3056 (vw), 2978 (m), 2939 (m), 2883 (s), 2833 (w), 2719 (vw), 2370 (s), 2316(s), 2249 (s), 2198 (s), 1942 (vw), 1874 (vw), 1817 (vw), 1668 (vw), 1595 (vs), 1504 (vs, with shoulder at 1477), 1441 (s), 1396 (s), 1338 (w), 1294 (w), 1244 (w), 1138 (s, with shoulder at 1176), 1103 (s), 1072 (s), 1032 (vs), 980 (vw), 920 (vw), 876 (vs, with shoulder at 835), 756 (vs), 702 (vs), 665 (s), 644 (w), 634 (m), 590 (m) cm^{-1}. Anal. Calcd. (%) for $C_{38}H_{58}B_2Eu_2O_2$ (872.43) (**3.1** with loss of 2x coordinated THF): C, 52.32; H, 6.70. Found: C, 51.25; H, 6.83.

[^{TMS}Cp$^{\#}$Eu(BH$_4$)(THF)$_2$]$_2$ (3.2). In a glovebox under a positive pressure of nitrogen gas, [Eu(BH$_4$)$_2$(THF)$_2$] (100 mg, 0.31 mmol, 1 eq.) and K^{TMS}Cp$^{\#}$ (72 mg, 0.31 mmol, 1 eq.) were dissolved in dry THF (5 mL) with stirring. The solution immediately attained a yellow-orange colour, and red-orange luminescence was observed when the solution was excited with a 405 nm laser pointer. The mixture was stirred for 48 hr at room temperature, during which a substantial quantity of precipitate formed. The mixture was filtered over a pad of Celite, and the pad rinsed with several 0.5 mL portions of THF until the washings ran colorless. The filtrate was concentrated *in vacuo* to *ca.* 2 mL, then crystallized via diffusion of *n*-hexane vapour into the concentrated filtrate at -35 °C to give **3.2** (112 mg, 72% yield) as large, greenish-yellow platelike crystals. IR: $\tilde{\nu}$ = 2970 (s), 2943 (s), 2883 (s), 2831 (w), 2721 (vw), 2380 (m), 2664 (m, br), 2197 (m, br, with shoulder at 2163), 1493 (m), 1433 (s), 1402 (m), 1385 (m), 1319 (s, with shoulder at 1340), 1244 (s), 1234 (s), 1117 (s), 1032 (vs), 910 (m), 877 (s), 827 (vs, with shoulder at 843), 748 (s), 677 (s), 627 (s) cm^{-1}. Despite several attempts, no sufficient or repeatable elemental analyses could be obtained from this compound. In addition to its high sensitivity to air, moisture and solvent loss, it is likely that this compound is especially prone to forming carbides given the presence of reducing organoeuropium(II) and its silicon content. However, single crystals were used for all analyses and the infrared and PL spectra are consistent with the expected composition.

[^{TMG}Cp$^{\#}$Eu(BH$_4$)(THF)$_2$]$_2$ (3.3). In a glovebox under a positive pressure of nitrogen gas, [Eu(BH$_4$)$_2$(THF)$_2$] (40 mg, 0.123 mmol, 1 eq.) and K^{TMG}Cp$^{\#}$ (34 mg, 0.123 mmol, 1 eq.) were dissolved in dry THF (3 mL) with stirring. The solution immediately attained a yellow colour, and red-orange luminescence was observed when the solution was excited with a 405 nm laser pointer. The mixture was stirred for 48 hr at room temperature, during which a substantial quantity of precipitate formed. The mixture was filtered over a pad of Celite, and the pad rinsed with several 0.5 mL portions of THF until the washings ran colorless. The filtrate was concentrated *in vacuo* to *ca.* 2 mL, then crystallized via diffusion of *n*-hexane vapour into the concentrated filtrate at -35 °C to give **3.3** (80 mg, 73% yield) as large yellow platelike crystals. IR: $\tilde{\nu}$ = 2974 (s, with shoulder at 2943), 2883 (s), 2833 (m), 2717 (vw), 2372 (s), 2316 (s), 2251 (s), 2197 (s, with shoulder at 2171), 1700 (w), 1647 (vw), 1543 (m), 1490 (m), 1431 (s), 1323 (s), 1238 (m), 1226 (s), 1109 (s, with shoulders at 1138 and 1174), 1036 (vs), 879 (vs, with shoulder at 910), 818 (vs), 748 (s), 667 (s), 584 (vs), 563 (vs) cm^{-1}. Anal. Calcd. (%) for $C_{40}H_{82}B_2Eu_2Ge_2O_4$ (1097.90) (**3.3** with loss of 4x coordinated THF): C, 35.61; H, 6.23. Found: C, 33.71; H, 6.10.

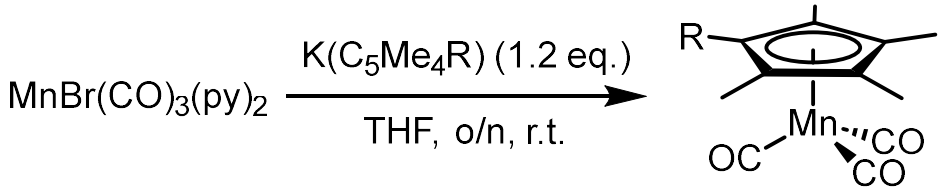
[^{bdp}Cp$^{\#}$Eu(BH$_4$)(THF)$_2$]$_2$ (3.4). In a glovebox under a positive pressure of nitrogen gas, [Eu(BH$_4$)$_2$(THF)$_2$] (40 mg, 0.123 mmol, 1 eq.) and K^{bdp}Cp$^{\#}$ (34 mg, 0.123 mmol, 1 eq.) were dissolved in dry THF (3 mL) with stirring. The solution immediately attained a yellow-orange colour, and red-orange luminescence was observed when the solution was excited with a 405 nm laser pointer. The mixture was stirred for 48 hr at

room temperature, during which a substantial quantity of precipitate formed. The mixture was filtered over a pad of Celite, and the pad rinsed with several 0.5 mL portions of THF until the washings ran colorless. The filtrate was concentrated *in vacuo* until incipient crystallization; then THF was added dropwise until all the solid just dissolved. The so-formed saturated solution was stored at −20 °C, resulting in the formation of yellow rodlike crystals. These were isolated by decantation of the supernatant and dried briefly *in vacuo*. This process was repeated with the supernatant to give **3.4** (26 mg, 38% yield over two crops). IR: $\tilde{\nu}$ = 2978 (m), 2937 (w), 2877 (s), 2845 (s), 2819 (s), 2777 (m), 2372 (m), 2306 (m), 2249 (m), 2193 (m), 1443 (m), 1400 (w), 1321 (s), 1255 (s), 1190 (s), 1138 (m), 1109 (m), 1034 (s), 966 (vs), 951 (vs), 897 (s), 877 (s), 823 (m), 752 (m), 656 (vs), 631 (s) cm^{-1}. Anal. Calcd. (%) for $C_{42}H_{88}B_2Eu_2N_4O_4P_2$ (1100.69): C, 45.83; H, 8.06; N, 5.09. Although the H and N analyses are within a reasonable expanded tolerance given the nature of the material and the known limitations of the method,[256] analysis repeatedly returned low carbon values for this compound despite our best efforts. The best results we obtained are as follows: C, 33.80; H, 7.36; N 4.39.

[Cp^{iPr4}Eu(BH$_4$)(THF)$_2$]$_\infty$ (3.5). In a glovebox under a positive pressure of nitrogen gas, [Eu(BH$_4$)$_2$(THF)$_2$] (40 mg, 0.123 mmol, 1 eq.) and KCp^{iPr4} (34 mg, 0.123 mmol, 1 eq.) were dissolved in dry THF (3 mL) with stirring. The solution immediately attained a yellow-orange colour, and yellowish luminescence was observed when the solution was excited with a 405 nm laser pointer. The mixture was stirred for 48 hr at room temperature, during which a substantial quantity of precipitate formed. The mixture was filtered over a pad of Celite, and the pad rinsed with several 0.5 mL portions of THF until the washings ran colorless. The filtrate was concentrated *in vacuo* to *ca.* 2 mL, then crystallized via diffusion of pentane vapour into the concentrated filtrate at -35 °C to give **3.5** (40 mg, 60% yield over two crops) as greenish-yellow blocklike crystals. IR: $\tilde{\nu}$ = 2970 (m), 2949 (m), 2883 (m), 2862 (m), 2833 (vw), 2397 (m), 2264 (m, with shoulder at 2299), 2224 (m, with shoulder at 2189), 1527 (vw), 1473 (w), 1441 (m), 1409 (vw), 1373 (m), 1358 (m), 1311 (w), 1284 (w), 1246 (m), 1188 (m), 1176 (m), 1157 (vw), 1138 (w), 1113 (m), 1066 (vs), 1026 (m), 1014 (m), 985 (m), 864 (vs), 835 (m), 764 (s), 731 (vw), 679 (s), 661 (w) cm^{-1}. Anal. Calcd. (%) for $C_{25}H_{49}BEuO_2$ (544.44, the monomeric unit of the polymer): C, 55.15; H, 9.07. Found: C, 50.22; H, 8.88.

[Cp*Eu(BH$_4$)(DME)]$_2$ (3.6). In a glovebox under a positive pressure of nitrogen gas, [Eu(BH$_4$)$_2$(THF)$_2$] (40 mg, 0.123 mmol, 1 eq.) and KCp* (22mg, 0.123 mmol) were dissolved in dry DME (10 mL) with stirring. The solution immediately attained a yellow colour, and orange luminescence was observed when the solution was excited with a 405 nm laser pointer. (On one occasion, we observed this solution to attain an unexpected dark orange colour at this stage, however the expected luminescence remained, and the reaction outcome was not affected.) The mixture was stirred for 72 hr at room temperature, during which a substantial quantity of precipitate formed. The mixture was filtered over a pad of Celite, and the pad rinsed with several 0.5 mL portions of DME until the washings were no longer luminescent. The filtrate was concentrated *in vacuo* until incipient crystallization; then DME was added in small portions with vigorous manual shaking until all the solid just dissolved. The so-formed saturated solution was stored at −35 °C, resulting in the formation of deep yellow blocklike crystals. These were isolated by decantation of the supernatant and dried briefly *in vacuo* to give **3.6** (36 mg, 60% yield). IR: $\tilde{\nu}$ = 3000 (vw), 2972 (vw), 2939 (m), 2898 (m), 2835 (m), 2723 (vw), 2374 (m), 2322 (m), 2241 (m), 2194 (m, br), 1443 (m, br, with shoulder at 1410), 1286 (w), 1242 (m), 1192 (m), 1142 (vw), 1109 (s), 1066 (vs), 1014 (m), 856 (vs), 829 (m), 798 (vw), 561 (vw) cm^{-1}. Anal. Calcd. (%) for $C_{20}H_{38}B_2Eu_2$ (604.07) (**3.6** with loss of 2x coordinated DME): C, 39.77; H, 6.34. Found: C, 39.54; H, 5.86.

[Cp^{iPr4}Eu(BH$_4$)(DME)]$_2$ (3.7). In a glovebox under a positive pressure of nitrogen gas, [Eu(BH$_4$)$_2$(THF)$_2$] (40 mg, 0.123 mmol, 1 eq.) and KCp^{iPr4} (34mg, 0.123 mmol, 1 eq.) were dissolved in dry DME (5 mL) with stirring. The solution immediately attained a yellow colour, and orange luminescence was observed when the solution was excited with a 405 nm laser pointer. The mixture was stirred for 48 hr at room temperature, during which a substantial quantity of precipitate formed. The mixture was filtered over a pad of Celite, and the pad rinsed with several 0.5 mL portions of DME until the washings were no longer luminescent. The filtrate was concentrated *in vacuo* to *ca.* 1 mL, then crystallized via diffusion of pentane vapour into the concentrated filtrate at -35 °C to give **3.7** (19 mg, 32% yield) as bright green blocklike crystals. IR: $\tilde{\nu}$ = 2970 (m), 2949 (s), 2883 (m), 2862 (m), 2832 (w), 2397 (m, br), 2264 (m, br, with shoulder at 2285), 2224 (m, br, with shoulder at 2190), 1473 (w), 1440 (m), 1409 (w), 1373 (m), 1358 (m), 1305 (w), 1284 (w), 1246 (m), 1188 (m), 1176 (m), 1140 (w), 1113 (s), 1066 (vs), 1026 (m), 1014 (m), 985 (m), 864 (vs), 835 (m), 764 (s), 731 (w), 679 (s), 661 (w) cm^{-1}. Anal. Calcd. (%) for $C_{42}H_{86}B_2Eu_2O_4$ (980.69): C, 51.44; H, 8.84. Found: C, 50.70; H, 9.04.



General procedure 1 (GP1) for the synthesis of substituted cymantrenes. Using a modified literature procedure,[6] a pear-shaped Schlenk flask was charged with MnBr(CO)$_3$(py)$_2$ (40 mg, 0.11 mmol, 1 eq.), the corresponding potassium cyclopentadienide (0.13 mmol, 1.2 eq.), and a stir bar in a glovebox under a positive pressure of nitrogen gas. THF (2 mL) was added, and the mixture stirred overnight at room temperature. The solvent was removed *in vacuo*, then the solid was treated with a small volume of hexanes to remove traces of pyridine before evaporating again. The flask was then sealed with a micro cold finger before transferring to a Schlenk line. The crude solid was carefully heated with a heat gun under dynamic vacuum to sublime the cymantrene, which was collected from the dry-ice-cooled cold finger in air.

1-phenyl-2,3,4,5-tetramethylcyclopentadienylmanganese(I) tricarbonyl (3.8). Following GP1, the title compound was obtained as a yellow microcrystalline solid (36 mg, quantitative yield). ^{1}H NMR (600 MHz, $CDCl_3$) δ: 7.44 – 7.28 (m, 5H, phenyl, overlapping $CDCl_3$ residual), 1.96 (s, 6H, 2,5-C$\underline{H}_3$), 1.85 (s, 6H, 3,4-C$\underline{H}_3$). ^{13}C NMR (151 MHz, $CDCl_3$) δ: 226.5 (-$\underline{C}$O), [132.8, 131.8, 128.3, 127.7] (aryl C), [101.1, 99.0, 94.8] (cyclopentadienyl C), [11.1, 10.5] (-$\underline{C}$H$_3$). IR: $\tilde{\nu}_{CO}$ = 1992, 1898 cm^{-1}. HRMS-EI (*m/z*): [M]$^+$ calc'd for $C_{18}H_{17}MnO_3$: 336.0558; found 336.0583 (32.75% abundance, 2.38 mmu deviation).

1-(trimethylsilyl)-2,3,4,5-tetramethylcyclopentadienylmanganese(I) tricarbonyl (3.9). Following GP1, the title compound was obtained as a pale yellow powder (30 mg, 81% yield). ^{1}H NMR (300 MHz, $CDCl_3$) δ: 1.91 (s, 6H, cyclopentadienyl -C$\underline{H}_3$), 1.89 (s, 6H, cyclopentadienyl -C$\underline{H}_3$), 0.31 (s, 9H, -Si(C$\underline{H}_3$)$_3$). ^{13}C NMR (151 MHz, $CDCl_3$) δ: 226.6 (-$\underline{C}$O), [105.1, 99.7, 80.3] (cyclopentadienyl C), [13.1, 10.6] (cyclopentadienyl -$\underline{C}$H$_3$), 2.0 (-Si($\underline{C}$H$_3$)$_3$). ^{29}Si NMR (60 MHz, $CDCl_3$) δ: -3.98 (s). IR: $\tilde{\nu}_{CO}$ = 1988, 1900 (with shoulder at 1874) cm^{-1}. HRMS-EI (*m/z*): [M]$^+$ calc'd for $C_{15}H_{21}MnO_3Si$: 332.0640; found 332.0653 (21.75% abundance, 1.20 mmu deviation).

1-(trimethylgermanyl)-2,3,4,5-tetramethylcyclopentadienylmanganese(I) tricarbonyl (3.10). Following GP1, the title compound was obtained as a pale yellow microcrystalline solid (42 mg, 93% yield). ^{1}H NMR (600 MHz, $CDCl_3$) δ: 1.89 (s, 6H, cyclopentadienyl -C$\underline{H}_3$), 1.88 (s, 6H, cyclopentadienyl -C$\underline{H}_3$), 0.45 (s, 9H,

-Ge($C\underline{H}_3$)$_3$). ^{13}C NMR (151 MHz, $CDCl_3$) δ: 226.8 (-$\underline{C}$O), [104.2, 99.1, 83.5] (cyclopentadienyl C), [12.9, 10.6] (cyclopentadienyl -$\underline{C}H_3$), 1.6 (-Ge($\underline{C}H_3$)$_3$). IR: $\tilde{\nu}_{CO}$ = 1986, 1898 (with shoulder at 1873) cm^{-1}. HRMS-EI (*m/z*): [M]$^+$ calc'd for $C_{15}H_{21}MnO_3{}^{74}Ge$: 378.0083; found 378.0099 (1.32% abundance, 0.83 mmu deviation).

1-(bis(dimethylamino)phosphino)-2,3,4,5-tetramethylcyclopentadienylmanganese(I) tricarbonyl (3.11). Following GP1, the title compound was obtained as a pale yellow microcrystalline solid (36 mg, 86% yield). ^{1}H NMR (300 MHz, $CDCl_3$) δ: 2.65 (d, 12H, -N($C\underline{H}_3$)$_2$), $^3J_{P\text{-}H}$ = 9 Hz), 1.94 (s, 6H, 2,5-$C\underline{H}_3$), 1.90 (s, 6H, 3,4-$C\underline{H}_3$). ^{13}C NMR (151 MHz, $CDCl_3$) δ: 226.4 (-$\underline{C}$O), 101.0 (d, $^2J_{C\text{-}P}$ = 9.4 Hz, 2,5-cyclopentadienyl), 97.9 (3,4-cyclopentadienyl), 92.8 (d, $^1J_{P\text{-}C}$ = 12.4 Hz, $\underline{C}$-P(NMe_2)$_2$), 41.4 (d, -N($\underline{C}H_3$)$_2$, $^2J_{P\text{-}C}$ = 17.7 Hz), 11.6 (d, $^3J_{C\text{-}P}$ = 3.2 Hz, 2,5-$\underline{C}H_3$), 10.4 (3,4-$\underline{C}H_3$). ^{31}P{^{1}H} NMR (122 MHz, $CDCl_3$) δ: 96.6 (s; without decoupling, a poorly resolved m). IR: $\tilde{\nu}_{CO}$ = 1990, 1902 (with shoulder at 1874) cm^{-1}. HRMS-EI (*m/z*): [M]$^+$ calc'd for $C_{16}H_{24}MnN_2O_3P$: 378.0905; found 378.0908 (18.65% abundance, 0.28 mmu deviation).

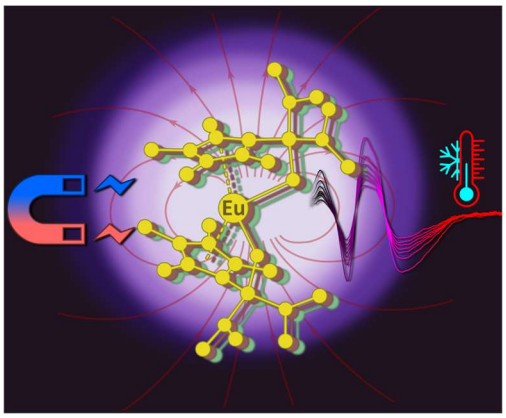
Cymantrenes **3.8**, **3.9** and **3.10** were found to be indefinitely stable in the solid state under ambient conditions, their NMR spectra unchanged after more than one year of storage. However, **3.11** is only moderately air-stable, having intractably decomposed with loss of the -P(NMe_2)$_2$ fragment within the same time; this compound should be stored under inert gas for best longevity.

Endnotes

[i]. It is perhaps important to note that for **3.4**, the crystallographic axes were adjusted to be the same across all the different datasets to facilitate comparison, but the b-axis of the unit cell actually contracts faster than the a-axis upon cooling. However, we observe no striking anomalies in the temperature-dependence of the metrical parameters that could be ascribed to this anisotropy in contraction, thus we will not consider it further.

CHAPTER 4
Exploring a New Family of (Phosphinochalcogenoyl)Europocenes for Magneto-Optical Thermometry

4.1 Preface



The work detailed in this chapter was published as an Open-Access Article in *Angewandte Chemie International Edition* and is reprinted from Diaz-Rodriguez, R. M., Gálico, D. A., Murugesu, M., *Angew. Chem. Int. Ed.* **2025**, *64*, e202517812 under the terms of the Creative Commons Attribution Non-Commercial No Derivatives License.

R. M. Diaz-Rodriguez performed all chemical synthesis; characterized the synthesized compounds by IR and NMR spectroscopy; performed and interpreted DFT calculations of vibrational spectra for **KCp$^{\#}$PCh**; collected, solved, refined and interpreted all SCXRD data; collected, processed and interpreted magnetometry data; collected, processed and interpreted diffuse reflectance, photoluminescence, and MCD data; and wrote the original manuscript. D. A. Gálico contributed to and substantially advised on the design of MCD thermometry experiments, collection and interpretation of MCD, diffuse reflectance and photoluminescence data, as well as writing and editing of parts of the manuscript. M. Murugesu oversaw all aspects of the project.

Additional data and discussion pertaining to this chapter are given in Appendix C.

4.2 Abstract

The development of novel materials based on lanthanide metallocenes remains a valuable endeavour, due to the synthetic accessibility, compositional tunability, and impressive magnetic and luminescent properties of this class of well-studied compounds. Europium(II) complexes are particularly interesting in this regard, given the relative stability, strong paramagnetism, and characteristic Laporte-allowed *5d→4f* emission of this ion. In this study, we tap into the powerful class of phosphinocyclopentadienyl ligands to develop a novel family of potassium (bis(dimethylamino)phosphinochalcogenoyl)cyclopentadienides $K[C_5Me_4(PCh(NMe_2)_2]$ of sulfur, selenium, and tellurium, and explore their coordination chemistry with Eu^{II}. These ligands readily form homoleptic europocenes where the pendant phosphine chalcogenide arms also coordinate the europium center, and these are characterized via single-crystal X-ray diffraction, absorbance, and photoluminescence spectroscopy. Characterization via magnetic circular dichroism (MCD) spectroscopy reveals that these complexes act as extremely sensitive probes for MCD-based magneto-optical thermometry, reaching relative thermal sensitivities up to 170 % K^{-1} at cryogenic

temperatures, with temperature uncertainties as low as 0.003 K. These complexes represent the first examples of organometallic MCD thermometers, and their remarkable properties and interesting structures highlight the promise of this new class of ligands and the utility of the Eu^{II} ion in lanthanide-based functional materials research.

4.3 Introduction

Molecular materials featuring divalent lanthanide ions have attracted significant attention due to their remarkable optical[30,89,211,262,263] and magnetic[264–268] properties. Among the divalent lanthanides, the classical Eu^{II} is of particular interest for several reasons. It is the most accessible and stable of all divalent lanthanide ions, with the Eu^{II}-Eu^{III} redox couple having a small negative reduction potential of only -0.35 V vs. the standard hydrogen electrode.[167] Consequently, the chemistry of the Eu^{II} ion is rich,[86,269,270] and a variety of coordination and organometallic constructs containing Eu^{II} have been reported. In terms of optical properties, the spectra of divalent ions like Eu^{II} are dominated by Laporte-allowed *d-f* transitions which are intense and broad.[30,46,54] Unlike the Laporte-forbidden, narrow-bandwidth, and long-lived *f-f* transitions typical of trivalent lanthanide ions, the *d-f* transitions of a divalent ion are highly sensitive to the coordination environment,[48,166] given the spatially expanded and diffuse nature of the excited-state 5d orbitals.[106,271] As a result, molecular systems based on Eu^{II} form a family of luminescent materials which together cover the entire visible spectrum and encroach upon the near-infrared.[55–61] This sensitivity to environmental stimulus also means that Eu^{II}-based luminescent materials can be employed for band-shift luminescence thermometry,[106,211,224,270,272] complementarily to the ratiometric or lifetime-based methods commonly demonstrated for trivalent lanthanide complexes.[91–93,207,209,273]

Additionally, the strong paramagnetism of Eu^{II} makes it interesting from a magnetochemical perspective as well. Eu^{II} is isoelectronic with Gd^{III}, thus has maximal single-ion ground-state spin owing to its $4f^7$, $^8S_{7/2}$ ground state electronic configuration. Eu^{II}-based materials have been successfully employed in magnetic resonance imaging[274–276] and, despite the formally isotropic electron density distribution of the free ion, have even demonstrated slow magnetic relaxation in a tailored ligand field.[277] Unlike Gd^{III}, Eu^{II} can emit in the visible region,[21] so multifunctional materials that can simultaneously exhibit interesting optical and magnetic properties become accessible with Eu^{II}. Thus, developing new (magneto-)optical materials based on Eu^{II} is a focal point of our research.

Our endeavours toward novel Eu^{II}-based molecular materials led us to the first organoeuropium(II) band-shift luminescence thermometer, the hemimetallocene dimer $[Cp^*Eu(BH_4)(THF)_2]_2$,[224] and later to a systematic study of how different ligands, especially different cyclopentadienides, affect the emission properties in complexes of that nature.[270] Among these, the ligand $^{bdp}Cp^{\#}$ (1-(bis(dimethylamino)phosphino)-2,3,4,5-tetramethylcyclopentadienyl)[227] stood out to us because the complex $[^{bdp}Cp^{\#}Eu(BH_4)(THF)_2]_2$ bearing this esoteric phosphinocyclopentadienide demonstrated the second-best thermometric performance of the complexes we investigated. Phosphinocyclopentadienides are highly versatile ambident ligands, having already been extensively studied in the coordination and organometallic chemistry of main group, transition metal, and f-block elements, and combinations thereof;[278–287] one need only look at the ubiquity of substituted phosphinoferrocenes as an example.[288–297] Furthermore, the free phosphine moiety of such ligands is poised for further chemical elaboration, offering a functional handle from which more diverse and complex systems can be constructed and evaluated for their potential favourable properties.

Phosphinocyclopentadienyl ligands can be conveniently derivatized by transforming the formally P^{III} phosphine component into a tetracoordinate phosphorus analogue. Doing so allows the electronic properties of the ligand to be modulated, and offers a way to diversify the nature of the potential

phosphorus-based coordinating moiety. Such an approach has generated a variety of lanthanide complexes bearing cyclopentadienylideneaminophosphorane ligands[298,299] that, by virtue of their nature as "constrained-geometry complexes" (CGCs),[300,301] have demonstrated utility in small-molecule activation and polymerization catalysis.[302–304] However, in this sense we are more interested in the ability of phosphines to be oxidized to formally P^V phosphino(chalcogenoyl) species, e.g. by direct oxidation with elemental chalcogens.[305] We take inspiration from the binary Eu^{II} chalcogenides EuCh (Ch = O, S, Se, Te),[306,307] which are a famous class of magneto-optical materials that have been thoroughly studied since the 1960s. These compounds exhibit interesting properties such as ferromagnetic semiconductivity, magneto-optic Kerr effect,[308] and strong magnetic circular dichroism (MCD). The bis(dimethylamino)phosphino moiety borne by $^{bdp}Cp^{\#}$ is particularly disposed toward oxidative reactivity with chalcogens because it is highly Lewis basic, allowing it to form a stable phosphine selenide or telluride and addressing the lability typically intrinsic to such species,[305,309–315] thus enabling a survey of structure-property relationships across the whole chalcogen group.

Given that Eu^{II} metallocenes are already well-known for their luminescence properties,[270] we envisioned that combining guidance from the field of solid-state materials with the well-understood chemistry of lanthanide metallocenes would be a promising avenue toward new magneto-optical materials. Further, despite its advantageous characteristics, $^{bdp}Cp^{\#}$ is unexpectedly understudied, and to the best of our knowledge, there exist only two other reports which discuss it or its derivatives,[227,316] and phosphine chalcogenide derivatives thereof are heretofore unknown. Thus, we report herein the synthesis and characterization of a new family of potassium 1-(bis(dimethylamino)phosphinochalcogenoyl)-cyclopentadienides. These salts serve as convenient ligand precursors in the synthesis of the corresponding homoleptic Eu^{II} metallocenes, in which the pendant phosphine chalcogenide moieties are coordinated to the Eu center. This work focuses on the heavier chalcogens (S, Se, Te) because we are most interested in investigating the properties of soft-donor ligands. These are still less well-studied in lanthanide chemistry given the preference of hard lanthanide ions for hard donors, and are advantageous for luminescent materials applications due to their lower phonon energy.[211,317] Further, Eu^{II} is, among lanthanides, a relatively large and soft ion, which is more amenable to accommodating a soft-donor ligand like a heavy chalcogen.[211] The Eu^{II} metallocenes are characterized spectroscopically and found to be highly sensitive probes for MCD-based thermometry in the cryogenic regime, becoming the first examples of organometallic MCD thermometers.

4.4 Synthesis and characterization of ligand precursors

Beginning from the phosphinocyclopentadiene $H^{bdp}Cp^{\#}$,[227] the synthesis of the phosphinochalcogenoyl-substituted proligands studied here is straightforward and high-yielding at the gram-scale (Figure 4.1). In a two-step, one-pot procedure, a toluene solution of $H^{bdp}Cp^{\#}$ is first oxidized with elemental chalcogen (sulfur, selenium, or, gratifyingly, tellurium) to furnish the phosphine chalcogenide, followed immediately by deprotonation with potassium hexamethyldisilazide (KHMDS) to give the corresponding potassium cyclopentadienide. We designate these compounds **$KCp^{\#}PCh$** (Ch = S, Se, Te), in analogy to the cyclopentadienylphosphazene "CpPN" ligands of Sundermeyer et al.[298,302,318] It should be noted that the best results are obtained from these protocols when the starting material $H^{bdp}Cp^{\#}$ is very pure (see Section 4.10). Each of the ligand precursors **$KCp^{\#}PCh$** is well-soluble in polar solvents like tetrahydrofuran (THF) and pyridine, but insoluble in aromatic solvents or alkanes.

Analysis of the multinuclear NMR spectra of all compounds (See Appendix C, Section C.1) in pyridine-d_5 reveals the expected pattern of resonances, and the spectral features are largely unremarkable.

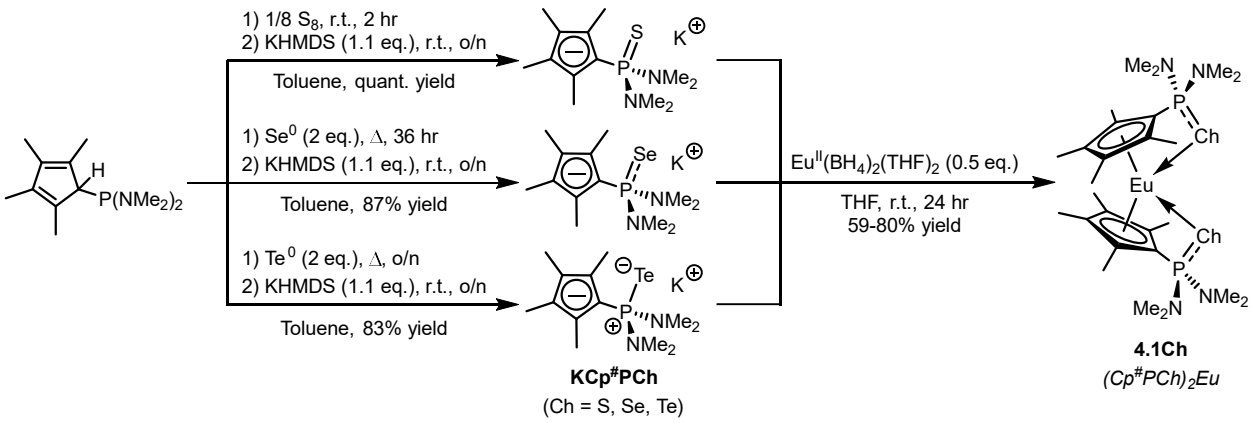


Figure 4.1. Synthesis of (phosphinochalcogenoyl)cyclopentadienides **KCp#PCh** and their corresponding Eu^{II} complexes **4.1Ch**.

In the case of **KCp#PSe** and **KCp#PTe**, an uncommonly-observed $^{4}J_{C\text{-}P}$ coupling is resolved in the ^{13}C resonance ascribed to the 3,4-methyl substituents, due to the "rigid W" effect.[319] Oxidation of the phosphinyl substituent engenders a significant upfield shift in the ^{31}P resonances, which occur within the typical range for the corresponding (dimethylamino)phosphine chalcogenide[320] in all cases (**KCp#PS** 74.8 ppm, **KCp#PSe** 68.2 ppm, **KCp#PTe** 28.7 ppm *cf.* the free phosphine $K^{bdp}Cp^{\#}$ at 115.9 ppm). A ^{31}P-coupled doublet at -167 ppm is observed in the ^{77}Se spectrum of **KCp#PSe**, well downfield of $(Me_2N)_3PSe$ or $(Me_2N)_2PhPSe$ (ca. -370 ppm). The magnitude of the coupling constant $^{1}J_{P\text{-}Se}$ (660 Hz) is rather smaller than those observed in $(Me_2N)_3PSe$ or $(Me_2N)_2PhPSe$ (ca. 800 Hz), and is instead closer to 1,1′-bis(alkylphosphino)ferrocene diselenides (ca. 700 Hz) or even Me_3PSe (684 Hz). These observations may imply a significant contribution of the P=Se multiple-bonded resonance form of the phosphinoselenoyl substituent in this compound, compared to the usually predominant dipolar P^{+}-Se^{-} form.[321]

A freshly prepared, room-temperature solution of **KCp#PTe** in pyridine-d_5 is golden-yellow and shows the expected pattern of ^{1}H resonances, analogously to its lighter congeners. However, the ^{31}P and ^{125}Te resonances are noticeably broadened and/or diminished in intensity, as are the ^{13}C resonances originating from the 1- and (3,4)-carbons of the cyclopentadienyl ring. Further investigation revealed that the ^{31}P resonances gradually sharpened upon cooling and broadened upon heating (Figure 4.2), accompanied by slight changes in chemical shift. Furthermore, we noticed that the colour of the solution changed from golden-yellow to a grey-green colour over several hours, with no apparent change in the NMR spectra. This behaviour was reminiscent of that observed previously in solutions of partially detellurated mono- or oligophosphine tellurides, where fast exchange of tellurium among various free Lewis basic phosphorus sites leads to broadening and loss of observed P-Te coupling.[310–313] Hence, we added a small amount of elemental Te directly to the NMR sample in an attempt to suppress any potential detelluration of **KCp#PTe**. However, the NMR spectra remained unaffected by this, exhibiting precisely the same behaviour. On the other hand, we were surprised to find that these solutions attain a red-violet colour upon standing for one week. The NMR spectra at that point exhibited the expected pattern[313] of sharp resonances for all nuclei at room temperature, with only slight differences in chemical shift *cf.* the others. We therefore ascribe this behaviour to coordinative fluxionality of the phosphinotelluroyl substituent, wherein the dissolved species might interconvert between metallocene-like polymers (*vide infra*), smaller oligomers or clusters, and monomers, which eventually reaches a (meta)stable equilibrium.

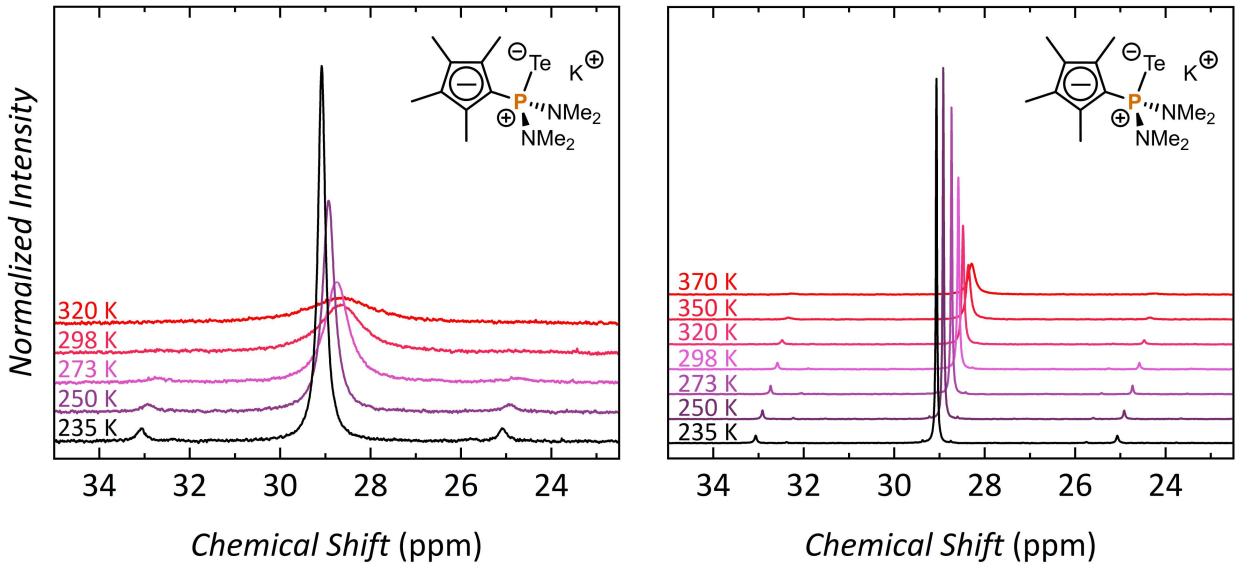
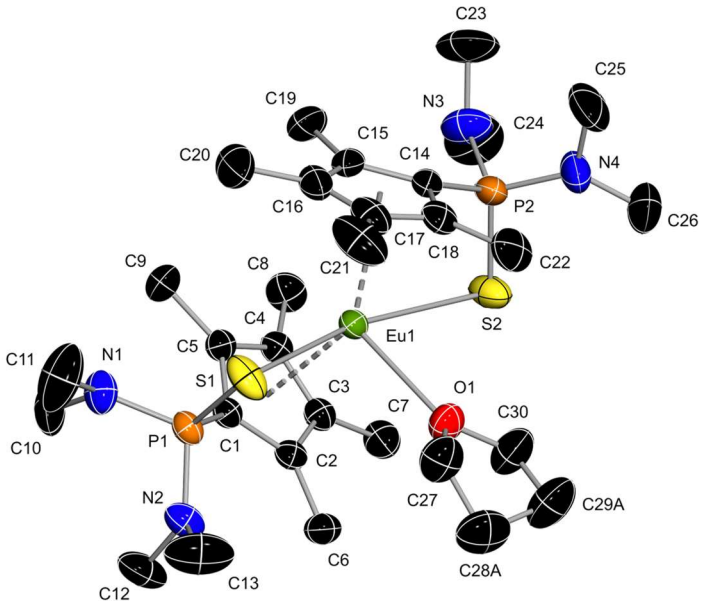


Figure 4.2. Variable-temperature $^{31}P\{^{1}H\}$ NMR spectra of **KCp$^{\#}$PTe** within 6 hr of sample preparation (left) and after one week of stabilization time (right). Spectra are normalized to the room-temperature spectrum in both cases.

4.5 Synthesis of europocenes

With the ligand precursors in hand, we proceeded to investigate their complexation reactivity with Eu^{II}. The reaction of $[Eu^{II}(BH4)_2(THF)_2]$[56] with 2 eq. **KCp$^{\#}$PS** in THF followed by crystallization from THF/pentane at -35 °C yielded yellow blocklike crystals suitable for X-ray diffraction analysis, which were found to be the metallocene solvate $[(Cp^{\#}PS)_2Eu(THF)]\cdot THF$ (**4.1S·THF**, Figures 4.3 and 4.4). The lanthanide borohydrides $[Ln^{X}(BH_4)_x(THF)_{2\text{-}4}]$ typically exhibit the useful property of allowing stepwise exchange of their tetrahydroborate ligands, thus serving as a useful platform for the synthesis of heteroleptic complexes.[107] Given this, we were surprised to find that we could not obtain any mono(cyclopentadienyl) products from the equimolar reaction of $[Eu^{II}(BH4)_2(THF)_2]$ and **KCp$^{\#}$PS**. Instead, the metallocene product was always formed, leaving 0.5 eq. of $[Eu^{II}(BH4)_2(THF)_2]$ unreacted.

We discovered that crystals of **4.1S·THF** are extremely easily desolvated, quickly collapsing to a bright orange powder when not protected by their mother liquor or immersed in oil. Indeed, treatment of these crystals with an excess of any non-coordinating solvent afforded complete deterioration to give said orange powder, which is well-soluble in aromatic solvents. This behaviour precluded any further characterization of **4.1S·THF**, so this complex will not be discussed further. It is necessary to conduct the metathesis reaction in THF to ensure solubility of both precursors. However, removal of THF upon completion of the reaction and redissolution of the residue in fluorobenzene gives, after a facile workup, the pure, solvent-free homoleptic europocene $[(Cp^{\#}PS)_2Eu]$ (**4.1S**) as an orange powder in good yield. Accordingly, the corresponding solvent-free phosphinoselenoyl and phosphinotelluroyl complexes $[(Cp^{\#}PSe)_2Eu]$ (**4.1Se**) and $[(Cp^{\#}PTe)_2Eu]$ (**4.1Te**) were synthesized in an analogous manner and were obtained as orange powders in good yield. Complexes **4.1Ch** are well-soluble in aromatic solvents and sparingly soluble in alkanes; their alkane solubility decreases on going down the chalcogen group. These complexes were found to be indefinitely stable in the solid state under inert conditions. Notably, solid **4.1Ch** can be handled briefly in air, decomposing over the course of minutes or hours instead of instantaneously. Their resistance towards aerobic decomposition decreases on going down the chalcogen group, as expected.



Metrical Parameter	Value
Avg. Eu-Cp(cent) distance	2.6378(3)
Cp(cent)-Eu-Cp(cent) angle	144.13(1)
Eu-S1 distance	3.0477(9)
Eu-S2 distance	3.1260(9)
S-Eu-S angle	166.76(2)
Torsional twist angle τ	170.3(2)
Avg. P-C(Cp) distance	1.753(2)
Avg. P-S distance	1.977(1)
Avg. P-N distance	1.661(2)
Avg. N-P-N angle	110.7(1)
Planarity at N1	0.238(3)
Planarity at N2	0.157(2)
Planarity at N3	0.190(3)
Planarity at N4	0.086(3)

Figure 4.3. Solid-state structure of **4.1S·THF**. Thermal ellipsoids are shown at 50% probability. For clarity, only one component of the disorder is shown; hydrogen atoms and THF of solvation are omitted. Selected metrical parameters are also given in the appended table (right). Distances are given in Å and angles are given in degrees. Twist angle τ is the torsion angle C-Cp(cent)-Cp(cent)-C between the cyclopentadienyl carbon atoms directly bound to the P atoms of the phosphinothioyl moiety and the corresponding cyclopentadienyl centroids.[289] The value obtained for this complex corresponds to an antiperiplanar staggered geometry. N planarity is defined as the distance between the nitrogen atom and the plane defined by the phosphorus atom and the two methyl carbon atoms on N.[293] This complex contains one planarized and three pyramidal dimethylamino substituents.

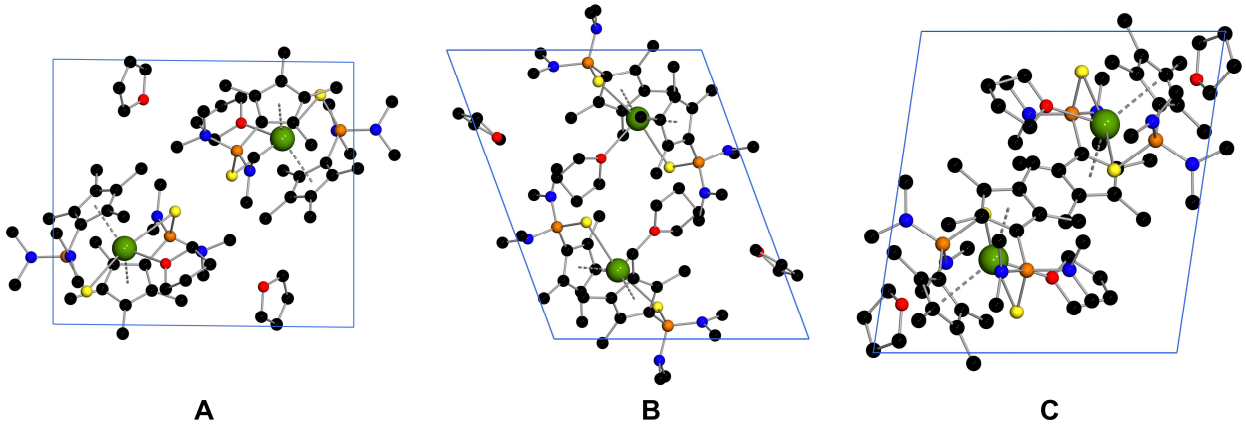


Figure 4.4. Crystallographic packing diagrams of **4.1S·THF**, shown along the a) *a*-axis, b) *b*-axis, and c) *c*-axis of the unit cell. For clarity, only one component of the disorder is shown, and hydrogen atoms are omitted.

4.6 Structural analysis

The ease with which **4.1S·THF** is desolvated was surprising to us, given that removal of coordinated THF from highly oxophilic lanthanide ions, where possible at all, typically requires forcing conditions.[322] Such behaviour is uncommon but not unprecedented, having been observed in e.g. the bulky thiophenolate $Eu^{II}(SAr^{*})_2$ (Ar* = 2,6-bis(2,4,6-triisopropylphenyl)phenyl)),[323] the samarocenes $(COT)Sm^{III}(C_5R^1{}_4PR^2{}_2)(THF)_n$ (COT = cyclooctatetraenyl dianion, R^1 = H or Me, R^2 = Me or Ph, n = 1 or 4),[324] and other "CGC-type" complexes of cyclopentadienylideneaminophosphoranes.[298,325] Clearly, the stereoelectronic characteristics of $(Cp^{\#}PCh)^-$ reduce the affinity of its metallocene complexes to bind solvent ligands, thereby avoiding the often undesirable "permanent coordination" of e.g. THF to lanthanide centers. This is a valuable characteristic, demonstrated even for a relatively large ion like Eu^{II} which would normally demand a high coordination number. The solvent-free europocenes **4.1Ch** can each be recrystallized from fluorobenzene or fluorobenzene/pentane to furnish orange blocklike crystals suitable for X-ray diffraction analysis, and their solid-state structures are shown in Figure 4.5.

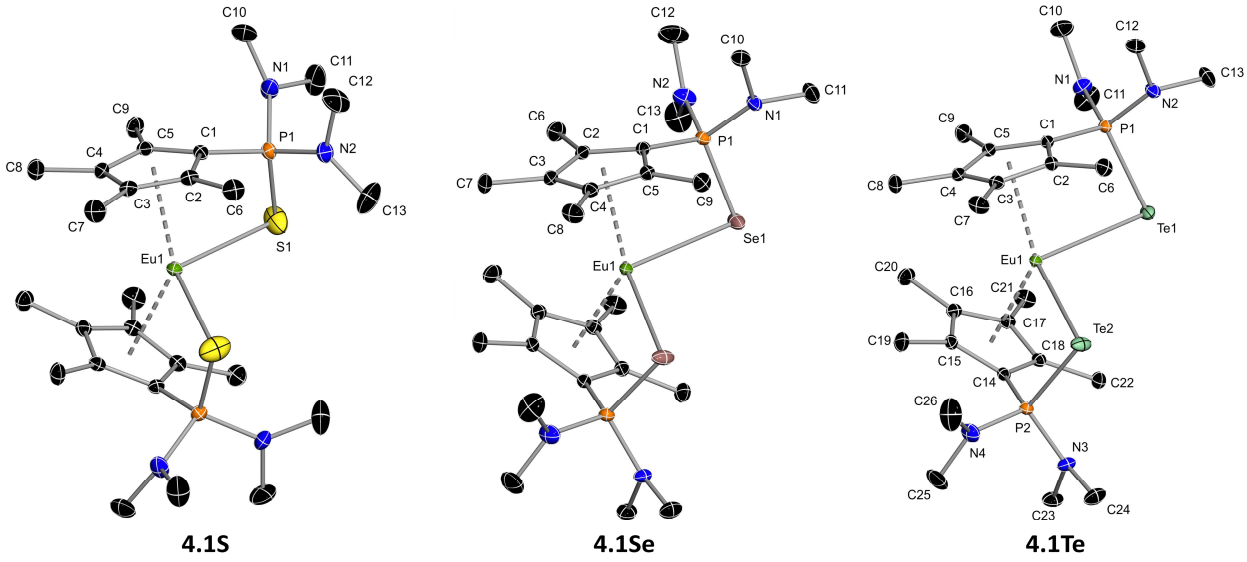


Figure 4.5. Solid-state structures of Eu^{II} complexes **4.1Ch**. Labels are given only to crystallographically unique atoms. Thermal ellipsoids are shown at 50% probability; hydrogen atoms are omitted for clarity. Packing diagrams are given in Figures C2-4.

These complexes are isomorphous in terms of molecular geometry but differ in their crystalline arrangement. Each complex demonstrates a typical bent-metallocene coordination environment courtesy of the two η^5-cyclopentadienyl moieties, and the two chalcogen atoms from the pendant phosphinochalcogenoyl substituents complete the coordination sphere of Eu. The complexes are helically chiral as a result of the coordination of the phosphinochalcogenoyl arms,[325,326] but crystallize as racemates in non-Sohncke space groups in all cases. These structural features are reminiscent of the remarkable ytterbocene $[(Ph_2P(C_5Me_4)NAd)_2Yb^{II}]$ reported by Petrov et al.[325] **4.1S** crystallizes in the orthorhombic space group Pbcn, with one half-molecule in the asymmetric unit. **4.1Te** also crystallizes in an orthorhombic space group ($Pna2_1$), but with one complete molecule in the asymmetric unit. Meanwhile, **4.1Se** instead crystallizes in the monoclinic space group P2/c, with two halves of two different molecules (one of each enantiomer) composing the asymmetric unit (see Figure C5 and Table C1).

Although we were unsuccessful in obtaining X-ray quality crystals of any of the ligand precursors **KCp$^{\#}$PCh**, it is important to note that the infrared spectra of the precursors are extremely similar to their corresponding complexes **4.1Ch** (Figures C8-10). Only small shifts in vibrational frequencies are observed, which are ascribable simply to coordination to Eu^{II}. This implies that the solid-state structures of **KCp$^{\#}$PCh** probably also contain metallocene-like motifs.[327] To corroborate this, the vibrational frequencies of **KCp$^{\#}$PCh** formulated as "half-metallocene" fragments resembling the asymmetric unit of **4.1S** (Figure C11) were calculated via DFT at the CAM-B3LYP[328]/def2-TZVPD[329,330] level. The calculated frequencies were scaled using a single linear scaling equation[331] (see Section 4.9), ultimately giving calculated infrared spectra that agree well with the experimental spectra (Figures 4.6-4.8). From this analysis, we can observe that the vibrational modes most affected by coordination to Eu are those dominated by motions of the -$(NMe_2)_2$PCh substituent. These results uphold that the most likely solid-state structure of each **KCp$^{\#}$PCh** consists of chains of potassium cations sandwiched between $(Cp^{\#}PCh)^-$ anions, which also explains the similarity in the infrared spectra between **KCp$^{\#}$PCh** and their corresponding Eu^{II} complexes **1-Ch**.

Selected metrical parameters of all **4.1Ch** are shown in Table 4.1. The Eu-Cp(cent) distances are, overall, average among related europocenes,[i] and become progressively slightly elongated on going down the chalcogen group. The Cp(cent)-Eu-Cp(cent) angles are also average among bent europocenes[ii] and show no correlation with the identity of the chalcogen. However, **4.1S** is distinctly less bent than its heavier congeners, which is probably due to decreased steric demand from the comparatively smaller sulfur atoms. Similarly, our europocenes are considerably less bent than $[(Ph_2P(C_5Me_4)NAd)_2Yb^{II}]$ (Cp(cent)-Yb-Cp(cent) angle 132.6(1)°)[325] which bears bulkier ligands.

Table 4.1. Selected metrical parameters of **4.1Ch**. Distances are given in Å and angles are given in degrees.

	4.1S	**4.1Se**[a]	**4.1Te**
Eu-Cp(cent) distance	2.5337(1)	2.5379(1)	2.5492(4)[b]
Cp(cent)-Eu-Cp(cent) angle	143.749(1)	137.728(2)	138.83(2)
Eu-Ch distance	2.951(1)	3.0816(4)	3.2760(5)[b]
Ch-Eu-Ch angle	111.09(3)	109.91(1)	108.30(1)
Torsional twist angle τ[c]	85.3(2)	118.8(1)	116.2(1)
P-C(Cp) distance	1.755(3)	1.764(2)	1.763(2)[b]
P-Ch distance	1.997(1)	2.1540(6)	2.3967(6)[b]
Avg. P-N distance	1.654(4)	1.656(2)	1.662(2)[b]
N-P-N angle	109.9(2)	108.14(8)	109.3(1)
Planarity at N[d]	0.192(4)	0.217(2)	0.060(2)
	0.044(4)	0.003(2)	0.269(2)
			0.244(2)
			0.020(2)

[a] The two half-molecules in the asymmetric unit differ slightly in their metrical parameters but are similar (Figure C5), so one molecule is taken as representative. The difference between values is not crystallographically significant (Table C1), so this value is given as the average. [b] The asymmetric unit of this structure contains one complete molecule with two slightly different distances (or four, in the case of the P-N distance), so this value is given as the average. [c] Torsion angle C-Cp(cent)-Cp(cent)-C between the cyclopentadienyl carbon atoms directly bound to the P atoms of the phosphinochalcogenoyl moiety and the corresponding cyclopentadienyl centroids.[289] [d] The distance between the nitrogen atom and the plane defined by the phosphorus atom and the two methyl carbon atoms on N.[293] Listed in order of atom labeling, i.e. P1-N1, P1-N2, etc.

With reference to the phosphinochalcogenoyl substituents and torsional angle τ,[289,326] complex **4.1S** adopts a synclinal eclipsed conformation of the cyclopentadienyl rings, whereas complexes **4.1Se** and **4.1Te** adopt

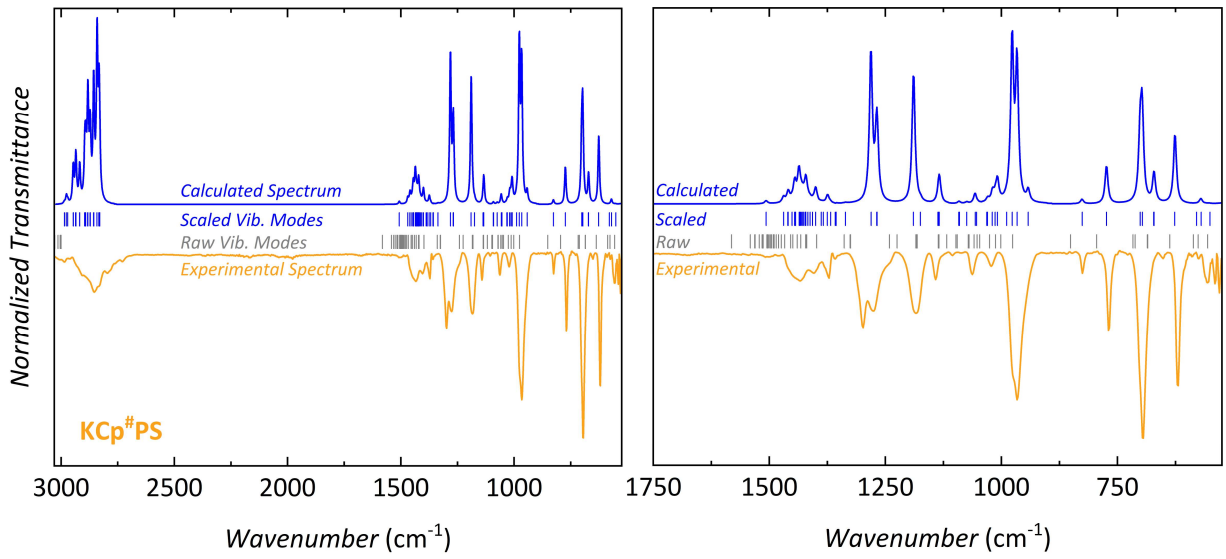


Figure 4.6. Experimental infrared spectrum of **KCp#PS** (yellow curve) compared to the corresponding simulated spectrum (obtained from vibrational frequencies calculated via DFT at the CAM-B3LYP/def2-TZVPD level) (blue curve). The raw (grey ticks) and scaled (blue ticks) vibrational frequencies are also shown. The simulated spectrum was obtained by applying a 4 cm^{-1} Gaussian broadening to the calculated vibrational frequencies. *Left:* full spectra. *Right:* closeup of the fingerprint region (525–1750 cm^{-1}).

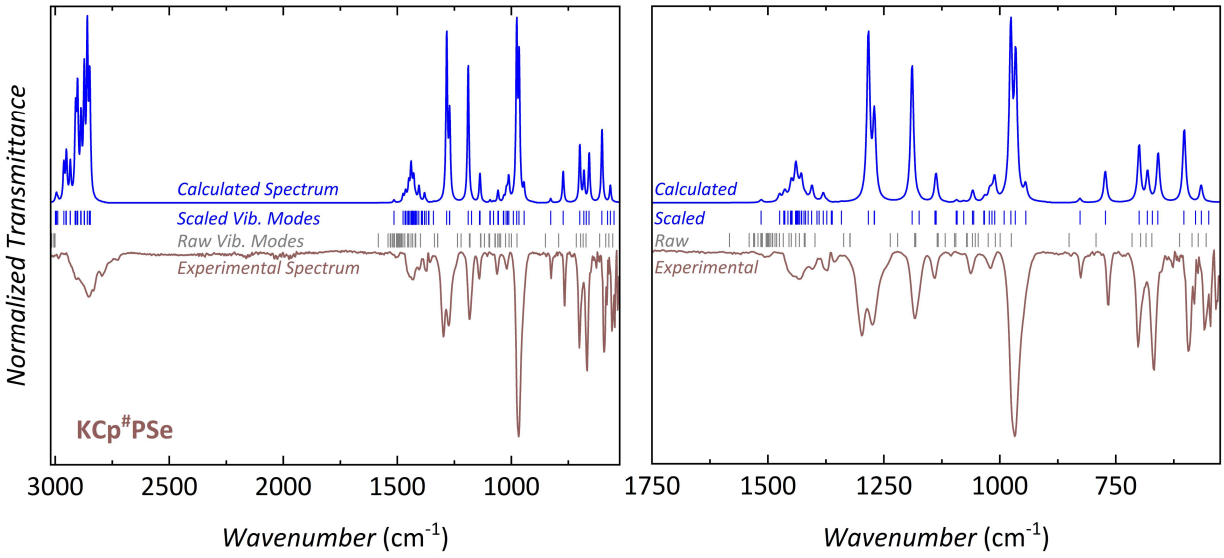


Figure 4.7. Experimental infrared spectrum of **KCp#PSe** (brown curve) compared to the corresponding simulated spectrum (obtained from vibrational frequencies calculated via DFT at the CAM-B3LYP/def2-TZVPD level) (blue curve). The raw (grey ticks) and scaled (blue ticks) vibrational frequencies are also shown. The simulated spectrum was obtained by applying a 4 cm^{-1} Gaussian broadening to the calculated vibrational frequencies. *Left:* full spectra. *Right:* closeup of the fingerprint region (525–1750 cm^{-1}).

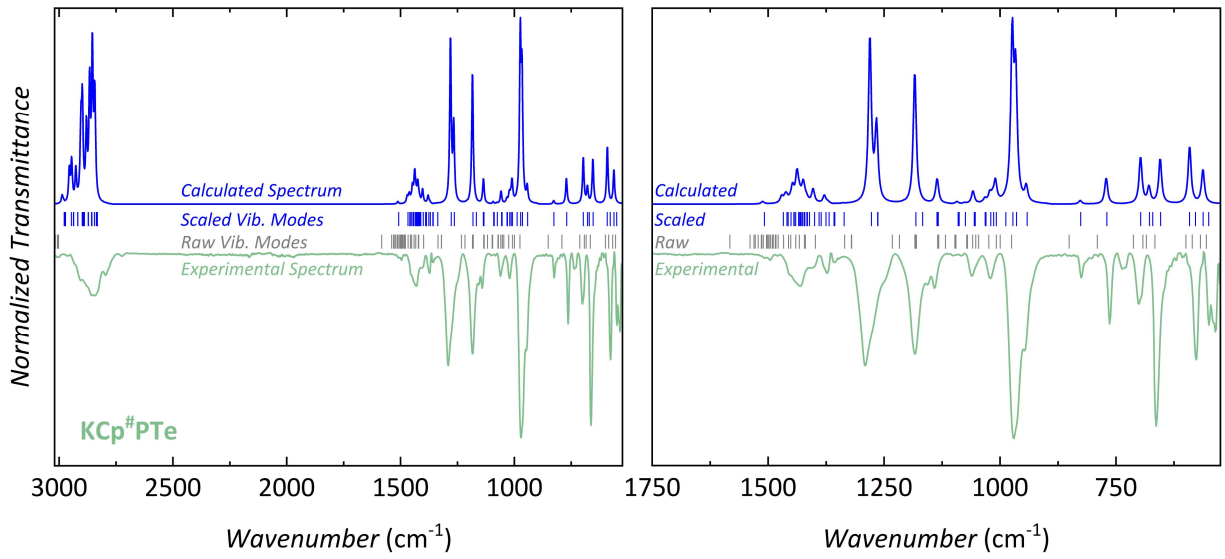


Figure 4.8. Experimental infrared spectrum of **KCp#PTe** (green curve) compared to the corresponding simulated spectrum (obtained from vibrational frequencies calculated via DFT at the CAM-B3LYP/def2-TZVPD level) (blue curve). The raw (grey ticks) and scaled (blue ticks) vibrational frequencies are also shown. The simulated spectrum was obtained by applying a 4 cm^{-1} Gaussian broadening to the calculated vibrational frequencies. *Left:* full spectra. *Right:* closeup of the fingerprint region (525–1750 cm^{-1}).

anticlinal staggered conformations instead (Figure 4.9), which is likely due again to reasons of steric demand.

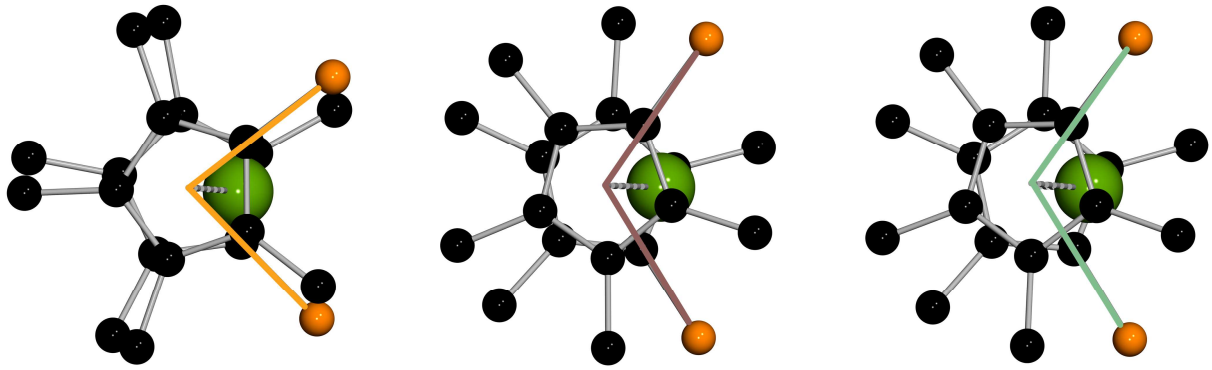


Figure 4.9. Top-down view of truncated structures of **4.1S** (left), **4.1Se** (middle) and **4.1Te** (right) highlighting the torsional angle τ that defines the metallocene conformation. Hydrogen and chalcogen atoms as well as dimethylamino substituents have been omitted. Black = C, orange = P, green = Eu.

The Eu-Ch distances in **4.1Ch** are in all cases shorter than the corresponding sum of covalent radii and are average among corresponding Eu^{II}-Ch bonds.[iii] Especially for **4.1Se**, it is interesting to note that the P-Se distance is similar to the average Eu-alkene(cent) distance in the structurally related tethered olefin complex

$[(C_5Me_4)SiMe_2(CH_2CH{=}CH_2)]_2Eu^{II}]$ (3.09 Å).[332] Due to coordination to Eu, the P-Ch distances in **4.1Ch** are between that of a typical (alkylamino)phosphine chalcogenide that features some P-Ch multiple bond character (S 1.95 Å,[iv] Se 2.11 Å,[v] Te 2.36 Å[vi]) and that of a typical P-Ch single bond (S 2.08 Å,[vii] Se 2.22 Å,[viii] Te 2.50 Å[ix]). The P-S distance in **4.1S** is noticeably longer than the average P-S distance in the dithioimidodiphosphinate $[Eu^{II}\{(NSPPh_2)_2\}_2(THF)_2]$ (1.96 Å)[211] and is more akin to those found in the phosphinodithioate $[Eu^{II}(Ph_2PS_2)_2(DME)_2]$ (2.00 Å)[333] or the phosphoranylidene $[(Eu^{II}\{CH(iPr_2P{-}S)(C_9H_6N\text{-}2)\}_2)_2]$ (2.01 Å).[334] Meanwhile, the P-Se distance in **4.1Se** is similar to the average P-Se distance in the diselenoimidodiphosphinate $[Eu^{II}\{(NSePPh_2)_2\}_2(THF)_2]$ (2.16 Å),[211] and the phosphinodiselenoate $[Eu^{II}(Ph_2PSe_2)_2(DME)_2]$ (2.14 Å)[333] as well as to the CGC-type zirconocene $(\eta^7\text{-}C_7H_7)Zr^{IV}(iPr_2PSe(C_5H_4))$ (2.15 Å)[281] which bears a similar coordinated phosphine selenide arm. We were unable to find any other crystallographically-characterized P-Te-Eu fragments with which to compare **4.1Te**, but the P-Te distance in this complex is slightly shorter than average for metal-bound P-Te motifs.[x] In all cases, each phosphinochalcogenoyl moiety of **4.1Ch** contains one planarized and one pyramidal dimethylamino substituent,[315] as observed previously in (dialkylaminophosphino)ferrocene chalcogenides.[293] The P-N distances are within the expected range for aminophosphines,[315] and the P-C(Cp) distance is ~1.76 Å in all cases; both metrics are average for a (diaminophosphinochalcogenoyl)cyclopentadienyl motif.[xi]

4.7 Photoluminescence spectroscopy and luminescence thermometry

Initially, we were disappointed to observe that crystals of **4.1S·THF** exhibited only weak yellow-green luminescence, whose intensity and emission colour were, qualitatively, minimally affected by temperature. However, no spectroscopic characterization of this complex was possible due to its instability toward desolvation. On the other hand, the solvent-free **4.1S** exhibited qualitatively much more intense red-orange emission, which became red upon cooling to 77 K. It therefore appears that coordination of THF to the Eu^{II} center in this complex has a deleterious effect on its emission characteristics. This is in direct contrast to the behaviour of our previously reported thermochromic emitter $[Cp^*Eu(BH_4)(THF)_2]_2$,[224] which loses its interesting properties upon loss of its THF ligands.

The intense and visibly thermochromic emission of **4.1S** prompted us to investigate its temperature-dependent emission in the solid state, to evaluate its performance for band-shift luminescence thermometry. Excitation and emission spectra obtained at 10 K are shown in Figure 4.10. The excitation spectrum shows the expected bands from the Eu^{II} *5d* state in conjunction with ligand-based states over the UV and blue spectral region, and excitation at 395 nm results in an intense, broad $d{\rightarrow}f$ emission band peaking at 636 nm. Beginning at 70 K, a small blueshift is observed with increasing temperature. The band peak shifts from 15 671 to 16 027 cm^{-1} (ΔE = 356 cm^{-1}) over this temperature range, corroborating the observed colour change from red-orange to red (Figure 4.11). As previously described, the temperature-dependence of the maximum band energy can be fitted using a Boltzmann function, and the absolute sensitivity S_a can be obtained via the first derivative of the fitted function (Figure 4.12).[224] Unfortunately, the performance of **4.1S** as a luminescence thermometer is greatly diminished relative to our previously-reported thermochromic emitters $[(C_5Me_4R)Eu^{II}(BH_4)(solv)_n]_2$,[270] exhibiting a small ΔE and maximum S_a of only 1.5 cm^{-1} K^{-1} at 330 K.

The phosphinoselenoyl analogue **4.1Se** shows dramatically different luminescence properties. While no visible emission is observed at room temperature, the complex begins to emit bright red upon cooling to 77 K. At 10 K in the solid state, the excitation spectrum of **4.1Se** shows analogous features to that of **4.1S**, and the corresponding $d{\rightarrow}f$ emission is redshifted *cf.* **4.1S** to 650 nm (Figure 4.13). Unexpectedly, **4.1Se** is not thermochromic. We observe no band-shift in the temperature-dependent emission spectra of

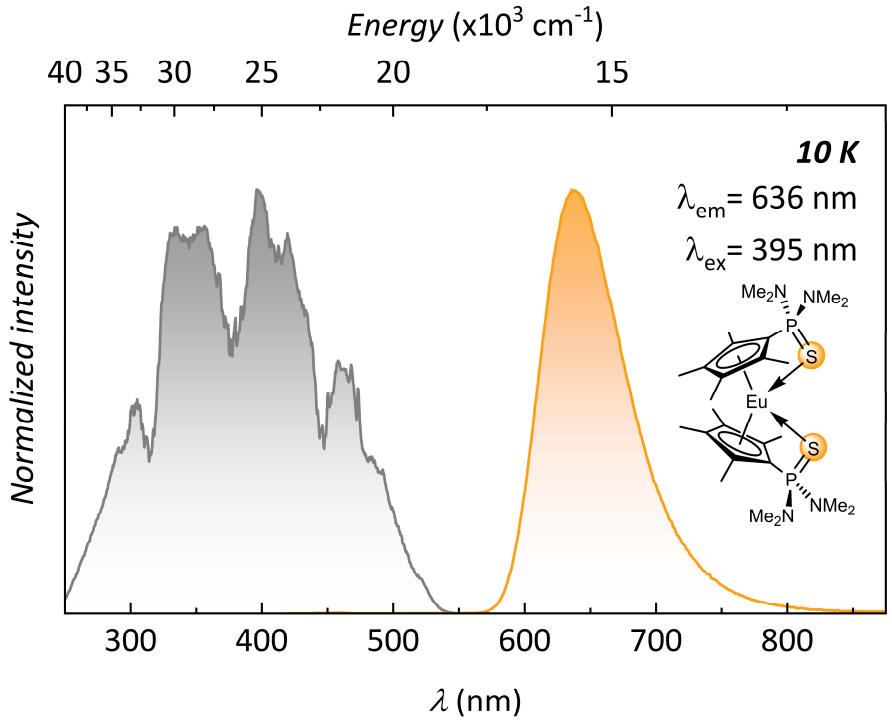


Figure 4.10. Solid-state excitation (grey) and emission (yellow) spectra for **4.1S** obtained at 10 K.

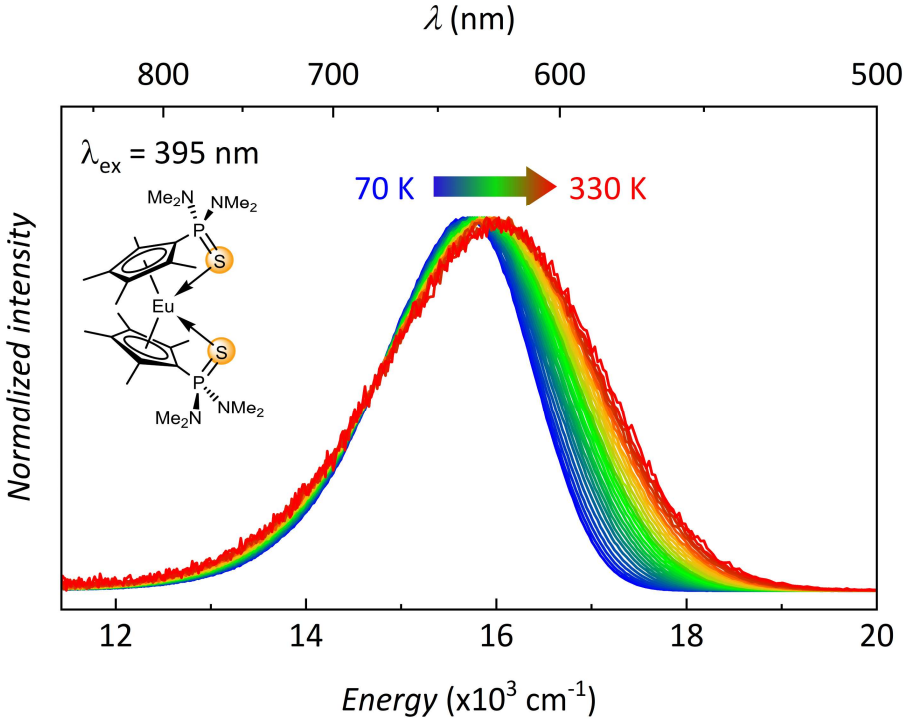


Figure 4.11. Temperature-dependent emission spectra (λ_{ex} = 395 nm) for **4.1S** obtained in the solid state over the 70–330 K range with steps of 10 K.

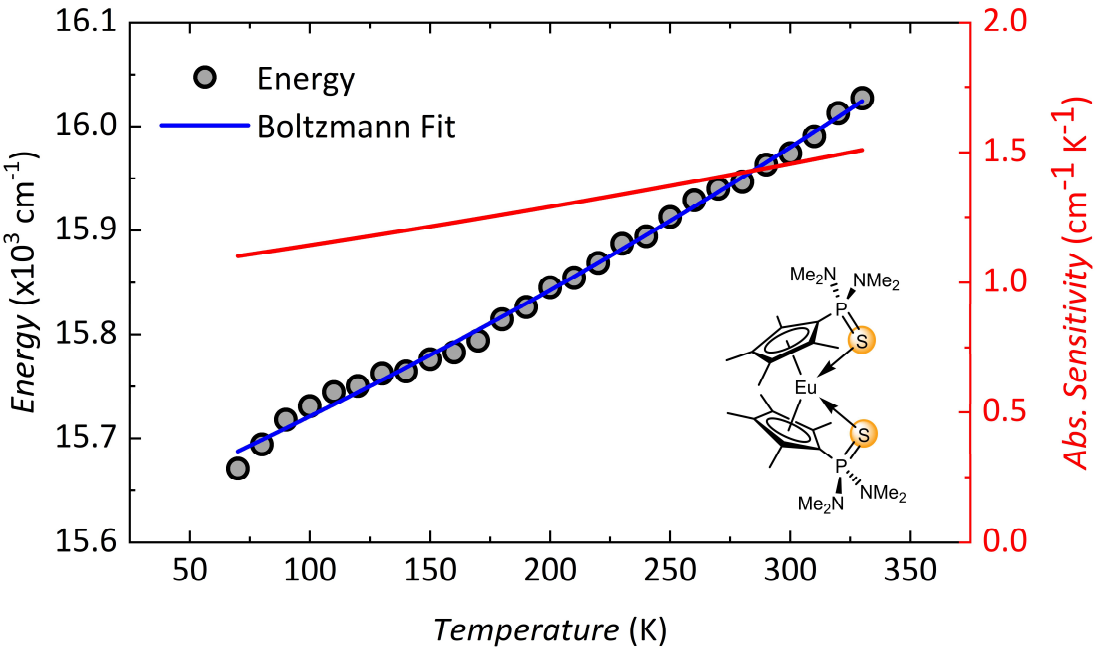


Figure 4.12. Temperature dependence of the energy at the emission band maximum of **4.1S**, extracted from the emission spectra shown in Figure 4.11 (left axis). The blue line represents the Boltzmann function fitted to the experimental data. Best fitting parameters: $A_1 = 14838$, $A_2 = 33468$, $x_0 = 2308$, $R^2 = 0.9954$. Absolute sensitivity obtained as the first derivative of the fitted function (right axis).

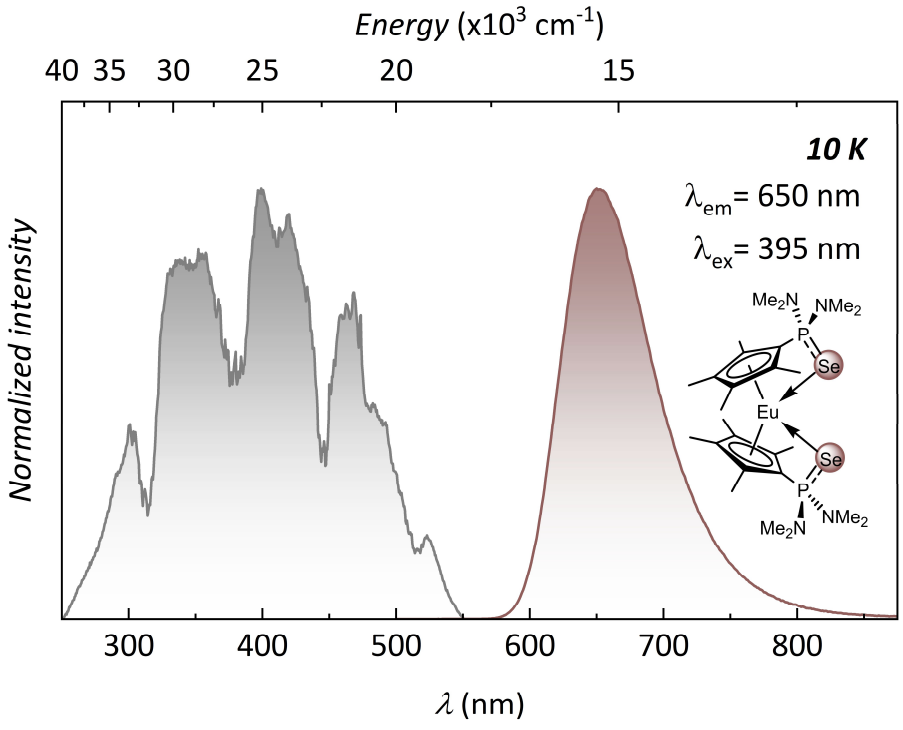


Figure 4.13. Solid-state excitation (grey) and emission (brown) spectra for **4.1Se** obtained at 10 K.

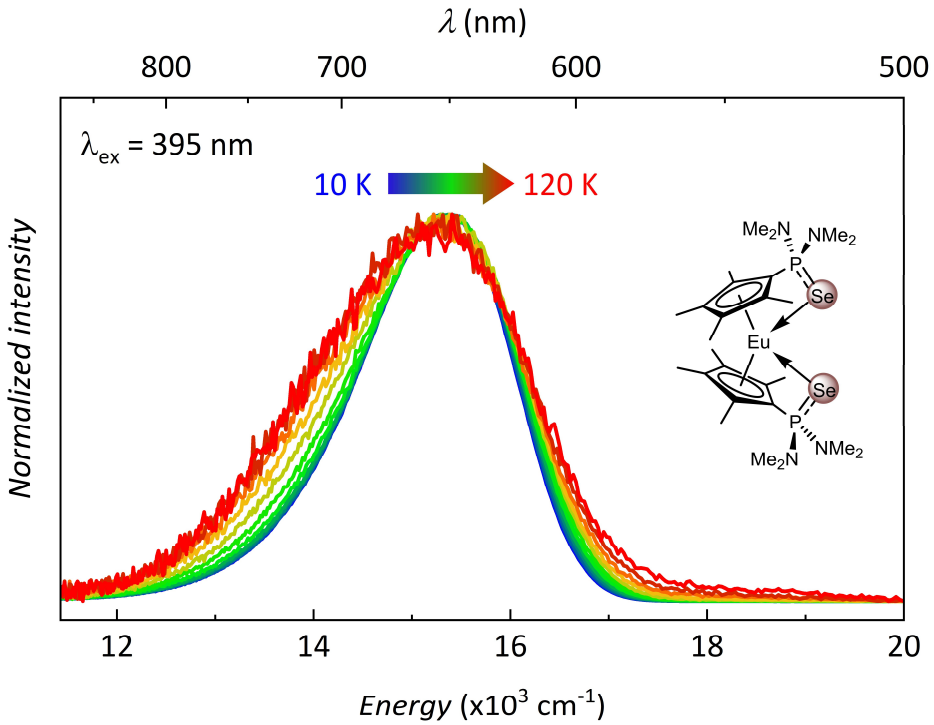


Figure 4.14. Temperature-dependent emission spectra (λ_{ex} = 395 nm) for **4.1Se** obtained in the solid state over the 10–120 K range with steps of 10 K.

4.1Se (Figure 4.14), with the emission band simply broadening and diminishing in intensity with increasing temperature until it is no longer measurable above 120 K. More surprisingly, the tellurium analogue **4.1Te** exhibits no emission whatsoever at any temperature. Given the trend defined by **4.1S** and **4.1Se**, we considered that the emission might be redshifted into the NIR, but no measurable luminescence was observed until 1600 nm.

We ascribe this pattern of luminescence behaviour to an energetic overlap of the n–π* transitions of the phosphine chalcogenide moiety with the metal-centered d-f transitions of Eu^{II}. In the solid-state diffuse reflectance spectra of **4.1S**, a broad peak centered at ~395 nm is observed, which is consistent with the excitation spectrum and is assigned generally to the *f-d* vertical transitions of Eu^{II} (Figure 4.15c). Alongside this, an intense tail extending into the ultraviolet is observed, which is assigned to ligand-based π–π* transitions involving the cyclopentadienyl fragment. In **4.1Se**, a similar broad band consistent with the excitation spectrum and assignable to the metal-centered transitions is observed, but now a partial peak is observed inside the spectral window that can be assigned to the P-Se n–π* transition (Figure 4.15d). The spectrum of **4.1Te** (shown in Figure 4.15a,b) shows a distinct peak at ~300 nm overlapping the high-energy tail, which we ascribe to the P-Te n–π* transition, and the broad band assigned to Eu^{II}-based transitions is slightly redshifted to ~405 nm. These assignments are consistent with the known spectral positions of n–π* transitions in tris(dimethylamino)phosphine chalcogenides[313,315] and the extended conjugation imparted by the appended cyclopentadienide. Therefore, luminescence in **4.1Se** and **4.1Te** might be quenched either by preferential excitation of the P-Ch n–π* transition or by introduction of an additional nonradiative decay pathway via the associated states. To further analyze the quenching pathways operant in these complexes, the temperature-dependence of the photoluminescence intensity was interrogated for **4.1S** and **4.1Se** using the Mott-Seitz model (Eqn. 4.1),

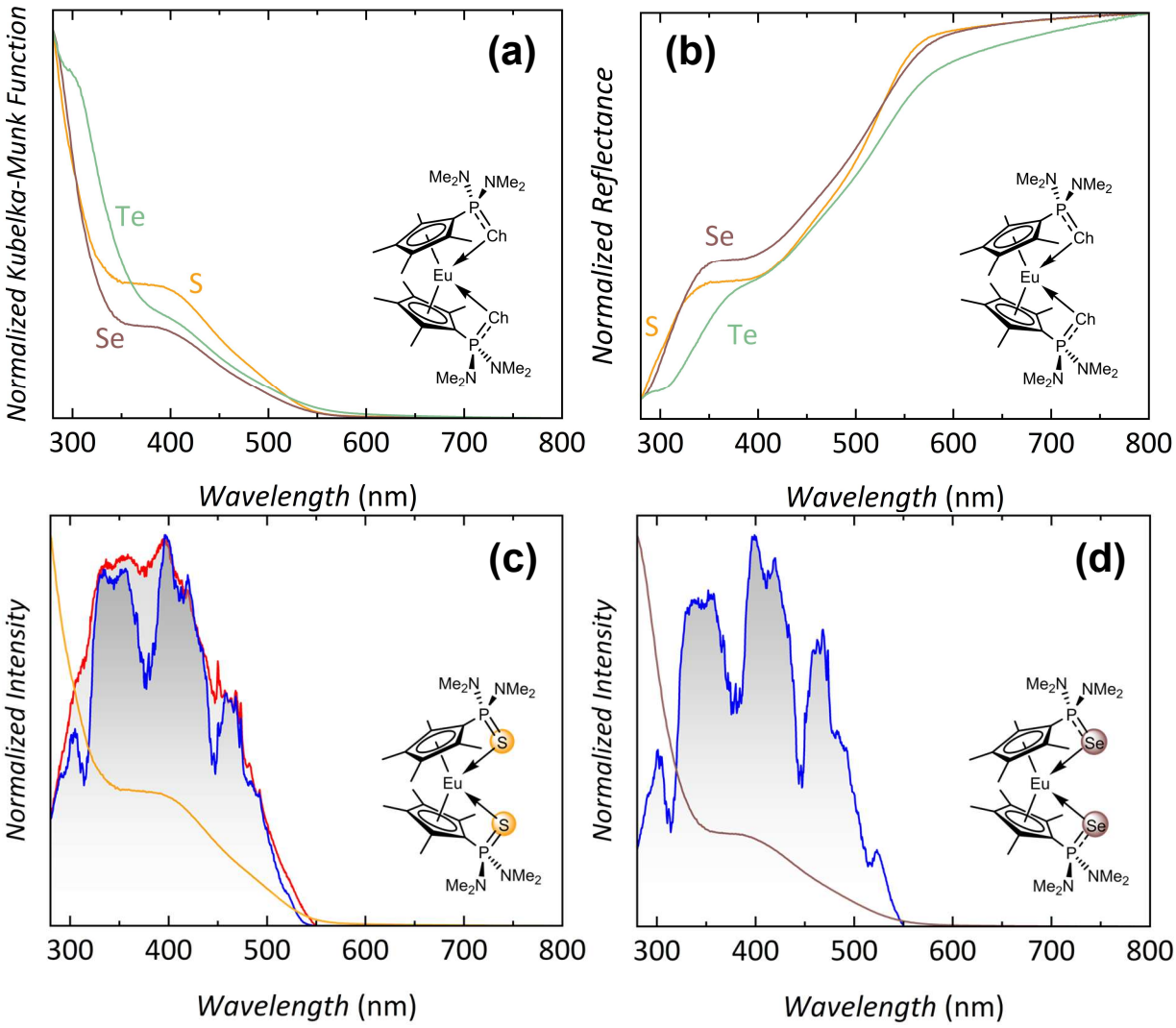


Figure 4.15. Solid-state diffuse reflectance spectra for **4.1Ch** transformed via the Kubelka-Munk function (a) and as raw reflectance (b). Comparison of the Kubelka-Munk-transformed diffuse reflectance spectra for **4.1S** (c) and **4.1Se** (d) (yellow and brown lines, respectively) with their solid-state photoluminescence excitation spectra at 10 K (blue curve) and room temperature, where applicable (red curve).

$$\frac{I}{I_0} = \frac{1}{1+\sum_i A_i e^{\left(-\frac{\Delta E_i}{kT}\right)}} \tag{4.1}$$

where $\frac{I}{I_0}$ is the photoluminescence intensity normalized to the intensity at the lowest measured temperature, A_i is the ratio between the nonradiative and radiative decay rates in the limit of $T \rightarrow 0$ K, and ΔE_i is the energy difference between the emitter level and the quencher level (Figure 4.16).[335] We find a two-component model accurately describes the experimental temperature-dependence of the intensities of both **4.1S** and **4.1Se**, with crossovers occurring at ΔE = 2479 and 202 cm^{-1} for **1-S** and ΔE = 223 and 50 cm^{-1} for 1-**Se**. These results are consistent with an increased density of states in **1-Se**, leading to greater overlap and therefore a stronger quenching pathway, and explaining the dramatic diminution of intensity with increasing temperature. Following this trend and in combination with the behaviour observed in the diffuse reflectance spectra, we hypothesize that the density and overlap of states in **4.1Te** is larger still, resulting in

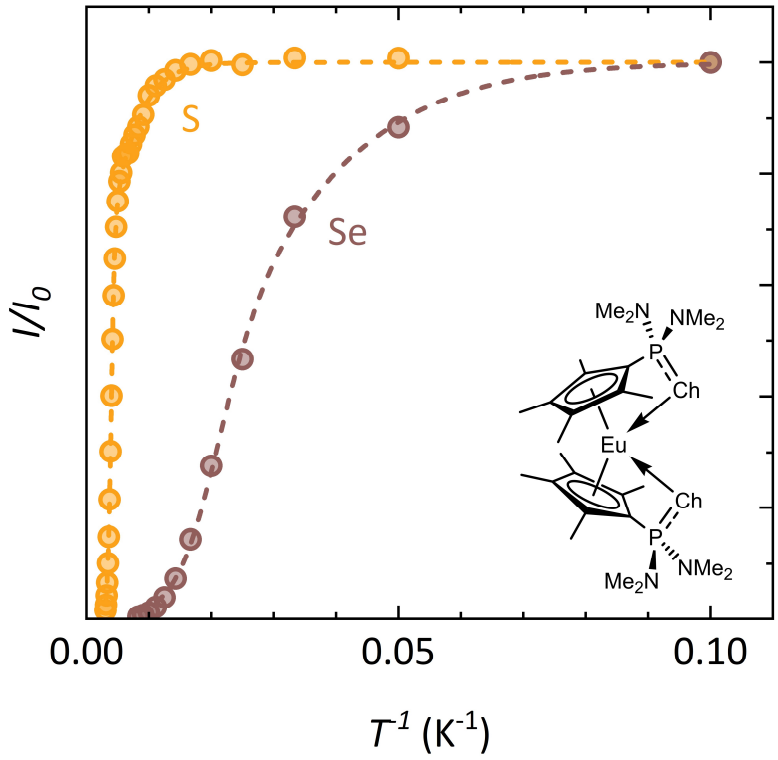


Figure 4.16. Mott-Seitz plots for the relative photoluminescence intensity of **4.1S** (yellow points) and **4.1Se** (brown points). A double-crossover model was employed, and the best-fitting parameters are as follows: for **4.1S**, $A_1 = 1.79\,\text{x}10^6$, $A_2 = 1.29$, $\Delta E_1 = 2479$, $\Delta E_2 = 202$, $R^2 = 0.9993$; for **4.1Se**, $A_1 = 4.13$, $A_2 = 1090$, $\Delta E_1 = 50$, $\Delta E_2 = 223$, $R^2 = 0.9989$.

a complete quenching of the emission even at cryogenic temperatures.

4.7 Magneto-optical properties and MCD thermometry

Despite becoming interested in the temperature-dependent emission properties of **4.1Ch** upon observing intense, visibly thermochromic photoluminescence in the solvent-free **4.1S**, we ultimately determined, as detailed above, that the photoluminescence characteristics of **4.1Ch** are not conducive to their application as luminescence thermometers. However, the strong paramagnetism of Eu^{II} opens another avenue for applications of these complexes based on their optical properties. Namely, such systems are excellent candidates as probes for MCD thermometry, a magneto-optical thermometry technique recently introduced by our group.[336] MCD spectroscopy[337] measures the differential absorption (ΔA) of left and right circularly polarized components of light (lcp and rcp, respectively), induced by a magnetic field oriented parallel (positive H) or antiparallel (negative H) to the direction of the light propagation. The ΔA signal results from the magnetic perturbation of the states involved in the optical transitions due to the Zeeman effect. Magneto-optical thermometers have the potential to show greatly improved relative sensitivity (S_r) compared to typical luminescence thermometers, since the technique relies on the presence of a highly temperature-dependent C-term in the MCD spectra of paramagnetic species at low temperature.[337,338] This behaviour enables magneto-optical thermometers to operate at cryogenic temperatures, complementing conventional luminescence thermometers[91] that tend to be poorly sensitive in this important temperature range for quantum technologies, spintronics, and superconductors. Hence, we aimed to study the variable-

temperature and variable-field MCD (VTVH-MCD) spectra of **4.1Ch** in the solid state to evaluate their performance in this area.

Firstly, the bulk magnetic properties of **4.1Ch** were probed via direct current (DC) SQUID magnetometry. The DC magnetic susceptibility χ of each complex **4.1Ch** was measured at 1000 Oe between 300 and 1.9 K (Figure 4.17), and the room-temperature χT products (**4.1S** 7.88, **4.1Se** 7.84, **4.1Te** 7.83 cm^3 K mol^{-1}) agree well with the theoretical value of 7.88 cm^3 K mol^{-1} for an isolated Eu^{II} ion ($^8S_{7/2}$, $S = 7/2$, $g_J = 1.997 \cong 2$). The χT product of **4.1S** remains expectedly nearly constant over the measured temperature range, while the χT products of **4.1Se** and **4.1Te** decrease gently with decreasing temperature, with the latter decreasing more quickly than the former.

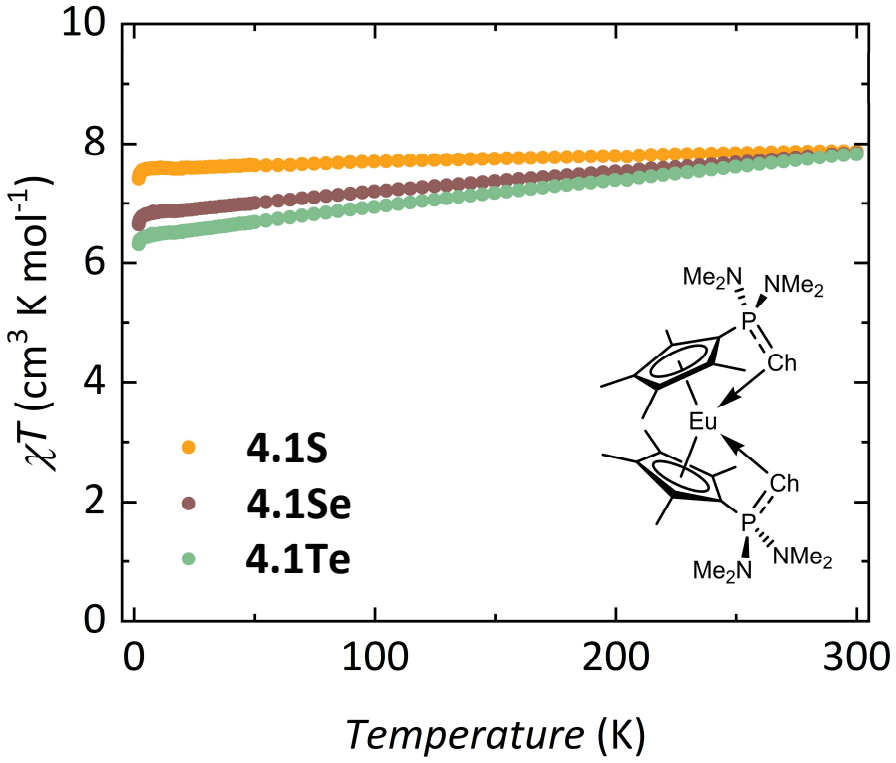


Figure 4.17. Temperature dependence of the χT product at 1000 Oe for complexes **4.1Ch**, with χ representing the molar magnetic susceptibility per molecule defined as *M*/*H*.

The isothermal magnetization shows typical field-dependence in all cases (Figure 4.18a,b,c). Molecular divalent europium systems tend to exhibit $4f^7$, $^8S_{7/2}$ ground states consisting of four Kramers doublets separated by a zero-field splitting of up to a few wavenumbers.[224,277,339] There is a slight downturn in the χT products of all **4.1Ch** at very low temperatures and a slight nesting of reduced magnetization isotherms (Figure 4.18d,e,f), which are consistent with this model. The saturation magnetization for **4.1S** (6.84 Nβ) at 1.9 K and 7.0 T is close to the expected value (7 Nβ). However, in conjunction with the behaviour of the χT product, the saturation values for **4.1Se** (6.16 Nβ) and **4.1Te** (5.81 Nβ) under the same conditions are lower than expected. The polarizability of the chalcogens increases on going down the group, as does the polarization of the P-Ch bonds,[340] placing progressively greater electron density at the metal-bound chalcogen atoms of **4.1Ch**. Thus, we attribute the somewhat unusual magnetic behaviour observed in **4.1Se** and **4.1Te** to an increased nephelauxetic effect in these heavier chalcogen analogues.[66,277,341]

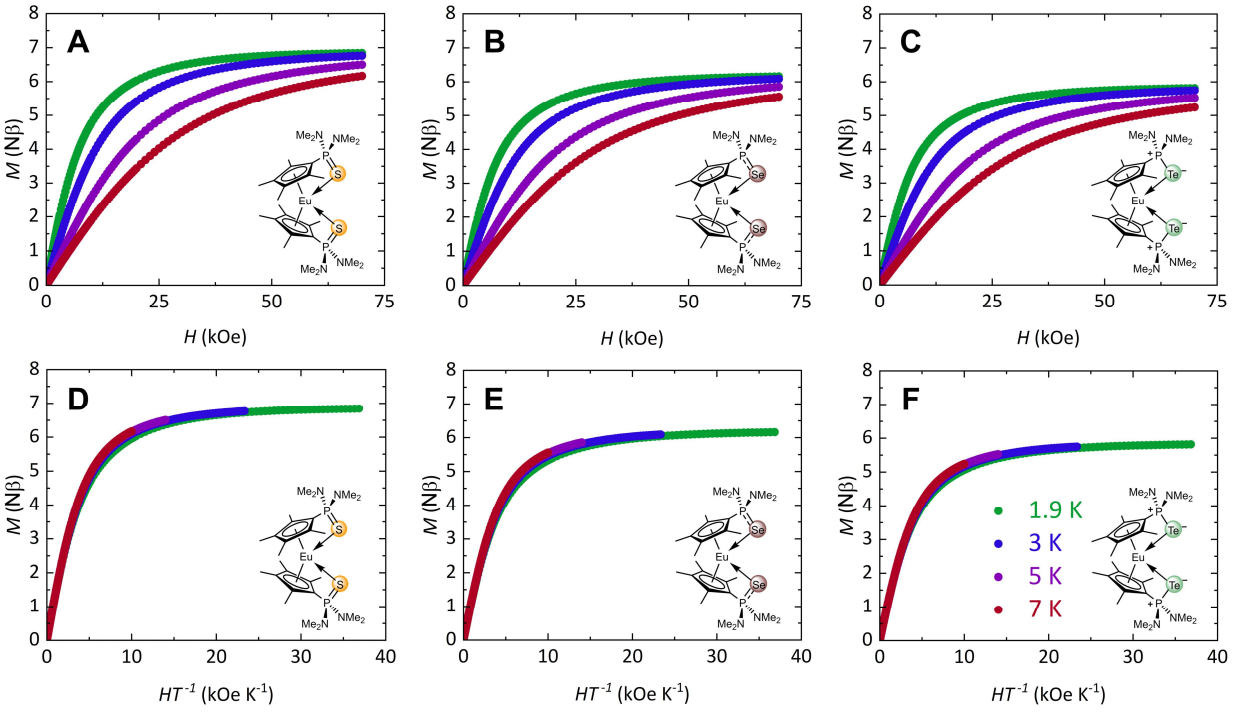


Figure 4.18. Isothermal field-dependence of the magnetization for **4.1S** (a), **4.1Se** (b), and **4.1Te** (c), and reduced magnetization for **4.1S** (d), **4.1Se** (e), and **4.1Te** (f) at the indicated temperatures.

Next, we recorded the VH-MCD spectra of these complexes, which are shown in Figures 4.19-4.21. Following the trend observed from the DC magnetometry data, the MCD intensity of **4.1Ch** is strong for **4.1S** and weakens on going down the chalcogen group. Six distinguishable components are selected for analysis in all cases, arranged into two positive (lcp-absorption dominated) and two negative (rcp-absorption dominated) bands. The components are 310.3, 350.6, 380, 393.4, 439.8, and 498.3 nm for **4.1S**, 281.9, 332, 351.5, 394, 447.3, and 490 nm for **4.1Se**, and 300, 322, 346.1, 408.5, 475.8, and 497.1 nm for **4.1Te**. In all cases, the transitions observed in the MCD spectra of **4.1Ch** correspond with their diffuse reflectance spectra and, where applicable, with their photoluminescence excitation spectra (Figure 4.22). As observed in the diffuse reflectance spectra, transitions occurring below ~315 nm are predominantly ligand-based, whereas those occurring above this wavelength are primarily *f-d* in nature. For **4.1S** and **4.1Se**, the *f-d* transitions giving rise to the greatest emission intensity (especially those around 400 nm) also exhibit the greatest MCD intensity. Transitions at 281.9 nm (**4.1Se**) and 300 nm (**4.1Te**), assigned as putative P-Ch n–π^* transitions (see Section 4.7), are likewise clearly visualized in the MCD spectra. The application of an equivalent antiparallel magnetic field to all complexes results in the expected mirror images.

The magnetic isotropy of the Eu^{II} ion, combined with the low symmetry of the complexes (C_2),[342] the large number of overlapping states, and the known complexity of the energetic landscape of Eu^{II} systems,[186,307] would render disambiguation of the exact nature of each transition infeasible. Hence, we have not attempted a more detailed assignment of the MCD spectra. Nevertheless, a highly detailed assignment of the MCD spectra is not required for application in MCD thermometry, so we proceeded to analyze the

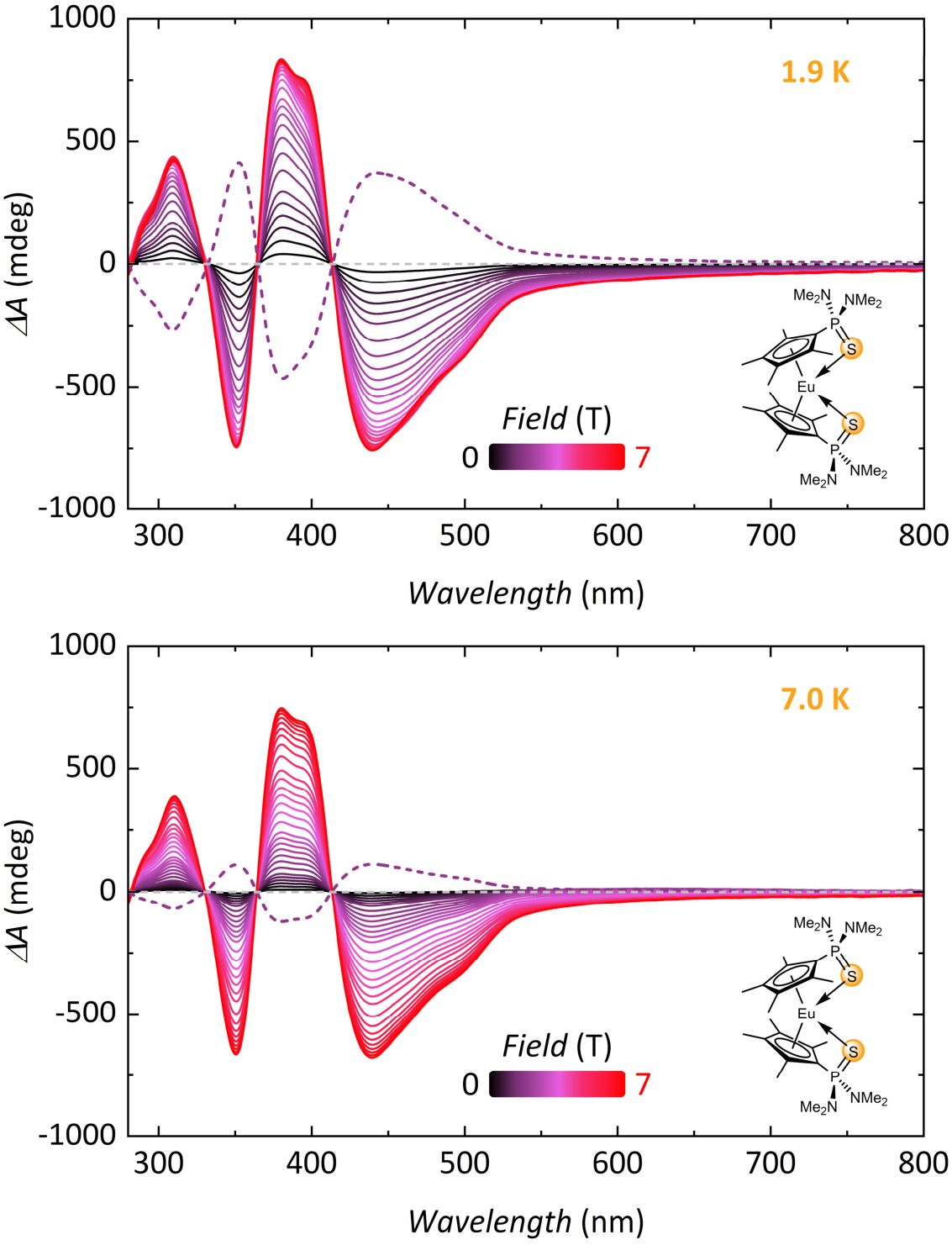


Figure 4.19. Variable-field magnetic circular dichroism (VH-MCD) spectra of **4.1S** at 1.9 K (top) and 7.0 K (bottom) under applied magnetic fields of 0.1 – 7 T. Spectra were collected with the magnetic field oriented parallel to the direction of light propagation ("positive field", solid lines) and a spectrum was also collected with a 1 T magnetic field oriented antiparallel to the direction of light propagation ("negative" 1 T), indicated by the dashed line.

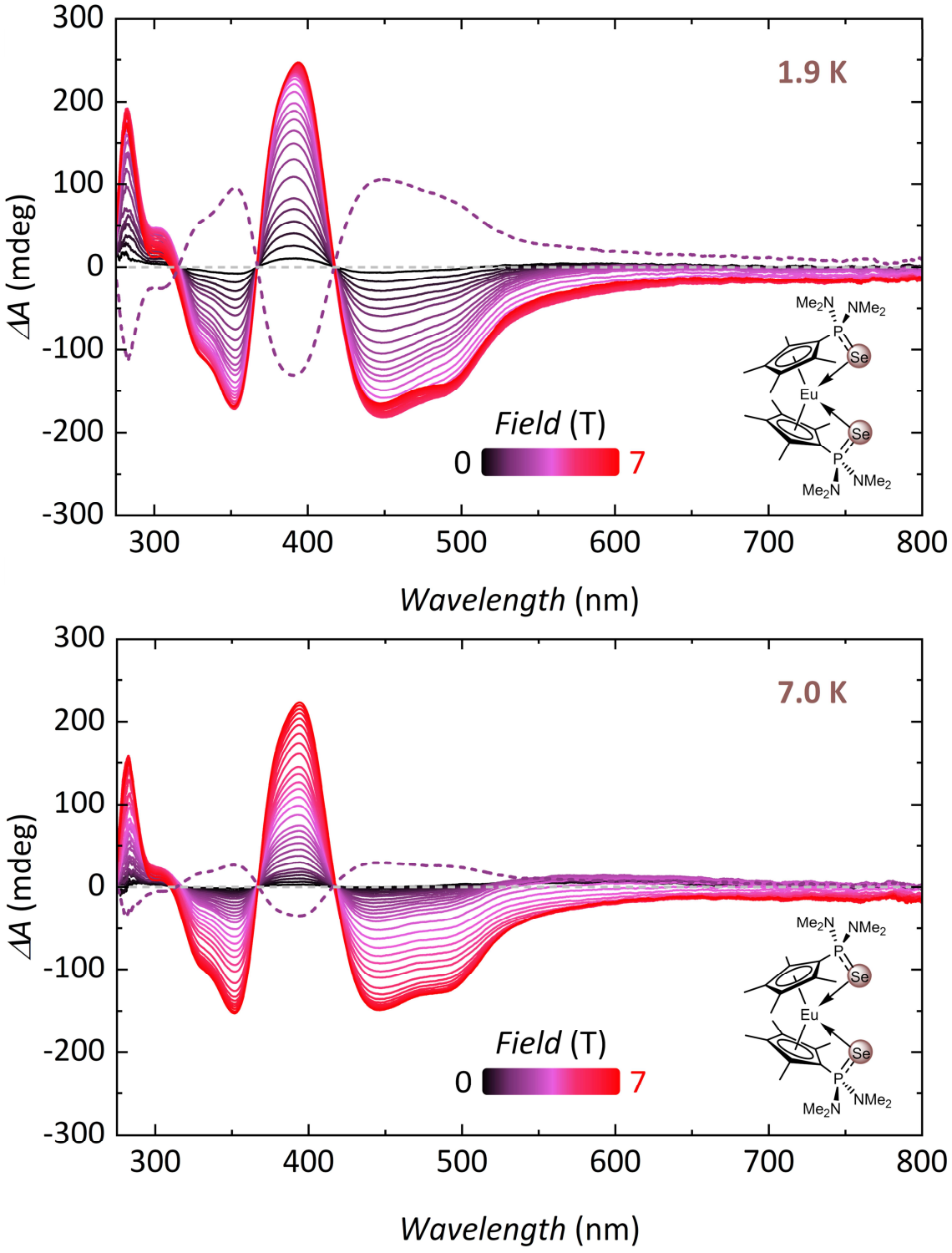


Figure 4.20. Variable-field magnetic circular dichroism (VH-MCD) spectra of **4.1Se** at 1.9 K (top) and 7.0 K (bottom) under applied magnetic fields of 0.1 – 7 T. Spectra were collected with the magnetic field oriented parallel to the direction of light propagation ("positive field", solid lines) and a spectrum was also collected with a 1 T magnetic field oriented antiparallel to the direction of light propagation ("negative" 1 T), indicated by the dashed line.

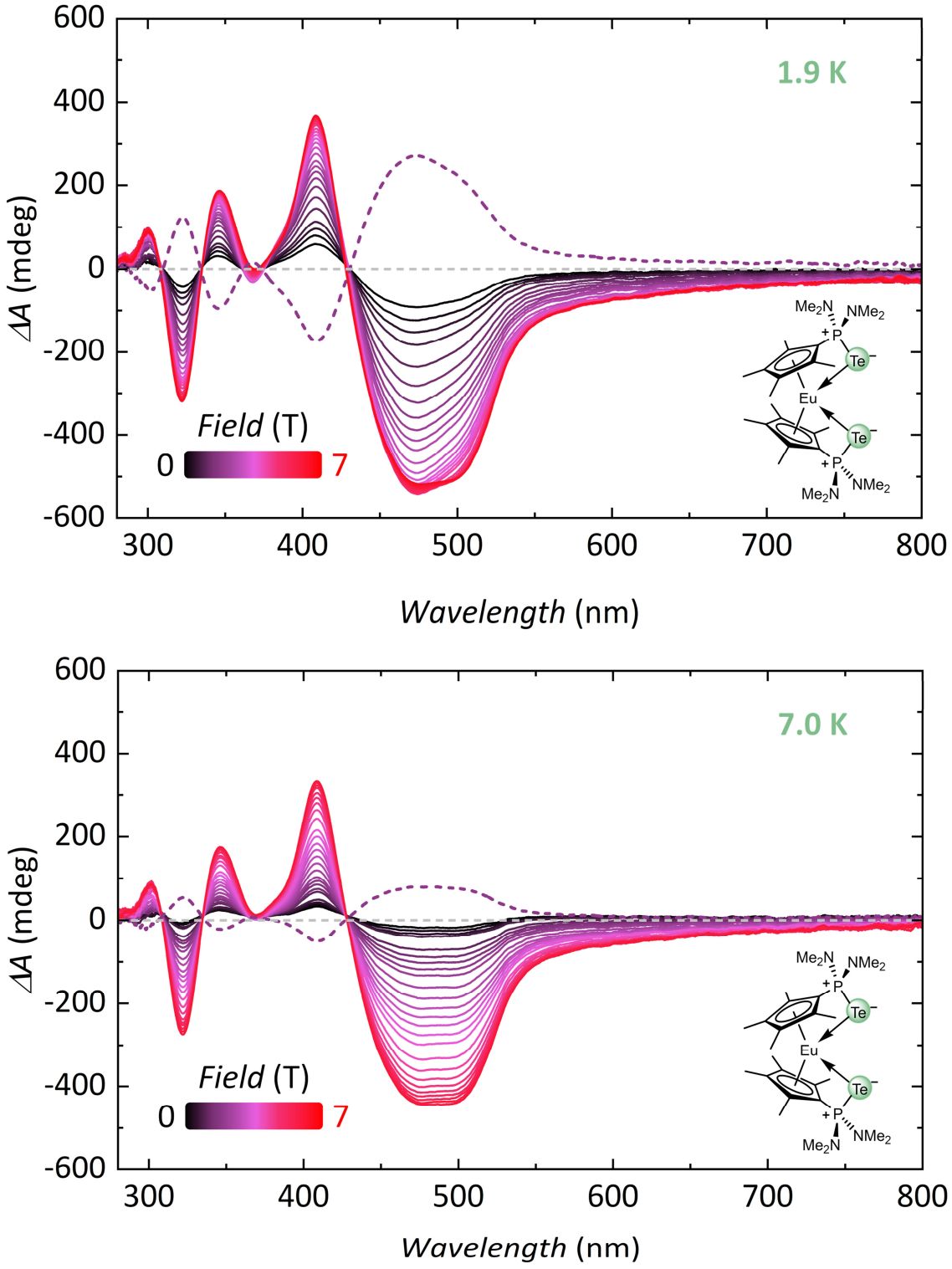


Figure 4.21. Variable-field magnetic circular dichroism (VH-MCD) spectra of **4.1Te** at 1.9 K (top) and 7.0 K (bottom) under applied magnetic fields of 0.1 – 7 T. Spectra were collected with the magnetic field oriented parallel to the direction of light propagation ("positive field", solid lines) and a spectrum was also collected with a 1 T magnetic field oriented antiparallel to the direction of light propagation ("negative" 1 T), indicated by the dashed line.

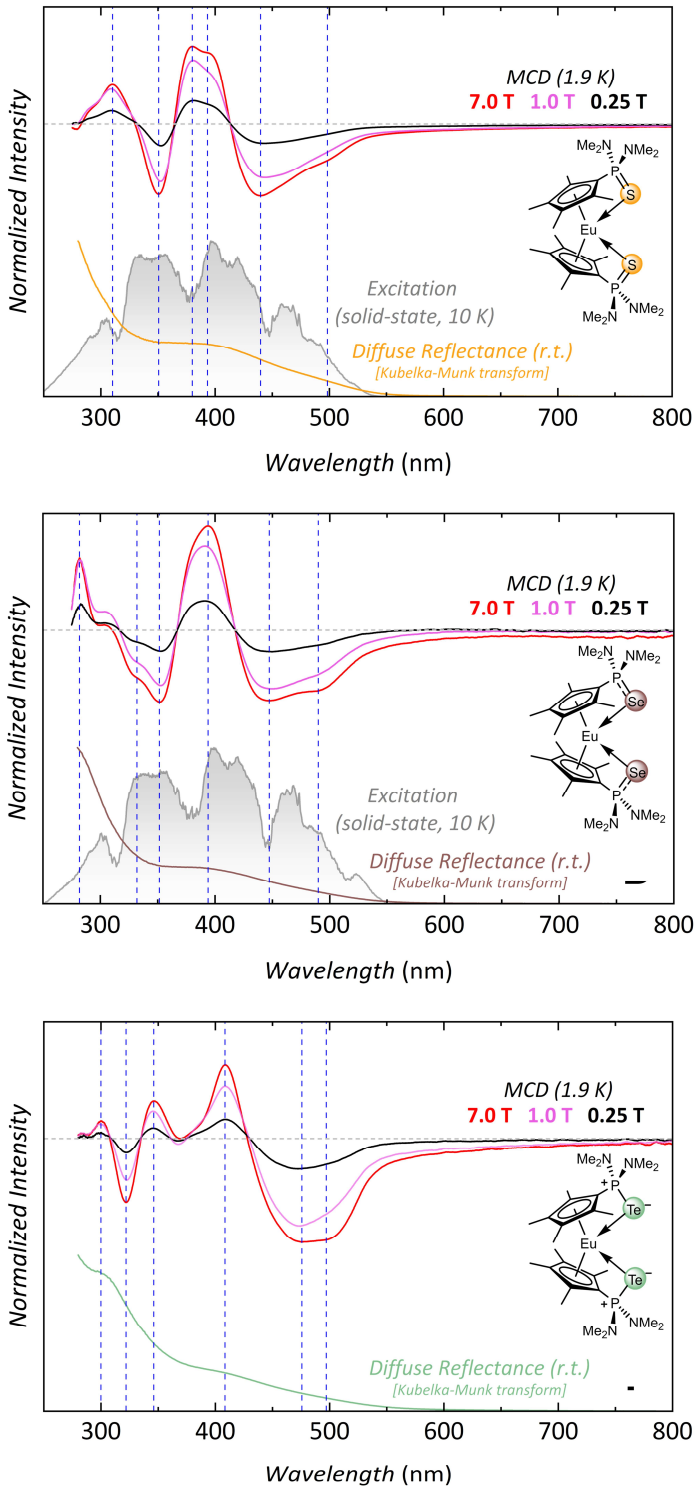


Figure 4.22. Comparison of VH-MCD spectra at selected fields with solid-state diffuse reflectance (coloured lines in lower portion) and photoluminescence excitation spectra (where applicable, filled grey curves in lower portion) for **4.1S** (top), **4.1Se** (middle), and **4.1Te** (bottom). Dotted blue lines indicate the distinguishable components observed in the MCD spectra, as described in the text.

VT-MCD spectra for **4.1Ch** under several applied magnetic fields (0.1, 0.25, 0.5 and 1.0 T) (Figures 4.23-4.25). Upon increasing the temperature, positive bands become less positive and negative bands become less negative. Thus, by taking the difference in integrated area between a lcp- and a rcp-dominated transition band, we can implement a highly sensitive thermometric parameter $\Delta = I_{lcp} - I_{rcp}$. In accordance with the strong MCD intensity of **4.1S**, an acceptable signal-to-noise ratio was obtained at 0.1 T, while for **4.1Se** and **4.1Te** with weaker intensity, the minimum usable field was 0.25 T. A sigmoidal logistic function (Eqn. 4.2) was used to fit the Δ parameters:[xii]

$$\Delta = \frac{A_1 - A_2}{1 + \left(x/x_0\right)^p} - A_2 \tag{4.2}$$

and S_r can then be calculated by dividing the derivative of the fitted function by the fitted Δ values (Eqn. 1.2):

$$S_r(\%) = \left[\frac{\left(\frac{\partial \Delta}{\partial T}\right)}{\Delta}\right] \cdot 100 \tag{1.2}$$

Various thermometric parameters consisting of combinations of I_{lcp} and I_{rcp} were evaluated to find the best performance (Figures 4.26-4.28), and the corresponding S_r values were calculated for each combination (Figures 4.29-4.31). A summary of the single-parameter thermometric figures of merit of **4.1Ch** is given in Table 4.2. We therefore find that complexes **4.1Ch** can behave as extraordinarily sensitive MCD thermometers; in particular, **4.1S** shows an unprecedented single-parameter maximum S_r of 93.9 % K^{-1} at T = 1.7 K and H = 0.1 T. To further validate the thermometric performance of these complexes, the temperature uncertainty δT was calculated as reported previously.[336] At the temperature of maximum sensitivity, values of δT in the range 10^{-3} – 10^{-2} K are obtained (Figures 4.32-4.34 and C13-C15). In accordance with our previous findings regarding MCD thermometers, these results demonstrate that increasing the applied magnetic field broadens the operational range at the expense of maximum S_r, when distinguishable signal-to-noise ratio is taken as the only criterion of merit. For a more quantitative comparison, we take a δT value of 1.0 K as the "useful" threshold and define the sensing range as the temperature range over which $\delta T \leq 1.0$ K.

The thermal sensing performance of these complexes can be further enhanced by considering all combinations of I_{lcp} and I_{rcp} simultaneously, via a multiparametric thermal readout method.[343] This method applies a multiple non-linear regression to calculate one new S_r from the sum of individual parameters, according to (Eqn. 4.3):

$$S_{r,mp}(\%) = \sqrt{\sum_{i=1}^{n} \left[\frac{\left(\frac{\partial \Delta}{\partial T}\right)}{\Delta}\right]^2} \cdot 100 \tag{4.3}$$

and correspondingly one new δT calculated based on the new S_r.[336] Using this approach, dramatic improvements in maximum S_r and δT are achieved in all cases, with **4.1S** attaining a maximum S_r of 170 % K^{-1} with δT = 0.003 at T = 1.7 K and H = 0.1 T. Overall, improvements in sensitivity and temperature uncertainty of 50-60% are observed using the multiparametric approach, except for **4.1S** at 1.0 T and **4.1Te** at 0.25 T, where the improvements are somewhat less at *ca.* 25 and 41%, respectively. A summary of the thermometric figures of merit obtained from the multiparametric readout approach is also given in Table 4.2.

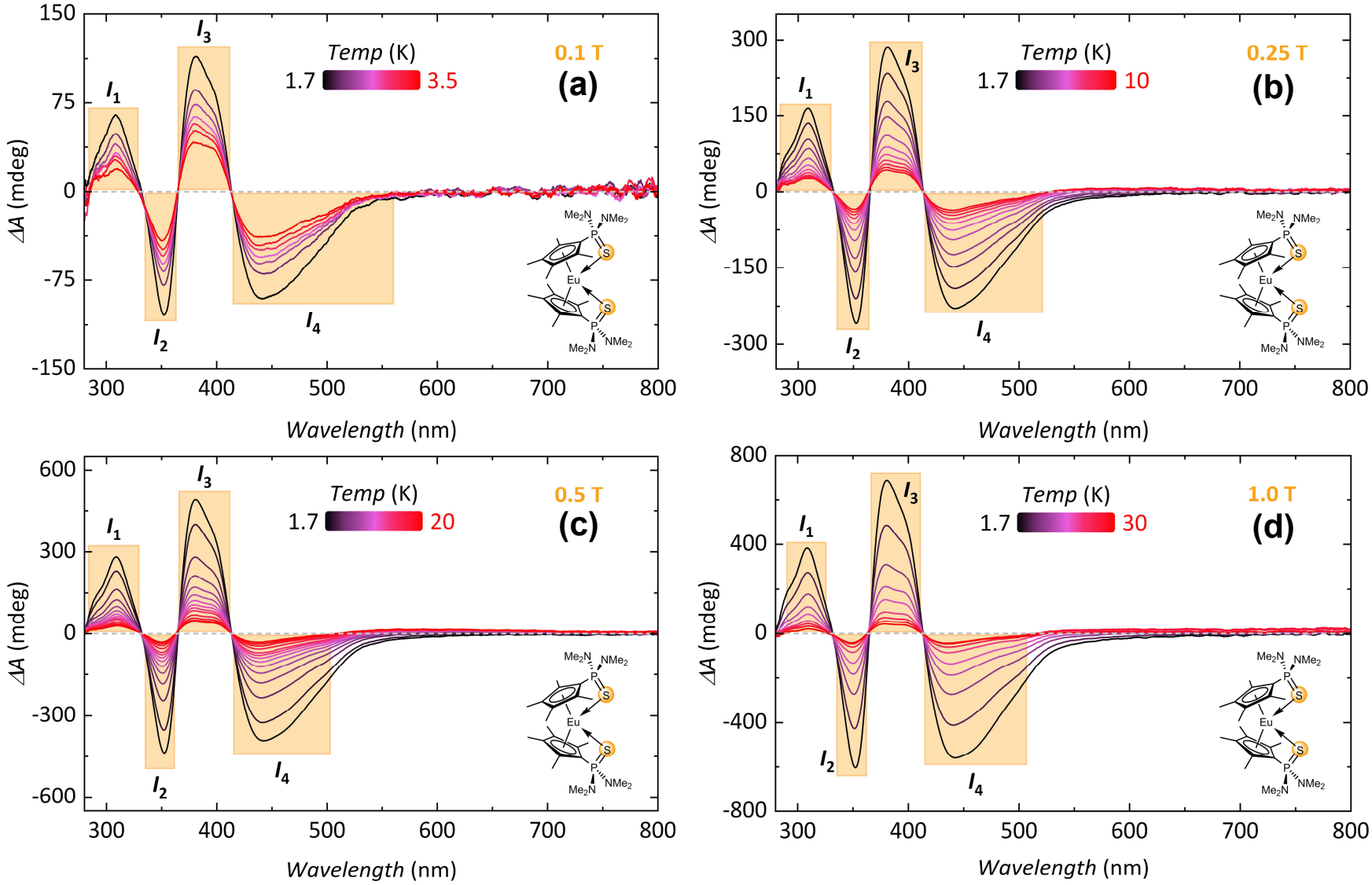


Figure 4.23. Variable-temperature magnetic circular dichroism (VT-MCD) spectra of **1-S** under applied magnetic fields of (a) 0.1, (b) 0.25, (c) 0.5, and (d) 1.0 T. Regions I_n of the spectra from which MCD thermometric parameters Δ are derived are indicated by yellow boxes.

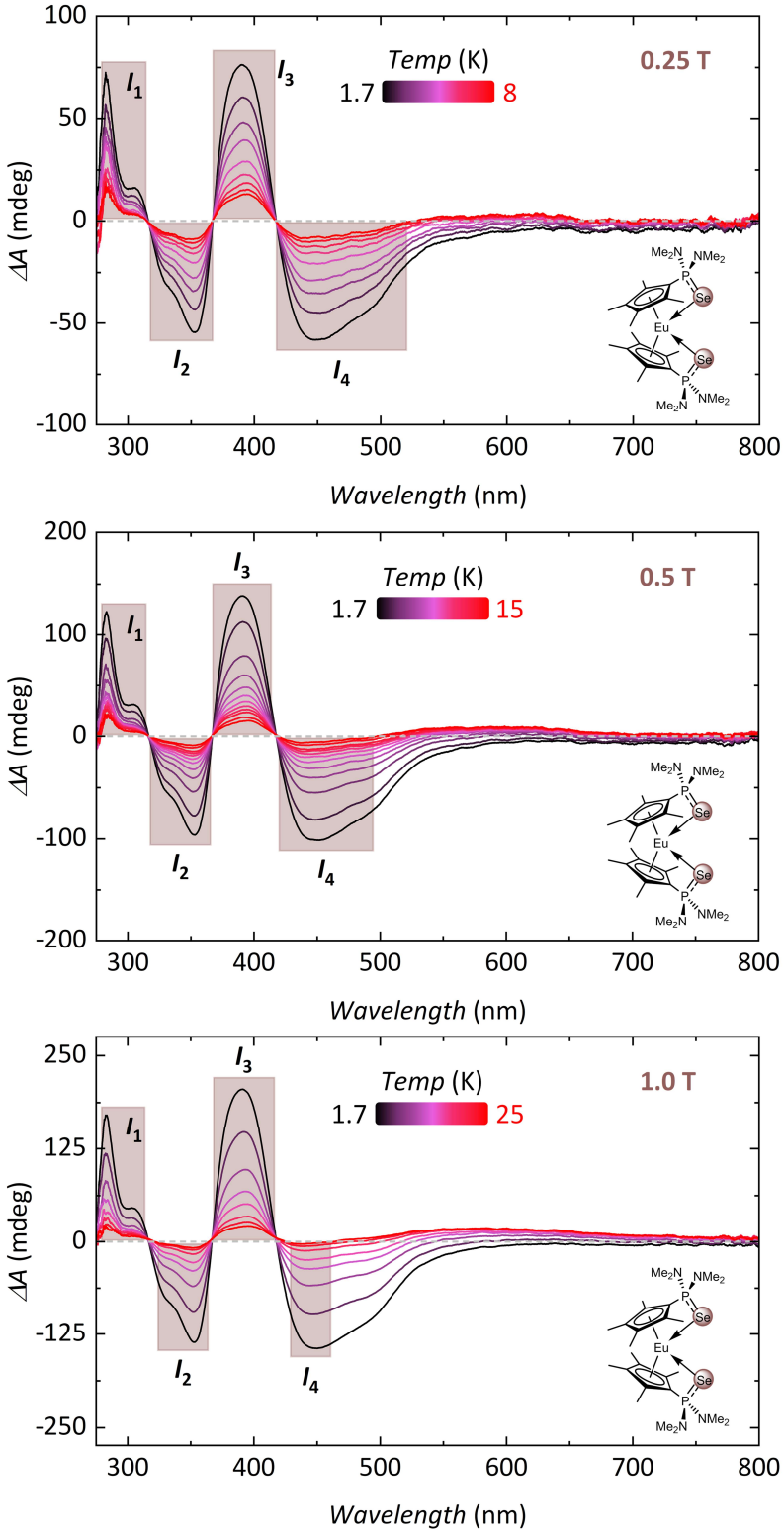


Figure 4.24. Variable-temperature magnetic circular dichroism (VT-MCD) spectra of **4.1Se** under applied magnetic fields of 0.25 (top), 0.5 (middle), and 1.0 T (bottom). Regions I_n of the spectra from which MCD thermometric parameters Δ are derived are indicated by brown boxes.

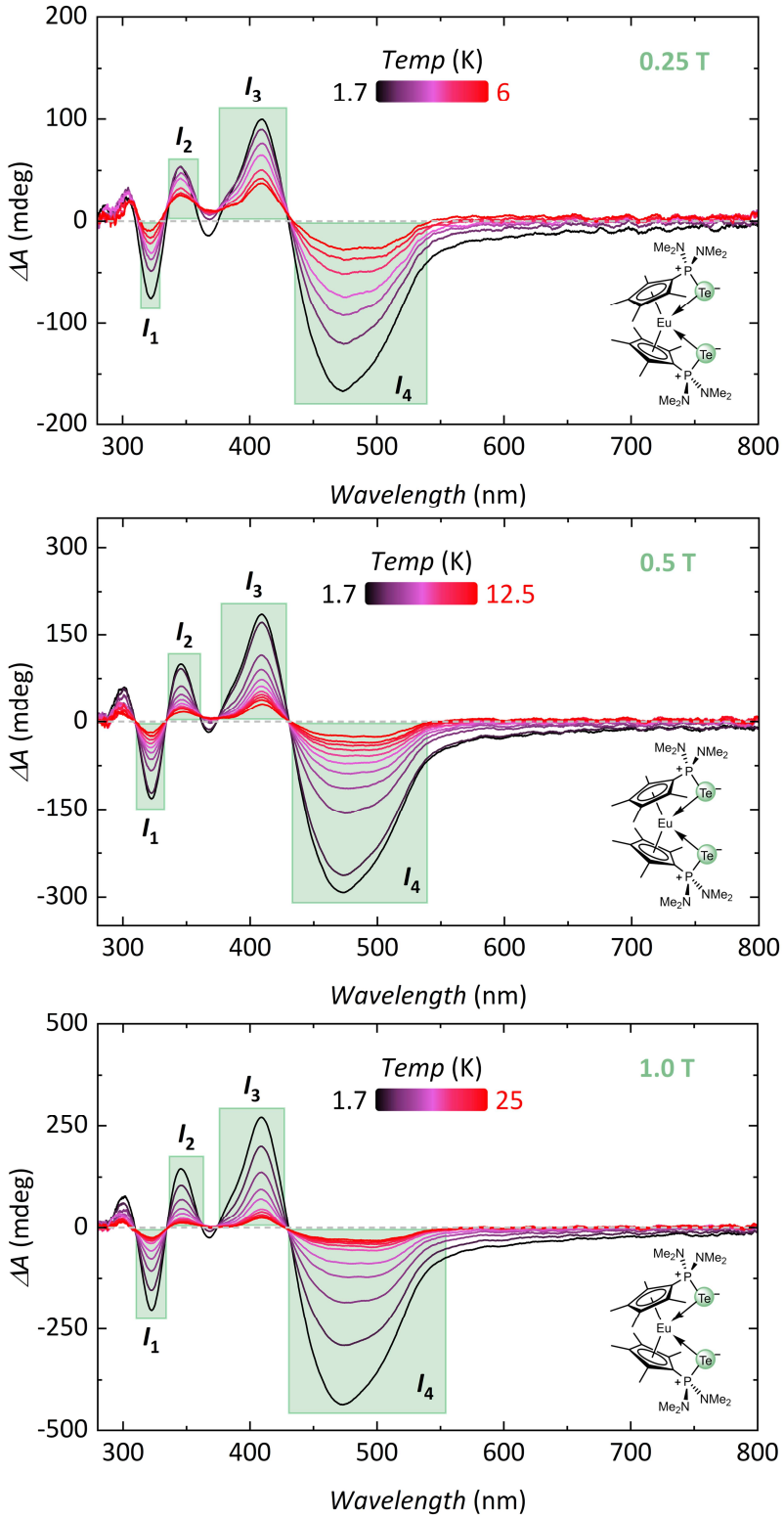


Figure 4.25. Variable-temperature magnetic circular dichroism (VT-MCD) spectra of **4.1Te** under applied magnetic fields of 0.25 (top), 0.5 (middle), and 1.0 T (bottom). Regions I_n of the spectra from which MCD thermometric parameters Δ are derived are indicated by green boxes.

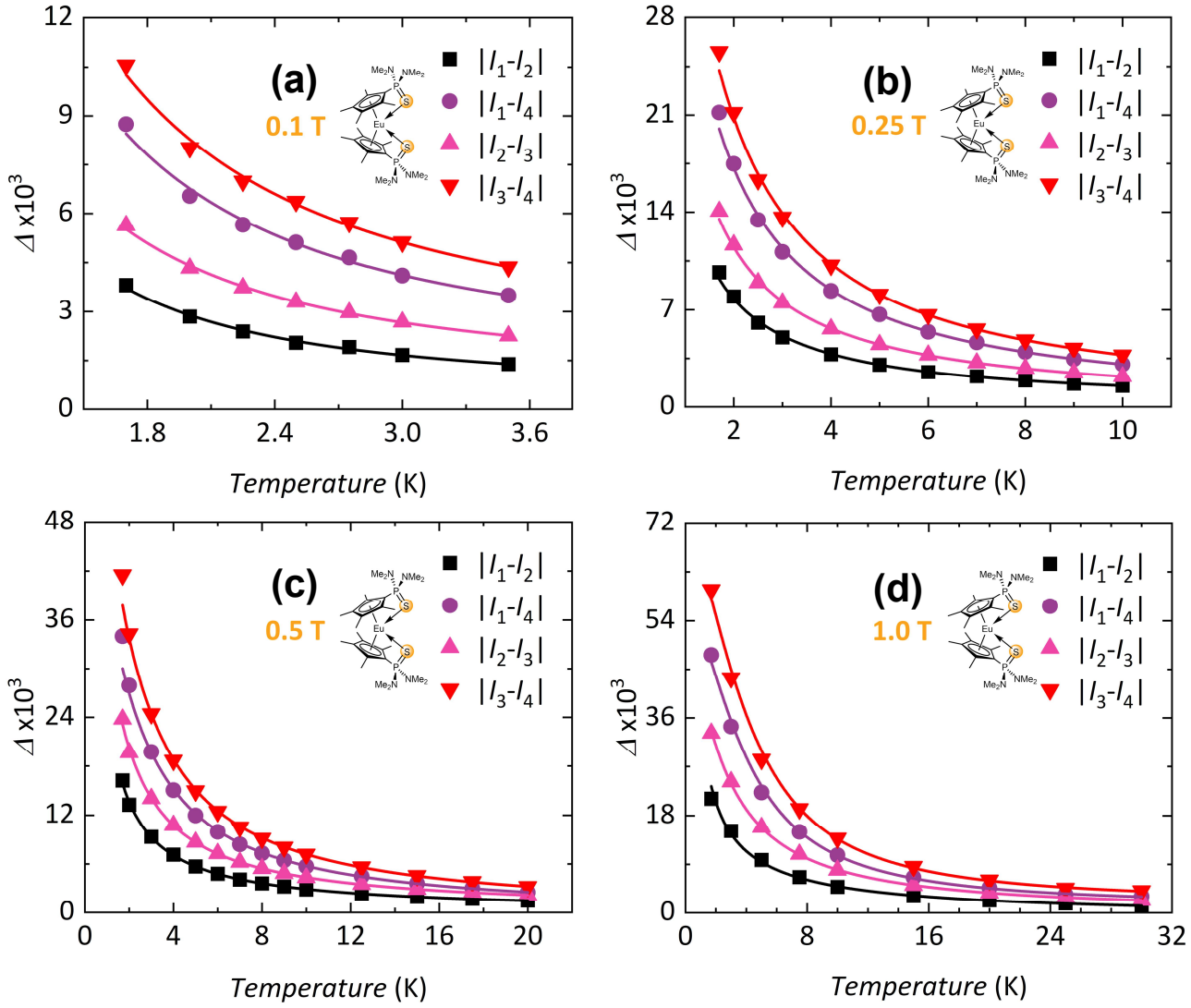


Figure 4.26. Temperature-dependence of the Δ parameters of **4.1S** under applied magnetic fields of (a) 0.1, (b) 0.25, (c) 0.5, and (d) 1.0 T. The solid lines represent the sigmoidal logistic function fitted to the experimental data; best fitting parameters are given in Table C6.

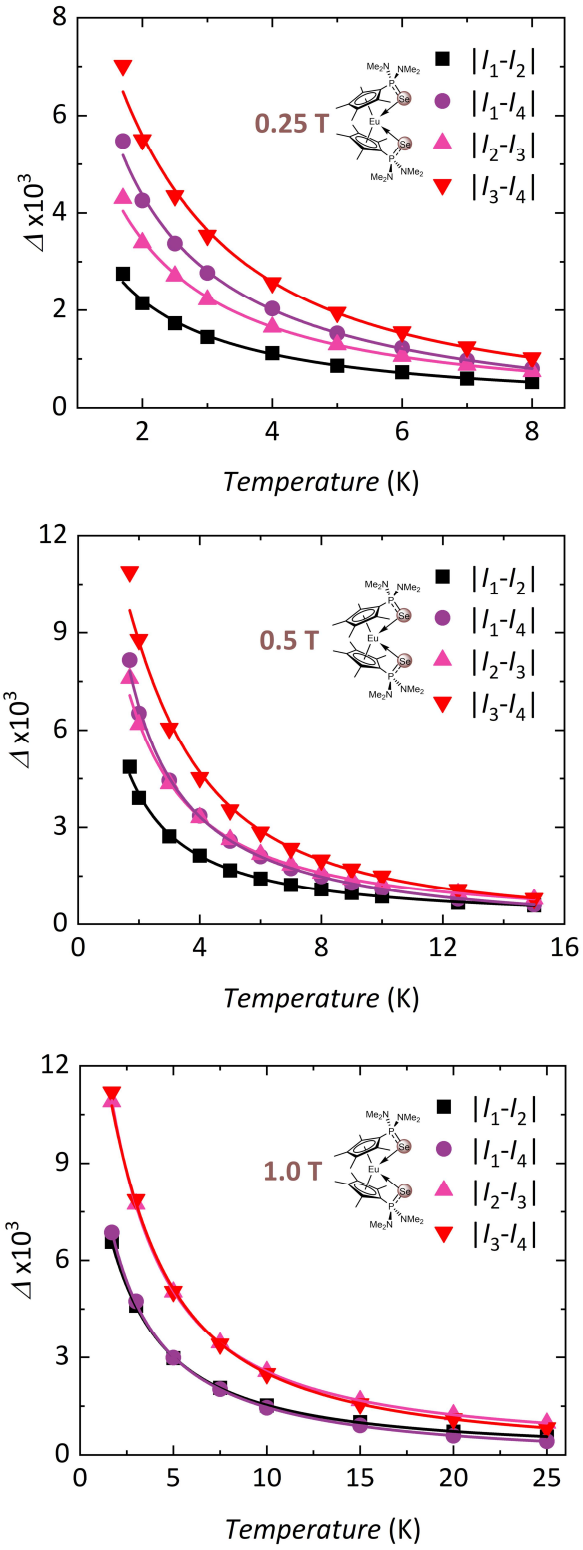


Figure 4.27. Temperature-dependence of the Δ parameters of **4.1Se** under applied magnetic fields of 0.25 (top), 0.5 (middle), and 1.0 T (bottom). The solid lines represent the sigmoidal logistic function fitted to the experimental data; best fitting parameters are given in Table C6.

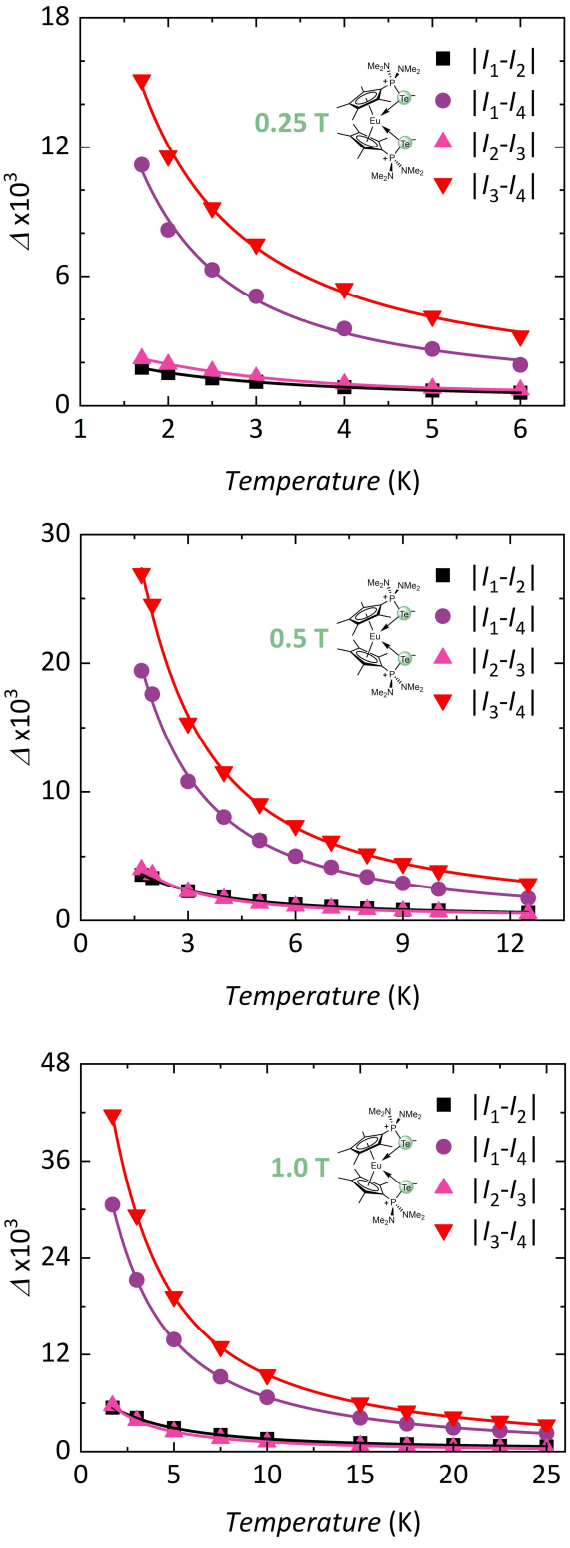


Figure 4.28. Temperature-dependence of the Δ parameters of **4.1Te** under applied magnetic fields of 0.25 (top), 0.5 (middle), and 1.0 T (bottom). The solid lines represent the sigmoidal logistic function fitted to the experimental data; best fitting parameters are given in Table C6.

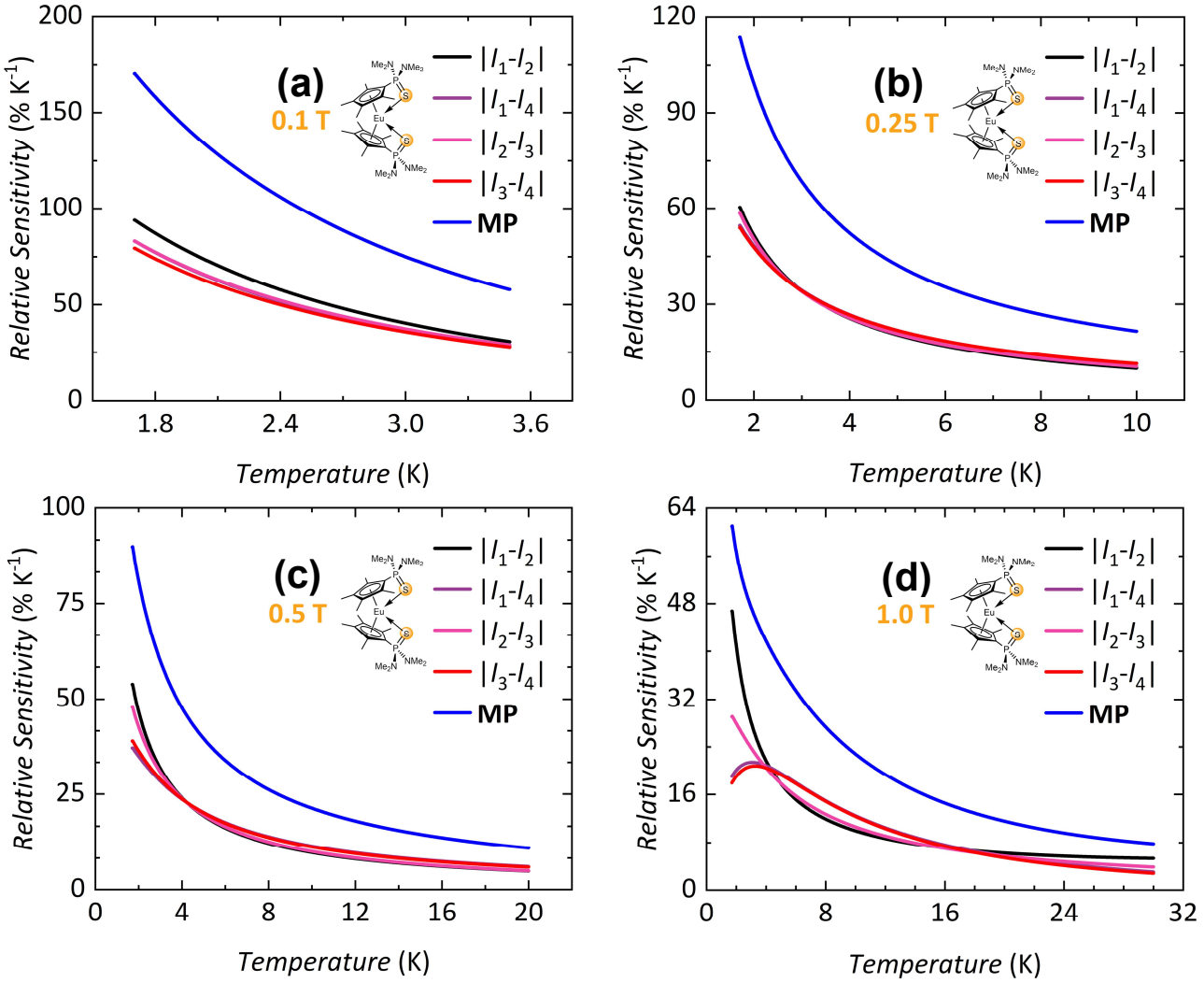


Figure 4.29. Relative sensitivities calculated for each Δ parameter of **4.1S** under applied magnetic fields of (a) 0.1, (b) 0.25, (c) 0.5, and (d) 1.0 T. The blue line labelled "MP" indicates the sensitivity derived from a multiparametric thermal readout method that combines the temperature-dependence of all Δ for a given set of conditions into one parameter.

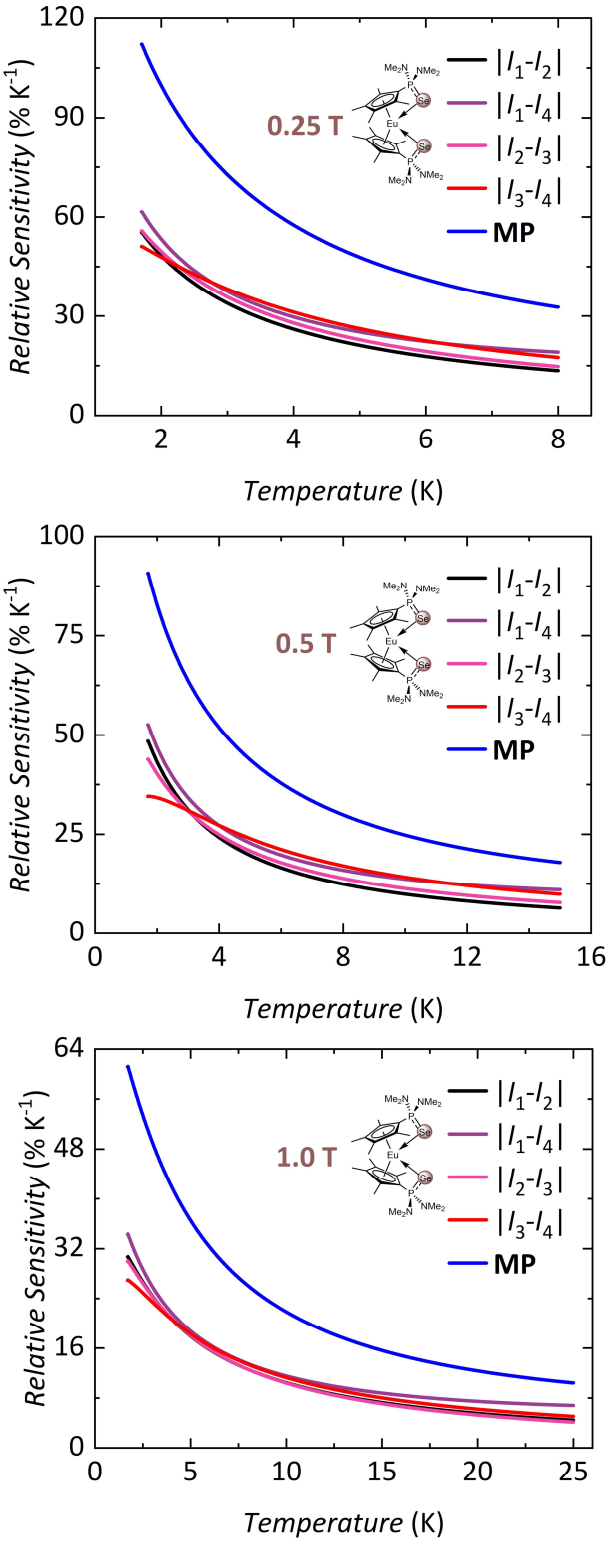


Figure 4.30. Relative sensitivities calculated for each Δ parameter of **4.1Se** under applied magnetic fields of 0.25 (top), 0.5 (middle) and 1.0 T (bottom). The blue line labelled "MP" indicates the sensitivity derived from a multiparametric thermal readout method that combines the temperature-dependence of all Δ for a given set of conditions into one parameter.

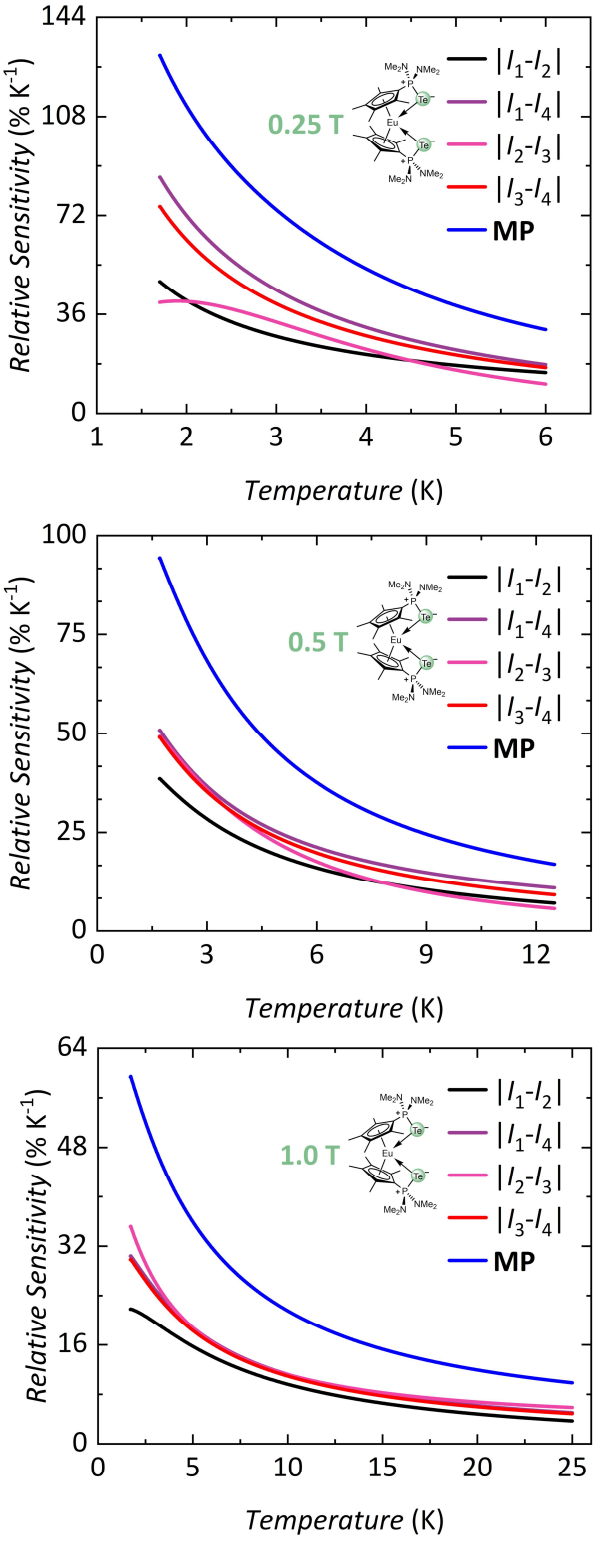


Figure 4.31. Relative sensitivities calculated for each Δ parameter of **4.1Te** under applied magnetic fields of 0.25 (top), 0.5 (middle) and 1.0 T (bottom). The blue line labelled "MP" indicates the sensitivity derived from a multiparametric thermal readout method that combines the temperature-dependence of all Δ for a given set of conditions into one parameter.

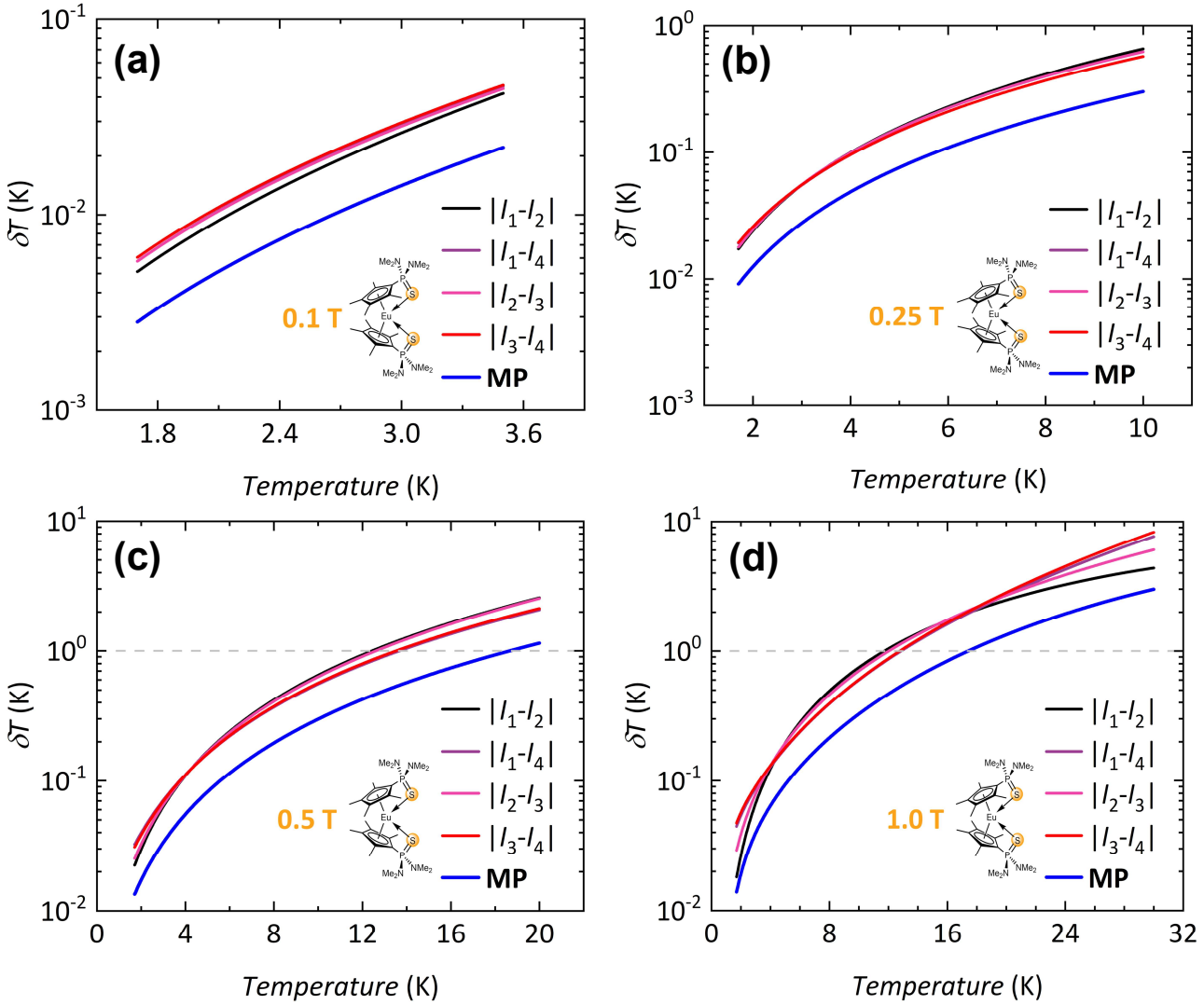


Figure 4.32. Temperature uncertainty δT obtained for **4.1S** under applied magnetic fields of (a) 0.1, (b) 0.25, (c) 0.5, and (d) 1.0 T, based on the temperature-dependent signal fluctuations shown in Figure C13. The dashed grey line indicates the "useful threshold" of δT = 1.0 K.

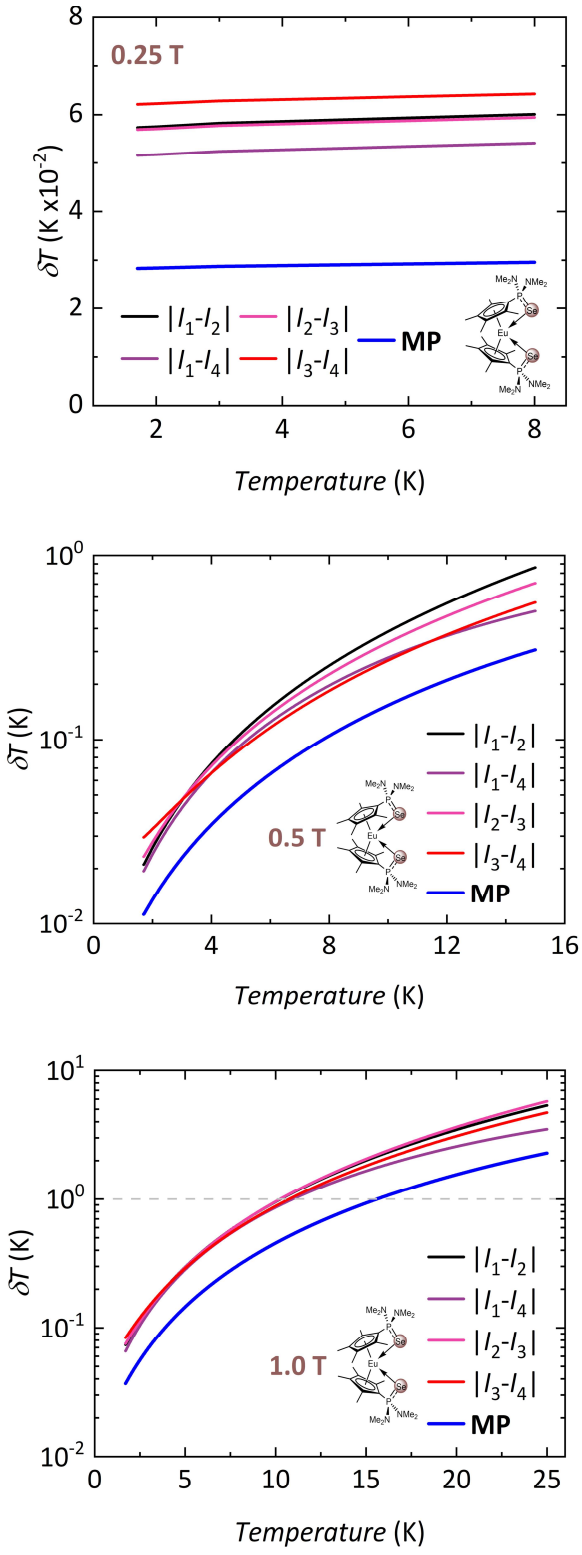


Figure 4.33. Temperature uncertainty ***δT*** obtained for **4.1Se** under applied magnetic fields of 0.25 (top), 0.5 (middle), and 1.0 T (bottom), based on the temperature-dependent signal fluctuations shown in Figure C14. The dashed grey line indicates the "useful threshold" of δT = 1.0 K.

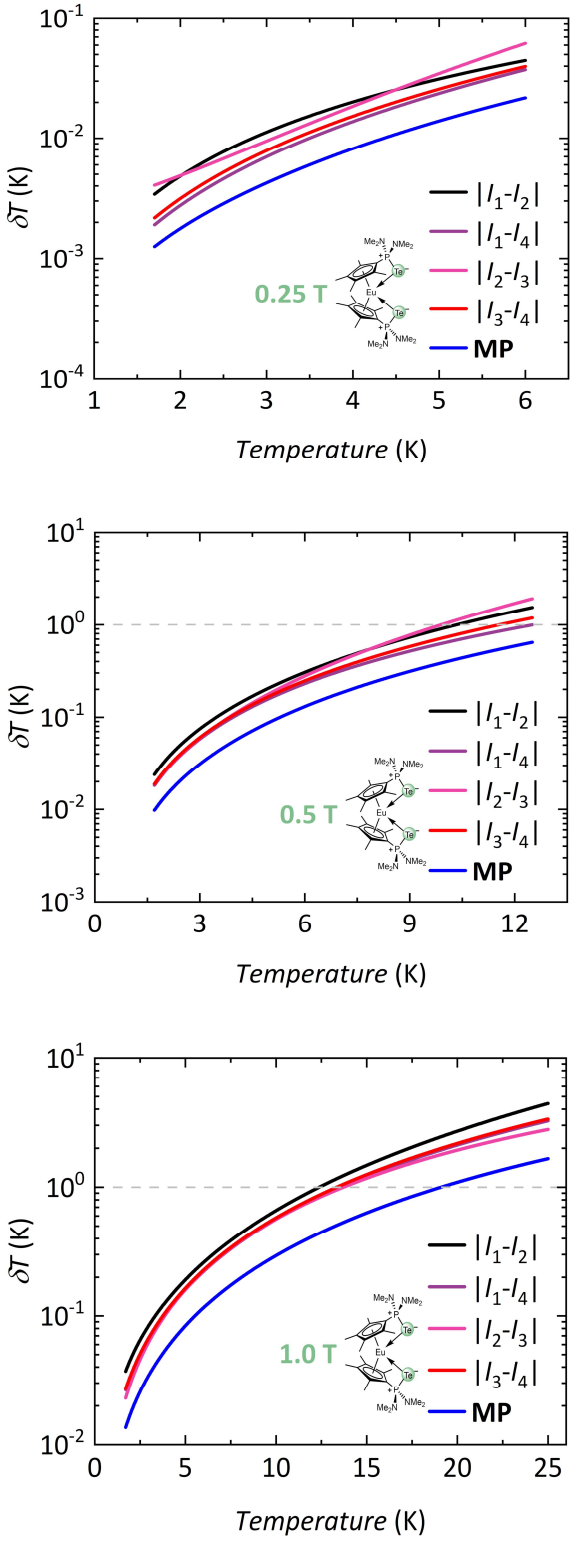


Figure 4.34. Temperature uncertainty δT obtained for **4.1Te** under applied magnetic fields of 0.25 (top), 0.5 (middle), and 1.0 T (bottom), based on the temperature-dependent signal fluctuations shown in Figure C15. The dashed grey line indicates the "useful threshold" of δT = 1.0 K.

Table 4.2. Summary of thermometric figures of merit obtained for **4.1Ch** applied as probes for MCD-based thermometry.

		0.1 T		0.25 T		0.5 T		1.0 T	
		Single-Parameter	**Multi-parametric**	**Single-Parameter**	**Multi-parametric**	**Single-Parameter**	**Multi-parametric**	**Single-Parameter**	**Multi-parametric**
4.1S	Max. S_r (% K^{-1})[a]	93.9	170	60.3	114	53.8	89.9	46.7	61.0
	δT (K)[b]	0.005	0.003	0.02	0.009	0.02	0.01	0.02	0.01
	Sensing Range (K)[c]	1.7 – 3.5		1.7 – 10		1.7 – 12.4	1.7 – 18.7	1.7 – 11.7	1.7 – 17.4
4.1Se	Max. S_r (% K^{-1})[a]	n.d.		61.5	112	52.6	90.7	34.3	61.2
	δT (K)[b]	n.d.		0.05	0.03	0.02	0.01	0.07	0.04
	Sensing Range (K)[c]	n.d.		1.7 – 8		1.7 – 15		1.7 – 10.9	
4.1Te	Max. S_r (% K^{-1})[a]	n.d.		85.9	130	50.8	94.4	35.2	59.4
	δT (K)[b]	n.d.		0.002	0.001	0.02	0.01	0.02	0.01
	Sensing Range (K)[c]	n.d.		1.7 – 6		1.7 – 12.5		1.7 – 13.7	

[a] Maximum S_r is attained at 1.7 K under all conditions. [b] Temperature uncertainty at the temperature of maximum S_r. [c] Temperature range for which δT is ≤ 1.0 K. n.d. = not determined.

Complexes **4.1Ch** are thus the first examples of organometallic complexes employed for MCD thermometry, and highlight the huge potential of Eu^{II} complexes as magneto-optical thermometers. We predict that further engineering of Eu^{II} complexes will yield magneto-optical materials with higher stability and potentially further improvements in thermometric performance.

4.8 Conclusion

Three novel potassium cyclopentadienides featuring bis(dimethylamino)phosphinochalcogenoyl substituents containing sulfur, selenium, and tellurium, as well as their homoleptic complexes with Eu^{II}, were prepared and characterized. The chalcogen atom of these ligands coordinates to the lanthanide center and, in doing so, disfavours the coordination of solvent ligands. Photoluminescence studies show that the identity of the chalcogen atom has an important effect on the luminescence properties of the Eu^{II} complexes, as the emission is progressively quenched on going down the chalcogen group. These complexes show highly temperature-dependent MCD and represent the first examples of organometallic complexes as probes for magneto-optical thermometry via MCD spectroscopy. In this application, values of relative sensitivity up to 170 % K^{-1} with temperature uncertainty as low as 0.003 K at cryogenic temperatures are obtained, far surpassing what is attainable with conventional luminescence thermometry. Further investigation of lanthanide complexes of these useful and interesting ligands is a continuing area of research in our group.

4.9 Methods

General remarks. All manipulations were conducted under stringently oxygen- and moisture-free conditions under argon or nitrogen atmospheres using Schlenk line and glovebox techniques. All chemicals were purchased from STREM Chemicals, Oakwood Scientific, Sigma-Aldrich, or Fisher Scientific and used as received unless otherwise noted. Tetrahydrofuran (THF), hexanes, pentane, diethyl ether, and toluene were dried on columns of activated alumina using a J.C. Meyer Phoenix solvent system and degassed via repeated freeze-pump-thaw cycles, then stored over activated 4 Å molecular sieves. Pyridine-d_5 was degassed via repeated freeze-pump-thaw cycles then stored over activated 4 Å molecular sieves. Fluorobenzene was pre-dried by stirring over P_2O_5 for one week, then distilled under an atmosphere of argon, degassed via repeated freeze-pump-thaw cycles, and stored over activated 4 Å molecular sieves. Ultrapure barium sulfate (99.998% trace metals basis, Fisher Scientific AA010651) was dried under vacuum at 120 °C before use. 1-(bis(dimethylamino)phosphino)-2,3,4,5-tetramethylcyclopentadiene (*vide infra,* Figure 4.35)[227,270] and $[Eu^{II}(BH_4)_2(THF)_2]$[56] were prepared according to reported procedures.

Elemental analysis. Elemental analysis was performed by Midwest Microlab (Indianapolis, IN, USA). Organolanthanide complexes, especially those of divalent ions, are well known to suffer incomplete combustion and formation of carbides during microanalysis, yielding consistently and artificially low values.[60,284] Complexes bearing solvent ligands are further plagued by artificially low values due to loss of coordinated solvent during sample loading and/or combustion; thus microanalysis values should be considered within a wider tolerance than usually expected.[256] Here, elemental analysis has been treated in a manner consistent with the literature regarding divalent organolanthanide compounds.

NMR spectroscopy. All NMR spectra were recorded using either a Bruker AVANCE III HD 500 MHz spectrometer or a Bruker AVANCE III HD 600 MHz spectrometer equipped with a triple resonance inverse 5 mm H-C/N-D cryoprobe. ^{1}H chemical shifts are reported in ppm relative to tetramethylsilane using the

pyridine-d_5 residual solvent signal at δ = 8.74 as an internal standard. ^{13}C chemical shifts are reported in ppm relative to tetramethylsilane referenced to the pyridine-d_5 resonance at δ = 150.35. ^{31}P chemical shifts are reported in ppm, externally referenced to 85% aqueous H_3PO_4 (δ = 0.00). ^{77}Se chemical shifts are reported in ppm, externally referenced to Me_2Se (δ = 0.00). ^{125}Te chemical shifts are reported in ppm, externally referenced to Me_2Te (δ = 0.00).

Infrared spectroscopy. Fourier transform infrared (FTIR) spectra were recorded in the $\tilde{\nu}$ = 4000-525 cm^{-1} range on a Nicolet 6700 FTIR spectrometer equipped with an attenuated total reflectance (ATR) attachment. Samples of air-sensitive materials comprised suspensions of crushed polycrystalline solid in a thin layer of Cargille Type NVH immersion oil (MiTeGen); background spectra were corrected for the presence of the oil.

X-ray crystallography. X-ray crystallography was performed using a Bruker AXS KAPPA single-crystal diffractometer equipped with an APEX II CCD detector, using graphite-monochromated Mo Kα radiation (λ = 0.710173 Å) from a sealed tube source. The crystals chosen were mounted on the tips of 100 or 200 μm MicroLoops (depending on the crystal size) using Cargille Type NVH immersion oil and cooled to the indicated temperatures. Raw data collection and processing were performed with the Bruker APEX II software package.[195,196] A multiscan absorption correction was applied (SADABS).[197] The crystal structures were solved via direct methods and refined using a full-matrix least-squares method on F^2 using the SHELXTL program suite[191–193] and the Olex2 user interface.[194] Non-hydrogen atoms were refined anisotropically. The positions of all hydrogen atoms were calculated based on the geometry of their respective atoms and are included at geometrically idealized positions [riding model]. All diagrams were prepared using Diamond 4[198,199] or Mercury 2024.3.1[200] and POV-Ray.[201] The data have been deposited with the Cambridge Crystallographic Data Centre under the deposition numbers indicated in Section C.2.

SQUID magnetometry. DC magnetic measurements were performed using a Quantum Design MPMS-XL7 SQUID magnetometer operating in the temperature range 1.8–300 K, on crushed polycrystalline samples of **4.1Ch** restrained in a matrix of vacuum grease (Corning) and wrapped in a polyethylene membrane. The magnetization data were collected at 100 K to check for ferromagnetic impurities, which were absent. Diamagnetic corrections were applied for the sample holder, and the inherent diamagnetism of the prepared sample was estimated with the use of Pascal's constants.

Diffuse reflectance spectroscopy. Diffuse reflectance spectra were recorded using an Agilent DRA-2500 PMT/PbS internal diffuse reflectance accessory mounted inside an Agilent Cary 5000 UV-Vis-NIR spectrophotometer. Samples were prepared in the glovebox by diluting the compound of interest to 5 ± 1 wt% in ultrapure $BaSO_4$ and homogenizing to a very fine powder in an agate mortar and pestle. The powder was enclosed in an Agilent "small" powder cell (cat. No. 9910111400) whose base was sealed with paraffin wax and whose threads were sealed with several wraps of high-density Teflon tape. The cell was jacketed by a gentle flow of argon during data collection to protect the sample. To facilitate comparison, the so-obtained reflectance spectra were transformed into pseudo-absorbance spectra by applying the Kubelka-Munk function[344,345] $F(R) = \frac{K}{S} = \frac{(1-R)^2}{2R}$.

Photoluminescence spectroscopy. Photoluminescence data were obtained using a Horiba QuantaMaster 8075-21 spectrofluorometer. An ozone-free PowerArc 75 W xenon lamp was used as the radiation source.

The excitation spectra were corrected in real time according to the lamp intensity and the optical system of the excitation monochromator using a silicon diode as a reference. The emission spectra were corrected according to the optical system of the emission monochromator and the photomultiplier response (Hamamatsu R13456 red-extended PMT). Samples were prepared inside the glovebox and comprised a small amount of crystalline solid placed inside a screw-top quartz cuvette, which was then sealed with additional layers of high-density Teflon and electrical tapes. Low-temperature measurements were performed with the samples mounted inside a CS202*E-DMX-1AL closed-cycle helium cryostat system (Advanced Research Systems), controlled via a LakeShore 335 temperature controller.

Magnetic circular dichroism spectroscopy. MCD measurements were performed using a Jasco J-1700 circular dichroism spectrometer and an Oxford Instruments SpectromagPT cryogen-free magneto-optical superconducting magnet system. MCD spectra were recorded on a mull of the solid compound in Cargille type NVH immersion oil, prepared in the glovebox. For **4.1S** and **4.1Se**, a portion of the mull was sandwiched between quartz slides. To compensate for the significantly lower MCD intensity of **4.1Te**, the optical path length was increased by introducing a 2 mm titanium spacer between the quartz slides; the intervening space was then filled with the mull. The spectrum in the absence of an applied field was used as the background for the measurements.

Computational details. All DFT calculations were performed using Gaussian 09 via the WebMO version 18.1.002e interface, running on a computing cluster administered by the Woo Lab at the University of Ottawa. Geometry optimizations and calculations of vibrational frequencies were carried out at the CAM-B3LYP[328]/def2-TZVPD[329,330] level of theory. Gaussian 09 does not natively include the Weigend-Ahlrichs family of basis sets, so these were downloaded from the Environmental Molecular Sciences Laboratory Basis Set Exchange database[346–348] and introduced manually to the calculation using the *gen* instruction. For **KCp$^{\#}$PTe**, an effective core potential included in the def2-TZVPD basis set[349] was used on tellurium. As we surmised that the solid-state structure of **KCp$^{\#}$PCh** contained metallocene-like motifs, a molecular geometry consisting of an (η^5-Cp,κ^1-Ch)-coordinated potassium ion was given as input (Figure C11). Geometry optimizations converged to energy minima in all cases, as evidenced by the lack of imaginary vibrational frequencies, and the resulting optimized geometries exhibited reasonable metrical parameters resembling the SCXRD structures of the corresponding Eu complexes **4.1Ch**. The calculated vibrational frequencies were expectedly systematically overestimated, so they were corrected using a single linear scaling equation,[331] derived by comparing the experimental and calculated frequencies of several prominent vibrations in each spectrum (Figure C12 and Tables C2 and C3). This procedure gave simulated spectra in good agreement with the experimental spectra (Figures 4.6-4.8).

4.10 Synthesis

Potassium 1-(bis(dimethylamino)phosphinothioyl)-2,3,4,5-tetramethylcyclopentadienide (KCp$^{\#}$PS). In a glove box under a positive pressure of nitrogen gas, H^{bdp}Cp$^{\#}$ (1.0 g, 4.16 mmol, 1 eq.) was dissolved in toluene (7 mL) with stirring. Crystalline sulfur (134 mg, 4.16 mmol, 1 eq.) was added, and the mixture was stirred at room temperature until the sulfur was fully dissolved (ca. 10 min), then for an additional 2 hr. A solution of KHMDS (913 mg, 4.58 mmol, 1.1 eq.) in toluene (8 mL) was then added dropwise, causing the solution to become bright yellow and precipitate a large quantity of light-coloured solid. The mixture was stirred overnight at room temperature. The resulting precipitate was collected on a fine-porosity fritted glass filter, washed with toluene (5x 5 mL) and pentane (5x 5 mL), then dried in vacuo to give the title

compound as an off-white powder (1.25 g, quantitative yield). IR: $\tilde{\nu}$ = 3007 (vw), 2985 (vw), 2964 (vw), 2904 (vw), 2852 (w, with shoulder at 2835), 2796 (vw), 2729 (vw), 1433 (vw), 1404 (vw), 1371 (vw), 1298 (m), 1277 (w, with shoulder at 1250), 1184 (w), 1142 (vw), 1105 (vw), 1063 (vw), 1022 (vw), 966 (s, with shoulder at 974), 825 (vw), 769 (m), 694 (vs), 652 (vw), 619 (s), 555 (vw) cm^{-1}. ^{1}H NMR (500 MHz, pyridine-d_5) δ: 3.04 (d, 12H, $^{3}J_{H\text{-}P}$ = 10.4 Hz, -NMe_2), 2.44 (s, 6H, 2,5-Cp-CH_3), 2.25 (s, 6H, 3,4-Cp-CH_3). ^{13}C NMR (126 MHz, pyridine-d_5) δ: 116.2 (d, 3,4-Cp, $^{3}J_{C\text{-}P}$ = 8.7 Hz), 116.1 (d, 2,5-Cp, $^{2}J_{C\text{-}P}$ = 7.0 Hz), 93.4 (d, 1-Cp, $^{1}J_{C\text{-}P}$ = 152 Hz), 38.8 (d, -NMe_2, $^{2}J_{C\text{-}P}$ = 2.9 Hz), 13.1 (2,5-Cp-CH_3), 12.4 (3,4-Cp-CH_3). $^{31}P\{^{1}H\}$ NMR (203 MHz, pyridine-d_5) δ: 74.8 (s). Anal. Calcd. (%) for $C_{13}H_{24}N_2PSK$ (310.48): C, 50.29; H, 7.79; N 9.02. Found: C, 50.01; H, 7.81; N, 9.00.

Unlike sulfur, powdered selenium and tellurium are not soluble in toluene, so the reaction of $H^{bdp}Cp^{\#}$ with these elements is slower and dependent on the particle size of the powder employed in the protocol. As detailed below, for **$KCp^{\#}PSe$**, we used 2 eq. of selenium and a reaction time of 36 hr. in refluxing toluene to generate the corresponding phosphine selenide. In the case of **$KCp^{\#}PTe$**, the oxidation is complete within 18 hr. due to the more finely divided tellurium we used.

Potassium 1-(bis(dimethylamino)phosphinoselenoyl)-2,3,4,5-tetramethylcyclopentadienide ($KCp^{\#}PSe$). In a glove box under a positive pressure of nitrogen gas, $H^{bdp}Cp^{\#}$ (860 mg, 3.58 mmol, 1 eq.) was dissolved in toluene (8 mL) with stirring. Selenium powder (100 mesh, 567 mg, 7.16 mmol, 2 eq.) was added, and the mixture was stirred at reflux for 36 hr, during which the solution became pale yellow. The mixture was filtered over a pad of Celite to give a clear pale yellow solution, rinsing with toluene until the washings ran colourless. To the filtrate, a solution of KHMDS (786 mg, 3.94 mmol, 1.1 eq.) in toluene (8 mL) was added dropwise with stirring, causing the filtrate to darken in colour and precipitate a large quantity of light-coloured solid. The mixture was stirred overnight at room temperature. The resulting precipitate was collected on a fine-porosity fritted glass filter, washed with toluene (5x 5 mL) and pentane (5x 5 mL), then dried in vacuo to give the title compound as a white powder (1.11 g, 87% yield). IR: $\tilde{\nu}$ = 2729 (vw), 2794 (vw), 2833 (w), 2852 (w), 2902 (vw), 2985 (vw), 1431 (vw, with shoulder at 1445), 1404 (vw), 1373 (vw), 1358 (vw), 1298 (m), 1275 (m, with shoulder at 1244), 1182 (m), 1140 (vw), 1105 (vw), 1084 (vw), 1062 (vw), 1020 (vw), 966 (vs), 825 (vw), 766 (w), 700 (m), 667 (s), 625 (vw), 594 (s), 571 (vw), 557 (m), 548 (w), 534 (w) cm^{-1}. ^{1}H NMR (500 MHz, pyridine-d_5) δ: 3.04 (d, 12H, $^{3}J_{H\text{-}P}$ = 10.7 Hz, -NMe_2), 2.41 (s, 6H, 2,5-Cp-CH_3), 2.25 (s, 6H, 3,4-Cp-CH_3). ^{13}C NMR (126 MHz, pyridine-d_5) δ: 116.5 (d, 3,4-Cp, $^{3}J_{C\text{-}P}$ = 18.2 Hz), 116.1 (d, 2,5-Cp, $^{2}J_{C\text{-}P}$ = 16.4 Hz), 93.7 (d, 1-Cp, $^{1}J_{C\text{-}P}$ = 141 Hz), 39.2 (d, -NMe_2, $^{2}J_{C\text{-}P}$ = 3.4 Hz), 13.2 (2,5-Cp-CH_3), 12.3 (d, 3,4-Cp-CH_3, $^{4}J_{C\text{-}P}$ = 2.5 Hz). $^{31}P\{^{1}H\}$ NMR (203 MHz, pyridine-d_5) δ: 68.2 (s with ^{77}Se satellites, $^{1}J_{P\text{-}Se}$ = 660 Hz). ^{77}Se NMR (95 MHz, pyridine-d_5) δ: -167.0 (d, $^{1}J_{P\text{-}Se}$ = 660 Hz). Anal. Calcd. (%) for $C_{13}H_{24}N_2PSeK$ (357.39): C, 43.69; H, 6.77; N 7.84. Found: C, 43.32; H, 6.36; N, 7.58.

Potassium 1-(bis(dimethylamino)phosphinotelluroyl)-2,3,4,5-tetramethylcyclopentadienide ($KCp^{\#}PTe$). In a glove box under a positive pressure of nitrogen gas, $H^{bdp}Cp^{\#}$ (1.00 g, 4.16 mmol, 1 eq.) was dissolved in toluene (12 mL) with stirring. Tellurium powder (60 mesh, 1.06 g, 8.32 mmol, 2 eq.) was added, upon which the solution immediately became yellow. The mixture was stirred at reflux for 24 hr, during which the colour darkened significantly. The mixture was filtered over a pad of Celite to give a clear, deep yellow-orange solution, rinsing with toluene until the washings ran colourless. To the filtrate, a solution of KHMDS (913 mg, 4.58 mmol, 1.1 eq.) in toluene (7 mL) was added dropwise with stirring, causing the filtrate to darken to a brown colour and precipitate a large quantity of brownish solid. The mixture was

stirred overnight at room temperature. The resulting precipitate was collected on a fine-porosity fritted glass filter, washed with toluene (4x 4 mL) and pentane (5x 5 mL), then dried in vacuo to give the title compound as a tan powder (1.41 g, 83% yield). IR: $\tilde{\nu}$ = 2900 (vw), 2856 (w), 2845 (w), 2796 (vw), 2727 (vw), 1495 (vw), 1431 (vw, with shoulder at 1410), 1373 (vw), 1358 (vw), 1292 (s), 1184 (m, with shoulder at 1157), 1142 (vw), 1103 (vw), 1082 (vw), 1061 (vw), 1022 (vw), 972 (vs, with shoulder at 947), 885 (vw), 825 (w, with shoulder at 833), 791 (vw), 764 (w), 737 (vw), 702 (w, with shoulder at 694), 663 (vs, with shoulders at 644, 634, 627), 600 (vw), 577 (m), 546 (m), 542 (m), 534 (w) cm^{-1}. ^{1}H NMR (500 MHz, pyridine-d_5 after 1 week of stabilization time) δ: 2.97 (d, 12H, $^{3}J_{H-P}$ = 11.0 Hz, -NMe_2), 2.38 (s, 6H, 2,5-Cp-CH_3), 2.25 (s, 6H, 3,4-Cp-CH_3). ^{13}C NMR (126 MHz, pyridine-d_5 after 1 week of stabilization time) δ: 116.9 (d, 3,4-Cp, $^{3}J_{C-P}$ = 17.8 Hz), 116.0 (d, 2,5-Cp, $^{2}J_{C-P}$ = 16.5 Hz), 95.2 (d, 1-Cp, $^{1}J_{C-P}$ = 125 Hz), 39.7 (d, -NMe_2, $^{2}J_{C-P}$ = 3.3 Hz), 13.4 (2,5-Cp-CH_3), 12.2 (d, 3,4-Cp-CH_3, $^{4}J_{C-P}$ = 2.5 Hz). $^{31}P\{^{1}H\}$ NMR (203 MHz, pyridine-d_5 after 1 week of stabilization time) δ: 28.6 (s with ^{125}Te satellites, $^{1}J_{P-Te}$ = 1621 Hz). $^{125}Te\{^{1}H\}$ NMR (158 MHz, pyridine-d_5 after 1 week of stabilization time) δ: -433.4 (d, $^{1}J_{P-Te}$ = 1621 Hz). Anal. Calcd. (%) for $C_{13}H_{24}N_2PTeK$ (406.02): C, 38.46; H, 5.96; N 6.90. Found: C, 38.63; H, 5.99; N, 6.72.

General procedure 1 (GP1) for the synthesis of homoleptic (Cp#PCh)$_2$Eu complexes. In a glove box under a positive pressure of nitrogen gas, [Eu(BH$_4$)$_2$(THF)$_2$] (1 eq.) was dissolved in a minimum volume of THF with stirring. A solution of the corresponding **KCp#PCh** (2 eq.) in an equal volume of THF was added dropwise, and the mixture stirred at room temperature for 24 hr. The solvent was removed *in vacuo*, then the solid residue was taken up in fluorobenzene and filtered through a 0.45 μM PTFE syringe filter to give a clear solution. These solutions were evaporated *in vacuo* and the solid residue was triturated with pentane (2 mL) to give the title compounds as powders. The powders were isolated via suction filtration on a fine-porosity fritted glass filter, washed with pentane (3x 2 mL), and dried *in vacuo*. X-ray quality crystals could be obtained from a fluorobenzene solution of the corresponding compound either by slow evaporation or by slow diffusion of a pentane layer at -35 °C.

Bis(1-(bis(dimethylamino)phosphinothioyl)-2,3,4,5-tetramethylcyclopentadienyl)europium(II) (4.1S). Following GP1, 50 mg (0.153 mmol) [Eu(BH$_4$)$_2$(THF)$_2$] and 96 mg (0.307 mmol) **KCp#PS** gave the title compound as an orange powder or orange crystals (63 mg, 59% yield). IR: $\tilde{\nu}$ = 3016 (vw), 2993 (vw), 2960 (vw), 2889 (w), 2860 (w), 2845 (w), 2800 (vw), 2725 (vw), 1595 (vw), 1506 (vw), 1494 (vw), 1481 (vw), 1435 (w, with shoulder at 1450), 1410 (w), 1371 (w, with shoulder at 1381), 1358 (vw), 1302 (m, with shoulder at 1317), 1282 (w), 1238 (vw), 1217 (vw), 1180 (m), 1142 (w, with shoulder at 1124), 1103 (vw), 1063 (w), 1024 (vw), 968 (vs, with shoulder at 976), 894 (vw), 860 (vw), 825 (w), 806 (vw), 771 (m, with shoulder at 752), 717 (m), 692 (vs, with shoulders at 659 and 642), 611 (s), 561 (w, with shoulder at 548), 532 (vw) cm^{-1}. Anal. Calcd. (%) for $C_{26}H_{48}EuN_4P_2S_2$ (694.73): C, 44.95; H, 6.96; N 8.06. Found: C, 42.66; H, 7.21; N, 7.60.

Bis(1-(bis(dimethylamino)phosphinoselenoyl)-2,3,4,5-tetramethylcyclopentadienyl)europium(II) (4.1Se). Following GP1, 50 mg (0.153 mmol) [Eu(BH$_4$)$_2$(THF)$_2$] and 110 mg (0.307 mmol) **KCp#PSe** gave the title compound as an orange powder or orange crystals (80 mg, 66% yield). IR: $\tilde{\nu}$ = 3003 (vw), 2964 (vw), 2883 (w, with shoulder at 2910), 2860 (w), 2841 (w), 2799 (w), 2725 (vw), 1504 (vw), 1481 (vw), 1441 (w, with shoulder at 1450), 1431 (w), 1408 (w), 1402 (vw), 1377 (vw), 1358 (vw), 1302 (m), 1279 (m), 1174 (s, with shoulder at 1184), 1140 (w), 1061 (w), 1022 (w), 964 (vs), 827 (w), 806 (vw), 769 (m, with shoulder

at 754), 712 (s), 673 (vs, with shoulders at 655 and 642), 586 (s), 555 (m) cm^{-1}. Anal. Calcd. (%) for $C_{26}H_{48}EuN_4P_2Se_2$ (788.51): C, 39.60; H, 6.14; N 7.11. Found: C, 38.47; H, 6.00; N, 6.51.

Bis(1-(bis(dimethylamino)phosphinotelluroyl)-2,3,4,5-tetramethylcyclopentadienyl)europium(II) (4.1Te). Following GP1, 50 mg (0.153 mmol) $[Eu(BH_4)_2(THF)_2]$ and 125 mg (0.307 mmol) **KCp#PTe** gave the title compound as an orange powder or dark orange crystals (109 mg, 80% yield). IR: $\tilde{\nu}$ = 3003 (vw), 2979 (vw), 2964 (vw), 2912 (vw), 2885 (w, with shoulder at 2864), 2841 (vw), 2796 (vw), 2723 (vw), 1674 (vw), 1635 (vw), 1595 (vw), 1495 (vw, with shoulder at 1504), 1481 (vw), 1441 (w, with shoulder at 1452), 1431 (w), 1408 (vw), 1402 (vw), 1375 (w, with shoulder at 1385), 1359 (vw), 1302 (m), 1273 (m), 1217 (vw), 1169 (m, with shoulder at 1180), 1142 (w), 1099 (vw), 1085 (vw), 1059 (w), 1020 (vw), 962 (vs), 895 (vw), 825 (w), 806 (vw), 768 (m), 752 (vw), 708 (m), 685 (vw), 663 (vs), 579 (ms), 544 (s) cm^{-1}. Anal. Calcd. (%) for $C_{26}H_{48}EuN_4P_2Te_2$ (885.81): C, 35.25; H, 5.46; N 6.33. Found: C, 35.57; H, 5.66; N, 6.14.

Notes on the synthesis of $H^{bdp}Cp^{\#}$

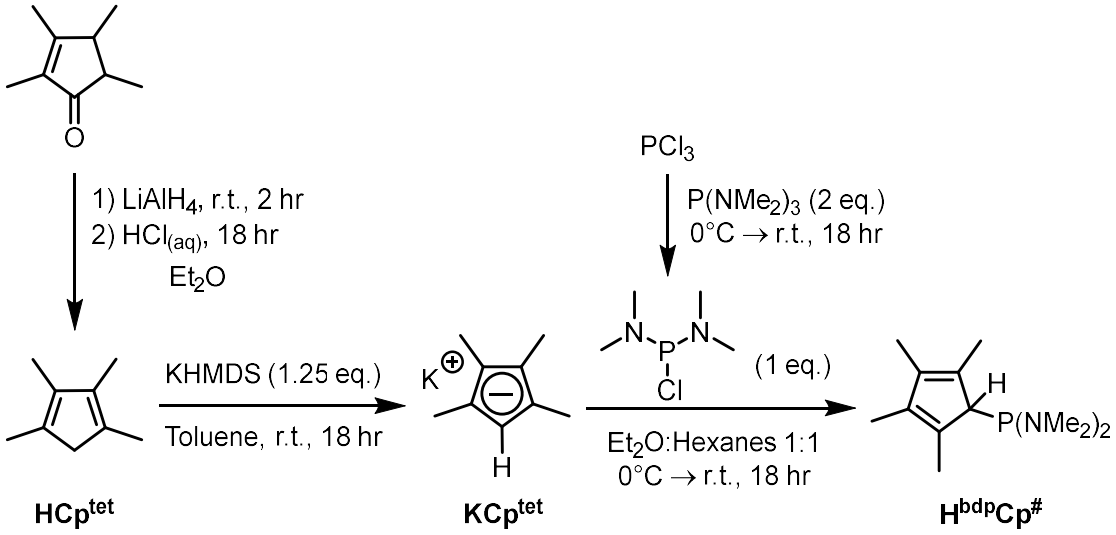


Figure 4.35. Reaction scheme for the synthesis of $H^{bdp}Cp^{\#}$.

We initially used commercial HCp^{tet} (Sigma-Aldrich 424471, 85% technical grade) and bis(dimethylamino)chlorophosphine (Sigma-Aldrich 750654, 96%, which is discontinued as of the time of writing) as received in this protocol. However, it should be noted that the best results are obtained in the syntheses of proligands **KCp#PCh** when the purity of all precursors is as high as possible. For this reason, reagents were prepared and purified as follows:

Lithium aluminum hydride[350] was extracted into dry diethyl ether in a nitrogen-filled glovebox. The cloudy grey suspension was filtered over Celite to give a clear, colourless solution, which was evaporated to give a hard white solid residue that was pulverized and dried in vacuo at 60 °C for 3 hr. ***DANGER:*** lithium aluminum hydride purified in this manner is EXTREMELY reactive with water and highly pyrophoric; it should always be stored in a glovebox and handled only under rigorously anhydrous conditions.

Phosphorus trichloride[350] (Thermo Scientific AA44436) was refluxed for 2 hr under an atmosphere of argon and then distilled under argon to give a clear, colourless liquid devoid of impurities by ^{31}P NMR spectroscopic analysis. It was stored under argon in a Schlenk storage flask.

Hexamethylphosphorous triamide[350] (tris(dimethylamino)phosphine, Thermo Scientific A12571) was distilled *in vacuo* with gentle heating (ca. 50 °C) to give a clear, colourless liquid devoid of impurities by ^{31}P NMR spectroscopic analysis. It was stored under argon in a Schlenk storage flask.

2,3,4,5-tetramethylcyclopenten-2-one (Thermo Scientific L09617) was dried over activated 4 Å molecular sieves for 48 hr, then distilled *in vacuo* to give a clear, colourless liquid devoid of impurities by ^{1}H NMR spectroscopic analysis. It was stored under argon in a Schlenk storage flask.

Bis(dimethylamino)chlorophosphine was synthesized according to modified literature procedures[351–353] as follows: under an atmosphere of argon, a Schlenk flask was charged with phosphorus trichloride (5.7 mL, 65 mmol, 1 eq.) and a stir bar and cooled to 0 °C using an ice bath. With stirring, tris(dimethylamino)phosphine (21.2 g, 130 mmol, 2 eq.) was added slowly via syringe. White fumes evolved above the liquid as the addition proceeded. The mixture was allowed to warm to room temperature with stirring overnight, giving a clear, colourless liquid which fumes in air. An aliquot of this mixture was analysed by ^{1}H and ^{31}P NMR spectroscopy and found to contain pure bis(dimethylamino)chlorophosphine (29.6 g, quant. yield), which was cannulated into a Schlenk storage flask and used without further purification. It is indefinitely stable under inert conditions, but even fleeting exposure to air and moisture when dispensing from the storage vessel is enough to cause a yellowing of the material over time; it should be redistilled when significantly deteriorated.

HCp^{tet} was prepared according to a reported procedure[354] and distilled *in vacuo* to give a yellowish oil. This material can be successfully used in this synthesis, but purification via chromatography on silica, eluting with an alkane (R_f = 0.91 in 20/80 Et_2O/hexanes), is probably preferred.

The commercial reagents originally employed in this protocol (and sometimes HCp^{tet} synthesized by us) tended to be yellow in colour rather than colourless as expected. The impurities giving rise to these yellow colours often carried through the protocol, leaving variably yellow coloured, rather than colourless, H^{bdp}Cp$^{\#}$. The yellow impurity has the same solubility as H^{bdp}Cp$^{\#}$ (i.e. highly soluble in alkanes even at low temperature), meaning it cannot be washed out of the product, even if the product is recrystallized. H^{bdp}Cp$^{\#}$ containing this yellow impurity can still be carried forward to the synthesis of **KCp$^{\#}$PCh**, and in the case of **KCp$^{\#}$PS**, is washed out during the workup and does not affect the final product. However, **KCp$^{\#}$PSe** and **KCp$^{\#}$PTe** synthesized using discoloured H^{bdp}Cp$^{\#}$ were noticeably discoloured compared to the same materials synthesized using colourless H^{bdp}Cp$^{\#}$ made from purified precursors, despite appearing pure via NMR spectroscopic analysis. Furthermore, the Eu complexes **4.1Se** and **4.1Te** prepared from discoloured **KCp$^{\#}$PSe** or **KCp$^{\#}$PTe** were also irreparably discoloured. Therefore, to prevent potential interference to optical measurements, it is crucial that **KCp$^{\#}$PCh** be synthesized from highly pure H^{bdp}Cp$^{\#}$.

The product obtained from the reported synthesis[227,270] of H^{bdp}Cp$^{\#}$ is a crystalline solid, and more specifically, is the 2,4-diene isomer which is the kinetic product of the reaction.[227] We found that discoloured H^{bdp}Cp$^{\#}$ could be purified fairly conveniently under inert conditions by filtration over a plug of activated alumina, eluted with pentane. Although this is a very effective method of removing the yellow impurities, we found

that the evaporated eluent gave a mixture of colourless solid and colourless oil. Further investigation concluded that contact with alumina and prolonged time in solution causes the cyclopentadiene to isomerize such that the product obtained from the alumina plug is mostly (ca. 75%) the thermodynamically favoured 1,3-diene isomer. Fortunately, both the 2,4- and 1,3-isomers have essentially identical reactivity toward deprotonation, unlike e.g. bis(diphenylphosphino)tetramethylcyclopentadiene, whose thermodynamic 1,3-isomer was demonstrated to react extremely slowly *cf.* the kinetic 2,4-isomer.[227]

Endnotes

[i]. A search of the Cambridge Structural Database for the terms "europium" and "cyclopentadienyl" returned 80 hits, from which 27 structures were selected for comparison that contained metallocene-like cyclopentadienyleuropium(II) structural motifs where the cyclopentadienyl ligands were fully substituted. The Eu-Cp(cent) distances among this population ranged from 2.49–2.68 Å, with an average value of 2.56 Å and standard deviation 0.04 Å. A list of structures used in this analysis is included in Appendix C.

[ii]. A subset of the above population was selected for this comparison, excluding linear metallocenes and any complex bearing a polyhapto ligand other than a fully substituted cyclopentadienide (nine structures were excluded based on these criteria).

[iii]. (a) A search of the Cambridge Structural Database for the fragment "Eu-[any bond]-S" returned 91 hits, from which 17 structures were selected for comparison that contained Eu in oxidation state II. The Eu-S distances among this population ranged from 2.80-3.37 Å, with an average value of 3.03 Å and standard deviation 0.09 Å. A list of structures used in this analysis is included in Appendix C. (b) A search of the Cambridge Structural Database for the fragment "Eu-[any bond]-Se" returned 21 hits, from which 8 structures were selected for comparison that contained Eu in oxidation state II. The Eu-Se distances among this population ranged from 3.06-3.35 Å, with an average value of 3.16 Å and standard deviation 0.08 Å. (c) A search of the Cambridge Structural Database for the fragment "Eu-[any bond]-Te" returned 8 hits, and it is interesting to note that all crystallographically characterized Eu-Te contacts to date are in complexes of Eu^{II}. The Eu-Te distances ranged from 3.16-3.52 Å, with an average value of 3.33 Å and standard deviation 0.09 Å. A list of structures used in this analysis is included in Appendix C.

[iv]. (a) for tris(dimethylamino)phosphine sulfide, CSD refcode NAHWUO (*Acta. Chem. Scand.* 1996, *50*, 759–744; (b) for 1,1'-bis(bis(dimethylamino(phosphinothioyl))ferrocene, CSD refcode ORIYAQ ([293]).

[v]. (a) for tris(dimethylamino)phosphine selenide, CSD refcode DMAPSE (*Acta. Chem. Scand.* 1979, *33*, 187–197; (b) for 1,1'-bis(bis(dimethylamino(phosphinoselenoyl))ferrocene, CSD refcode ORIXUJ ([293]).

[vi]. for tris(pyrrolidino)phosphine telluride, CSD refcode COJFUC, *Acta. Chem. Scand.* 1984, *38*, 349–357.

[vii]. for bis(hexamethylthiophosphoramido)sulfonium bis(tribromide), CSD refcode HOJMAU (*J. Chem. Soc. Dalton Trans.* 1999, 2225–2230).

[viii]. for tris(dimethylamino)phosphaneselenide)iodine(I) triiodide, CSD refcode RIJQAC (*Acta. Chem. Scand.* 1997, *51*, 689–708).

[ix]. average distance in bis(tri-*tert*-butylphosphine)tritellurium bis(hexafluoroantimonate), CSD refcode FIWDEU (*Chem. Commun.* 1987, 1257–1258).

[x]. A search of the Cambridge Structural Database for the fragment "P-Te-[any metal] returned 87 hits, 15 of which were excluded that were duplicate structures or did not contain a formally P^{V}-Te-M motif. The P-Te distances among the remaining 72 structures ranged from 2.383–2.509 Å, with an average value of 2.44 Å and standard deviation 0.03 Å. A list of structures used in this analysis is included in Appendix C.

[xi]. The analyses were performed on complexes of any metal bearing a (diaminophosphino-chalcogenoyl)cyclopentadienyl ligand. A list of structures used in this analysis is included in Appendix C. The P-N distances fall within the expected range described in ref. [315] and have an average value of

1.66 Å with standard deviation 0.02 Å. The P-C(Cp) distances are rather consistent and range from 1.74-1.80 Å, with an average value of 1.78 Å and standard deviation 0.01 Å.

[xii]. It should be noted that this equation has no physical significance; it is only used to provide a fit for Δ.

CHAPTER 5
Concluding Remarks and Future Directions

5.1 Organoeuropium(II) complexes as optical thermometers

Ever since the discovery of ferrocene, organometallic complexes have been pushing the boundaries of chemical synthesis and challenging the paradigms of chemical structure, bonding, and properties. The work presented in this thesis investigates a series of discrete molecular, organometallic complexes of Eu^{II}, which display thermosensitive (magneto-)optical properties that can be leveraged for optical thermometry. The field of optical thermometry with Eu^{II}-based materials has been saturated with doped inorganic solids and thermometers operating on the LIR principle, with a distinct lack of molecular systems and thermometers operating *via* other approaches, such as temperature-induced band-shift. The goal of our studies was to uncover previously unexplored Eu^{II}-based molecular systems with thermochromic luminescence, exploiting the highly environment-sensitive nature of the $4f^6 5d^1 \rightarrow 4f^7$ transition that characterizes this ion for non-LIR optical thermometry.

After having identified $[Eu^{II}(BH_4)_2(THF)_2]$ as an optimal starting material for the preparation of new luminescent materials, in Chapter 2 we studied its temperature-dependent luminescence. Gratifyingly, we discovered that this simple Ln^{II} starting material, in addition to all of its existing favourable properties, also exhibits substantial temperature-induced band-shift (1178 cm^{-1} from 30-320 K), to the point where it already lands among the best-performing band-shift thermometers reported to date (having a maximum S_a of 5.37 cm^{-1} K^{-1} at 220 K with a ΔT as low as ~0.02 K). The observable colour shift from cyan to green is distinctive, and this result further validates the concept that borohydride-based coordination environments are well-positioned to yield luminophores with emission characteristics that vary significantly with changes in their surroundings. More importantly, substituting 1 eq. of borohydride ligands with Cp* yields the hemimetallocene dimer $[Cp^*Eu(\mu\text{-}BH_4)(THF)_2]_2$ (complex **2.1**), a modification which shifts the emission towards red and improves the S_a by 53% (to 8.2 cm^{-1} K^{-1} at 320 K with a ΔT as low as 0.09 K), yielding the highest-performing lanthanide-based band shift thermometer to date. A careful comparison of structural metrics as a function of temperature in this complex, and correlation to emission properties, revealed how small structural distortions, including as minor a modification as substitution of deuterium for protium, could have a large effect on the luminescence. These findings clearly demonstrated the concept that organometallic Eu^{II}-based systems can behave as excellent optical thermometers.

Following that discovery, we continued to study how the emission characteristics of Eu^{II} hemimetallocenes could be modified and controlled. To this end, in Chapter 3 we undertook the synthesis and (opto-)structural characterization of seven novel Eu^{II} hemimetallocenes $[Cp^REu(\mu\text{-}BH_4)(solv)_n]_m$ (solv = THF, DME; n = 1 or 2; m = 2 or ∞) (complexes **3.1**-**3.7**) bearing systematically varying ligand sets. Among these isostructural complexes, we observed a remarkable variability in luminescence behaviour despite sometimes minor substitutional changes, which translated to a similarly wide range of thermometric performances. As in Chapter 2, a detailed analysis of temperature-dependent metrical parameters and correlation to emission properties in complexes **3.1**-**3.4** and **3.6** revealed a complex relationship between structure and luminescence; a metrical parameter that correlated with emission behaviour in one complex did not always affect the others in the same way. We were, however, able to identify a few factors of particular influence, including the donor strength of the cyclopentadienyl ligand, the Eu-basal plane distance in their square-pyramidal coordination polyhedra, the intramolecular Eu-Eu distance, and the metal-ligand flexibility of the construct. Although we were ultimately unsuccessful in identifying a system

which improved upon the performance demonstrated by **2.1**, we nevertheless showed that Eu^{II} hemimetallocenes are a highly tunable family of complexes well worth further exploration.

Finally, the work discussed in Chapter 3 identified a standout substituted cyclopentadienyl moiety, the bis(dimethylamino)phosphino-substituted $^{bdp}Cp^{\#}$, whose hemimetallocene **3.4** demonstrated very good thermometric performance and which we envisioned could be further elaborated by oxidation with chalcogens. Additionally, this was an opportunity to study heavy-atom effects, as the aminophosphine fragment is well-suited to stabilizing the usually unstable heavy phosphine chalcogenides. Hence, in Chapter 4, we discussed the synthesis and characterization of a new family of (bis(dimethylamino)phosphinochalcogenoyl)cyclopentadienides [$\mathbf{Cp^{\#}PCh}$]$^-$ (Ch = S, Se, Te), which can be smoothly synthesized on gram scale in excellent yields by oxidation of $H^{bdp}Cp^{\#}$ with elemental S, Se, or Te. When exploring the coordination chemistry of these new ligands with Eu^{II}, we were surprised to find that they subverted the usual propensities of a) lanthanides to favour saturating themselves with O-donor solvent ligands and b) lanthanide borohydrides to allow stepwise substitution of their borohydride ligands to make heteroleptic complexes. What ensued were a series of homoleptic europocenes(II) featuring these ligands (complexes **4.1Ch**), in which Eu bound the pendant phosphinochalcogenoyl arms as well as the η^5-cyclopentadienide. We investigated them for band-shift thermometry and found them to be either poorly performing (**4.1S**), not thermochromic (**4.1Se**), or not emissive at all (**4.1Te**). However, we also investigated their temperature-dependent MCD spectra and found that they are extremely sensitive cryogenic magneto-optical thermometers, with relative sensitivities reaching 170% K^{-1} at ultralow temperatures inaccessible to conventional luminescence thermometry. These results further develop our seminal work on MCD thermometry[336] and also further cement organoeuropium(II) complexes as excellent candidates for optical thermometry systems, via approaches that are understudied for lanthanide-based materials.

5.2 Future directions

Although the thermometric performance of Eu^{II}-based systems is demonstrably impressive, and further research into Eu^{II}-based luminescence thermometers is already expanding,[272] the air- and moisture-sensitivity of such materials, especially in discrete molecular form, is currently their most major limitation. This is exacerbated when considering our finding that a high degree of metal-ligand flexibility tends to produce better thermometric performance. Increasing metal-ligand flexibility usually means moving to lower coordination numbers or reducing steric encumbrance, both of which necessarily decrease the degree of protection that an easily oxidized metal center such as Eu^{II} experiences. It is therefore a formidable synthetic (and kinetic, and thermodynamic) challenge to produce complexes of this nature that are both flexible and stable, but this is the clear path forward both to improving performance and realizing broader applications. There already exist air-stable Eu^{II} complexes, for example, bound by bespoke tris(pyrazolyl)borates[57,85] or by crown ether and cryptand-type ligands.[66,71] Although bulky tris(pyrazolyl)borates and small encapsulating ethers may not be expected to engender high-performance thermometers with Eu^{II} on account of having rather inflexible coordination spheres, flexible macrocycles might indeed be a means of addressing this challenge. To that end, a promising candidate family that warrants further investigation are the "mausolate" ligands of Berg and co-workers (Figure 5.1).[355] These are in fact a direct confluence of a tris(pyrazolyl)borate and a cryptand, have already been shown to be ambident ligands for various cations including lanthanides,[355,356] and can produce complexes with unusual interelement bonding.[357] However, this approach would require the "equatorial" pyridine groups of the construct to be substituted for something else, as pyridine is a known quencher of the Eu^{II} $d \rightarrow f$ emission.[70] In keeping with the theme of organometallic systems, N-heterocyclic carbenes (NHCs) and their many derivatives might be choice moieties for the next generation of organometallic Eu^{II} optical thermometers.

These concepts could even be combined, as an NHC-based fragment would be a potential replacement for the pyridine, and/or a tris(imidazolylidene)borate or related carbene-based scorpionate[358,359] could be used in place of the tris(pyrazolyl)borate component, in a mausolate architecture.

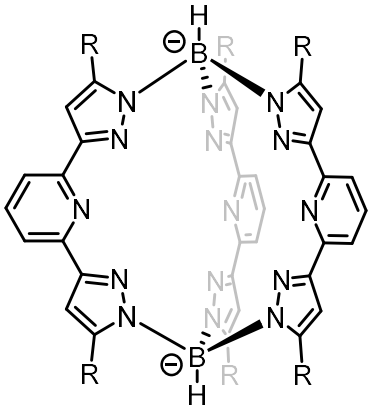


Figure 5.1. Chemical structure of the "mausolate" dianion.[355]

Interest in the areas of molecular (opto)electronics[360,361] and quantum devices is burgeoning, thus a variety of practical applications for these materials can also be imagined. Molecular systems based on Eu^{II} have already demonstrated utility as emitters for OLEDs[43,71,81,84,85,214,216] and as qubits.[268] Organometallic Eu^{II}-based complexes such as ours might therefore be envisioned as spintronic components with the valuable ability to report their own temperature; onboard thermal sensors for molecular electronic circuitry requiring nanometric resolution; thermochromic phosphors for sensing and lighting applications, and so on. The aforementioned limitations due to air- and moisture-sensitivity can nevertheless be reasonably circumvented if the device of interest is fully encapsulated. The redox behaviour of Eu might also potentially be harnessed, e.g. as part of a molecular capacitor that indicates its charge state via luminescence.[360] There is also a huge potential for bioimaging applications with a suitable Eu^{II} complex stable under ambient conditions. The applicability of Eu^{II} as a contrast agent for magnetic resonance imaging due to its strong paramagnetism,[362] as well as its environment-sensitive luminescence, means that there is a possibility to realize multimodal magnetic resonance and luminescence imaging with simultaneous temperature readout. The technology is nascent, and we anticipate a continued advancement of the fundamental understanding of this promising class of material with application-focused intent.

APPENDIX A
Corresponding to Chapter 2

A.1 Nuclear magnetic resonance spectra

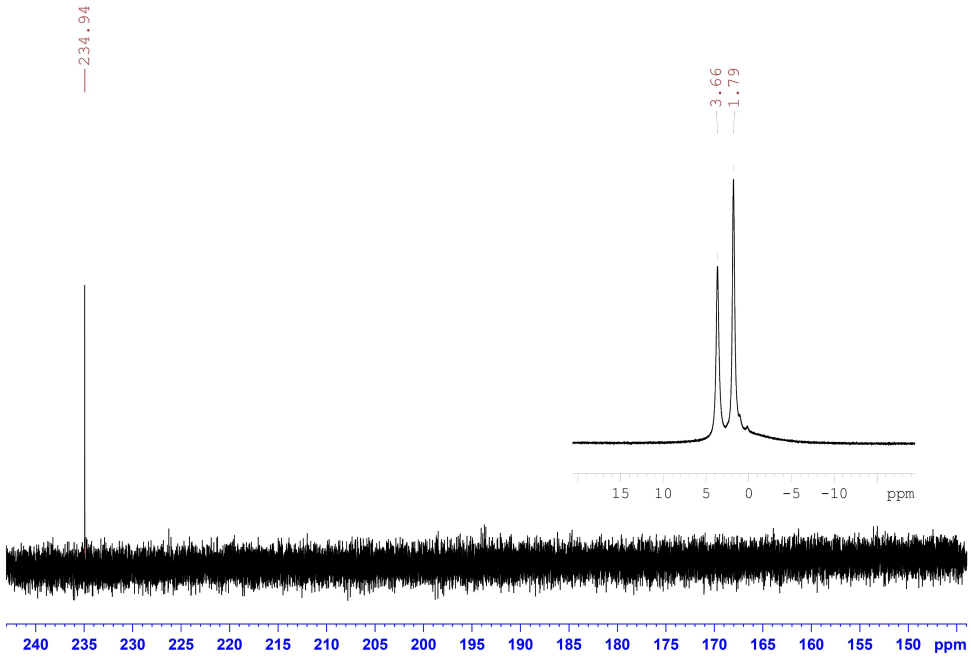


Figure A1. ^{1}H NMR spectrum of complex **2.1** in THF-d_8. Note the extremely downfield-shifted resonance ascribable to the Cp* methyl substituents, in addition to the resonances at 3.66 and 1.79 ppm that are attributable to THF. Residual THF and coordinated THF are indistinguishable due to the broadness of the resonances.

A.2 Electronic structure calculations

Calculations have been carried out using the ORCA 4.1 program package on the crystal structure of **2.1** at 203.15 K. Energies and corresponding spin densities have been computed with the B3LYP functional and def2-TZVP basis set on Eu^{II} and def2-SVP for the rest of the molecule. The exchange interaction has been computed using the broken-symmetry approach. The broken-symmetry solution is an open-shell singlet state, which corresponds to a spin flip on one of the sites. The exchange coupling constant (J) is then computed as

$$J = -\frac{E_{HS} - E_{BS}}{\langle S^2 \rangle_{HS} - \langle S^2 \rangle_{BS}} \tag{C.1}$$

where E_{HS} and $\langle S^2 \rangle_{HS}$ are the energy and the expectation value of the squared spin operator of the maximum multiplicity state; E_{BS} is the energy of the open-shell singlet; and $\langle S^2 \rangle_{BS}$ its non-zero expectation value. This approach assumes the $\mathcal{H} = -2JS_1S_2$ Hamiltonian. Zero-field splitting (ZFS) and the *g*-tensor, as well as the energies of the *f-f* transitions, were calculated with OpenMolcas v19 with all-electron relativistic basis sets ANO-RCC-VTZP on lanthanides and ANO-RCC-VDZ for the rest of the

molecule. One of the Eu^{II} ions was substituted by a diamagnetic Yb^{II} ion. The active space consists of seven 4*f*-orbitals with 7 electrons. 1 octet, 48 sextet and 392 quartet states were calculated and mixed via spin-orbit coupling with the RASSI module.

The exchange coupling was found to be ferromagnetic, $\boldsymbol{J = +0.06\ cm^{-1}}$, that agrees well with the experimentally extracted parameter of 0.04 cm^{-1}.

S(High-Spin) = 7.0
<S**2>(High-Spin) = 56.0169
<S**2>(BrokenSym) = 7.0168
E(High-Spin) = -3182.058714 E_h
E(BrokenSym) = -3182.058701 E_h

The spin density plot shows an almost spherical spin distribution about each Eu^{II} site, characteristic for the half-filled *f*-shell. There is almost no spin delocalisation onto the bridging BH_4 fragments.

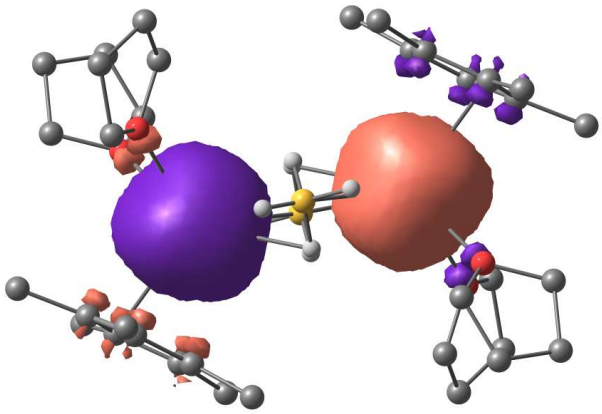


Figure A2. Spin density plot (iso-value 0.001) of the broken-symmetry solution for **2.1**.

The ZFS of the Eu^{II} octet ground state is within 1 cm^{-1}. The exact energies (in cm^{-1}) are:

0.000
0.000
0.159
0.159
0.386
0.386
0.743
0.743

and this can be described by the relatively small ZFS parameters $D = 0.0598\ cm^{-1}$ and $E = 0.0066\ cm^{-1}$. The *g*-tensor is isotropic, and the *g*-factor is 1.9972 (≅ 2.00).

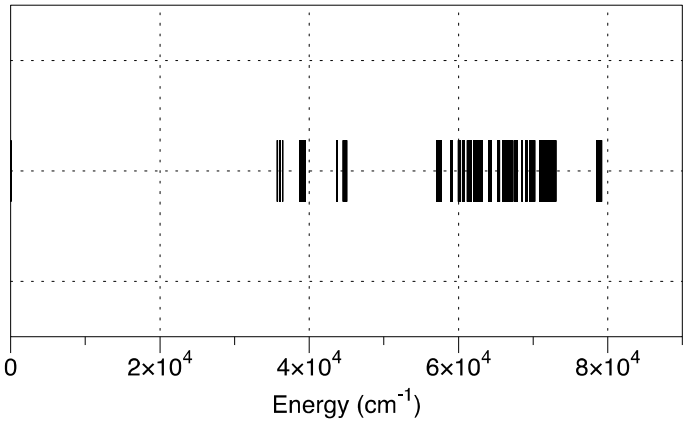


Figure A3. Computed energies of the excited states arising from *f-f* transitions in 2.1.

Ab initio ligand field calculations were performed on monomeric fragments of the 90 K and 270 K crystal structures (*vide infra*) with SOC-CASSCF(7,7)/NEVPT2 using def2-TZVP basis set for Eu and def2-SVP for the rest of the molecule. The *f*-orbital splitting and ligand field parameters are extracted based on the energy and wavefunctions of 1 octet and 48 sextet states.

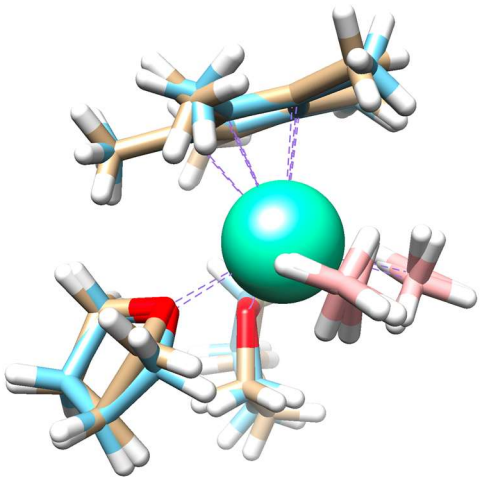


Figure A4. Comparison of the 90 K and 270 K crystal structures of a mononuclear fragment of **2.1**.

270 K ligand field parameters:

F2 = 0.398686471 a.u. = 10.849 eV = 87501.6 cm^{-1}
F4 = 0.262175443 a.u. = 7.134 eV = 57540.9 cm^{-1}
F6 = 0.186061113 a.u. = 5.063 eV = 40835.7 cm^{-1}

The ligand field one-electron eigenfunctions:

Orbital	Energy (eV)	Energy (cm^{-1})	f-3	f-2	f-1	f0	f+1	f+2	f+3
1	0.000	0.0	0.270410	0.790765	0.008013	0.351294	-0.176909	0.346090	-0.164386
2	0.004	35.5	0.428549	-0.214254	0.240480	-0.571289	-0.102834	0.531293	-0.305602
3	0.013	102.3	0.035528	0.521000	-0.228208	-0.705449	0.104280	-0.395614	0.100865
4	0.019	157.3	-0.589526	0.135966	0.154814	-0.212454	-0.245708	0.483538	0.520276
5	0.029	233.3	0.567544	-0.043216	0.348976	0.068088	-0.222140	-0.215457	0.673675
6	0.038	310.2	0.007398	0.134945	0.390450	0.034509	0.884770	0.160460	0.139743
7	0.048	389.3	0.268812	-0.137042	-0.769301	0.039991	0.233918	0.368050	0.354059

90 K ligand field parameters:

F2 = 0.398940993 a.u. = 10.856 eV = 87557.4 cm^{-1}
F4 = 0.262619569 a.u. = 7.146 eV = 57638.3 cm^{-1}
F6 = 0.186198988 a.u. = 5.067 eV = 40866.0 cm^{-1}

The ligand field one electron eigenfunctions:

Orbital	Energy (eV)	Energy (cm^{-1})	f-3	f-2	f-1	f0	f+1	f+2	f+3
1	0.000	0.0	-0.413362	-0.719885	0.003531	-0.161426	0.181931	-0.443433	0.234725
2	0.008	65.1	-0.331818	0.387737	-0.331091	0.637455	0.066340	-0.431596	0.181416
3	0.012	94.8	-0.078206	-0.434326	0.216702	0.679037	-0.136765	0.520968	0.084156
4	0.022	179.0	-0.527007	0.270000	0.049019	-0.307912	-0.287688	0.356941	0.584791
5	0.031	251.8	0.630161	-0.016727	0.168905	0.077971	-0.020887	-0.213430	0.722510
6	0.042	340.4	-0.156983	0.243054	0.598420	0.038706	0.741924	0.068005	0.040009
7	0.050	404.8	0.115888	-0.102629	-0.674069	-0.064145	0.556905	0.410002	0.198265

The ligand field parameters are very similar for both geometries (the same within the accuracy of the *ab initio* ligand field fitting).

A.2 Photoluminescence

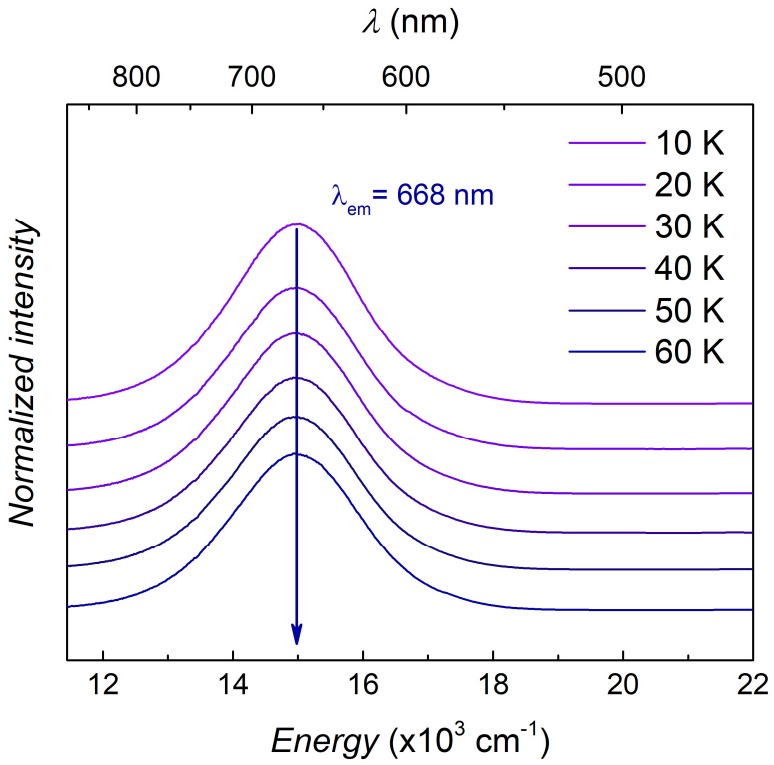


Figure A5. Solid-state emission spectra of crystalline **2.1** (λ_{ex} = 330 nm) obtained in the 10-60 K range. Note that the emission peak energy remains constant over this temperature range.

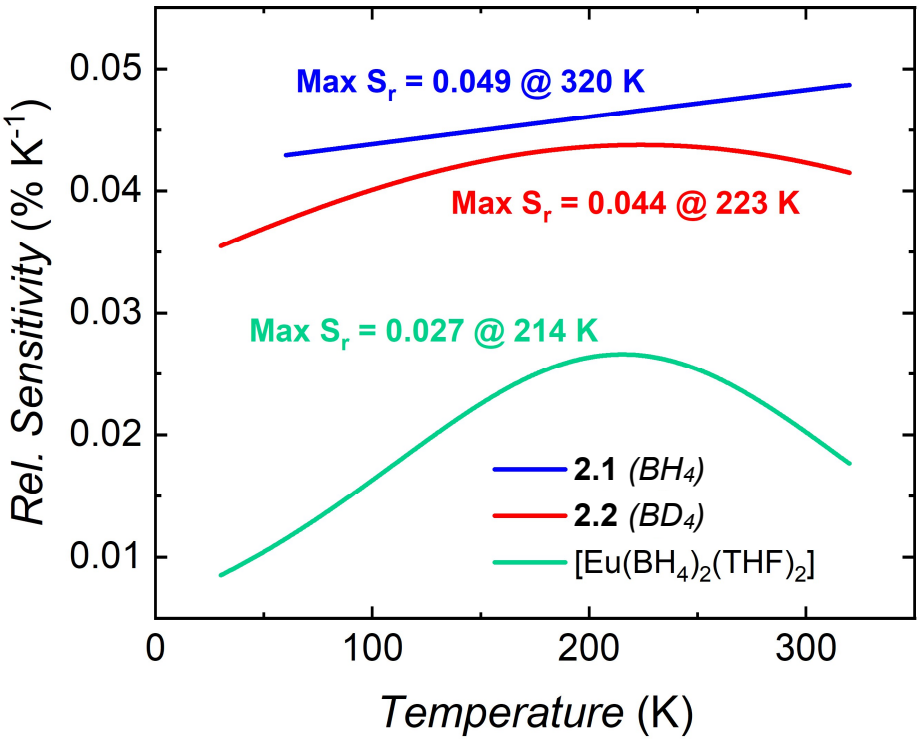


Figure A6. Relative sensitivities for **2.1**, **2.2**, and $[Eu^{II}(BH_4)_2(THF)_2]$. Relative sensitivities were calculated with the equation: S_r (%) = [(∂*Peak position* / ∂*T*) / *Peak position*] x 100.

A.3 Crystallographic information

	2.1	**2.2**	**2.1 (VT 90 K)**
CCDC deposition no.	2107457	2126609	210458
Temperature (K)	203	203	90
Empirical formula	$C_{36}H_{70}B_2Eu_2O_4$	$C_{36}H_{62}D_8B_2Eu_2O_4$	$C_{36}H_{70}B_2Eu_2O_4$
Formula weight (amu)	892.46	900.51	892.46
Crystal system	Monoclinic	Monoclinic	Monoclinic
Space group	$P2_1/n$	$P2_1/n$	$P2_1/n$
Unit cell dimensions (Å and °)	a = 12.1778(6)	a = 12.172(4)	a = 12.1457(9)
	b = 13.4959(7)	b = 13.562(4)	b = 13.2645(9)
	c = 13.4000(7)	c = 13.407(4)	c = 13.2504(9)
	α = 90	α = 90	α = 90
	β = 109.838(1)	β = 109.450(5)	β = 109.234(4)
	γ = 90	γ = 90	γ = 90
Volume (Å^3)	2071.6(2)	2086.90(11)	2015.6(2)
Z	2	2	2
Density (calc., g/cm^3)	1.431	1.433	1.471
Abs. coefficient (mm^{-1})	3.032	3.009	16.242
F(000)	908.0	908.0	908.0
Crystal size (mm^3)	0.330 x 0.300 x 0.240	0.410 x 0.370 x 0.300	0.180 x 0.14 x 0.11
Radiation (wavelength, Å)	Mo Kα (0.71073)	Mo Kα (0.71073)	Ga Kα (1.34139)
Theta range (°)	1.955 to 30.666	1.960 to 29.573	3.729 to 55.093
Index ranges (h,k,l)	- 17 to 17, -19 to 19, -19 to 19	-16 to 16, -18 to 18, -18 to 18	-14 to 14, -16 to 15, -16 to 14
Reflections collected	104787	37801	10258
Independent reflections	6410	5857	3725
R(int)	0.0271	0.0293	0.0544
Completeness (%) to $\theta = \sin^{-1}(0.6\lambda)$	99.9	99.9	96.8
Max. and min. transmission	0.746 and 0.632	0.746 and 0.384	0.657 and 0.299
Data / restraints / parameters	6410 / 18 / 220	5857 / 60 / 218	3725 / 467 / 310
Goodness-of-fit on F^2	1.075	1.157	1.091
R indices (all data)	R_1 = 0.0308	R_1 = 0.0455	R_1 = 0.0841
	wR_2 = 0.0568	wR_2 = 0.0927	wR_2 = 0.2234
Final R indices [$I > 2\sigma(I)$]	R_1 = 0.0226	R_1 = 0.0374	R_1 = 0.0688
	wR_2 = 0.0515	wR_2 = 0.0849	wR_2 = 0.2019
Largest diff. peak and hole (e.Å^{-3})	0.74 and -0.83	1.11 and -2.22	2.10 and -1.63

	2.1 (VT 175 K)	**2.1 (VT 200 K)**	**2.1 (VT 270 K)**
CCDC deposition no.	210459	210460	2107461
Temperature (K)	175	200	270
Empirical formula	$C_{36}H_{70}B_2Eu_2O_4$	$C_{36}H_{70}B_2Eu_2O_4$	$C_{36}H_{70}B_2Eu_2O_4$
Formula weight (amu)	892.46	892.46	892.46
Crystal system	Monoclinic	Monoclinic	Monoclinic
Space group	$P2_1/n$	$P2_1/n$	$P2_1/n$
Unit cell dimensions (Å and °)	a = 12.1622(4)	a = 12.2030(7)	a = 12.3321(7)
	b = 13.4570(4)	b = 13.4553(8)	b = 13.5012(7)
	c = 13.3393(4)	c = 13.3956(7)	c = 13.5298(7)
	α = 90	α = 90	α = 90
	β = 109.486(1)	β = 109.887(3)	β = 110.596(3)
	γ = 90	γ = 90	γ = 90
Volume (Å^3)	2058.15(11)	2068.3(2)	2108.7(2)
Z	2	2	2
Density (calc., g/cm^3)	1.440	1.433	1.406
Abs. coefficient (mm^{-1})	16.242	15.827	15.524
F(000)	908.0	908.0	908.0
Crystal size (mm^3)	0.180 x 0.14 x 0.11	0.180 x 0.140 x 0.110	0.260 x 0.200 x 0.195
Radiation (wavelength, Å)	Ga Kα (1.34139)	Ga Kα (1.34139)	Ga Kα (1.34139)
Theta range (°)	3.729 to 55.093	3.688 to 54.852	3.634 to 54.771
Index ranges (h,k,l)	-17 to 16, -18 to 18, -16 to 18	-14 to 14, -16 to 15, -14 to 16	-14 to 14, -16 to 15, -16 to 14
Reflections collected	34610	10644	10846
Independent reflections	5983	3848	3915
R(int)	0.0606	0.0488	0.0497
Completeness (%) to $\theta = \sin^{-1}(0.6\lambda)$	97.1	97.0	97.1
Max. and min. transmission	0.258 and 0.091	0.657 and 0.302	0.657 and 0.270
Data / restraints / parameters	5983 / 85 / 248	3848 / 461 / 311	3915 / 413 / 308
Goodness-of-fit on F^2	1.084	1.082	1.057
R indices (all data)	R_1 = 0.0420	R_1 = 0.0745	R_1 = 0.0837
	wR_2 = 0.1129	wR_2 = 0.1613	wR_2 = 0.2067
Final R indices [$I > 2\sigma(I)$]	R_1 = 0.0386	R_1 = 0.0585	R_1 = 0.0659
	wR_2 = 0.1093	wR_2 = 0.1829	wR_2 = 0.1818
Largest diff. peak and hole (e.Å^{-3})	1.29 and -1.35	1.04 and -1.83	1.44 and -1.54

Table A1. Selected bond lengths/interatomic distances and angles around europium of **2.1**.

Bond or Interatomic distance	Length (Å)	Entry	Angle (°)
Eu1-Cp*(cent)	2.5185(3)	Cp*(cent)-Eu1-B1	115.064(59)
Eu1-O1	2.6064(16)	B1-Eu1-O2	85.661(71)
Eu1-O2	2.6097(20)	O2-Eu1-O1	72.878(65)
Eu1-B1	2.8746(26)	O1-Eu1-Cp*(cent)	115.866(46)
Eu1-B1′	2.9389(36)	O2-Eu1-B1′	136.792(73)
Eu1-Eu1′	4.2616(5)	O1-Eu1-B1	128.736(68)

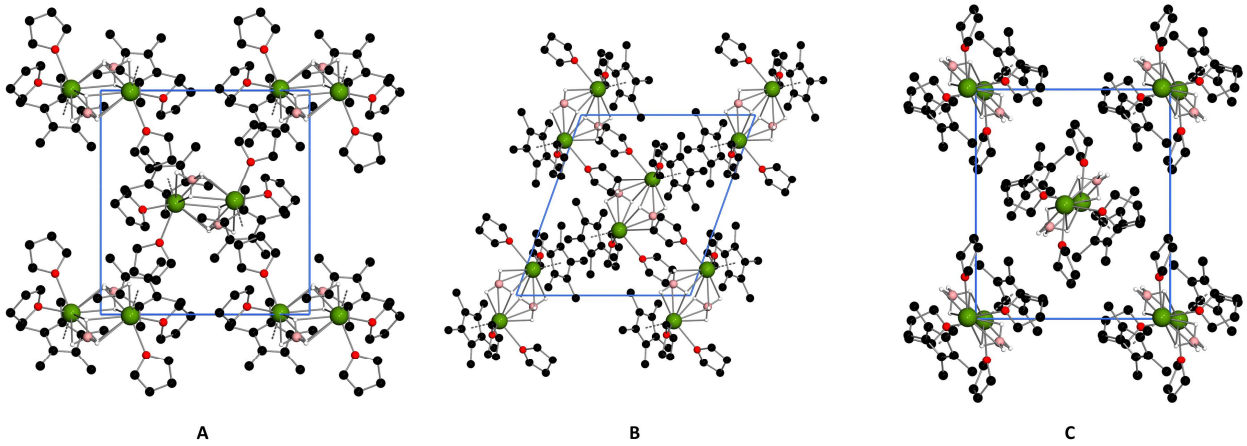


Figure A7. Crystallographic packing diagrams of **2.1**, shown along the (a) *a*-axis, (b) *b*-axis, and (c) *c*-axis of the unit cell. Hydrogen atoms bonded to carbon are omitted for clarity.

Table A2. Shape analysis of **2.1**, from the 203 K crystal structure, using SHAPE 2.1. Values in table are the continuous shape measures (dimensionless) for each idealized geometry.

Complex	Pentagon (D_{5h})	Vacant octahedron (C_{4v})	Trigonal bipyramid (D_{3h})	***Spherical square pyramid (C_{4v})***	Johnson trigonal bipyramid J12 (D_{3h})
2.1	32.724	4.752	4.856	***1.236***	8.129

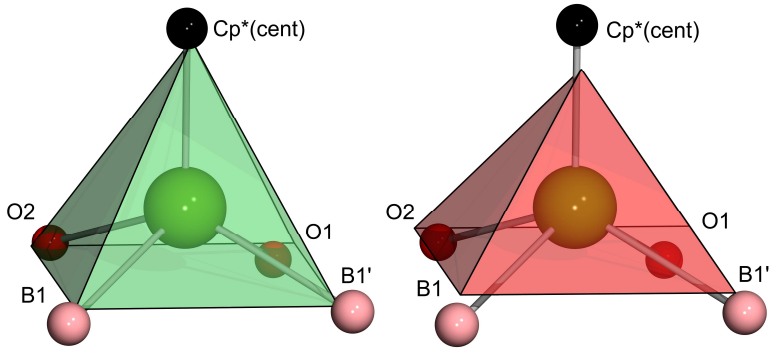


Figure A8. *Left:* comparison of the idealized square pyramidal geometry (green polyhedron) to the actual coordination sphere of **2.1**. *Right:* comparison of the next-best-fitting idealized geometry (vacant octahedron, red polyhedron), demonstrating the poor agreement of this model with the real structure.

A.4 Absorption spectra calculations

TD-DFT absorption spectra were calculated for the same monomeric fragments derived from the 90 K and 270 K crystal structures (Figure A4), with the B3LYP functional and def2-TZVP basis set on Eu and def2-SVP on the rest of the molecule, considering the first 50 excited states.

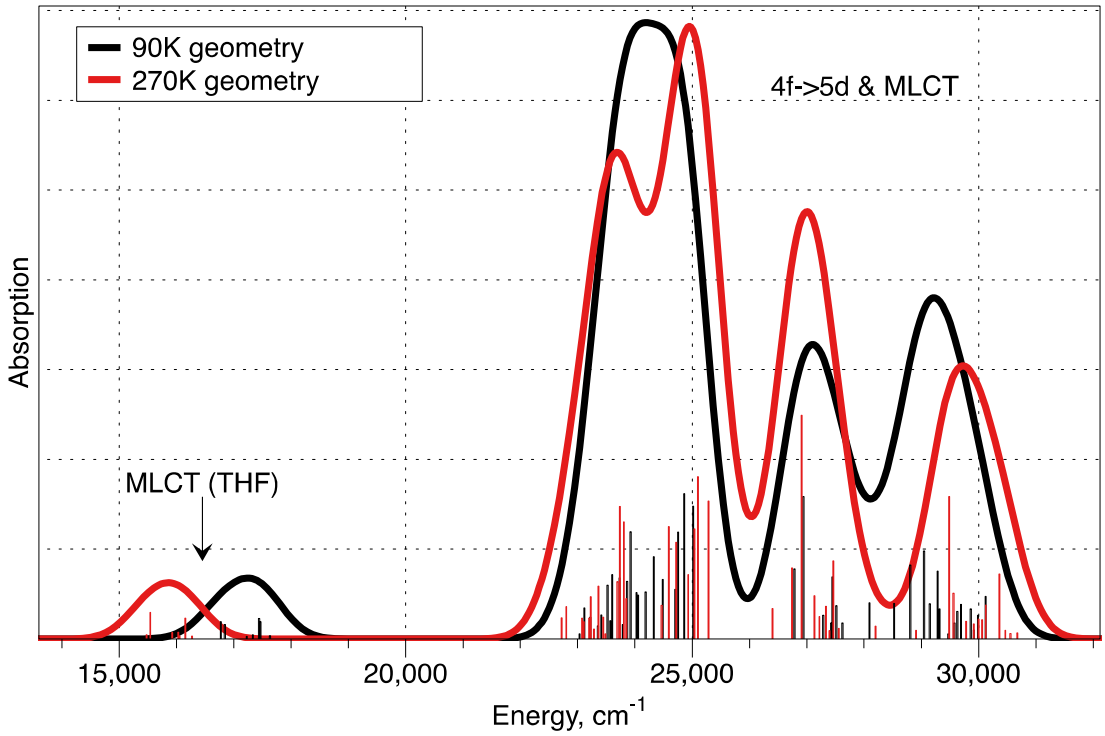
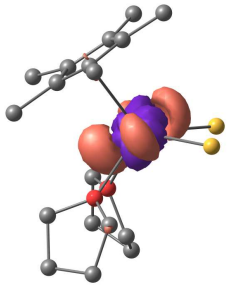
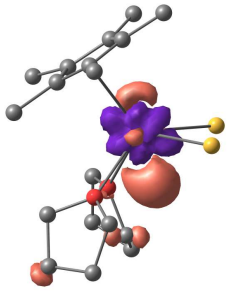
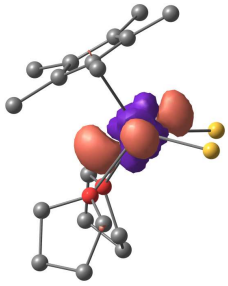
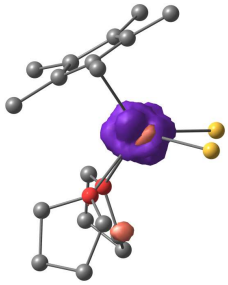
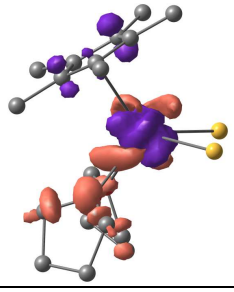


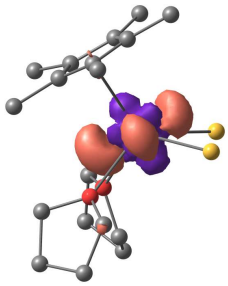
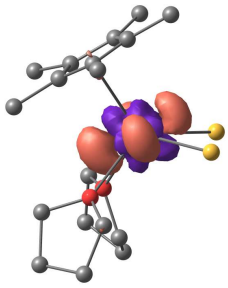
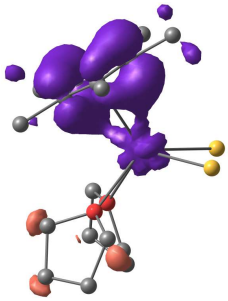
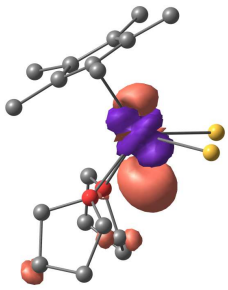
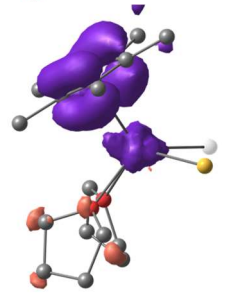
Figure A9. Computed TD-DFT absorption spectra of 2.1 calculated based on the crystal structures at 90 K (black) and 270 K (red). The bars represent vertical electronic transitions, and the envelope is obtained with 1000 cm^{-1} Gaussian broadening.

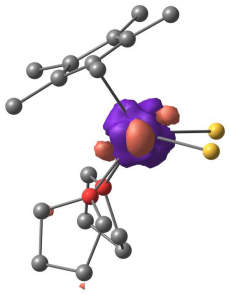
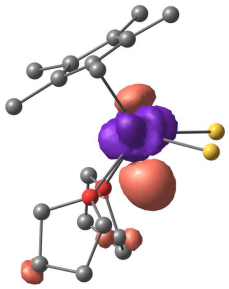
Small changes in the structure caused by the temperature increase seem to affect the low-lying metal to ligand (THF) charge transfer band (15000-17000 cm^{-1}) the most, by shifting it ~1500 cm^{-1} to lower energy. Meanwhile, the 4*f*-5*d* bands (some of which are coupled with the MLCT band) exhibit much smaller shifts of ~500 cm^{-1} to higher energies, accompanied by small changes in intensity.

The nature of transitions with large oscillator strength were identified using the difference in electronic densities between excited and ground states.

Table A3. TD-DFT (B3LYP) calculated vertical excitations for the first 50 electronic transitions, with the corresponding oscillator strength and difference densities of **2.1** (truncated structure) measured at 90 K (isovalue 0.003). Transitions are sorted by their oscillator strength.

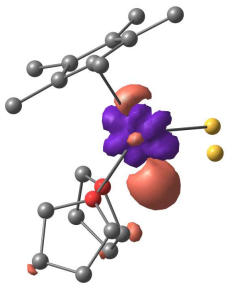
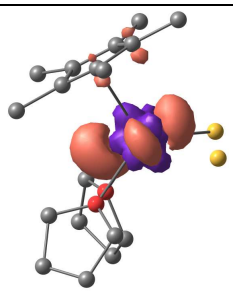
Excited state	Energy (cm^{-1})	Oscillator strength $x10^{-3}$	Difference density	Assignment
27	24 862	1.49		*4f-5d*
30	26 943	1.46		*4f-5d* + MLCT
28	25 019	1.36		*4f-5d*
19	23 925	1.10		MLCT+*4f-5d*
26	24 753	1.10		CT+ *4f-5d*

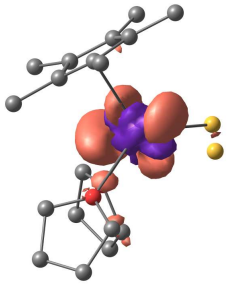
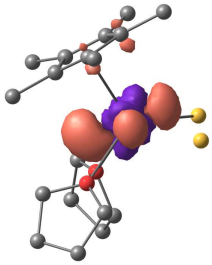
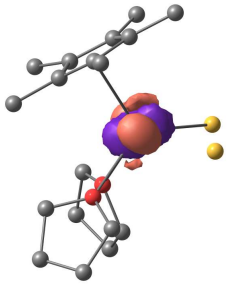
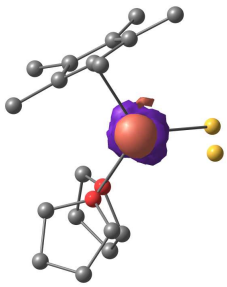
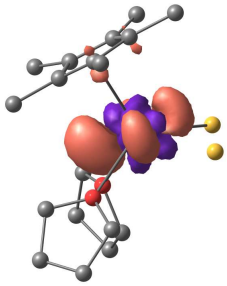
39	29 046	0.902		*4f-5d*
23	24 331	0.846		*4f-5d*
38	28 808	0.758		intraligand +MLCT
29	26 783	0.720		*4f-5d*+MLCT
41	29 282	0.697		intraligand +MLCT

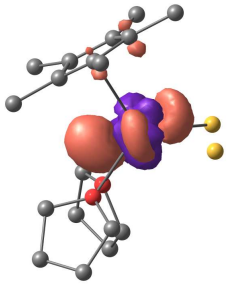
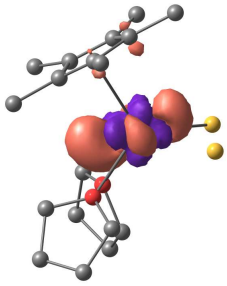
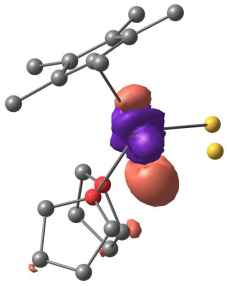
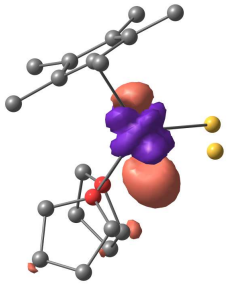
15	23 602	0.662		*4f-5d*
33	27 446	0.636		*4d-5d*+MLCT
16	23 732	0.629		
24	24 489	0.609		
18	23 863	0.592		
13	23 522	0.552		
25	24 706	0.511		
22	24 188	0.482		
20	24 029	0.476		
21	24 054	0.450		
50	30 120	0.436		
36	28 093	0.370		
37	28 523	0.364		
40	29 147	0.362		
46	29 689	0.356		
34	27 517	0.341		
9	23 120	0.317		
42	29 319	0.309		
47	29 861	0.308		
45	29 628	0.282		
12	23 413	0.247		
31	27 287	0.244		
49	29 988	0.244		

10	23 221	0.223
5	17 441	0.211
14	23 572	0.188
6	17 464	0.177
1	16 774	0.177
44	29 576	0.166
32	27 425	0.165
35	27 624	0.163
17	23 789	0.149
2	16 844	0.148
11	23 354	0.137
48	29 915	0.0924
8	23 032	0.0535
43	29 471	0.0524
4	17 333	0.0427
7	17 630	0.0319
3	17 225	0.0271

Table A4. TD-DFT (B3LYP) calculated vertical excitations for the first 50 electronic transitions with the corresponding oscillator strength and difference densities of **2.1** (truncated structure) measured at 270 K (isovalue 0.003). Transitions are sorted by their oscillator strength.

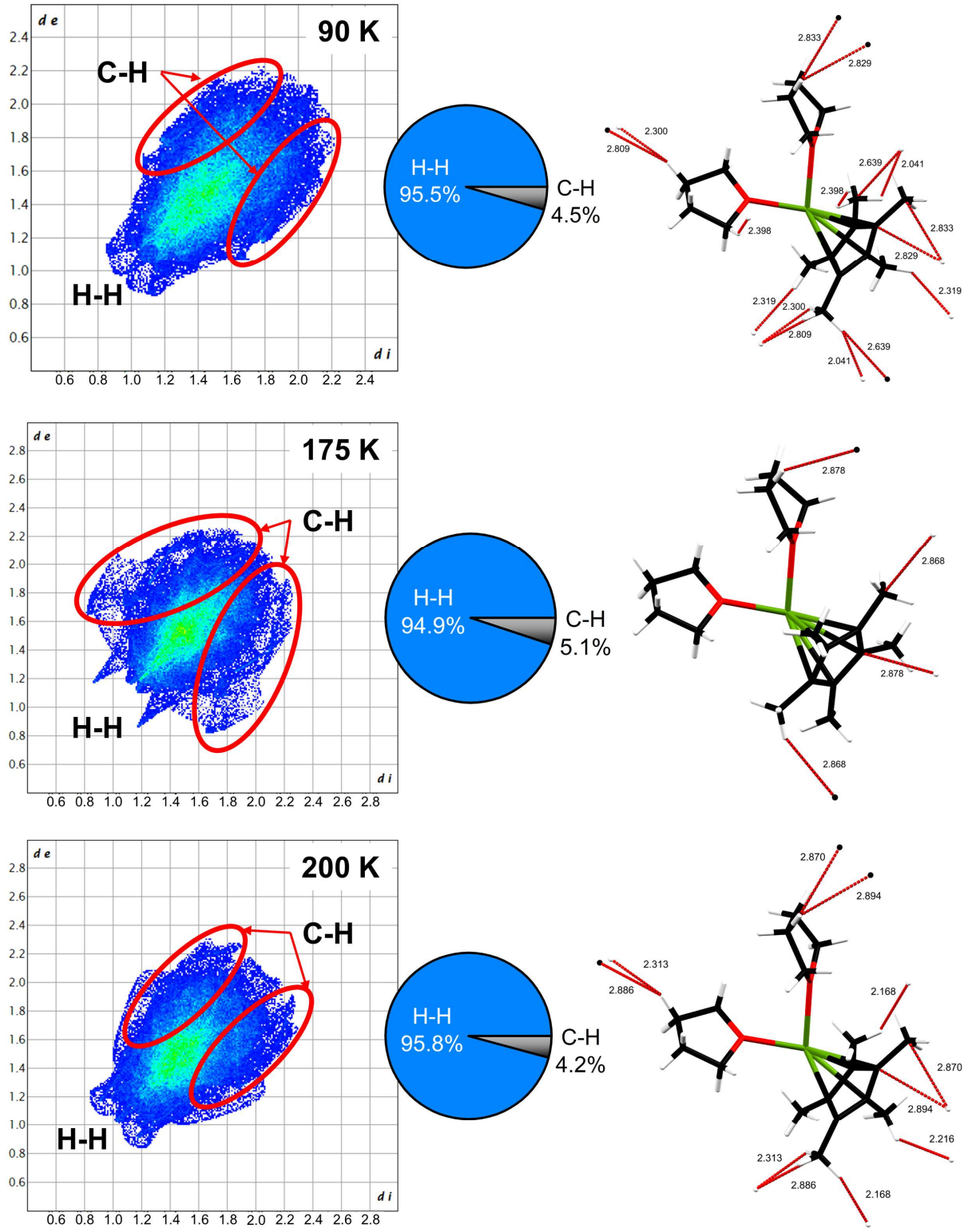
Excited state	Energy (cm^{-1})	Oscillator strength $x10^{-3}$	Difference density	Assignment
31	26 911	2.30		*4f-5d* + MLCT (THF)
27	25100	1.66E-03		*4f-5d* + MLCT (Cp*)

40	29487	1.46E-03		*4f-5d* + MLCT (THF)
28	25287	1.42E-03		*4f-5d* + MLCT (Cp*)
19	23740	1.36E-03		*4f-5d*
20	23807	1.20E-03		*4f-5d*
23	24 593	1.15		*4f-5d*

26	25 039	1.13		*4f-5d*
24	24 722	0.992		*4f-5d*
36	27 465	0.801		*4f-5d* +MLCT
30	26 741	0.731		*4f-5d* +MLCT
47	30 360	0.667		
25	24 929	0.660		
18	23 695	0.588		
15	23 364	0.544		
41	29 560	0.471		
32	27 135	0.444		
13	23 232	0.435		
21	23 851	0.412		

46	30 125	0.347
22	24 467	0.345
34	27 333	0.338
9	22 802	0.331
29	26 403	0.313
2	15 542	0.273
33	27 219	0.231
16	23 448	0.225
8	22 720	0.217
6	16 152	0.214
10	23 080	0.213
12	23 204	0.212
44	30 000	0.205
45	30 059	0.198
42	29 780	0.181
11	23 109	0.177
43	29 913	0.156
38	28 201	0.132
37	27 557	0.110
14	23 285	0.101
39	28 907	0.0912
48	30 466	0.0902
35	27 394	0.0879
4	16 031	0.0688
3	15 923	0.0666
50	30 675	0.0625
49	30 554	0.0556
17	23 485	0.0519
1	15 479	0.0450

5	16 049	0.0288
7	16 271	0.0286


d e
90 K
C-H
H-H
d i
0.6 0.8 1.0 1.2 1.4 1.6 1.8 2.0 2.2 2.4
H-H
95.5%
C-H
4.5%
2.833
2.829
2.300
2.809
2.639
2.041
2.398
2.398
2.833
2.829
2.319
2.319
2.300
2.809
2.639
2.041
d e
175 K
C-H
H-H
d i
0.6 0.8 1.0 1.2 1.4 1.6 1.8 2.0 2.2 2.4 2.6 2.8
H-H
94.9%
C-H
5.1%
2.878
2.868
2.878
2.868
d e
200 K
C-H
H-H
d i
0.6 0.8 1.0 1.2 1.4 1.6 1.8 2.0 2.2 2.4 2.6 2.8
H-H
95.8%
C-H
4.2%
2.870
2.894
2.313
2.886
2.168
2.870
2.894
2.216
2.313
2.886
2.168

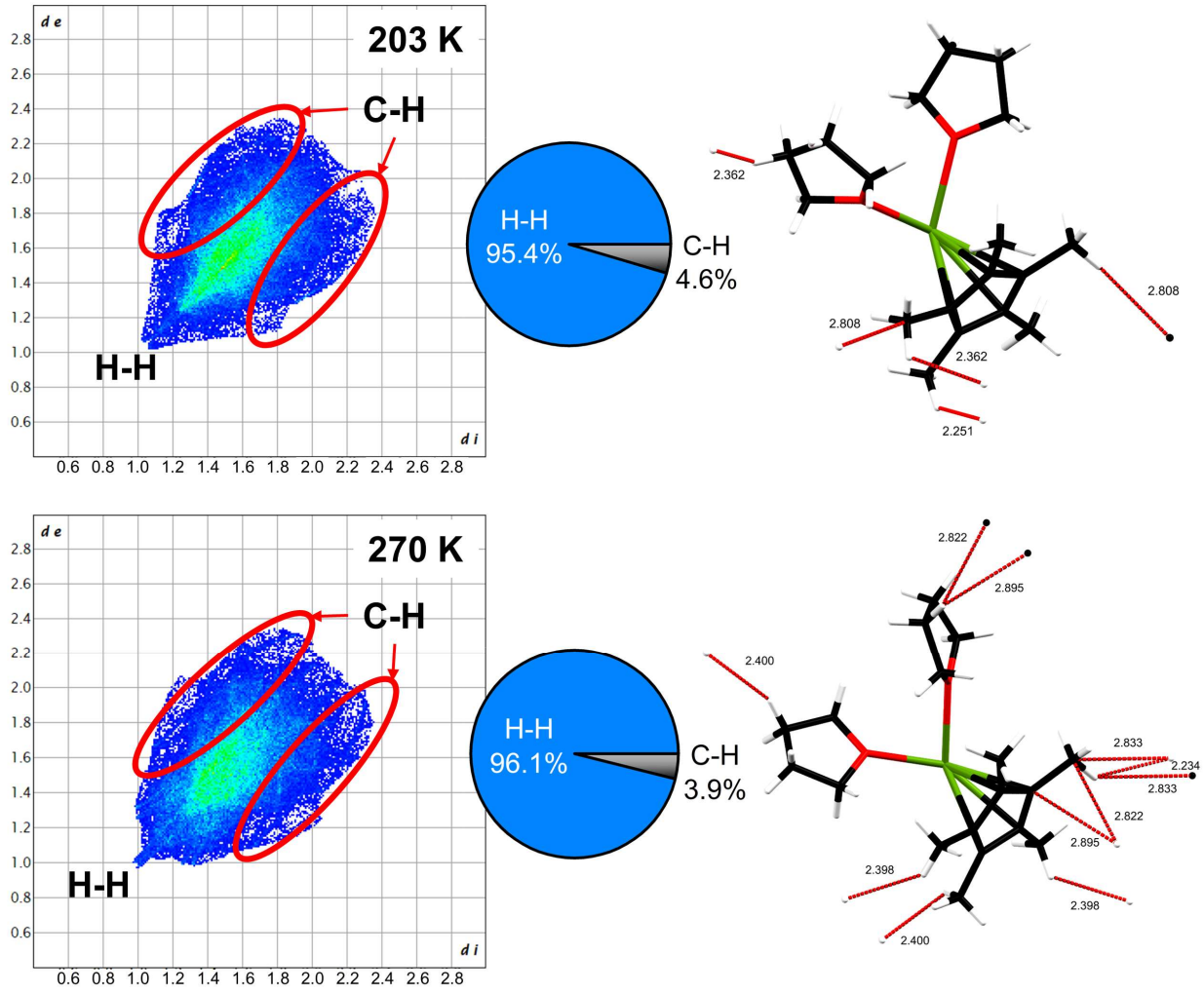
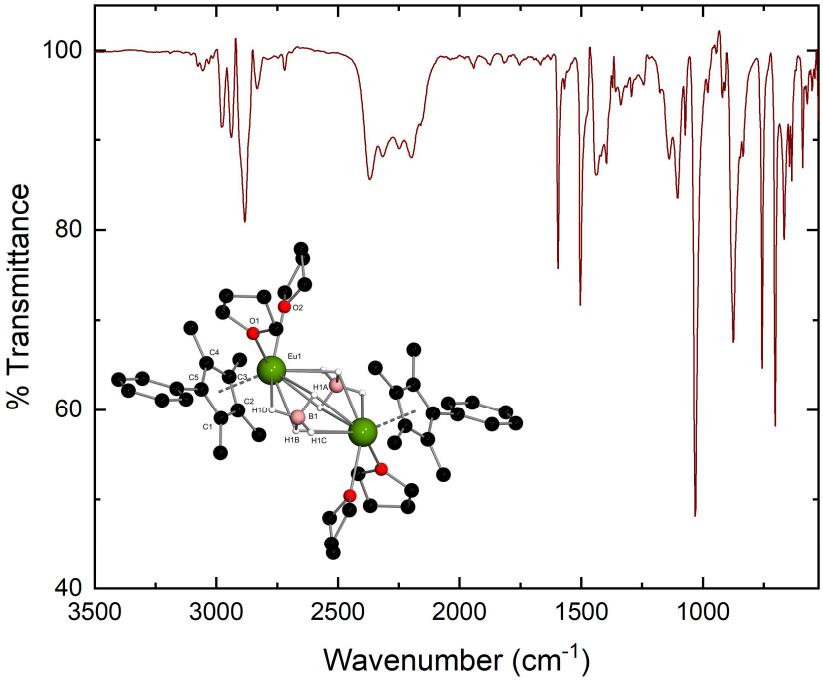


Figure A10. Visualization of the intermolecular interactions in **2.1** at various temperatures. Left to right: Hirshfeld fingerprint plot; sum of intermolecular contacts derived from the Hirshfeld surface analysis; and specific intermolecular contacts in the crystal structure, at each indicated temperature. Only the asymmetric unit is shown, and components of the molecule that do not participate in any intermolecular contacts are omitted for clarity. X-axis labels were added manually for clarity.

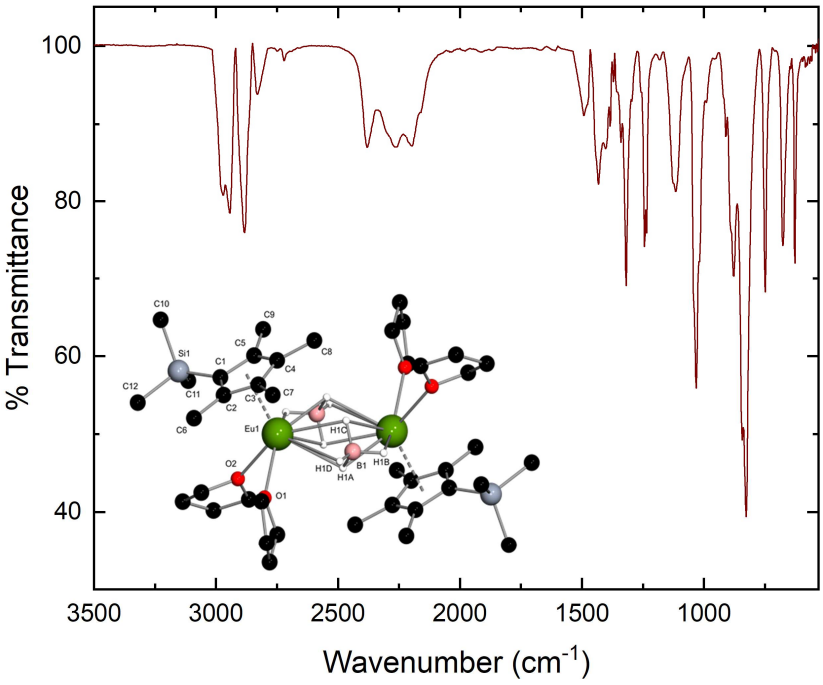
APPENDIX B
Corresponding to Chapter 3

B.1 Infrared spectra

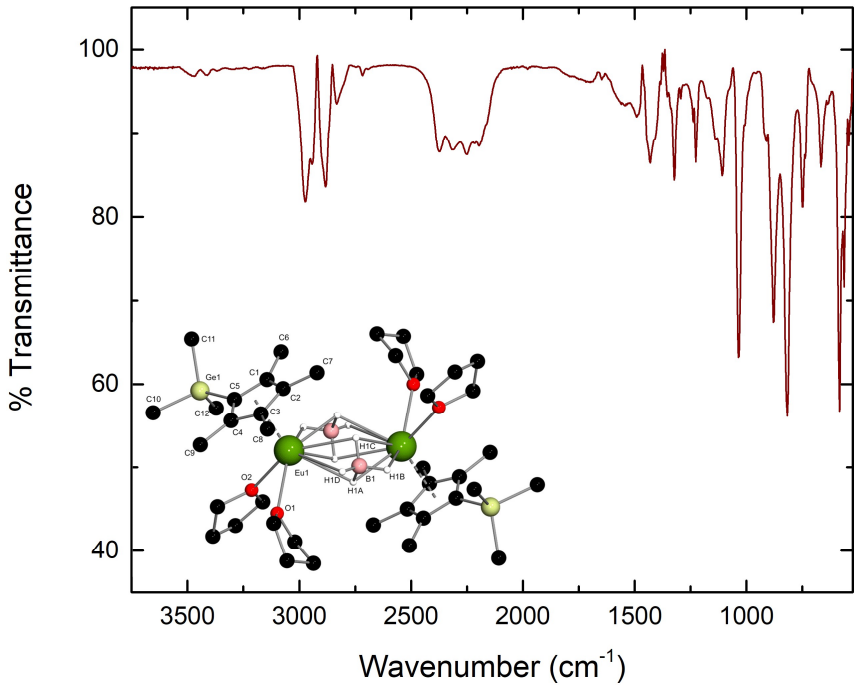
$[Cp^{xph}Eu(BH_4)(THF)_2]_2$ (**3.1**)



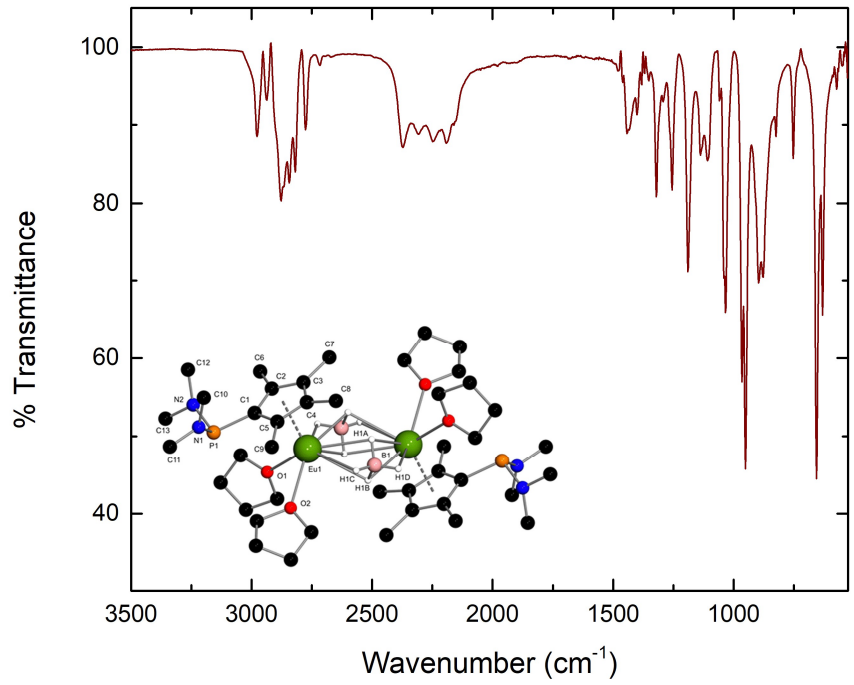
$[^{TMS}Cp^{\#}Eu(BH_4)(THF)_2]_2$ (**3.2**)



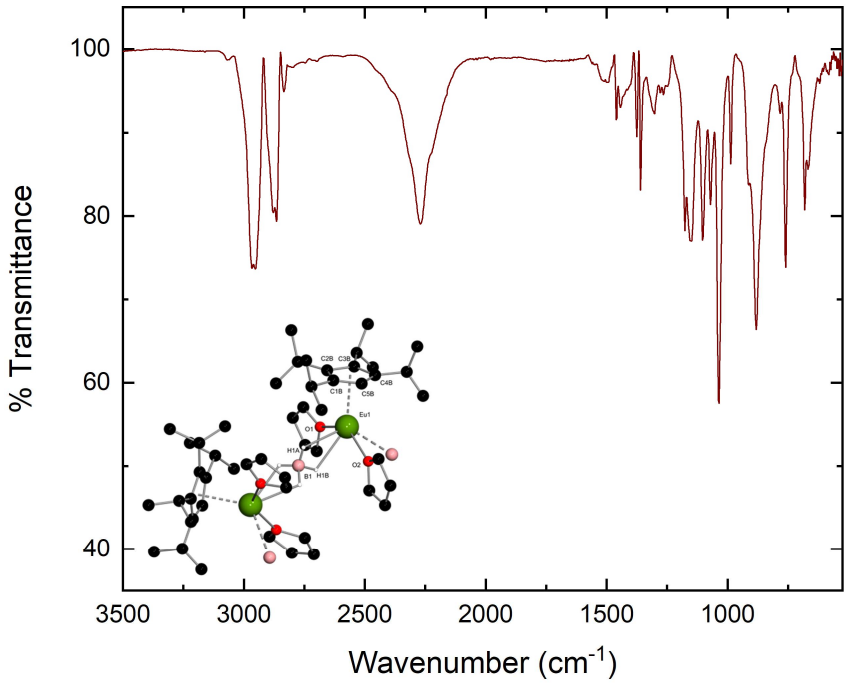
[^{TMG}Cp$^{\#}$Eu(BH$_4$)(THF)$_2$]$_2$ (**3.3**)



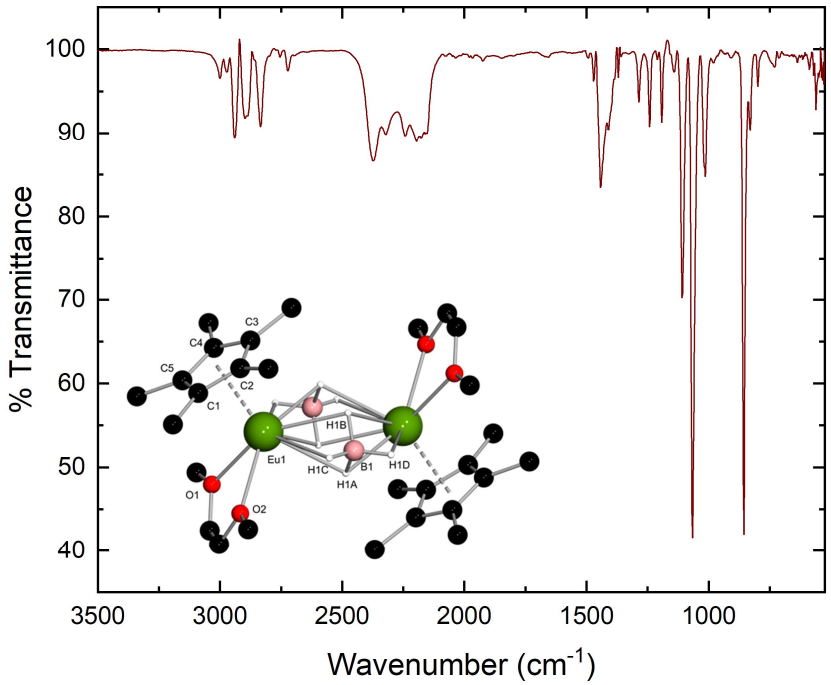
[^{bdp}Cp$^{\#}$Eu(BH$_4$)(THF)$_2$]$_2$ (**3.4**)



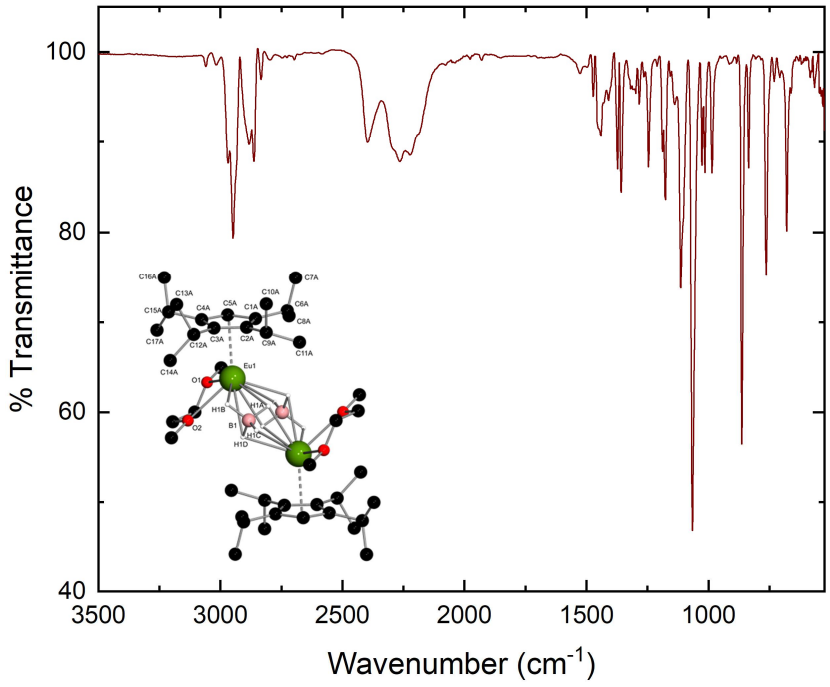
$[Cp^{iPr4}Eu(BH_4)(THF)_2]_\infty$ (**3.5**)



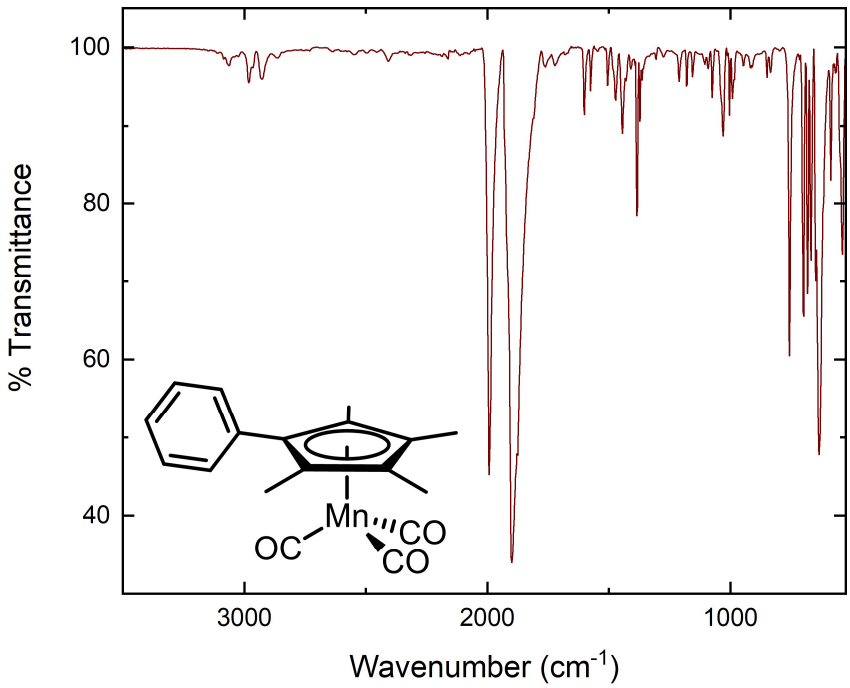
$[Cp^*Eu(BH_4)(DME)]_2$ (**3.6**)



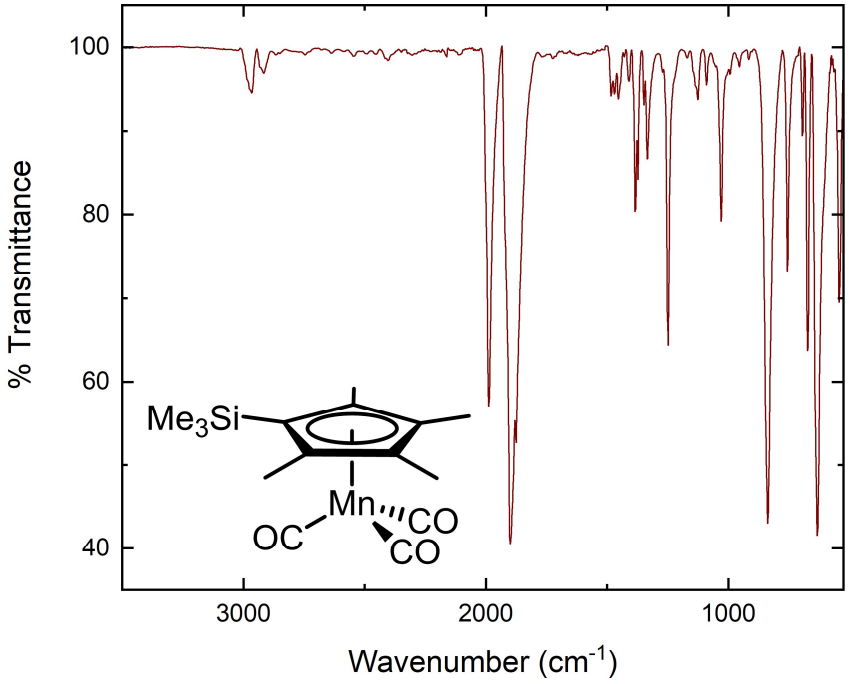
$[Cp^{iPr4}Eu(BH_4)(DME)]_2$ (**3.7**)



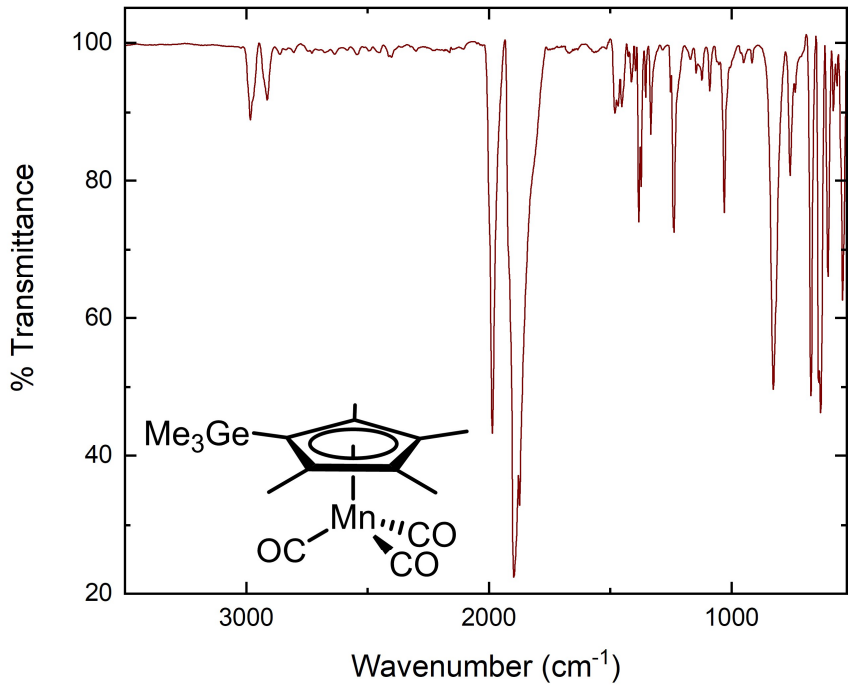
1-phenyl-2,3,4,5-tetramethylcyclopentadienylmanganese(I) tricarbonyl (**3.8**)



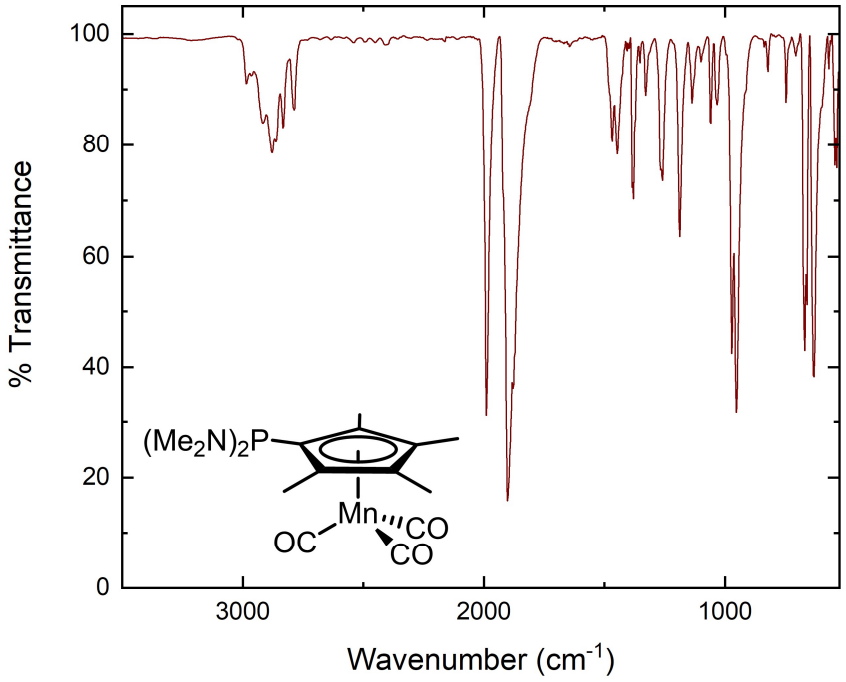
1-(trimethylsilyl)-2,3,4,5-tetramethylcyclopentadienylmanganese(I) tricarbonyl (**3.9**)



1-(trimethylgermanyl)-2,3,4,5-tetramethylcyclopentadienylmanganese(I) tricarbonyl (**3.10**)



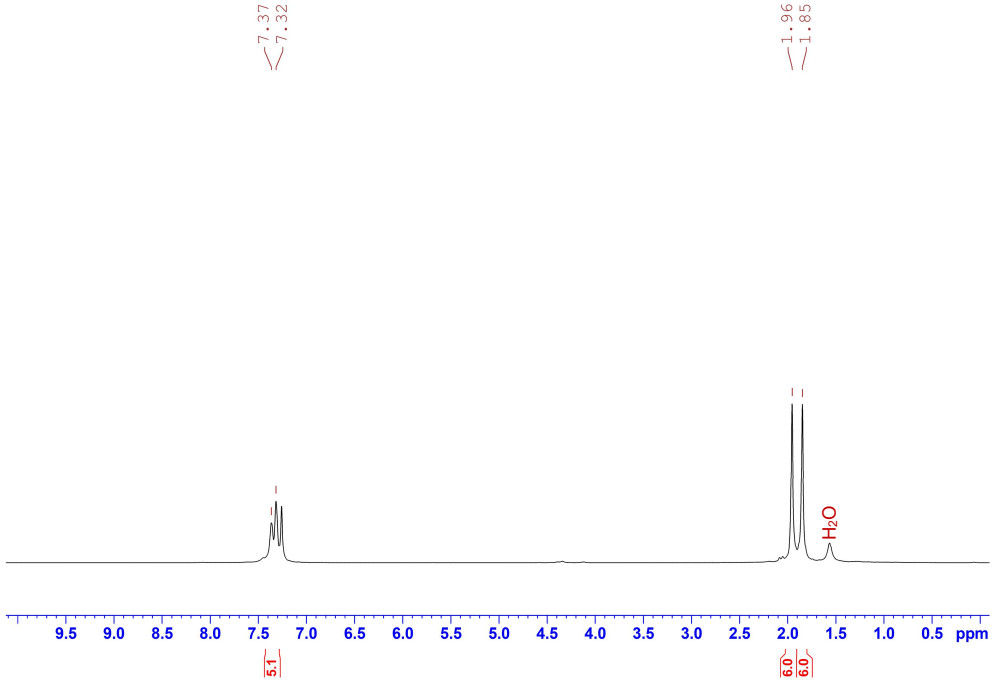
1-(bis(dimethylamino)phosphino)-2,3,4,5-tetramethylcyclopentadienylmanganese(I) tricarbonyl (**3.11**)



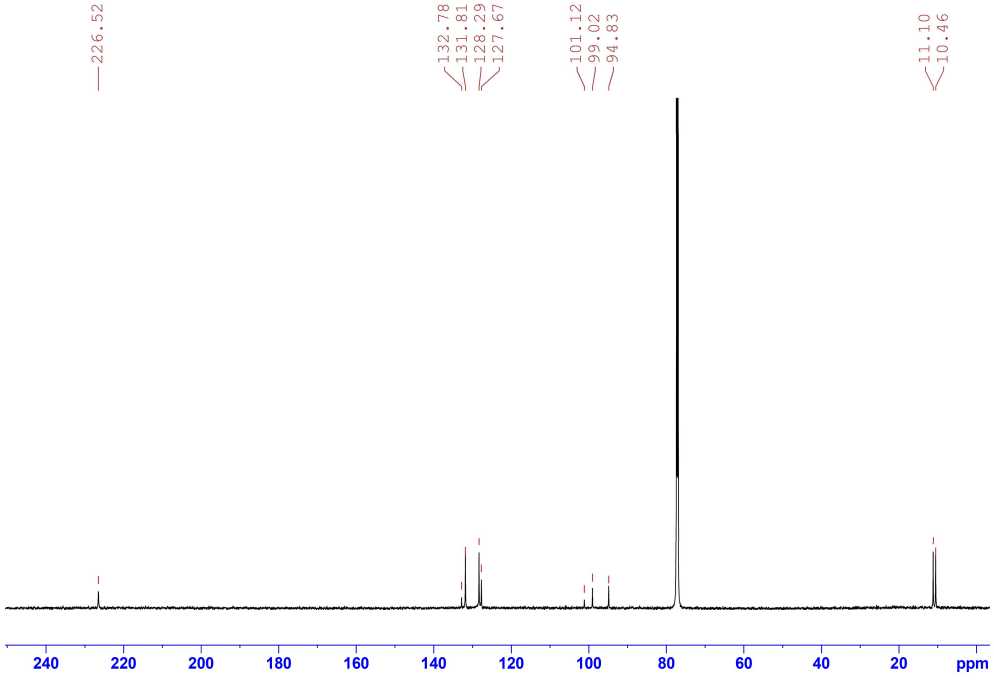
B.2 Nuclear magnetic resonance spectra

1-phenyl-2,3,4,5-tetramethylcyclopentadienylmanganese(I) tricarbonyl (**3.8**)

^{1}H NMR (600 MHz, $CDCl_3$)

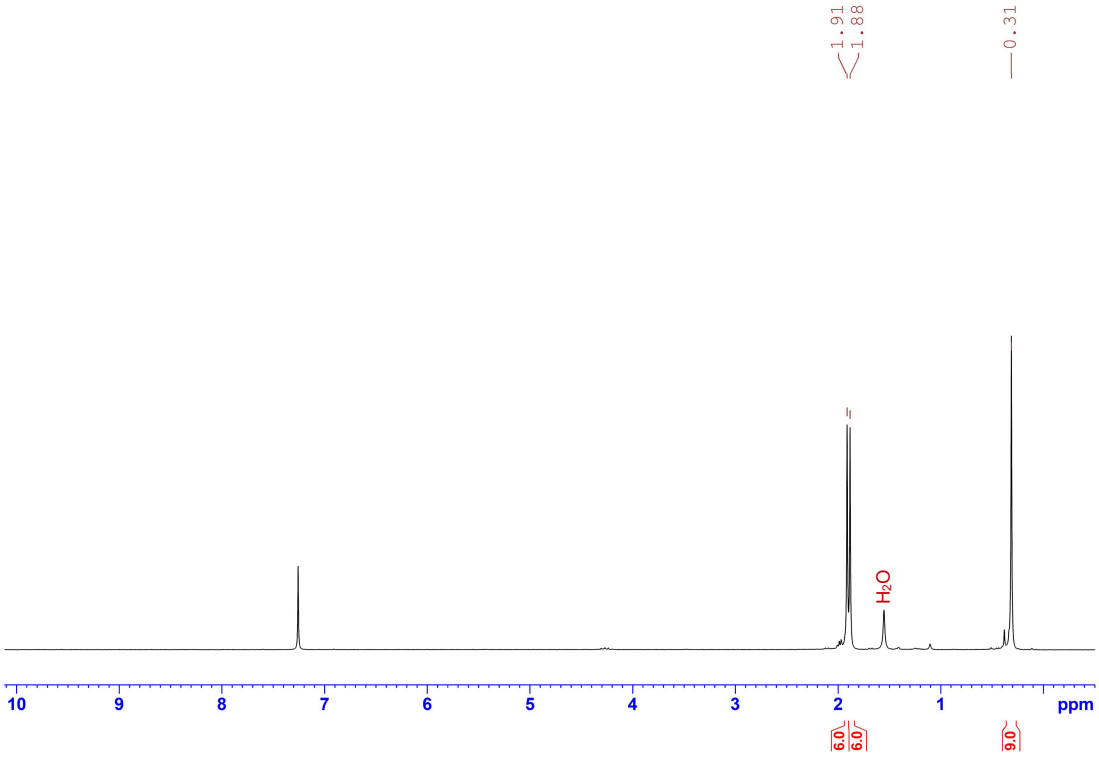


^{13}C NMR (151 MHz, $CDCl_3$)

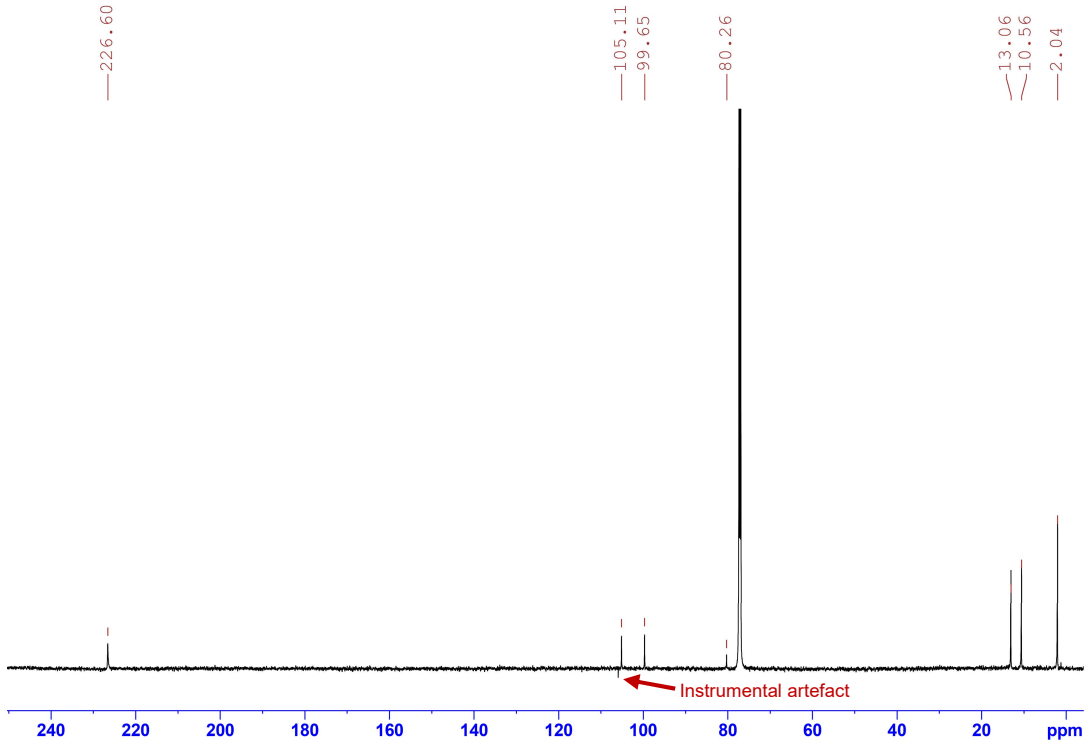


1-(trimethylsilyl)-2,3,4,5-tetramethylcyclopentadienylmanganese(I) tricarbonyl (**3.9**)

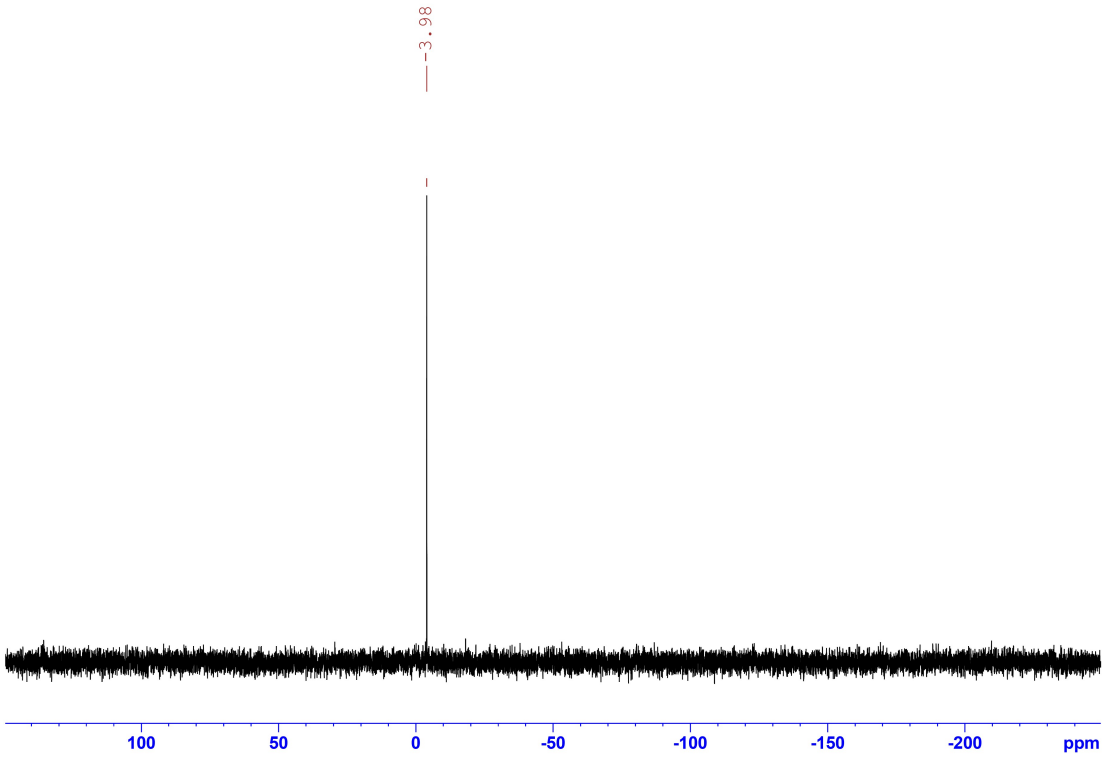
^{1}H NMR (300 MHz, $CDCl_3$)



^{13}C NMR (151 MHz, $CDCl_3$)

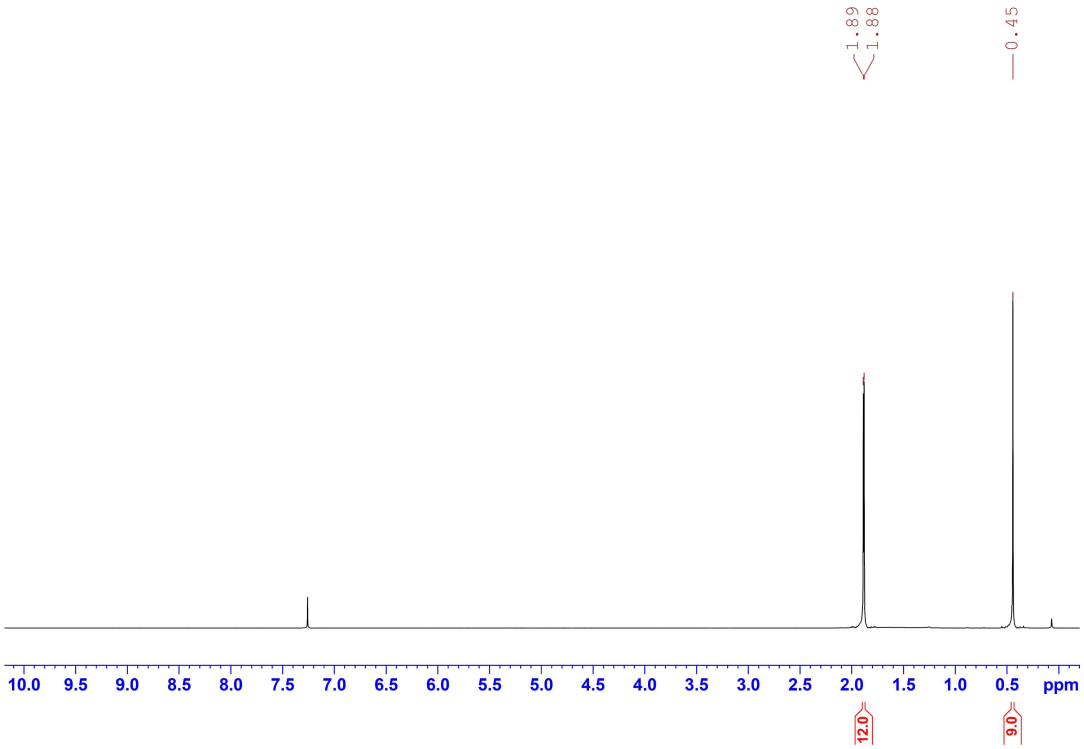


^{29}Si DEPT35 NMR (60 MHz, $CDCl_3$)

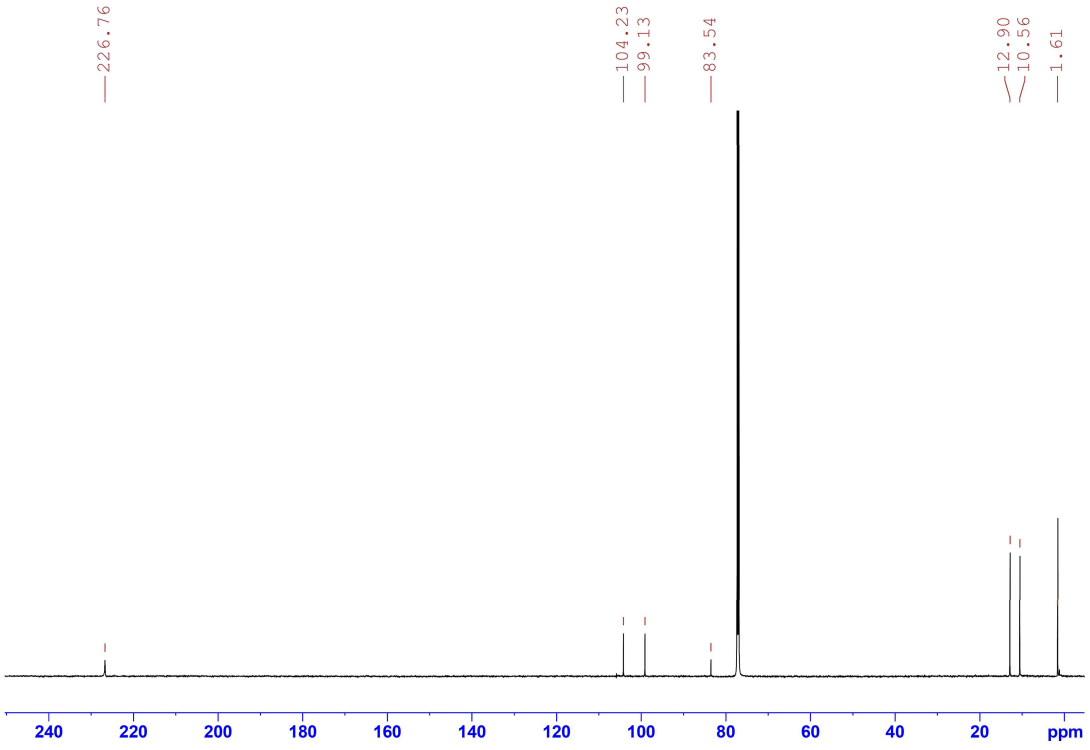


1-(trimethylgermanyl)-2,3,4,5-tetramethylcyclopentadienylmanganese(I) tricarbonyl (**3.10**)

^{1}H NMR (600 MHz, $CDCl_3$)

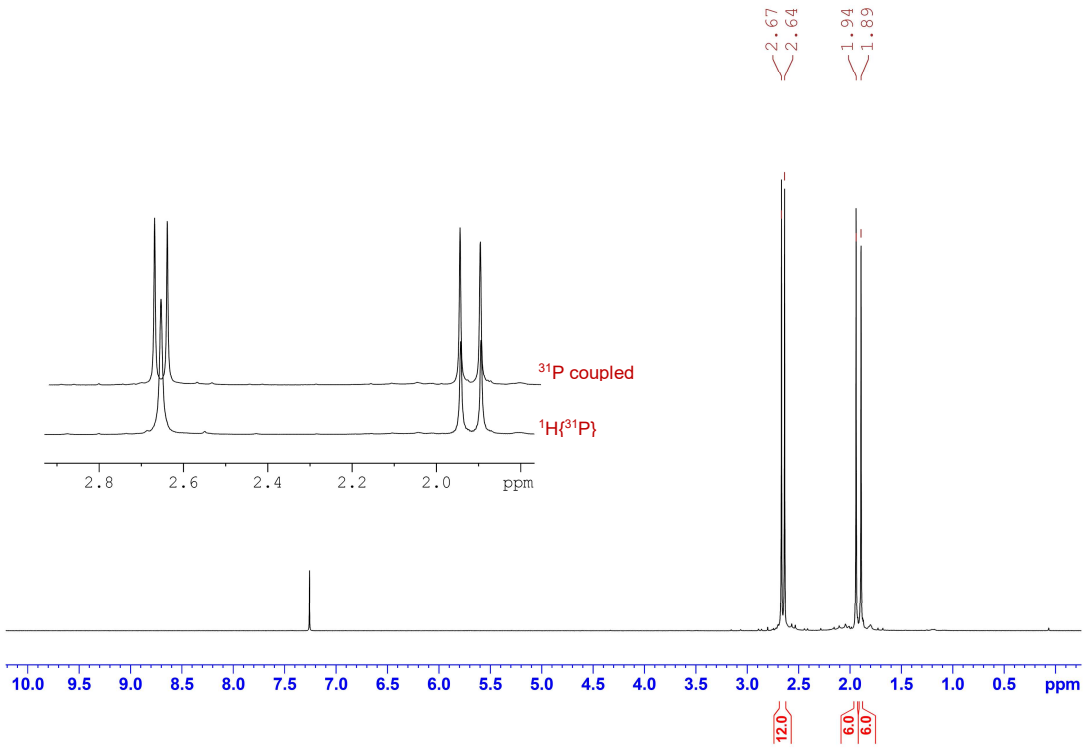


^{13}C NMR (151 MHz, $CDCl_3$)

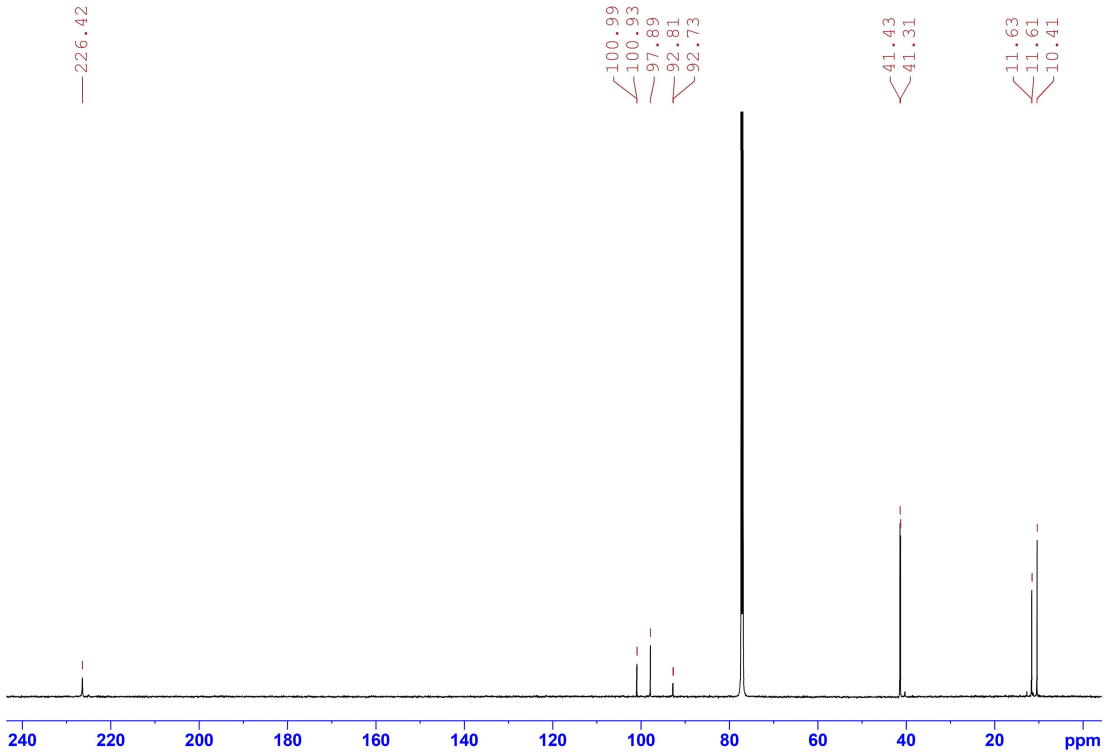


1-(bis(dimethylamino)phosphino)-2,3,4,5-tetramethylcyclopentadienylmanganese(I) tricarbonyl (**3.11**)

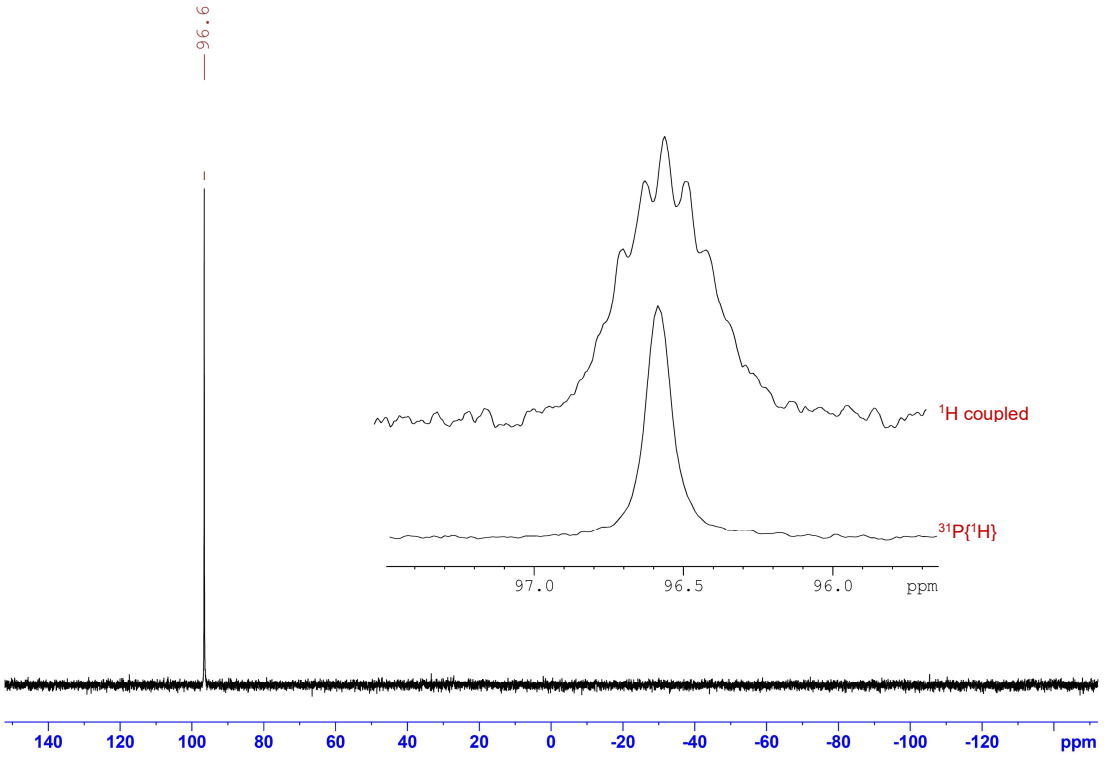
^{1}H NMR (300 MHz, $CDCl_3$)



^{13}C NMR (151 MHz, $CDCl_3$)



$^{31}P\{^{1}H\}$ NMR (122 MHz, $CDCl_3$)



B.3 Crystallographic information

	3.1 (VT 90 K) | NoSpherA2	**3.1 (VT 150 K)**	**3.1 (VT 175 K)**	**3.1**
CCDC deposition no.	2387284 | 2387285	2387286	2387287	2387288
Temperature (K)	90	150	175	208
Empirical formula	$C_{46}H_{74}B_2Eu_2O_4$	$C_{46}H_{74}B_2Eu_2O_4$	$C_{46}H_{74}B_2Eu_2O_4$	$C_{46}H_{74}B_2Eu_2O_4$
Formula weight (amu)	1016.59	1016.59	1016.59	1016.59
Crystal system	Triclinic	Triclinic	Triclinic	Triclinic
Space group	$P\bar{1}$	$P\bar{1}$	$P\bar{1}$	$P\bar{1}$
Unit cell dimensions (Å and °)	a = 9.3300(3)	a = 9.3609(7)	a = 9.3721(4)	a = 9.4186(5)
	b = 10.6241(4)	b = 10.6777(8)	b = 10.6847(5)	b = 10.6972(6)
	c = 12.6111(5)	c = 12.587(1)	c = 12.5959(5)	c = 12.6534(7)
	α = 70.761(1)	α = 71.188(3)	α = 71.258(2)	α = 71.205(1)
	β = 85.438(2)	β = 86.138(4)	β = 86.304(2)	β = 86.288(1)
	γ = 75.659(1)	γ = 75.893(4)	γ = 75.978(2)	γ = 76.085(1)
Volume (Å^3)	1143.46(7)	1154.93(16)	1158.73(9)	1171.35(11)
Z	1	1	1	1
Density (calc., g/cm^3)	1.476	1.462	1.457	1.441
Abs. coefficient (mm^{-1})	14.365	14.222	14.175	2.691
F(000)	518.0	518.0	518.0	518.0
Crystal size (mm^3)	0.120 x 0.070 x 0.040	0.113 x 0.076 x 0.050	0.113 x 0.076 x 0.050	0.261 x 0.251 x 0.114
Radiation (wavelength, Å)	Ga Kα (1.34139)	Ga Kα (1.34139)	Ga Kα (1.34139)	Mo Kα (0.71073)
Theta range (°)	3.229 to 65.986	3.227 to 57.293	3.224 to 62.215	1.7 to 25.5
Index ranges (h,k,l)	-12 to 11, -14 to 11, -17 to 17	-10 to 11, -13 to 13, -14 to 15	-11 to 12, -12 to 13, -16 to 16	-11 to 11, -12 to 12, -15 to 15
Reflections collected	14470	17795	16286	28016
Independent reflections	5553	4673	5306	4358
R(int)	0.0399	0.0583	0.0468	0.0153
Completeness (%)	91.5	97.7	95.3	99.9
Max. and min. transmission	0.318 and 0.141	0.458 and 0.279	0.124 and 0.032	0.746 and 0.649
Data / restraints / parameters	5553 / 0 / 264 | 5553 / 69 / 577	4673 / 516 / 349	5306 / 522 / 349	4605 / 18 / 264
Goodness-of-fit on F^2	1.059 | 1.065	1.110	1.119	1.121
R indices (all data)	R_1 = 0.0272 | 0.0255	R_1 = 0.0777	R_1 = 0.0558	R1 = 0.0267
	wR_2 = 0.0633 | 0.0589	wR_2 = 0.1662	wR_2 = 0.1433	wR2 = 0.0697
Final R indices [$I > 2\sigma(I)$]	R_1 = 0.0254 | 0.0237	R_1 = 0.0585	R_1 = 0.0488	R1 = 0.0254
	wR_2 = 0.0624 | 0.0580	wR_2 = 0.1466	wR_2 = 0.1347	wR2 = 0.0680
Largest diff. peak and hole (e.Å^{-3})	1.36 and -1.14 | 1.34 and -1.29	1.63 and -2.16	1.51 and -2.43	1.53 and -0.65

	3.1 (VT 270 K)	3.2 (VT 90 K)	3.2 (VT 150 K)	3.2 (VT 175 K)
CCDC deposition no.	2387289	2387290	2387291	2387292
Temperature (K)	270	90	150	175
Empirical formula	$C_{46}H_{74}B_2Eu_2O_4$	$C_{40}H_{82}B_2Eu_2O_4Si_2$	$C_{40}H_{82}B_2Eu_2O_4Si_2$	$C_{40}H_{82}B_2Eu_2O_4Si_2$
Formula weight (amu)	1016.59	1008.77	1008.77	1008.77
Crystal system	Triclinic	Triclinic	Triclinic	Triclinic
Space group	$P\bar{1}$	$P\bar{1}$	$P\bar{1}$	$P\bar{1}$
Unit cell dimensions (Å and °)	a = 9.4713(4)	a = 9.4323(3)	a = 9.4696(4)	a = 9.4805(3)
	b = 10.7205(5)	b = 9.9211(4)	b = 9.9544(4)	b = 9.9933(3)
	c = 12.7004(6)	c = 13.9777(5)	c = 14.0626(6)	c = 14.0995(5)
	α = 71.377(2)	α = 88.033(2)	α = 87.966(2)	α = 87.988(2)
	β = 86.650(2)	β = 76.710(1)	β = 76.610(2)	β = 76.604(1)
	γ = 76.527(2)	γ = 67.350(1)	γ = 67.134(2)	γ = 67.144(1)
Volume ($Å^3$)	1188.23(9)	1172.67(7)	1186.03(9)	1195.19(7)
Z	1	1	1	1
Density (calc., g/cm^3)	1.421	1.428	1.412	1.402
Abs. coefficient (mm^{-1})	13.824	14.310	14.149	14.041
F(000)	518.0	518.0	518.0	518.0
Crystal size (mm^3)	0.162 x 0.072 x 0.069	0.131 x 0.061 x 0.050	0.120 x 0.084 x 0.077	0.114 x 0.060 x 0.050
Radiation (wavelength, Å)	Ga Kα (1.34139)	Ga Kα (1.34139)	Ga Kα (1.34139)	Ga Kα (1.34139)
Theta range (°)	3.195 to 58.320	4.759 to 58.343	4.742 to 58.326	4.734 to 58.480
Index ranges (h,k,l)	-11 to 11, -12 to 13, -15 to 15	-11 to 11, -12 to 12, -16 to 16	-12 to 11, -11 to 11, -17 to 17	-11 to 11, -12 to 12, -17 to 17
Reflections collected	10964	11224	11405	11876
Independent reflections	4628	4470	4578	4649
R(int)	0.0424	0.0322	0.0320	0.0389
Completeness (%)	91.3	89.1	90.2	90.3
Max. and min. transmission	0.372 and 0.169	0.752 and 0.414	0.372 and 0.235	0.752 and 0.409
Data / restraints / parameters	4628 / 504 / 350	4470 / 6 / 260	4578 / 6 / 259	4649 / 6 / 260
Goodness-of-fit on F^2	1.084	1.052	1.052	1.050
R indices (all data)	R_1 = 0.0437	R_1 = 0.0268	R_1 = 0.0285	R_1 = 0.0307
	wR_2 = 0.1113	wR_2 = 0.0664	wR_2 = 0.0646	wR_2 = 0.0726
Final R indices [$I > 2\sigma(I)$]	R_1 = 0.0395	R_1 = 0.0257	R_1 = 0.0262	R_1 = 0.0287
	wR_2 = 0.1069	wR_2 = 0.0657	wR_2 = 0.0636	wR_2 = 0.0715
Largest diff. peak and hole ($e.Å^{-3}$)	0.76 and -1.37	1.62 and -1.17	1.05 and -0.56	1.04 and -1.51

	3.2	**3.2 (VT 270 K)**	**3.3 (VT 90 K)**	**3.3 (VT 150 K)**
CCDC deposition no.	2387293	2387294	2387295	2387296
Temperature (K)	213	270	90	150
Empirical formula	$C_{40}H_{82}B_2Eu_2O_4Si_2$	$C_{40}H_{82}B_2Eu_2O_4Si_2$	$C_{40}H_{82}B_2Eu_2Ge_2O_4$	$C_{40}H_{82}B_2Eu_2Ge_2O_4$
Formula weight (amu)	1008.77	1008.77	1097.77	1097.77
Crystal system	Triclinic	Triclinic	Triclinic	Triclinic
Space group	$P\bar{1}$	$P\bar{1}$	$P\bar{1}$	$P\bar{1}$
Unit cell dimensions (Å and °)	a = 9.5365(6)	a = 9.5688(5)	a = 9.2172(4)	a = 9.228(2)
	b = 10.0324(7)	b = 10.0867(6)	b = 10.5375(5)	b = 10.614(2)
	c = 14.1862(9)	c = 14.2469(8)	c = 14.0415(6)	c = 14.085(2)
	α = 87.864(2)	α = 87.708(3)	α = 91.518(2)	α = 91.740(6)
	β = 76.390(2)	β = 76.086(3)	β = 108.275(2)	β = 108.054(6)
	γ = 66.967(2)	γ = 66.903(3)	γ = 114.242(2)	γ = 114.210(6)
Volume (Å^3)	1211.70(14)	1225.46(12)	1161.68(9)	1176.5(3)
Z	1	1	1	1
Density (calc., g/cm^3)	1.382	1.367	1.569	1.549
Abs. coefficient (mm^{-1})	2.647	13.694	15.048	14.859
F(000)	518.0	518.0	554.0	554.0
Crystal size (mm^3)	0.216 x 0.138 x 0.092	0.080 x 0.070 x 0.045	0.120 x 0.085 x 0.073	0.110 x 0.070 x 0.040
Radiation (wavelength, Å)	Mo Kα (0.71073)	Ga Kα (1.34139)	Ga Kα (1.34139)	Ga Kα (1.34139)
Theta range (°)	2.21 to 26.496	4.684 to 58.530	2.931 to 58.182	2.919 to 56.996
Index ranges (h,k,l)	-11 to 11, -12 to 12, -17 to 17	-11 to 11, -12 to 11, -17 to 17	-11 to 11, -12 to 13, -15 to 17	-10 to 10, -12 to 13, -17 to 17
Reflections collected	27079	12334	10406	11378
Independent reflections	5011	4786	4396	4501
R(int)	0.0239	0.0429	0.0319	0.0499
Completeness (%)	100	90.8	88.7	93.2
Max. and min. transmission	0.745 and 0.673	0.752 and 0.525	0.308 and 0.147	0.751 and 0.321
Data / restraints / parameters	5011 / 55 / 268	4786 / 67 / 268	4396 / 0 / 250	4501 / 12 / 250
Goodness-of-fit on F^2	1.036	1.074	1.035	1.060
R indices (all data)	R_1 = 0.0210	R_1 = 0.0469	R_1 = 0.0299	R_1 = 0.0436
	wR_2 = 0.0414	wR_2 = 0.0855	wR_2 = 0.0674	wR_2 = 0.1098
Final R indices [$I > 2\sigma(I)$]	R_1 = 0.0172	R_1 = 0.0355	R_1 = 0.0259	R_1 = 0.0418
	wR_2 = 0.0398	wR_2 = 0.0816	wR_2 = 0.0658	wR_2 = 0.1073
Largest diff. peak and hole (e.Å^{-3})	0.98 and -0.35	1.01 and -0.57	1.03 and -1.13	2.09 and -1.68

	3.3 (VT 175 K)	**3.3**	**3.3 (VT 270 K)**	**3.4 (VT 90 K) | NoSpherA2**
CCDC deposition no.	2387297	2387298	2387299	2387300 | 2387301
Temperature (K)	175	213	270	90
Empirical formula	$C_{40}H_{82}B_2Eu_2Ge_2O_4$	$C_{40}H_{82}B_2Eu_2Ge_2O_4$	$C_{40}H_{82}B_2Eu_2Ge_2O_4$	$C_{42}H_{88}B_2Eu_2N_4O_4P_2$
Formula weight (amu)	1097.77	1097.77	1097.77	1100.64
Crystal system	Triclinic	Triclinic	Triclinic	Triclinic
Space group	$P\bar{1}$	$P\bar{1}$	$P\bar{1}$	$P\bar{1}$
Unit cell dimensions (Å and °)	a = 9.2265(3)	a = 9.2382(9)	a = 9.266(1)	a = 9.9301(6)
	b = 10.6361(4)	b = 10.7559(10)	b = 10.900(2)	b = 9.7997(6)
	c = 14.1029(5)	c = 14.1388(13)	c = 14.204(2)	c = 14.1919(9)
	α = 91.839(2)	α = 92.109(2)	α = 92.603(6)	α = 75.485(2)
	β = 108.137(2)	β = 108.188(2)	β = 108.507(6)	β = 84.427(2)
	γ = 114.179(1)	γ = 114.393(2)	γ = 114.960(5)	γ = 72.658(2)
Volume (Å^3)	1179.32(7)	1193.1(2)	1206.2(3)	1275.81(14)
Z	1	1	1	1
Density (calc., g/cm^3)	1.546	1.528	1.511	1.433
Abs. coefficient (mm^{-1})	14.823	3.874	14.493	13.293
F(000)	554.0	554.0	554.0	566.0
Crystal size (mm^3)	0.120 x 0.085 x 0.073	0.238 x 0.160 x 0.096	0.150 x 0.140 x 0.130	0.090 x 0.083 x 0.050
Radiation (wavelength, Å)	Ga Kα (1.34139)	Mo Kα (0.71073)	Ga Kα (1.34139)	Ga Kα (1.34139)
Theta range (°)	2.918 to 58.326	2.118 to 29.573	2.918 to 58.655	2.799 to 58.383
Index ranges (h,k,l)	-11 to 11, -12 to 12, -17 to 17	-12 to 12, -14 to 14, -19 to 19	-11 to 11, -13 to 13, -17 to 17	-11 to 11, -11 to 12, -17 to 17
Reflections collected	11334	41493	10825	13016
Independent reflections	4580	6683	4675	4916
R(int)	0.0345	0.0213	0.0499	0.0337
Completeness (%)	90.9	100	89.9	90.0
Max. and min. transmission	0.752 and 0.275	0.746 and 0.586	0.308 and 0.121	0.751 and 0.470
Data / restraints / parameters	4580 / 17 / 260	6683 / 0 / 249	4675 / 29 / 268	4916 / 0 / 278 | 4915 / 81 / 650
Goodness-of-fit on F^2	1.062	1.027	1.098	1.065 | 1.074
R indices (all data)	R_1 = 0.0307	R_1 = 0.0217	R_1 = 0.0695	R_1 = 0.0275 | 0.0259
	wR_2 = 0.0708	wR_2 = 0.0460	wR_2 = 0.1811	wR_2 = 0.0702 | 0.0650
Final R indices [$I > 2\sigma(I)$]	R_1 = 0.0273	R_1 = 0.0184	R_1 = 0.0588	R_1 = 0.0263 | 0.0246
	wR_2 = 0.0694	wR_2 = 0.0443	wR_2 = 0.1659	wR_2 = 0.0687 | 0.0633
Largest diff. peak and hole (e.Å^{-3})	0.87 and -0.78	0.93 and -0.85	1.90 and -1.56	1.36 and -1.30 | 1.42 and -1.28

	3.4 (VT 150 K)	**3.4 (VT 175 K)**	**3.4**	**3.4 (VT 270 K)**
CCDC deposition no.	2387302	2387303	2387304	2387305
Temperature (K)	150	175	213	270
Empirical formula	$C_{42}H_{88}B_2Eu_2N_4O_4P_2$	$C_{42}H_{88}B_2Eu_2N_4O_4P_2$	$C_{42}H_{88}B_2Eu_2N_4O_4P_2$	$C_{42}H_{88}B_2Eu_2N_4O_4P_2$
Formula weight (amu)	1100.64	1100.64	1100.64	1100.64
Crystal system	Triclinic	Triclinic	Triclinic	Triclinic
Space group	$P\bar{1}$	$P\bar{1}$	$P\bar{1}$	$P\bar{1}$
Unit cell dimensions (Å and °)	a = 9.9308(4)	a = 9.8973(8)	a = 9.9374(5)	a = 9.9052(9)
	b = 9.8697(4)	b = 9.9064(8)	b = 9.9655(5)	b = 10.0179(9)
	c = 14.2559(6)	c = 14.299(1)	c = 14.3146(7)	c = 14.366(1)
	α = 75.479(2)	α = 75.729(4)	α = 75.551(1)	α = 75.737(4)
	β = 83.963(2)	β = 83.494(4)	β = 83.483(1)	β = 83.184(4)
	γ = 72.600(2)	γ = 73.319(4)	γ = 72.776(1)	γ = 73.421(4)
Volume (Å^3)	1290.06(9)	1300.2(2)	1309.99(11)	1322.4(2)
Z	1	1	1	1
Density (calc., g/cm^3)	1.417	1.406	1.395	1.382
Abs. coefficient (mm^{-1})	13.146	13.044	2.472	12.825
F(000)	566.0	566.0	566.0	566.0
Crystal size (mm^3)	0.099 x 0.057 x 0.040	0.105 x 0.079 x 0.073	0.239 x 0.143 x 0.096	0.105 x 0.079 x 0.073
Radiation (wavelength, Å)	Ga Kα (1.34139)	Ga Kα (1.34139)	Mo Kα (0.71073)	Ga Kα (1.34139)
Theta range (°)	2.787 to 58.334	4.972 to 58.492	2.148 to 27.484	2.765 to 58.664
Index ranges (h,k,l)	-11 to 11, -12 to 12, -18 to 17	-11 to 11, -12 to 12, -18 to 17	-12 to 12, -12 to 12, -18 to 18	-11 to 11, -12 to 12, -18 to 17
Reflections collected	12739	12631	31323	12607
Independent reflections	4986	5061	6001	5152
R(int)	0.0416	0.0445	0.0192	0.0448
Completeness (%)	90.4	90.5	100	89.9
Max. and min. transmission	0.751 and 0.432	0.372 and 0.194	0.746 and 0.656	0.752 and 0.445
Data / restraints / parameters	4986 / 0 / 278	5061 / 131 / 314	6001 / 10 / 277	5152 / 131 / 315
Goodness-of-fit on F^2	1.086	1.058	1.048	1.084
R indices (all data)	R_1 = 0.0366	R_1 = 0.0575	R1 = 0.0205	R_1 = 0.0523
	wR_2 = 0.0872	wR_2 = 0.1515	wR2 = 0.0450	wR_2 = 0.1353
Final R indices [$I > 2\sigma(I)$]	R_1 = 0.0337	R_1 = 0.0497	R1 = 0.0178	R_1 = 0.0455
	wR_2 = 0.0850	wR_2 = 0.1414	wR2 = 0.0434	wR_2 = 0.1264
Largest diff. peak and hole (e.Å^{-3})	1.04 and -1.23	1.62 and -1.08	1.09 and -0.34	1.50 and -0.95

	3.5	3.6 (VT 90 K)	3.6 (VT 150 K)	3.6 (VT 175 K)
CCDC deposition no.	2387306	2387307	2387308	2387309
Temperature (K)	200	90	150	175
Empirical formula	$C_{25}H_{48}BEuO_2$	$C_{28}H_{58}B_2Eu_2O_4$	$C_{28}H_{58}B_2Eu_2O_4$	$C_{28}H_{58}B_2Eu_2O_4$
Formula weight (amu)	543.40	784.28	784.28	784.28
Crystal system	Orthorhombic	Orthorhombic	Orthorhombic	Orthorhombic
Space group	Pbcn	Pbca	Pbca	Pbca
Unit cell dimensions (Å and °)	a = 16.1650(5)	a = 15.763(1)	a = 15.7534(7)	a = 15.7648(4)
	b = 22.5065(7)	b = 13.5204(9)	b = 13.6045(6)	b = 13.6923(4)
	c = 14.3146(7)	c = 16.335(1)	c = 16.3907(7)	c = 16.4126(5)
	α = 90	α = 90	α = 90	α = 90
	β = 90	β = 90	β = 90	β = 90
	γ = 90	γ = 90	γ = 90	γ = 90
Volume ($Å^3$)	6409.7(3)	3481.3(4)	3512.8(3)	3542.8(2)
Z	8	4	4	4
Density (calc., g/cm^3)	1.126	1.496	1.483	1.470
Abs. coefficient (mm^{-1})	1.971	18.753	18.585	18.428
F(000)	2256	1576.0	1576.0	1576.0
Crystal size (mm^3)	0.320 x 0.190 x 0.140	0.600 x 0.100 x 0.080	0.600 x 0.100 x 0.080	0.145 x 0.093 x 0.084
Radiation (wavelength, Å)	Mo Kα (0.71073)	Ga Kα (1.34139)	Ga Kα (1.34139)	Ga Kα (1.34139)
Theta range (°)	2.5 to 26.2	4.882 to 60.594	5.293 to 60.743	5.287 to 54.933
Index ranges (h,k,l)	-19 to 15, -26 to 27, -21 to 21	-20 to 20, -17 to 11, -21 to 17	-20 to 16, -17 to 16, -18 to 20	-19 to 19, -16 to 16, -19 to 20
Reflections collected	69121	18446	25255	25330
Independent reflections	5964	3965	3983	3358
R(int)	0.0396	0.0477	0.0456	0.0606
Completeness (%)	99.9	99.2	98.3	99.5
Max. and min. transmission	0.745 and 0.663	0.311 and 0.145	0.311 and 0.150	0.512 and 0.302
Data / restraints / parameters	5964 / 176 / 440	3965 / 0 / 186	3983 / 175 / 206	3358 / 175 / 205
Goodness-of-fit on F^2	1.066	1.044	1.038	1.059
R indices (all data)	R1 = 0.0582	R_1 = 0.0473	R_1 = 0.0370	R_1 = 0.0340
	wR2 = 0.1291	wR_2 = 0.0927	wR_2 = 0.0609	wR_2 = 0.0824
Final R indices [$I > 2\sigma(I)$]	R1 = 0.0446	R_1 = 0.0339	R_1 = 0.0259	R_1 = 0.0306
	wR2 = 0.1163	wR_2 = 0.0856	wR_2 = 0.0570	wR_2 = 0.0805
Largest diff. peak and hole ($e.Å^{-3}$)	2.04 and -0.54	1.52 and -1.25	0.61 and -0.45	0.71 and -1.08

	3.6	**3.6 (VT 270 K)**	**3.7**
CCDC deposition no.	2387310	2387311	2387312
Temperature (K)	208	270	200
Empirical formula	$C_{28}H_{58}B_2Eu_2O_4$	$C_{28}H_{58}B_2Eu_2O_4$	$C_{42}H_{86}B_2Eu_2O_4$
Formula weight (amu)	784.28	784.28	980.64
Crystal system	Orthorhombic	Orthorhombic	Triclinic
Space group	Pbca	Pbca	$P\bar{1}$
Unit cell dimensions (Å and °)	a = 15.794(2)	a = 15.8323(4)	a = 8.7437(8)
	b = 13.7602(18)	b = 13.8905(3)	b = 12.0548(11)
	c = 16.479(2)	c = 16.5101(4)	c = 12.5759(11)
	α = 90	α = 90	α = 98.283(2)
	β = 90	β = 90	β = 98.853(2)
	γ = 90	γ = 90	γ = 109.052(2)
Volume (Å^3)	3581.3(8)	3630.9(2)	1210.9(2)
Z	4	4	1
Density (calc., g/cm^3)	1.455	1.435	1.345
Abs. coefficient (mm^{-1})	3.496	17.981	2.600
F(000)	1576.0	1576.0	506.0
Crystal size (mm^3)	0.176 x 0.125 x 0.067	0.145 x 0.093 x 0.084	0.178 x 0.173 x 0.095
Radiation (wavelength, Å)	Mo Kα (0.71073)	Ga Kα (1.34139)	Mo Kα (0.71073)
Theta range (°)	2.32 to 27.088	4.359 to 60.659	1.675 to 25.681
Index ranges (h,k,l)	-12 to 20, -16 to 17, -21 to 21	-19 to 20, -18 to 17, -13 to 21	-10 to 10, -14 to 14, -15 to 15
Reflections collected	40798	25421	18957
Independent reflections	3946	4148	4608
R(int)	0.0533	0.0438	0.0359
Completeness (%)	100	99.4	100
Max. and min. transmission	0.746 and 0.663	0.311 and 0.140	0.745 and 0.605
Data / restraints / parameters	3946 / 12 / 186	4148 / 450 / 301	4608 / 129 / 414
Goodness-of-fit on F^2	1.079	1.036	1.165
R indices (all data)	R_1 = 0.0679	R_1 = 0.0387	R1 = 0.0359
	wR_2 = 0.0780	wR_2 = 0.0772	wR2 = 0.0533
Final R indices [$I > 2\sigma(I)$]	R_1 = 0.0305	R_1 = 0.0288	R1 = 0.0258
	wR_2 = 0.0622	wR_2 = 0.0718	wR2 = 0.0492
Largest diff. peak and hole (e.Å^{-3})	1.73 and -0.70	0.79 and -0.38	2.16 and -1.00

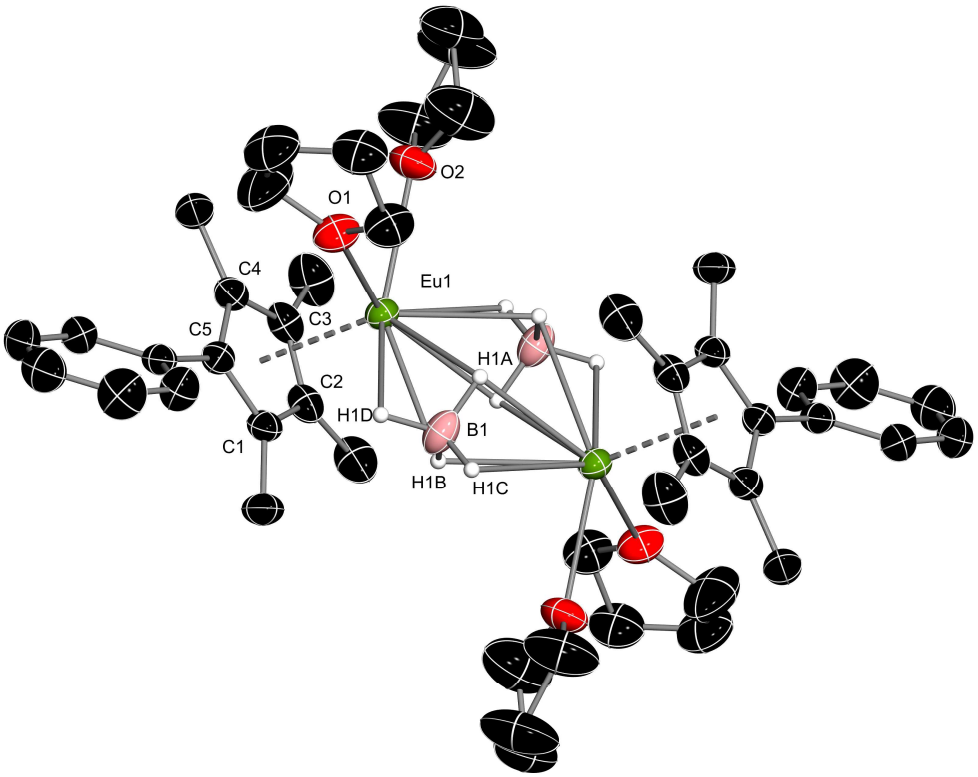


Figure B1. Thermal ellipsoid diagram (50% probability) of **3.1**. Hydrogen atoms bonded to carbon are omitted for clarity. Labels are given only to the crystallographically unique atoms which coordinate the Eu^{II} centre.

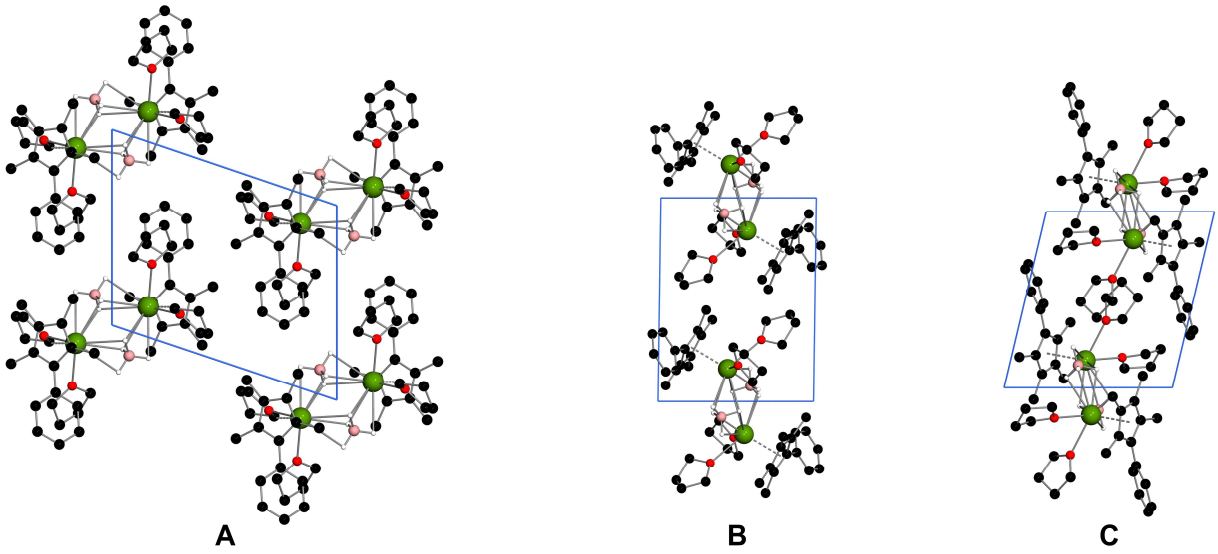


Figure B2. Crystallographic packing diagrams of **3.1**, shown along the (a) *a*-axis, (b) *b*-axis, and (c) *c*-axis of the unit cell. Hydrogen atoms bonded to carbon are omitted for clarity.

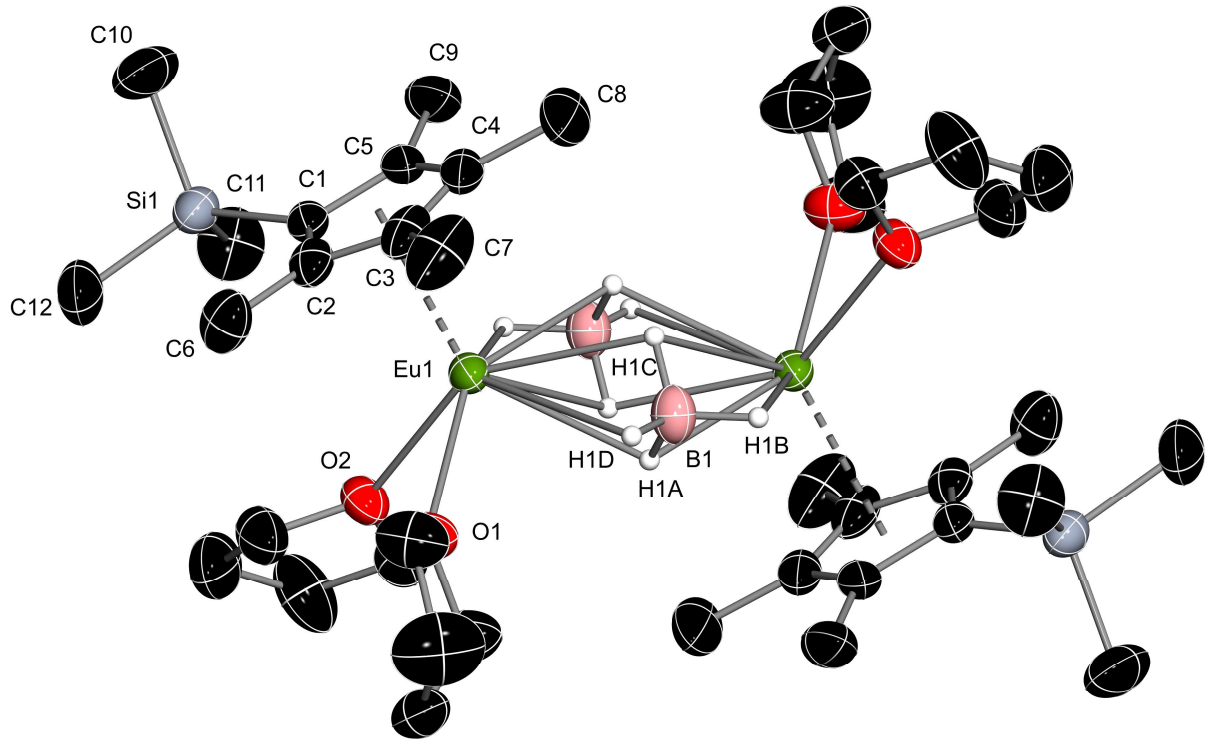


Figure B3. Thermal ellipsoid diagram (50% probability) of **3.2**. Hydrogen atoms bonded to carbon are omitted and only one component of the disorder [of O1-THF] is shown for clarity. Labels are given only to the crystallographically unique atoms which coordinate the Eu^{II} centre.

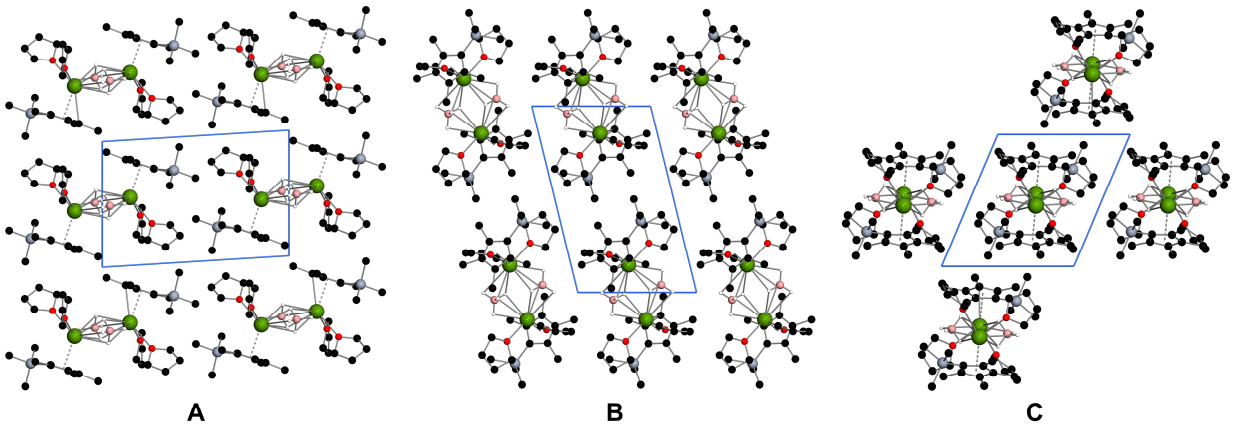


Figure B4. Crystallographic packing diagrams of **3.2**, shown along the (a) *a*-axis, (b) *b*-axis, and (c) *c*-axis of the unit cell. Hydrogen atoms bonded to carbon are omitted for clarity.

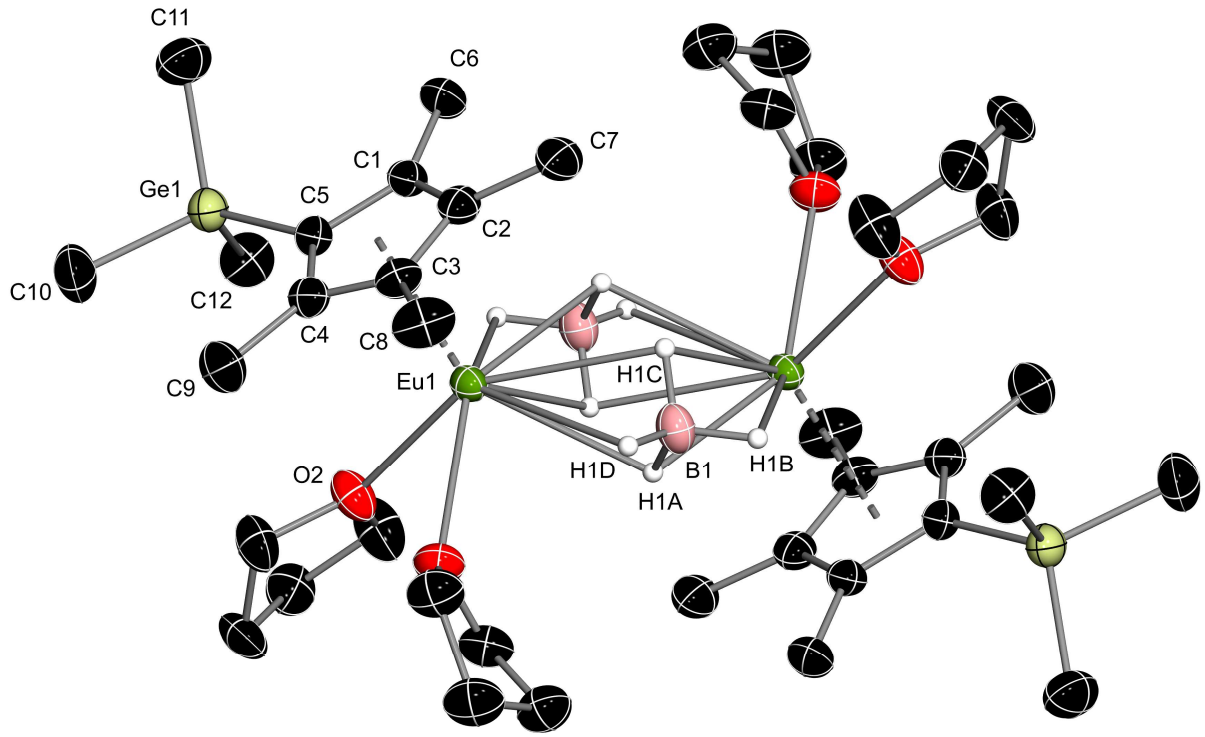


Figure B5. Thermal ellipsoid diagram (50% probability) of **3.3**. Hydrogen atoms bonded to carbon are omitted and only one component of the disorder [of O2-THF] is shown for clarity. Labels are given only to the crystallographically unique atoms which coordinate the Eu^{II} centre.

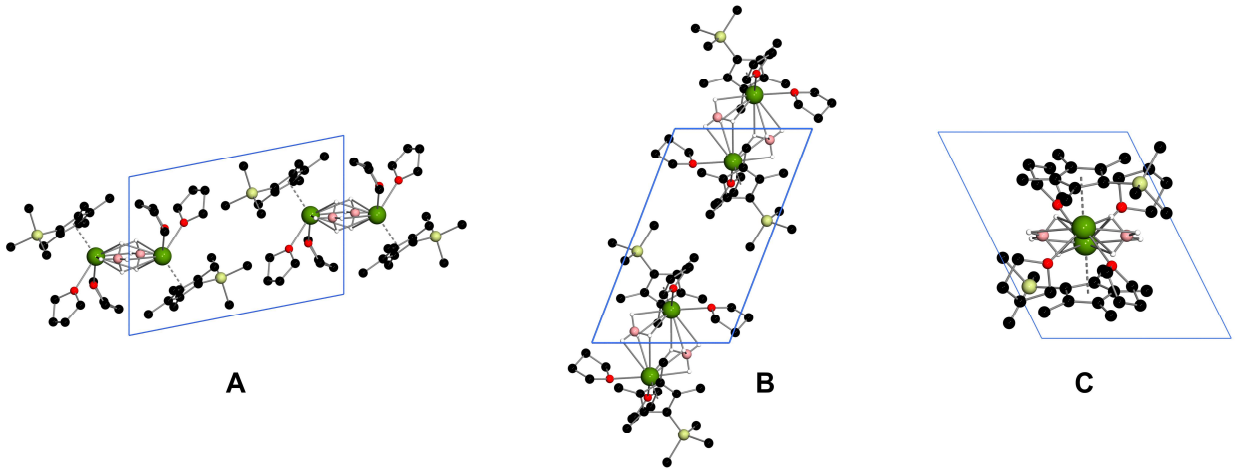


Figure B6. Crystallographic packing diagrams of **3.3**, shown along the (a) *a*-axis, (b) *b*-axis, and (c) *c*-axis of the unit cell. Hydrogen atoms bonded to carbon are omitted for clarity.

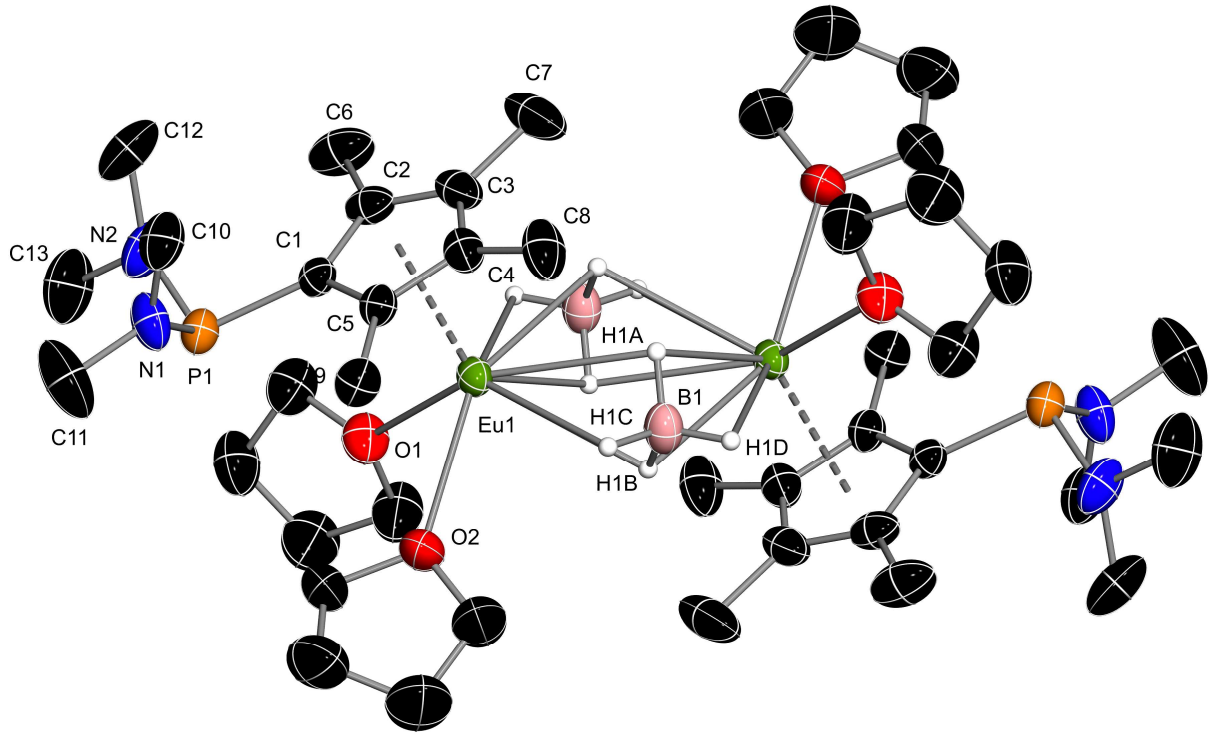


Figure B7. Thermal ellipsoid diagram (50% probability) of **3.4**. Hydrogen atoms bonded to carbon are omitted for clarity. Labels are given only to the crystallographically unique atoms which coordinate the Eu^{II} centre.

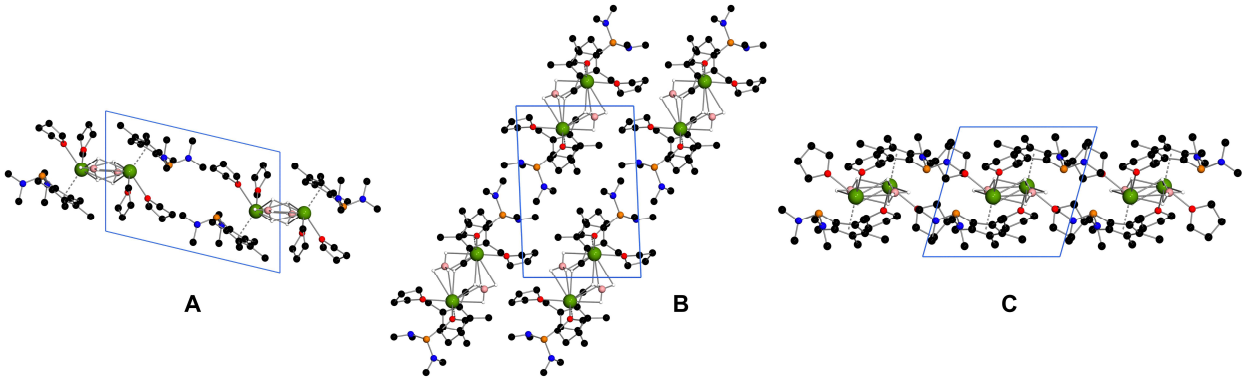


Figure B8. Crystallographic packing diagrams of **3.4**, shown along the (a) *a*-axis, (b) *b*-axis, and (c) *c*-axis of the unit cell. Hydrogen atoms bonded to carbon are omitted for clarity.

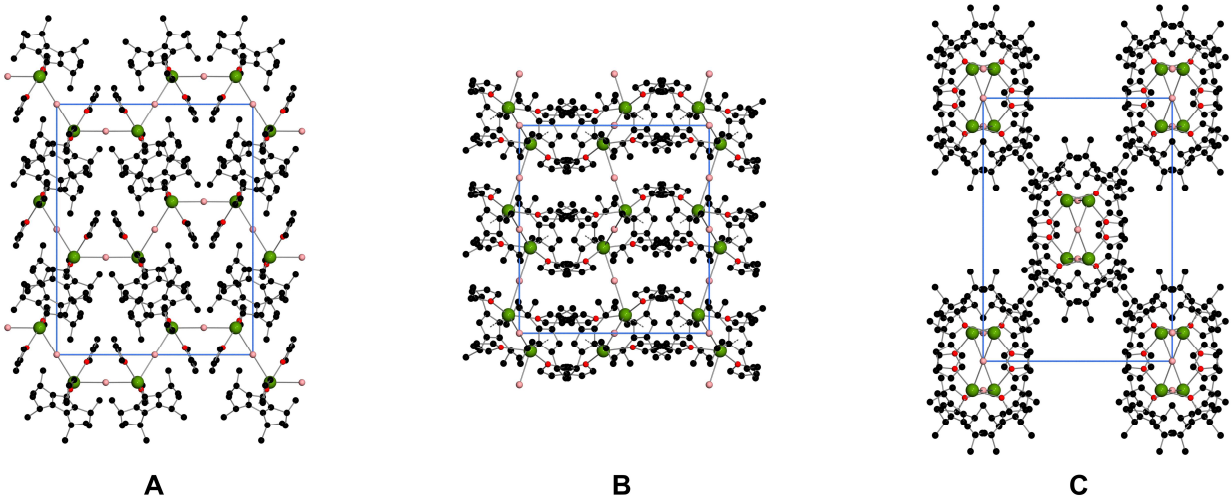


Figure B9. Crystallographic packing diagrams of **3.5**, shown along the (a) *a*-axis, (b) *b*-axis, and (c) *c*-axis of the unit cell. Only one component of the disorder is shown for clarity. Hydrogen atoms bonded to carbon are omitted for clarity.

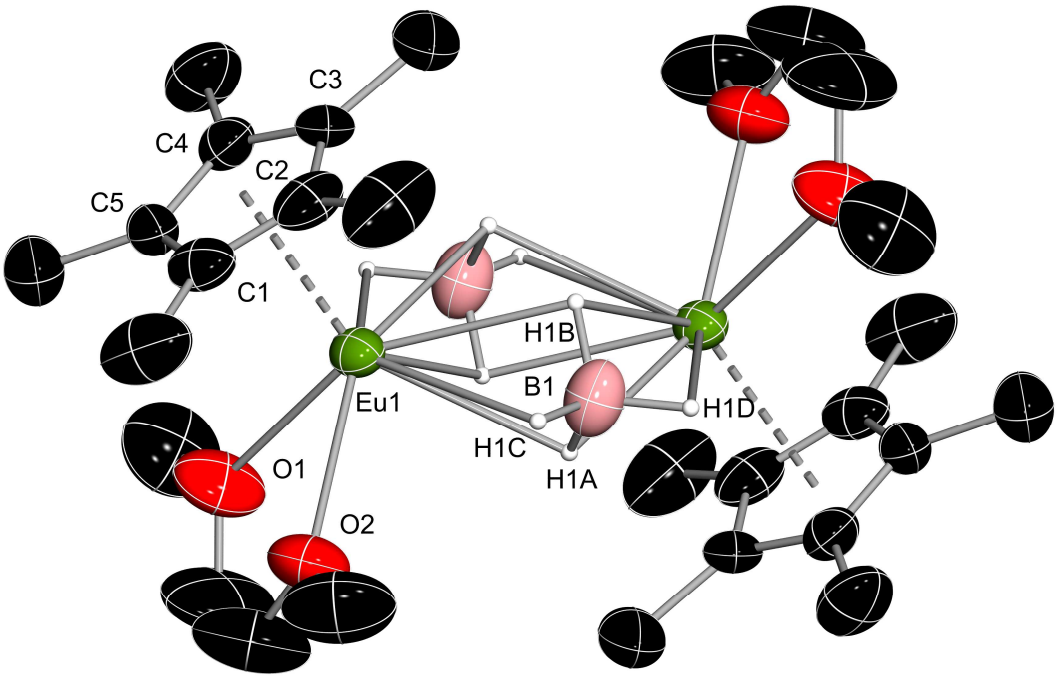


Figure B10. Thermal ellipsoid diagram (50% probability) of **3.6**. Hydrogen atoms bonded to carbon are omitted for clarity. Labels are given only to the crystallographically unique atoms which coordinate the Eu^{II} centre.

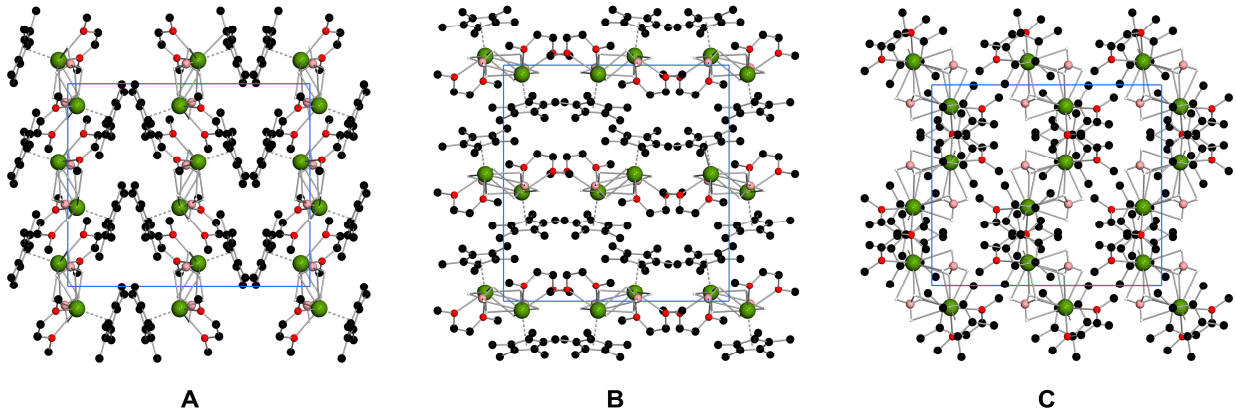


Figure B11. Crystallographic packing diagrams of **3.6**, shown along the (a) *a*-axis, (b) *b*-axis, and (c) *c*-axis of the unit cell. Hydrogen atoms bonded to carbon are omitted for clarity.

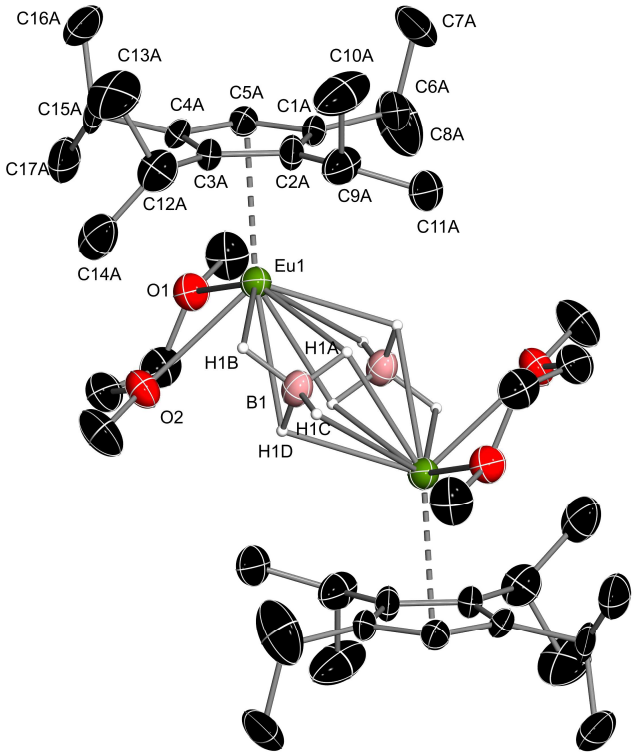


Figure B12. Thermal ellipsoid diagram (50% probability) of **3.7**. Only one component of the disorder is shown for clarity. Hydrogen atoms bonded to carbon are omitted for clarity. Labels are given only to the crystallographically unique atoms which coordinate the Eu^{II} centre.

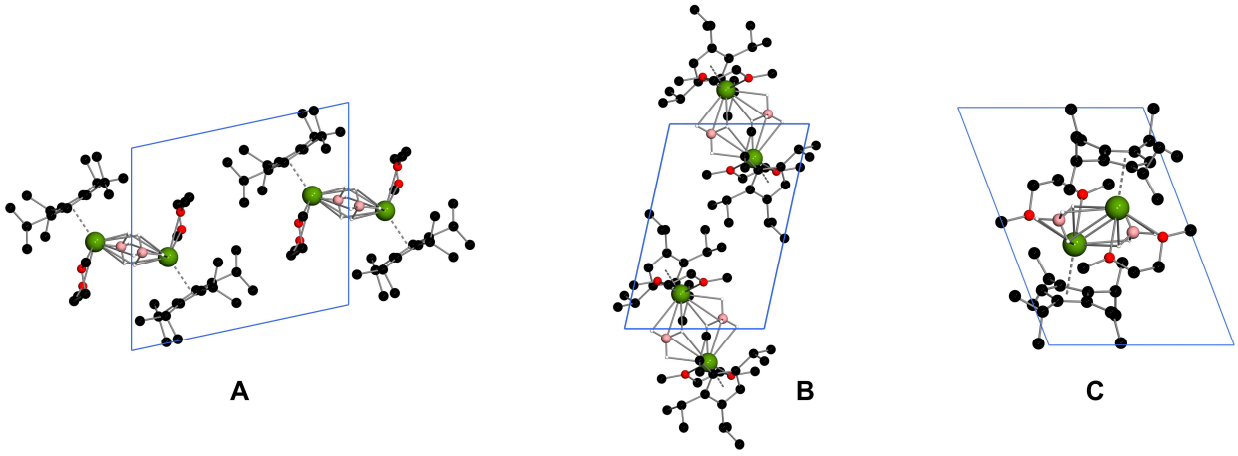


Figure B13. Crystallographic packing diagrams of **3.7**, shown along the (a) *a*-axis, (b) *b*-axis, and (c) *c*-axis of the unit cell. Only one component of the disorder is shown for clarity. Hydrogen atoms bonded to carbon are omitted for clarity.

B.4 Photoluminescence

Table B1. Best-fitting parameters for the Boltzmann-type function $y = A_2 + \frac{(A_1 - A_2)}{1+e^{[(x-x_0)/dx]}}$ fitted to the energies at the emission band maxima for complexes **3.1–3.4**, **3.6** and **3.7** (Figure 3.18a). Best-fitting parameters for **2.1** are given in Figure 2.6.

Compound	A_1	A_2	x_0	R^2
3.1	17296	18107	245	0.9963
3.2	16272	17880	147	0.9997
3.3	16653	17907	210	0.9989
3.4	15240	17890	113	0.9980
3.6	15730	17259	223	0.9967
3.7	17782	286226	928	0.9902

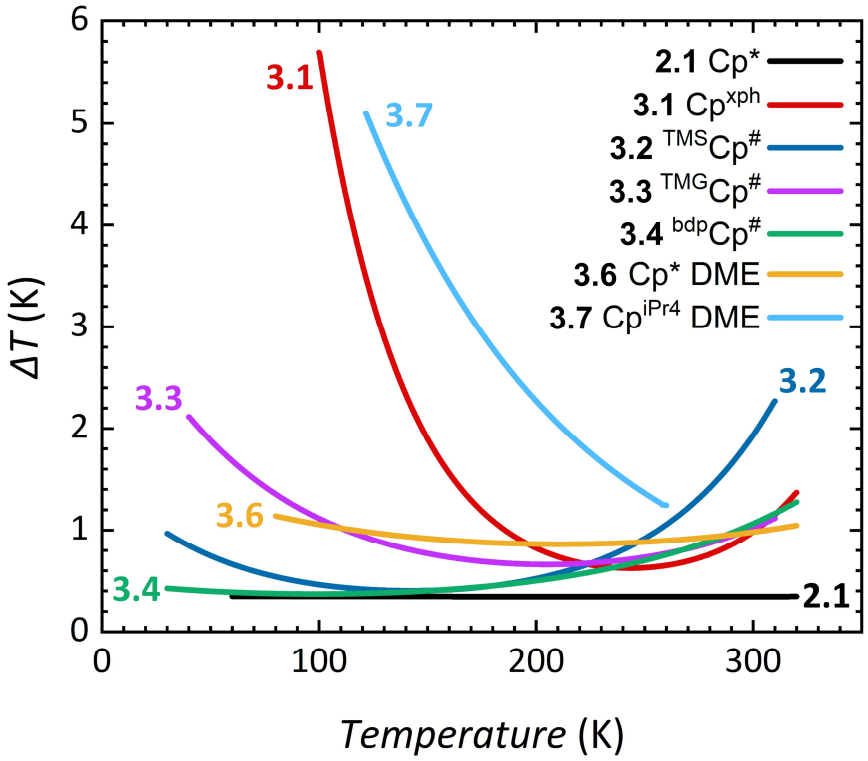


Figure B14. Temperature uncertainty of complexes **3.1–3.4**, **3.6** and **3.7** in comparison to the original complex **2.1**, assuming a wavelength resolution of 0.1 nm (lower is better).[224]

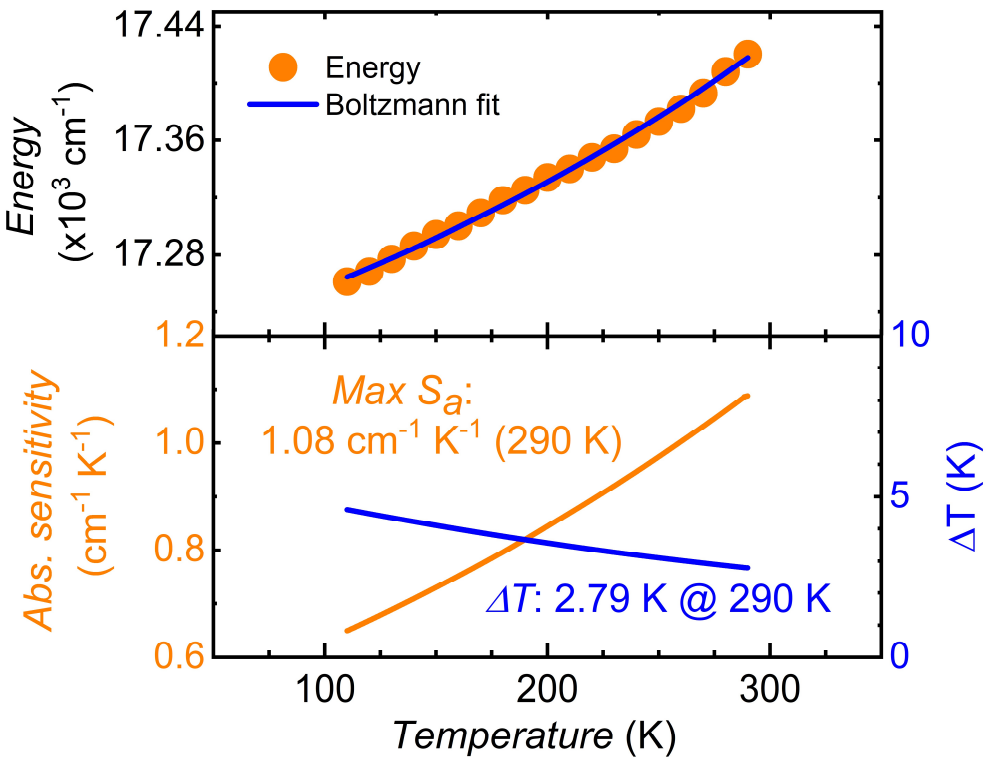


Figure B15. Thermometric performance of complex **3.5**. *Top:* Temperature dependence of the energy at the emission band maximum, extracted from the temperature-dependent emission spectra shown in Figure 3.13. The solid line represents the Boltzmann function fitted to the experimental data. Best fitting parameters: $A_1 = 17050$, $A_2 = 24466$, $x_0 = 1236$, $R^2 = 0.9950$. *Bottom:* Absolute sensitivity obtained as the first derivative of the fitted function (left axis), and the temperature uncertainty assuming a wavelength resolution of 0.1 nm (right axis).[224]

B.5 Metrical analysis

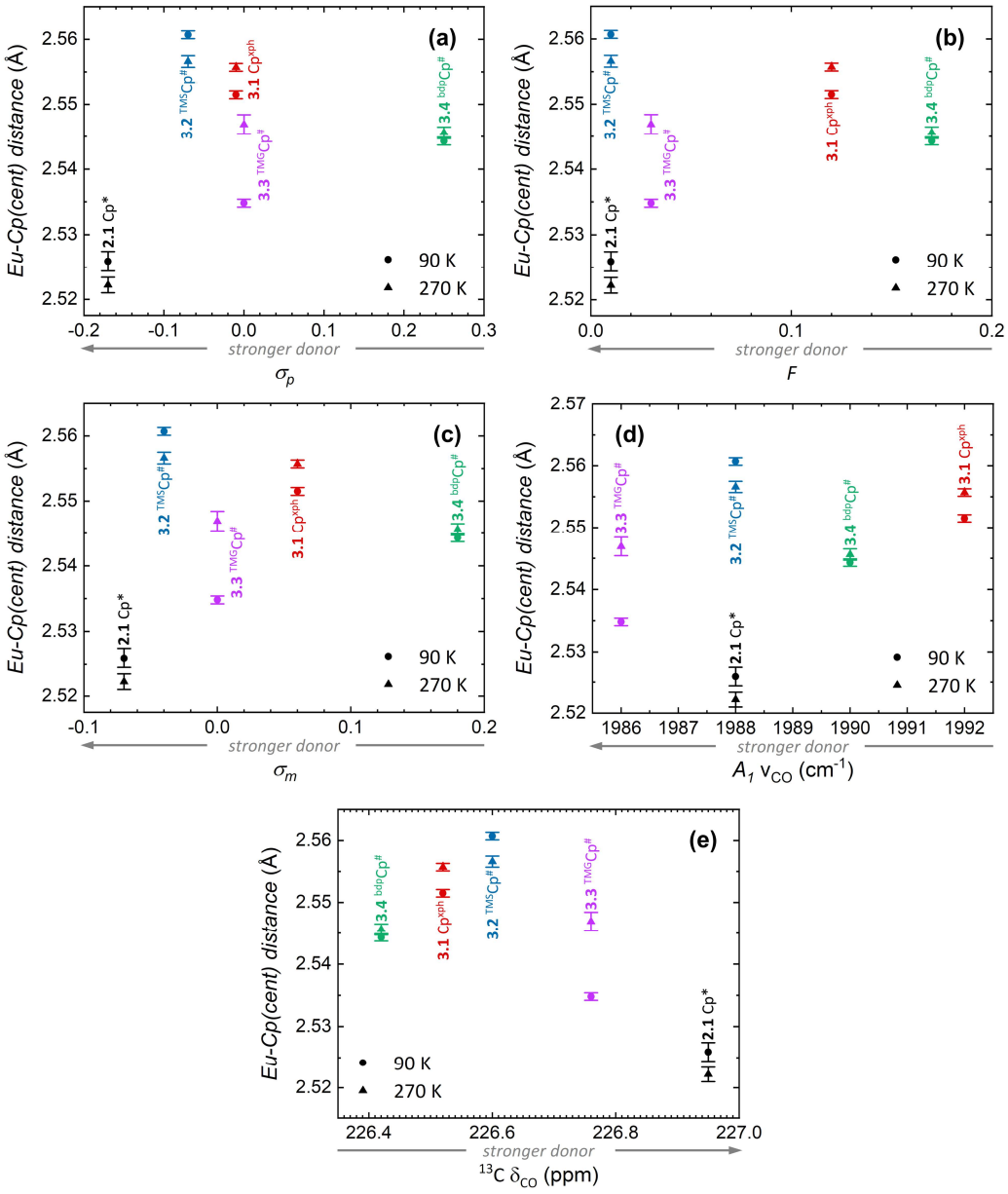


Figure B16. Distance between the cyclopentadienyl centroid and the Eu ion for complexes **2.1**, **3.1–3.4** as a function of the donor strength of the cyclopentadienyl ligand C_5Me_4R, as estimated via the Hammett σ_P parameter (a), the modified Swain-Lupton F parameter (b), and the Hammett σ_M parameter (c) of the substituent R, as well as the A_1 carbonyl stretching frequency (d) and the ^{13}C δ_{CO} of the corresponding complex $(C_5Me_4R)Mn^I(CO)_3$, demonstrating the lack of meaningful correlation between these parameters. Error bars are shown as ±3x esu of the measurement.

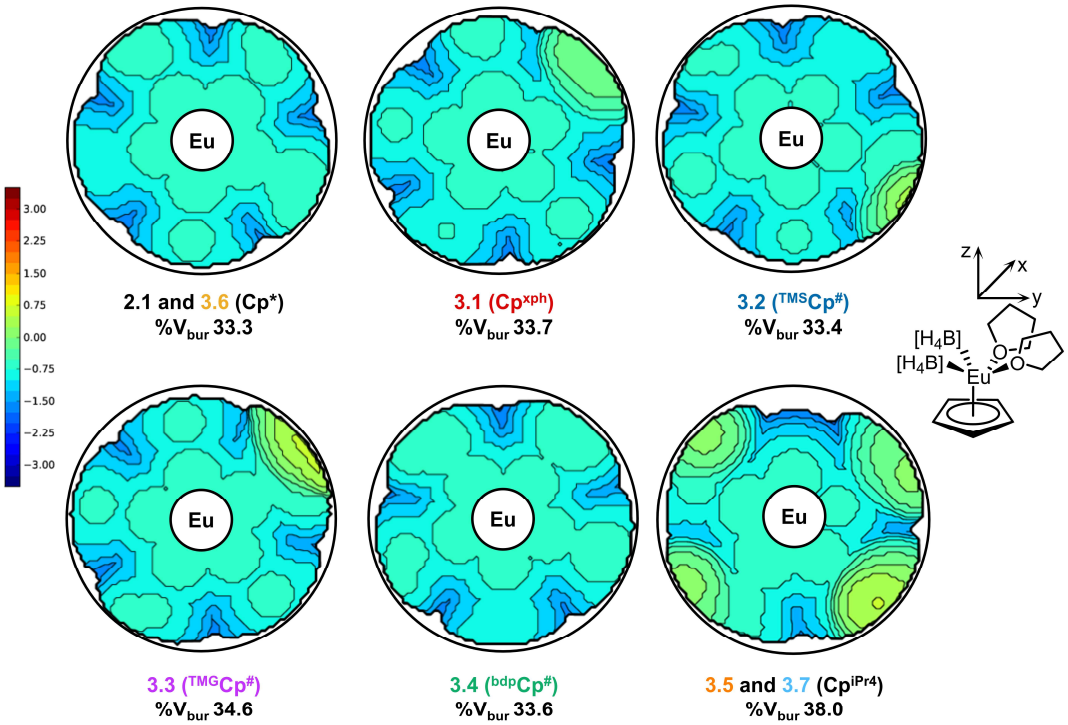


Figure B17. Steric maps of the ligands used in complexes **2.1**, **3.1**–**3.7**.

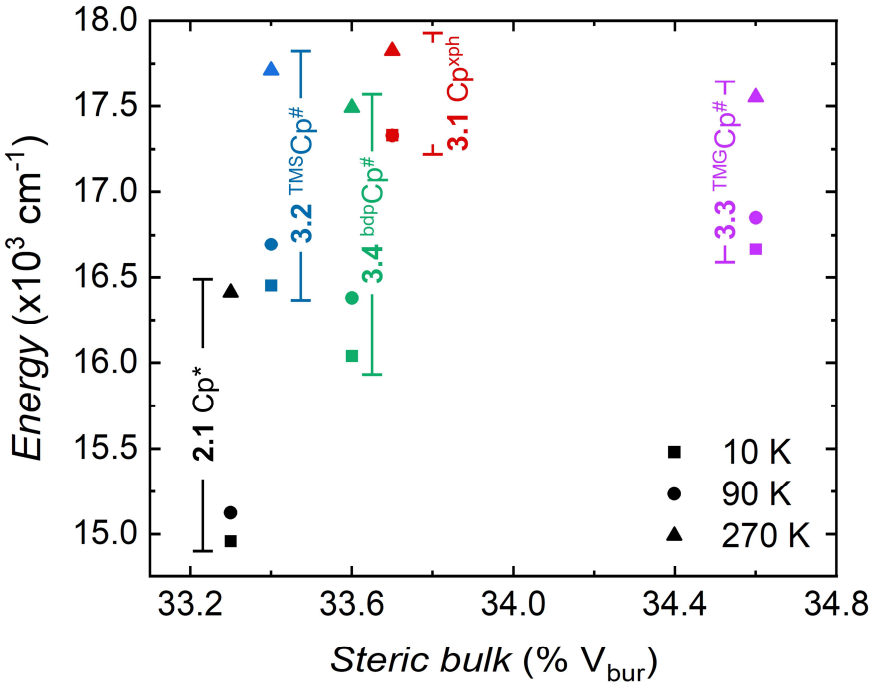


Figure B18. Energy at the emission band maximum for complexes **2.1**, **3.1**–**3.4** as a function of steric bulk (measured as $\%V_{bur}$), demonstrating the lack of meaningful correlation between these parameters. The 10 and 90 K points for **3.1** overlap.

Table B2. Thermal expansion coefficients[56,176] for complexes studied via variable-temperature SCXRD.

Complex	α_V (K^{-1} x10^{-4})
2.1[224]	2.54
3.1	2.21
3.2	2.61
3.3	2.15
3.4	2.07
3.6	2.49

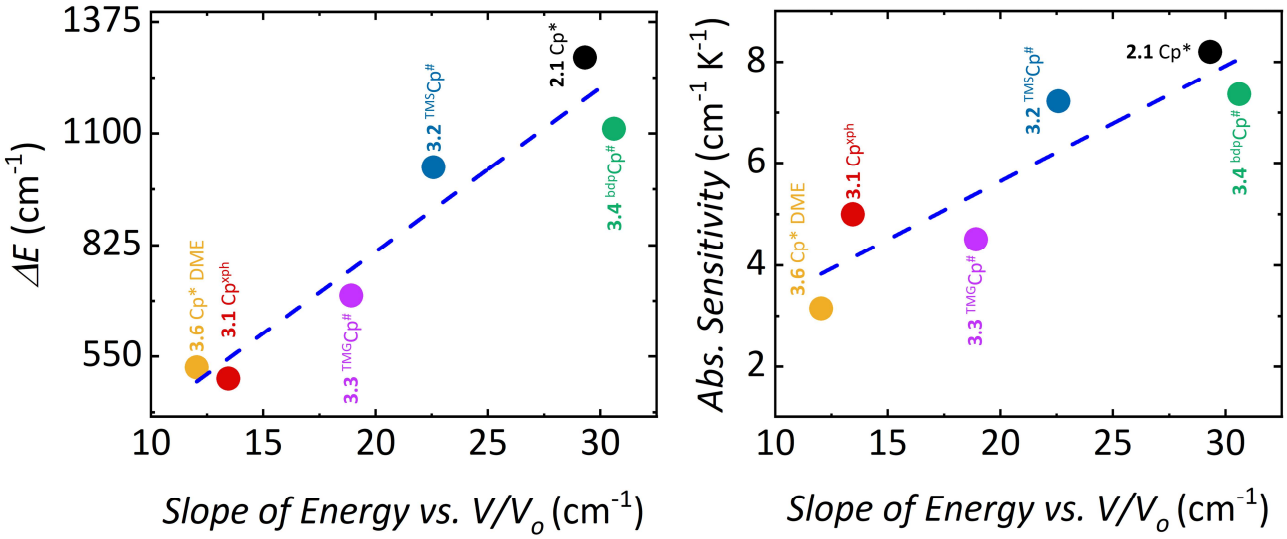


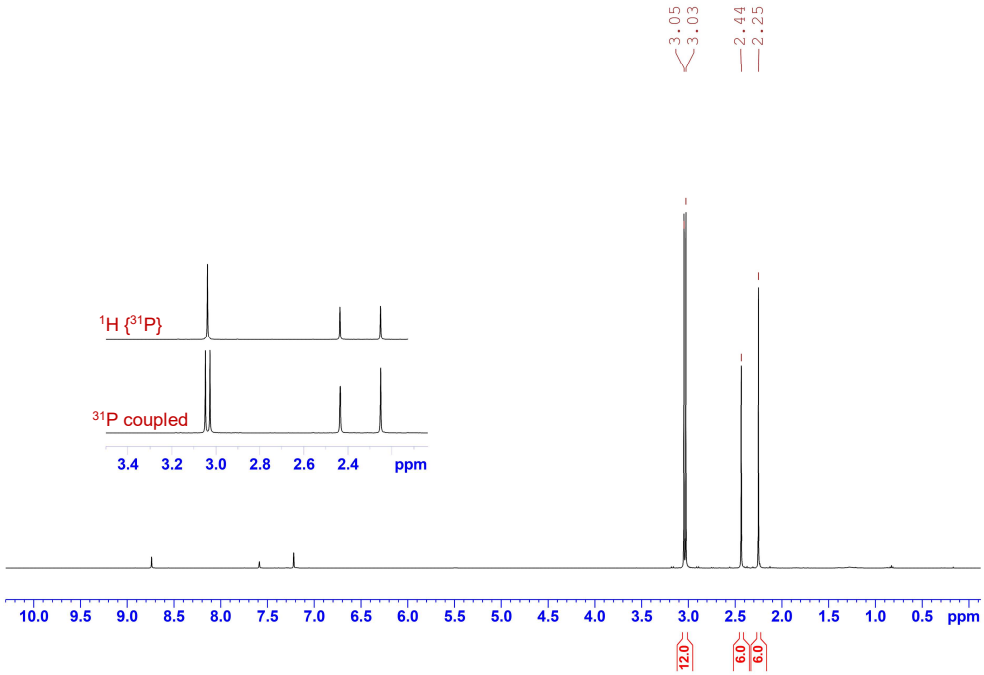
Figure B19. Total change in emission energy ΔE of each complex **2.1**, **3.1–3.4**, and **3.6** over the temperature range 90-270 K (left) and the maximum values of the absolute sensitivity of **2.1**, **3.1–3.4**, and **3.6** (right) plotted against the slopes of the linear fits calculated for plots of energy vs. relative compression of the lattice (i.e., the rate of change of emission energy as a function of lattice compression, see Tables 3.[5, 8, 11, 14, 17]) of each complex. This demonstrates that in general, complexes with a more compressible lattice are expected to show better thermometric performance. Best fitting parameters are (left) $m = 40.3$, $b = 2.38$, $R^2 = 0.8963$; (right) $m = 0.23$, $b = 1.09$, $R^2 = 0.7671$.

APPENDIX C
Corresponding to Chapter 4

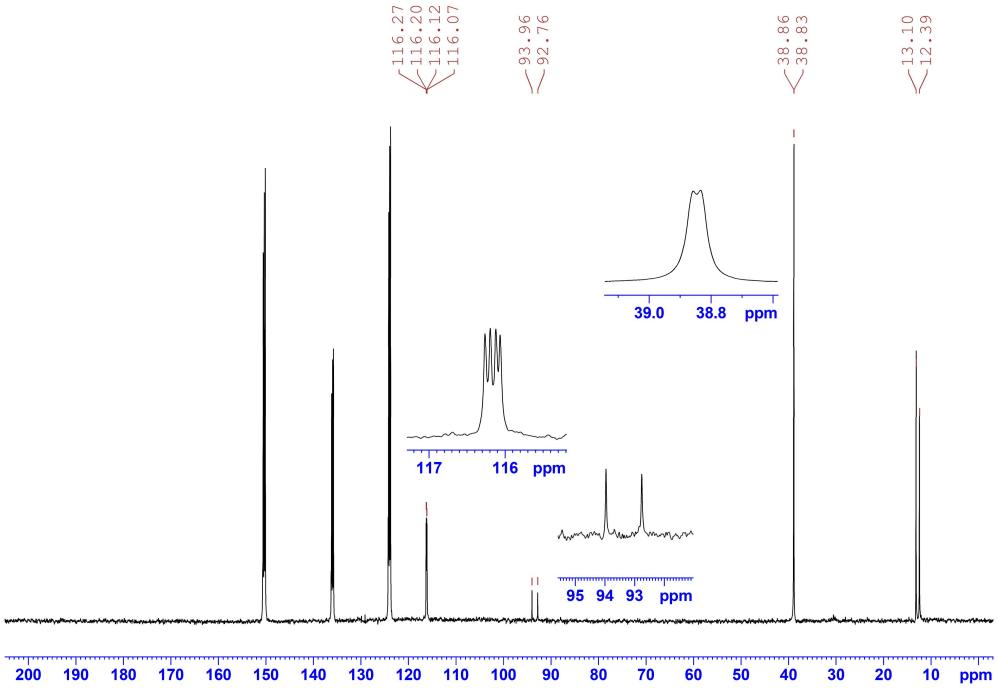
C.1 Nuclear magnetic resonance spectra

Potassium 1-(bis(dimethylamino)phosphinothioyl)-2,3,4,5-tetramethylcyclopentadienide (**KCp$^{\#}$PS**)

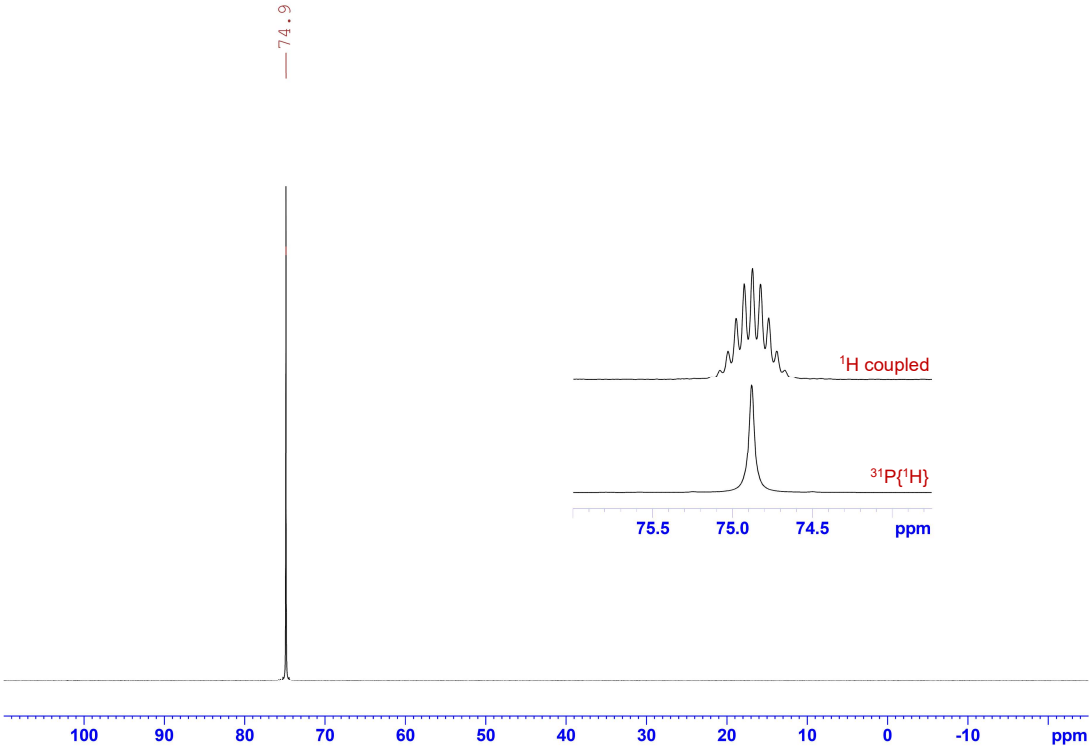
^{1}H NMR (500 MHz, pyridine-d_5*)*



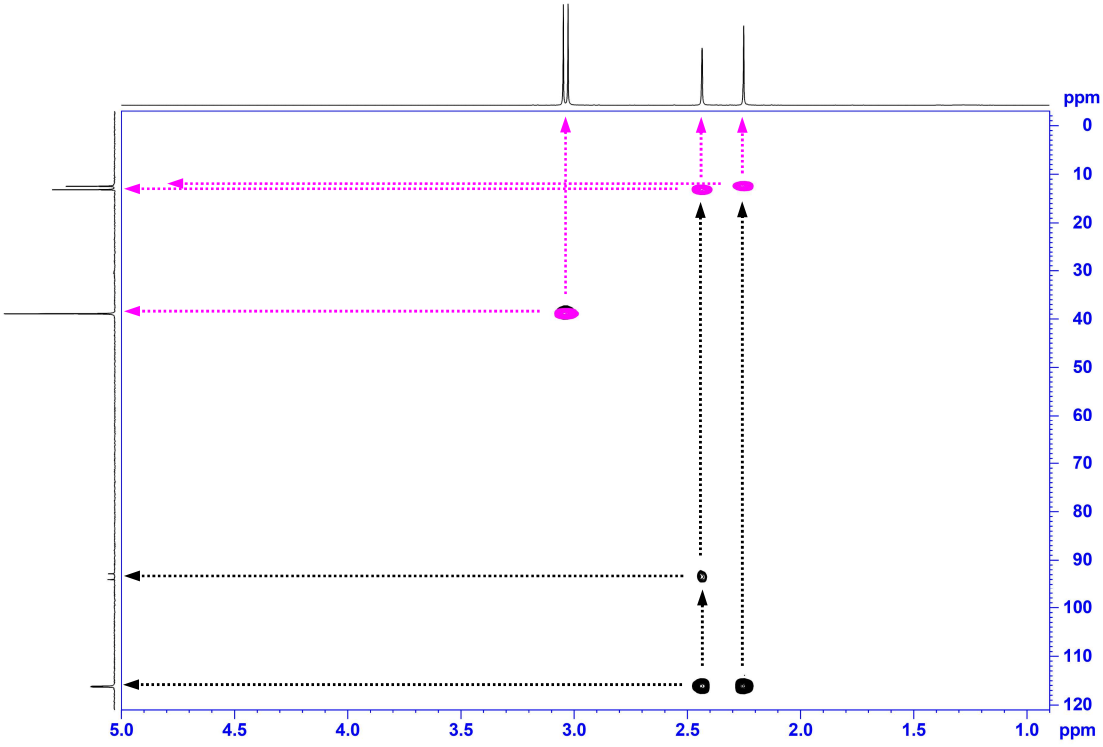
^{13}C NMR (126 MHz, pyridine-d_5*)*



$^{31}P\{^{1}H\}$ NMR (203 MHz, pyridine-d_5)

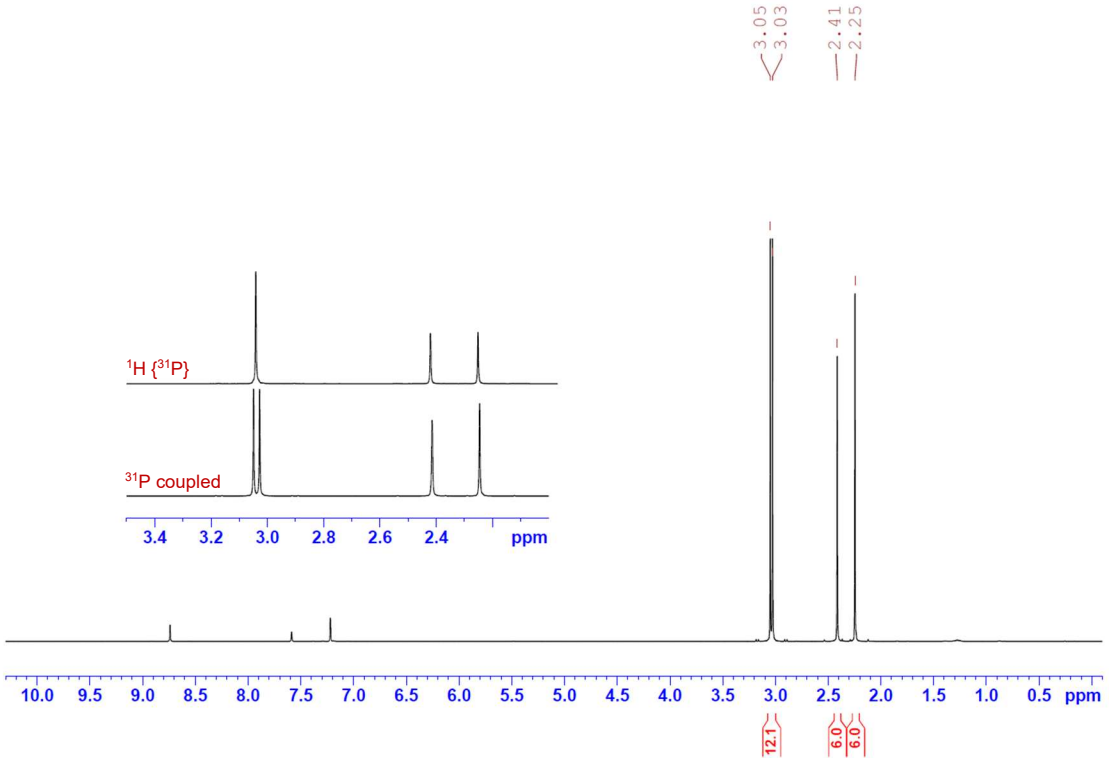


^{1}H-^{13}C HMBC (black) and HSQC (magenta) (pyridine-d_5)

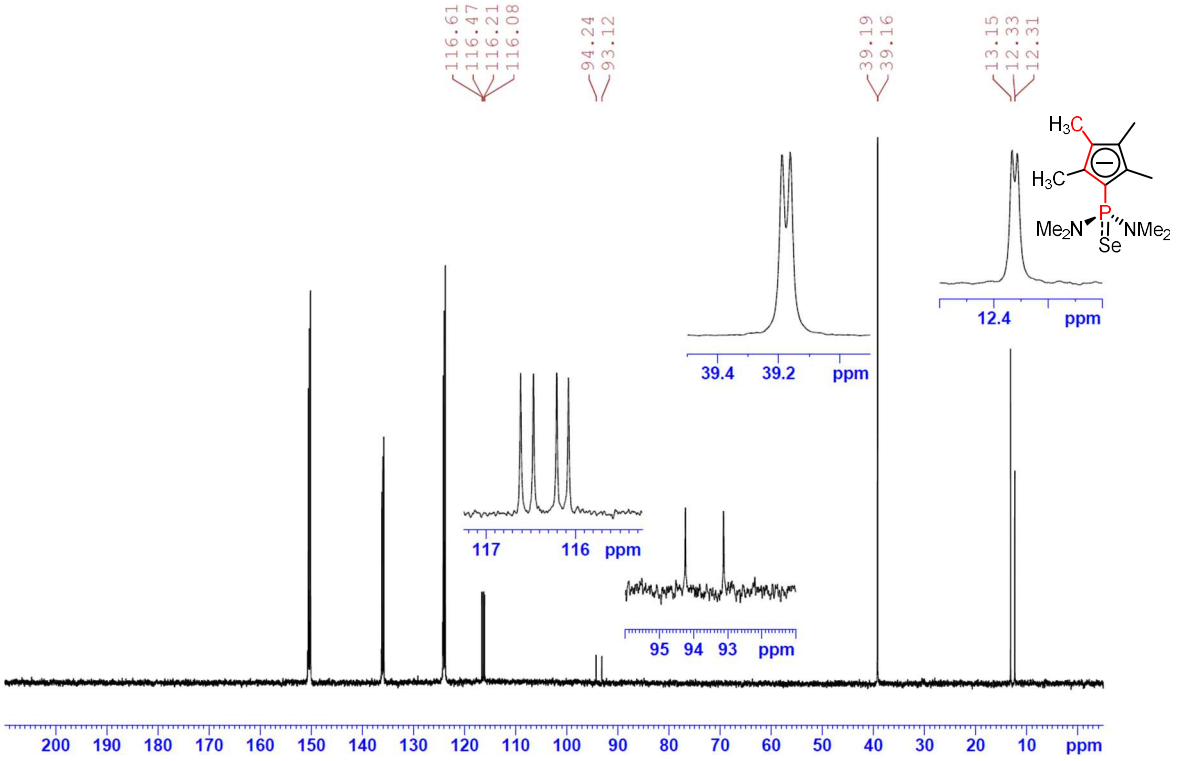


Potassium 1-(bis(dimethylamino)phosphinoselenoyl)-2,3,4,5-tetramethylcyclopentadienide (**KCp$^{\#}$PSe**)

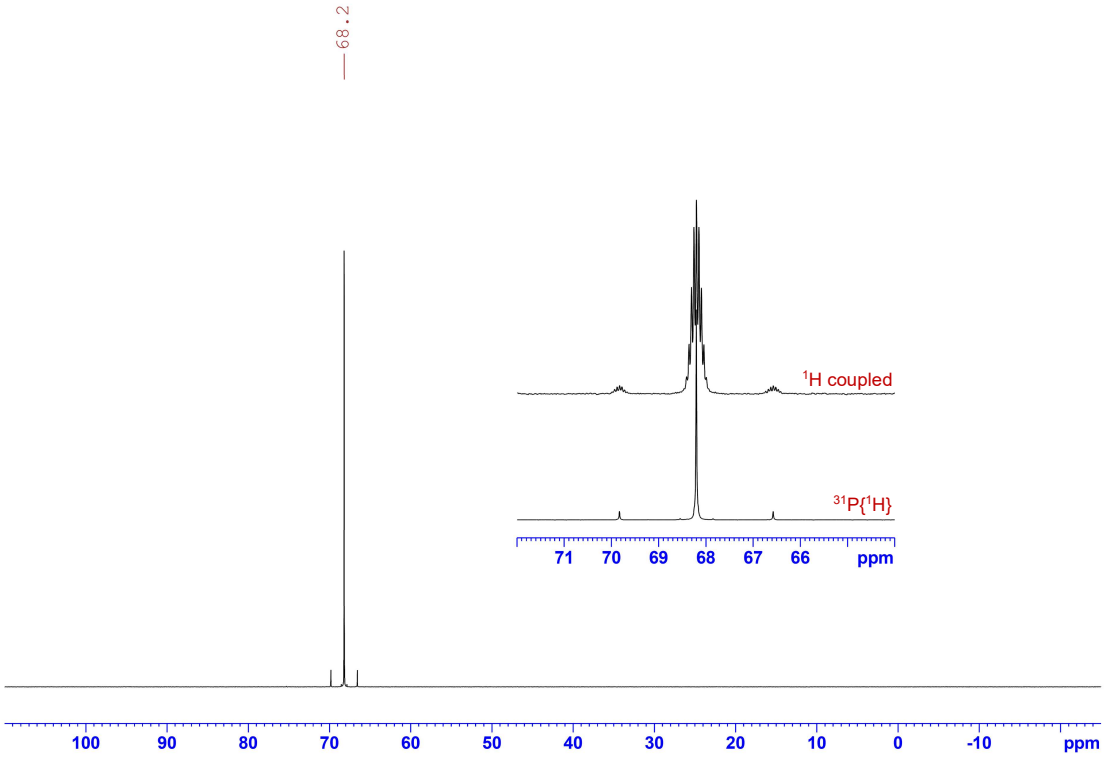
^{1}H NMR (500 MHz, pyridine-d_5*)*



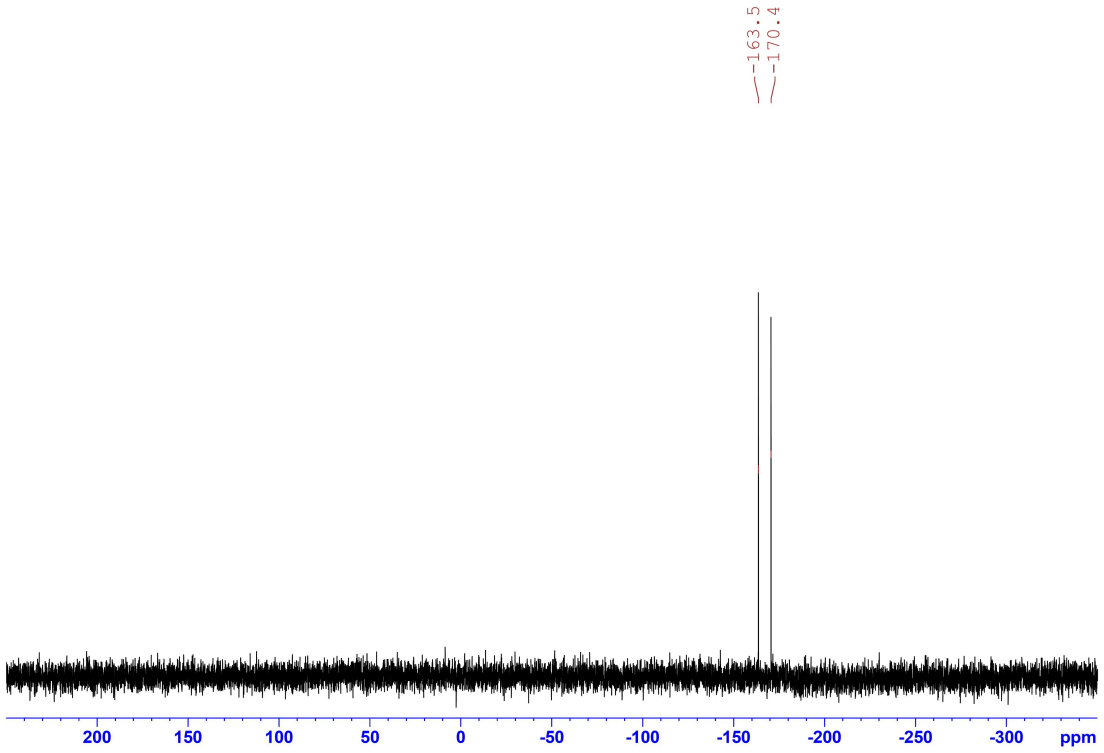
^{13}C NMR (126 MHz, pyridine-d_5*)*



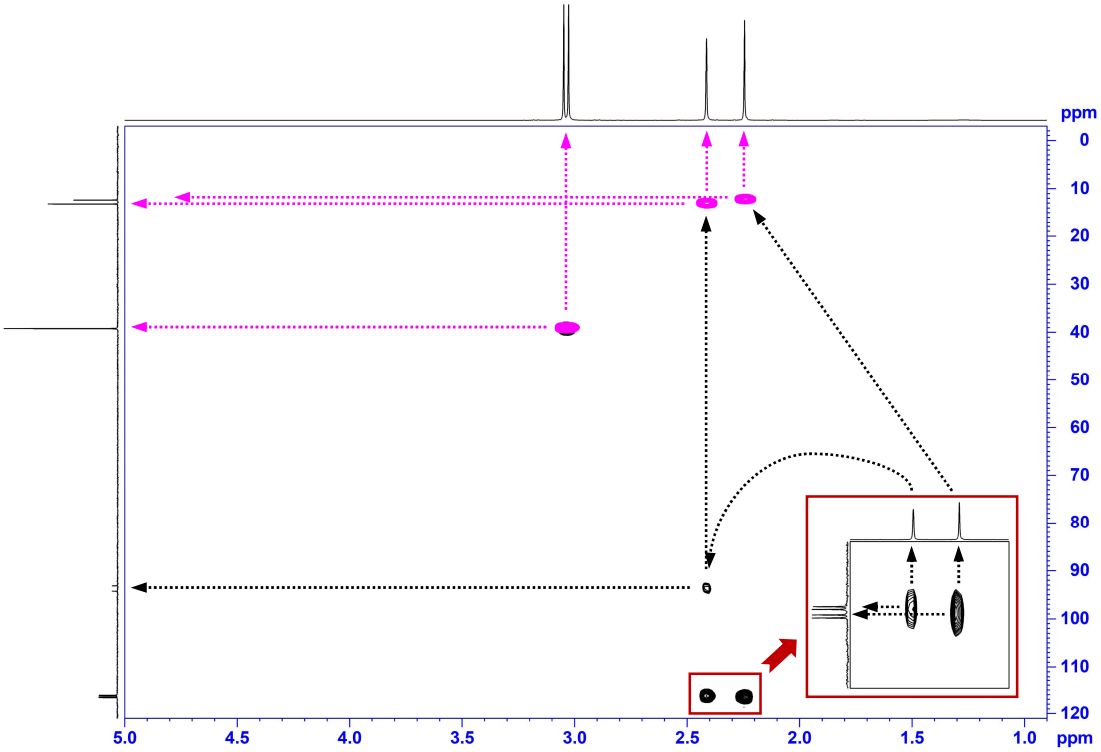
$^{31}P\{^{1}H\}$ NMR (203 MHz, pyridine-d_5)



^{77}Se NMR (95 MHz, pyridine-d_5)

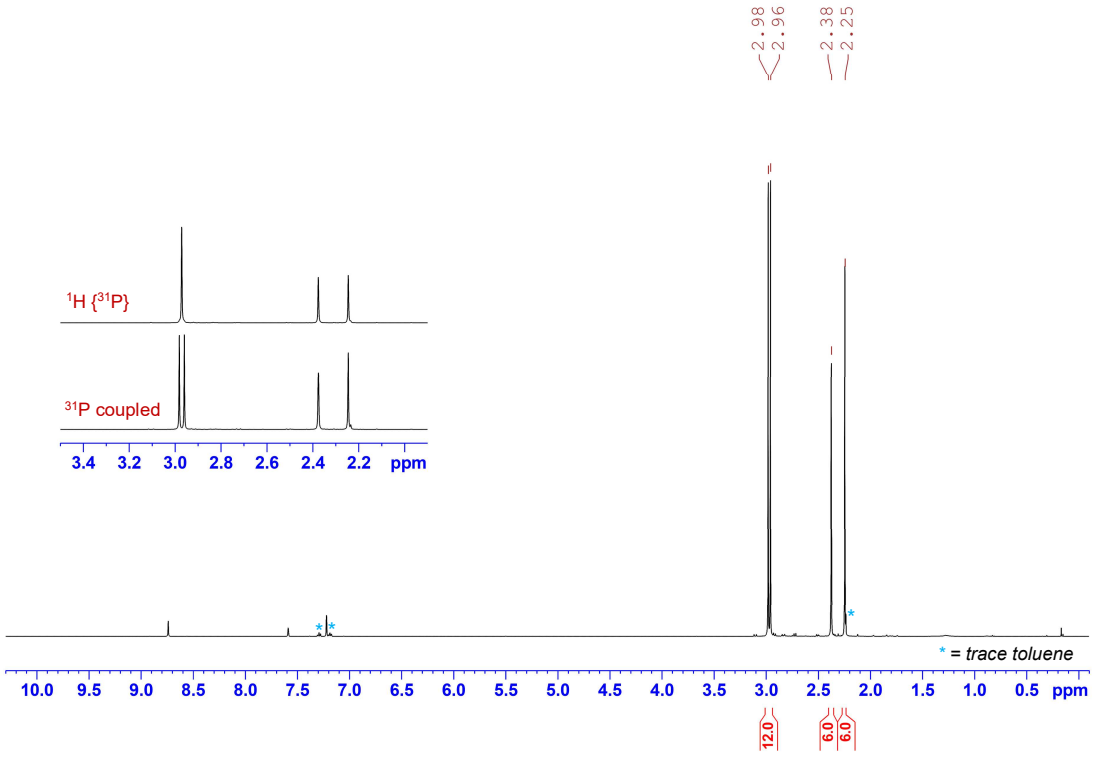


^{1}H-^{13}C HMBC (black) and HSQC (magenta) (pyridine-d_5)

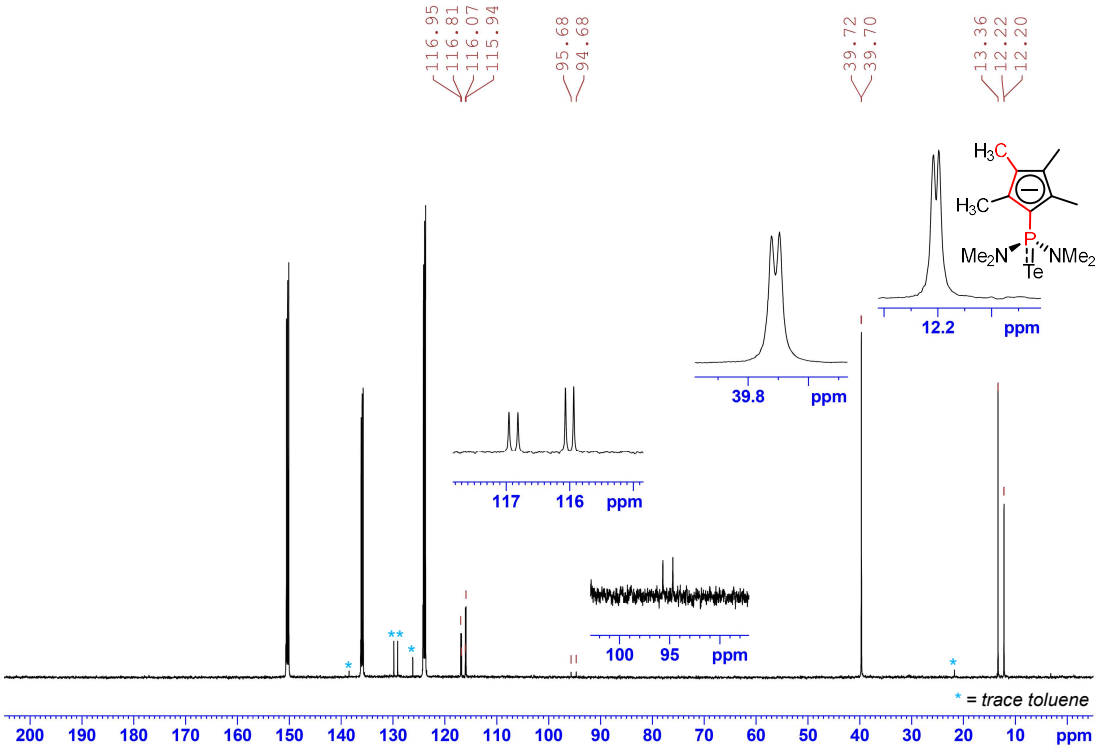


Potassium 1-(bis(dimethylamino)phosphinotelluroyl)-2,3,4,5-tetramethylcyclopentadienide (**KCp#PTe**)

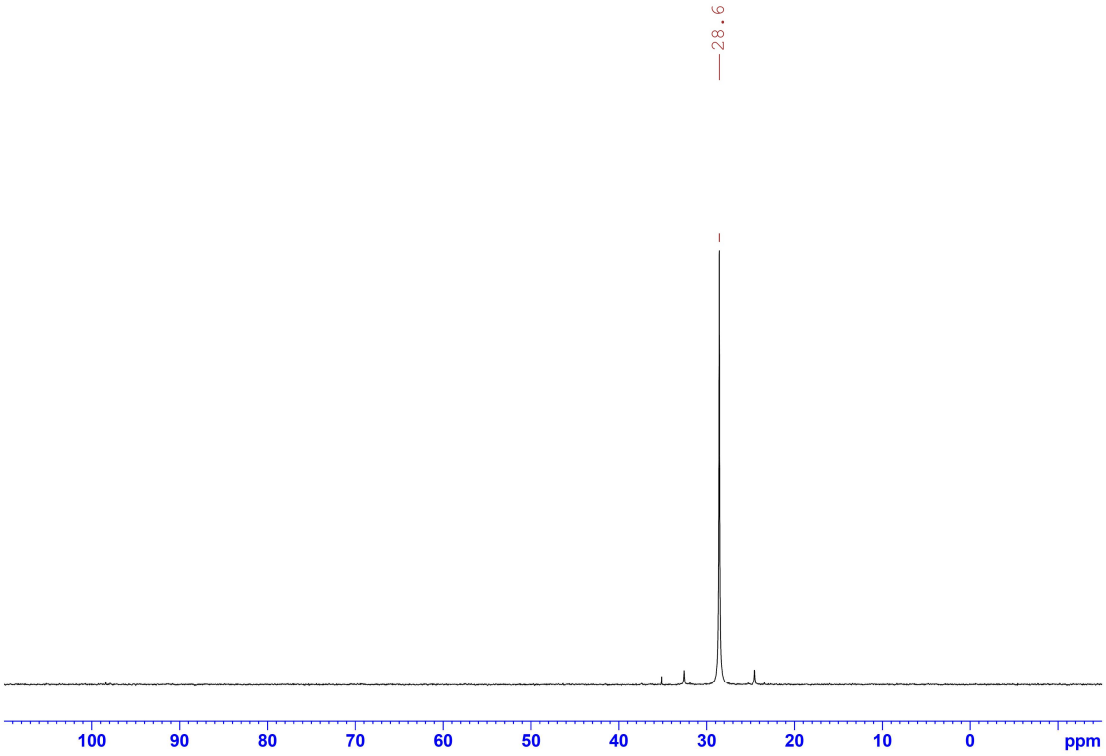
^{1}H NMR (500 MHz, pyridine-d$_5$ after 1 week of stabilization time)



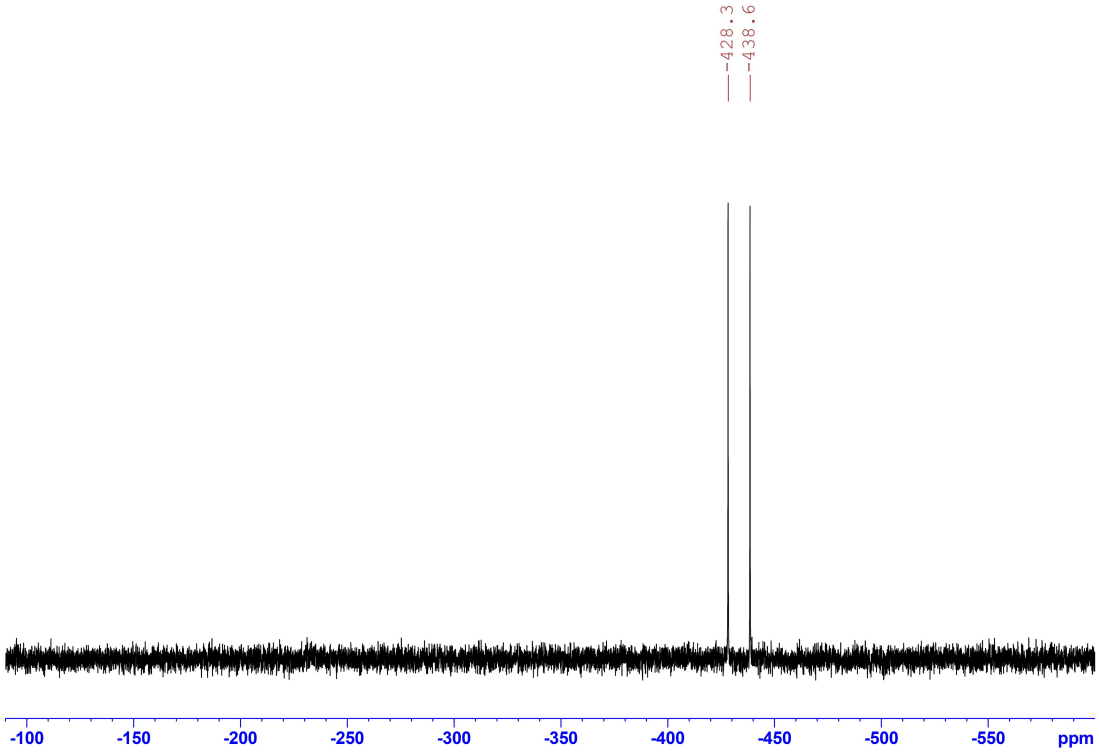
^{13}C NMR (126 MHz, pyridine-d$_5$ after 1 week of stabilization time)



$^{31}P\{^{1}H\}$ NMR (203 MHz, pyridine-d_5 after 1 week of stabilization time)



$^{125}Te\{^{1}H\}$ NMR (158 MHz, pyridine-d_5 after 1 week of stabilization time)



^{1}H-^{13}C HMBC (black) and HSQC (magenta) (pyridine-d_5 after 1 week of stabilization time)

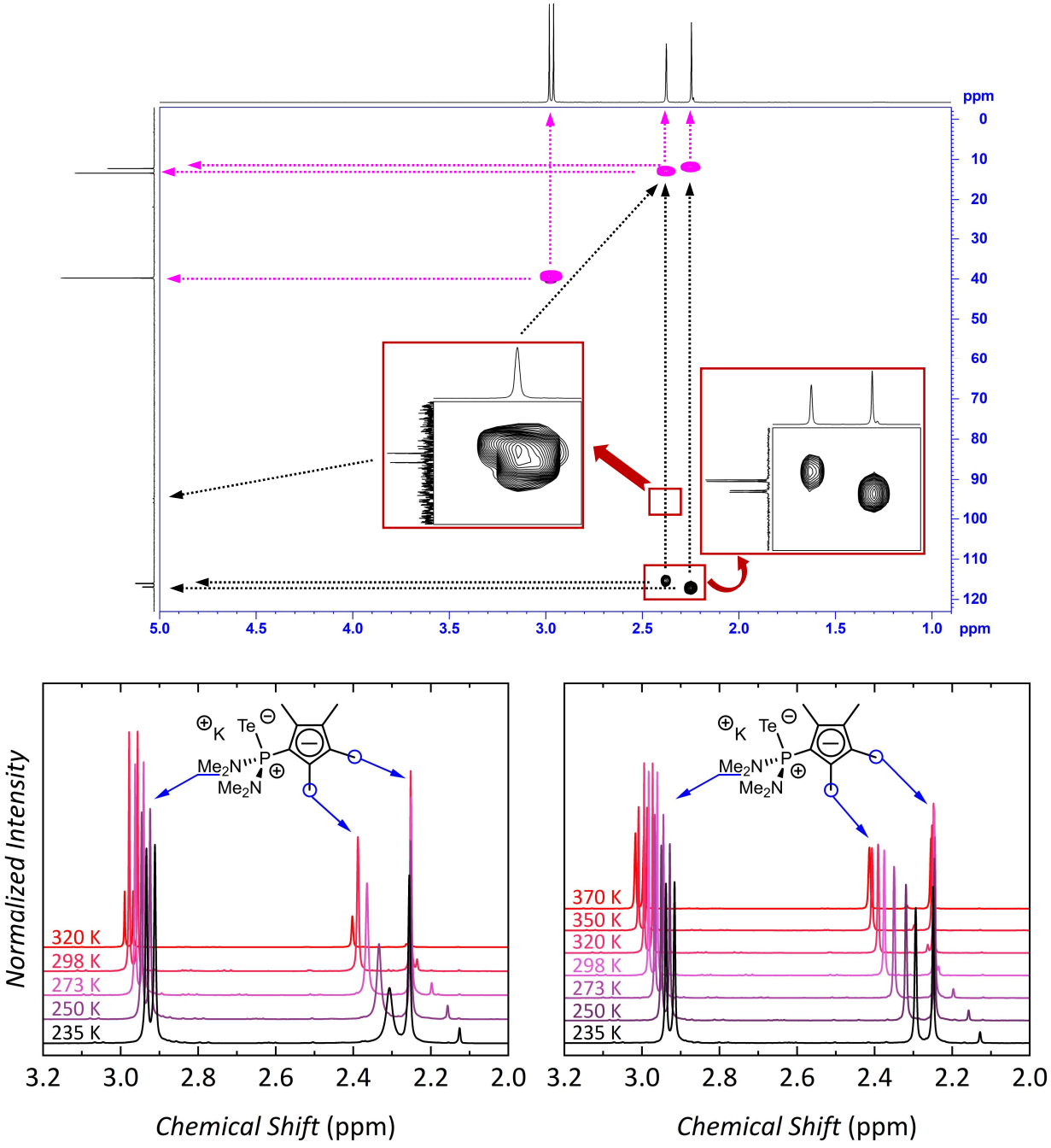


Figure C1. Variable-temperature ^{1}H NMR spectra of **KCp$^{\#}$PTe** within 6 hr of sample preparation (left) and after one week of stabilization time (right). Spectra are normalized to the room-temperature spectrum in both cases.

C.2 Crystallographic information

	4.1S·THF	**4.1S**	**4.1Se**	**4.1Te**
CCDC deposition no.	2477059	2477057	2477058	2477060
Temperature (K)	200	100	100	100
Empirical formula	$C_{34}H_{64}EuN_4O_2P_2S_2$	$C_{26}H_{48}EuN_4P_2S_2$	$C_{26}H_{48}EuN_4P_2Se_2$	$C_{26}H_{48}EuN_4P_2Te_2$
Formula weight (amu)	838.91	694.70	788.50	885.78
Crystal system	Triclinic	Orthorhombic	Monoclinic	Orthorhombic
Space group	$P\bar{1}$	Pbcn	P2/c	$Pna2_1$
Unit cell dimensions (Å and °)	a = 12.2404(9)	a = 18.4146(8)	a = 21.0493(12)	a = 21.1214(18)
	b = 12.2684(9)	b = 15.9712(7)	b = 8.2933(4)	b = 8.4038(8)
	c = 14.6566(11)	c = 10.8486(5)	c = 20.8630(11)	c = 18.2791(15)
	α = 86.165(2)	α = 90	α = 90	α = 90
	β = 69.291(2)	β = 90	β = 119.627(2)	β = 90
	γ = 80.645(2)	γ = 90	γ = 90	γ = 90
Volume (Å^3)	2031.3(3)	3190.6(2)	3165.9(3)	3244.5(5)
Z	2	4	4	4
Density (calc., g/cm^3)	1.372	1.446	1.654	1.813
Abs. coefficient (mm^{-1})	1.758	2.218	4.403	3.815
F(000)	874.0	1428.0	1572.0	1716.0
Crystal size (mm^3)	0.290 x 0.220 x 0.033	0.173 x 0.134 x 0.120	0.294 x 0.201 x 0.159	0.304 x 0.152 x 0.146
Radiation (wavelength, Å)	Mo Kα (0.71073)	Mo Kα (0.71073)	Mo Kα (0.71073)	Mo Kα (0.71073)
Theta range (°)	1.485 to 27.103	1.688 to 30.503	1.113 to 38	1.928 to 41.151
Index ranges (h,k,l)	- 15 to 15, -15 to 15, -18 to 18	-26 to 26, -21 to 22, -15 to 15	-36 to 36, -14 to 14, -36 to 36	-39 to 39, -15 to 13, -33 to 33
Reflections collected	47881	41705	316529	172006
Independent reflections	8986	4868	17257	21553
R(int)	0.0340	0.0827	0.0772	0.0608
Completeness (%)	100	99.7	100	100
Max. and min. transmission	0.746 and 0.663	0.527 and 0.470	0.558 and 0.433	0.619 and 0.476
Data / restraints / parameters	8986 / 260 / 485	4868 / 0 / 167	17257 / 0 / 333	21553 / 1 / 333
Goodness-of-fit on F^2	1.030	1.245	1.258	1.066
R indices (all data)	R_1 = 0.0338	R_1 = 0.0579	R_1 = 0.0400	R_1 = 0.0230
	wR_2 = 0.0620	wR_2 = 0.1335	wR_2 = 0.0614	wR_2 = 0.0476
Final R indices [$I > 2\sigma(I)$]	R_1 = 0.0249	R_1 = 0.0493	R_1 = 0.0302	R_1 = 0.0204
	wR_2 = 0.0583	wR_2 = 0.1286	wR_2 = 0.0587	wR_2 = 0.0464
Largest diff. peak and hole (e.Å^{-3})	0.80 and -0.37	1.27 and -0.92	1.12 and -0.97	1.63 and -0.53

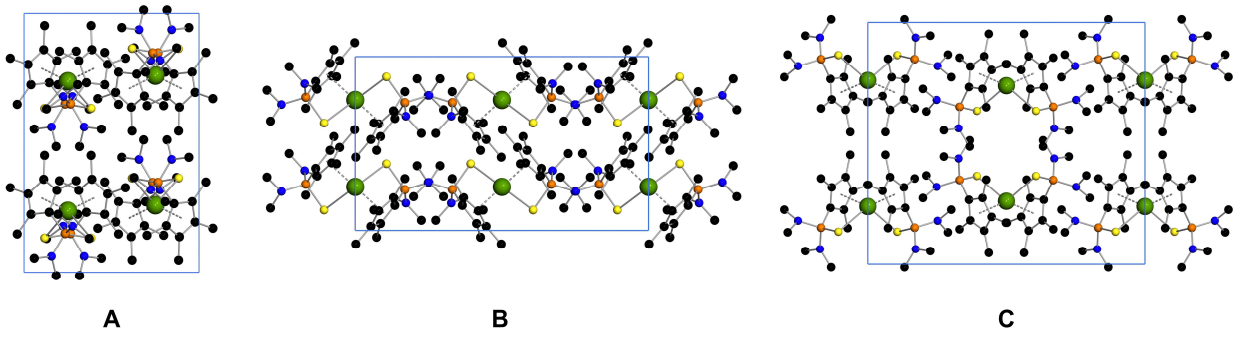


Figure C2. Crystallographic packing diagrams of **4.1S**, shown along the (a) *a*-axis, (b) *b*-axis, and (c) *c*-axis of the unit cell. Hydrogen atoms are omitted for clarity.

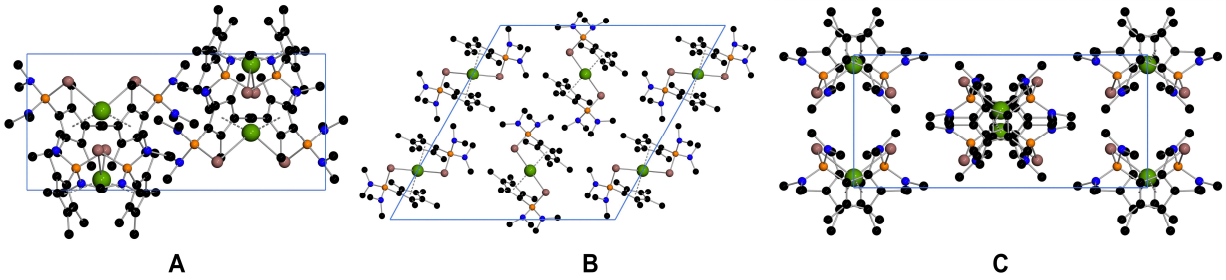


Figure C3. Crystallographic packing diagrams of **4.1Se**, shown along the (a) *a*-axis, (b) *b*-axis, and (c) *c*-axis of the unit cell. Hydrogen atoms are omitted for clarity.

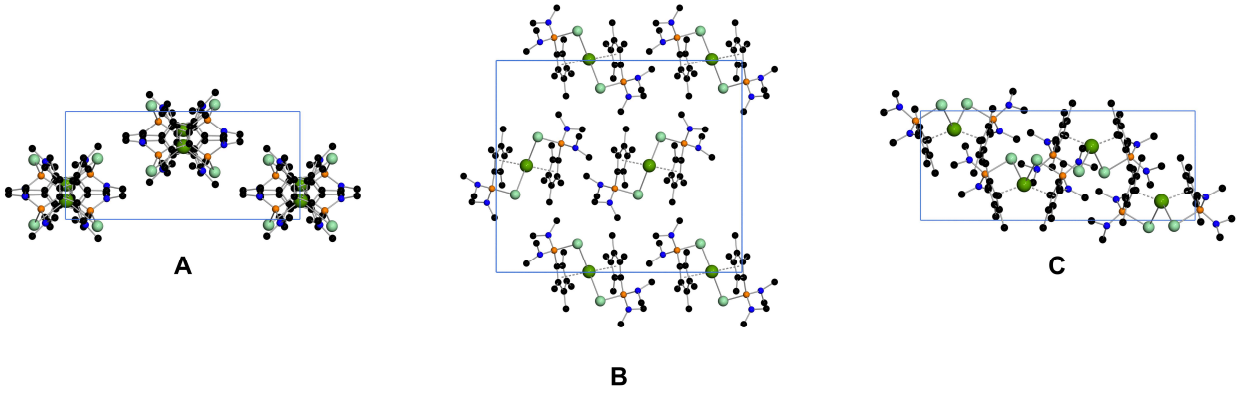


Figure C4. Crystallographic packing diagrams of **4.1Te**, shown along the (a) *a*-axis, (b) *b*-axis, and (c) *c*-axis of the unit cell. Hydrogen atoms are omitted for clarity.

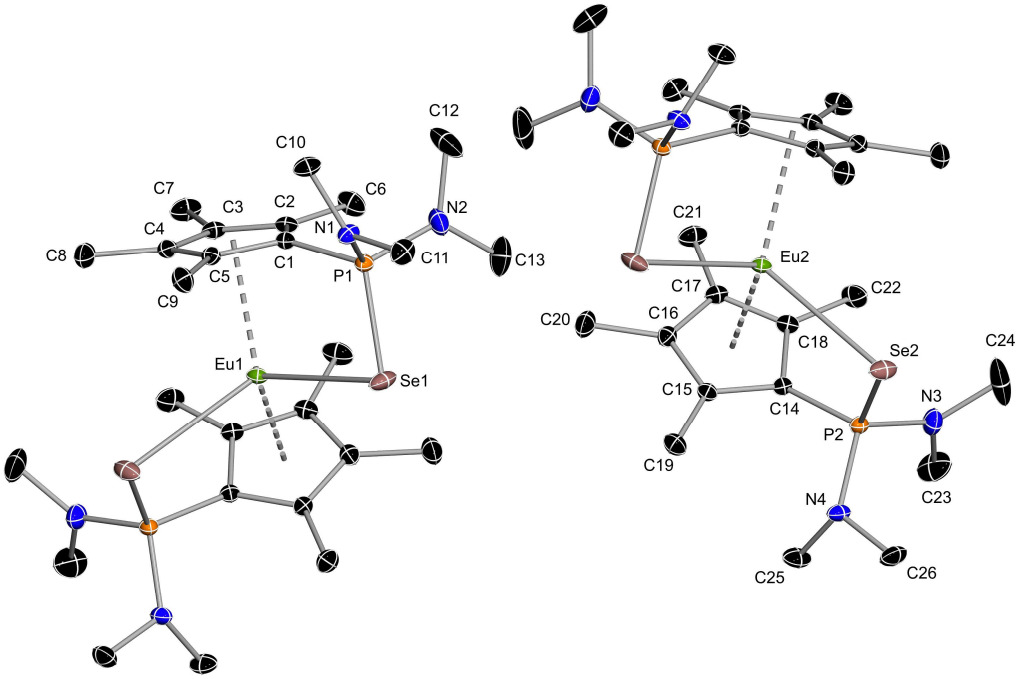


Figure C5. Solid-state structures of both unique molecules in the unit cell of **4.1Se** (two half molecules are uniquely defined). These are similar but differ slightly in their metrical parameters; the differences are listed in Table C1. Thermal ellipsoids are shown at 50% probability, and hydrogen atoms have been omitted for clarity.

Table C1. Comparison of metrical parameters between the two uniquely-defined half-molecules in the asymmetric unit of the crystal structure of **4.1Se**. "Fragment 1" contains Eu1 and associated atoms, and "Fragment 2" contains Eu2 and associated atoms. All distances are given in angstroms, and all angles are given in degrees.

	Fragment 1	**Fragment 2**	
Eu-Cp(cent) distance	2.5379(1)	2.5385(1)	
Cp(cent)-Eu-Cp(cent) angle	137.728(2)	136.733(3)	
Torsional twist angle τ	118.8(1)	115.0(1)	
C1-C2 distance	1.438(2)	1.437(2)	C14-C15 distance
C2-C3 distance	1.408(3)	1.404(2)	C15-C16 distance
C3-C4 distance	1.429(2)	1.426(3)	C16-C17 distance
C4-C5 distance	1.399(3)	1.405(2)	C17-C18 distance
C5-C1 distance	1.437(2)	1.440(2)	C18-C14 distance
C2-C6 distance	1.503(2)	1.506(2)	C15-C19 distance
C3-C7 distance	1.504(2)	1.503(2)	C16-C20 distance
C4-C8 distance	1.504(3)	1.503(2)	C17-C21 distance
C5-C9 distance	1.504(2)	1.504(3)	C18-C22 distance
C1-P1 distance	1.764(2)	1.763(1)	C14-P2 distance
P1-Se1 distance	2.1540(6)	2.1503(7)	P2-Se2 distance
P1-N1 distance	1.658(2)	1.656(1)	P2-N3 distance
P1-N2 distance	1.654(2)	1.662(2)	P2-N4 distance
N1-P1-N2 angle	108.15(8)	108.51(9)	N3-P2-N4 angle
Eu1-Se1 distance	3.0816(4)	3.0835(3)	Eu2-Se2 distance
Se1′-Eu1-Se1 angle	109.91(1)	109.088(9)	Se2′-Eu2-Se2 angle

Structural comparisons

Eu-Cp(cent) distances. A search of the Cambridge Structural Database for the terms "europium" and "cyclopentadienyl" returned 80 hits, from which 25 structures were selected for comparison that contained metallocene-like cyclopentadienyleuropium(II) structural motifs where the cyclopentadienyl ligands were fully substituted:

BEDMAC	JINDOA	TUYZAO
BIJMEM	MIZTAQ	VEPNIO
CALXIZ	NILROT	VISBEG
CIBMEJ	PUYKAX	VURHOG
CIBMIN	QIQSAN	VURJAU
DIVYEQ	SERGUS	YUKDUF
DUHYIO	SERHED	ZESRAQ
HIYKOS	TIMWAO	TUYZAO
JACLIJ	TUYYOB	VEPNIO

The Eu-Cp(cent) distances among this population ranged from 2.49–2.68 Å, with an average value of 2.56 Å and standard deviation 0.04 Å.

Metal-bound P-Te distances. A search of the Cambridge Structural Database for the fragment "P-Te-[any metal] returned 87 hits, 15 of which were excluded that were duplicate structures or did not contain a formally P^{V}-Te-M motif. The P-Te distances among the remaining 72 structures:

AFOGUB	DOMMUO	NEWZIZ	PICCOU	SUBZAS	WOXREI
BOYMEI	EDIKAE	NEXBIC	PICCUA	TAKMAV	WUDSOE
BOYMIM	FAQLOB	NUMPES	PIWLEN	TAKMEZ	WUDSUK
BOYMOS	JISPAG	OGOHOH	PIWLIR	TAKMID	WUDTAR
BOYMUY	JISRIQ	OGOHUN	PIWLOX	TAKMOJ	WUDTEV
BOYNAF	KAWSEH	ONEFAQ	PODDUI	TASHOL	WUDTOF
BOYNEJ	KAWSIL	ONEFEU	PODFEU	TASJAZ	WUDVAT
CEPSOG	KAWSOR	ONEFIY	PODFIY	TASJED	XORYEJ
CEPVAV01	KOBYOQ	ONEFOE	PODFOE	TASJIH	XORYIN
DEGTIS	LUNGIK	PICCAG	RACQIV	TASJON	XORYOT
DOMMEY	MECYOJ	PICCEK	RIWRUL	WEMREN	XORYUZ
DOMMIC	MECYUP	PICCIO	RIWSAS	WEMRIR	XUMXEJ

ranged from 2.38–2.51 Å, with an average value of 2.44 Å and standard deviation 0.03 Å.

Eu^{II}-S distances. A search of the Cambridge Structural Database for the fragment "Eu-[any bond]-S" returned 91 hits, from which 18 structures were selected for comparison that contained Eu in oxidation state II:

AFECAS	HOXJIR	NOQYOH	UBUFOM	ZIMZEA	ZIPNUH
CUYPAO	LUPGOU	PORBIH	WAZBIL	ZIMZIE	ZIPPAP
HIPLID	NERTUD01	TICYIO01	WUVCOI	ZIMZOK	

The Eu-S distances among this population ranged from 2.80-3.37 Å, with an average value of 3.03 Å and standard deviation 0.09 Å.

Eu^{II}-Se distances. A search of the Cambridge Structural Database for the fragment "Eu-[any bond]-Se" returned 21 hits, from which 8 structures were selected for comparison that contained Eu in oxidation state II:

INOHUR	NOQYEX	YAVXAU	ZIMKUB
LIBLUD	WAZBOR	YAVXEY	ZIMLAI

The Eu-Se distances among this population ranged from 3.06-3.35 Å, with an average value of 3.16 Å and standard deviation 0.08 Å.

Eu^{II}-Te distances. A search of the Cambridge Structural Database for the fragment "Eu-[any bond]-Te" returned 8 hits, and it is interesting to note that all crystallographically characterized Eu-Te contacts to date are in complexes of Eu^{II}:

FIJJAN	FIJJOB	LIBCUU	PITJOR
FIJJER	FIJJUH	LIBDAB	TOMTIA

The Eu-Te distances among this population ranged from 3.16-3.52 Å, with an average value of 3.33 Å and standard deviation 0.09 Å.

Distances about P in (diaminophosphinochalcogenoyl)cyclopentadienyl metal complexes. These are:

FIWPOS	FIWQIN	FIXDEX	HOVXEV	ORIXOD	VAYPER
FIWPUY	FIWQOT	FIXDIB	NAYFEY	ORIXUJ	XUTTAJ
FIWQAF	FIWQUZ	FIXDOH	NAYFIC	ORIYAQ	
FIWQEJ	FIWRAG	FIXDOH01	ORIXIX	UXEHAI	

The P-N distances among this population ranged from 1.63–1.70 Å, with an average value of 1.66 Å and standard deviation 0.02 Å. The P-C(Cp) distances are rather consistent and range from 1.74-1.80 Å, with an average value of 1.78 Å and standard deviation 0.01 Å.

C.3 Infrared spectra

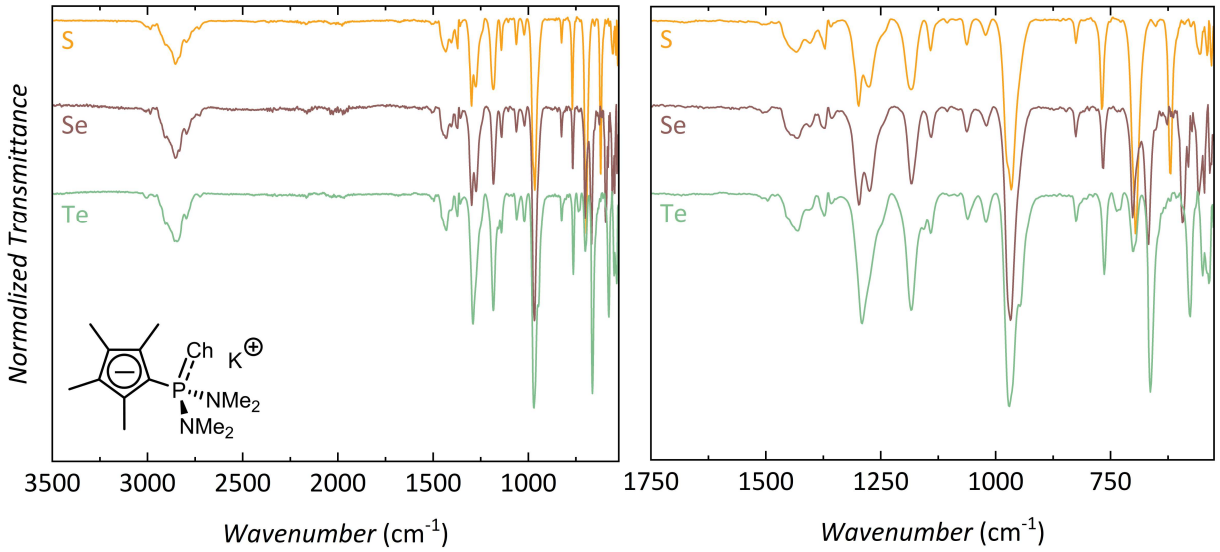


Figure C6. Infrared spectra of ligand precursors **KCp#PCh**. *Left:* full spectra. *Right:* closeup of the fingerprint region (525–1750 cm^{-1}).

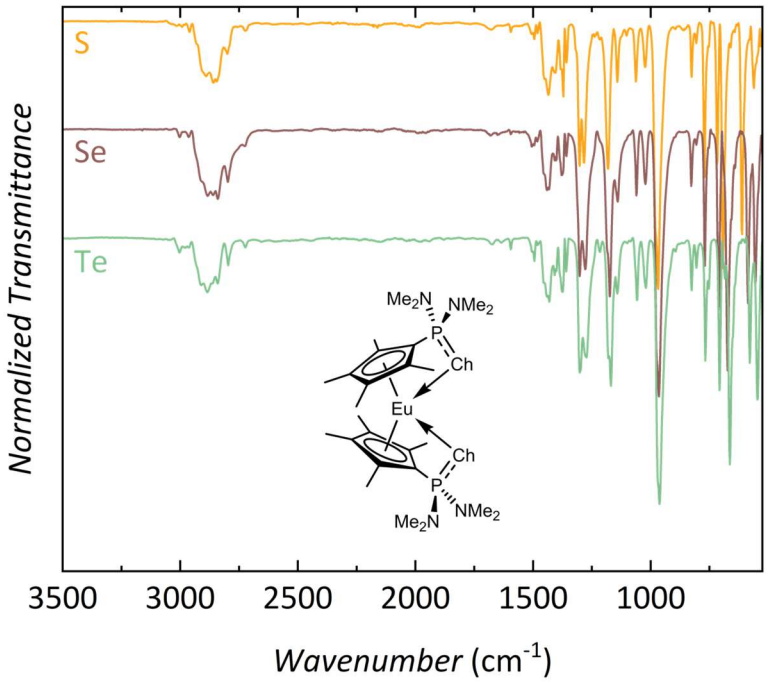


Figure C7. Infrared spectra of complexes **4.1Ch**.

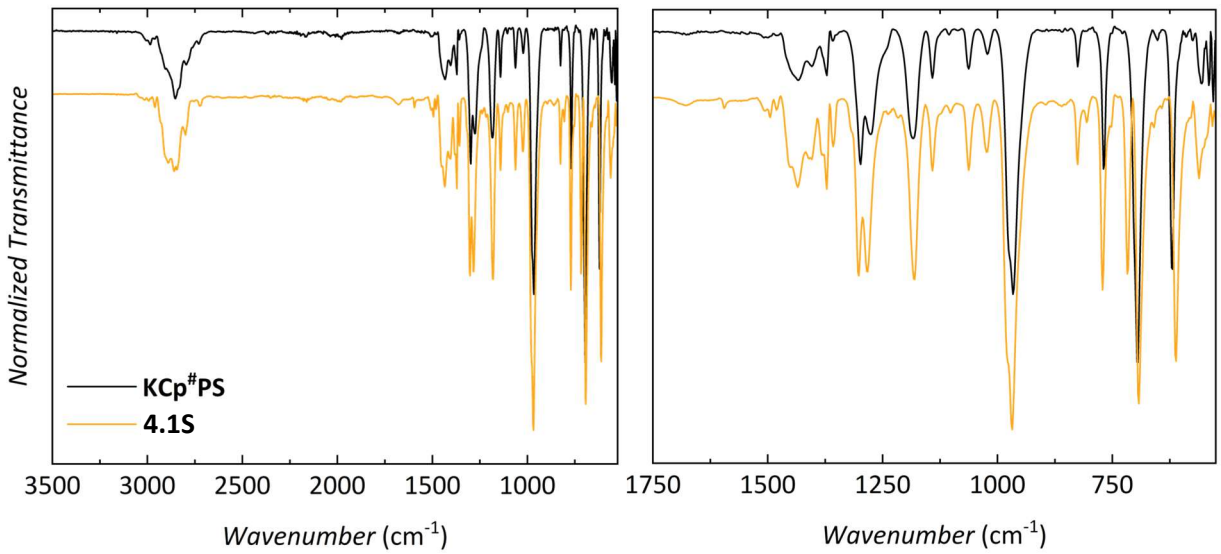


Figure C8. Infrared spectrum of **KCp#PS** (black curve) compared to the corresponding Eu complex **4.1S** (yellow curve). *Left:* full spectra. *Right:* closeup of the fingerprint region (525–1750 cm^{-1}).

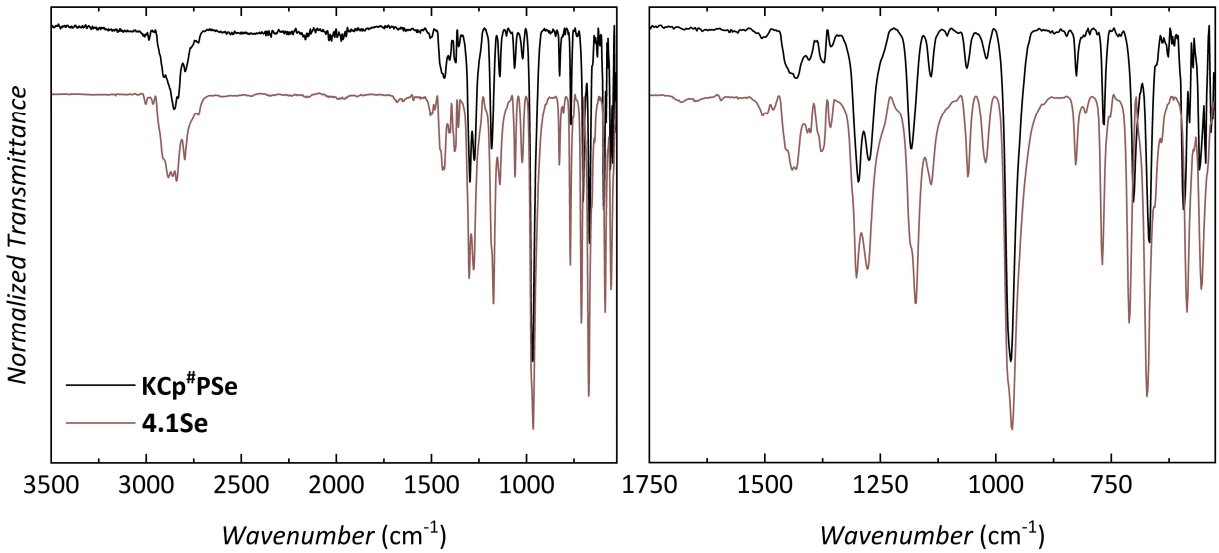


Figure C9. Infrared spectrum of **KCp#PSe** (black curve) compared to the corresponding Eu complex **4.1Se** (brown curve). *Left:* full spectra. *Right:* closeup of the fingerprint region (525–1750 cm^{-1}).

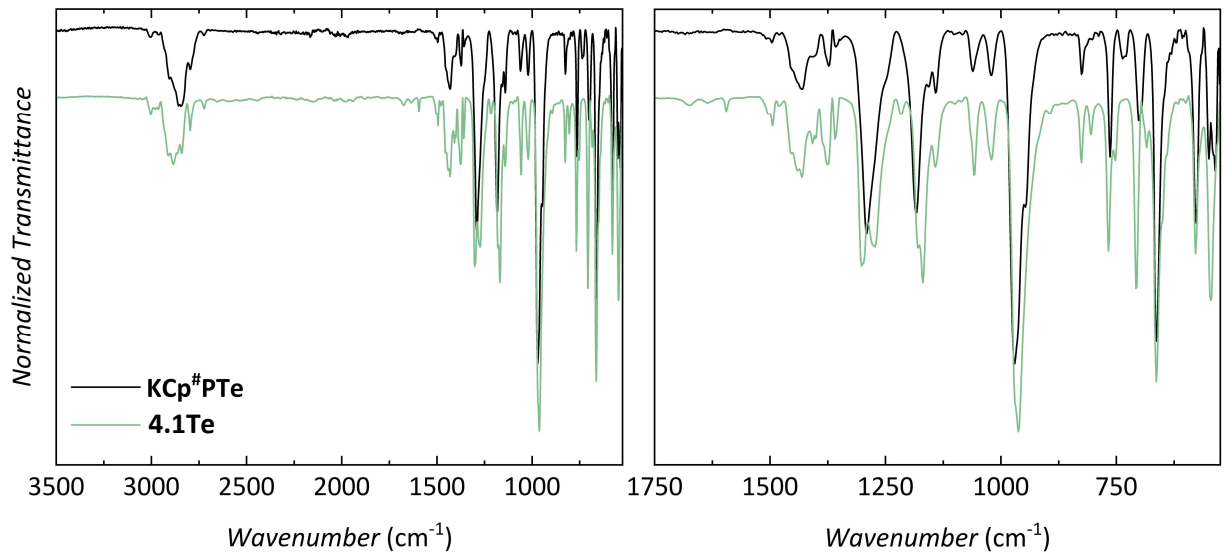


Figure C10. Infrared spectrum of **KCp#PTe** (black curve) compared to the corresponding Eu complex **4.1Te** (green curve). *Left:* full spectra. *Right:* closeup of the fingerprint region (525–1750 cm^{-1}).

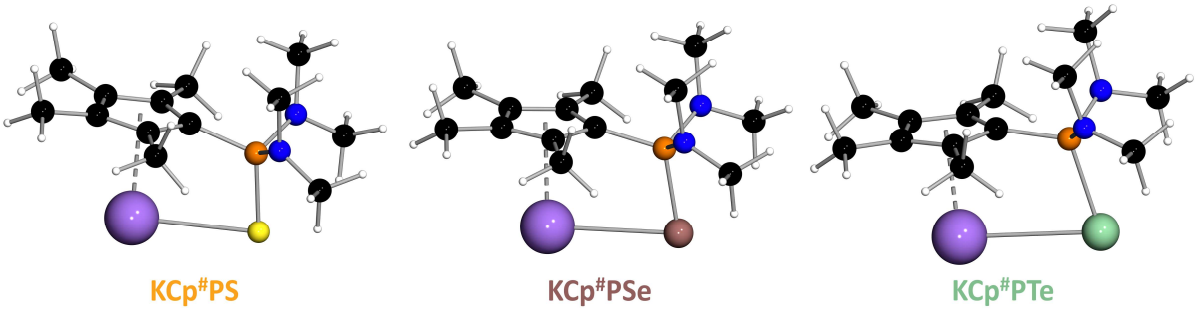


Figure C11. CAM-B3LYP/def2-TZVPD optimized geometries of **KCp#PCh**. White = H, black = C, blue = N, orange = P, yellow = S, purple = K, brown = Se, light green = Te.

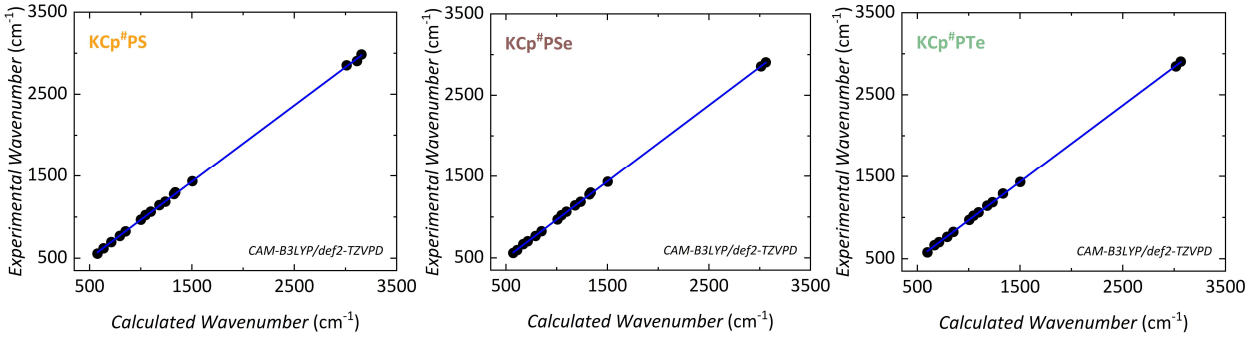


Figure C12. Comparison of experimental and calculated vibrational frequencies for **KCp#PS** (left), **KCp#PSe** (middle), and **KCp#PTe** (right) The solid blue lines are linear fits of the equation $y = mx + b$ to the data. Best-fitting parameters are given in Table C2.

Table C2. Best-fitting parameters for the linear fits given in Figure C12.

	KCp#PS	**KCp#PSe**	**KCp#PTe**
m	0.932 ± 0.004	0.939 ± 0.003	0.936 ± 0.003
b	33 ± 6	28 ± 4	32 ± 4
R^2	0.9998	0.9999	0.9999

Table C3. Selected vibrational modes used to scale the frequencies of **KCp#PCh**, and their assignments. Raw calculated frequencies were scaled according to the parameters in Table C2.

	Experimental wavenumber (cm^{-1})	Raw calculated wavenumber (cm^{-1})	Percent difference	Scaled calculated wavenumber (cm^{-1})	Percent difference	Mode number: assignment
KCp#PS	555	578	4.06	572	2.93	37: Symmetric in-plane stretching of ring and 2,5-Me with C-C bending of Cp esp. of 1,2,5-Cp
	619	637	2.87	627	1.21	39: A symmetric mode of several convoluted coupled vibrations
	694	713	2.70	697	0.48	42: Symmetric P-S stretching with P-N stretching and "envelope" bending of Cp ring
	769	796	3.45	775	0.74	44: Symmetric P-C stretching with in-plane stretching of Cp along 1,2-, 1,5-, and 3,4-C bonds, stretching of 3,4-Me, and some P-S stretching
	825	852	3.22	827	0.24	45: Asymmetric in-plane stretching of Cp along 2,3- and 4,5-C bonds, with asymmetric ring Me stretching
	966	1002	3.66	967	0.08	47: Asymmetric N-C-N stretching of both -$P(NMe_2)_2$ with asymmetric N-P-N stretching
	1022	1047	2.42	1009	1.31	50: Wagging of 3,4-Me with some P-C stretching
	1063	1099	3.33	1057	0.55	56: Symmetric C-N-C rocking of -NMe_2 with some P-N wagging
	1142	1182	3.44	1135	0.65	60: Symmetric bending of 1,2,5-Cp with P-C and 2,5-Me stretching
	1184	1241	4.70	1190	0.47	65: P-N wagging of -$P(NMe_2)_2$
	1277	1325	3.69	1268	0.72	66/67: overlapping symmetric and asymmetric N-P-N stretching of -$P(NMe_2)_2$
	1298	1338	3.03	1280	1.40	68: P-C stretching with symmetric ring stretching/bending (elongation of 1,2-, 1,5-, and 3,4-C with compression of 2,3- and 4,5-C)
	1433	1505	4.90	1436	0.18	87/88: Overlapping symmetric and asymmetric methyl C-H bending
	2852	3012	5.46	2840	0.41	100: Symmetric C-H stretching of -NMe_2 pointing away from ring
	2904	3113	6.95	2935	1.05	113: Asymmetric C-H stretching esp. of 3,4-Me
	2985	3157	5.60	2976	0.32	118: Symmetric C-H stretching of -NMe_2 pointing towards ring with some N-C wagging
	RMS error[a] →		86.1		11.9	

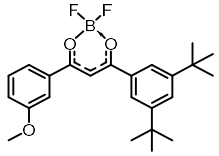
	559	572	2.30	565	1.11	37: Symmetric in-plane stretching of ring and 2,5-Me with C-C bending of Cp esp. of 1,2,5-Cp
	594	611	2.82	602	1.32	39: A symmetric mode of several convoluted coupled vibrations
	667	671	0.60	658	1.32	40: Symmetric out-of-plane ring bending (driven by 2,5-C motion) with P-N and P-Se stretching
	702	715	1.83	700	0.35	43: Asymmetric in-plane ring twisting (esp. of 2,3,4,5-C) with in-plane C-P "pendulum" motion and N-P-N stretching of -$P(NMe_2)_2$
	766	792	3.34	772	0.76	44: Symmetric P-C stretching with in-plane stretching of Cp along 1,2-, 1,5-, and 3,4-C bonds, stretching of 3,4-Me, and some P-S stretching
	825	851	3.10	827	0.27	45: Asymmetric ring Me stretching with in-plane Cp stretching (2,3- and 4,5-C bonds)
	968	1009	4.15	976	0.79	48: Symmetric N-C-N stretching of both -$P(NMe_2)_2$ with symmetric N-P-N stretching
	1020	1048	2.71	1012	0.76	50: Wagging of 3,4-Me with some P-C stretching
$KCp^{\#}PSe$	1063	1097	3.15	1058	0.45	56: Symmetric C-N-C rocking of -NMe_2 with some P-N wagging
	1140	1181	3.53	1137	0.25	60: Symmetric bending of 1,2,5-Cp with P-C and 2,5-Me stretching
	1184	1236	4.30	1189	0.40	65: P-N wagging of -$P(NMe_2)_2$
	1275	1323	3.70	1270	0.35	66/67: Overlapping symmetric and asymmetric N-P-N stretching of -$P(NMe_2)_2$
	1298	1336	2.89	1283	1.19	68: P-C stretching with symmetric ring stretching/bending (elongation of 1,2-, 1,5-, and 3,4-C with compression of 2,3- and 4,5-C)
	1431	1503	4.91	1440	0.59	87/88: Overlapping symmetric and asymmetric methyl C-H bending
	2854	3014	5.45	2858	0.16	100: Symmetric C-H stretching of -NMe_2 pointing away from ring
	2904	3061	5.26	2903	0.05	106: Asymmetric C-H stretching of -NMe_2
	RMS error[a] →		65.8		6.82	
	577	599	3.74	592	2.54	39: A symmetric mode of several convoluted coupled vibrations
	663	667	0.60	655	1.15	40: Symmetric out-of-plane ring bending (driven by 2,5-C motion) with P-N and P-Te stretching
	700	712	1.70	698	0.35	43: Asymmetric in-plane ring twisting (esp. of 2,3,4,5-C) with in-plane C-P "pendulum" motion and N-P-N stretching of -$P(NMe_2)_2$
$KCp^{\#}PTe$	764	792	3.60	772	1.09	44: Symmetric P-C stretching with in-plane stretching of Cp along 1,2-, 1,5-, and 3,4-C bonds, stretching of 3,4-Me, and some P-S stretching
	825	851	3.10	828	0.31	45: Asymmetric ring Me stretching with in-plane Cp stretching (2,3- and 4,5-C bonds)
	970	1006	3.64	973	0.27	48: Symmetric N-C-N stretching of both -$P(NMe_2)_2$ with symmetric N-P-N stretching
	1020	1047	2.61	1011	0.89	50: Wagging of 3,4-Me with some P-C stretching

1061	1097	3.37	1058	0.31	56: Symmetric C-N-C rocking of -NMe_2 with some P-N wagging
1142	1181	3.36	1136	0.50	60/61: Symmetric bending of 1,2,5-Cp with P-C and 2,5-Me stretching, overlapping asymmetric N-C wagging of both -NMe_2 with N-P-N rocking
1184	1233	4.06	1185	0.08	65: P-N wagging of -$P(NMe_2)_2$
1290	1334	3.35	1279	0.82	68: P-C stretching with symmetric ring stretching/bending (elongation of 1,2-, 1,5-, and 3,4-C with compression of 2,3- and 4,5-C)
1431	1502	4.84	1437	0.39	87/88: Overlapping symmetric and asymmetric methyl C-H bending
2846	3018	5.87	2855	0.31	100: Symmetric C-H stretching of -NMe_2 pointing away from ring
2904	3065	5.40	2899	0.18	105: Asymmetric C-H stretching of -NMe_2
RMS error[a] →		71.6		7.28	

[a] RMS error is calculated as $\sqrt{\frac{1}{n}\sum_i^n (\upsilon_{i,calc} - \upsilon_{i,expt})^2}$.[323] The percentage errors given in the columns above are not related to the calculation of RMS error, but serve to aid in visualizing the differences between experimental and calculated values.

C.5 Photoluminescence and luminescence thermometry

Table C5. Performance comparison of selected band-shift luminescence thermometers.

Thermometer	Ref.	S_a ($cm^{-1}\,K^{-1}$)	Sensing Range (K)	ΔE (cm^{-1})
Bromo(methylpyridinium)-paracyclophane chloride	363	17.7 @ 178 K	143-223	1046
$Cs_6Cu_3AgBr_{10}$	364	15.3 @ 300 K	80-300	2657
Ag_2S quantum dots	173	11	295-317	500[d]
$[Cp^*Eu(\mu\text{-}BH_4)(THF)_2]_2$	224	8.2 @ 320 K	60-320	1899
γ-Al_2O_3:Sm^{II}	99	8.0 @ 298 K[b]	298-648	1500[d]
$[^{bdp}Cp^{\#}Eu(\mu\text{-}BH_4)(THF)_2]_2$	270	7.36 @ 113 K	30-320	1647
$[^{TMS}Cp^{\#}Eu(\mu\text{-}BH_4)(THF)_2]_2$	270	7.22 @ 150 K	30-300	1350
$[Cp^*Eu(\mu\text{-}BD_4)(THF)_2]_2$	224	7.07 @260 K	30-320	1858
$\{Eu^{II}[B(CN)_4]_2{\cdot}THF\}_n$[c]	272	5.65	77-500	2450
	164	5.57	77-380	1687
$[Eu(BH_4)_2(THF)_2]$	56,224	5.37 @ 220 K	30-320	1178
$[Cp^{xph}Eu(\mu\text{-}BH_4)(THF)_2]_2$	270	5.00 @ 243 K	100-320	622
CdTe quantum dots	174	5	300-353	283
$[^{TMG}Cp^{\#}Eu(\mu\text{-}BH_4)(THF)_2]_2$	270	4.51 @ 210 K	40-310	939
Dipyren-1-yl(2,4,6-triisopropylphenyl)borane	365	3.34	223-373	1881[d]
$[Cp^*Eu(\mu\text{-}BH_4)(DME)]_2$	270	3.15 @ 220 K	80-320	786
$[Cp^{iPr4}Eu(\mu\text{-}BH_4)(DME)]_2$	270	2.61 @ 260 K	120-260	207
$Na_4Mg(WO_4)_3$:Mn^{IV}	366	1.99 @ 300 K	100-300	597
$[(Cp^{\#}PS)_2Eu]$ (**4.1S**)	[a]	1.5 @ 330 K	70-330	356

$[Cp^{iPr4}Eu(\mu\text{-}BH_4)(THF)_2]_n$ [270]	1.08 @ 290 K	110-290	60
$Mg_2SiO_4:Cr^{III}$ [367]	0.25 @ 310 K	125-330	40[d]
$Mg_2TiO_4:Cr^{III}$ [368]	0.21[d] @ 460 K	50-460	61

[a] This work. [b] using the barycentre of the entire Sm^{II} emission band as the sensor. [c] without annealing. [d] estimated.

C.6 Magneto-optical properties and MCD thermometry

Table C6. Best-fitting parameters for the sigmoidal logistic function $\Delta = \frac{A_1 - A_2}{1+\left(x/x_0\right)^p} - A_2$ fitted to the thermometric parameters Δ shown in Figures 4.26-4.28.

Figure	Δ	A_1	A_2	x_0	p	R^2
4.26a	$\lvert I_1 - I_2\rvert$	844108	615	0.09	1.92	1.0000
	$\lvert I_1 - I_4\rvert$	678007	1508	0.13	1.74	1.0000
	$\lvert I_2 - I_3\rvert$	847771	915	0.08	1.71	1.0000
	$\lvert I_3 - I_4\rvert$	739898	1797	0.12	1.66	1.0000
4.26b	$\lvert I_1 - I_2\rvert$	811953	95	0.02	1.05	1.0000
	$\lvert I_1 - I_4\rvert$	99208	0.96	0.52	1.17	1.0000
	$\lvert I_2 - I_3\rvert$	261261	8.50	0.11	1.05	1.0000
	$\lvert I_3 - I_4\rvert$	113102	0.95	0.56	1.17	1.0000
4.26c	$\lvert I_1 - I_2\rvert$	227778	11	0.13	0.99	1.0000
	$\lvert I_1 - I_4\rvert$	60086	0.03	1.70	1.27	1.0000
	$\lvert I_2 - I_3\rvert$	93561	161	0.61	1.10	1.0000
	$\lvert I_3 - I_4\rvert$	82259	0.08	1.49	1.23	1.0000
4.26d	$\lvert I_1 - I_2\rvert$	787378	-1359	0.02	0.79	1.0000
	$\lvert I_1 - I_4\rvert$	57272	1345	3.90	1.71	1.0000
	$\lvert I_2 - I_3\rvert$	56029	68	2.36	1.25	1.0000
	$\lvert I_3 - I_4\rvert$	70458	2009	4.04	1.75	1.0000
4.27 top	$\lvert I_1 - I_2\rvert$	16929	0.12	0.36	1.11	1.0000
	$\lvert I_1 - I_4\rvert$	1855253	-465	0.004	0.97	1.0000
	$\lvert I_2 - I_3\rvert$	17777	0.05	0.63	1.23	1.0000
	$\lvert I_3 - I_4\rvert$	15511	0.02	1.36	1.50	1.0000
4.27 middle	$\lvert I_1 - I_2\rvert$	17509	78	0.68	1.14	1.0000

	$\|I_1 - I_4\|$	37917	-328	0.52	1.10	1.0000
	$\|I_2 - I_3\|$	18439	0.01	1.15	1.22	1.0000
	$\|I_3 - I_4\|$	15504	0.0008	2.35	1.56	1.0000
4.27 bottom	$\|I_1 - I_2\|$	11460	28	2.14	1.23	1.0000
	$\|I_1 - I_4\|$	14217	-247	1.66	1.12	1.0000
	$\|I_2 - I_3\|$	18405	144	2.27	1.27	1.0000
	$\|I_3 - I_4\|$	16466	0.002	2.75	1.33	1.0000
4.28 top	$\|I_1 - I_2\|$	8727422	-87	0.00003	0.78	0.9990
	$\|I_1 - I_4\|$	5.0 x10^7	672	0.007	1.56	0.9874
	$\|I_2 - I_3\|$	3243	503	2.07	2.29	0.9992
	$\|I_3 - I_4\|$	3.8 x10^7	919	0.005	1.37	0.9924
4.28 middle	$\|I_1 - I_2\|$	7432	177	1.58	1.32	0.9981
	$\|I_1 - I_4\|$	51454	-24	1.21	1.40	0.9974
	$\|I_2 - I_3\|$	8798	309	1.47	1.62	0.9978
	$\|I_3 - I_4\|$	68045	471	1.27	1.41	0.9976
4.28 bottom	$\|I_1 - I_2\|$	7587	165	3.35	1.33	1.0000
	$\|I_1 - I_4\|$	51372	-64	2.30	1.28	1.0000
	$\|I_2 - I_3\|$	11951	-131	1.60	1.14	0.9999
	$\|I_3 - I_4\|$	69958	-50	2.32	1.26	1.0000

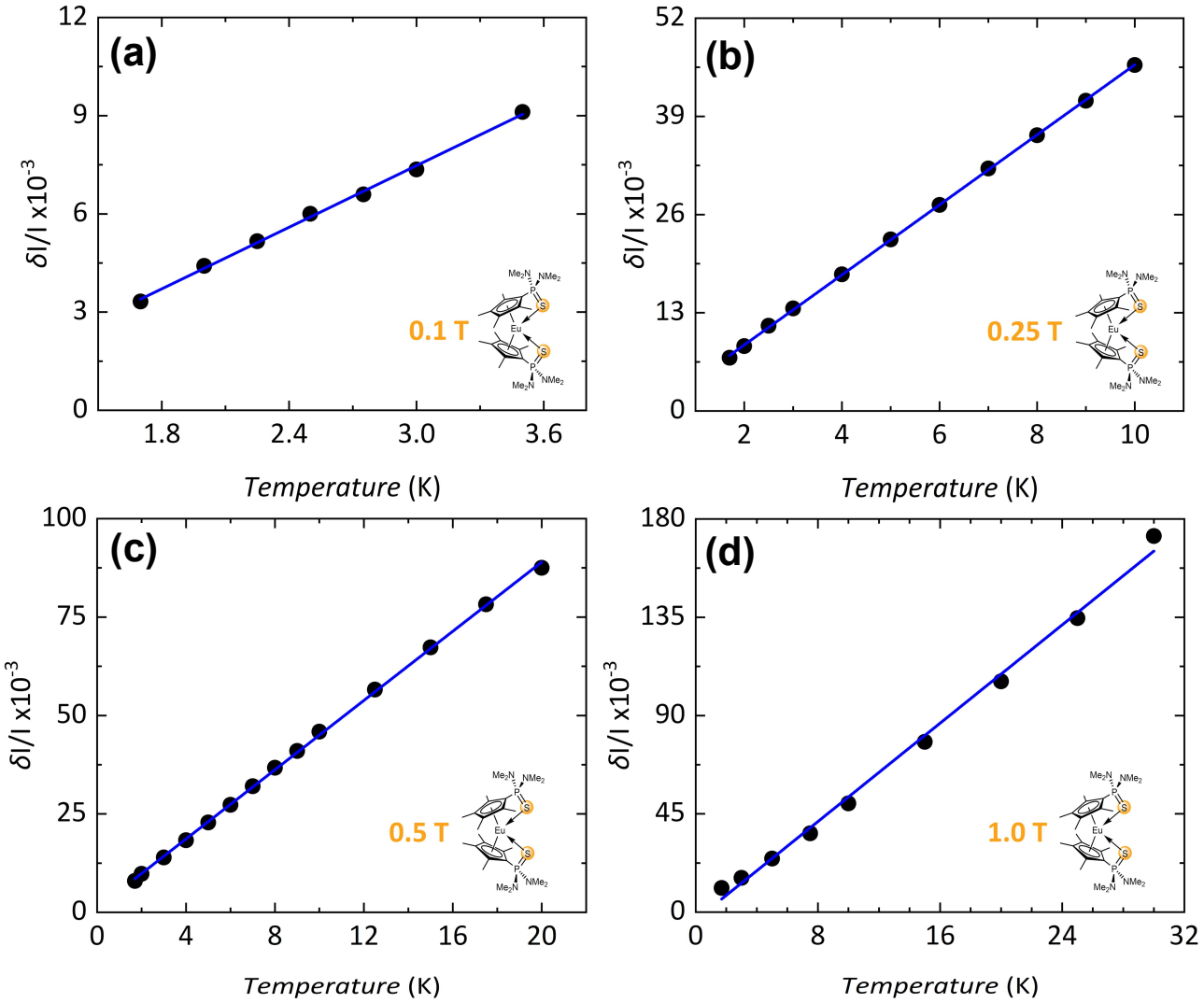


Figure C13. Temperature-dependent signal fluctuation $\delta I/I$ in the range 675-775 nm (outside the Eu^{II} components) for **4.1S** under applied magnetic fields of (a) 0.1, (b) 0.25, (c) 0.5, and (d) 1.0 T. The solid blue lines are linear fits of the equation $y = mx + b$ to the data. Best-fitting parameters are given in Table C7.

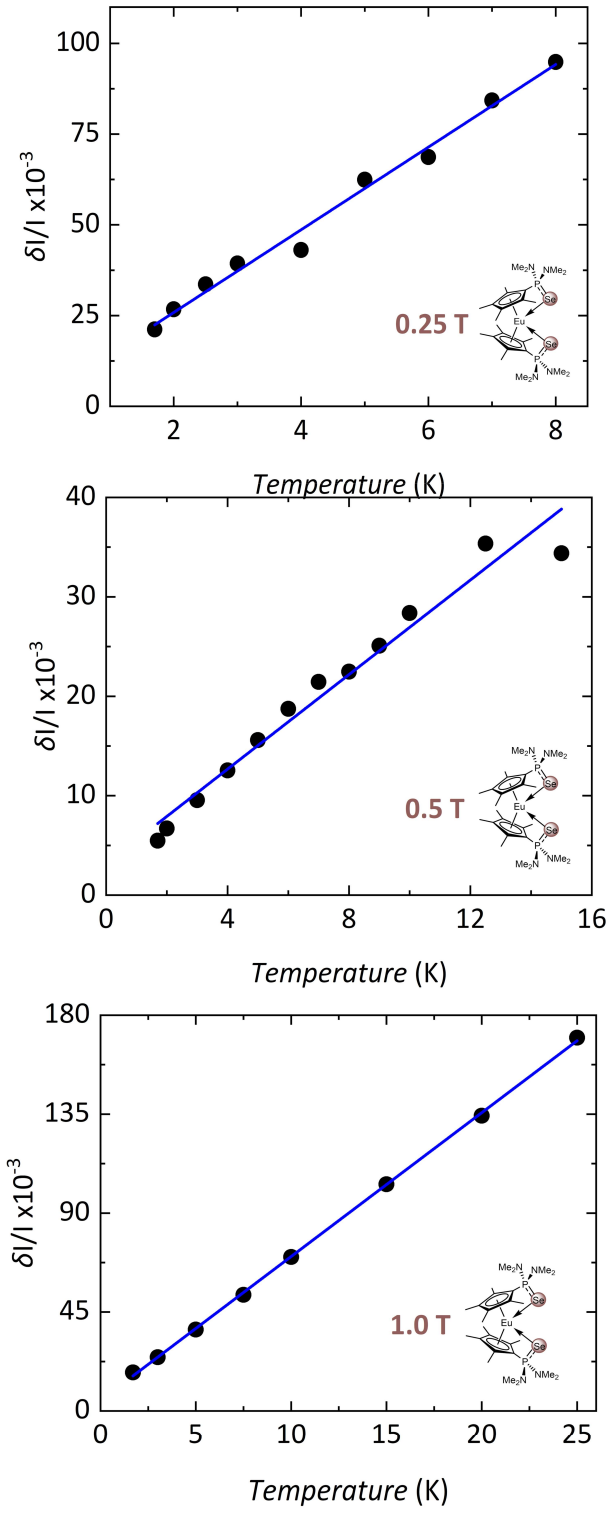


Figure C14. Temperature-dependent signal fluctuation $\delta I/I$ in the range 675-775 nm (outside the Eu^{II} components) for **4.1Se** under applied magnetic fields of 0.25 (top), 0.5 (middle), and 1.0 T (bottom). The solid blue lines are linear fits of the equation $y = mx + b$ to the data. Best-fitting parameters are given in Table C7.

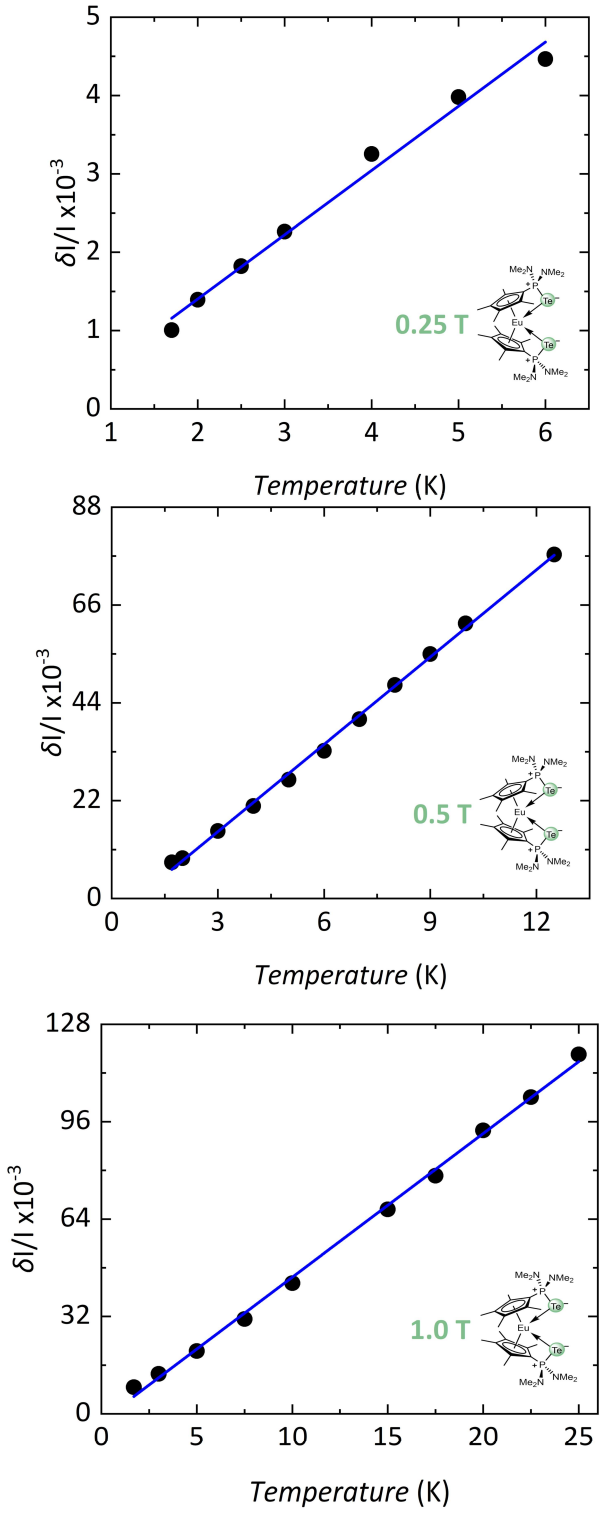


Figure C15. Temperature-dependent signal fluctuation $\delta I/I$ in the range 675-775 nm (outside the Eu^{II} components) for **4.1Te** under applied magnetic fields of 0.25 (top), 0.5 (middle), and 1.0 T (bottom). The solid blue lines are linear fits of the equation $y = mx + b$ to the data. Best-fitting parameters are given in Table C7.

Table C7. Best-fitting parameters for the linear fits given in Figures C13-15.

Figure	m	b	R^2
C13a	0.0314	-0.002	0.9973
C13b	0.0046	0.0005	0.9998
C13c	0.0044	0.001	0.9994
C13d	0.0056	-0.004	0.9947
C14 top	0.0114	0.003	0.9879
C14 middle	0.0024	0.003	0.9626
C14 bottom	0.0065	0.005	0.9996
C15 top	0.0008	0.0002	0.9851
C15 middle	0.0065	-0.005	0.9979
C15 bottom	0.0047	-0.002	0.9975

Table C8. Performance comparison of magnetic circular dichroism thermometers reported to date.

		0.1 T		0.25 T		0.5 T		1.0 T	
		Single-Parameter	**Multi-parametric**	**Single-Parameter**	**Multi-parametric**	**Single-Parameter**	**Multi-parametric**	**Single-Parameter**	**Multi-parametric**
4.1S	Max. S_r (% K^{-1})[a]	93.9	170	60.3	114	53.8	89.9	46.7	61.0
	δT (K)[b]	0.005	0.003	0.02	0.009	0.02	0.01	0.02	0.01
	Sensing Range (K)[c]	1.7 – 3.5		1.7 – 10		1.7 – 12.4	1.7 – 18.7	1.7 – 11.7	1.7 – 17.4
4.1Se	Max. S_r (% K^{-1})[a]	n.d.		61.5	112	52.6	90.7	34.3	61.2
	δT (K)[b]	n.d.		0.05	0.03	0.02	0.01	0.07	0.04
	Sensing Range (K)[c]	n.d.		1.7 – 8		1.7 – 15		1.7 – 10.9	
4.1Te	Max. S_r (% K^{-1})[a]	n.d.		85.9	130	50.8	94.4	35.2	59.4
	δT (K)[b]	n.d.		0.002	0.001	0.02	0.01	0.02	0.01
	Sensing Range (K)[c]	n.d.		1.7 – 6		1.7 – 12.5		1.7 – 13.7	
{Nd}	Max. S_r (% K^{-1})	n.d.		44.8 @ 2.38 K	n.d.	36.8 @ 2.66 K	n.d.	24.1 @ 1.55 K	n.d.
	δT (K)	n.d.		n.d.	n.d.	n.d.	n.d.	n.d.	n.d.
	Sensing Range (K)	n.d.		1.55 – 5.0	n.d.	1.55 – 8.0	n.d.	1.55 – 15.0	n.d.
{Dy}	Max. S_r (% K^{-1})	n.d.		37.7 @ 1.55 K	n.d.	22.3 @ 2.13 K	n.d.	11.2 @ 5.57 K	n.d.
	δT (K)	n.d.		n.d.	n.d.	n.d.	n.d.	n.d.	n.d.
	Sensing Range (K)	n.d.		1.55 – 5.0	n.d.	1.55 – 12.5	n.d.	1.55 – 20.0	n.d.
{Ho}	Max. S_r (% K^{-1})	n.d.		42.3 @ 2.50 K	95.3 @ 2.50 K	22.9 @ 3.44 K	n.d.	10.3 @ 4.71 K	n.d.
	δT (K)	n.d.		0.02	0.008	n.d.	n.d.	n.d.	n.d.
	Sensing Range (K)	n.d.		1.55 – 3.5	1.55 – 3.5	1.55 – 9.0	n.d.	1.55 – 20.0	n.d.

{Ln} = Ln(acac)$_3$(phen) from ref. [336]. [a] Maximum S_r is attained at 1.7 K under all conditions. [b] Temperature uncertainty at the temperature of maximum S_r. [c] Temperature range for which δT is ≤ 1.0 K. n.d. = not determined.

REFERENCES

(1) Tessitore, G.; Mandl, G. A.; Maurizio, S. L.; Kaur, M.; Capobianco, J. A. The Role of Lanthanide Luminescence in Advancing Technology. *RSC Adv.* **2023**, *13* (26), 17787–17811. https://doi.org/10.1039/D3RA00991B.

(2) Blomqvist, L.; Nordberg, G. F.; Nurchi, V. M.; Aaseth, J. O. Gadolinium in Medical Imaging—Usefulness, Toxic Reactions and Possible Countermeasures—A Review. *Biomolecules* **2022**, *12* (6), 742. https://doi.org/10.3390/biom12060742.

(3) Ramalho, M.; Ramalho, J.; Burke, L. M.; Semelka, R. C. Gadolinium Retention and Toxicity—An Update. *Adv. Chronic Kidney Dis.* **2017**, *24* (3), 138–146. https://doi.org/10.1053/j.ackd.2017.03.004.

(4) Wang, X.; Wu, W.; Yun, B.; Huang, L.; Chen, Z.-H.; Ming, J.; Zhai, F.; Zhang, H.; Zhang, F. An Emerging Toolkit of Ho^{3+} Sensitized Lanthanide Nanocrystals with NIR-II Excitation and Emission for *in Vivo* Bioimaging. *J. Am. Chem. Soc.* **2025**, *147* (2), 2182–2192. https://doi.org/10.1021/jacs.4c16451.

(5) Altaee, Z. M. Y.; Ayyed, A. A.; Khaleel, R. W. Influence of Stone Location on Rate of Stone Clearance and Complication for Holmium Laser Lithotripsy. *Int. J. Urol. Res.* **2024**, *6* (1), 84–90. https://doi.org/10.33545/26646617.2024.v6.i1b.38.

(6) Fiber Laser Overview and Medical Applications. In *Tunable Laser Applications*; Duarte, F. J., Ed.; CRC Press, 2016.

(7) Canadian Nuclear Society. *Smoke detectors and americium-241 fact sheet*. https://web.archive.org/web/20160325003327/https://cns-snc.ca/media/uploads/teachers/smoke_am241.pdf (accessed 2026-05-11).

(8) Natural Resources Canada. *Uranium and nuclear power facts*. https://natural-resources.canada.ca/minerals-mining/mining-data-statistics-analysis/minerals-metals-facts/uranium-nuclear-power-facts (accessed 2026-05-11).

(9) International Atomic Energy Agency. *Near Term and Promising Long Term Options for the Deployment of Thorium Based Nuclear Energy*; text IAEA-TECDOC-2009; IAEA: Vienna, 2022; p 174. http://www.iaea.org/publications/15215/near-term-and-promising-long-term-options-for-the-deployment-of-thorium-based-nuclear-energy (accessed 2026-05-11).

(10) Dejneka, M.; Samson, B. Rare-Earth-Doped Fibers for Telecommunications Applications. *MRS Bull.* **1999**, *24* (9), 39–45. https://doi.org/10.1557/S0883769400053057.

(11) Sorace, L.; Gatteschi, D. Electronic Structure and Magnetic Properties of Lanthanide Molecular Complexes. *Lanthan. Actin. Mol. Magn.* **2015**, *2*, 1–26. https://doi.org/10.1002/9783527673476.ch1.

(12) Rinehart, J. D.; Long, J. R. Exploiting Single-Ion Anisotropy in the Design of f-Element Single-Molecule Magnets. *Chem. Sci.* **2011**, *2* (11), 2078–2085. https://doi.org/10.1039/c1sc00513h.

(13) Harriman, K. L. M.; Errulat, D.; Murugesu, M. Magnetic Axiality: Design Principles from Molecules to Materials. *Trends Chem.* **2019**, 1–15. https://doi.org/10.1016/j.trechm.2019.04.005.

(14) Lu, J.-B.; Jiang, X.-L.; Hu, H.-S.; Li, J. Norm-Conserving 4f-in-Core Pseudopotentials and Basis Sets Optimized for Trivalent Lanthanides. ChemRxiv 2022. https://doi.org/10.26434/chemrxiv-2022-zv7cx.

(15) Jiang, S.-D.; Wang, B.-W.; Gao, S. Advances in Lanthanide Single-Ion Magnets. In *Structure and Bonding*; 2014; Vol. 164. https://doi.org/10.1007/430_2014_153.

(16) *The Rare Earth Elements: Fundamentals and Applications*; Atwood, D. A., Ed.; EIC Books; Wiley-VCH Verlag GmbH & Co. KGaA: West Sussex, UK, 2012.

(17) Nash, K. L. Chapter 121 Separation Chemistry for Lanthanides and Trivalent Actinides. In *Handbook on the Physics and Chemistry of Rare Earths*; Handbook on the Physics and Chemistry of Rare Earths; Elsevier, 1994; Vol. 18, pp 197–238. https://doi.org/10.1016/S0168-1273(05)80044-3.

(18) Marsh, J. K. The Separation of the Lanthanons (Rare-Earth Elements). *Q. Rev. Chem. Soc.* **1947**, *1* (2), 126–143. https://doi.org/10.1039/QR9470100126.

(19) Cheisson, T.; Schelter, E. J. Rare Earth Elements: Mendeleev's Bane, Modern Marvels. *Science* **2019**, *363* (6426), 489–493. https://doi.org/10.1126/science.aau7628.

(20) Marin, R.; Brunet, G.; Murugesu, M. Shining New Light on Multifunctional Lanthanide Single-Molecule Magnets. *Angew. Chem. Int. Ed.* **2021**, *60* (4), 1728–1746. https://doi.org/10.1002/anie.201910299.

(21) Bünzli, J. C. G. Lanthanide Luminescence: From a Mystery to Rationalization, Understanding, and Applications. *Handb. Phys. Chem. Rare Earths* **2016**, *50*, 141–176. https://doi.org/10.1016/bs.hpcre.2016.08.003.

(22) Gálico, D. A.; Calado, C. M. S.; Murugesu, M. Lanthanide Molecular Cluster-Aggregates as the next Generation of Optical Materials. *Chem. Sci.* **2023**, *14* (22), 5827–5841. https://doi.org/10.1039/D3SC01088K.

(23) Dieke, G. H. *Spectra and Energy Levels of Rare Earth Ions in Crystals*; Interscience Publishers, 1968.

(24) Carnall, W. T.; Goodman, G. L.; Rajnak, K.; Rana, R. S. A Systematic Analysis of the Spectra of the Lanthanides Doped into Single Crystal LaF_3. *J. Chem. Phys.* **1989**, *90* (7), 3443–3457. https://doi.org/10.1063/1.455853.

(25) Dieke, G. H.; Crosswhite, H. M. The Spectra of the Doubly and Triply Ionized Rare Earths. *Appl. Opt.* **1963**, *2* (7), 675–686. https://doi.org/10.1364/AO.2.000675.

(26) Nielsen, V. R. M.; Sørensen, T. J. Electronic Energy Levels and Optical Spectra of Trivalent Lanthanide Ions in Water – Ce(III), Pr(III), Nd(III), Sm(III), Eu(III), Gd(III), Tb(III), Dy(III), Ho(III), Er(III), Tm(III), and Yb(III). *Nat. Commun.* **2025**, *16* (1), 10754. https://doi.org/10.1038/s41467-025-65784-y.

(27) Laporte, O.; Meggers, W. F. Some Rules of Spectral Structure. *J. Opt. Soc. Am.* **1925**, *11* (5), 459–463. https://doi.org/10.1364/JOSA.11.000459.

(28) Landi Degl'Innocenti, E. Selection Rules and Line Strengths. In *Atomic Spectroscopy and Radiative Processes*; Landi Degl'Innocenti, E., Ed.; Springer Milan: Milano, 2014; pp 291–305. https://doi.org/10.1007/978-88-470-2808-1_12.

(29) Kitos, A. A.; Gálico, D. A.; Castañeda, R.; Ovens, J. S.; Murugesu, M.; Brusso, J. L. Stark Sublevel-Based Thermometry with Tb(III) and Dy(III) Complexes Cosensitized via the 2-Amidinopyridine Ligand. *Inorg. Chem.* **2020**, *59* (15), 11061–11070. https://doi.org/10.1021/acs.inorgchem.0c01534.

(30) Suta, M.; Wickleder, C. Synthesis, Spectroscopic Properties and Applications of Divalent Lanthanides Apart from Eu^{2+}. *J. Lumin.* **2019**, *210* (October 2018), 210–238. https://doi.org/10.1016/j.jlumin.2019.02.031.

(31) Nief, F. Non-Classical Divalent Lanthanide Complexes. *Dalton Trans.* **2010**, *39* (29), 6589–6598. https://doi.org/10.1039/C001280G.

(32) Molander, G. A. Reductions with Samarium(II) Iodide. In *Organic Reactions*; John Wiley & Sons, Ltd, 2004; pp 211–367. https://doi.org/10.1002/0471264180.or046.03.

(33) Mahieu, N.; Piątkowski, J.; Simler, T.; Nocton, G. Back to the Future of Organolanthanide Chemistry. *Chem. Sci.* **2023**, *14* (3), 443–457. https://doi.org/10.1039/D2SC05976B.

(34) Kagan, H. B. Lanthanide Derivatives as Reagents or Catalysts for Organic Reactions. *Inorganica Chim. Acta* **1987**, *140*, 3–6. https://doi.org/10.1016/S0020-1693(00)81036-1.

(35) Ding, H.; Lu, C.; Hu, X.; Zhao, B.; Wu, B.; Yao, Y. Addition of Terminal Alkynes to Aromatic Nitriles Catalyzed by Divalent Lanthanide Amides Supported by Amidates: Synthesis of Ynones. *Synlett* **2013**, *24* (10), 1269–1274. https://doi.org/10.1055/s-0033-1338446.

(36) Pindwal, A.; Ellern, A.; Sadow, A. D. Homoleptic Divalent Dialkyl Lanthanide-Catalyzed Cross-Dehydrocoupling of Silanes and Amines. *Organometallics* **2016**, *35* (11), 1674–1683. https://doi.org/10.1021/acs.organomet.6b00138.

(37) Moinet, E. C.; Wolf, B. M.; Tardif, O.; Maichle-Mössmer, C.; Anwander, R. Divalent Lanthanide Tetraisobutylaluminates: Reactivity and Living Isoprene Polymerization. *Angew. Chem. Int. Ed.* **2023**, *62* (17), e202219316. https://doi.org/10.1002/anie.202219316.

(38) Nakayama, Y.; Yasuda, H. Developments of Rare Earth Metal Catalysts for Olefin Polymerization. *J. Organomet. Chem.* **2004**, *689* (24), 4489–4498. https://doi.org/10.1016/j.jorganchem.2004.05.056.

(39) Szostak, M.; Procter, D. J. Beyond Samarium Diiodide: Vistas in Reductive Chemistry Mediated by Lanthanides(II). *Angew. Chem. Int. Ed.* **2012**, *51* (37), 9238–9256. https://doi.org/10.1002/anie.201201065.

(40) Mansell, J. I.; Romano, C.; Procter, D. J. Contemporary Strategies in SmI_2 Catalysis: A Reagent Reborn. *Angew. Chem. Int. Ed.* **2025**, *64* (46), e202519678. https://doi.org/10.1002/anie.202519678.

(41) Basalov, I. V.; Roşca, S. C.; Lyubov, D. M.; Selikhov, A. N.; Fukin, G. K.; Sarazin, Y.; Carpentier, J.-F.; Trifonov, A. A. Divalent Heteroleptic Ytterbium Complexes – Effective Catalysts for Intermolecular Styrene Hydrophosphination and Hydroamination. *Inorg. Chem.* **2014**, *53* (3), 1654–1661. https://doi.org/10.1021/ic4027859.

(42) Andriessen, J.; Dorenbos, P.; Van Eijk, C. W. E. The Centroid Shift of the 5d Levels of Ce^{3+} with Respect to the 4f Levels in Ionic Crystals, a Theoretical Investigation. *Nucl. Instrum. Methods Phys. Res. Sect. Accel. Spectrometers Detect. Assoc. Equip.* **2002**, *486* (1–2), 399–402. https://doi.org/10.1016/S0168-9002(02)00741-6.

(43) Wang, L.; Fang, P.; Zhao, Z.; Huang, Y.; Liu, Z.; Bian, Z. Rare Earth Complexes with 5d–4f Transition: New Emitters in Organic Light-Emitting Diodes. *J. Phys. Chem. Lett.* **2022**, *13* (12), 2686–2694. https://doi.org/10.1021/acs.jpclett.2c00400.

(44) Pandey, P.; Yang, Q.; Gau, M. R.; Schelter, E. J. Evaluating the Photophysical and Photochemical Characteristics of Green-Emitting Cerium(III) Mono-Cyclooctatetraenide Complexes. *Dalton Trans.* **2023**, *52* (18), 5909–5917. https://doi.org/10.1039/D3DT00351E.

(45) Qiao, Y.; Sergentu, D.-C.; Yin, H.; Zabula, A. V.; Cheisson, T.; McSkimming, A.; Manor, B. C.; Carroll, P. J.; Anna, J. M.; Autschbach, J.; Schelter, E. J. Understanding and Controlling the Emission Brightness and Color of Molecular Cerium Luminophores. *J. Am. Chem. Soc.* **2018**, *140* (13), 4588–4595. https://doi.org/10.1021/jacs.7b13339.

(46) Qin, X.; Liu, X.; Huang, W.; Bettinelli, M.; Liu, X. Lanthanide-Activated Phosphors Based on 4f-5d Optical Transitions: Theoretical and Experimental Aspects. *Chem. Rev.* **2017**, *117* (5), 4488–4527. https://doi.org/10.1021/acs.chemrev.6b00691.

(47) Cao, Z.; Wei, X.; Zhao, L.; Chen, Y.; Yin, M. Investigation of SrB_4O_7:Sm^{2+} as a Multimode Temperature Sensor with High Sensitivity. *ACS Appl. Mater. Interfaces* **2016**, *8* (50), 34546–34551. https://doi.org/10.1021/acsami.6b10917.

(48) Dorenbos, P. Energy of the First $4f^7 \rightarrow 4f^6 5d$ Transition of Eu^{2+} in Inorganic Compounds. *J. Lumin.* **2003**, *104* (4), 239–260. https://doi.org/10.1016/S0022-2313(03)00078-4.

(49) Aull, B. F.; Jenssen, H. P. Impact of Ion-Host Interactions on the 5d-to-4f Spectra of Lanthanide Rare-Earth-Metal Ions. I. A Phenomenological Crystal-Field Model. *Phys. Rev. B* **1986**, *34* (10), 6640–6646. https://doi.org/10.1103/PhysRevB.34.6640.

(50) Poe, T. N.; Molinari, S.; Beltran-Leiva, M. J.; Celis-Barros, C.; Ramanantoanina, H.; Albrecht-Schönzart, T. E. Influence of Outer-Sphere Anions on the Photoluminescence from Samarium(II) Crown Complexes. *Inorg. Chem.* **2021**, *60* (20), 15196–15207. https://doi.org/10.1021/acs.inorgchem.1c01606.

(51) Parker, D.; Suturina, E. A.; Kuprov, I.; Chilton, N. F. How the Ligand Field in Lanthanide Coordination Complexes Determines Magnetic Susceptibility Anisotropy, Paramagnetic NMR Shift, and Relaxation Behavior. *Acc. Chem. Res.* **2020**. https://doi.org/10.1021/acs.accounts.0c00275.

(52) Aime, S.; Botta, M.; Fasano, M.; Terreno, E. Chemical Shift and Relaxation Reagents in NMR. In *Encyclopedia of Spectroscopy and Spectrometry (Third Edition)*; Lindon, J. C., Tranter, G. E., Koppenaal, D. W., Eds.; Academic Press: Oxford, 2017; pp 195–202. https://doi.org/10.1016/B978-0-12-409547-2.10946-1.

(53) von Ammon, R.; Fischer, R. D. Shift Reagents in NMR Spectroscopy. *Angew. Chem. Int. Ed. Engl.* **1972**, *11* (8), 675–692. https://doi.org/10.1002/anie.197206751.

(54) Bünzli, J.-C. G. On the Design of Highly Luminescent Lanthanide Complexes. *Coord. Chem. Rev.* **2015**, *293–294*, 19–47. https://doi.org/10.1016/j.ccr.2014.10.013.

(55) Jenks, T. C.; Bailey, M. D.; Corbin, B. A.; Kuda-Wedagedara, A. N. W.; Martin, P. D.; Schlegel, H. B.; Rabuffetti, F. A.; Allen, M. J. Photophysical Characterization of a Highly Luminescent Divalent-Europium-Containing Azacryptate. *Chem. Commun.* **2018**, *54* (36), 4545–4548. https://doi.org/10.1039/c8cc01737a.

(56) Marks, S.; Heck, J. G.; Habicht, M. H.; Oña-Burgos, P.; Feldmann, C.; Roesky, P. W. $[Ln(BH_4)_2(THF)_2]$ (Ln = Eu, Yb)—A Highly Luminescent Material. Synthesis, Properties, Reactivity, and NMR Studies. *J. Am. Chem. Soc.* **2012**, *134* (41), 16983–16986. https://doi.org/10.1021/ja308077t.

(57) Qi, H.; Zhao, Z.; Zhan, G.; Sun, B.; Yan, W.; Wang, C.; Wang, L.; Liu, Z.; Bian, Z.; Huang, C. Air Stable and Efficient Rare Earth Eu(II) Hydro-Tris(Pyrazolyl)Borate Complexes with Tunable Emission Colors. *Inorg. Chem. Front.* **2020**, *7* (23), 4593–4599. https://doi.org/10.1039/d0qi00762e.

(58) Kawasaki, K.; Sugiyama, R.; Tsuji, T.; Iwasa, T.; Tsunoyama, H.; Mizuhata, Y.; Tokitoh, N.; Nakajima, A. A Designer Ligand Field for Blue-Green Luminescence of Organoeuropium(II) Sandwich Complexes with Cyclononatetraenyl Ligands. *Chem. Commun.* **2017**, *53* (49), 6557–6560. https://doi.org/10.1039/C7CC03045B.

(59) Kuda-Wedagedara, A. N. W.; Wang, C.; Martin, P. D.; Allen, M. J. Aqueous Eu^{II}-Containing Complex with Bright Yellow Luminescence. *J. Am. Chem. Soc.* **2015**, *137* (15), 4960–4963. https://doi.org/10.1021/jacs.5b02506.

(60) Kelly, R. P.; Bell, T. D. M.; Cox, R. P.; Daniels, D. P.; Deacon, G. B.; Jaroschik, F.; Junk, P. C.; Le Goff, X. F.; Lemercier, G.; Martinez, A.; Wang, J.; Werner, D. Divalent Tetra- and Penta-Phenylcyclopentadienyl Europium and Samarium Sandwich and Half-Sandwich Complexes: Synthesis, Characterization, and Remarkable Luminescence Properties. *Organometallics* **2015**, *34* (23), 5624–5636. https://doi.org/10.1021/acs.organomet.5b00842.

(61) Thomas, A. C.; Ellis, A. B. Diethyl Ether Adducts of Bis(Pentamethylcyclopentadienyl)Europium(II) and -Ytterbium(II). Excited-State Energy Transfer with Organolanthanoid Complexes. *Organometallics* **1985**, *4* (12), 2223–2225. https://doi.org/10.1021/om00131a029.

(62) Jagannathan, R.; Rao, R. P.; Kutty, T. R. N. Eu^{2+} Luminescence in MAl_3BO_7 Aluminoborates (M = Ca, Sr, Ba). *Mater. Res. Bull.* **1992**, *27* (4), 459–466. https://doi.org/10.1016/0025-5408(92)90023-S.

(63) Galimov, D. I.; Bulgakov, R. G. The First Example of Fluorescence of the Solid Individual Compounds of Eu^{2+} Ion: $EuCl_2$, EuI_2, $EuBr_2$. *Luminescence* **2019**, *34* (1), 127–129. https://doi.org/10.1002/bio.3580.

(64) Halmurat, D.; Zhang, X.; Aihaiti, L.; Xie, R. J. Near-Infrared Emission of Eu^{2+} in $M_4Li(BN_2)_3$ (M = Ca, Sr, Ba). *J. Rare Earths* **2026**, *44* (3), 733–741. https://doi.org/10.1016/j.jre.2025.03.004.

(65) Jiang, J.; Higashiyama, N.; Machida, K. I.; Adachi, G. Y. The Luminescent Properties of Divalent Europium Complexes of Crown Ethers and Cryptands. *Coord. Chem. Rev.* **1998**, *170* (1), 1–29. https://doi.org/10.1016/S0010-8545(98)00070-8.

(66) Poe, T. N.; Beltrán-Leiva, M. J.; Celis-Barros, C.; Nelson, W. L.; Sperling, J. M.; Baumbach, R. E.; Ramanantoanina, H.; Speldrich, M.; Albrecht-Schönzart, T. E. Understanding the Stabilization and Tunability of Divalent Europium 2.2.2B Cryptates. *Inorg. Chem.* **2021**, *60* (11), 7815–7826. https://doi.org/10.1021/acs.inorgchem.1c00300.

(67) Sabbatini, N.; Ciano, M.; Dellonte, S.; Bonazzi, A.; Bolletta, F.; Balzani, V. Photophysical Properties of Europium(II) Cryptates. *J. Phys. Chem.* **1984**, *88* (8), 1534–1537. https://doi.org/10.1021/j150652a018.

(68) Starynowicz, P. Europium(II) Complexes with Unsubstituted Crown Ethers. *Polyhedron* **2003**, *22* (2), 337–345. https://doi.org/10.1016/S0277-5387(02)01358-X.

(69) Adachi, G.-Y.; Sorita, K.; Kawata, K.; Tomokiyo, K.; Shiokawa, J. Luminescence of Divalent Europium Complexes with Crown Ethers, Cryptands and Polyethylene Glycols. *J. Common Met.* **1983**, *93* (1), 81–87. https://doi.org/10.1016/0022-5088(83)90450-2.

(70) Christoffers, J.; Starynowicz, P. A Europium(II) Complex with Bis-Pyridino-18-Crown-6. *Polyhedron* **2008**, *27* (12), 2688–2692. https://doi.org/10.1016/j.poly.2008.05.028.

(71) Li, J.; Wang, L.; Zhao, Z.; Sun, B.; Zhan, G.; Liu, H.; Bian, Z.; Liu, Z. Highly Efficient and Air-Stable Eu(II)-Containing Azacryptates Ready for Organic Light-Emitting Diodes. *Nat. Commun.* **2020**, *11* (1), 5218. https://doi.org/10.1038/s41467-020-19027-x.

(72) Adachi, G.-Y.; Fujikawa, H.; Tomokiyo, K.; Sorita, K.; Kawata, K.; Shiokawa, J. Luminescence Properties of Divalent Europium Complexes with 15-Crown-5 Derivatives. *Inorganica Chim. Acta* **1986**, *113* (1), 87–90. https://doi.org/10.1016/S0020-1693(00)86864-4.

(73) Adachi, G.-Y.; Sorita, K.; Kawata, K.; Tomokiyo, K.; Shiokawa, J. Luminescence of Divalent Europium Complexes with 18-Crown-6 Derivatives. *Inorganica Chim. Acta* **1985**, *109* (2), 117–121. https://doi.org/10.1016/S0020-1693(00)84551-X.

(74) Starynowicz, P.; Bukietyńska, K.; Gołąb, S.; Ryba-Romanowski, W.; Sokolnicki, J. Europium(II) Complexes With Benzo-18-Crown-6. *Eur. J. Inorg. Chem.* **2002**, *2002* (9), 2344–2347. https://doi.org/10.1002/1099-0682(200209)2002:9%3C2344::AID-EJIC2344%3E3.0.CO;2-N.

(75) Starynowicz, P.; Bukietyńska, K. A Europium(II) Complex with Benzo-15-Crown-5. *Eur. J. Inorg. Chem.* **2002**, *2002* (7), 1835–1838. https://doi.org/10.1002/1099-0682(200207)2002:7%3C1835::AID-EJIC1835%3E3.0.CO;2-%23.

(76) Sabbatini, N.; Ciano, M.; Dellonte, S.; Bonazzi, A.; Balzani, V. Absorption and Emission Properties of a Europium(II) Cryptate in Aqueous Solution. *Chem. Phys. Lett.* **1982**, *90* (4), 265–268. https://doi.org/10.1016/0009-2614(82)83236-3.

(77) Higashiyama, N.; Takemura, K.; Kimura, K.; Adachi, G. Luminescence of Divalent Europium Complexes with N-Pivot Lariat Azacrown Ethers. *Inorganica Chim. Acta* **1992**, *194* (2), 201–206. https://doi.org/10.1016/S0020-1693(00)82663-8.

(78) Yan, W.; Li, T.; Cai, Z.; Qi, H.; Guo, R.; Huo, P.; Liu, Z.; Bian, Z. Systematic Tuning of the Emission Colors and Redox Potential of Eu(II)-Containing Cryptates by Changing the N/O Ratio of Cryptands. *Inorg. Chem. Front.* **2022**, *9* (18), 4794–4800. https://doi.org/10.1039/D2QI01216B.

(79) Higashiyama, N.; Izumi, Y.; Adachi, G. Fluorescence Properties of Europium(II) and Other Divalent Metal Ion Doubly-Doped Poly(Methacrylate Containing 15-Crown-5 Structure) Complexes. *Inorganica Chim. Acta* **1993**, *207* (2), 233–240. https://doi.org/10.1016/S0020-1693(00)90715-1.

(80) Shinoda, S.; Nishioka, M.; Tsukube, H. In Situ Generation of Fluorescent Macrocyclic Europium(II) Complexes via Zinc Reduction. *J. Alloys Compd.* **2009**, *488* (2), 603–605. https://doi.org/10.1016/j.jallcom.2008.10.034.

(81) Qi, H.; Huo, P.; Han, B.; Zheng, J.; Wang, L.; Yan, W.; Guo, R.; Li, T.; Yu, K.; Liu, Z.; Bian, Z. High-Performance Circularly Polarized Electroluminescence from d-f Transition Europium(II) Complexes. *Cell Rep. Phys. Sci.* **2022**, *3* (11), 101107. https://doi.org/10.1016/j.xcrp.2022.101107.

(82) Guo, R.; Zhao, Z.; Wu, A.; Li, Y.; Wang, K.; Bian, Z.; Liu, Z. Rare Earth Complexes of Europium(II) and Substituted Bis(Pyrazolyl)Borates with High Photoluminescence Efficiency. *Molecules* **2022**, *27* (22), 8053. https://doi.org/10.3390/molecules27228053.

(83) Suta, M.; Kühling, M.; Liebing, P.; Edelmann, F. T.; Wickleder, C. Photoluminescence Properties of the "Bent Sandwich-like" Compounds $[Eu(Tp^{iPr2})_2]$ and $[Yb(Tp^{iPr2})_2]$ – Intermediates between Nitride-Based Phosphors and Metallocenes. *J. Lumin.* **2017**, *187*, 62–68. https://doi.org/10.1016/j.jlumin.2017.02.054.

(84) Shipley, C. P.; Capecchi, S.; Salata, O. V.; Etchells, M.; Dobson, P. J.; Christou, V. Orange Electroluminescence from a Divalent Europium Complex. *Adv. Mater.* **1999**, *11* (7), 533–536. https://doi.org/10.1002/(SICI)1521-4095(199905)11:7%3C533::AID-ADMA533%3E3.0.CO;2-U.

(85) Zhan, G.; Wang, L.; Zhao, Z.; Fang, P.; Bian, Z.; Liu, Z. Highly Efficient and Air-Stable Lanthanide Eu^{II} Complex: New Emitter in Organic Light Emitting Diodes. *Angew. Chem. - Int. Ed.* **2020**, *59* (43), 19011–19015. https://doi.org/10.1002/anie.202008423.

(86) Garcia, J.; Allen, M. J. Developments in the Coordination Chemistry of Europium(II). *Eur. J. Inorg. Chem.* **2012**, *2012* (29), 4550–4563. https://doi.org/10.1002/ejic.201200159.

(87) Williams, A. F.; Grandjean, F.; Long, G. J.; Ulibarri, T. A.; Evans, W. J. Europium-151 Moessbauer Effect Study of Several Organoeuropium(II) Complexes. *Inorg. Chem.* **1989**, *28* (26), 4584–4588. https://doi.org/10.1021/ic00325a010.

(88) Shephard, A. C. G.; Delon, A.; Chevreux, S.; Martinez, A.; Guo, Z.; Deacon, G. B.; Lemercier, G.; McClenaghan, N.; Jonusauskas, G.; Junk, P. C.; Jaroschik, F. Divalent Ansa-Octaphenyllanthanocenes: Synthesis, Structures, and Eu^{II} Luminescence. *Inorg. Chem.* **2023**. https://doi.org/10.1021/acs.inorgchem.3c01062.

(89) Harder, S.; Naglav, D.; Ruspic, C.; Wickleder, C.; Adlung, M.; Hermes, W.; Eul, M.; Pöttgen, R.; Rego, D. B.; Poineau, F.; Czerwinski, K. R.; Herber, R. H.; Nowik, I. Physical Properties of Superbulky Lanthanide Metallocenes: Synthesis and Extraordinary Luminescence of $[Eu^{II}(Cp^{BIG})_2]$ (Cp^{BIG}=(4-*n*Bu-$C_6H_4)_5$-Cyclopentadienyl). *Chem. – Eur. J.* **2013**, *19* (37), 12272–12280. https://doi.org/10.1002/chem.201302021.

(90) Dramićanin, M. D. Sensing Temperature via Downshifting Emissions of Lanthanide-Doped Metal Oxides and Salts. A Review. *Methods Appl. Fluoresc.* **2016**, *4* (4), 042001. https://doi.org/10.1088/2050-6120/4/4/042001.
(91) Brites, C. D. S.; Balabhadra, S.; Carlos, L. D. Lanthanide-Based Thermometers: At the Cutting-Edge of Luminescence Thermometry. *Adv. Opt. Mater.* **2019**, *7* (5), 1801239. https://doi.org/10.1002/adom.201801239.
(92) Dramićanin, M. D. Trends in Luminescence Thermometry. *J. Appl. Phys.* **2020**, *128* (4), 040902. https://doi.org/10.1063/5.0014825.
(93) Quintanilla, M.; Liz-Marzán, L. M. Guiding Rules for Selecting a Nanothermometer. *Nano Today* **2018**, *19*, 126–145. https://doi.org/10.1016/j.nantod.2018.02.012.
(94) Moerner, W. E.; Fromm, D. P. Methods of Single-Molecule Fluorescence Spectroscopy and Microscopy. *Rev. Sci. Instrum.* **2003**, *74* (8), 3597–3619. https://doi.org/10.1063/1.1589587.
(95) Yu, D.; Li, H.; Zhang, D.; Zhang, Q.; Meijerink, A.; Suta, M. One Ion to Catch Them All: Targeted High-Precision Boltzmann Thermometry over a Wide Temperature Range with Gd^{3+}. *Light Sci. Appl.* **2021**, *10* (1), 236. https://doi.org/10.1038/s41377-021-00677-5.
(96) Balabhadra, S.; Debasu, M. L.; Brites, C. D. S.; Ferreira, R. A. S.; Carlos, L. D. Upconverting Nanoparticles Working As Primary Thermometers In Different Media. *J. Phys. Chem. C* **2017**, *121* (25), 13962–13968. https://doi.org/10.1021/acs.jpcc.7b04827.
(97) Bao, G.; Wong, K.-L.; Jin, D.; Tanner, P. A. A Stoichiometric Terbium-Europium Dyad Molecular Thermometer: Energy Transfer Properties. *Light Sci. Appl.* **2018**, *7* (1), 96. https://doi.org/10.1038/s41377-018-0097-7.
(98) Gil, Y.; Corredoira-Vázquez, J.; Santana, R. C. de; Brites, C. D. S.; Carlos, L. D.; Spodine, E.; Aravena, D.; Fuentealba, P. Tunable Nd^{3+} Dimer Luminescent Molecular Thermometer via Stark Sublevels. *Inorg. Chem. Front.* **2026**, *13* (10), 4229–4238. https://doi.org/10.1039/D5QI02484F.
(99) Ćirić, A.; Stojadinović, S.; Ristić, Z.; Zeković, I.; Kuzman, S.; Antić, Ž.; Dramićanin, M. D. Supersensitive Sm^{2+}-Activated Al_2O_3 Thermometric Coatings for High-Resolution Multiple Temperature Read-Outs from Luminescence. *Adv. Mater. Technol.* **2021**, *2001201*, 2001201. https://doi.org/10.1002/admt.202001201.
(100) Yue, D.; Li, Z.; Chen, D.; Li, W.; Qin, B.; Zhang, B.; Li, Y.; Zhao, D.; Wang, Z. Ratiometric Luminescent Thermometer Based on a Mixed Ce/Tb Metal-Organic Framework. *J. Solid State Chem.* **2023**, *327*, 124279. https://doi.org/10.1016/j.jssc.2023.124279.
(101) Samal, S. K.; Yadav, J.; Naidu, B. S. Rare Earth Ion-Doped Luminescent Materials for Optical Thermometry. In *Materials Science for Future Applications*; CRC Press, 2025.
(102) Kusama, H.; Sovers, O. J.; Yoshioka, T. Line Shift Method for Phosphor Temperature Measurements. *Jpn. J. Appl. Phys.* **1976**, *15* (12), 2349. https://doi.org/10.1143/JJAP.15.2349.
(103) Rocha, U.; Jacinto da Silva, C.; Ferreira Silva, W.; Guedes, I.; Benayas, A.; Martínez Maestro, L.; Acosta Elias, M.; Bovero, E.; van Veggel, F. C. J. M.; García Solé, J. A.; Jaque, D. Subtissue Thermal Sensing Based on Neodymium-Doped LaF_3 Nanoparticles. *ACS Nano* **2013**, *7* (2), 1188–1199. https://doi.org/10.1021/nn304373q.
(104) Ćirić, A.; Stojadinović, S.; Dramićanin, M. D. Time-Integrated Luminescence Thermometry of Eu^{3+} and Dy^{3+} Doped YVO_4. *Sens. Actuators Phys.* **2019**, *295*, 450–455. https://doi.org/10.1016/j.sna.2019.06.035.
(105) Kolesnikov, I. E.; Kalinichev, A. A.; Kurochkin, M. A.; Golyeva, E. V.; Kolesnikov, E. Y.; Kurochkin, A. V.; Lähderanta, E.; Mikhailov, M. D. YVO_4:Nd^{3+} Nanophosphors as NIR-to-NIR Thermal Sensors

in Wide Temperature Range. *Sci. Rep.* **2017**, *7* (1), 18002. https://doi.org/10.1038/s41598-017-18295-w.

(106) Wylezich, T.; Sontakke, A. D.; Castaing, V.; Suta, M.; Viana, B.; Meijerink, A.; Kunkel, N. One Ion, Many Facets: Efficient, Structurally and Thermally Sensitive Luminescence of Eu^{2+} in Binary and Ternary Strontium Borohydride Chlorides. *Chem. Mater.* **2019**. https://doi.org/10.1021/acs.chemmater.9b03048.

(107) Visseaux, M.; Bonnet, F. Borohydride Complexes of Rare Earths, and Their Applications in Various Organic Transformations. *Coord. Chem. Rev.* **2011**, *255* (3–4), 374–420. https://doi.org/10.1016/j.ccr.2010.09.016.

(108) Shi, R.; Ning, L.; Huang, Y.; Tao, Y.; Zheng, L.; Li, Z.; Liang, H. Li 4 $SrCa(SiO_4)_2:Eu^{2+}$: A Potential Temperature Sensor with Unique Optical Thermometric Properties. *ACS Appl. Mater. Interfaces* **2019**, *11* (10), 9691–9695. https://doi.org/10.1021/acsami.8b22754.

(109) Wu, M.; Deng, D.; Ruan, F.; Chen, B.; Xu, S. A Spatial/Temporal Dual-Mode Optical Thermometry Based on Double-Sites Dependent Luminescence of $Li_4SrCa(SiO_4)_2:Eu^{2+}$ Phosphors with Highly Sensitive Luminescent Thermometer. *Chem. Eng. J.* **2020**, *396*, 125178. https://doi.org/10.1016/j.cej.2020.125178.

(110) Ruan, F.; Deng, D.; Wu, M.; Chen, B.; Lei, R.; Xu, S. Multichannel Luminescence of Eu^{2+}/Eu^{3+} Co-Activated $Ca_9Mg_{1.5}(PO_4)_7$ Phosphors for Self-Referencing Optical Thermometry. *J. Lumin.* **2019**, *213* (May), 117–126. https://doi.org/10.1016/j.jlumin.2019.04.047.

(111) Stefańska, D.; Stefanski, M.; Dereń, P. J. Unusual Emission Generated from $Ca_2Mg_{0.5}AlSi_{1.5}O_7:Eu^{2+}$ and Its Potential for UV-LEDs and Non-Contact Optical Thermometry. *J. Alloys Compd.* **2021**, *863*, 1–7. https://doi.org/10.1016/j.jallcom.2021.158770.

(112) Ojo, A. O.; Fond, B.; Abram, C.; Van Wachem, B. G. M.; Heyes, A. L.; Beyrau, F. Thermographic Laser Doppler Velocimetry Using the Phase-Shifted Luminescence of BAM:Eu^{2+} Phosphor Particles for Thermometry. *Opt. Express* **2017**, *25* (10), 11833. https://doi.org/10.1364/OE.25.011833.

(113) Yin, Z.; Fond, B.; Eckel, G.; Abram, C.; Meier, W.; Boxx, I.; Beyrau, F. Investigation of BAM:Eu^{2+} Particles as a Tracer for Temperature Imaging in Flames. *Combust. Flame* **2017**, *184*, 249–251. https://doi.org/10.1016/j.combustflame.2017.06.005.

(114) Chen, D.; Liu, S.; Wan, Z.; Ji, Z. EuF 3 /Ga 2 O 3 Dual-Phase Nanostructural Glass Ceramics with Eu^{2+}/Cr^{3+} Dual-Activator Luminescence for Self-Calibrated Optical Thermometry. *J. Phys. Chem. C* **2016**, *120* (38), 21858–21865. https://doi.org/10.1021/acs.jpcc.6b08271.

(115) Zhou, R.; Liu, C.; Lin, L.; Huang, Y.; Liang, H. Multi-Site Occupancies of Eu^{2+} in $Ca_6BaP_4O_{17}$ and Their Potential Optical Thermometric Applications. *Chem. Eng. J.* **2019**, *369* (February), 376–385. https://doi.org/10.1016/j.cej.2019.03.073.

(116) Zhao, L.; Mao, J.; Jiang, B.; Wei, X.; Chen, Y.; Yin, M. Temperature-Dependent Persistent Luminescence of $SrAl_2O_4:Eu^{2+},Dy^{3+},Tb^{3+}$: A Strategy of Optical Thermometry Avoiding Real-Time Excitation. *Opt. Lett.* **2018**, *43* (16), 3882. https://doi.org/10.1364/OL.43.003882.

(117) Zhou, X.; Geng, W.; Ding, J.; Zhao, Z.; Wang, Y. $Ca_2Na_2La_6(SiO_4)_4(PO_4)_2O:Eu^{2+}/Eu^{3+}$: A Visual Dual-emitting Fluorescent Ratiometric Temperature Sensor. *J. Am. Ceram. Soc.* **2019**, *102* (9), 5443–5453. https://doi.org/10.1111/jace.16431.

(118) Liu, W.; Liu, L.; Wang, Y.; Chen, L.; McLeod, J. A.; Yang, L.; Zhao, J.; Liu, Z.; Diwu, J.; Chai, Z.; Albrecht-Schmitt, T. E.; Liu, G.; Wang, S. Tuning Mixed-Valent Eu^{2+}/Eu^{3+} in Strontium Formate Frameworks for Multichannel Photoluminescence. *Chem. - Eur. J.* **2016**, *22* (32), 11170–11175. https://doi.org/10.1002/chem.201602621.

(119) Stefańska, D.; Dereń, P. J. High Efficiency Emission of Eu^{2+} Located in Channel and Mg-Site of $Mg_2Al_4Si_5O_{18}$ Cordierite and Its Potential as a Bi-Functional Phosphor toward Optical Thermometer and White LED Application. *Adv. Opt. Mater.* **2020**, *8* (22), 2001143. https://doi.org/10.1002/adom.202001143.

(120) Zhou, R.; Lin, L.; Zhao, H.; Deng, T.; Li, J. Constructing Sensitive Luminescent Thermometers via Energy Transfer in Ce^{3+} and Eu^{2+} Co-Doped $Ca_8Mg_3Al_2Si_7O_{28}$ Phosphors. *Mater. Chem. Front.* **2021**, *5* (16), 6071–6081. https://doi.org/10.1039/D1QM00555C.

(121) Liu, F.; Deng, D.; Wu, M.; Chen, B.; Zhou, L.; Xu, S. Luminescent and Thermometric Properties of Dual Emitting Eu^{2+}/Sm^{3+} Co-Doped $Sr_4La(PO_4)_3O$ Phosphor Based on Energy Transfer. *J. Rare Earths* **2021**, *39* (3), 261–268. https://doi.org/10.1016/j.jre.2020.06.003.

(122) Zhang, X.; Zhu, Z.; Guo, Z.; Sun, Z.; Chen, Y. A Ratiometric Optical Thermometer with High Sensitivity and Superior Signal Discriminability Based on $Na_3Sc_2P_3O_{12}:Eu^{2+},Mn^{2+}$ Thermochromic Phosphor. *Chem. Eng. J.* **2019**, *356*, 413–422. https://doi.org/10.1016/j.cej.2018.09.075.

(123) Liu, F.; Deng, D.; Wu, M.; Chen, B.; Zhou, L.; Xu, S. Alkali Ions Substitution Induced Tuning of Sensitivity in Mixed-Valence Europium Ion Co-Doped $NaZr_2(PO_4)_3$ Thermochromic Phosphor for Optical Thermometry. *J. Alloys Compd.* **2021**, *865*, 158820. https://doi.org/10.1016/j.jallcom.2021.158820.

(124) Li, C.; Chen, B.; Deng, D.; Yu, H.; Li, H.; Shen, C.; Wang, L.; Xu, S. A Ratiometric Optical Thermometer with Tunable Sensitivity and Superior Signal Discriminability Based on Eu^{2+}/Eu^{3+} Co-Doped $La_{1-y}Gd_yAlO_3$ Phosphors. *J. Lumin.* **2020**, *221*, 117036. https://doi.org/10.1016/j.jlumin.2020.117036.

(125) Kolesnikov, I. E.; Afanaseva, E. V.; Kurochkin, M. A.; Kolesnikov, E. Y.; Lähderanta, E. Mixed-Valent $MgAl_2O_4:Eu^{2+}/Eu^{3+}$ Phosphor for Ratiometric Optical Thermometry. *Phys. B Condens. Matter* **2022**, *624*, 413456. https://doi.org/10.1016/j.physb.2021.413456.

(126) Wu, M.; Deng, D.; Ruan, F.; Chen, B.; Lei, L.; Lei, R.; Xu, S. Double-Site Emission of Eu^{2+} Ions in $Sr_4Al_{14}O_{25}:Eu^{2+}$ Phosphors for Self-Calibrated Optical Thermometry. *Opt. Mater.* **2019**, *88*, 704–710. https://doi.org/10.1016/j.optmat.2018.12.058.

(127) Zhang, D.; Zheng, B.; Zheng, Z.; Li, L.; Yang, Q.; Song, Y.; Zou, B.; Zou, H. Multifunctional $Ca_9NaZn_{1-y}Mg_y(PO_4)_7:Eu^{2+}$ Phosphor for Full-Spectrum Lighting, Optical Thermometry and Pressure Sensor Applications. *Chem. Eng. J.* **2022**, *431*, 133805. https://doi.org/10.1016/j.cej.2021.133805.

(128) Yu, H.; Ruan, F.; Chen, L.; Deng, D. Dual-Emitting Eu^{2+}/Eu^{3+} Co-Doped $Ca_9Zn_{1.5}(PO_4)_7$ Phosphor for Self-Calibrated Optical Thermometry. *Opt. Mater.* **2020**, *100*, 109678. https://doi.org/10.1016/j.optmat.2020.109678.

(129) Xue, J.; Song, M.; Noh, H. M.; Park, S. H.; Choi, B. C.; Kim, J. H.; Jeong, J. H.; Du, P. Achieving Non-Contact Optical Thermometer via Inherently Eu^{2+}/Eu^{3+}-Activated $SrAl_2Si_2O_8$ Phosphors Prepared in Air. *J. Alloys Compd.* **2020**, *843*, 155858. https://doi.org/10.1016/j.jallcom.2020.155858.

(130) Hu, T.; Gao, Y.; Molokeev, M.; Xia, Z.; Zhang, Q. Non-Stoichiometry in $Ca_2Al_2SiO_7$ Enabling Mixed-Valent Europium toward Ratiometric Temperature Sensing. *Sci. China Mater.* **2019**, *62* (12), 1807–1814. https://doi.org/10.1007/s40843-019-1202-x.

(131) Chen, D.; Xu, M.; Liu, S.; Li, X. Eu^{2+}/Eu^{3+} Dual-Emitting Glass Ceramic for Self-Calibrated Optical Thermometry. *Sens. Actuators B Chem.* **2017**, *246*, 756–760. https://doi.org/10.1016/j.snb.2017.02.159.

(132) Chen, B.; Li, C.; Deng, D.; Ruan, F.; Wu, M.; Wang, L.; Zhu, Y.; Xu, S. Temperature Sensitive Properties of Eu^{2+}/Eu^{3+} Dual-Emitting $LaAlO_3$ Phosphors. *J. Alloys Compd.* **2019**, *792*, 702–712. https://doi.org/10.1016/j.jallcom.2019.04.013.

(133) Yu, H.; Su, W.; Chen, L.; Deng, D.; Xu, S. Excellent Temperature Sensing Characteristics of Europium Ions Self-Reduction $Sr_3P_4O_{13}$ Phosphors for Ratiometric Luminescence Thermometer. *J. Alloys Compd.* **2019**, *806*, 833–840. https://doi.org/10.1016/j.jallcom.2019.07.338.

(134) Nair, G. B.; Kumar, A.; Dhoble, S. J.; Swart, H. C. Synergistic Effect from the Dual Oxidation States of Europium in the Color-Tuning of $Ca_3Mg_3(PO_4)_4:Eu^{2+},Eu^{3+}$ Thermometric Phosphor. *Mater. Res. Bull.* **2020**, *122*, 110644. https://doi.org/10.1016/j.materresbull.2019.110644.

(135) Zhao, D.; Zhang, S.-R.; Zhang, R.-J.; Liu, B.-Z.; Yao, Q.-X. Warm White Light Emission, Thermochromic Property and Long Persistent Luminescence Derived from Multi-Sites of Eu^{2+}/Eu^{3+} in Host Lattice. *Chem. Eng. J.* **2022**, *428*, 131023. https://doi.org/10.1016/j.cej.2021.131023.

(136) Qian, F.; Zhang, J. Various Strategies for Optical Thermometry with High Sensitivities Based on Rare Earth Ions Doped $BaY_2Si_3O_{10}$ Phosphors. *Mater. Res. Bull.* **2020**, *122*, 110660. https://doi.org/10.1016/j.materresbull.2019.110660.

(137) Xu, Y.; Sun, Z.; Wei, Y.; Jia, M.; Hou, B.; Li, X.; Lin, F.; Zhang, M.; Wang, H.; Fu, Z. Optical Properties of the $CaEuAl_3O_7$ Phosphor with Dual-Activator Eu^{2+}/Eu^{3+} for Multifunctional Applications. *J. Am. Ceram. Soc.* **2020**, *103* (10), 5721–5730. https://doi.org/10.1111/jace.17289.

(138) Du, P.; Luo, L.; Li, W.; Yan, F.; Xing, G. Multi-Site Occupancies and Photoluminescence Characteristics in Developed Eu^{2+}-Activated $Ba_5SiO_4Cl_6$ Bifunctional Platform: Towards Manufacturable Optical Thermometer and Indoor Illumination. *J. Alloys Compd.* **2020**, *826*, 154233. https://doi.org/10.1016/j.jallcom.2020.154233.

(139) Zhou, L.; Du, P.; Li, L. Facile Modulation the Sensitivity of Eu^{2+}/Eu^{3+}-Coactivated Li_2CaSiO_4 Phosphors through Adjusting Spatial Mode and Doping Concentration. *Sci. Rep.* **2020**, *10* (1), 20180. https://doi.org/10.1038/s41598-020-77185-w.

(140) Ruan, F.; Deng, D.; Wu, M.; Chen, B.; Lei, L.; Lei, R.; Xu, S. Multichannel Luminescence Properties and Ultrahigh-Sensitive Optical Temperature Sensing of Mixed-Valent Eu^{2+}/Eu^{3+} Co-Activated $Ca_8ZrMg(PO_4)_6(SiO_4)$ Phosphors. *J. Alloys Compd.* **2019**, *784*, 1153–1161. https://doi.org/10.1016/j.jallcom.2019.01.092.

(141) Pan, Y.; Xie, X.; Huang, Q.; Gao, C.; Wang, Y.; Wang, L.; Yang, B.; Su, H.; Huang, L.; Huang, W. Inherently Eu^{2+}/Eu^{3+} Codoped Sc_2O_3 Nanoparticles as High-Performance Nanothermometers. *Adv. Mater.* **2018**, *30* (14), 1705256. https://doi.org/10.1002/adma.201705256.

(142) Yu, T.; Liu, B.; Ma, Z.; Jiang, Y.; Zeng, Q.; Wen, D.; Guo, Y. Regulation of Double Luminescence Centers Based on the Evolution of Disordered Local Structure for Ratiometric Temperature Sensing Applications. *Mater. Chem. Front.* **2021**, *5* (16), 6256–6264. https://doi.org/10.1039/D1QM00722J.

(143) Zhou, L.; Zhou, L.; Du, P.; Du, P.; Li, W.; Li, W.; Luo, L.; Luo, L.; Xing, G.; Xing, G. Composition Regulation Triggered Multicolor Emissions in Eu^{2+}-Activated $Li_4(Sr_{1-x}Ca_{1+x})(SiO_4)_2$ for a Highly Sensitive Thermometer. *Ind. Eng. Chem. Res.* **2020**, *59* (21), 9989–9996. https://doi.org/10.1021/acs.iecr.0c00967.

(144) Li, C.; Chen, B.; Deng, D.; Wu, M.; Yu, H.; Li, H.; Shen, C.; Wang, L.; Xu, S. Ratiometric Optical Thermometer with High-Sensitive Temperature Sensing Based on Synergetic Luminescence of Ce^{3+}-Eu^{2+} in $LiSr_4(BO_3)_3$ Phosphors. *J. Alloys Compd.* **2020**, *838*, 155675. https://doi.org/10.1016/j.jallcom.2020.155675.

(145) Wang, Z.; Huang, F.; Li, D.; Lei, R.; Zhang, J.; Xu, S. An Environmental Amorphous Solid by Local Crystallization for Multifunctional Optical Applications. *J. Clean. Prod.* **2020**, *270*, 122441. https://doi.org/10.1016/j.jclepro.2020.122441.

(146) Zhou, L.; Liu, F.; Ye, R.; Lei, L.; Guo, W.; Chen, L.; Deng, D.; Xu, S. Tunable Photoluminescence and Temperature Sensing Properties of Ce^{3+}, Eu^{2+} Co-Doped $Ca_{2-x}Sr_xMgSi_2O_7$ Phosphors. *J. Lumin.* **2021**, *240*, 118417. https://doi.org/10.1016/j.jlumin.2021.118417.

(147) Zhang, J.; Yang, D.; Chen, G.; Zhang, Y. Emission-Tunable $Sr_{1-n-2x-y}Ba_nMg_2(PO_4)_2$:*X*$Ce^{3+}$,*y*$Eu^{2+}$,*x*$Na^+$ Phosphors for Optical Temperature Sensing. *J. Alloys Compd.* **2017**, *725*, 1055–1062. https://doi.org/10.1016/j.jallcom.2017.07.267.

(148) Su, F.; Lou, B.; Ou, Y.; Yang, Y.; Zhou, W.; Duan, C.-K.; Liang, H. VUV–UV–Vis Luminescence, Energy Transfer Dynamics, and Potential Applications of Ce^{3+}- and Eu^{2+}-Doped $CaMgSi_2O_6$. *J. Phys. Chem. C* **2021**, *125* (10), 5957–5967. https://doi.org/10.1021/acs.jpcc.1c01320.

(149) Su, K.; Guo, Q.; Shuai, P.; Liu, N.; Mei, L.; Liao, L. A Novel Eu^{2+}/Tb^{3+} Co-Doped Phosphor with Pyroxene Structure Applied for Cryogenic Thermometric Sensing. *J. Am. Ceram. Soc.* **2022**, *105* (4), 2903–2913. https://doi.org/10.1111/jace.18275.

(150) Gálico, D. A.; Marin, R.; Brunet, G.; Errulat, D.; Hemmer, E.; Sigoli, F. A.; Moilanen, J. O.; Murugesu, M. Triplet-State Position and Crystal-Field Tuning in Opto-Magnetic Lanthanide Complexes: Two Sides of the Same Coin. *Chem. - Eur. J.* **2019**, *25* (64), 14625–14637. https://doi.org/10.1002/chem.201902837.

(151) Parke, S. M.; Narreto, M. A. B.; Hupf, E.; McDonald, R.; Ferguson, M. J.; Hegmann, F. A.; Rivard, E. Understanding the Origin of Phosphorescence in Bismoles: A Synthetic and Computational Study. *Inorg. Chem.* **2018**, *57* (13), 7536–7549. https://doi.org/10.1021/acs.inorgchem.8b00149.

(152) Chan, K.-T.; Lam, T.-L.; Yu, D.; Du, L.; Phillips, D. L.; Kwong, C.-L.; Tong, G. S. M.; Cheng, G.; Che, C.-M. Strongly Luminescent Tungsten Emitters with Emission Quantum Yields of up to 84 %: TADF and High-Efficiency Molecular Tungsten OLEDs. *Angew. Chem. Int. Ed.* **2019**, *58* (42), 14896–14900. https://doi.org/10.1002/anie.201906698.

(153) Baudron, S. A. Luminescent Dipyrrin Based Metal Complexes. *Dalton Trans.* **2013**, *42* (21), 7498–7509. https://doi.org/10.1039/c3dt50493j.

(154) Carlotto, A.; Babetto, L.; Carlotto, S.; Miozzi, M.; Seraglia, R.; Casarin, M.; Bottaro, G.; Rancan, M.; Armelao, L. Luminescent Thermometers: From a Library of Europium(III) β-Diketonates to a General Model for Predicting the Thermometric Behaviour of Europium-Based Coordination Systems. *ChemPhotoChem* **2020**, *4* (9), 674–684. https://doi.org/10.1002/cptc.202000116.

(155) Kim, J. M.; Jeong, Y. K.; Sohn, Y.; Kang, J. G. Synthesis and Photophysical Properties of an Eu(II)-Complex/PS Blend: Role of Ag Nanoparticles in Surface-Enhanced Luminescence. *Langmuir* **2012**, *28* (25), 9842–9848. https://doi.org/10.1021/la301547z.

(156) Starynowicz, P. Complexes of Divalent Europium with Dotp and Dotpph. *New J. Chem.* **2021**, *45* (13), 5879–5889. https://doi.org/10.1039/d1nj00393c.

(157) Pan, C. L.; Pan, Y. S.; Wang, J.; Song, J. F. A Heterometallic Sandwich Complex of Europium(II) for Luminescent Studies. *Dalton Trans.* **2011**, *40* (24), 6361–6363. https://doi.org/10.1039/c1dt10635j.

(158) Kühling, M.; Wickleder, C.; Ferguson, M. J.; Hrib, C. G.; McDonald, R.; Suta, M.; Hilfert, L.; Takats, J.; Edelmann, F. T. Investigation of the "Bent Sandwich-like" Divalent Lanthanide Hydro-Tris(Pyrazolyl)Borates $Ln(Tp^{iPr2})_2$ (Ln = Sm, Eu, Tm, Yb). *New J. Chem.* **2015**, *39* (10), 7617–7625. https://doi.org/10.1039/c5nj00568j.

(159) Qu, J.; Xia, Q.; Ji, W.; Jing, S.; Zhu, D.; Li, L.; Huang, L.; An, Z.; Xin, C.; Ni, Y.; Li, M.; Jia, J.; Song, Y.; Huang, W. A Ferrocene∩europium Assembly Showing Phototriggered Anticancer Activity and Fluorescent Modality Imaging. *Dalton Trans.* **2018**, *47* (5), 1479–1487. https://doi.org/10.1039/c7dt04492e.

(160) Errulat, D.; Marin, R.; Gálico, D. A.; Harriman, K. L. M.; Pialat, A.; Gabidullin, B.; Iikawa, F.; Couto, O. D. D.; Moilanen, J. O.; Hemmer, E.; Sigoli, F. A.; Murugesu, M. A Luminescent Thermometer Exhibiting Slow Relaxation of the Magnetization: Toward Self-Monitored Building Blocks for Next-Generation Optomagnetic Devices. *ACS Cent. Sci.* **2019**, *5* (7), 1187–1198. https://doi.org/10.1021/acscentsci.9b00288.

(161) Kitagawa, Y.; Kumagai, M.; Ferreira da Rosa, P. P.; Fushimi, K.; Hasegawa, Y. Long-Range LMCT Coupling in Eu^{III} Coordination Polymers for an Effective Molecular Luminescent Thermometer. *Chem. - Eur. J.* **2021**, *27* (1), 264–269. https://doi.org/10.1002/chem.202002628.

(162) Wang, J.; Zakrzewski, J. J.; Zychowicz, M.; Vieru, V.; Chibotaru, L. F.; Nakabayashi, K.; Chorazy, S.; Ohkoshi, S. I. Holmium(III) Molecular Nanomagnets for Optical Thermometry Exploring the Luminescence Re-Absorption Effect. *Chem. Sci.* **2021**, *12* (2), 730–741. https://doi.org/10.1039/d0sc04871b.

(163) Outis, M.; Laia, C. A. T.; Oliveira, M. C.; Monteiro, B.; Pereira, C. C. L. A Europium(III) Complex with an Unusual Anion–Cation Interaction: A Luminescent Molecular Thermometer for Ratiometric Temperature Sensing. *ChemPlusChem* **2020**, *85* (3), 580–586. https://doi.org/10.1002/cplu.202000034.

(164) Wang, J. X.; Yu, Y. S.; Niu, L. Y.; Zou, B.; Wang, K.; Yang, Q. Z. A Difluoroboron β-Diketonate Based Thermometer with Temperature-Dependent Emission Wavelength. *Chem. Commun.* **2020**, *56* (46), 6269–6272. https://doi.org/10.1039/d0cc01505a.

(165) Zhao, Y.; Wang, X.; Zhang, Y.; Li, Y.; Yao, X. Optical Temperature Sensing of Up-Conversion Luminescent Materials: Fundamentals and Progress. *J. Alloys Compd.* **2020**, *817*, 152691. https://doi.org/10.1016/j.jallcom.2019.152691.

(166) Lefevre, G.; Herfurth, A.; Kohlmann, H.; Sayede, A.; Wylezich, T.; Welinski, S.; Duarte Vaz, P.; Parker, S. F.; Blach, J. F.; Goldner, P.; Kunkel, N. Electron-Phonon Coupling in Luminescent Europium-Doped Hydride Perovskites Studied by Luminescence Spectroscopy, Inelastic Neutron Scattering, and First-Principles Calculations. *J. Phys. Chem. C* **2018**, *122* (19), 10501–10509. https://doi.org/10.1021/acs.jpcc.8b01011.

(167) Morss, L. R. Thermochemical Properties of Yttrium, Lanthanum, and the Lanthanide Elements and Ions. *Chem. Rev.* **1976**, *76* (6), 827–841. https://doi.org/10.1021/cr60304a007.

(168) Sharma, M.; Didelot, E.; Spyratou, A.; Lawson Daku, L. M.; Černý, R.; Hagemann, H. Halide Free $M(BH_4)_2$ (M = Sr, Ba, and Eu) Synthesis, Structure, and Decomposition. *Inorg. Chem.* **2016**, *55* (14), 7090–7097. https://doi.org/10.1021/acs.inorgchem.6b00931.

(169) Cendrowski-Guillaume, S. M.; Nierlich, M.; Lance, M.; Ephritikhine, M. First Chemical Transformations of Lanthanide Borohydride Compounds: Synthesis and Crystal Structures of $[(\eta\text{-}C_8H_8)Nd(BH_4)(THF)]_2$ and $[(\eta\text{-}C_8H_8)Nd(THF)_4][BPh_4]$. *Organometallics* **1998**, *17* (5), 786–788. https://doi.org/10.1021/om9709446.

(170) Jaroschik, F.; Bonnet, F.; Le Goff, X.-F.; Ricard, L.; Nief, F.; Visseaux, M. Synthesis of Samarium(II) Borohydrides and Their Behaviour as Initiators in Styrene and ε-Caprolactone Polymerisation. *Dalton Trans.* **2010**, *39* (29), 6761. https://doi.org/10.1039/c001795g.

(171) Cendrowski-Guillaume, S. M.; Le Gland, G.; Nierlich, M.; Ephritikhine, M. Lanthanide Borohydrides as Precursors to Organometallic Compounds. Mono(Cyclooctatetraenyl)

Neodymium Complexes. *Organometallics* **2000**, *19* (26), 5654–5660. https://doi.org/10.1021/om000558f.

(172) Marks, T. J.; Kolb, J. R. Covalent Transition Metal, Lanthanide, and Actinide Tetrahydroborate Complexes. *Chem. Rev.* **1977**, *77* (2), 263–293. https://doi.org/10.1021/cr60306a004.

(173) Shen, Y.; Santos, H. D. A.; Ximendes, E. C.; Lifante, J.; Sanz-Portilla, A.; Monge, L.; Fernández, N.; Chaves-Coira, I.; Jacinto, C.; Brites, C. D. S.; Carlos, L. D.; Benayas, A.; Iglesias-de la Cruz, M. C.; Jaque, D. Ag_2S Nanoheaters with Multiparameter Sensing for Reliable Thermal Feedback during In Vivo Tumor Therapy. *Adv. Funct. Mater.* **2020**, *30* (49). https://doi.org/10.1002/adfm.202002730.

(174) Liang, R.; Tian, R.; Shi, W.; Liu, Z.; Yan, D.; Wei, M.; Evans, D. G.; Duana, X. A Temperature Sensor Based on CdTe Quantum Dots-Layered Double Hydroxide Ultrathin Films via Layer-by-Layer Assembly. *Chem. Commun.* **2013**, *49* (10), 969–971. https://doi.org/10.1039/c2cc37553b.

(175) Srivastava, A. M.; Comanzo, H. A.; Camardello, S.; Chaney, S. B.; Aycibin, M.; Happek, U. Unusual Luminescence of Octahedrally Coordinated Divalent Europium Ion in $Cs_2M^{2+}P_2O_7$ (M^{2+} = Ca, Sr). *J. Lumin.* **2009**, *129* (9), 919–925. https://doi.org/10.1016/j.jlumin.2009.03.018.

(176) Batsanov, A. S. Weak Interactions in Crystals: Old Concepts, New Developments. *Acta Crystallogr. Sect. E Crystallogr. Commun.* **2018**, *74*, 570–574. https://doi.org/10.1107/S2056989018005339.

(177) Ruiṕrez, F.; Seijo, L.; Barandiarán, Z. Prediction of Pressure-Induced Redshift of $f^1 \rightarrow d(t_{2g})^1$ Excitations in $Cs_2NaYCl_6:Ce^{3+}$ and Its Connection with Bond-Length Shortening. *J. Chem. Phys.* **2005**, *122* (23), 1–5. https://doi.org/10.1063/1.1935512.

(178) Dorenbos, P. Relating the Energy of the [Xe]$5d^1$ Configuration of Ce^{3+} in Inorganic Compounds with Anion Polarizability and Cation Electronegativity. *Phys. Rev. B* **2002**, *65* (23), 235110. https://doi.org/10.1103/PhysRevB.65.235110.

(179) Poort, S. H. M.; Meyerink, A.; Blasse, G. Lifetime Measurements in Eu^{2+}-Doped Host Lattices. *J. Phys. Chem. Solids* **1997**, *58* (9), 1451–1456. https://doi.org/10.1016/S0022-3697(97)00010-3.

(180) Schouwink, P.; Ley, M. B.; Tissot, A.; Hagemann, H.; Jensen, T. R.; Smrčok, L; Černý, R. Structure and Properties of Complex Hydride Perovskite Materials. *Nat. Commun.* **2014**, *5* (May), 1–10. https://doi.org/10.1038/ncomms6706.

(181) Albasiny, E. L.; Cooper, J. R. A. Amendments to the Calculated Polarizabilities of BH_4^-, CH_4 and NH^{4+}. *Proc. Phys. Soc.* **1963**, *82* (5), 801–802. https://doi.org/10.1088/0370-1328/82/5/116.

(182) Jurca, T.; Farghal, A.; Lin, P. H.; Korobkov, I.; Murugesu, M.; Richeson, D. S. Single-Molecule Magnet Behavior with a Single Metal Center Enhanced through Peripheral Ligand Modifications. *J. Am. Chem. Soc.* **2011**, *133* (40), 15814–15817. https://doi.org/10.1021/ja204562m.

(183) Valiente, R.; Rodríguez, F.; González, J.; Güdel, H. U.; Martín-Rodríguez, R.; Nataf, L.; Sanz-Ortiz, M. N.; Krämer, K. High Pressure Optical Spectroscopy of Ce^{3+}-Doped $Cs_2NaLuCl_6$. *Chem. Phys. Lett.* **2009**, *481* (1–3), 149–151. https://doi.org/10.1016/j.cplett.2009.09.059.

(184) Grinberg, M. High Pressure Spectroscopy of Rare Earth Ions Doped Crystals-New Results. *Opt. Mater.* **2006**, *28* (1–2), 26–34. https://doi.org/10.1016/j.optmat.2004.10.029.

(185) Mahlik, S.; Grinberg, M.; Shi, L.; Seo, H. J. Pressure Evolution of $LiBaF_3:Eu^{2+}$ Luminescence. *J. Phys. Condens. Matter* **2009**, *21* (23). https://doi.org/10.1088/0953-8984/21/23/235603.

(186) Joos, J. J.; Smet, P. F.; Seijo, L.; Barandiarán, Z. Insights into the Complexity of the Excited States of Eu-Doped Luminescent Materials. *Inorg. Chem. Front.* **2020**, *7* (4), 871–888. https://doi.org/10.1039/c9qi01455a.

(187) Monreal, M. J.; Thomson, R. K.; Cantat, T.; Travia, N. E.; Scott, B. L.; Kiplinger, J. L. UI_4(1,4-Dioxane)$_2$, [UCl_4(1,4-Dioxane)]$_2$, and UI_3(1,4-Dioxane)$_{1.5}$: Stable and Versatile Starting Materials for

Low- and High-Valent Uranium Chemistry. *Organometallics* **2011**, *30* (7), 2031–2038. https://doi.org/10.1021/om200093q.
(188) SAINT; Bruker AXS: Madison, WI, USA, 2008.
(189) APEX II; Bruker AXS: Madison, WI, USA, 2008.
(190) SADABS; Bruker AXS: Madison, WI, USA, 2009.
(191) Sheldrick, G. M. A Short History of SHELX. *Acta Crystallogr. A* **2008**, *64* (1), 112–122. https://doi.org/10.1107/S0108767307043930.
(192) Sheldrick, G. M. SHELXT - Integrated Space-Group and Crystal-Structure Determination. *Acta Crystallogr. A* **2015**, *71* (1), 3–8. https://doi.org/10.1107/S2053273314026370.
(193) Sheldrick, G. M. Crystal Structure Refinement with SHELXL. *Acta Crystallogr. Sect. C Struct. Chem.* **2015**, *71* (Md), 3–8. https://doi.org/10.1107/S2053229614024218.
(194) Dolomanov, O. V.; Bourhis, L. J.; Gildea, R. J.; Howard, J. A. K.; Puschmann, H. OLEX2 : A Complete Structure Solution, Refinement and Analysis Program. *Journal of Applied Crystallography*, 2009, *42*, 339–341. https://doi.org/10.1107/S0021889808042726.
(195) APEX 3; Bruker AXS: Madison, WI, USA, 2018.
(196) SAINT; Bruker AXS: Madison, WI, USA, 2016.
(197) SADABS; Bruker AXS: Madison, WI, USA, 2016.
(198) Putz, H.; Brandenburg, K. Diamond - Crystal and Molecular Structure Visualization. Bonn, Germany.
(199) Bergerhoff, G.; Berndt, M.; Brandenburg, K. Evaluation of Crystallographic Data with the Program DIAMOND. *J. Res. Natl. Inst. Stand. Technol.* **1996**, *101* (3), 221. https://doi.org/10.6028/jres.101.023.
(200) Macrae, C. F.; Bruno, I. J.; Chisholm, J. A.; Edgington, P. R.; McCabe, P.; Pidcock, E.; Rodriguez-Monge, L.; Taylor, R.; van de Streek, J.; Wood, P. A. Mercury CSD 2.0 – New Features for the Visualization and Investigation of Crystal Structures. *J. Appl. Crystallogr.* **2008**, *41* (2), 466–470. https://doi.org/10.1107/S0021889807067908.
(201) Buck, D. K.; Collins, Aaron. A.; Enzmann, A. Persistence of Vision Ray Tracer (POV-Ray). 1991.
(202) Llunel, M.; Casanova, D.; Cirera, J.; Alemany, P.; Alvarez, S. SHAPE: Program for the Stereochemical Analysis of Molecular Fragments by Means of Continuous Shape Measures and Associated Tools. Barcelona, Spain 2013.
(203) Cirera, J.; Ruiz, E.; Alvarez, S. Continuous Shape Measures as a Stereochemical Tool in Organometallic Chemistry. *Organometallics* **2005**, *24* (7), 1556–1562. https://doi.org/10.1021/om049150z.
(204) Spackman, P. R.; Turner, M. J.; McKinnon, J. J.; Wolff, S. K.; Grimwood, D. J.; Jayatilaka, D.; Spackman, M. A. CrystalExplorer : A Program for Hirshfeld Surface Analysis, Visualization and Quantitative Analysis of Molecular Crystals. *J. Appl. Crystallogr.* **2021**, *54* (3), 1006–1011. https://doi.org/10.1107/S1600576721002910.
(205) Chilton, N. F.; Anderson, R. P.; Turner, L. D.; Soncini, A.; Murray, K. S. PHI: A Powerful New Program for the Analysis of Anisotropic Monomeric and Exchange-Coupled Polynuclear d- and f-Block Complexes. *J. Comput. Chem.* **2013**, *34* (13), 1164–1175. https://doi.org/10.1002/jcc.23234.
(206) Ferreira, R. A. S.; Mamontova, E.; Botas, A. M. P.; Shestakov, M.; Vanacken, J.; Moshchalkov, V.; Guari, Y.; Chibotaru, L. F.; Luneau, D.; André, P. S.; Larionova, J.; Long, J.; Carlos, L. D. Synchronous Temperature and Magnetic Field Dual-Sensing by Luminescence in a Dysprosium Single-Molecule Magnet. *Adv. Opt. Mater.* **2021**, *9* (24), 2101495. https://doi.org/10.1002/adom.202101495.

(207) Gálico, D. A.; Mazali, I. O.; Sigoli, F. A. Nanothermometer Based on Intensity Variation and Emission Lifetime of Europium(III) Benzoylacetonate Complex. *J. Lumin.* **2017**, *192*, 224–230. https://doi.org/10.1016/j.jlumin.2017.06.062.

(208) Lapaev, D. V.; Nikiforov, V. G.; Lobkov, V. S.; Knyazev, A. A.; Galyametdinov, Y. G. Reusable Temperature-Sensitive Luminescent Material Based on Vitrified Film of Europium(III) β-Diketonate Complex. *Opt. Mater.* **2018**, *75*, 787–795. https://doi.org/10.1016/j.optmat.2017.11.042.

(209) Calado, C. M. S.; Gálico, D. A.; Murugesu, M. Intra-Cluster Energy Transfer Editing in a Dual-Emitting System to Tap into Lifetime Thermometry. *Chem. Commun.* **2023**, *59* (92), 13715–13718. https://doi.org/10.1039/D3CC03658H.

(210) Ilichev, V. A.; Silantyeva, L. I.; Rogozhin, A. F.; Yablonskiy, A. N.; Andreev, B. A.; Rumyantsev, R. V.; Fukin, G. K.; Bochkarev, M. N. Luminescence Thermochromism in Novel Mixed Eu(II)–Cu(I) Iodide. *Dalton Trans.* **2021**, *50* (40), 14244–14251. https://doi.org/10.1039/D1DT02384E.

(211) Stewart, O. C.; Marwitz, A. C.; Swanson, J.; Bertke, J. A.; Hartman, T.; Monteiro, J. H. S. K.; de Bettencourt-Dias, A.; Knope, K. E.; Stoll, S. L. Lanthanide Luminescence and Thermochromic Emission from Soft-Atom Donor Dichalcogenoimidodiphosphinate Ligands. *Inorg. Chem.* **2022**. https://doi.org/10.1021/acs.inorgchem.2c02260.

(212) Kim, D.; Park, S.; Kim, S.; Kang, S.-G.; Park, J.-C. Blue-Emitting Eu^{2+}-Activated LaOX (X = Cl, Br, and I) Materials: Crystal Field Effect. *Inorg. Chem.* **2014**, *53* (22), 11966–11973. https://doi.org/10.1021/ic5015576.

(213) Bao, Q.; Wang, Z.; Wang, Z.; Meng, X.; Qiu, K.; Chen, Y.; Li, Y.; Sun, J.; Yang, Z.; Li, P. Role of H_3BO_3 and Sr^{2+}/K^+ in the Luminescent Property of $NaBaB_9O_{15}:Eu^{2+}$. *J. Lumin.* **2020**, *218* (June 2019), 116840. https://doi.org/10.1016/j.jlumin.2019.116840.

(214) Qi, H.; Zhong, T.; Huo, P.; Zheng, J.; Zhao, Z.; Yan, W.; Bian, Z.; Liu, Z. Europium(II) Complexes with Substituted Triethylenetetramine: New Emitters to Construct Efficient Deep Blue Organic Light Emitting Diodes by Spin Coating. *J. Mater. Chem. C* **2023**, *11* (12), 4136–4142. https://doi.org/10.1039/D2TC05500G.

(215) Starynowicz, P. Europium(II) Complexes with Nitrilotriacetic Acid (NTA). *Polyhedron* **2003**, *22* (20), 2761–2765. https://doi.org/10.1016/S0277-5387(03)00452-2.

(216) Wu, A.; Huo, P.; Yu, G.; Guo, R.; Zhao, Z.; Yan, W.; Wang, L.; Bian, Z.; Liu, Z. Europium(II) Complexes with Substituted Tris(2-Aminoethyl)Amine/Triethanolamine Ligand and Their Application in Blue Spin-Coated Organic Light-Emitting Diodes. *Adv. Opt. Mater.* **2022**, *10* (22), 2200952. https://doi.org/10.1002/adom.202200952.

(217) Straub, L. C.; Adlung, M.; Wickleder, C.; Wickleder, M. S.; Rasche, B. Impact of 1,10-Phenanthroline-Induced Intermediate Valence on the Luminesence of Divalent Europium Halides. *Inorg. Chem.* **2023**, *62* (1), 497–507. https://doi.org/10.1021/acs.inorgchem.2c03647.

(218) Silantyeva, L. I.; Ilichev, V. A.; Shavyrin, A. S.; Yablonskiy, A. N.; Rumyantcev, R. V.; Fukin, G. K.; Bochkarev, M. N. Unexpected Findings in a Simple Metathesis Reaction of Europium and Ytterbium Diiodides with Perfluorinated Mercaptobenzothiazolates of Alkali Metals. *Organometallics* **2020**, *39* (16), 2972–2983. https://doi.org/10.1021/acs.organomet.0c00334.

(219) Carvalho, A.; Domingos, Â.; Isolani, P. C.; Marques, N.; Pires de Matos, A.; Vicentini, G. Synthesis, Luminescence Studies and Crystal Structures of Two Europium(II) Hydrotris(Pyrazol-1-yl)Borate Complexes: $Eu(HBpz_3)_2{\cdot}2DPSO$ and $Eu(HBpz_3)_2{\cdot}2BPMU$. *Polyhedron* **2000**, *19* (14), 1707–1712. https://doi.org/10.1016/S0277-5387(00)00445-9.

(220) Chowdhury, T.; Evans, M. J.; Coles, M. P.; Bailey, A. G.; Peveler, W. J.; Wilson, C.; Farnaby, J. H. Reduction Chemistry Yields Stable and Soluble Divalent Lanthanide Tris(Pyrazolyl)Borate Complexes. *Chem. Commun.* **2023**. https://doi.org/10.1039/D2CC03189B.

(221) Corbin, B. A.; Hovey, J. L.; Thapa, B.; Schlegel, H. B.; Allen, M. J. Luminescence Differences between Two Complexes of Divalent Europium. *J. Organomet. Chem.* **2018**, *857*, 88–93. https://doi.org/10.1016/j.jorganchem.2017.09.007.

(222) Basal, L. A.; Kajjam, A. B.; Bailey, M. D.; Allen, M. J. Systematic Tuning of the Optical Properties of Discrete Complexes of Eu^{II} in Solution Using Counterions and Solvents. *Inorg. Chem.* **2020**, *59* (14), 9476–9480. https://doi.org/10.1021/acs.inorgchem.0c01516.

(223) Bokouende, S. S.; Ward, C. L.; Allen, M. J. Understanding the Coordination Chemistry and Structural and Photophysical Properties of Eu^{II}- and Sm^{II}-Containing Complexes of Hexamethylhexacyclen and Noncyclic Tetradentate Amines. *Inorg. Chem.* **2024**, *63* (37), 16991–17004. https://doi.org/10.1021/acs.inorgchem.4c02590.

(224) Diaz-Rodriguez, R. M.; Gálico, D. A.; Chartrand, D.; Suturina, E. A.; Murugesu, M. Toward Opto-Structural Correlation to Investigate Luminescence Thermometry in an Organometallic Eu(II) Complex. *J. Am. Chem. Soc.* **2022**, *144* (2), 912–921. https://doi.org/10.1021/jacs.1c11076.

(225) Evans, W. J.; Kozimor, S. A.; Ziller, J. W.; Fagin, A. A.; Bochkarev, M. N. Facile Syntheses of Unsolvated UI_3 and Tetramethylcyclopentadienyl Uranium Halides. *Inorg. Chem.* **2005**, *44* (11), 3993–4000. https://doi.org/10.1021/ic0482685.

(226) Windorff, C. J.; Evans, W. J. ^{29}Si NMR Spectra of Silicon-Containing Uranium Complexes. *Organometallics* **2014**, *33* (14), 3786–3791. https://doi.org/10.1021/om500512q.

(227) Lichtenberg, C.; Elfferding, M.; Finger, L.; Sundermeyer, J. Investigation of Novel and Reinvestigation of Known Cyclopentadienylphosphanes: News on [1,5] Sigmatropic Rearrangements. *J. Organomet. Chem.* **2010**, *695* (17), 2000–2006. https://doi.org/10.1016/j.jorganchem.2010.05.001.

(228) Weismann, D.; Saurenz, D.; Boese, R.; Bläser, D.; Wolmershäuser, G.; Sun, Y.; Sitzmann, H. Cyclopentadiene Alkylation and Nickel Complexes with Tri-, Tetra-, or Pentaisopropylcyclopentadienide or an Even Bulkier Lithium Alkylcyclopentadienide. *Organometallics* **2011**, *30* (23), 6351–6364. https://doi.org/10.1021/om200372j.

(229) Sitzmann, H.; Dezember, T.; Schmitt, O.; Weber, F.; Wolmershäuser, G.; Ruck, M. Reactions of Free Cyclopentadienyl Radicals. 3 Metallocenes of Samarium, Europium, and Ytterbium with the Especially Bulky Cyclopentadienyl Ligands $C_5H(CHMe_2)_4$, $C_5H_2(CMe_3)_3$, and $C_5(CHMe_2)_5$. *Z. Anorg. Allg. Chem.* **2000**, *626* (11), 2241–2244. https://doi.org/10.1002/1521-3749(200011)626:11%3C2241::AID-ZAAC2241%3E3.0.CO;2-0.

(230) Randall McClain, K.; Gould, C. A.; Chakarawet, K.; Teat, S. J.; Groshens, T. J.; Long, J. R.; Harvey, B. G. High-Temperature Magnetic Blocking and Magneto-Structural Correlations in a Series of Dysprosium(III) Metallocenium Single-Molecule Magnets. *Chem. Sci.* **2018**, *9* (45), 8492–8503. https://doi.org/10.1039/c8sc03907k.

(231) Dehmlow, E. V.; Bollmann. Verbesserte präparative Darstellung von Polyisopropyl- und Poly-tert-butylcyclopentadienen. *Z. Naturforschung - Sect. B J. Chem. Sci.* **1993**, *48*, 457–460.

(232) Dezember, T.; Sitzmann, H. Die Fulven-Route Zum Pentaisopropylcyclopentadienid. *Z. Naturforschung - Sect. B J. Chem. Sci.* **1997**, *52* (8), 911–918.

(233) Díaz-Torres, R.; Alvarez, S. Coordinating Ability of Anions and Solvents towards Transition Metals and Lanthanides. *Dalton Trans.* **2011**, *40* (40), 10742. https://doi.org/10.1039/c1dt11000d.

(234) Di Bernardo, P.; Melchior, A.; Tolazzi, M.; Zanonato, P. L. Thermodynamics of Lanthanide(III) Complexation in Non-Aqueous Solvents. *Coord. Chem. Rev.* **2012**, *256* (1–2), 328–351. https://doi.org/10.1016/j.ccr.2011.07.010.
(235) Hansch, Corwin.; Leo, A.; Taft, R. W. A Survey of Hammett Substituent Constants and Resonance and Field Parameters. *Chem. Rev.* **1991**, *91* (2), 165–195. https://doi.org/10.1021/cr00002a004.
(236) Tolman, C. A. Steric Effects of Phosphorus Ligands in Organometallic Chemistry and Homogeneous Catalysis. *Chem. Rev.* **1977**, *77* (3), 313–348. https://doi.org/10.1021/cr60307a002.
(237) Perrin, L.; Clot, E.; Eisenstein, O.; Loch, J.; Crabtree, R. H. Computed Ligand Electronic Parameters from Quantum Chemistry and Their Relation to Tolman Parameters, Lever Parameters, and Hammett Constants. *Inorg. Chem.* **2001**, *40* (23), 5806–5811. https://doi.org/10.1021/ic0105258.
(238) Huynh, H. V. Recent Applications of the Huynh Electronic Parameter (HEP). *Chem. Lett.* **2021**, *50* (10), 1831–1841. https://doi.org/10.1246/cl.210435.
(239) Falivene, L.; Credendino, R.; Poater, A.; Petta, A.; Serra, L.; Oliva, R.; Scarano, V.; Cavallo, L. SambVca 2. A Web Tool for Analyzing Catalytic Pockets with Topographic Steric Maps. *Organometallics* **2016**, *35* (13), 2286–2293. https://doi.org/10.1021/acs.organomet.6b00371.
(240) Falivene, L.; Cao, Z.; Petta, A.; Serra, L.; Poater, A.; Oliva, R.; Scarano, V.; Cavallo, L. Towards the Online Computer-Aided Design of Catalytic Pockets. *Nat. Chem.* **2019**, *11* (10), 872–879. https://doi.org/10.1038/s41557-019-0319-5.
(241) Llunel, M.; Casanova, D.; Cirera, J.; Alemany, P.; Alvarez, S. SHAPE: Program for the Stereochemical Analysis of Molecular Fragments by Means of Continuous Shape Measures and Associated Tools, 2013. http://www.ee.ub.edu/index.php?option=com_content&view=article&id=575:shape-available&catid=80:news&Itemid=466.
(242) Kleemiss, F.; Dolomanov, O. V.; Bodensteiner, M.; Peyerimhoff, N.; Midgley, L.; Bourhis, L. J.; Genoni, A.; Malaspina, L. A.; Jayatilaka, D.; Spencer, J. L.; White, F.; Grundkötter-Stock, B.; Steinhauer, S.; Lentz, D.; Puschmann, H.; Grabowsky, S. Accurate Crystal Structures and Chemical Properties from NoSpherA2. *Chem. Sci.* **2021**, *12* (5), 1675–1692. https://doi.org/10.1039/D0SC05526C.
(243) Kohout, M. A Measure of Electron Localizability. *Int. J. Quantum Chem.* **2004**, *97* (1), 651–658. https://doi.org/10.1002/qua.10768.
(244) Adamo, C.; Barone, V. Toward Reliable Density Functional Methods without Adjustable Parameters: The PBE0 Model. *J. Chem. Phys.* **1999**, *110* (13), 6158–6170. https://doi.org/10.1063/1.478522.
(245) Vetere, V.; Adamo, C.; Maldivi, P. Performance of the 'parameter Free' PBE0 Functional for the Modeling of Molecular Properties of Heavy Metals. *Chem. Phys. Lett.* **2000**, *325* (1), 99–105. https://doi.org/10.1016/S0009-2614(00)00657-6.
(246) Pollak, P.; Weigend, F. Segmented Contracted Error-Consistent Basis Sets of Double- and Triple-ζ Valence Quality for One- and Two-Component Relativistic All-Electron Calculations. *J. Chem. Theory Comput.* **2017**, *13* (8), 3696–3705. https://doi.org/10.1021/acs.jctc.7b00593.
(247) Winter, M. *The Orbitron: a gallery of atomic orbitals on the WWW*. https://winter.group.shef.ac.uk/orbitron/ (accessed 2024-09-03).
(248) Pons, M.; Herberich, G. E.; Kirk, P. N.; Castellani, M. P.; Rizzo, M. J.; Atwood, J. D. Bromotricarbonyldi(Pyridine)Manganese(I). In *Inorganic Syntheses: Volume 36*; John Wiley & Sons, Ltd, 2014; pp 148–149. https://doi.org/10.1002/9781118744994.ch28.

(249) Kirk, P. N.; Castellani, M. P.; Rizzo, M.; Atwood, J. D. (η^5-Cyclopentadienyl)Tricarbonylmanganese(I) Complexes. In *Inorganic Syntheses: Volume 36*; John Wiley & Sons, Ltd, 2014; pp 62–64. https://doi.org/10.1002/9781118744994.ch13.

(250) Evans, P.; Reta, D.; Goodwin, C. A. P.; Ortu, F.; Chilton, N. F.; Mills, D. P. A Double-Dysprosocenium Single-Molecule Magnet Bound Together with Neutral Ligands. *Chem. Commun.* **2020**, *56* (42), 5677–5680. https://doi.org/10.1039/c9cc08945d.

(251) Bochkarev, M. N.; Fagin, A. A.; Khoroshenkov, G. V. Specific Chemical Behavior of Nd^{II} and Dy^{II} Iodides in Reactions with Aromatic Compounds. *Russ. Chem. Bull.* **2002**, *51* (10), 1909–1914. https://doi.org/10.1023/A:1021364804963.

(252) Liu, J.; Reta, D.; Cleghorn, J. A.; Yeoh, Y. X.; Ortu, F.; Goodwin, C. A. P.; Chilton, N. F.; Mills, D. P. Light Lanthanide Metallocenium Cations Exhibiting Weak Equatorial Anion Interactions. *Chem. - Eur. J.* **2019**, *25* (32), 7749–7758. https://doi.org/10.1002/chem.201901167.

(253) Evans, P.; Reta, D.; Whitehead, G. F. S.; Chilton, N. F.; Mills, D. P. Bis-Monophospholyl Dysprosium Cation Showing Magnetic Hysteresis at 48 K. *J. Am. Chem. Soc.* **2020**, *141* (50), 19935–19940. https://doi.org/10.1021/jacs.9b11515.

(254) Rachor, S. G.; Cleaves, P. A.; Robertson, S. D.; Mansell, S. M. NMR Spectroscopic Study of the Adduct Formation and Reactivity of Homoleptic Rare Earth Amides with Alkali Metal Benzyl Compounds, and the Crystal Structures of $[Li(TMEDA)_2][Nd\{N(SiMe_3)_2\}_3(CH_2Ph)]$ and $[\{Li(TMP)\}_2\{Li(Ph)\}]_2$. *J. Organomet. Chem.* **2018**, *857*, 101–109. https://doi.org/10.1016/j.jorganchem.2017.10.022.

(255) Liu, J.; Nodaraki, L. E.; Cobb, P. J.; Giansiracusa, M. J.; Ortu, F.; Tuna, F.; Mills, D. P. Synthesis and Characterisation of Light Lanthanide Bis-Phospholyl Borohydride Complexes. *Dalton Trans.* **2020**, *49* (19), 6504–6511. https://doi.org/10.1039/D0DT01241F.

(256) Kuveke, R. E. H.; Barwise, L.; van Ingen, Y.; Vashisth, K.; Roberts, N.; Chitnis, S. S.; Dutton, J. L.; Martin, C. D.; Melen, R. L. An International Study Evaluating Elemental Analysis. *ACS Cent. Sci.* **2022**, *8* (7), 855–863. https://doi.org/10.1021/acscentsci.2c00325.

(257) Piotto, M.; Bourdonneau, M.; Elbayed, K.; Wieruszeski, J. M.; Lippens, G. New DEFT Sequences for the Acquisition of One-Dimensional Carbon NMR Spectra of Small Unlabelled Molecules. *Magn. Reson. Chem.* **2006**, *44* (10), 943–947. https://doi.org/10.1002/mrc.1884.

(258) Neese, F. The ORCA Program System. *WIREs Comput. Mol. Sci.* **2012**, *2* (1), 73–78. https://doi.org/10.1002/wcms.81.

(259) Neese, F.; Wennmohs, F.; Becker, U.; Riplinger, C. The ORCA Quantum Chemistry Program Package. *J. Chem. Phys.* **2020**, *152* (22), 224108. https://doi.org/10.1063/5.0004608.

(260) Neese, F. Software Update: The ORCA Program System—Version 5.0. *WIREs Comput. Mol. Sci.* **2022**, *12* (5), e1606. https://doi.org/10.1002/wcms.1606.

(261) Björgvinsson, M.; Halldorsson, S.; Arnason, I.; Magull, J.; Fenske, D. Preparation and Characterization of $(C_5Me_4Ph)TiCl_3$, the Oxochloride Complexes $[(C_5Me_4Ph)TiCl_2]_2(\mu\text{-}O)$ and $[(C_5Me_4Ph)TiCl(\mu\text{-}O)]_3$ and the Oxo-Complex$[(C_5Me_4Ph)Ti]_4(\mu\text{-}O)_6$. The X-Ray Crystal Structures of $[(C_5Me_4Ph)TiCl_2]_2(\mu\text{-}O)$ and $[(C_5Me_4Ph)Ti]_4(\mu\text{-}O)_6$. *J. Organomet. Chem.* **1997**, *544* (2), 207–215. https://doi.org/10.1016/s0022-328x(97)00327-6.

(262) Schuyt, J. J.; Chong, S. V.; Williams, G. V. M. Luminescence of Isoelectronic Lanthanide Pairs (Ln^{2+}/Ln^{3+}): A Relative Compression Factor for Isoelectronic Ln $4f^n$ Levels. *J. Lumin.* **2023**, *264*, 120171. https://doi.org/10.1016/j.jlumin.2023.120171.

(263) De Jong, M.; Meijerink, A.; Seijo, L.; Barandiarán, Z. Energy Level Structure and Multiple $4f^{12}5d^{1}$ Emission Bands for Tm^{2+} in Halide Perovskites: Theory and Experiment. *J. Phys. Chem. C* **2017**, *121* (18), 10095–10101. https://doi.org/10.1021/acs.jpcc.7b01902.
(264) McClain, K. R.; Gould, C. A.; Marchiori, D. A.; Kwon, H.; Nguyen, T. T.; Rosenkoetter, K. E.; Kuzmina, D.; Tuna, F.; Britt, R. D.; Long, J. R.; Harvey, B. G. Divalent Lanthanide Metallocene Complexes with a Linear Coordination Geometry and Pronounced 6s–5d Orbital Mixing. *J. Am. Chem. Soc.* **2022**, *144* (48), 22193–22201. https://doi.org/10.1021/jacs.2c09880.
(265) Gould, C. A.; McClain, K. R.; Yu, J. M.; Groshens, T. J.; Furche, F.; Harvey, B. G.; Long, J. R. Synthesis and Magnetism of Neutral, Linear Metallocene Complexes of Terbium(II) and Dysprosium(II). *J. Am. Chem. Soc.* **2019**, *141* (33), 12967–12973. https://doi.org/10.1021/jacs.9b05816.
(266) Liu, M.; Chen, Y.-C.; Wang, H.; Shang, T.; Tong, M.-L.; Layfield, R. A.; Mansikkamäki, A.; Guo, F.-S. A Linear Dysprosium(II) Metallocene with a High Effective Energy Barrier and Magnetic Hysteresis up to 70 Kelvin. *J. Am. Chem. Soc.* **2025**, *147* (21), 18307–18316. https://doi.org/10.1021/jacs.5c06222.
(267) Jin, P.-B.; Luo, Q.-C.; Gransbury, G. K.; Vitorica-Yrezabal, I. J.; Hajdu, T.; Strashnov, I.; McInnes, E. J. L.; Winpenny, R. E. P.; Chilton, N. F.; Mills, D. P.; Zheng, Y.-Z. Thermally Stable Terbium(II) and Dysprosium(II) Bis-Amidinate Complexes. *J. Am. Chem. Soc.* **2023**, *145* (51), 27993–28009. https://doi.org/10.1021/jacs.3c07978.
(268) Hu, Z.; Ullah, A.; Prima-Garcia, H.; Chin, S.-H.; Wang, Y.; Aragó, J.; Shi, Z.; Gaita-Ariño, A.; Coronado, E. Binding Sites, Vibrations and Spin-Lattice Relaxation Times in Europium(II)-Based Metallofullerene Spin Qubits. *Chem. – Eur. J.* **2021**, *27* (52), 13242–13248. https://doi.org/10.1002/chem.202101922.
(269) Schäfer, S.; Kaufmann, S.; S. Rösch, E.; W. Roesky, P. Divalent Metallocenes of the Lanthanides – a Guideline to Properties and Reactivity. *Chem. Soc. Rev.* **2023**, *52* (12), 4006–4045. https://doi.org/10.1039/D2CS00744D.
(270) Diaz-Rodriguez, R. M.; Gálico, D. A.; Chartrand, D.; Murugesu, M. Ligand Effects on the Emission Characteristics of Molecular Eu(II) Luminescence Thermometers. *J. Am. Chem. Soc.* **2024**. https://doi.org/10.1021/jacs.4c13805.
(271) Jenks, T. C.; Allen, M. J. Divalent Lanthanide Luminescence in Solution. In *Modern Applications of Lanthanide Luminescence*; de Bettencourt-Dias, A., Ed.; Springer Series on Fluorescence; Springer International Publishing: Cham, 2023; pp 67–92. https://doi.org/10.1007/4243_2020_19.
(272) Ilichev, V. A.; Rogozhin, A. F.; Balashova, T. V.; Polyakova, S. K.; Efimov, N. N.; Vasilev, P. N.; Ugolkova, E. A.; Bernhardt, E.; Rumyantcev, R. V.; Fukin, G. K.; Bochkarev, M. N. Tetracyanidoborates of Divalent Eu and Yb 3D Metal–Organic Frameworks with Cubic Structure. Thermochromic Luminescence and Slow Relaxation of Magnetization of $Eu[B(CN)_4]_2$. *Chem. Mater.* **2025**. https://doi.org/10.1021/acs.chemmater.4c03507.
(273) Brites, C. D. S.; Marin, R.; Suta, M.; Carneiro Neto, A. N.; Ximendes, E.; Jaque, D.; Carlos, L. D. Spotlight on Luminescence Thermometry: Basics, Challenges, and Cutting-Edge Applications. *Adv. Mater.* **2023**, *35* (36), 2302749. https://doi.org/10.1002/adma.202302749.
(274) Batchev, A. L.; Rashid, M. M.; Allen, M. J. Chapter 328 - Divalent Europium-Based Contrast Agents for Magnetic Resonance Imaging. In *Handbook on the Physics and Chemistry of Rare Earths*; Bünzli, J.-C. G., Kauzlarich, S. M., Eds.; Including Actinides; Elsevier, 2023; Vol. 63, pp 55–98. https://doi.org/10.1016/bs.hpcre.2023.03.001.

(275) Funk, A. M.; Clavijo Jordan, V.; Sherry, A. D.; Ratnakar, S. J.; Kovacs, Z. Oxidative Conversion of a Europium(II)-Based T_1 Agent into a Europium(III)-Based paraCEST Agent That Can Be Detected In Vivo by Magnetic Resonance Imaging. *Angew. Chem. Int. Ed.* **2016**, *55* (16), 5024–5027. https://doi.org/10.1002/anie.201511649.

(276) Han, G.; Deng, Y.; Sun, J.; Ling, J.; Shen, Z. Research into Europium Complexes as Magnetic Resonance Imaging Contrast Agents (Review). *Exp. Ther. Med.* **2015**, *9* (5), 1561–1566. https://doi.org/10.3892/etm.2015.2297.

(277) Errulat, D.; Harriman, K. L. M.; Gálico, D. A.; Salerno, E. V.; van Tol, J.; Mansikkamäki, A.; Rouzières, M.; Hill, S.; Clérac, R.; Murugesu, M. Slow Magnetic Relaxation in a Europium(II) Complex. *Nat. Commun.* **2024**, *15* (1), 3010. https://doi.org/10.1038/s41467-024-46196-w.

(278) Lin, G.; McDonald, R.; Takats, J. Synthesis and Structure of [Sm(η^5-$CpPPh_2$)(κ^3-$TpMe_2$)(I)(THF)]; a Samarium Complex with Four Different Ligands. *J. Organomet. Chem.* **2001**, *626* (1), 76–81. https://doi.org/10.1016/S0022-328X(01)00660-X.

(279) Daniels, D. P.; Guo, Z.; Shephard, A. C. G.; Deacon, G. B.; Jaroschik, F.; Junk, P. C. Synthesis and Characterisation of Divalent Di(1,3-Bis(Diphenylphosphano)Cyclopentadienyl)Lanthanoid and Alkaline Earth Complexes as Potential Platforms for Heterometallic Complexes. *Z. Für Anorg. Allg. Chem.* **2022**, *648* (23), e202200251. https://doi.org/10.1002/zaac.202200251.

(280) Wang, H.; Wang, H.; Li, H.-W.; Xie, Z. Synthesis, Structural Characterization, and Reactivity of Rare-Earth Complexes Derived from A New Phosphorus-Bridged Versatile Ligand, $^{i}Pr_2NP(C_9H_7)(C_2B_{10}H_{11})$. *Organometallics* **2004**, *23* (4), 875–885. https://doi.org/10.1021/om034268l.

(281) Büschel, S.; Daniliuc, C.; Jones, P. G.; Tamm, M. Ambiphilic Reactivity of a Phosphane-Functionalized Cycloheptatrienyl–Cyclopentadienyl Zirconium Sandwich Complex. *Organometallics* **2010**, *29* (3), 671–675. https://doi.org/10.1021/om9009763.

(282) Schumann, H.; Meese-Marktscheffel, J. A.; Gorella, B.; Görlitz, F. H. Metallorganische Verbindungen Der Lanthanoide: LXXI. Synthese Und Röntgenstrukturanalyse von $CpLa(C_5H_4PPh_2)_2(THF)$, Einem Zweizähnigen Liganden Zur Herstellung Heterobimetallischer Lanthanoidkomplexe. *J. Organomet. Chem.* **1992**, *428* (3), C27–C32. https://doi.org/10.1016/0022-328X(92)83105-Q.

(283) Lin, G.; Wong, W.-T. Preparation and Structural Characterization of a Functionalized Trigonal Organoerbium Cluster with Two Bridging Hydroxyl Groups and a μ^3-Oxo Group. *Polyhedron* **1995**, *14* (20), 3167–3169. https://doi.org/10.1016/0277-5387(95)00148-L.

(284) Deacon, G. B.; Fallon, G. D.; Gatehouse, B. M.; Rabinovich, A.; Skelton, B. W.; White, A. H. Organolanthanoids XIX. The X-Ray Crystal Structures of Di [μ-(Acetato-O,O:O′)Bis(Diphenylphosphino-η^5-Cyclopentadienyl)Ytterbium(III)] and Di[μ-(Acetato-O,O:O′)Bis(η^5-Cyclopentadienyl)Ytterbium(III)] — Unexpected Examples of Formal Nine Coordination in Lanthanoid Organometallics. *J. Organomet. Chem.* **1995**, *501* (1), 23–30. https://doi.org/10.1016/0022-328X(95)05592-D.

(285) Müller-Buschbaum, K.; Deacon, G. B.; Forsyth, C. M. $[Yb(THF)_3(C_5H_4PPh_2)_2W(CO)_4]\cdot 0.5THF$ and $^{1}_{\infty}[Yb(THF)(C_5H_4PPh_2)_2(\mu\text{-}OC)W(CO)_3]$: Two New Heterobimetallic Complexes Containing Yb^{II} and W^0. *Eur. J. Inorg. Chem.* **2002**, *2002* (12), 3172–3177. https://doi.org/10.1002/1099-0682(200212)2002:12%3C3172::AID-EJIC3172%3E3.0.CO;2-Q.

(286) Steiner, M. R.; Hlina, J. A.; Uher, J. M.; Fischer, R. C.; Neshchadin, D.; Wilfling, T. Phosphinoindenyl and Phosphazidoindenyl Complexes of Lanthanum and Samarium: Synthesis, Characterisation, and

Hydroamination Catalysis. *Dalton Trans.* **2022**, *51* (5), 1819–1828. https://doi.org/10.1039/D1DT03219D.
(287) Müller, C.; Warken, J.; Huch, V.; Morgenstern, B.; Bischoff, I. A.; Zimmer, M.; Schäfer, A. Diphosphanylmetallocenes of Main-Group Elements. *Chem. - Eur. J.* **2021**, 1–12. https://doi.org/10.1002/chem.202005198.
(288) Siddiqui, M. M.; Radhakrishna, L.; Mague, J. T.; Balakrishna, M. S. 1,1′-Bis(Dipyrrolylphosphino)Ferrocene: Synthesis, Coordination Chemistry and Structural Studies. *J. Organomet. Chem.* **2016**, *824*, 15–24. https://doi.org/10.1016/j.jorganchem.2016.09.027.
(289) Bandoli, G.; Dolmella, A. Ligating Ability of 1,1′-Bis(Diphenylphosphino)Ferrocene: A Structural Survey (1994–1998). *Coord. Chem. Rev.* **2000**, *209* (1), 161–196. https://doi.org/10.1016/S0010-8545(00)00229-0.
(290) Gómez Arrayás, R.; Adrio, J.; Carretero, J. C. Recent Applications of Chiral Ferrocene Ligands in Asymmetric Catalysis. *Angew. Chem. Int. Ed.* **2006**, *45* (46), 7674–7715. https://doi.org/10.1002/anie.200602482.
(291) Colacot, T. J. A Concise Update on the Applications of Chiral Ferrocenyl Phosphines in Homogeneous Catalysis Leading to Organic Synthesis. *Chem. Rev.* **2003**, *103* (8), 3101–3118. https://doi.org/10.1021/cr000427o.
(292) Barbaro, P.; Bianchini, C.; Giambastiani, G.; Parisel, S. L. Progress in Stereoselective Catalysis by Metal Complexes with Chiral Ferrocenyl Phosphines. *Coord. Chem. Rev.* **2004**, *248* (21), 2131–2150. https://doi.org/10.1016/j.ccr.2004.03.022.
(293) Seibert, A. R.; Dougherty, W. G.; Kassel, W. S.; Nataro, C. Bis(Dialkylaminophosphino)Ferrocenes: Reactivity and Electrochemistry. *Inorganica Chim. Acta* **2010**, *364* (1), 30–38. https://doi.org/10.1016/j.ica.2010.06.061.
(294) Spichal, Z.; Hegrova, B.; Moravec, Z.; Pinkas, J.; Necas, M. Synthesis and Structure of Lanthanide Complexes with Large-Bite Diphosphine Dioxide Ligands. *Polyhedron* **2011**, *30* (9), 1620–1627. https://doi.org/10.1016/j.poly.2011.03.027.
(295) Sonawane, S. C.; Kunchur, H. S.; Pandey, S. P.; Balakrishna, M. S. Synthesis, Reactivity and Transition Metal Complexes of 1,1′-Bis(Diethynylphosphino)Ferrocene. *J. Coord. Chem.* **2022**, *74* (17–20), 2959–2971. https://doi.org/10.1080/00958972.2021.2004310.
(296) Horký, F.; Císařová, I.; Schulz, J.; Štěpnička, P. Synthesis and Structural Characterisation of 1'-(Diphenylphosphino)Ferrocene-1-Phosphonic Acid, Its Ammonium Salts and Pd(II) Complexes. *J. Organomet. Chem.* **2019**, *891*, 44–53. https://doi.org/10.1016/j.jorganchem.2019.04.012.
(297) Sameer Prasad, P.; Pandey, M. K.; Balakrishna, M. S. Synthesis and Transition Metal Complexes of 1,1′-Bis(Diphenylethynylphosphino)Ferrocene. *Polyhedron* **2019**, *158*, 173–182. https://doi.org/10.1016/j.poly.2018.10.063.
(298) Rufanov, K. A.; Petrov, A. R.; Kotov, V. V.; Laquai, F.; Sundermeyer, J. A Lutetium Cyclopentadienyl-Phosphazene Constrained Geometry Complex (CGC): First Isolobal Analogues of Group 4 Cyclopentadienyl-Silylamido CGC Systems. *Eur. J. Inorg. Chem.* **2005**, *2005* (19), 3805–3807. https://doi.org/10.1002/ejic.200500529.
(299) Hangaly, N. K.; Petrov, A. R.; Elfferding, M.; Harms, K.; Sundermeyer, J. Tetrahydropentalenyl-Phosphazene Constrained Geometry Complexes of Rare-Earth Metal Alkyls. *Dalton Trans.* **2014**, *43* (19), 7109–7120. https://doi.org/10.1039/C3DT53596G.
(300) Braunschweig, H.; Breitling, F. M. Constrained Geometry Complexes—Synthesis and Applications. *Coord. Chem. Rev.* **2006**, *250* (21), 2691–2720. https://doi.org/10.1016/j.ccr.2005.10.022.

(301) Cano, J.; Kunz, K. How to Synthesize a Constrained Geometry Catalyst (CGC) – A Survey. *J. Organomet. Chem.* **2007**, *692* (21), 4411–4423. https://doi.org/10.1016/j.jorganchem.2007.05.015.
(302) Hangaly, N. K.; Petrov, A. R.; Rufanov, K. A.; Harms, K.; Elfferding, M.; Sundermeyer, J. Cyclopentadienylphosphazene (CpPN) Complexes of Rare-Earth Metals: Synthesis, Structural Characterization, and Hydroamination Catalysis. *Organometallics* **2011**, *30* (17), 4544–4554. https://doi.org/10.1021/om200264n.
(303) Jian, Z.; Petrov, A. R.; Hangaly, N. K.; Li, S.; Rong, W.; Mou, Z.; Rufanov, K. A.; Harms, K.; Sundermeyer, J.; Cui, D. Phosphazene-Functionalized Cyclopentadienyl and Its Derivatives Ligated Rare-Earth Metal Alkyl Complexes: Synthesis, Structures, and Catalysis on Ethylene Polymerization. *Organometallics* **2012**, *31* (11), 4267–4282. https://doi.org/10.1021/om300263p.
(304) Jian, Z.; Rong, W.; Mou, Z.; Pan, Y.; Xie, H.; Cui, D. Intramolecular C–H Bond Activation Induced by a Scandium Terminal Imido Complex. *Chem. Commun.* **2012**, *48* (60), 7516–7518. https://doi.org/10.1039/C2CC33179A.
(305) Davies, R.; Patel, L. Chalcogen–Phosphorus (and Heavier Congener) Compounds. **2013**. https://doi.org/10.1039/9781849737456-00238.
(306) Mauger, A.; Godart, C. The Magnetic, Optical, and Transport Properties of Representatives of a Class of Magnetic Semiconductors: The Europium Chalcogenides. *Phys. Rep.* **1986**, *141* (2), 51–176. https://doi.org/10.1016/0370-1573(86)90139-0.
(307) Wachter, P. Chapter 19 Europium Chalcogenides: EuO, EuS, EuSe and EuTe. In *Handbook on the Physics and Chemistry of Rare Earths*; Alloys and Intermetallics; Elsevier, 1979; Vol. 2, pp 507–574. https://doi.org/10.1016/S0168-1273(79)02010-9.
(308) Zhou, X.; Zhang, K. H.; Xiong, J.; Park, J.-H.; Dickerson, J. H.; He, W. Size- and Dimensionality-Dependent Optical, Magnetic and Magneto-Optical Properties of Binary Europium-Based Nanocrystals: EuX (X = O, S, Se, Te). *Nanotechnology* **2016**, *27* (19), 192001. https://doi.org/10.1088/0957-4484/27/19/192001.
(309) Capps, K. B.; Wixmerten, B.; Bauer, A.; Hoff, C. D. Thermochemistry of Sulfur Atom Transfer. Enthalpies of Reaction of Phosphines with Sulfur, Selenium, and Tellurium, and of Desulfurization of Triphenylarsenic Sulfide, Triphenylantimony Sulfide, and Benzyl Trisulfide. *Inorg. Chem.* **1998**, *37* (12), 2861–2864. https://doi.org/10.1021/ic9715862.
(310) Jeremias, L.; Babiak, M.; Kubát, V.; Calhorda, M. J.; Trávníček, Z.; Novosad, J. Successful Oxidation of $Ph_2P(CH_2)_nPPh_2$ (n = 2, 4, 6) by Tellurium Leading to $Ph_2P(Te)(CH_2)_nP(Te)Ph_2$. *RSC Adv.* **2014**, *4* (30), 15428–15430. https://doi.org/10.1039/C4RA00157E.
(311) Jones, C. H. W.; Sharma, R. D. Tellurium-125 NMR and Moessbauer Spectroscopy of Tellurium-Phosphine Complexes and the Tellurocyanates. *Organometallics* **1987**, *6* (7), 1419–1423. https://doi.org/10.1021/om00150a009.
(312) Sun, H.; Wang, F.; Buhro, W. E. Tellurium Precursor for Nanocrystal Synthesis: Tris(Dimethylamino)Phosphine Telluride. *ACS Nano* **2018**, *12* (12), 12393–12400. https://doi.org/10.1021/acsnano.8b06468.
(313) Nordheider, A.; Woollins, J. D.; Chivers, T. Organophosphorus–Tellurium Chemistry: From Fundamentals to Applications. *Chem. Rev.* **2015**, *115* (18), 10378–10406. https://doi.org/10.1021/acs.chemrev.5b00279.
(314) Buß, F.; Röthel, M. B.; Werra, J. A.; Rotering, P.; Wilm, L. F. B.; Daniliuc, C. G.; Löwe, P.; Dielmann, F. Tris(Tetramethylguanidinyl)Phosphine: The Simplest Non-Ionic Phosphorus Superbase and

Strongly Donating Phosphine Ligand. *Chem. – Eur. J.* **2022**, *28* (3), e202104021. https://doi.org/10.1002/chem.202104021.

(315) Gopalakrishnan, J. Aminophosphines: Their Chemistry and Role as Ligands and Synthons. *Appl. Organomet. Chem.* **2009**, *23* (8), 291–318. https://doi.org/10.1002/aoc.1515.

(316) Schröder, F. G.; Lichtenberg, C.; Elfferding, M.; Sundermeyer, J. Deprotonated P-Ylides As Templates for Novel Cyclopentadienyl Phosphonioalkyl, -Alkylidene, and -Alkylidyne (CpPC) Constrained-Geometry Complexes. *Organometallics* **2013**, *32* (18), 5082–5091. https://doi.org/10.1021/om4005548.

(317) Pushkarev, A. P.; Yablonskiy, A. N.; Yunin, P. A.; Burin, M. E.; Andreev, B. A.; Bochkarev, M. N. Features of Spectral Properties of Sm^{3+} Complexes with Dithia- and Diselenophosphinate Ligands. *Spectrochim. Acta. A. Mol. Biomol. Spectrosc.* **2016**, *163*, 134–139. https://doi.org/10.1016/j.saa.2016.03.026.

(318) Petrov, A. R.; Rufanov, K. A.; Ziemer, B.; Neubauer, P.; Kotov, V. V.; Sundermeyer, J. P-Amino-Cyclopentadienylidene-Phosphoranes versus P-Cyclopentadienyl-Iminophosphoranes—Tautomeric Protic Forms of a New Bidentate CpPN ligand System. *Dalton Trans* **2008**, *2* (7), 909–915. https://doi.org/10.1039/B710419G.

(319) Kühl, O. The Range of Chemical Shifts, Coupling Constants, and What Influences Each. In *Phosphorus-31 NMR Spectroscopy*; Springer, Berlin, Heidelberg, 2008; pp 7–23. https://doi.org/10.1007/978-3-540-79118-8_2.

(320) Reich, H. *NMR Spectroscopy :: 31P NMR Chemical Shifts*. Organic Chemistry Data. https://organicchemistrydata.org/hansreich/resources/nmr/?index=nmr_index%2F31P_shift (accessed 2025-07-05).

(321) McFarlane, W.; Rycroft, D. S. Studies of Organophosphorus Selenides by Heteronuclear Magnetic Triple Resonance. *J. Chem. Soc. Dalton Trans.* **1973**, No. 20, 2162–2166. https://doi.org/10.1039/DT9730002162.

(322) Evans, W. J.; Hughes, L. A.; Hanusa, T. P. Synthesis and X-Ray Crystal Structure of Bis(Pentamethylcyclopentadienyl) Complexes of Samarium and Europium: $(C_5Me_5)_2Sm$ and $(C_5Me_5)_2Eu$. *Organometallics* **1986**, *5* (7), 1285–1291. https://doi.org/10.1021/om00138a001.

(323) Niemeyer, M. σ-Donor versus η^6-π-Arene Interactions in Monomeric Europium(II) and Ytterbium(II) Thiolates – An Experimental and Computational Study. *Eur. J. Inorg. Chem.* **2001**, *2001* (8), 1969–1981. https://doi.org/10.1002/1099-0682(200108)2001:8%3C1969::AID-EJIC1969%3E3.0.CO;2-0.

(324) Visseaux, M.; Dormond, A.; Kubicki, M. M.; Moïse, C.; Baudry, D.; Ephritikhine, M. Metalloligands Containing Samarium(III). Access to Binuclear f-Metal (Samarium)-d-Metal (Rhodium) Complexes. *J. Organomet. Chem.* **1992**, *433* (1), 95–106. https://doi.org/10.1016/0022-328X(92)80132-H.

(325) Petrov, A. R.; Rufanov, K. A.; Hangaly, N. K.; Elfferding, M.; Harms, K.; Sundermeyer, J. Air-Stable Helical Bis(Cyclopentadienylphosphazene) Complexes of Divalent Ytterbium. *Mendeleev Commun.* **2010**, *20* (4), 197–199. https://doi.org/10.1016/j.mencom.2010.06.004.

(326) Dietz, C.; Jouikov, V.; Jurkschat, K. Diastereoselective Ortho-Metalation of a Chiral Ferrocenylphosphonic Diamide and Its Organotin Derivatives. *Organometallics* **2013**, *32* (20), 5906–5917. https://doi.org/10.1021/om4004797.

(327) Evans, W. J.; Brady, J. C.; Fujimoto, C. H.; Giarikos, D. G.; Ziller, J. W. The Bent Metallocene Geometries of Potassium Polyalkyl Cyclopentadienyl THF Solvates: Monosolvated [(THF)K(μ-

$C_5Me_5)]_n$, Disolvated $[(THF)_2K(\mu\text{-}C_5Me_5)]_n$ and the Tethered Olefin Complex $[(THF)K(\mu\text{-}C_5Me_4SiMe_2CH_2CH{=}CH2)]_n$. *J. Organomet. Chem.* **2002**, *649* (2), 252–257. https://doi.org/10.1016/S0022-328X(02)01138-5.

(328) Yanai, T.; Tew, D. P.; Handy, N. C. A New Hybrid Exchange–Correlation Functional Using the Coulomb-Attenuating Method (CAM-B3LYP). *Chem. Phys. Lett.* **2004**, *393* (1), 51–57. https://doi.org/10.1016/j.cplett.2004.06.011.

(329) Weigend, F.; Ahlrichs, R. Balanced Basis Sets of Split Valence, Triple Zeta Valence and Quadruple Zeta Valence Quality for H to Rn: Design and Assessment of Accuracy. *Phys. Chem. Chem. Phys.* **2005**, *7* (18), 3297–3305. https://doi.org/10.1039/B508541A.

(330) Rappoport, D.; Furche, F. Property-Optimized Gaussian Basis Sets for Molecular Response Calculations. *J. Chem. Phys.* **2010**, *133* (13), 134105. https://doi.org/10.1063/1.3484283.

(331) Palafox, M. A. DFT Computations on Vibrational Spectra: Scaling Procedures to Improve the Wavenumbers. *Phys. Sci. Rev.* **2018**, *3* (6). https://doi.org/10.1515/psr-2017-0184.

(332) Evans, W. J.; Perotti, J. M.; Brady, J. C.; Ziller, J. W. Tethered Olefin Studies of Alkene versus Tetraphenylborate Coordination and Lanthanide Olefin Interactions in Metallocenes. *J. Am. Chem. Soc.* **2003**, *125* (17), 5204–5212. https://doi.org/10.1021/ja020957x.

(333) Burin, M. E.; Pushkarev, A. P.; Fukin, G. K.; Rumyantsev, R. V.; Konev, A. N.; Bochkarev, M. N. Synthesis of EuS and EuSe Particles via Thermal Decomposition of Dithio- and Diselenophosphinate Europium Complexes. *Nanotechnologies Russ.* **2017**, *12* (1), 66–72. https://doi.org/10.1134/S1995078017010025.

(334) Leung, W.-P.; Chan, Y.-C.; Mak, T. C. W. Synthesis and Structural Characterization of Thiophosphinoyl Late-Transition-Metal and Divalent Lanthanide Complexes Derived from 2-Quinolyl-Linked (Thiophosphorano)Methane. *Eur. J. Inorg. Chem.* **2013**, *2013* (36), 6103–6110. https://doi.org/10.1002/ejic.201300797.

(335) Ćirić, A.; Dramićanin, M. D. LumTHools - Software for Fitting the Temperature Dependence of Luminescence Emission Intensity, Lifetime, Bandshift, and Bandwidth and Luminescence Thermometry and Review of the Theoretical Models. *J. Lumin.* **2022**, *252*, 119413. https://doi.org/10.1016/j.jlumin.2022.119413.

(336) Gálico, D. A.; Murugesu, M. Toward Magneto-Optical Cryogenic Thermometers with High Sensitivity: A Magnetic Circular Dichroism Based Thermometric Approach. *Angew. Chem. Int. Ed.* **2023**, *62* (40), e202309152. https://doi.org/10.1002/anie.202309152.

(337) Mason, W. R. *A Practical Guide to Magnetic Circular Dichroism Spectroscopy*; John Wiley & Sons, Ltd, 2006. https://doi.org/10.1002/9780470139233.

(338) Wolford, N. J.; Radovic, A.; Neidig, M. L. C-Term Magnetic Circular Dichroism (MCD) Spectroscopy in Paramagnetic Transition Metal and f-Element Organometallic Chemistry. *Dalton Trans.* **2021**, *50* (2), 416–428. https://doi.org/10.1039/D0DT03730C.

(339) Carpenter, S. H.; Mengell, J.; Chen, J.; Jones, M. R.; Kirk, M. L.; Tondreau, A. M. Determining the Effects of Zero-Field Splitting and Magnetic Exchange in Dimeric Europium(II) Complexes. *Inorg. Chem.* **2024**, *63* (19), 8516–8520. https://doi.org/10.1021/acs.inorgchem.4c00694.

(340) Sandblom, N.; Ziegler, T.; Chivers, T. A Density Functional Study of the Bonding in Tertiary Phosphine Chalcogenides and Related Molecules. *Can. J. Chem.* **1996**, *74* (11), 2363–2371. https://doi.org/10.1139/v96-263.

(341) Errulat, D.; Harriman, K. L. M.; Gálico, D. A.; Kitos, A. A.; Mansikkamäki, A.; Murugesu, M. A Trivalent 4f Complex with Two Bis-Silylamide Ligands Displaying Slow Magnetic Relaxation. *Nat. Chem.* **2023**, *15* (8), 1100–1107. https://doi.org/10.1038/s41557-023-01208-y.

(342) Hayashi, T.; Yamamoto, A.; Hojo, M.; Ito, Y. A New Chiral Ferrocenylphosphine Ligand with C_2 Symmetry: Prepration and Use for Palladium-Catalysed Asymmetric Cross-Coupling. *J. Chem. Soc. Chem. Commun.* **1989**, No. 8, 495–496. https://doi.org/10.1039/C39890000495.

(343) Maturi, F. E.; Brites, C. D. S.; Ximendes, E. C.; Mills, C.; Olsen, B.; Jaque, D.; Ribeiro, S. J. L.; Carlos, L. D. Going Above and Beyond: A Tenfold Gain in the Performance of Luminescence Thermometers Joining Multiparametric Sensing and Multiple Regression. *Laser Photonics Rev.* **2021**, *15* (11), 2100301. https://doi.org/10.1002/lpor.202100301.

(344) Landi, S.; Segundo, I. R.; Freitas, E.; Vasilevskiy, M.; Carneiro, J.; Tavares, C. J. Use and Misuse of the Kubelka-Munk Function to Obtain the Band Gap Energy from Diffuse Reflectance Measurements. *Solid State Commun.* **2022**, *341*, 114573. https://doi.org/10.1016/j.ssc.2021.114573.

(345) Myrick, M.; English, C.; Kitzhaber, Z. A Brief Look at Optical Diffuse Reflection (ODR) Spectroscopy. *Spectroscopy* **2023**, *38*, 31–36. https://doi.org/10.56530/spectroscopy.mj8589f4.

(346) Feller, D. The Role of Databases in Support of Computational Chemistry Calculations. *J. Comput. Chem.* **1996**, *17* (13), 1571–1586. https://doi.org/10.1002/(SICI)1096-987X(199610)17:13%3C1571::AID-JCC9%3E3.0.CO;2-P.

(347) Schuchardt, K. L.; Didier, B. T.; Elsethagen, T.; Sun, L.; Gurumoorthi, V.; Chase, J.; Li, J.; Windus, T. L. Basis Set Exchange: A Community Database for Computational Sciences. *J. Chem. Inf. Model.* **2007**, *47* (3), 1045–1052. https://doi.org/10.1021/ci600510j.

(348) Pritchard, B. P.; Altarawy, D.; Didier, B.; Gibson, T. D.; Windus, T. L. New Basis Set Exchange: An Open, Up-to-Date Resource for the Molecular Sciences Community. *J. Chem. Inf. Model.* **2019**, *59* (11), 4814–4820. https://doi.org/10.1021/acs.jcim.9b00725.

(349) Peterson, K. A.; Figgen, D.; Goll, E.; Stoll, H.; Dolg, M. Systematically Convergent Basis Sets with Relativistic Pseudopotentials. II. Small-Core Pseudopotentials and Correlation Consistent Basis Sets for the Post-d Group 16–18 Elements. *J. Chem. Phys.* **2003**, *119* (21), 11113–11123. https://doi.org/10.1063/1.1622924.

(350) Armarego, W. L. F.; Chai, C. L. L. *Purification of Laboratory Chemicals*, 6th ed.; Elsevier: USA, 2009.

(351) Bentrude, W. G.; Setzer, W. N.; Sopchik, A. E.; Chandrasekaran, Subramanian.; Ashby, M. T. Conformations of Saturated Six-Membered Ring Phosphorus Heterocycles. 2-Aryl-1,3,2λ^5-Oxazaphosphorinanes. *J. Am. Chem. Soc.* **1988**, *110* (21), 7119–7127. https://doi.org/10.1021/ja00229a027.

(352) Berens, U.; Englert, U.; Geyser, S.; Runsink, J.; Salzer, A. A Flexible Approach to Different Families of Bidentate P,P Ligands as Highly Efficient Ligands for Asymmetric Catalysis. *Eur. J. Org. Chem.* **2006**, *2006* (9), 2100–2109. https://doi.org/10.1002/ejoc.200500937.

(353) Dellinger, D. J.; Sheehan, D. M.; Christensen, N. K.; Lindberg, J. G.; Caruthers, M. H. Solid-Phase Chemical Synthesis of Phosphonoacetate and Thiophosphonoacetate Oligodeoxynucleotides. *J. Am. Chem. Soc.* **2003**, *125* (4), 940–950. https://doi.org/10.1021/ja027983f.

(354) Beagley, P.; Davies, P.; Adams, H.; White, C. Chiral Metallocenes: The Synthesis and X-Ray Crystal Structures of $TiCl_2(\eta^5{:}\eta^5\text{-}C_5Me_4SiMe_2C_5H_3R^*)$ (R^* = Menthyl or Neomenthyl) and Related Compounds. *Can. J. Chem.* **2001**, *79* (5–6), 731–741. https://doi.org/10.1139/v01-034.

(355) Ackroyd, A. J.; Gajecki, L.; Gogoulis, A. T.; Smart, J. F.; Oliver, A. G.; McIndoe, J. S.; Berg, D. J. Mausolates: Large-Cavity Chelates with Potential as Delivery Vehicles in Nuclear Medicine. *Chem. – Eur. J.* **2024**, *30* (45), e202401987. https://doi.org/10.1002/chem.202401987.

(356) Smart, J. F.; Krueckl, L. D. N.; Schmidt, R. Q.; Gajecki, L.; Frederiksen, L. E. K.; Oliver, A. G.; Berg, D. J.; McIndoe, J. S. Mausolate Complexes of the Alkaline Earth Metals. *ChemistryEurope* **2026**, *4* (3), e70225. https://doi.org/10.1002/ceur.70225.

(357) Smart, J.; Oliver, A.; LaPierre, E.; Berg, D.; McIndoe, J. S. In(II) the Void: Mausolate Complexes of Divalent Diindium. ChemRxiv September 29, 2025. https://doi.org/10.26434/chemrxiv-2025-zjr5s.

(358) Pellei, M.; Lobbia, G. G.; Papini, G.; Santini, C. Synthesis and Properties of Poly(Pyrazolyl)Borate and Related Boron-Centered Scorpionate Ligands. Part B: Imidazole-, Triazole- and Other Heterocycle-Based Systems. *Mini-Rev. Org. Chem.* **2010**, *7* (3), 173–203. https://doi.org/10.2174/157019310791384146.

(359) Scott, J. S.; Schneider, J. E.; Tewelde, E. G.; Gardner, J. G.; Anferov, S. W.; Filatov, A. S.; Anderson, J. S. Combining Donor Strength and Oxidative Stability in Scorpionates: A Strongly Donating Fluorinated Mesoionic Tris(Imidazol-5-Ylidene)Borate Ligand. *Inorg. Chem.* **2023**, *62* (51), 21224–21232. https://doi.org/10.1021/acs.inorgchem.3c03251.

(360) Mathew, P. T.; Fang, F. Advances in Molecular Electronics: A Brief Review. *Engineering* **2018**, *4* (6), 760–771. https://doi.org/10.1016/j.eng.2018.11.001.

(361) Zhang, H.; Li, J.; Yang, C.; Guo, X. Single-Molecule Functional Chips: Unveiling the Full Potential of Molecular Electronics and Optoelectronics. *Acc. Mater. Res.* **2024**, *5* (8), 971–986. https://doi.org/10.1021/accountsmr.4c00125.

(362) Rodgers, C. B.; Deal, M. P.; Garman, L. C.; Guzei, I. A.; Allen, M. J.; Boros, E. Single Molecule $Eu^{2+/3+}$ Complex Platform for Optical and Magnetic Resonance Imaging In Vivo. *J. Am. Chem. Soc.* **2026**, *148* (23), 24520–24530. https://doi.org/10.1021/jacs.6c08257.

(363) Qiu, X.; Zheng, T.; Runowski, M.; Woźny, P.; Martín, I. R.; Soler-Carracedo, K.; Piñero, C. E.; Lebedkin, S.; Fuhr, O.; Bräse, S. Constructing [2.2]Paracyclophane-Based Ultrasensitive Optical Fluorescent-Phosphorescent Thermometer with Cucurbit[8]Uril Supramolecular Assembly. *Adv. Funct. Mater.* **2024**, *34* (47), 2313517. https://doi.org/10.1002/adfm.202313517.

(364) Wang, S.; Liu, R.; Li, J.; Sun, F.; Yang, Q.; Li, S.; Liu, J.; Chen, J.; Cheng, P. Achieving Highly Efficient Warm-White Light Emission in All-Inorganic Copper-Silver Halides via Structural Regulation. *Adv. Sci.* **2023**, *10* (28), 2303501. https://doi.org/10.1002/advs.202303501.

(365) Feng, J.; Tian, K.; Hu, D.; Wang, S.; Li, S.; Zeng, Y.; Li, Y.; Yang, G. A Triarylboron-Based Fluorescent Thermometer: Sensitive Over a Wide Temperature Range. *Angew. Chem. Int. Ed.* **2011**, *50* (35), 8072–8076. https://doi.org/10.1002/anie.201102390.

(366) Amarasinghe, D. K.; Rabuffetti, F. A. Bandshift Luminescence Thermometry Using Mn^{4+}:$Na_4Mg(WO_4)_3$ Phosphors. *Chem. Mater.* **2019**, *31* (24), 10197–10204. https://doi.org/10.1021/acs.chemmater.9b03886.

(367) Ristić, Z.; Đorđević, V.; Medić, M.; Kuzman, S.; Sekulić, M.; Antić, Ž.; Dramićanin, M. D. Triple-Temperature Readout in Luminescence Thermometry with Cr^{3+}-Doped Mg_2SiO_4 Operating from Cryogenic to Physiologically Relevant Temperatures. *Meas. Sci. Technol.* **2021**, *32* (5), 054004. https://doi.org/10.1088/1361-6501/abdc9a.

(368) Ristić, Z.; Đorđević, V.; Medić, M.; Kuzman, S.; Brik, M. G.; Antić, Ž.; Dramićanin, M. D. Temperature Dependence of the Cr^{3+}-Doped Mg_2TiO_4 near-Infrared Emission. *Opt. Mater.* **2021**, *120*, 111468. https://doi.org/10.1016/j.optmat.2021.111468.

LIST OF COPYRIGHT PERMISSIONS

For Figure 1.1:



CCC Marketplace

This is a License Agreement between Roberto Diaz-Rodriguez ("User") and Copyright Clearance Center, Inc. ("CCC") on behalf of the Rightsholder identified in the order details below. The license consists of the order details, the Marketplace Permissions General Terms and Conditions below, and any Rightsholder Terms and Conditions which are included below.

All payments must be made in full to CCC in accordance with the Marketplace Permissions General Terms and Conditions below.

Order Date	11-May-2026	Type of Use	Republish in a thesis/dissertation
Order License ID	1728867-1		
ISSN	2041-6539	Publisher	Royal Society of Chemistry
		Portion	Image/photo/illustration

LICENSED CONTENT

Publication Title	Chemical science	Rightsholder	Royal Society of Chemistry
Article Title	Exploiting single-ion anisotropy in the design of f-element single-molecule magnets	Publication Type	e-Journal
		Start Page	2078
		Issue	11
Author / Editor	Royal Society of Chemistry (Great Britain)	Volume	2
		URL	http://www.rsc.org/Publishing/Journals/SC/Index.asp
Date	01/01/2010		
Language	English		
Country	United Kingdom of Great Britain and Northern Ireland		

REQUEST DETAILS

Portion Type	Image/photo/illustration	Distribution	Canada
Number of Images / Photos / Illustrations	2	Translation	Original language of publication
Format (select all that apply)	Print, Electronic	Copies for the Disabled?	No
		Minor Editing Privileges?	Yes
Who Will Republish the Content?	Academic institution	Incidental Promotional Use?	No
Duration of Use	Life of current edition	Currency	CAD
Lifetime Unit Quantity	Up to 499		
Rights Requested	Main product		

NEW WORK DETAILS

Title	Optical Thermometry with Organoeuroplum(II) Complexes	Institution Name	University of Ottawa
		Expected Presentation Date	2026-07-31
Instructor Name	Dr. Muralee Murugesu		

ADDITIONAL DETAILS

Order Reference Number	N/A	The Requesting Person / Organization to Appear on the License	Roberto Diaz-Rodriguez

REQUESTED CONTENT DETAILS

Title, Description or Numeric Reference of the Portion(s)	Fig. 3, Fig. 4	Title of the Article / Chapter the Portion Is From	Exploiting single-ion anisotropy in the design of f-element single-molecule magnets
Editor of Portion(s)	Rinehart, Jeffrey D.; Long, Jeffrey R.	Author of Portion(s)	Rinehart, Jeffrey D.; Long, Jeffrey R.
Volume / Edition	2	Issue, if Republishing an Article From a Serial	11
Page or Page Range of Portion	2078	Publication Date of Portion	2011-10-11

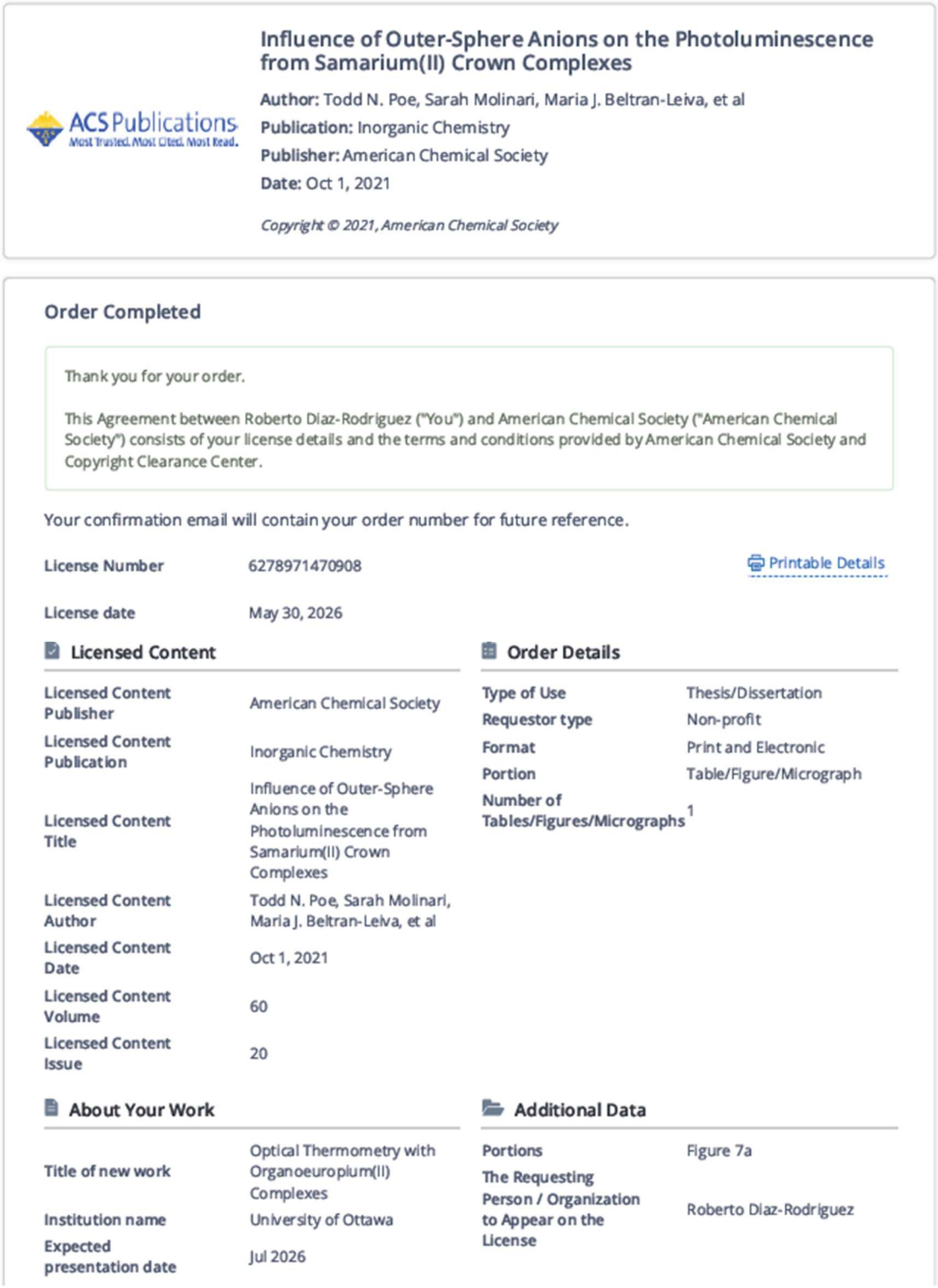
For Figure 1.2:

This Agreement between Roberto Diaz-Rodriguez ("You") and John Wiley and Sons ("John Wiley and Sons") consists of your license details and the terms and conditions provided by John Wiley and Sons and Copyright Clearance Center.

License Number	6266790136321
License date	May 12, 2026
Licensed Content Publisher	John Wiley and Sons
Licensed Content Publication	Angewandte Chemie International Edition
Licensed Content Title	Shining New Light on Multifunctional Lanthanide Single-Molecule Magnets
Licensed Content Author	Riccardo Marin, Gabriel Brunet, Muralee Murugesu
Licensed Content Date	Sep 15, 2020
Licensed Content Volume	60
Licensed Content Issue	4
Licensed Content Pages	19
Type of use	Dissertation/Thesis
Requestor type	University/Academic

Format	Print and electronic
Portion	Figure/table
Number of figures/tables	1
Will you be translating?	No
Title of new work	Optical Thermometry with Organoeuropium(II) Complexes
Institution name	University of Ottawa
Expected presentation date	Jul 2026
Portions	Figure 2
The Requesting Person / Organization to Appear on the License	Roberto Diaz-Rodriguez

For Figure 1.5:



Influence of Outer-Sphere Anions on the Photoluminescence from Samarium(II) Crown Complexes

Author: Todd N. Poe, Sarah Molinari, Maria J. Beltran-Leiva, et al
Publication: Inorganic Chemistry
Publisher: American Chemical Society
Date: Oct 1, 2021

Copyright © 2021, American Chemical Society

Order Completed

Thank you for your order.

This Agreement between Roberto Diaz-Rodriguez ("You") and American Chemical Society ("American Chemical Society") consists of your license details and the terms and conditions provided by American Chemical Society and Copyright Clearance Center.

Your confirmation email will contain your order number for future reference.

License Number	6278971470908
License date	May 30, 2026

Printable Details

Licensed Content

Licensed Content Publisher	American Chemical Society
Licensed Content Publication	Inorganic Chemistry
Licensed Content Title	Influence of Outer-Sphere Anions on the Photoluminescence from Samarium(II) Crown Complexes
Licensed Content Author	Todd N. Poe, Sarah Molinari, Maria J. Beltran-Leiva, et al
Licensed Content Date	Oct 1, 2021
Licensed Content Volume	60
Licensed Content Issue	20

Order Details

Type of Use	Thesis/Dissertation
Requestor type	Non-profit
Format	Print and Electronic
Portion	Table/Figure/Micrograph
Number of Tables/Figures/Micrographs	1

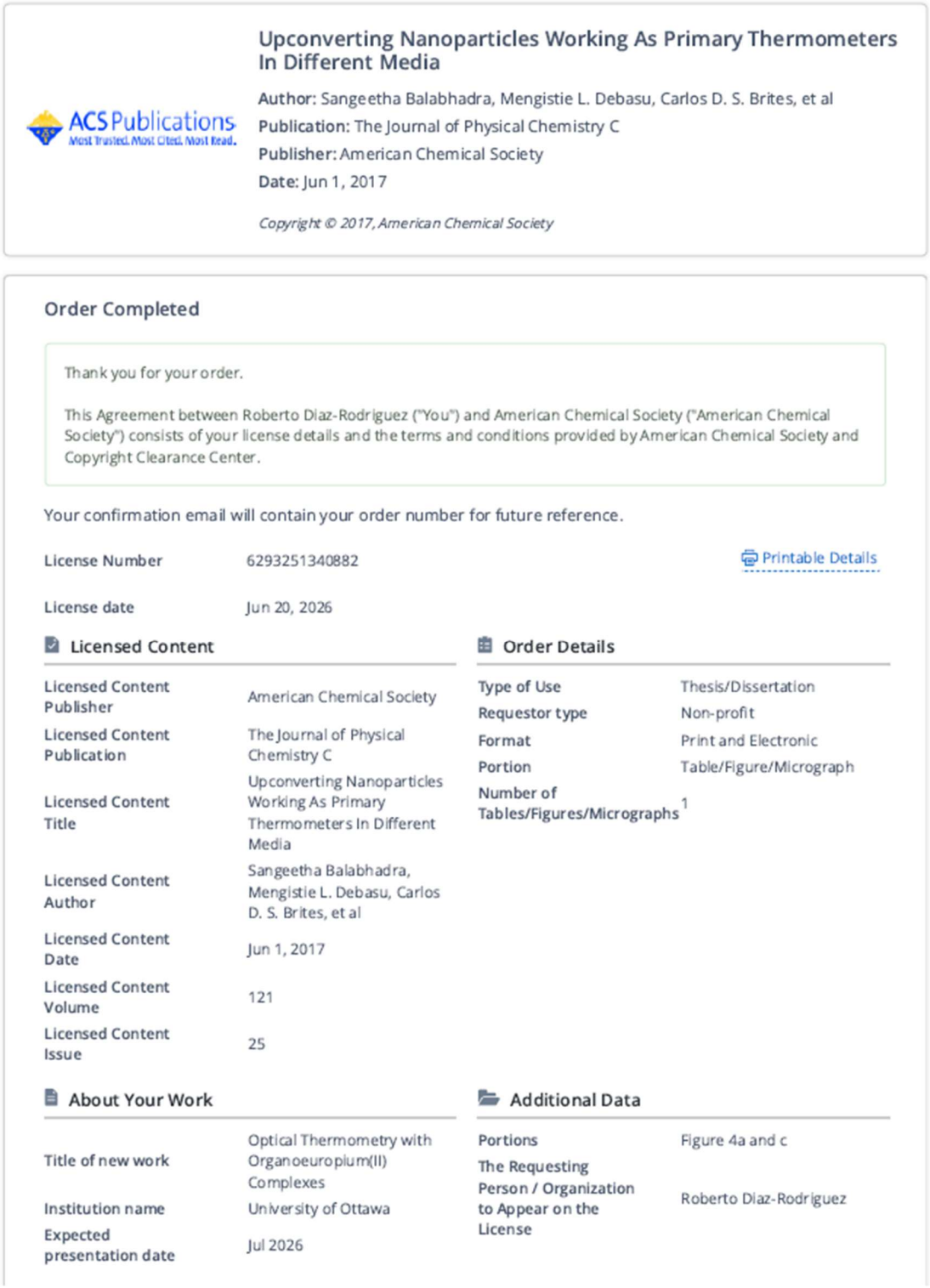
About Your Work

Title of new work	Optical Thermometry with Organoeuropium(II) Complexes
Institution name	University of Ottawa
Expected presentation date	Jul 2026

Additional Data

Portions	Figure 7a
The Requesting Person / Organization to Appear on the License	Roberto Diaz-Rodriguez

For Figure 1.6:



Upconverting Nanoparticles Working As Primary Thermometers In Different Media

Author: Sangeetha Balabhadra, Mengistie L. Debasu, Carlos D. S. Brites, et al
Publication: The Journal of Physical Chemistry C
Publisher: American Chemical Society
Date: Jun 1, 2017

Copyright © 2017, American Chemical Society

Order Completed

Thank you for your order.

This Agreement between Roberto Diaz-Rodriguez ("You") and American Chemical Society ("American Chemical Society") consists of your license details and the terms and conditions provided by American Chemical Society and Copyright Clearance Center.

Your confirmation email will contain your order number for future reference.

License Number	6293251340882
License date	Jun 20, 2026

Printable Details

Licensed Content

Licensed Content Publisher	American Chemical Society
Licensed Content Publication	The Journal of Physical Chemistry C
Licensed Content Title	Upconverting Nanoparticles Working As Primary Thermometers In Different Media
Licensed Content Author	Sangeetha Balabhadra, Mengistie L. Debasu, Carlos D. S. Brites, et al
Licensed Content Date	Jun 1, 2017
Licensed Content Volume	121
Licensed Content Issue	25

Order Details

Type of Use	Thesis/Dissertation
Requestor type	Non-profit
Format	Print and Electronic
Portion	Table/Figure/Micrograph
Number of Tables/Figures/Micrographs	1

About Your Work

Title of new work	Optical Thermometry with Organoeuropium(II) Complexes
Institution name	University of Ottawa
Expected presentation date	Jul 2026

Additional Data

Portions	Figure 4a and c
The Requesting Person / Organization to Appear on the License	Roberto Diaz-Rodriguez

For Figure 1.7:



CCC Marketplace

This is a License Agreement between Roberto Diaz-Rodriguez ("User") and Copyright Clearance Center, Inc. ("CCC") on behalf of the Rightsholder identified in the order details below. The license consists of the order details, the Marketplace Permissions General Terms and Conditions below, and any Rightsholder Terms and Conditions which are included below.

All payments must be made in full to CCC in accordance with the Marketplace Permissions General Terms and Conditions below.

Order Date	21-Jun-2026	Type of Use	Republish in a thesis/dissertation
Order License ID	1742203-1		
ISSN	2052-1553	Publisher	Royal Society of Chemistry
		Portion	Chart/graph/table/figure

LICENSED CONTENT

Publication Title	Inorganic Chemistry Frontiers	Publication Type	e-Journal
		Start Page	4229
Article Title	Tunable Nd 3+ dimer luminescent molecular thermometer via Stark sublevels	End Page	4238
		Issue	10
		Volume	13
Author / Editor	Royal Society of Chemistry (Great Britain),, Zhongguo hua xue hui (Beijing, China),, Beijing da xue,	URL	http://pubs.rsc.org/en/journals/journalissues/qi#issues
Date	01/01/2014		
Language	English		
Country	United Kingdom of Great Britain and Northern Ireland		
Rightsholder	Royal Society of Chemistry		

REQUEST DETAILS

Portion Type	Chart/graph/table/figure	Distribution	United States and Canada
Number of Charts / Graphs / Tables / Figures Requested	1	Translation	Original language of publication
		Copies for the Disabled?	No
Format (select all that apply)	Print, Electronic	Minor Editing Privileges?	Yes
Who Will Republish the Content?	Academic institution	Incidental Promotional Use?	No
Duration of Use	Life of current edition	Currency	CAD
Lifetime Unit Quantity	Up to 499		
Rights Requested	Main product		

NEW WORK DETAILS

Title	Optical Thermometry with Organoeuropium(II) Complexes	Institution Name	University of Ottawa
		Expected Presentation Date	2026-08-20
Instructor Name	Muralee Murugesu		

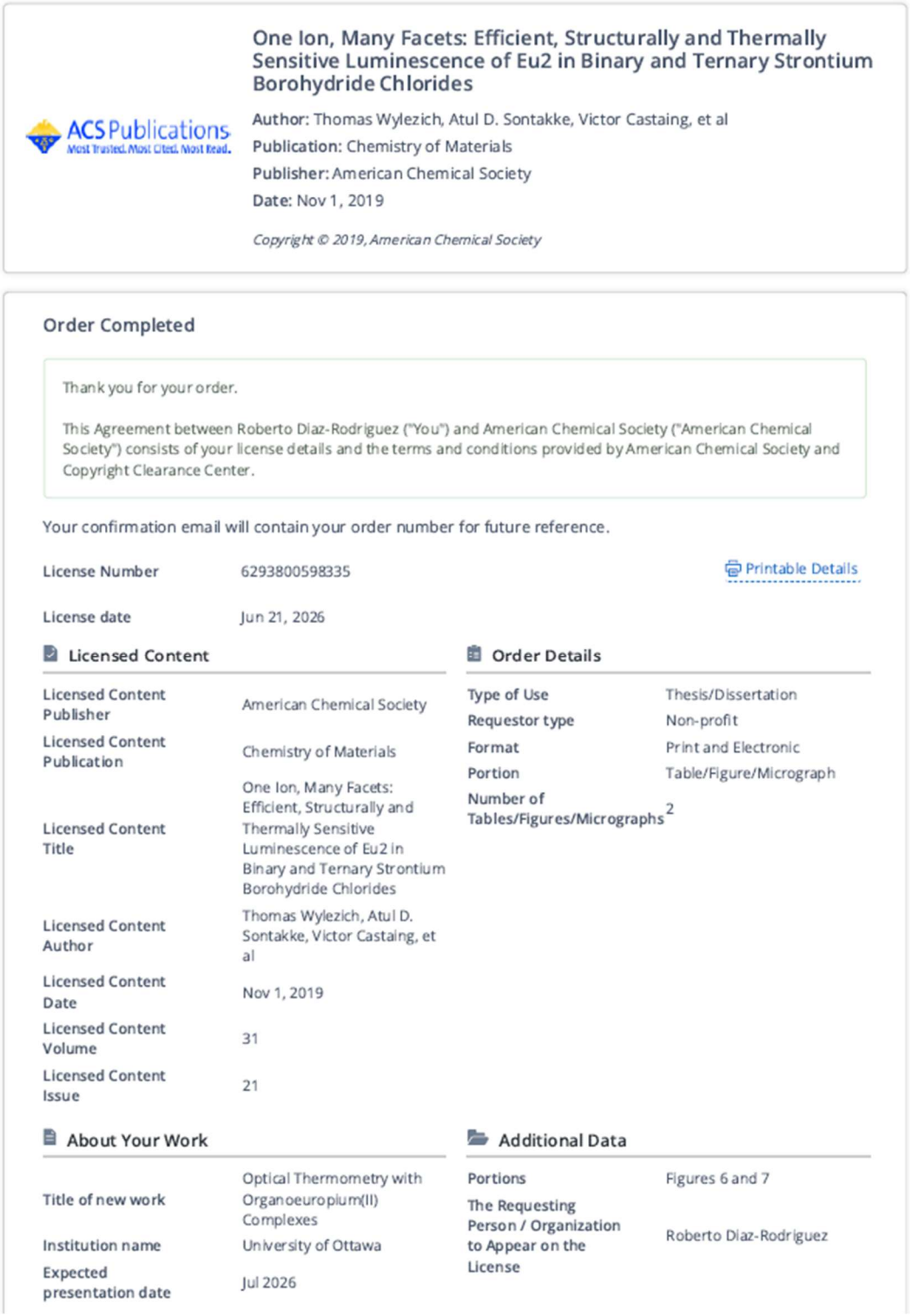
ADDITIONAL DETAILS

Order Reference Number	N/A	The Requesting Person / Organization to Appear on the License	Roberto Diaz-Rodriguez

REQUESTED CONTENT DETAILS

Title, Description or Numeric Reference of the Portion(s)	Figure 4	Title of the Article / Chapter the Portion Is From	Tunable Nd 3+ dimer luminescent molecular thermometer via Stark sublevels
Editor of Portion(s)	Gil, Yolimar; Corredoira-Vázquez, Julio; Costa de Santana, Ricardo; Brites, Carlos D. S.; Carlos, Luís D.; Spodine, Evgenia; Aravena, Daniel; Fuentealba, Pablo	Author of Portion(s)	Gil, Yolimar; Corredoira-Vázquez, Julio; Costa de Santana, Ricardo; Brites, Carlos D. S.; Carlos, Luís D.; Spodine, Evgenia; Aravena, Daniel; Fuentealba, Pablo
Volume / Edition	13		
Page or Page Range of Portion	4229-4238	Issue, if Republishing an Article From a Serial	10
		Publication Date of Portion	2026-05-19

For Figure 1.8:



One Ion, Many Facets: Efficient, Structurally and Thermally Sensitive Luminescence of Eu2 in Binary and Ternary Strontium Borohydride Chlorides

Author: Thomas Wylezich, Atul D. Sontakke, Victor Castaing, et al
Publication: Chemistry of Materials
Publisher: American Chemical Society
Date: Nov 1, 2019

Copyright © 2019, American Chemical Society

Order Completed

Thank you for your order.

This Agreement between Roberto Diaz-Rodriguez ("You") and American Chemical Society ("American Chemical Society") consists of your license details and the terms and conditions provided by American Chemical Society and Copyright Clearance Center.

Your confirmation email will contain your order number for future reference.

License Number	6293800598335
License date	Jun 21, 2026

Printable Details

Licensed Content

Licensed Content Publisher	American Chemical Society
Licensed Content Publication	Chemistry of Materials
Licensed Content Title	One Ion, Many Facets: Efficient, Structurally and Thermally Sensitive Luminescence of Eu2 in Binary and Ternary Strontium Borohydride Chlorides
Licensed Content Author	Thomas Wylezich, Atul D. Sontakke, Victor Castaing, et al
Licensed Content Date	Nov 1, 2019
Licensed Content Volume	31
Licensed Content Issue	21

Order Details

Type of Use	Thesis/Dissertation
Requestor type	Non-profit
Format	Print and Electronic
Portion	Table/Figure/Micrograph
Number of Tables/Figures/Micrographs	2

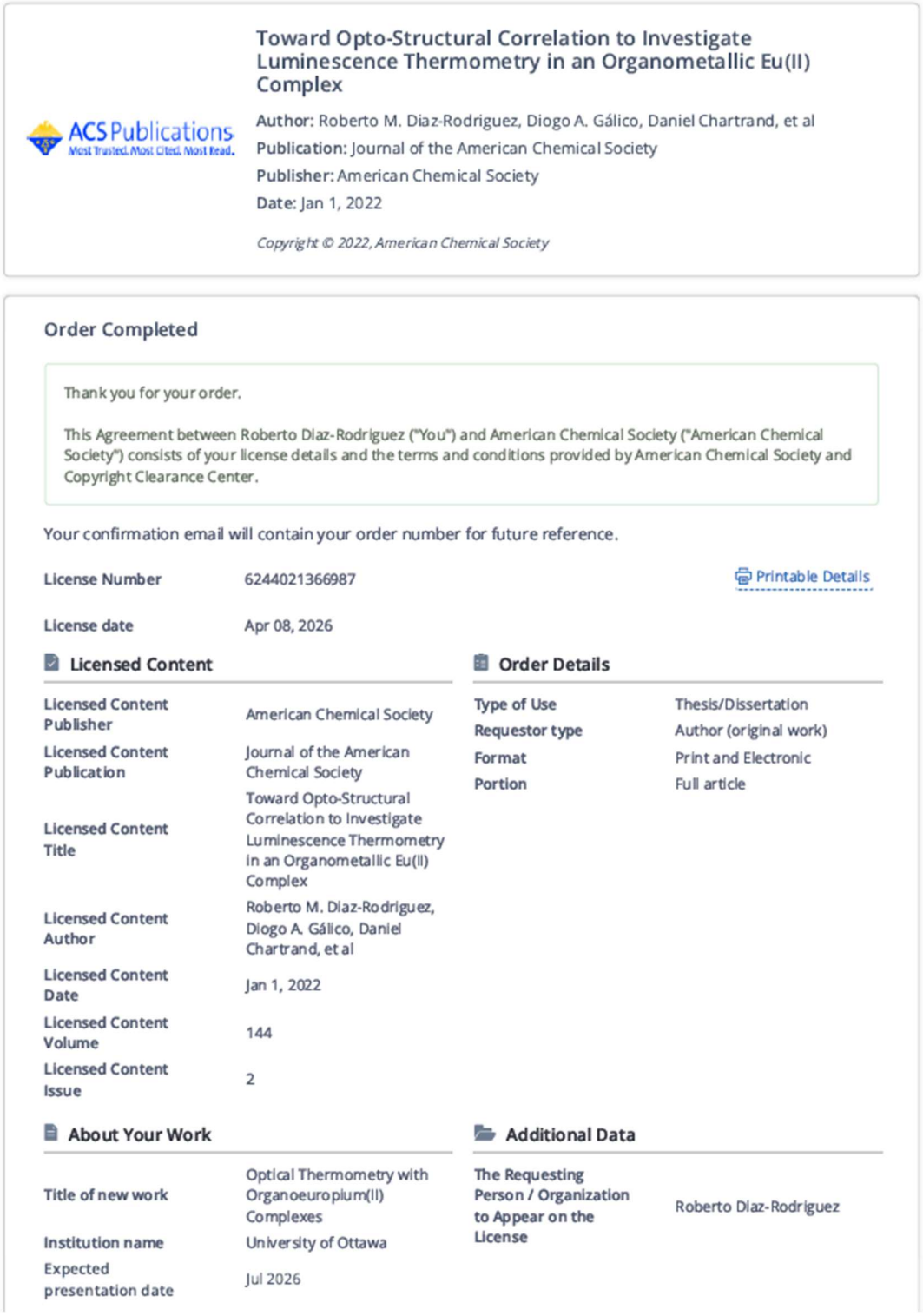
About Your Work

Title of new work	Optical Thermometry with Organoeuropium(II) Complexes
Institution name	University of Ottawa
Expected presentation date	Jul 2026

Additional Data

Portions	Figures 6 and 7
The Requesting Person / Organization to Appear on the License	Roberto Diaz-Rodriguez

Chapter 2:



Toward Opto-Structural Correlation to Investigate Luminescence Thermometry in an Organometallic Eu(II) Complex

Author: Roberto M. Diaz-Rodriguez, Diogo A. Gálico, Daniel Chartrand, et al
Publication: Journal of the American Chemical Society
Publisher: American Chemical Society
Date: Jan 1, 2022

Copyright © 2022, American Chemical Society

Order Completed

Thank you for your order.

This Agreement between Roberto Diaz-Rodriguez ("You") and American Chemical Society ("American Chemical Society") consists of your license details and the terms and conditions provided by American Chemical Society and Copyright Clearance Center.

Your confirmation email will contain your order number for future reference.

License Number	6244021366987
License date	Apr 08, 2026

Printable Details

Licensed Content

Licensed Content Publisher	American Chemical Society
Licensed Content Publication	Journal of the American Chemical Society
Licensed Content Title	Toward Opto-Structural Correlation to Investigate Luminescence Thermometry in an Organometallic Eu(II) Complex
Licensed Content Author	Roberto M. Diaz-Rodriguez, Diogo A. Gálico, Daniel Chartrand, et al
Licensed Content Date	Jan 1, 2022
Licensed Content Volume	144
Licensed Content Issue	2

Order Details

Type of Use	Thesis/Dissertation
Requestor type	Author (original work)
Format	Print and Electronic
Portion	Full article

About Your Work

Title of new work	Optical Thermometry with Organoeuropium(II) Complexes
Institution name	University of Ottawa
Expected presentation date	Jul 2026

Additional Data

The Requesting Person / Organization to Appear on the License	Roberto Diaz-Rodriguez

Chapter 3:



Ligand Effects on the Emission Characteristics of Molecular Eu(II) Luminescence Thermometers

Author: Roberto M. Diaz-Rodriguez, Diogo A. Gálico, Daniel Chartrand, et al
Publication: Journal of the American Chemical Society
Publisher: American Chemical Society
Date: Dec 1, 2024

Copyright © 2024, American Chemical Society

Order Completed

Thank you for your order.

This Agreement between Roberto Diaz-Rodriguez ("You") and American Chemical Society ("American Chemical Society") consists of your license details and the terms and conditions provided by American Chemical Society and Copyright Clearance Center.

Your confirmation email will contain your order number for future reference.

License Number	6244030078905
License date	Apr 08, 2026

Printable Details

Licensed Content

Licensed Content Publisher	American Chemical Society
Licensed Content Publication	Journal of the American Chemical Society
Licensed Content Title	Ligand Effects on the Emission Characteristics of Molecular Eu(II) Luminescence Thermometers
Licensed Content Author	Roberto M. Diaz-Rodriguez, Diogo A. Gálico, Daniel Chartrand, et al
Licensed Content Date	Dec 1, 2024
Licensed Content Volume	146
Licensed Content Issue	49

Order Details

Type of Use	Thesis/Dissertation
Requestor type	Author (original work)
Format	Print and Electronic
Portion	Full article

About Your Work

Title of new work	Optical Thermometry with Organoeuropium(II) Complexes
Institution name	University of Ottawa
Expected presentation date	Jul 2026

Additional Data

The Requesting Person / Organization to Appear on the License	Roberto Diaz-Rodriguez

Chapter 4:



Exploring a New Family of (Phosphinochalcogenoyl)Europocenes for Magneto-Optical Thermometry

Author: Roberto M. Diaz-Rodriguez, Diogo A. Gálico, Muralee Murugesu

Publication: Angewandte Chemie International Edition

Publisher: John Wiley and Sons

Date: Oct 17, 2025

© 2025 The Author(s). Angewandte Chemie International Edition published by Wiley-VCH GmbH

Quick Price Estimate

Content Delivery:
A copy of this content may be purchased following completion of your permissions order.
High Res Image files - please contact Wiley

This article is available under the terms of the Creative Commons Attribution Non-Commercial No Derivatives License CC BY-NC-ND (which may be updated from time to time) and permits **non-commercial** use, distribution, and reproduction in any medium, without alteration, provided the original work is properly cited and it is reproduced verbatim.

For an understanding of what is meant by the terms of the Creative Commons License, please refer to Wiley's Open Access Terms and Conditions.

Permission is not required for **non-commercial** reuse. For **commercial** reuse, please select the most appropriate **commercial** requestor type before completing your order.

If you wish to adapt, alter, translate or create any other derivative work from this article, permission must be sought from the Publisher. Please email your requirements to RightsLink@wiley.com.